SOURCE AND EFFECTS OF LIGHT TO MODERATE MAGNITUDE EARTHQUAKES

EDITED BY: Nicola Alessandro Pino, Vincenzo Convertito,
Jorge Miguel Gaspar-Escribano and Ruizhi Wen

PUBLISHED IN: Frontiers in Earth Science

frontiers Research Topics

ISSN 1664-8714
ISBN 978-2-88974-236-3
DOI 10.3389/978-2-88974-236-3

About Frontiers

Frontiers is more than just an open-access publisher of scholarly articles: it is a pioneering approach to the world of academia, radically improving the way scholarly research is managed. The grand vision of Frontiers is a world where all people have an equal opportunity to seek, share and generate knowledge. Frontiers provides immediate and permanent online open access to all its publications, but this alone is not enough to realize our grand goals.

Frontiers Journal Series

The Frontiers Journal Series is a multi-tier and interdisciplinary set of open-access, online journals, promising a paradigm shift from the current review, selection and dissemination processes in academic publishing. All Frontiers journals are driven by researchers for researchers; therefore, they constitute a service to the scholarly community. At the same time, the Frontiers Journal Series operates on a revolutionary invention, the tiered publishing system, initially addressing specific communities of scholars, and gradually climbing up to broader public understanding, thus serving the interests of the lay society, too.

Dedication to Quality

Each Frontiers article is a landmark of the highest quality, thanks to genuinely collaborative interactions between authors and review editors, who include some of the world's best academicians. Research must be certified by peers before entering a stream of knowledge that may eventually reach the public - and shape society; therefore, Frontiers only applies the most rigorous and unbiased reviews.
Frontiers revolutionizes research publishing by freely delivering the most outstanding research, evaluated with no bias from both the academic and social point of view. By applying the most advanced information technologies, Frontiers is catapulting scholarly publishing into a new generation.

What are Frontiers Research Topics?

Frontiers Research Topics are very popular trademarks of the Frontiers Journals Series: they are collections of at least ten articles, all centered on a particular subject. With their unique mix of varied contributions from Original Research to Review Articles, Frontiers Research Topics unify the most influential researchers, the latest key findings and historical advances in a hot research area! Find out more on how to host your own Frontiers Research Topic or contribute to one as an author by contacting the Frontiers Editorial Office: frontiersin.org/about/contact

SOURCE AND EFFECTS OF LIGHT TO MODERATE MAGNITUDE EARTHQUAKES

Topic Editors:
Nicola Alessandro Pino, Vesuvius Observatory, National Institute of Geophysics and Volcanology (INGV), Italy
Vincenzo Convertito, Vesuvius Observatory, National Institute of Geophysics and Volcanology (INGV), Italy
Jorge Miguel Gaspar-Escribano, Polytechnic University of Madrid, Spain
Ruizhi Wen, Institute of Engineering Mechanics, China Earthquake Administration, China

Citation: Pino, N. A., Convertito, V., Gaspar-Escribano, J. M., Wen, R., eds. (2022). Source and Effects of Light to Moderate Magnitude Earthquakes. Lausanne: Frontiers Media SA. doi: 10.3389/978-2-88974-236-3

Table of Contents

frontiers in Earth Science

EDITORIAL
published: 21 December 2021
doi: 10.3389/feart.2021.822481

Editorial: Source and Effects of Light to Moderate Magnitude Earthquakes

Nicola Alessandro Pino[1]*, *Vincenzo Convertito*[1], *Jorge M. Gaspar-Escribano*[2] and *Ruizhi Wen*[3]

[1]Istituto Nazionale di Geofisica e Vulcanologia, Osservatorio Vesuviano, Napoli, Italy, [2]Escuela Técnica Superior de Ingenieros en Topografía, Geodesia y Cartografía, Universidad Politécnica de Madrid, Madrid, Spain, [3]Institute of Engineering Mechanics, China Earthquake Administration Harbin, Harbin, China

Keywords: earthquake source, strong ground motion, historical earthquake catalogue, seismic hazard, damage scenarios

Editorial on the Research Topic

Source and Effects of Light to Moderate Magnitude Earthquakes

The predominant tectonic stress is generally released with strong earthquakes, which represent the principal element determining the seismic hazard in a region. However, major seismic events are less frequent and have relatively long return periods, typically hundreds to thousands of years. In 2000–2020 the worldwide occurrence of earthquakes with $M \geq 6.0$ was 152/yr on average, with the annual number ranging from 111/yr to 205/yr (https://www.usgs.gov/natural-hazards/earthquake-hazards/lists-maps-and-statistics). On a planetary scale, the frequency of occurrence of light to moderate magnitude ($4.0 \leq M \leq 5.9$) earthquakes is about two orders of magnitude larger than the stronger ones (Gutenberg and Richter, 1941). Thus, the investigation of their source represents a fundamental tool in the definition of active structures, and in the assessment of the stress level. Valuable indications on the characteristics of propagation of the seismic waves that contribute to determine the level of ground shaking derive from their analysis. Moreover, statistical investigations on the occurrence of light to moderate magnitude earthquakes, in time and space, are essential in the definition of the seismic hazard and themselves represent a threat to society, leading to injuries, possible casualties, and economic loss through structural and non-structural damage.

On the other hand, due to the low signal-to-noise ratio in their recording and to the lower level of permanent damage, the analysis of these relatively weaker earthquakes, either instrumental or macroseismic, often requires the development of specific methods to derive robust information.

Based on the above considerations we proposed to Frontiers in Earth Science a Research Topic that could encompass various aspects of the analysis of light to moderate magnitude earthquakes. The 2020–2021 world pandemic situation forced most researchers to work from home and to drastically reduce the profitable interaction with colleagues. Nevertheless the scientific community responded with interest and we could close the Research Topic with twelve articles published, involving sixty-five authors from 16 research institutions, distributed in seven countries (**Figure 1A**).

Most articles deal with the investigation of the source of specific earthquakes (**Figure 1B**), several of which occurred close to densely inhabited areas and caused casualties and intense damage in spite of their moderate magnitude. Some authors focused on the analysis of waveforms to retrieve ground motion parameters for selected areas, highlighting the larger difficulties to be faced in dealing with smaller earthquakes. Macroseismic studies of historical earthquakes and the development of damage scenarios are also part of the themes considered in the articles of this Research Topic.

In the following we briefly describe the content and the major results of the papers.

Edited and reviewed by:
Carolina Lithgow-Bertelloni, UCLA Department of Earth, Planetary, and Space Sciences, United States

***Correspondence:**
Nicola Alessandro Pino
alessandro.pino@ingv.it

Specialty section:
This article was submitted to Solid Earth Geophysics, a section of the journal Frontiers in Earth Science

Received: *25 November 2021*
Accepted: *30 November 2021*
Published: *21 December 2021*

Citation:
Pino NA, Convertito V, Gaspar-Escribano JM and Wen R (2021) Editorial: Source and Effects of Light to Moderate Magnitude Earthquakes. Front. Earth Sci. 9:822481. doi: 10.3389/feart.2021.822481

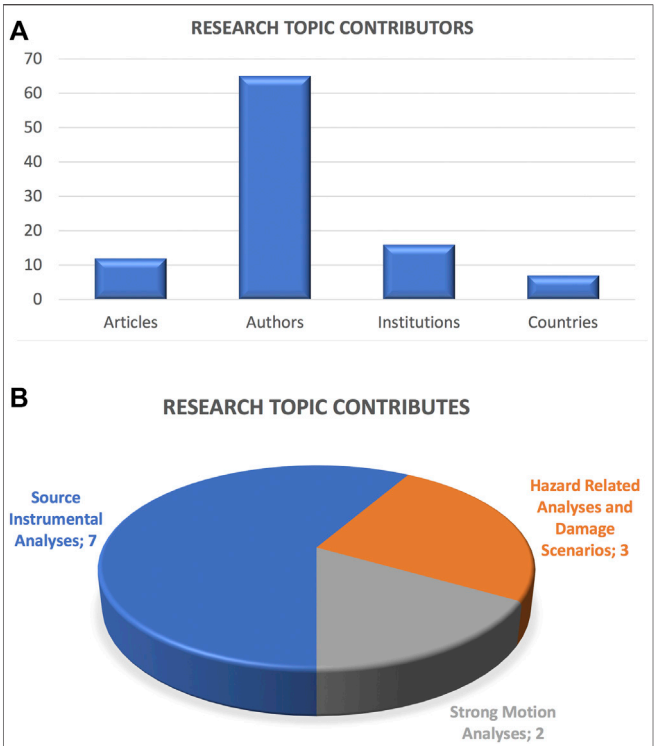

FIGURE 1 | (A) Cumulative graphic description of the authors of the articles included in the present Research Topic, along with their institution and country **(B)** Rough categorization of the articles by theme.

SOURCE INSTRUMENTAL ANALYSES

Stich et al. analyze the 2016 southern Alboran Sea earthquake sequence. They carry out a detailed relocation and moment tensor inversion of most events of the series and apparent source time functions for the main shock. They give a detailed description of the rupture and observe slip partitioning into strike-slip rupture and dip-slip aftershocks. They suggest that the 2016 event settled a slip deficit from previous ruptures that could not propagate into the stronger restraining segment.

Wang and Wen, by using of a nonparametric spectral inversion, separated the propagation path attenuation, and source spectra from the observed ground motions recorded in the junction of the northwest Tarim Basin and Kepingtage fold-and-thrust zone. The authors observed a slow seismic wave decaying as function of the distance, which reflects the strong anelastic attenuation, and the breakdown of earthquake self-similar scaling. They estimated a temporal variation of the stress drops indicating a short-term effect of the mainshock on the source characteristics of the earthquakes before and after the mainshock.

López-Comino et al. studied the 2017, Montesano Earthquake and the possible links with the Val d'Agri oilfield (Italy). They applied advanced seismological techniques to estimate the uncertainties derived from the moment tensor inversion and identify plausible directivity effects. Their findings support the activation of a deeper fault segment associated with the Eastern Agri Fault System and the natural tectonic origin of the Montesano event, rather than an induced or triggering mechanism related to hydrocarbon extraction.

In order to reduce the effect of approximations of the propagation structure in retrieving characteristics of the seismic source, Huo et al. obtained a solution for the event location and the moment tensor of the 2019, M_W = 5.7, Changning earthquake by modeling recorded waveforms using 3D Green's functions, including the effect of the topography. The authors also analyzed the effect of their assumptions with respect to solutions obtained with 1D models without topography.

Ciaccio et al. present a compilation of source mechanisms computed from first motion polarities for more than 100 earthquakes in the magnitude range 4.0–5.5, occurred in Italy in the time period 2015–2016. They also put a focus on two particular areas, for one of which they obtained focal mechanisms for events with magnitude between 3.0 and 3.6, contributing to improve the knowledge of the active tectonics in those areas.

Pastori et al. analysed the 2011–2014 Pollino swarms (Italy). Based on accurate relocations of ~6,000 earthquakes and shear-wave splitting analysis for ~22,600 event-station pairs, they found two main clusters around the major shocks. They propose a local faulting framework explaining this seismicity and relate it to regional tectonics.

Zhao et al. analyzed seismic data $M_L \geq 2.0$ earthquakes since 2009 near the epicenter of the 3 February 2020 M_S 5.1 Qingbaijiang earthquake in China to investigate the seismogenic structure of the region. The authors indicate that the seismicity along the central and northern segments of the Longquanshan fault zone has occurred mainly along the eastern branch and the M_S = 5.1 mainshock is a thrust faulting event based on the focal mechanism solution, and the seismogenic fault lies along the eastern branch of the Longquanshan fault zone.

STRONG MOTION ANALYSES

Sharma et al. developed stochastic ground motion simulation of two earthquakes occurred in Uttarakhand (India) in 2017 assuming a circular point source with a ω^{-2} decay (Brune's model). They compared synthetic spectra with the observed Fourier amplitude spectra and find a good match. They also compared observed and simulated PGA values with PGA predictions of well-known GMPEs for different distance ranges and discussed their applicability to the Himalayan region.

Dhakal analyzed 79 Japan earthquakes and derived ground motions parameters for the considered events, highlighting large peak ground acceleration during 15 earthquakes. The author compared the results with predictions from Ground Motion Equations (GMPE) available for the area, concluding that the GMPE underestimate the hazard associated with moderate magnitude events. Finally, focusing on the damaging 2018 North Osaka, M_W = 5.5, earthquake, Dhakal suggests that this might have been a high stress drop event.

Hazard Related Analyses and Damage Scenarios

Selva et al. reviewed and systematically re-analysed the available historical and instrumental seismic data to build an earthquake catalogue for Ischia (Italy) that includes a robust uncertainties characterization. They assessed data completeness and analysed the spatial, temporal, and magnitude distributions of seismicity in the Ischia area.

Gómez-Novell et al. presented a probabilistic seismic hazard analysis of Southeastern Spain explicitly including faults as seismic sources. They incorporated different multi-fault rupture scenarios in a logic tree and evaluated the relative impact of different parameters hazard estimates. They compared their results with recorded ground motion data, results of other studies of the region and with the national seismic code.

Pessina et al. presented an application of a rapid earthquake damage scenario assessment in the area of Mt. Etna (Italy). Using damage data on residential buildings collected after the December 26, 2018 earthquake, they tested different methodological approaches to simulate the damage scenario in the most affected municipalities. They discussed how these approaches are adapted to the target area and highlight their usefulness for emergency planning.

Conclusive Remark

Overall, the articles published in the present Research Topic highlight the importance of getting deeper knowledge of the characteristics of light to moderate magnitude earthquake, in terms of either stress release or effect on the anthropic environment, at the same time evidencing the complexity of such events. We hope that the results of this Research Topic will increase the interest of the scientific community in such earthquakes, in particular boosting the development of multidisciplinary techniques able to get deeper comprehension of these anyhow damaging events.

AUTHOR CONTRIBUTIONS

NP, VC, JG-E, and RW edited the Research Topic "Source and Effects of Light to Moderate Magnitude Earthquakes", and equally contributed the Editorial.

ACKNOWLEDGMENTS

We thank all the authors that submitted their manuscript to the research topic. In times when many scientists don't feel reviewing scholars manuscript as an essential part of the researcher's job, we are really grateful to the reviewers, which spent their time in reading the original manuscripts, providing useful comments and suggestions to improve them. We also thank the editorial staff for their fundamental help and support.

REFERENCES

Gutenberg, S., and Richter, C. F. (1941). Seismicity of the earth. *Geol. Soc. Am. Spec. Pap.* 34, 1–131.

Conflict of Interest: The authors declare that the research was conducted in the absence of any commercial or financial relationships that could be construed as a potential conflict of interest.

Publisher's Note: All claims expressed in this article are solely those of the authors and do not necessarily represent those of their affiliated organizations, or those of the publisher, the editors and the reviewers. Any product that may be evaluated in this article, or claim that may be made by its manufacturer, is not guaranteed or endorsed by the publisher.

frontiers in Earth Science

ORIGINAL RESEARCH
published: 29 September 2020
doi: 10.3389/feart.2020.587356

Slip Partitioning in the 2016 Alboran Sea Earthquake Sequence (Western Mediterranean)

Daniel Stich[1,2]*, *Rosa Martín*[1], *Jose Morales*[1,2], *José Ángel López-Comino*[3,1,2] and *Flor de Lis Mancilla*[1,2]

[1] Instituto Andaluz de Geofísica, Universidad de Granada, Granada, Spain, [2] Departamento de Física Teórica y Del Cosmos, Universidad de Granada, Granada, Spain, [3] Institute of Geosciences, University of Potsdam, Potsdam, Germany

A M_W = 5.1 earthquake on January 21st, 2016 marked the beginning of a significant seismic sequence in the southern Alboran Sea, culminating in a M_W = 6.3 earthquake on January 25th, and continuing with further moderate magnitude earthquakes until March. We use data from 35 seismic broadband stations in Spain, Morocco and Portugal to relocate the seismicity, estimate seismic moment tensors, and isolate regional apparent source time functions for the main earthquake. Relocation and regional moment tensor inversion consistently yield very shallow depths for the majority of events. We obtain 50 moment tensors for the sequence, showing a mixture of strike-slip faulting for the foreshock and the main event and reverse faulting for the major aftershocks. The leading role of reverse focal mechanisms among the aftershocks may be explained by the geometry of the fault network. The mainshock nucleates at a bend along the left-lateral Al-Idrisi fault, introducing local transpression within the transtensional Alboran Basin. The shallow depths of the 2016 Alboran Sea earthquakes may favor slip-partitioning on the involved faults. Apparent source durations for the main event suggest a ~21 km long, asymmetric rupture that propagates primarily toward NE into the restraining fault segment, with fast rupture speed of ~3.0 km/s. Consistently, the inversion for laterally variable fault displacement situates the main slip in the restraining segment. The partitioning into strike-slip rupture and dip-slip aftershocks confirms a non-optimal orientation of this segment, and suggests that the 2016 event settled a slip deficit from previous ruptures that could not propagate into the stronger restraining segment.

Keywords: slip partitioning, fault bend, moment tensor, source time function, shallow earthquakes

OPEN ACCESS

Edited by:
Jorge Miguel Gaspar-Escribano, Polytechnic University of Madrid, Spain

Reviewed by:
Dogan Kalafat, Boğaziçi University, Turkey
Francesca Di Luccio, Istituto Nazionale di Geofisica e Vulcanologia (INGV), Italy

***Correspondence:**
Daniel Stich
stich@ugr.es

Specialty section:
This article was submitted to Solid Earth Geophysics, a section of the journal Frontiers in Earth Science

Received: *25 July 2020*
Accepted: *31 August 2020*
Published: *29 September 2020*

Citation:
Stich D, Martín R, Morales J, López-Comino JÁ and Mancilla FdeL (2020). Front. Earth Sci. 8:587356. doi: 10.3389/feart.2020.587356

INTRODUCTION

Most earthquakes worldwide show directions of fault displacement close to horizontal or close to vertical, while oblique slip directions are less common (Célérier, 2008). This observation is usually thought to represent the influence of the Earth's free surface on crustal stresses. Vanishing shear stress at a free surface requires that one principal stress is oriented vertically, thus complicating the occurrence of general, oblique directions of shear, at least on shallow faults (Anderson, 1905). The predominance of strike-slip and dip-slip faulting still holds in many scenarios where regional deformation is actually oblique to the trend of the principal faults or belts of tectonic deformation. Such a behavior was first recognized at the convergent margin of Sumatra, where oblique motion between the Australian and Sunda plates is partitioned into shortening normal to the plate boundary

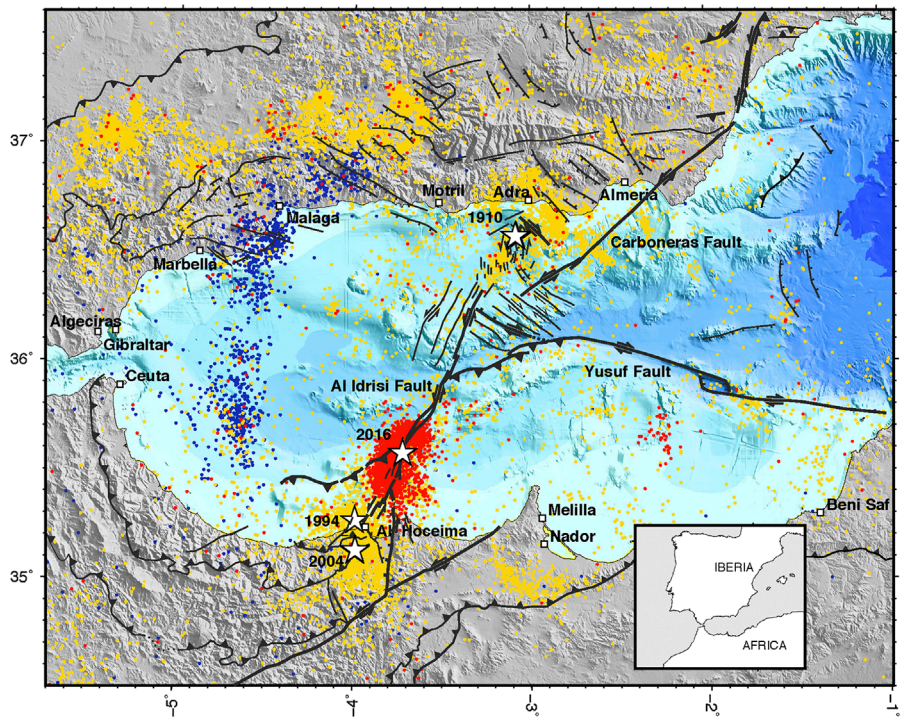

FIGURE 1 | Earthquake locations in the Alboran region from 1990 to 2020 (IGN catalog, www.ign.es), distinguishing between shallow events (yellow dots), intermediate depth events (deeper 40 km, blue dots), and shallow seismicity during 2016 (red dots), including the sequence in the southern Alboran Sea. The principal strike slip faults are labeled (left-lateral Al-Idrisi and Carboneras faults, right-lateral Yusuf fault; all faults from Gràcia et al., 2019). Stars mark the epicenters of the 2016 mainshock and the largest instrumental earthquakes in the Alboran region, including the 1910, M_W 6.1 Adra earthquake (Stich et al., 2003) and the 1994, M_W 5.9 and 2004, M_W 6.3 earthquakes near the city of Al Hoceima (El Alami et al., 1998; Stich et al., 2005). Bathymetry is taken from the EMODnet Bathymetry Consortium (2018). Squares mark selected coastal cities and towns around the Alboran Sea.

along the subduction interface, and strike slip faulting parallel to the plate boundary in the overriding plate (Fitch, 1972). The case of Sumatra is no exception, and slip partitioning has been analyzed on many plate boundaries since then (e.g., Yu et al., 1993; McCaffrey, 1996). Slip partitioning can also be active during single earthquakes, as demonstrated in an exemplary manner by the complex rupture cascade of the M_W 7.8, 2016 Kaikoura, New Zealand earthquake (Xu et al., 2018; Ulrich et al., 2019), or, previously, by concurrent strike-slip and reverse faulting during the M_W 7.9, 2002 Denali earthquake in Alaska (Eberhart-Phillips et al., 2003; Bemis et al., 2015). Even for very large events, partitioning of slip may occur over very close distances of order of km, as observed along the 400 km long surface rupture from the M_W 7.8, 2011 earthquake on the Kunlun fault in Tibet (Van der Woerd et al., 2002; King et al., 2005).

Slip partitioning for crustal deformation occurs at different length scales, from the order of plate-boundaries down to local structures. Case histories for slip partitioning in smaller earthquakes include the 2014 Northern Nagano earthquake (Japan, M_W 6.2) or the 2018 Hualien earthquake (Taiwan, M_W 6.4), with both events involving strike-slip and reverse motion in settings where fault curvature imposes local variation of the slip direction (Kobayashi et al., 2017; Lo et al., 2019). Local slip partitioning can be frequently inferred from geological observations, for example along the Dead Sea Fault System (Bartov and Sagy, 2004; Gomez et al., 2007), and also has been confirmed from the locations and mechanisms of microearthquakes in many different settings, (e.g., Yamini-Fard et al., 2006; Wenzheng and Hauksson, 2011). By definition, strike-slip faulting is an integral part of slip partitioning, and in general, local slip partitioning is linked to a nonplanar geometry of the faults. Irregularities of the fault trace are common for strike-slip faults, and may arise from the evolution of disconnected faults over time, compositional heterogeneity or fault interaction, among others, (e.g., Mann, 2007). If step-overs or bends are present along a fault, strike-slip motion has to deal with these obstacles, and local deformation will deviate from simple shear by a component of shortening or extension (Fossen and Tikoff, 1998; McClay and Bonora, 2001; Nabavi et al., 2017). Transtensional settings develop around fault releasing bends and extensional step overs, which occur where the sense of fault slip and the sense of the fault offset are the same, like for a right-stepping pull apart on a right-lateral fault. In turn, transpersonal settings develop around fault restraining bends and contractional step overs, which occur where the sense of fault slip and the sense of the offset are opposite to each other.

Here, we analyze the kinematics of an intense earthquake sequence that occurred in 2016 in the southern Alboran Sea (Buforn et al., 2017; Medina and Cherkaoui, 2017; Galindo-Zaldivar et al., 2018; Kariche et al., 2018; Gràcia et al., 2019).

Seismicity started with a foreshock, which was a moderate magnitude, M_W 5.1 earthquake on January 21st. This initial event was followed by a M_W 6.3 earthquake at 04:22 UTC on January 25th. Despite its offshore location, about 40 km from the African coast and 125 km from Iberia (**Figure 1**), this earthquake caused damage along the north Moroccan coast (I = VI) and was widely felt in southern Spain (I = IV, IGN, 2016). During the following months, aftershock activity was intense, including numerous felt, moderate magnitude earthquakes. Moment tensor solutions for this sequence are available from near real-time moment tensor determination at the Instituto Geográfico Nacional (Rueda and Mezcua, 2005) and dedicated studies (Buforn et al., 2017; Gràcia et al., 2019). According to published results, foreshock and mainshock show similar strike slip faulting solutions, while the aftershock series shows more complex characteristics of faulting. In addition to further strike-slip events, pure reverse faulting mechanisms occur, including many of the largest aftershocks. We investigate this case of slip partitioning through relocation and regional moment tensor inversion for further small-to-moderate magnitude aftershocks. We also use moderate aftershocks as empirical Greens functions to evaluate the rupture process of the mainshock and establish the spatial relationship between mainshock and aftershocks. We interpret our results in light of the local faulting geometry, originating transpression during the 2016 earthquake series, and in the regional tectonic context, characterized by present-day transtensional conditions in the Alboran basin.

FORMATION AND SEISMOTECTONICS OF THE ALBORAN BASIN

The Alboran Sea is the western termination of the Mediterranean and is located on the inner side of the Gibraltar Arc, formed by the Betic and Rif mountain belts in southern Spain and northern Morocco. The relationship between the extensional Alboran Basin and the tightly curved orogenic arc has been analyzed by means of diverse geodynamic models. Besides explanations in terms of subduction-related processes, (e.g., Royden, 1993; Lonergan and White, 1997; Gutscher et al., 2002; Spakman and Wortel, 2004; Gutscher et al., 2012; Faccenna et al., 2014), the configuration of the Alboran-Betic-Rif system also inspired less common geodynamic interpretations, like for example a radial extensional collapse (Platt and Vissers, 1989; Molnar and Houseman, 2004). Recent results from seismic tomography, based on dense station coverage in the Iberia–Maghreb region during several temporal deployments, show clearly the position and geometry of the lithospheric slab in the upper mantle beneath the Alboran region, (e.g., Bezada et al., 2013; Palomeras et al., 2014; Fichtner and Villaseñor, 2015). These images substantially strengthen geodynamic interpretations in terms of subduction related processes. The Alboran slab forms part of the Western Mediterranean subduction system that is characterized by fragmentation of the slab, generalized trench retreat and nearly complete consumption of the remaining Tethys lithosphere since the slowing down of African–Eurasian convergence about 25 Myr ago, (e.g., Faccenna et al., 2014). In particular, the formation of the Alboran Basin is tied to the rapid rollback of the Alboran slab during the Miocene. Receiver functions have imaged a narrow corridor of oceanic lithosphere that is still preserved below the Alboran units at the vertex of the Gibraltar arc, representing the Mesozoic connection between the spreading centers of the Alpine Tethys and the Central Atlantic (Molina-Aguilera et al., 2019; Santos-Bueno et al., 2019).

According to stratigraphy and structural evidence, the most significant extension recorded in the Alboran crust started around the beginning of the Miocene (23 Myr) and lasted until ~8 Myr in the middle Tortonian, (e.g., Bourgois et al., 1992; Comas et al., 1992; Billi et al., 2011; Giaconia et al., 2015). Kinematic reconstructions suggest that this extensional phase coincides with fast displacement of the Alboran domain, following the retreating Alboran slab for about 500–700 km from a position south of the Balearic Islands at the beginning of the Miocene, to nearly the present position at 8 Myr (Rosenbaum et al., 2002; Vergés and Fernàndez, 2012; van Hinsbergen et al., 2014). The reconstructions corroborate a WSW direction of slab rollback as a requirement to explain the length (>600 km) of the subducted Alboran slab seen in tomographic images. Slab rollback toward Gibraltar and the docking of the allochthonous Alboran units onto the passive continental margins of Iberia and Morocco is also recorded by a change in the geochemical signatures of late Miocene volcanic rocks (12–6 Myr), showing a spatial and temporal transition from subduction-related to intraplate type magmatism (Duggen et al., 2004; Duggen et al., 2005). Since the Tortonian, the Alboran domain slowed down significantly and became affected by slow, oblique convergence between the Iberian and Moroccan margins (e.g., Billi et al., 2011; Giaconia et al., 2015). This fundamental change led to shortening and partial basin inversion (e.g., in the southern Alboran Sea, Martínez-García et al., 2013; Martínez-García et al., 2017; Lafosse et al., 2020). Despite ongoing plate convergence and geological evidence for contraction since the end of the Miocene, the general present-day stress regime in the Alboran domain is transtensional, according to observed geodetic velocities and earthquake focal mechanisms (e.g., Stich et al., 2006; Serpelloni et al., 2007).

Moment tensor focal mechanisms for earthquakes in the Alboran domain show a clear predominance of strike-slip faulting, occasionally including components of normal faulting. The characteristic orientation of tension axes is near ENE–WSW (**Figure 2**, e.g., Martín et al., 2015; Custódio et al., 2016; Stich et al., 2019). Strike-slip faulting with optional normal components has also been observed for the so far largest instrumental earthquakes in the Alboran region, including the 1910, M_W 6.1 Adra earthquake (Stich et al., 2003a; Stich et al., 2003b) and the earthquakes in 1994 (M_W 5.9) and the 2004 (M_W 6.3) near Al Hoceima (Calvert et al., 1997; Bezzeghoud and Buforn, 1999; Stich et al., 2005; Biggs et al., 2006). In agreement with the dominant faulting style, overall transtensional stress conditions have been inferred for the Alboran region, with stress tensors closer to uniaxial extension

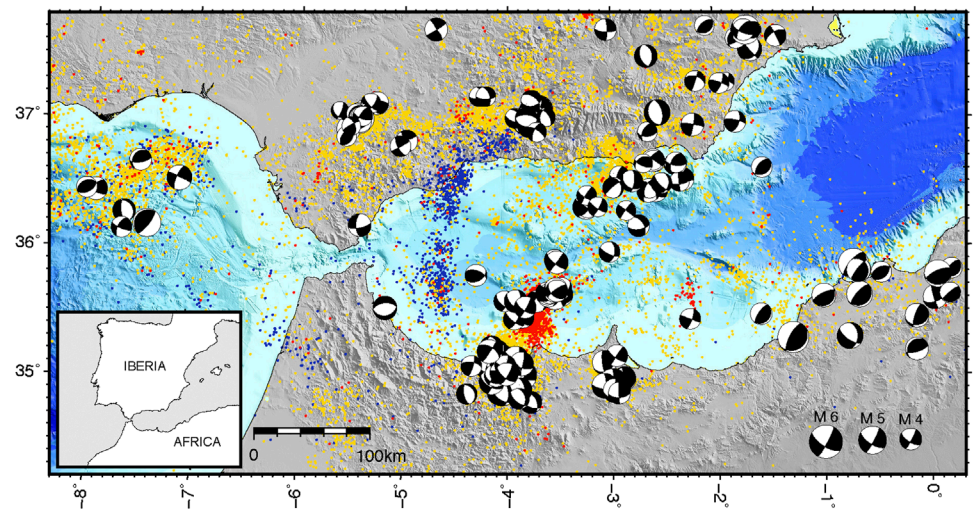

FIGURE 2 | Regional moment tensor solutions along the Iberia-Maghreb plate boundary zone until 2014 (Martín et al., 2015). We show double couple components of the mechanisms in lower hemisphere projection. The size of the beach-balls is scaled with magnitude (see bottom right). We use EMODnet Bathymetry, as well as source and representation of seismicity like in **Figure 1**. Strike slip and normal faulting earthquakes are dominant in the plate boundary zone between about 2°W and 5°W.

in the northern part, and closer to strike-slip condition in the southern part of the Alboran domain (Stich et al., 2006; De Vicente et al., 2008; Olaiz et al., 2009; Soumaya et al., 2018). Compressional principal stress axes show azimuths around N345°E and tensional principal axes around N75°E. Recent transtension is also documented geologically from active faults at the Moroccan margin (d'Acremont et al., 2014; Lafosse et al., 2017; Lafosse et al., 2020). The tectonic regime in the Alboran region is in a marked contrast with the adjacent sections of the plate boundary zone, where transpersonal environments with reverse and strike-slip focal mechanisms are characteristic for northern Algeria as well as for the SW-Iberian margin (e.g., Bezzeghoud and Buforn, 1999; Stich et al., 2003a; Stich et al., 2003b).

Extension in the central Betics and Alboran Sea is not straightforward to understand in the context of plate convergence between the Iberian and Maghrebian margins (e.g., Cunha et al., 2012). In fact, the Global Navigation Satellite System (GNSS) velocity field suggests that deformation in the Iberia-Maghreb region is a result of the superposition of two independent processes (e.g., Fadil et al., 2006; Stich et al., 2006; Serpelloni et al., 2007; Koulali et al., 2011; Mancilla et al., 2013; Palano et al., 2013). On regional scale, the Iberia-Maghreb region is subject to oblique Eurasia-Nubia plate convergence in WNW–ESE direction at a rate of ~4–5 mm/yr. The most striking anomaly in this context is the peculiar SW motion of the Rif mountain range in Morocco with respect to stable Nubia at a rate of ~3–4 mm/yr (Fadil et al., 2006; Koulali et al., 2011). Motion of the Rif block is aligned with the direction of extension in the central Betics (Mancilla et al., 2013) and Alboran Basin (Spakman et al., 2018). The anomalous emplacement of the Rif block can be modeled by applying a horizontal traction in SW direction to the base of the Rif (Pérouse et al., 2010), such that a local, subcrustal process superimposed on plate convergence can be considered causative for transtensional conditions in the Alboran Sea. A plausible origin of Rif motion is the present stage of slab rollback and detachment, where the mantle resistance to the hanging slab produces traction in direction opposite to the NW-directed absolute plate motion of the Alboran region with respect to the underlying mantle (Spakman et al., 2018; Capella et al., 2020). Strain tensors calculated from GNSS velocities around the Alboran Sea corroborate that a transtensional regime is characteristic of the Alboran Basin today (Serpelloni et al., 2007; Billi et al., 2011; Palano et al., 2013). The Alboran transtensional regime is characterized by ~2.5 mm/yr of extension in direction of present-day Alboran stretching (ENE–WSW), or ~3 mm/yr of left-lateral slip along the NNE–SSW faulting directions inferred from strike-slip moment tensors in the Basin (Stich et al., 2006).

The interplay of large-scale plate motion with local subcrustal processes is mapped in the regional fault network by changes in the seismotectonic pattern along the Maghrebian margin from east to west. While the Alboran-Rif domain is characterized by conjugate strike-slip faulting with normal component, seismotectonics along the coast of Algeria and Tunisia is dominated by reverse faulting and right-lateral strike-slip, (e.g., Bezzeghoud and Buforn, 1999; Braunmiller and Bernardi, 2005; Stich et al., 2006; Soumaya et al., 2018). Over the recent decade, marine multibeam and seismic reflection imaging in the Alboran basin was able to characterize the principal active faults in the offshore part of the Alboran domain, (e.g., Gràcia et al., 2006; Gràcia et al., 2012; Martínez-García et al., 2013; Perea et al., 2018). The dominant tectonic feature of the Alboran is the complex fault network of a major left-lateral shear zone that extends for more than 400 km in roughly NE–SW from SE Spain across the Alboran Sea to the eastern Rif Mountains near Al Hoceima (Trans-Alboran Shear Zone, Bousquet, 1979; De Larouzière et al., 1988; Stich et al., 2006). The two principal left-lateral lineaments that cross the Alboran Sea are the offshore part of the Carboneras fault system and the Al-Idrisi fault system, both with

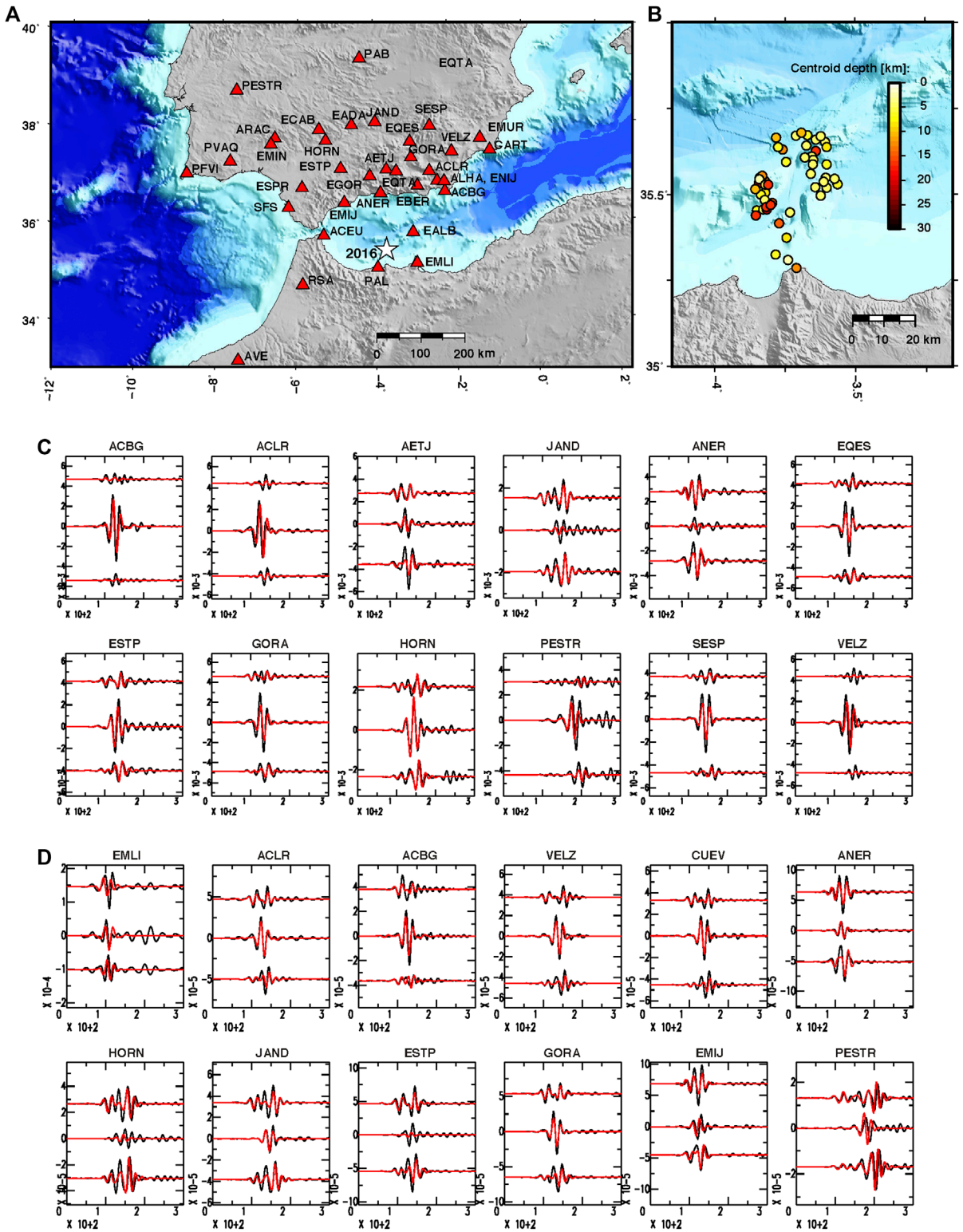

FIGURE 3 | (A) Distribution of 35 regional seismic broadband stations (triangles) used for waveform analysis of the 2016 Alboran sequence (star), **(B)** depth of the moment centroid from regional moment tensor inversion, **(C)** example of waveform fitting from moment tensor inversion at intermediate periods (20–50 s), showing results for the January 25 mainshock. Station panels show radial, transverse and vertical displacement waveforms from top to bottom, black for observations and red for predictions (time in s, amplitudes in m). The best-fitting solution was obtained at 6 km depth. **(D)** Example of waveform fitting (as in **C**) for the M_W 5.1 reverse faulting aftershock occurred on 2016/02/22, 03:46:03 UTC, at identical centroid depth (6 km).

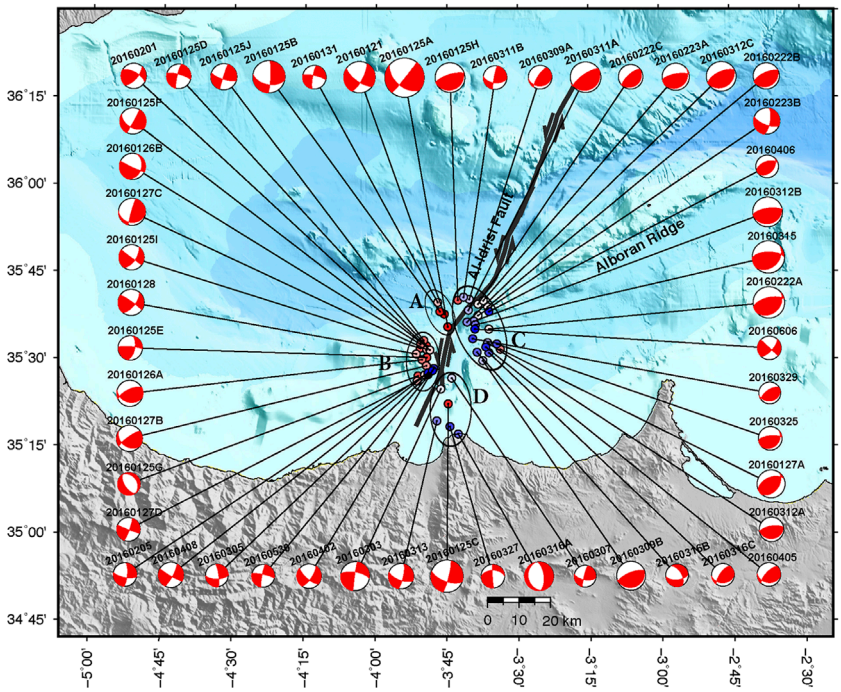

FIGURE 4 | Regional moment tensor solutions for earthquakes in the south-central Alboran Sea during 2016 (double couple components in lower hemisphere projection). Solutions are labeled with the year, month and day of the event (**Table 1**) and, where is necessary, a capital letter (A–J) is indexed for events in the same day, according to temporal order. Mechanisms are offset from the epicenter position for visibility. Epicenters are obtained from relocation in a 3D Earth model, and represented in different colors according to the temporal order of events (earliest events in red, latest events in blue). The black ellipses (labeled A–D) mark four separate groups of events that are referred to in the text. Bathymetry from EMODnet Bathymetry Consortium (2018); Al-Idrisi Fault from Gràcia et al. (2019).

~90 km length (**Figure 1**). The right-lateral Yusuf fault connects the Trans-Alboran Shear Zone with the Algerian continental margin. While in general the instrumental seismicity of the Alboran Basin shows little activity of these principal tectonic structures, the 2016 Alboran Sea earthquake is an exception from this rule. The 2016 earthquake sequence can been assigned to the Al-Idrisi fault, and the mainshock appears to nucleate right at a pronounced bend in the fault system (Buforn et al., 2017; Medina and Cherkaoui, 2017; Kariche et al., 2018; Gràcia et al., 2019).

RELOCATION AND REGIONAL MOMENT TENSOR INVERSION FOR THE 2016 ALBORAN SEA EARTHQUAKES

Source properties of small to moderate earthquakes have to be inferred from local and regional observations, because at far distances the signal of the elastic wavefield falls below noise level. We collect the recordings from 35 seismic broadband stations in Spain, Morocco and Portugal, including 30 near regional stations at distances less than 350 km, as well as five intermediate distance stations (350–500 km) to complement the dataset with additional observations in southwest, northwest and north directions from the earthquakes (**Figure 3**). In order to understand faulting processes during the 2016 Alboran Sea earthquake sequence, we perform time domain moment tensor inversion. Before moment tensor inversion, we relocate the mainshock, foreshock and major aftershocks. Relocation is motivated mainly by reported catalog depths, in excess of 20 km for many events of the sequence (e.g., IAG, iagpds.ugr.es, IGN, www.ign.es), which appears unrealistic in the extended continental crust of the Alboran Basin (e.g., Comas et al., 1999; Torne et al., 2000; Booth-Rea et al., 2007). Shallow source depths are expected for all events according to previous estimates for the seismogenic layer thickness (Fernández-Ibáñez and Soto, 2008; Grevemeyer et al., 2015). Relocation is performed by a grid-search algorithm (NonLinLoc, Lomax et al., 2000), involving a preliminary 3D Earth model for the region (Martín et al., unpublished manuscript). The Earth model was mainly built from available studies of crustal thickness, (e.g., Mancilla and Díaz, 2015), sediment thickness (e.g., Soto et al., 2008) and crustal structure inferred from seismic transects, (e.g., Gil et al., 2014).

Our relocation yields shallow hypocentral depths as expected, mostly below 15 km. It places the 2016 mainshock at the bend of the Al-Idrisi fault, suggesting a relationship between this major earthquake and the major strike-slip fault. This agrees with most previous interpretations (Buforn et al., 2017; Medina and Cherkaoui, 2017; Kariche et al., 2018; Gràcia et al., 2019), with the exception of Galindo-Zaldivar et al. (2018), who suggest that the earthquake could be related to newly formed faults like the 1994 and 2004 Al Hoceima earthquakes. Relocation resolves four separate groups of epicenters within the seismic sequence (**Figure 4**). The first group, according to chronological order,

TABLE 1 | Results from moment tensor inversion for 50 earthquakes of the 2016 sequence (compare **Figure 4**).

Event-ID/ date (aaaa/mm/ dd)	Origin time (UTC)	Lat (oN)	Lon (oE)	Depth (km)	Seismic moment (Nm)	Magn itude M_W	Double couple, planes #1, #2 strike dip rake strike dip rake						CLVD (%)
20160121	13:47:19	35.631	−3.760	12	5.69×10^{16}	5.1	125	68	−162	28	73	−22	9.0
20160125A	04:22:00	35.595	−3.748	6	3.49×10^{18}	6.3	131	51	−177	39	88	−38	3.8
20160125B	05:54:03	35.639	−3.775	6	7.52×10^{16}	5.2	99	50	−170	3	82	−39	0.8
20160125C	06:10:40	35.375	−3.745	8	6.06×10^{16}	5.2	15	81	−25	109	64	−170	0.1
20160125D	08:15:27	35.541	−3.823	12	1.17×10^{15}	4.0	286	75	−170	193	80	−14	8.1
20160125E	08:25:04	35.507	−3.821	8	6.78×10^{14}	3.9	11	59	12	275	79	149	9.1
20160125F	09:06:13	35.550	−3.841	8	3.52×10^{15}	4.3	122	50	−175	29	86	−39	9.4
20160125G	11:29:20	35.455	−3.852	6	3.66×10^{14}	3.7	148	60	−89	327	30	−90	9.1
20160125H	14:52:41	35.672	−3.712	4	1.82×10^{16}	4.8	253	72	92	66	18	84	1.0
20160125I	16:02:42	35.534	−3.844	18	1.63×10^{15}	4.1	35	61	−1	126	88	−151	0.5
20160125J	18:17:32	35.556	−3.832	12	2.62×10^{15}	4.2	198	87	16	107	74	177	1.4
20160126A	01:16:45	35.501	−3.838	6	3.21×10^{15}	4.3	107	33	129	243	65	68	0.2
20160126B	23:15:23	35.545	−3.842	2	2.87×10^{15}	4.3	115	85	−122	18	33	−8	0.8
20160127A	06:32:04	35.531	−3.564	6	6.50×10^{15}	4.5	41	42	71	246	51	107	5.9
20160127B	21:57:47	35.484	−3.823	4	1.91×10^{15}	4.2	126	36	157	234	77	56	0.5
20160127C	22:10:35	35.530	−3.821	4	4.59×10^{15}	4.4	96	23	169	196	86	67	0.7
20160127D	22:52:56	35.440	−3.855	16	5.77×10^{14}	3.8	19	82	−1	110	88	−172	2.4
20160128	19:48:50	35.517	−3.857	10	1.91×10^{15}	4.2	39	63	9	305	82	153	0.1
20160131	04:54:50	35.666	−3.782	10	6.38×10^{14}	3.8	283	76	−169	190	79	−13	3.8
20160201	23:50:48	35.529	−3.810	16	1.55×10^{15}	4.1	42	66	29	299	64	153	9.2
20160205	09:04:58	35.457	−3.829	4	5.08×10^{14}	3.8	101	70	−162	5	74	−20	0.1
20160222A	03:46:03	35.589	−3.603	6	5.14×10^{16}	5.1	256	64	102	50	29	67	1.3
20160222B	04:14:29	35.653	−3.608	4	3.27×10^{15}	4.3	245	69	92	59	22	84	1.1
20160222C	06:43:02	35.660	−3.642	4	7.21×10^{14}	3.9	56	19	99	227	71	87	0.7
20160223A	08:46:00	35.670	−3.623	4	4.06×10^{15}	4.4	49	20	62	259	72	100	2.5
20160223B	10:12:32	35.628	−3.642	16	2.94×10^{15}	4.3	111	67	−156	11	68	−24	2.9
20160303	11:36:25	35.417	−3.772	14	1.14×10^{16}	4.7	278	65	−178	188	88	−24	0.4
20160305	21:00:30	35.458	−3.816	18	3.46×10^{14}	3.7	89	65	−167	353	78	−25	0.8
20160307	02:38:19	35.449	−3.734	4	2.07×10^{14}	3.5	101	62	173	194	84	28	0.9
20160309A	23:04:19	35.674	−3.672	6	6.43×10^{14}	3.8	86	28	139	213	72	68	0.8
20160309B	23:46:07	35.498	−3.624	4	9.70×10^{15}	4.6	248	70	88	75	20	97	2.6
20160311A	04:16:47	35.643	−3.675	4	3.47×10^{16}	5.0	68	17	103	235	73	86	0.5
20160311B	09:40:19	35.681	−3.692	10	6.36×10^{14}	3.8	191	83	37	96	53	172	4.3
20160312A	09:20:00	35.550	−3.607	4	7.83×10^{14}	3.9	87	24	96	260	67	87	3.8
20160312B	15:04:05	35.612	−3.655	4	2.02×10^{16}	4.8	75	21	85	261	69	92	0.2
20160312C	15:17:11	35.609	−3.680	4	1.91×10^{16}	4.8	244	64	91	62	26	88	3.0
20160313	20:54:02	35.326	−3.785	6	1.35×10^{15}	4.1	13	75	−25	110	65	−164	0.1
20160315	04:40:38	35.601	−3.651	4	8.31×10^{16}	5.2	48	35	54	269	62	112	1.6
20160316A	16:27:33	35.288	−3.711	12	1.18×10^{16}	4.7	353	62	−86	167	28	−96	6.1
20160316B	19:43:09	35.522	−3.644	4	2.76×10^{14}	3.6	330	55	−38	85	59	−138	3.2
20160316C	23:10:46	35.521	−3.603	4	3.83×10^{14}	3.7	87	33	138	215	68	64	8.0
20160325	22:28:48	35.546	−3.575	4	5.94×10^{14}	3.8	47	26	56	264	69	105	5.7
20160327	23:56:21	35.310	−3.740	2	5.27×10^{14}	3.8	178	87	−43	270	46	−176	8.5
20160329	22:53:59	35.561	−3.660	4	2.27×10^{14}	3.5	79	29	111	235	63	78	2.9
20160402	14:48:04	35.476	−3.797	14	9.90×10^{14}	4.0	131	70	−160	34	71	−20	17.4
20160405	17:39:03	35.538	−3.614	4	5.93×10^{14}	3.8	97	32	139	223	69	64	8.7
20160406	03:17:47	35.639	−3.603	8	3.16×10^{14}	3.6	46	41	71	250	52	106	9.0
20160408	07:10:06	35.464	−3.817	16	1.76×10^{15}	4.1	29	78	−5	120	84	−168	0.2
20160530	22:03:49	35.470	−3.801	16	4.46×10^{14}	3.7	191	83	−10	282	79	−173	8.8
20160606	03:03:27	35.589	−3.652	4	5.44×10^{14}	3.8	133	89	−157	43	67	0	10.9

Origin time, latitude and longitude are given according to relocation of the earthquakes, while focal depth is given according to the best fitting trial depth in moment tensor inversion (increments of 2 km). Fault angle parameters assume strike counted clockwise from north. CLVD denotes the percentage of compensated linear vector dipoles to the deviatoric moment tensor, a measure for the deviation of the tensor from pure double-couple faulting. The CLVD components can be considered insignificant for all events.

is situated in the center of the 2016 earthquake series, and is formed solely by the epicenters of the January 21st foreshock, the January 25th main event and two aftershocks on January 25th and 31st (group A). This group is surrounded by a zone where no moderate aftershocks occurred. A second cluster toward the South (group B) is located ~5 km west of the trace of the Al-Idrisi fault, and contains large part of the early aftershocks. A third group toward the East (group C) concentrates most of the later aftershocks from February to March. Finally, a fourth group consists of more scattered events that extend from the southern cluster toward the Moroccan coastline (group D). Besides the fore- and main shocks, also the southern aftershock cluster could be associated with the Al-Idrisi fault within reasonable location errors. Overall, the relocated sequence is shifted eastward by

~5 km compared to routine catalog locations by the Instituto Geográfico Nacional (IGN). Results agree with other studies that use 3D velocity models (Buforn et al., 2017; Gràcia et al., 2019), and also with studies that keep a 1D model but incorporate additional stations in northern Morocco (Medina and Cherkaoui, 2017). A key role of azimuthal coverage for locating earthquakes beneath the Alboran Sea has been suggested previously (Santos-Bueno et al., 2019).

The first-order seismic moment tensor provides a general description of seismic wave radiation from a point source. Full waveforms are the preferred observable in moment tensor inversion, leading to a linear inversion scheme and a rather complete usage of the available information (Stich et al., 2003a; Stich et al., 2003b). We perform time-domain inversion for the deviatoric moment tensors, addressing small and moderate events of the 2016 earthquake sequence. We use three component displacement waveforms and filter in an intermediate period band from 15 to 35 s. Seismograms are rotated to a cylindrical coordinate system to approach a separation of radial and transverse components of the wavefield. Green's functions for waveform inversion are computed with a reflectivity code for an average regional 1D Earth model (Stich et al., 2003a; Stich et al., 2003b; Stich et al., 2005; Martín et al., 2015). To incorporate the non-linear dependence of Green's functions on source depth, we combine linear moment tensor inversion with a grid search among different trial depths and retain the best fitting combination of moment tensor and depth. We try centroid depths from 2 to 30 km, with 2 km increment. In this way, we also may assess the stability of the moment tensor solutions for different trial depths, and obtain an independent depth estimate for the seismotectonic interpretation of the sequence. The inversion involves careful manual weighting of individual waveforms to improve the overall waveform matches and explore the stability of the solutions (**Figure 3**). For the mainshock, an ad hoc centroid time shift of 3 s was assumed, to account for finite rupture duration, a choice that will be justified a posteriori through empirical Green function (EGF) analysis.

We were able to obtain stable moment tensor solutions for the foreshock, mainshock and 48 small and moderate aftershocks of the 2016 Alboran Sea sequence (**Figure 4**; **Table 1**). This includes the solutions that achieve a satisfactory match between observed and modeled waveforms, and do not show erratic changes for minor variations of seismogram weighting factors and centroid depths. Our solution for the mainshock shows strike-slip faulting with fault angle parameters of N39°E, 88°, −38° (strike, dip, rake) for the left-lateral nodal plane or N131°E, 51°, 183° for the right-lateral plane. The left lateral plane agrees with the kinematics and the local strike of the Al-Idrisi fault north of the fault bend, and can be likely considered the rupture plane (Buforn et al., 2017; Gràcia et al., 2019). The mainshock moment tensor shows a double-couple source with negligible compensated linear vector dipole contribution of 4%, and shallow centroid depth of 6 km. The estimated scalar moment of $M_0 = 3.5 \times 10^{18}$ Nm reveals the 2016 earthquake as the largest instrumental event at this part of the Africa–Eurasia plate boundary zone, larger than the 2004 Al Hoceima earthquake ($M_W = 6.3$, $M_0 = 2.9 \times 10^{18}$ Nm, using the same methodology; Stich et al., 2005) and the 1910 M_W 6.1 Adra earthquake (Stich et al., 2003a; Stich et al., 2003b). The collocated foreshock shows a very similar mechanism, with fault angle parameters of N28°E, 73°, −22° (strike, dip, rake) for the left-lateral nodal plane. Among the aftershock moment tensors, we obtain 28 solutions with magnitude M_W 4.0 and up, highlighting the importance of this sequence for the regional context. The remaining 20 moment tensor mechanisms correspond to minor aftershocks with magnitudes M_W between 3.5 and 3.9.

Compared to previous studies, we obtained a larger number of aftershock moment tensors [48, compared to 11 and 20 solutions, respectively, in Buforn et al. (2017) and Gràcia et al. (2019)], which is possibly a benefit from the denser station coverage in this study. Our mechanism for the mainshock is comparable to moment tensor solutions by Buforn et al. (2017) and Gràcia et al. (2019), showing similar seismic moment, although relatively minor double-couple rotation angles of 15° and 34°, respectively (Kagan, 2007), but our mechanism is different from the IGN automated moment tensor inversion showing a rotation angle of 60°. For the foreshock, we observe moderate rotations of 36° and 39° between our mechanism and solutions by IGN and Buforn et al. (2017), introduced mainly by the lower fault dip proposed in these studies for the NNE–SSW nodal plane (40°–46°). Our dip value of 73° appears more consistent with the steep dip angles of the mainshock mechanism and the Al-Idrisi fault. Instead, Gràcia et al. (2019) proposed for the foreshock a nearly opposite moment tensor mechanism (rotation angle of 93° with respect to our solution), showing right-lateral faulting along the NNE–SSW nodal plane. This orientation is not supported by the recorded waveforms, showing high similarity and identical polarity for fore- and main shocks, and also appears incompatible with the present-day stress field in the Alboran Basin and the left-lateral kinematics of the Al-Idrisi fault. From waveform and tectonic features, we think that faulting mechanisms for fore- and main shocks are likely similar. Our mechanisms are supporting a scenario of activity on one single fault segment at the beginning of the sequence, involved in the rupture of the foreshock, as well as the rupture nucleation for the mainshock four days later.

Centroid depths (**Figure 3**; **Table 1**) concentrate between 4 and 6 km and indicate shallow seismicity throughout (2–18 km), in agreement with relocated hypocenters and the shallow brittle-to-ductile transition in the area. These depth estimates from waveform inversion, although not tightly constrained, implicitly take into account the amplitude ratio between body and surface waves, and therefore are relevant support when near-source observations for shallow offshore earthquakes are lacking. Aftershock moment tensors reproduce the long duration of the 2016 Alboran Sea sequence, with 24 solutions over the first month, 18 more solutions during March, and six further moment tensor from April to June (**Table 1**). Our main focus in this study is the faulting style. The southern aftershock cluster (group B) is dominated by strike-slip faulting. These events tend to have different orientation compared to foreshock and mainshock; a majority of 12 solutions show strike values clustering between N5°E and N20°E for the left-lateral nodal plane, which seems more compatible with the trend of the southern Al-Idrisi fault (**Figure 4**). On the other hand, moment tensor inversion indicates reverse faulting for 21

aftershocks, and especially for the majority of the larger events ($M_W \geq 4.5$, **Table 1**). Reverse aftershocks are predominant in the eastern cluster (group C, **Figure 4**), showing ~NW–SE orientation of moment tensor P-axes, which rather resembles the compressional regime at the north Algerian margin or SW-Iberia (**Figure 2**). The cumulated seismic moment of major reverse faulting aftershocks for the 2016 earthquake is 2.3×10^{17} Nm (equivalent to a single M_W 5.5 earthquake). Overall, the combination of strike-slip faulting and reverse faulting in the 2016 earthquakes indicates a transpressional scenario, as opposed to the generally transtensional conditions inferred from previous moment tensors and the GNSS velocity field across the Alboran Sea (e.g., Stich et al., 2006; Serpelloni et al., 2007; De Vicente et al., 2008). We may characterize the 2016 sequence as a case of local slip-partitioning, where crustal deformation is taken up along subparallel strike-slip and dip-slip faults.

FINITE SOURCE MODELING FOR THE PRINCIPAL EARTHQUAKE

According to empirical source-scaling laws, a typical M_W 6.3, strike-slip earthquake has rupture length of about 22 km and rupture area of about 280 km^2 (Thingbaijam et al., 2017). Expected rupture areas of the largest aftershocks (M_W 5.2) are already one order of magnitude smaller. To establish the spatial relationship between the two principal clusters of aftershocks in the 2016 Alboran earthquake sequence (groups B and C in **Figure 4**) and the position and extension of the mainshock rupture area, we need to estimate finite source parameters for the main earthquake. In particular, we are interested in how far the rupture propagated from the nucleation zone into the restraining fault segment of the Al-Idrisi fault in one direction, and into the southern leg of the fault in the other direction.

The magnitude M_W 6.3 earthquake on January 25th is the only event of the 2016 Alboran sequence that has been recorded with sufficient quality at far distances, and teleseismic body wave recordings of this earthquake could be used to investigate the rupture process (Buforn et al., 2017; Gràcia et al., 2019). Both studies apply iterative time domain deconvolution (Kikuchi and Kanamori, 1991) to invert for the slip distribution. They use similar faulting parameters (hypocentral depth of 7 and 10 km, strike of N30°E and N214°E, and dip of 87° and 85°, respectively), and obtain overall similar slip distributions, showing maximum fault displacement of ~1 m, total rupture length of ~25–30 km, as well as an asymmetry of the slip distribution, with the rupture propagating predominantly northward for ~16–20 km (Buforn et al., 2017; Gràcia et al., 2019). In both studies, slip is confined to shallow depths between 1 and 15 km. In general, teleseismic body waves are more sensitive to vertical variations of slip because these waves propagate steeply downward from the source, but the resolving power for horizontal variations may be less. To confirm the horizontal directivity of the rupture, Buforn et al. (2017) analyze spectral amplitudes of teleseismic Rayleigh waves at different azimuths, indicating a rupture propagating to N30°E azimuth, and Gràcia et al. (2019) suggest that pulse durations in regional waveforms are shorter toward north, consistent with predominant rupture propagation toward this side.

Here, we estimate apparent source time functions (ASTFs) for the main earthquake from P- and S- waveforms recorded at near-regional stations in Morocco and Spain. Source time functions are time series of moment release. The prefix "apparent" points out that these moment rate functions vary according to the direction to the recording station and the type of wave involved in the analysis, hereby encoding finite source parameters like directivity and rupture speed (e.g., Ammon et al., 2006; López-Comino et al., 2012). We attempt to isolate the ASTFs from the mainshock broadband waveforms through deconvolution of the corresponding recordings for foreshock and aftershocks. This approach assumes that waveforms from collocated small earthquakes represent EGFs (Hartzell, 1978) that contain essentially the same propagation effects as the target earthquake, but lack a significant imprint from source finiteness and rupture propagation. We perform deconvolution through spectral division, stabilized by a waterlevel at 1% of the maximum spectral amplitude, as well as a Gaussian low pass with pulse width of ~0.75 s (at half the height of the maximum). We process time windows that contain 15 s of P-waves on radial and vertical components (except for stations EMLI and EALB, with shorter S–P times) and 10 s of S-waves on the transverse component, as well as 5 s of pre-arrival waveforms for both P- and S-waves. Several recordings saturate at the S-waves (EMLI, EALB, ANER), and amplitude information is lost. A concern with deconvolution in our case is given by the complicate and emergent waveforms recorded for shallow earthquakes at regional distances, due to multiple interactions with the crustal waveguide. We decide to enhance final ASTFs by stacking the deconvolution results for different candidate EGFs (Stich et al., 2005).

We initially include all strike-slip aftershocks (**Table 1**) into the analysis, without considering source proximity. The validity of EGFs and the success of individual deconvolutions are verified a posteriori according to the quality of the extracted ASTFs, validating the temporal concentration of the signal and the pre- and post signal noise level. In this step most of the deconvolved functions are discarded because of low quality, an outcome that we may relate to the characteristics of the signals, as well as the significant distances between mainshock and several trial EGF events. Used ASTFs are normalized before stacking to avoid that aftershocks with different magnitudes contribute differently to the result. We are able to retain stacked ASTFs with acceptable noise level for eight P- and eight S-waves (**Figure 5**). We measure apparent durations on the ASTFs from manual picks of onset and termination of the source signal. Termination is not well defined on several ASTFs where the time function fades away slowly (EADA, EBER, ALHA), in which case, we rely on nearby stations to guide the pick. We obtain apparent durations of 4.8–6.3 s for P-waves, and 4.8–8.3 s for S-waves. The longest durations for each wave type are to the southwest, and shortest durations toward north and northeast.

We model the azimuthal variability of ASTF durations as a function of finite source parameters with a propagating line

source (Cesca et al., 2011; López-Comino et al., 2012; López-Comino et al., 2016), **Eq. 1**:

$$\tau(\varphi)_{BI} = \max\left[t_r + (1-\chi)\left(\frac{L}{v_R} - \frac{L}{v_{P,S}}\cos(\varphi-\alpha)\right), t_r + \chi\left(\frac{L}{v_R} + \frac{L}{v_{P,S}}\cos(\varphi-\alpha)\right)\right] \quad (1)$$

Apparent durations depend on the angle between the fault strike φ and the azimuth of the recording station α, the rupture length L, the rupture speed v_R, the asymmetry of the rupture χ (defined between 0 for unilateral rupture and 0.5 for symmetric bilateral rupture), and the rise time t_R, which is the time that a particular point on the fault is slipping during the rupture. We solve the non-linear inverse problem through full grid search for the involved parameters in reasonable intervals and appropriate steps (**Table 2**). We assume local P-wave velocity of 6.1 km/s, and S-wave velocity of 3.5 km/s (Stich et al., 2005), as well as horizontal take off angles for the bulk energy of regional body waves for this shallow earthquake at regional distances. Model performance is evaluated through the average L1 misfit to P- and S-wave apparent durations at all stations.

The joint inversion of ASTF durations obtained from P- and S-waves yields low L1 misfit of 0.18 s (**Figure 5**), rupture duration of 5.2 s, rupture length of 21 km, azimuth of N24°E (corroborating left-lateral faulting) and an asymmetric pattern with 60% of the rupture propagating toward NE (**Table 2**). The rupture velocity is 3.0 km/s, corresponding to ~85% of the local S-wave speed, which is a high, yet plausible value. The rise time estimate of 1.0 s agrees with the initial ascent of most seismograms and ASTFs. There are intrinsic trade-offs among rise time, length and rupture speed, therefore we use the full grid search results for an appraisal of errors. We retain alternative models that perform reasonably well applying a conservative L1 misfit threshold of 0.36 s, twice the global minimum. Variations within this set show that total duration, azimuth and asymmetry are well resolved (**Table 2**), while the trade-offs among rise time, length and rupture speed remain unresolved. Inversion with fixed rupture speed and rise time does lead to a well constrained length estimate of 21 ± 1 km. Finally, we generalize inversion to account for a bended rupture as suggested by the surface expression of the Al-Idrisi fault around the mainshock hypocenter. Therefore, we treat the azimuths of the long and short legs of rupture propagation as independent variables (α_S and α_L instead of α). This modification leads to a marginal improvement of global L1 fit, and estimates of N32°E for α_L and N199°E for α_S. These estimates are remarkably similar to the mapped directions of the Al-Idrisi fault on either side of the epicenter (**Figure 4**), supporting the hypothesis of rupture of the 2016 mainshock into the restraining fault segment.

We further attempt to use the shape of ASTFs to resolve lateral variations of fault slip. To invert for variable slip, we discretize the fault model in a regular mesh with cell dimension of 0.5 × 0.5 km^2, using 80 mesh elements along strike and 24 mesh elements along dip. This allows for maximum rupture length of 40 km, well above the previous estimate from apparent source durations. The hypocenter is assumed in the center of the fault model. The chosen width of the rupture zone of 12 km appears a plausible scenario for the thickness of the seismogenic layer, close to estimates for the depth of the 450°C isotherm (10 km; Soto et al., 2008), the maximum depth of faulting from Ocean Bottom Seismometer data (15 km; Grevemeyer et al., 2015), as well as including the centroid depths for more than 80% of inverted moment tensors in this study. A fault width of 12 km translates to average fault slip of 46 cm when assuming a rectangular rupture with length of 21 km, scalar seismic moment of 3.5 × 10^{18} Nm and rigidity of crustal rocks of 30 GPa. We test a plane fault surface (moment tensor strike of N39°E), as well as a model that incorporates a fault bend according to the mapped fault geometry, with strike of N40°E north of the hypocenter and N10°E south of the hypocenter (the hypocenter is still placed in the center of the model, and both legs are 20 km long). Synthetic ASTFs are constructed by superposition of time-lagged, triangular slip velocity functions for constant rupture speed of 3 km/s (**Table 2**). The approach has to deal with shortcomings of ASTFs. Besides short windows and clipping at individual stations, ASTFs show significant noise, and the complexity of several ASTFs appears mutually inconsistent, for example very abrupt terminations or the coexistence of trapezoidal and triangular shapes (**Figure 5**). We suspect that ASTFs can be affected by ringing artifacts and other deconvolution instabilities (López-Comino et al., 2016).

Slip inversion is solved through a search approach (López-Comino et al., 2015; López-Comino et al., 2016) based on forward modeling for pseudorandom trial distributions with prescribed statistics for the slip heterogeneity (Mai and Beroza, 2002). According to the geometry of the regional wavefield, with predominately horizontal radiation into the crustal waveguide, we cannot expect resolution for variations of slip with depth, while data are expected to be sensitive to horizontal variation. We therefore exclude slip variations with depth, and restrict heterogeneity solely to variations along fault strike (**Figure 6**), where we impose a 1D von Karman distribution for fault slip, with correlation length of 20 km and Hurst exponent of one, which corresponds to the theoretical value for a 2D planar slip distribution. Predictions for 1,000 trial models are compared to actual ASTFs by normalized cross correlation. Similar correlation coefficients are achieved for a plane fault model (cc = 0.80) and a bended fault model (cc = 0.81), which cannot be discriminated from regional data. Fits are poor at several stations (**Figure 6**), confirming the anticipated inconsistencies in the set of ASTFs. In particular, the oscillatory nature of several ASTFs cannot be reproduced, suggesting that oscillations are an artifact from limited bandwidth and an incomplete fulfillment of the underlying assumptions in EGF analysis. Nevertheless, slip distributions are consistent with bulk rupture parameters inverted from apparent durations (**Table 2**) and show that: 1) Slip propagates longer into the NE segment, consistent with the asymmetry obtained from apparent durations, 2) Slip in the NE segment is larger, consistent with the overall faulting mechanism (N39°E), and 3) maximum slip (~0.6 m) occurs close the hypocenter, explaining the impulsive onsets of all ASTFs.

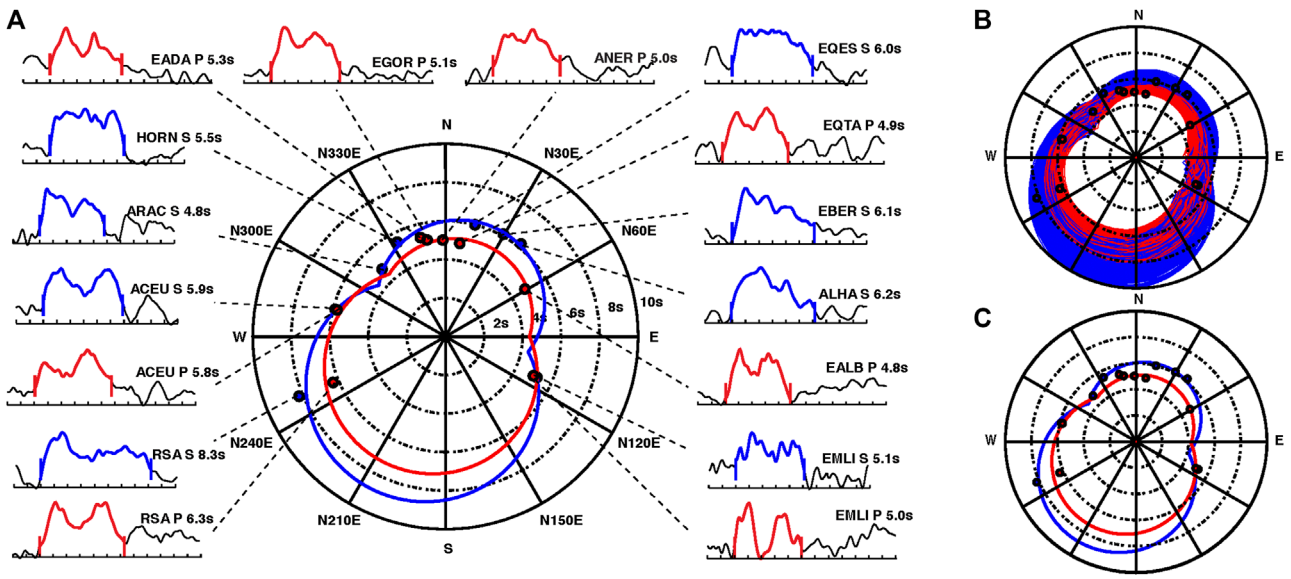

FIGURE 5 | (A) Stacked apparent source time functions at 13 near-regional stations (blue for P-waves, red for S-waves) and apparent source durations represented in a polar plot. Duration measurements on individual apparent source time functions are annotated by vertical bars and colored segments of the waveforms. Predictions for the P and S-durations from the best fitting line source model (L1 misfit of 0.18 s) are given by blue and red curves in the polar plot. **(B)** Overlay of alternative solutions with acceptable L1 misfit (range of L1 between 0.18 and 0.38 s), showing the resolution of the source model (compare **Table 2**). **(C)** Best fitting line source model for a bended fault with rupture nucleation at the bend and fault azimuths in either direction incorporated as free, independent variables. The bended fault model leads to marginal improvement of the fit, and results in best azimuths of N32°E and N199°E, close to the mapped geometry of the Al-Idrisi fault bend.

In comparison with previous studies, our total rupture duration of 5.2 s from regional recordings is significantly shorter than rupture duration inferred from the teleseismic wavefield. In the later case, the estimates range from a rupture duration of 11 s from automated processing of teleseismic source time functions (Vallée et al., 2011) or 12 s from inversion of teleseismic body waves (Buforn et al., 2017) up to significantly longer source time functions with about 20 s duration for the main slip pulse (Gràcia et al., 2019). A possible starting point to understand this inconsistency is the fact that teleseismic waves are modeled with synthetic Green functions, while on regional scale the empirical waveforms are used for this purpose. Regional source durations may suffer from deconvolution artifacts, while teleseismic source durations may be influenced by secondary body wave phases generated in slow sediments and the water layer, not reproduced completely by the models. Our estimate of a high rupture speed of 3 km/s is in agreement with rupture speed of 3.0 km/s from finite fault inversion and rupture speed of 2.9–3.0 km/s from modeling teleseismic Rayleigh waves by Buforn et al. (2017), but is in disagreement with the slow rupture speed of 2 km/s proposed by Gràcia et al. (2019). For offshore earthquakes like the 2016 sequence, geodetic information, that would help to reduce the non-uniqueness of finite fault inversion, is not available, and finite source models have to be inferred from seismic recordings alone. In this context, regional source analysis from small to moderate aftershocks plays an important role. In our case, the rupture length of 21 km estimated from regional data is close to the expectation for M_W 6.3, strike-slip earthquakes (22 km according to Thingbaijam et al., 2017), while teleseismic analyses yield longer ruptures.

TABLE 2 | Parameters for the in line source inversion of apparent source time function durations (column 1), parameter range and step size for full grid search (column 2), best model (column 3) and range of parameters in alternative trial models that lead to tolerable misfit (column 4). Columns 4–6 summarize the setup and results for an alternative grid search that reduces trade-offs through fixed rupture speed and rise time.

	Search 1 (minimum, increment, maximum)	Best L1	Error estimate	Search 2 (minimum, increment, maximum)	Best L1	Error estimate
Azimuth α (N°E)	[0, 2, 358]	24	[12, 60]	[0, 2, 358]	24	[14, 52]
Length L (km)	[10, 1, 30]	21	[10, 30]	[10, 1, 30]	21	[20, 22]
Rupture speed v_R (km/s)	[2.0, 0.25, 4.0]	3.0	[2, 4]	3.0, fixed	3.0	–
Symmetry χ (1)	[0.0, 0.05, 0.5]	0.4	[0.35, 0.45]	[0.0, 0.05, 0.5]	0.4	[0.4, 0.45]
Rise time t_R (s)	[0.0, 0.25, 2.5]	1.0	[0, 2.5]	1.0, fixed	1.0	–
Rupture duration t (s)	No preset	5.2	[4.5, 6.0]	No preset	5.2	[4.7, 5.4]

Symmetry of the rupture (χ) is counted from 0 for purely unilateral rupture to 0.5 for symmetric bilateral rupture. Rupture duration is a composite parameter ($t_R + [1-\chi] \times L/v_R$) not affected by trade-offs between rise time, length and rupture speed.

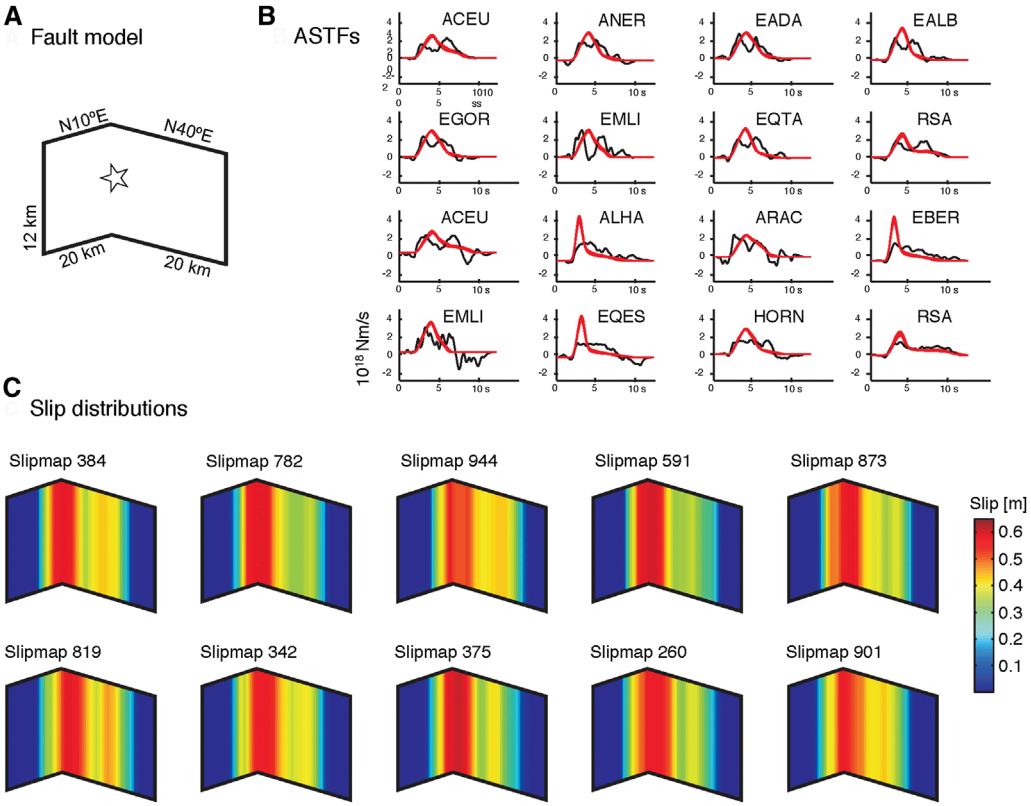

FIGURE 6 | (A) Fault model with 40 km length and 12 km width and slip initiation in the center (star), including two planar, N10°E and N40°E striking fault segments of the same length (perspective view from SE). **(B)** Comparison between best possible predictions (red) and deconvolved apparent source time functions (ASTFs) (black) from finite fault inversion at constant rupture speed (3 km/s) and slip varying only in horizontal direction. Inversion yields a partial fit, suggesting that oscillations in ASTFs may be attributed to deconvolution artifacts rather than actual partitioning of the rupture into subevents. Amplitudes of ASTFs are given for moment rate in Nm/s. **(C)** Best fitting slip distributions from random model search (slip amplitudes in m).

DISCUSSION

In regions of slow and distributed tectonic deformation, essential tectonic information has to be inferred from small-to-moderate earthquakes. In case of the Alboran region, even the analysis of the largest earthquakes of the instrumental period so far (M_W 6.3 for the 2004 Al Hoceima and 2016 Alboran Sea earthquakes) depend on the processing of aftershocks and requires the use of regional seismograms to understand its source process, context and implications. For seismic waves, the distance range places conditions on the geometry of observations. While the teleseismic wavefield is radiated steeply downward from the source, the part of the wavefield that appears in regional seismograms is injected laterally into the crustal waveguide. As a consequence, propagation effects are different. Teleseismic wavefields are characterized by well-understood multipathing and wave conversions, leading to well-defined packages of body waves. Regional wavefields for shallow earthquakes are characterized by complex reverberations within the crustal waveguide, leading to an emergent and ringing appearance of body waves and high sensitivity to changes in hypocenter position. These characteristics do not affect significantly the performance of moment tensor inversion in an intermediate period band, but turn out to complicate the extraction of broadband ASTFs in case of the 2016 mainshock. Yet, the analysis of regional seismograms is a key to understand the earthquake. On one hand, regional data suggest a shorter rupture than previously thought, limiting the section of the Al Idrisi fault that slipped during this earthquake. On the other hand, the regional analysis of aftershocks reveals the variability of focal mechanisms during this sequence.

The magnitude M_W 6.3, January 25th, 2016 Alboran Sea earthquake nucleated at a right-stepping bend of the Al-Idrisi fault (**Figure 4**). This has two interesting consequences. First, the 2016 mainshock is the first major earthquake recorded in the Alboran basin that can be assigned to a major structure. The left-lateral Al-Idrisi fault is an important tectonic accident in the Alboran Sea, composed of a ~60 km long, ~N20°E striking northern segment, a ~20 km long, N40°E striking central restraining bend and a southern segment striking ~N10°E, with length of at least 20 km (Martínez García et al., 2011; Martínez García et al., 2013; Gràcia et al., 2019). At the northern termination, the Al-Idrisi fault ends at a network of secondary right-lateral faults that separate this fault from the offshore Carboneras fault (Perea et al., 2018). The southern segment reaches into an area of distributed transtensional deformation at the Moroccan margin (d'Acremont et al., 2014;

Lafosse et al., 2017; Lafosse et al., 2020). No other mapped fault in the epicentral area shows appropriate strike and length to host the 2016 earthquake with a ~20 km long and NNE–SSW oriented rupture area, according to finite fault modeling from regional data. Our moment tensor, with near-vertical dip (88°), and non-horizontal rake estimate (−38°), agrees with high-resolution seismic profiles across the Al-Idrisi fault bend that show near-vertical dip and an exhumed crystalline basement with recent (Neogene) volcanic rocks in the eastern block of the fault, while subsidence and sedimentation occurs on the western block (Martínez García et al., 2011). Second, the location of the 2016 mainshock at the bend of the Al-Idrisi fault introduces local transpression around the restraining segment of the fault. According to moment tensor inversion, transpressional deformation is partitioned into strike-slip and dip-slip displacements in different fault structures.

The 2016 earthquake is the last out of three strong earthquakes that affected the Moroccan Mediterranean margin in recent times, following the 1994, M_W 5.9 and the 2004, M_W 6.3 Al Hoceima earthquakes. Unlike the last earthquake, the 1994 and 2004 earthquakes occurred on unmapped faults that have no recognized surface expression, (e.g., Stich et al., 2005; Biggs et al., 2006; van der Woerd et al., 2014). Both events show strike-slip mechanisms similar to the 2016 earthquake, (e.g., Biggs et al., 2006), but due to a lack of surface rupture, the discrimination between left-lateral and right-lateral faulting remains debatable. In SAR images suggest rupture along a NW–SE, right-lateral fault in case of the 2004 earthquake, and a NE–SW, left-lateral fault in 1994, thus attributing the two Al Hoceima earthquakes to conjugate faulting on previously unknown structures (Akoglu et al., 2006; Biggs et al., 2006; Cakir, 2006). The 1994 and 2004 Al Hoceima earthquakes reproduce a general trend of Alboran earthquakes, where small and moderate events correlate poorly with mapped faults, and the significance of these events and faults is not clear (Grevemeyer et al., 2015; Custódio et al., 2016). Among the larger events, also the 1910, M_W 6.1 Adra earthquake has been related to a secondary, oblique-right-lateral fault within the shear zone (Stich et al., 2003b; Gràcia et al., 2012). This leaves the 2016 earthquake as the first event associated to one of the principal left-lateral faults of the Trans-Alboran shear zone, and highlights the role of the Al-Idrisi fault in accommodating regional tectonic deformation in the Alboran region (Buforn et al., 2017; Medina and Cherkaoui, 2017; Kariche et al., 2018; Gràcia et al., 2019).

At regional scale, the Trans-Alboran shear zone can be considered a transform fault, accommodating differential deformation between the Algerian and Moroccan sectors of the plate boundary, the latter affected by stretching due to slab rollback and basal drag under the Rif (Rutter et al., 2012; Spakman et al., 2018). In particular, the Al-Idrisi fault aligns with the limit of independent southwestward motion of the Gibraltar Arc with respect to Nubia documented by onshore GNSS observations (Vernant et al., 2010; Koulali et al., 2011). The importance of long term motion along the Al-Idrisi fault is evidenced from subsurface imaging (Martínez García et al., 2011; Gràcia et al., 2019), as well as possibly by the interruption and left-lateral offset of about 10 km of the Alboran Ridge, a prominent basement high with overall trend of ~N60°E and length of ~130 km (**Figure 4**; Galindo-Zaldívar et al., 2018). This amount appears consistent with a Pliocene age of the southern Al-Idrisi fault (~3.5 Myr; Martínez-García et al., 2011; Gràcia et al., 2019) and fault slip rates of about 3 mm/a. Such slip rates coincide with GNSS-based estimates for the total left-lateral strain rates along the Trans-Alboran Shear Zone (Stich et al., 2006), indicating that the Al-Idrisi is one of the principal faults in the Alboran basin, and may possible concentrate a large part of regional strain in a single structure. This seems to contrast with the situation further south at the Moroccan margin, where the mapped fault network is becoming more distributed (d'Acremont et al., 2014; Lafosse et al., 2017; Lafosse et al., 2020), including the occurrence of strong events like the Al Hoceima earthquakes on previously unrecognized structures, which suggests the formation of new faults, and possibly a contemporary reorganization of tectonic deformation at the margin (Galindo-Zaldivar et al., 2018).

From finite source modeling, we observe asymmetric rupture propagation out from the nucleation zone at the Al-Idrisi fault bend. The rupture was propagating mainly into the restraining fault segment northeast of the hypocenter. We can compare the extend of the rupture surface with the spatial separation between the hypocenter of the main event and the locations of the two groups of aftershock toward south and northeast. In the southern aftershock cluster (group B), strike slip solutions with ~N10°E striking left-lateral planes emulate the orientation of the southern Al-Idrisi fault. From faulting style and locations, we may suppose that the southern cluster is located on the Al-Idrisi fault itself, and likely outlines the limit of the mainshock rupture in this direction. The distance to this aftershock cluster is ~8 km, identical to the length estimate inferred for the southern leg of the mainshock rupture. The separation of the northeastern aftershock cluster (group C) is less, and the entire cluster falls within the estimated rupture length of ~13 km for the northeastern leg of the mainshock. In this case, aftershock activity occurs off the Al-Idrisi fault, according to the fundamentally different fault dip and faulting style. This area aligns with the fault segment inside the double restraining bend of the Al-Idrisi fault, and shows a clear expression of slip partitioning: In a scenario of local transpressional deformation, we observe the concurrence of strike-slip motion on the vertical Al-Idrisi fault during the mainshock, with dip-slip motion during the aftershock sequence. The dip-slip aftershocks occur on subparallel, low-angle south-dipping reverse faults at the western end of the Alboran Ridge. The contrast between regional transtensional deformation and local transpressional deformation can be demonstrated by a comparison of seismicity in the southern Alboran basin before and during 2016 (**Figure 7**). Before 2016, only three out of 23 available moment tensor solutions (13%) indicate reverse faulting earthquakes, (i.e., the *T*-axes are the most vertical principal axes of the moment tensor), while during the 2016 earthquake sequence, 21 out of 50 solutions (42%) were

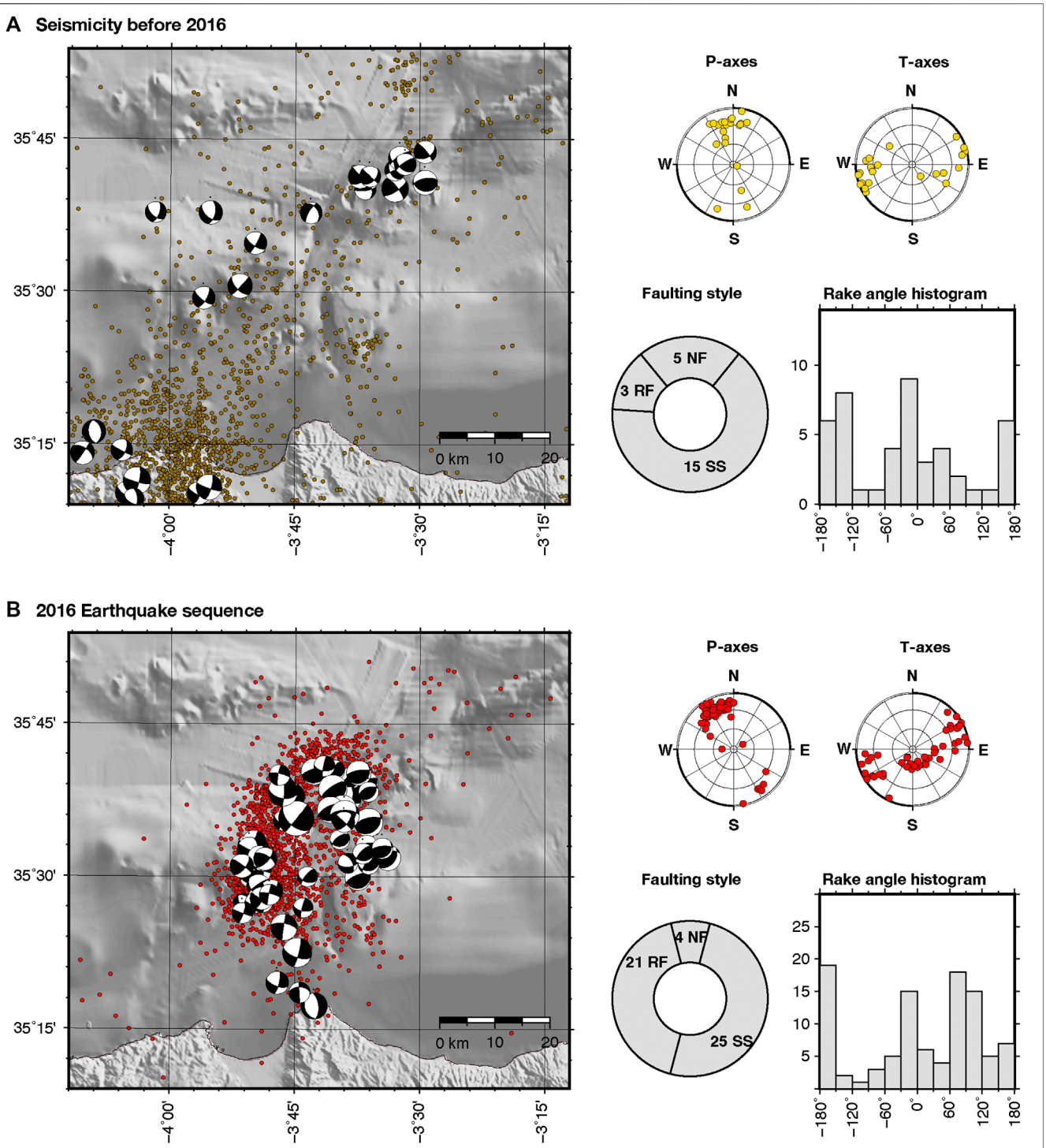

FIGURE 7 | Comparison of seismicity and focal mechanisms for the south-central Alboran Sea before **(A)** and during **(B)** the 2016 earthquake sequence. Bathymetry from EMODnet Bathymetry Consortium (2018); seismicity [red for events during 2016 in **(**B**)** yellow for other shallow earthquakes between 1990 and 2020 in **(A)**] according to IGN catalog (www.ign.es). For both sets of moment tensor solutions, for 23 and 50 events, respectively, we show orientations of principal compression (*P*-axes) and tension directions (*T*-axes) in polar plot, pie charts with distribution of faulting style (NF for normal faulting, i.e., *P*-axes is most vertical principal axes; RF for reverse faulting, i.e., *T*-axes is most vertical principal axes; and SS for strike-slip faulting, i.e., *N*-axes is most vertical principal axes) and histograms of rake angles measured indiscriminately on both nodal planes.

reverse faulting, and a pronounced peak appears in the rake angle histogram for directions between 60° and 120° (**Figure 7**).

Slip partitioning at the restraining bend appears consistent with the shallow centroid depths from moment tensor inversion and an influence of the stress-free boundary condition at the Earth's surface. However, an ideal realization of an Andersonian model of faulting disagrees with the outcome of a non-horizontal rake vector in the 2016 mainshock focal mechanism and the visible offset of the seafloor produced by accumulated motion on the Al-Idrisi fault (Galindo-Zaldívar et al., 2018; Gràcia et al., 2019). Otherwise, partitioning of fault motions in the brittle crust is favored by the contact with ductile rheologies at depth (Bowman et al., 2003), which is the case in the Alboran basin with shallow brittle-to-ductile transition (Fernández-Ibáñez and Soto, 2008). A more trivial way to understanding partitioning in the 2016 Alboran sequence is through the nearly vertical dip of the Al-Idrisi fault. The fault is not capable of taking up a component of horizontal shortening, and contraction produced around the restraining segment may localize on secondary faults, in this case reverse faults with low dip angles (mostly below 30°; **Table 1**) and the ability to take up large amounts of horizontal shortening. The 2016 sequence may have reactivated Alboran Ridge reverse faults that accommodated NW–SE shortening since the Pliocene (Martínez-García et al., 2011; Martínez-García et al., 2013) and puts on the agenda a potential role of the Alboran Ridge as source of tsunamis (Álvarez-Gómez et al., 2011). Slip partitioning during the 2016 Al Idrisi rupture provides a framework to understand the long and intense aftershock sequence of this earthquake. We finally recall other examples of local transpression along the Trans-Alboran shear zone. Slip partitioning into a reverse dip-slip component and left-lateral strike-slip has been proposed for a restraining bend in the Alhama de Murcia fault, based on geological evidence (Ferrater et al., 2017). Deep-rooted positive flower structures, cutting through the entire crust, were imaged in receiver function studies in southeastern Spain (Mancilla et al., 2018).

Finite source modeling reveals that the 2016 rupture was able to propagate at high rupture speed into both directions from the fault bend, suggesting that the northern and southern segments of the Al Idrisi fault link across a continuous fault bend at seismogenic depth, thus confirming the geological observations of a continuously curved surface trace of the fault (Martínez-García et al., 2011; Galindo-Zaldívar et al., 2018; Gràcia et al., 2019). Compared to the N10°E striking southern segment or the N20°E striking northern segment, the N40°E striking segment inside the bend of the Al-Idrisi fault is less favorably oriented with respect to the regional stress field: it forms a high angle with the maximum horizontal stress direction in the southern Alboran Sea (σ_1 at ~N345°E; Stich et al., 2006; Fernández-Ibáñez et al., 2007; De Vicente et al., 2008; Soumaya et al., 2018). Observed slip partitioning confirms the misalignment of the restraining segment and the regional shear stress. Fault bends may be efficient obstacles for rupture propagation, and frequently form the starting or termination points for earthquakes (e.g., King and Nábělek, 1985; Elliott et al., 2015), in agreement with numerical simulations of dynamic ruptures (e.g., Nielsen and Knopoff, 1998; Aochi et al., 2002; Kase and Day, 2006). In particular, during the rupture propagation into a restraining bend, the strength excess becomes larger due to an increase of compressional normal stress. The 2016 rupture nucleated in a high-angle bend of the Al Idrisi fault and died on apparently planar domains of the fault. For uniform long-term deformation along the fault, slip along the less favorably oriented fault segments is predicted to be smaller due to slip partitioning. The opposite pattern of fault slip in the 2016 earthquake is likely the result of an inherited slip deficit. In such a model, previous large ruptures that were approaching the restraining segment could not propagate past the 30° fault bend, but have contributed to stress buildup at the nucleation zone of the 2016 rupture.

CONCLUSIONS

- We may associate the 2016 Alboran Sea earthquake with the Al-Idrisi strike-slip fault, making it the first major earthquake in the Alboran basin that can be assigned to a principal fault within the Trans-Alboran shear zone.
- In contrast to adjacent areas with distributed deformation, the Al-Idrisi fault appears capable of concentrating in a single structure large part of the ~3 mm/yr, left-lateral deformation due to slab rollback and tearing beneath the Alboran basin.
- The M_W 6.3, 2016 Alboran Sea earthquake involved ~21 km of left-lateral faulting, and was nucleated in the bend between the southern, N10°E and central, N40°E segments of the Al Idrisi fault.
- ASTFs suggest a fast (~3 km/s) and asymmetric rupture, propagating primarily toward north, and showing main slip (>0.5 m) in the N40°E fault segments, consistent with the N39°E strike of the moment tensor mechanisms.
- Hence, main slip is located inside a double restraining bend, where fault strike forms a high angle with the maximum horizontal stress. Deformation along the restraining segment is partitioned between left-lateral strike-slip and reverse dip-slip faulting.
- Local transpression around the Al-Idrisi fault bend activates reverse faults at the Alboran Ridge, that make an important contribution to the intense and long-lasting aftershock activity in the 2016 Alboran Sea earthquake sequence.
- Strike-slip faulting aftershocks are observed mainly along the N10°E segments of the Al Idrisi fault, beyond the end of the 2016 mainshock rupture.
- The fore- and main shocks show nearby locations and similar mechanisms, supporting activity of the same fault segment involved in the M_W 5.1 rupture of the foreshock, and the rupture nucleation for the mainshock 4 days later.
- The 2016 earthquake appears to have settled a slip deficit in the restraining segment, suggesting that this segment may have remained unbroken in previous ruptures that could not propagate across the fault bend.

DATA AVAILABILITY STATEMENT

The raw data supporting the conclusions of this article will be made available by the authors, without undue reservation.

AUTHOR CONTRIBUTIONS

DS and RM have realized the point source modeling, DS and JA have realized the finite source modeling. All authors have contributed to the interpretation and discussion. DS prepared the initial draft, with contributions and editing from all authors.

FUNDING

This study was supported by FEDER/MINECO projects CGL2015–67130-C2-2-R and PID2019–109608GB-I00, FEDER/Junta de Andalucía project A-RNM-421-UGR18, and is part of the research group RNM104 of the Junta de Andalucía. JA has also received funding from the European Union's Horizon 2020 research and innovation program under the Marie Skłodowska-Curie grant agreement No. 754446 and UGR Research and Knowledge Transfer Found–Athenea3i; and by project 407141557 of the Deutsche Forschungsgemeinschaft (DFG, German Research Foundation).

ACKNOWLEDGMENTS

For this study we use seismic broadband data from stations operated by the Instituto Andaluz de Geofísica (IAG) in Granada, Spain, Instituto Geográfico Nacional (IGN) in Madrid, Spain, Center National pour la Recherche Scientifique et Technique (CNRST) in Rabat, Morocco, Instituto Português do Mar e da Atmosfera (IPMA) in Lisbon, Portugal, as well as the Western Mediterranean Network (WestMed) operated by the Real Observatorio de la Armada (Cádiz), Universidad Complutense de Madrid and the GeoForschungsZentrum in Potsdam, (ROA/UCM/GFZ).

REFERENCES

Akoglu, A. M., Cakir, Z., Meghraoui, M., Belabbes, S., El Alami, S. O., Ergintav, S., et al. (2006). The 1994–2004 Al Hoceima (Morocco) earthquake sequence: conjugate fault ruptures deduced from InSAR. *Earth Planet Sci. Lett.* 252, 467–480. doi:10.1016/j.epsl.2006.10.010

Álvarez-Gómez, J. A., Aniel-Quiroga, Í., González, M., Olabarrieta, M., and Carreño, E. (2011). Scenarios for earthquake-generated tsunamis on a complex tectonic area of diffuse deformation and low velocity: the Alboran Sea, Western Mediterranean. *Mar. Geol.* 284 (1), 55–73. doi:10.1016/j.margeo.2011.03.008

Ammon, C. J., Kanamori, H., Lay, T., and Velasco, A. (2006). The 17 July 2006 java tsunami earthquake. *Geophys. Res. Lett.* 33, 10. doi:10.1029/2006gl028005

Anderson, E. M. (1905). The dynamics of faulting. *Trans. Edinb. Geol. Soc.* 8, 387–402. doi:10.1144/transed.8.3.387

Aochi, H., Madariaga, R., and Fukuyama, E. (2002). Effect of normal stress during rupture propagation along nonplanar faults. *J. Geophys. Res.* 107 (B2), 2038. doi:10.1029/2001JB000500.

Bartov, Y., and Sagy, A. (2004). Late pleistocene extension and strike-slip in the Dead Sea basin. *Geol. Mag.* 141, 565–572. doi:10.1017/s001675680400963x

Bemis, S. P., Weldon, R. J., and Carver, G. A. (2015). Slip partitioning along a continuously curved fault: quaternary geologic controls on Denali fault system slip partitioning, growth of the Alaska Range, and the tectonics of south-central Alaska. *Lithosphere* 7, 235–246. doi:10.1130/l352.1

Bezada, M. J., Humphreys, E. D., Toomey, D. R., Harnafi, M., Dávila, J. M., and Gallart, J. (2013). Evidence for slab rollback in westernmost Mediterranean from improved upper mantle imaging. *Earth Planet Sci. Lett.* 368, 51–60. doi:10.1016/j.epsl.2013.02.024

Bezzeghoud, M., and Buforn, E. (1999). Source parameters of the 1992 Melilla (Spain, M_w = 4.8), 1994 Alhoceima (Morocco, M_w = 5.8), and 1994 Mascara (Algeria, M_w = 5.7) earthquakes and seismotectonic implications. *Bull. Seism. Soc. Am.* 89, 359–372.

Biggs, J., Bergman, E. A., Emmerson, B., Funning, G., Jackson, J., Parsons, B., et al. (2006). Fault identification for buried strike-slip earthquakes using InSAR: the 1994 and 2004 Al Hoceima, Morocco earthquakes. *Geophys. J. Int.* 166, 1347–1362. doi:10.1111/j.1365-246x.2006.03071.x

Billi, A., Faccenna, C., Bellier, O., Minelli, L., Neri, G., Piromallo, C., et al. (2011). Recent tectonic reorganization of the Nubia-Eurasia convergent boundary heading for the closure of the Western Mediterranean. *Bull. Soc. Geol. Fr.* 182, 279–303. doi:10.2113/gssgfbull.182.4.279

Booth-Rea, G., Ranero, C. R., Martínez-Martínez, J. M., and Grevemeyer, I. (2007). Crustal types and tertiary tectonic evolution of the Alborán sea, western Mediterranean. *Geochem. Geophys. Geosys.* 8, Q10005. 10.1029/2007GC001639

Bourgois, J., Mauffret, A., Ammar, A., and Demnati, A. (1992). Multichannel seismic data imaging of inversion tectonics of the Alboran ridge (western Mediterranean Sea). *Geo Mar. Lett.* 12, 117–122. doi:10.1007/bf02084921

Bousquet, J.-C. (1979). Quaternary strike-slip faults in southeastern Spain. *Tectonophysics* 52, 277–286. doi:10.1016/0040-1951(79)90232-4

Bowman, D., King, G., and Tapponnier, P. (2003). Slip partitioning by elastoplastic propagation of oblique slip at depth. *Science* 300, 1121–1123. doi:10.1126/science.1082180

Braunmiller, J., and Bernardi, F. (2005). The 2003 Boumerdes, Algeria earthquake: regional moment tensor analysis. *Geophys. Res. Lett.* 32, L06305. doi:10.1029/2004GL022038

Buforn, E., Pro, C., Sanz de Galdeano, C., Cantavella, J. V., Cesca, S., Caldeira, B., et al. (2017). The 2016 south Alboran earthquake (M_w = 6.4): a reactivation of the Ibero-Maghrebian region?. *Tectonophysics* 712–713, 704–715. doi:10.1016/j.tecto.2017.06.033

Cakir, Z., Meghraoui, M., Akoğlu, A. M., Jabour, N., Belabbès, S., and Ait-Brahim, L. (2006). Surface deformation associated with the M_w 6.4, 24 February 2004 Al Hoceima, Morocco, earthquake deduced from InSAR: implications for the active tectonics along north Africa. *Bull. Seismol. Soc. Am.* 96, 59–68. doi:10.1785/0120050108

Calvert, A., Gomez, F., Seber, D., Barazangi, M., Jabbour, N., Ibenbrahim, A., et al. (1997). An integrated geophysical investigation of recent seismicity in the Al-Hoceima region of North Morocco. *Bull. Seismol. Soc. Am.* 87, 637–651.

Capella, W., Spakman, W., Hinsbergen, D. J. J., Chertova, M. V., and Krijgsman, W. (2020). Mantle resistance against Gibraltar slab dragging as a key cause of the Messinian Salinity Crisis. *Terra. Nova.* 32, 141–150. doi:10.1111/ter.12442

Célérier, B. (2008). Seeking Anderson's faulting in seismicity: a centennial celebration. *Rev. Geophys.* 46. doi:10.1029/2007rg000240

Cesca, S., Heimann, S., and Dahm, T. (2011). Rapid directivity detection by azimuthal amplitude spectra inversion. *J. Seismol.* 15, 147–164. doi:10.1007/s10950-010-9217-4

Comas, M. C., García-Dueñas, V., and Jurado, M. J. (1992). Neogene tectonic evolution of the Alboran Sea from MCS data. *Geo Mar. Lett.* 12 (2–3), 157–164. doi:10.1007/bf02084927

Comas, M. C., Platt, J. P., Juan, S. I., and Watts, A. B. (1999). The origin and tectonic history of the Alboran basin: insights from leg 161 results. *Proc. Ocean Drill Progr. Sci. Results* 161, 555–579.

Cunha, T. A., Matias, L. M., Terrinha, P., Negredo, A. M., Rosas, F., Fernandes, R. M. S., et al. (2012). Neotectonics of the SW Iberia margin, Gulf of Cadiz and Alboran Sea: a reassessment including recent structural, seismic and geodetic data. *Geophys. J. Int.* 188 (3), 850–872. doi:10.1111/j.1365-246x.2011.05328.x

Custódio, S., Lima, V., Vales, D., Cesca, S., and Carrilho, F. (2016). Imaging active faulting in a region of distributed deformation from the joint clustering of focal mechanisms and hypocentres: application to the Azores-western Mediterranean region. *Tectonophysics* 676, 70–89. doi:10.1016/j.tecto.2016.03.013

d'Acremont, E., Gutscher, M.-A., Alain, R., Benard, M. de L., Manferd, L., Jeffrey, P., et al. (2014). High-resolution imagery of active faulting offshore Al Hoceima, Northern Morocco. *Tectonophysics* 632, 160–166.

De Larouzière, F. D., Bolze, J., Bordet, P., Hernandez, J., Montenat, C., and Ott d'Estevou, P. (1988). The Betic segment of the lithospheric Trans-Alboran shear zone during the Late Miocene. *Tectonophysics* 152, 41–52. doi:10.1016/0040-1951(88)90028-5

de Vicente, G., Cloetingh, S., Muñoz-Martín, A., Olaiz, A., Stich, D., Vegas, R., et al. (2008). Inversion of moment tensor focal mechanisms for active stresses around the microcontinent Iberia: tectonic implications. *Tectonics* 27, TC1009. doi:10.1029/2006TC002093

Duggen, S., Hoernle, K., Van den Bogaard, P., and Garbe-schönberg, D. (2005). Post-collisional transition from subduction- to intraplate-type magmatism in the westernmost Mediterranean: evidence for continental-edge delamination of subcontinental lithosphere. *J. Petrol.* 46, 1155–1201. doi:10.1093/petrology/egi013

Duggen, S., Hoernle, K., van den Bogaard, P., and Harris, C. (2004). Magmatic evolution of the Alboran region: the role of subduction in forming the western Mediterranean and causing the Messinian Salinity Crisis. *Earth Planet Sci. Lett.* 218, 91–108. doi:10.1016/s0012-821x(03)00632-0

Eberhart-Phillips, D., Haeussler, P. J., Freymueller, J. T., Frankel, A. D., Rubin, C. M., Craw, P., et al. (2003). The 2002 Denali fault earthquake, Alaska: a large magnitude, slip-partitioned event. *Science* 300, 1113–1118. doi:10.1126/science.1082703

El Alami, S. O., Tadili, B., Cherkaoui, T. E., Medina, F., Ramdani, M., et al. (1998). The Al Hoceima earthquake of 1994 and its aftershocks: a seismotectonic study. *Ann. Geophys.* 41, 519–537. doi:10.4401/ag-3801

Elliott, A. J., Oskin, M. E., Liu, J., and Shao, Y. (2015). Rupture termination at restraining bends: the last great earthquake on the Altyn Tagh Fault. *Geophys. Res. Lett.* 42, 2164–2170. doi:10.1002/2015GL063107

EMODnet Bathymetry Consortium. (2018). EMODnet digital bathymetry (DTM 2018). 10.12770/18ff0d48-b203-4a65-94a9-5fd8b0ec35f6

Faccenna, C., Becker, T. W., Auer, L., Billi, A., Boschi, L., Brun, J. P., et al. (2014). Mantle dynamics in the Mediterranean. *Rev. Geophys.* 52, 283–332. doi:10.1002/2013RG000444

Fadil, A., Vernant, P., McClusky, S., Reilinger, R., Gómez, F., Ben Sari, D., et al. (2006). Active tectonics of the western Mediterranean: geodetic evidence for rollback of a delaminated subcontinental lithospheric slab beneath the Rif Mountains, Morocco. *Geol.* 34 (7), 529–532. doi:10.1130/g22291.1

Fernández-Ibáñez, F., and Soto, J. I. (2008). Crustal rheology and seismicity in the Gibraltar arc (western Mediterranean). *Tectonics* 27. doi:10.1029/2007TC002192

Fernández-Ibáñez, F., Soto, J. I., Zoback, M. D., and Morales, J. (2007). Present-day stress field in the Gibraltar Arc (western Mediterranean). *J. Geophys. Res.* 112, B08404. doi:10.1029/2006JB004683

Ferrater, M., Ortuño, M., Masana, E., Martínez-Díaz, J. J., Pallàs, R., Perea, H., et al. (2017). Lateral slip rate of Alhama de Murcia fault (SE Iberian Peninsula) based on a morphotectonic analysis: comparison with paleoseismological data. *Quat. Int.* 451, 87–100. doi:10.1016/j.quaint.2017.02.018

Fichtner, A., and Villaseñor, A. (2015). Crust and upper mantle of the western Mediterranean - constraints from full-waveform inversion. *Earth Planet Sci. Lett.* 428, 52–62. doi:10.1016/j.epsl.2015.07.038

Fitch, T. J. (1972). Plate convergence, transcurrent faults, and internal deformation adjacent to Southeast Asia and the western Pacific. *J. Geophys. Res.* 77, 4432–4460. doi:10.1029/jb077i023p04432

Fossen, H., and Tikoff, B. (1998). Extended models of transpression and transtension, and application to tectonic settings. *Geol. Soc. Spec. Publ.* 135, 15–33. doi:10.1144/GSL.SP.1998.135.01.02

Galindo-Zaldivar, J., Ercilla, G., Estrada, F., Catalán, M., d'Acremont, E., Azzouz, O., et al. (2018). Imaging the growth of recent faults: the case of 2016–2017 seismic sequence sea bottom deformation in the Alboran Sea (western Mediterranean). *Tectonics* 37, 2513–2530. doi:10.1029/2017tc004941

Giaconia, F., Booth-Rea, G., Ranero, C. R., Gràcia, E., Bartolome, R., Calahorrano, A., et al. (2015). Compressional tectonic inversion of the Algero-Balearic basin: latemost Miocene to present oblique convergence at the Palomares margin (Western Mediterranean). *Tectonics* 34 (7), 1516–1543. doi:10.1002/2015tc003861

Gil, A., Gallart, J., Diaz, J., Carbonell, R., Torne, M., Levander, A., et al. (2014). Crustal structure beneath the Rif Cordillera, North Morocco, from the RIFSIS wide-angle reflection seismic experiment. *Geochem. Geophys. Geosyst.* 15, 4712–4733. doi:10.1002/2014gc005485

Gomez, F., Nemer, T., Tabet, C., Khawlie, M., Meghraoui, M., and Barazangi, M. (2007). "Strain partitioning of active transpression within the Lebanese restraining bend of the dead sea fault (Lebanon and SW Syria)," in *Tectonics of strike-slip restraining and releasing bends*. Editors W. D Cunninham and P. Mann (London, UK: Geological Society), 285–303.

Gràcia, E., Bartolomé, R., Lo Iacono, C., Moreno, X., Stich, D., Martínez-Diaz, J. J., et al. (2012). Acoustic and seismic imaging of the active Adra fault (NE Alboran Sea): in search for the source of the 1910 Adra earthquake. *Nat. Hazards Earth Syst. Sci.* 12, 3255–3267. doi:10.5194/nhess-12-3255-2012

Gràcia, E., Pallàs, R., Soto, J. I., Comas, M., Moreno, X., Masana, E., et al. (2006). Active faulting offshore SE Spain (Alboran Sea): implications for earthquake hazard assessment in the southern Iberian Margin. *Earth Planet Sci. Lett.* 241, 734–749. doi:10.1016/j.epsl.2005.11.009

Gràcia, E., Grevemeyer, I., Bartolomé, R., Perea, H., Martínez-Loriente, S., Gómez de la Peña, L., et al. (2019). Earthquake crisis unveils the growth of an incipient continental fault system. *Nat. Commun.* 10, 3482. doi:10.1038/s41467-019-11064-5

Grevemeyer, I., Gràcia, E., Villaseñor, A., Leuchters, W., and Watts, A. B. (2015). Seismicity and active tectonics in the Alboran Sea, Western Mediterranean: constraints from an offshore-onshore seismological network and swath bathymetry data. *J. Geophys. Res. Solid Earth* 120, 8348–8368. doi:10.1002/2015JB012073.

Gutscher, M.-A., Dominguez, S., Westbrook, G. K., Le Roy, P., Rosas, F., Duarte, J. C., et al. (2012). The Gibraltar subduction: a decade of new geophysical data. *Tectonophysics* 574–575, 72–91. doi:10.1016/j.tecto.2012.08.038

Gutscher, M.-A., Malod, J., Rehault, J.-P., Contrucci, I., Klingelhoefer, F., Mendes-Victor, L., et al. (2002). Evidence for active subduction beneath Gibraltar. *Geol.* 30, 1071–1074. doi:10.1130/0091-7613(2002)030<1071:efasbg>2.0.co;2

Hartzell, S. H. (1978). Earthquake aftershocks as Green's functions. *Geophys. Res. Lett.* 5, 1–4. doi:10.1029/gl005i001p00001

IGN (2016). Informe de la actividad sísmica en el Mar de Alborán. Available at: http://www.ign.es/web/resources/noticias/Terremoto_Alboran.pdf (Accessed May 19, 2020).

Kagan, Y. Y. (2007). Simplified algorithms for calculating double-couple rotation. *Geophys. J. Int.* 171, 411–418. doi:10.1111/j.1365-246x.2007.03538.x

Kariche, J., Meghraoui, M., Timoulali, Y., Cetin, E., and Toussaint, R. (2018). The Al Hoceima earthquake sequence of 1994, 2004, and 2016: stress transfer and poroelasticity in the Rif and Alboran Sea region. *Geophys. J. Int.* 212, 42–53. doi:10.1093/gji/ggx385

Kase, Y., and Day, S. M. (2006). Spontaneous rupture processes on a bending fault. *Geophys. Res. Lett.* 33, L10302. doi:10.1029/2006GL025870

Kikuchi, M., and Kanamori, H. (1991). Inversion of complex body waves-III. *Bull. Seismol. Soc. Am.* 81, 2335–2350.

King, G., and Nábělek, J. (1985). Role of fault bends in the initiation and termination of earthquake rupture. *Science* 228, 984–987. doi:10.1126/science.228.4702.984

King, G., Klinger, Y., Bowman, D., and Tapponnier, P. (2005). Slip-partitioned surface breaks for the M_w 7.8 2001 Kokoxili earthquake, China. *Bull. Seismol. Soc. Am.* 95, 731–738. doi:10.1785/0120040101

Kobayashi, T., Morishita, Y., and Yarai, H. (2017). SAR-revealed slip partitioning on a bending fault plane for the 2014 Northern Nagano earthquake at the northern Itoigawa–Shizuoka tectonic line. *Tectonophysics* 733, 85–99. doi:10.1016/j.tecto.2017.12.001

Koulali, A., Ouazar, D., Tahayt, A., King, R. W., Vernant, P., Reilinger, R. E., et al. (2011). New GPS constraints on active deformation along the Africa-Iberia plate boundary. *Earth Planet Sci. Lett.* 308, 211–217. doi:10.1016/j.epsl.2011.05.048

Lafosse, M., d'Acremont, E., Rabaute, A., Estrada, F., Jollivet-Castelot, M., Vazquez, J. T., et al. (2020). Plio-quaternary tectonic evolution of the southern margin of the Alboran basin (western Mediterranean). *Solid Earth* 11, 741–765. doi:10.5194/se-11-741-2020

Lafosse, M., d'Acremont, E., Rabaute, A., Mercier de Lépinay, B., Tahayt, A., Ammar, A., et al. (2017). evidence of quaternary transtensional tectonics in the nekor basin (NE Morocco). *Basin Res.* 29 (4), 470–489. doi:10.1111/bre.12185

Lo, Y.-C., Yue, H., Jianbao, S., Li, Z., and Mingjia, L. (2019). The 2018 M_w 6.4 Hualien earthquake: dynamic slip partitioning reveals the spatial transition from mountain building to subduction. *Earth Planet Sci. Lett.* 524, 115729. doi:10.1016/j.epsl.2019.115729

Lomax, A., Virieux, J., Volant, P., and Berge, C. (2000). "Probabilistic earthquake location in 3D and layered models: introduction of a Metropolis-Gibbs method and comparison with linear locations," in *Advances in seismic event location thurber*. Editors C. H. Thurber and N. Rabinowitz (Amsterdam, Netherlands: Kluwer), 101–134.

Lonergan, L., and White, N. (1997). Origin of the Betic-Rif mountain belt. *Tectonics* 16, 504–522. doi:10.1029/96tc03937

López-Comino, J. A., Mancilla, F., Morales, J., and Stich, D. (2012). Rupture directivity of the 2011, M_w 5.2 lorca earthquake (Spain). *Geophys. Res. Lett.* 39, L03301. doi:10.1029/2011gl050498

López-Comino, J. A., Stich, D., Ferreira, A., and Morales, J. (2015). Extended fault inversion with random slipmaps: a resolution test for the 2012 M_w 7.6 Nicoya, Costa Rica earthquake. *Geophys. J. Int.* 202, 77–93. doi:10.1093/gji/ggv235

López-Comino, J. A., Stich, D., Morales, J., and Ferreira, A. (2016). Resolution of rupture directivity in weak events: 1D versus 2D source parameterizations for the 2011, M_w 4.6 and 5.2 Lorca earthquakes, Spain. *J. Geophys. Res.* 121, 6608–6626. doi:10.1002/2016JB013227

Mai, P. M., and Beroza, G. C. (2002). A spatial random-field model to characterize complexity in earthquake slip. *J. Geophys. Res.* 107 (B11), 2308. doi:10.1029/2001JB000588

Mancilla, F. d. L., and Díaz, J. (2015). High resolution Moho topography map beneath Iberia and Northern Morocco from receiver function analysis. *Tectonophysics* 663, 203–211. doi:10.1016/j.tecto.2015.06.017

Mancilla, F. d. L., Heit, B., Morales, J., Yuan, X., Stich, D., Molina-Aguilera, A., et al. (2018). A STEP fault in Central Betics, associated with lateral lithospheric tearing at the northern edge of the Gibraltar arc subduction system. *Earth Planet Sci. Lett.* 486, 32–40. doi:10.1016/j.epsl.2018.01.008

Mancilla, F., Stich, D., Berrocoso, M., Martin, R., Morales, J., Fernández-Ros, A., et al. (2013). Delamination in the betic range: deep structure, seismicity, and GPS motion. *Geology* 41, 307–310. doi:10.1130/G33733.1

Mann, P. (2007). "Global catalogue, classification and tectonic origins of restraining- and releasing bends on active and ancient strike-slip fault systems." in *Tectonics of strike-slip restraining and releasing bends*. Editors W. D Cunninham and P Mann (London, UK: Geological Society), 13–142.

Martín, R., Stich, D., Morales, J., and Mancilla, F. (2015). Moment tensor solutions for the Iberian-Maghreb region during the IberArray deployment (2009–2013). *Tectonophysics* 663, 261–274. doi:10.1016/j.tecto.2015.08.012

Martínez-García, P., Comas, M., Lonergan, L., and Watts, A. B. (2017). From extension to shortening: tectonic inversion distributed in time and space in the Alboran sea, western Mediterranean. *Tectonics* 36, 2777–2805. doi:10.1002/2017tc004489

Martínez-García, P., Comas, M., Soto, J. I., Lonergan, L., and Watts, A. B. (2013). Strike-slip tectonics and basin inversion in the western Mediterranean: the post-Messinian evolution of the Alboran Sea. *Basin Res.* 25, 361–387. doi:10.1111/bre.12005

Martínez-García, P., Soto, J. I., and Comas, M. (2011). Recent structures in the Alboran Ridge and Yusuf fault zones based on swath bathymetry and sub-bottom profiling: evidence of active tectonics. *Geo Mar. Lett.* 31, 19–36. doi:10.1007/s00367-010-0212-0

McCaffrey, R. (1996). Slip partitioning at convergent plate boundaries of SE Asia. *Geol. Soc. Spec. Publ.* 106, 3–18. doi:10.1144/GSL.SP.1996.106.01.02

McClay, K., and Bonora, M. (2001). Analog models of restraining stepovers in strike-slip fault systems. *Am. Assoc. Pet. Geol. Bull.* 85, 233–260.

Platt, J. P., and Vissers, R. L. M. (1989). Extensional collapse of thickened continental lithosphere: a working hypothesis for the Alboran Sea and Gibraltar arc. *Geology* 17, 540–543. doi:10.1130/0091-7613(1989)017<0540:ecotcl>2.3.co;2

Medina, F., and Cherkaoui, T.-E. (2017). The south-western Alboran earthquake sequence of January-March 2016 and its associated Coulomb stress changes. *Ojer* 06 (1), 35–54. doi:10.4236/ojer.2017.61002

Molina-Aguilera, A., Mancilla, F., Morales, J., Stich, D., Yuan, X., and Heit, B. (2019). Connection between the Jurassic oceanic lithosphere of the Gulf of Cádiz and the Alboran slab imaged by Sp receiver functions. *Geology* 47, 227–230. doi:10.1130/G45654.1

Molnar, P., and Houseman, G. A. (2004). The effects of buoyant crust on the gravitational instability of thickened mantle lithosphere at zones of intracontinental convergence. *Geophys. J. Int.* 158, 1134–1150. doi:10.1111/j.1365-246x.2004.02312.x

Nabavi, S. T., Alavi, S. A., Mohammadi, S., Ghassemi, M. R., and Frehner, M. (2017). Analysis of transpression within contractional fault steps using finite-element method. *J. Struct. Geol.* 96, 1–20. doi:10.1016/j.jsg.2017.01.004

Nielsen, S. B., and Leon, K. (1998). The equivalent strength of geometrical barriers to earthquakes. *J. Geophys. Res.* 103, 9953–9965. doi:10.1029/97jb03293

Olaiz, A. J., Muñoz-Martín, A., de Vicente, G., Vegas, R., and Cloetingh, S. (2009). European continuous active tectonic strain-stress Map. *Tectonophysics* 474, 33–40. doi:10.1016/j.tecto.2008.06.023

Palano, M., González, P. J., and Fernández, J. (2013). Strain and stress fields along the Gibraltar Orogenic Arc: constraints on active geodynamics. *Gondwana Res.* 23 (3), 1071–1088. doi:10.1016/j.gr.2012.05.021

Palomeras, I., Thurner, S., Levander, A., Liu, K., Villasenor, A., Carbonell, R., et al. (2014). Finite-frequency Rayleigh wave tomography of the western Mediterranean: mapping its lithospheric structure. *Geochem. Geophys. Geosyst.* 15, 140–160. doi:10.1002/2013GC004861

Perea, H., Gràcia, E., Martinez Loriente, S., Bartolomé, R., Gómez de la Peña, L., Mol, B., et al. (2018). Kinematic analysis of secondary faults within a distributed shear-zone reveals fault linkage and increased seismic hazard. *Mar. Geol.* 399, 23–33. doi:10.1016/j.margeo.2018.02.002

Pérouse, E., Vernant, P., Chéry, J., Reilinger, R., and Simon, M. (2010). Active surface deformation and sub-lithospheric processes in the western Mediterranean constrained by numerical models. *Geology* 38, 823–826. doi:10.1130/g30963.1

Rosenbaum, G., Lister, G., and Duboz, C. (2002). Reconstruction of the tectonic evolution of the western Mediterranean since the oligocene. *J. Virtual Explor.* 8, 107–130. doi:10.3809/jvirtex.2002.00053

Royden, L. H. (1993). Evolution of retreating subduction boundaries formed during continental collision. *Tectonics* 12, 6299638. doi:10.1029/92tc02641

Rueda, J., and Mezcua, J. (2005). Near-real-time seismic moment-tensor determination in Spain. *Seismol Res. Lett.* 76, 455–465. doi:10.1785/gssrl.76.4.455

Rutter, E., Faulkner, D., and Burgess, R. (2012). Structure and geological history of the Carboneras Fault Zone, SE Spain: part of a stretching transform fault system. *J. Struct. Geol.* 45, 68–71. doi:10.1016/j.jsg.2012.08.009

Santos-Bueno, N., Fernández-García, C., Stich, D., Mancilla, F., Rose, M., Antonio, M.-A., et al. (2019). Focal mechanisms for subcrustal earthquakes beneath the Gibraltar arc. *Geophys. Res. Lett.* 46, 2534–2543. doi:10.1029/2018GL081587

Serpelloni, E., Vannucci, G., Pondrelli, S., Argnani, A., Casula, G., Anzidei, M., et al. (2007). Kinematics of the western Africa–Eurasia plate boundary from focal mechanisms and gps data. *Geophys. J. Int.* 25, 10. doi:10.1111/j.1365-246X.2007.03367.x

Soto, J. I., Fernández-Ibáñez, F., Fernández, M., and García-Casco, A. (2008). Thermal structure of the crust in the Gibraltar Arc: influence on active tectonics in the Western Mediterranean. *Geochem. Geophys. Geosyst.* 9. doi:10.1029/2008GC002061

Soumaya, A., Ben Ayed, N., Rajabi, M., Meghraoui, M., Delvaux, D., Kadri, A., et al. (2018). Active faulting geometry and stress pattern near complex strike-slip systems along the Maghreb region: constraints on active convergence in the western Mediterranean. *Tectonics* 37, 3148–3173. doi:10.1029/2018tc004983

Spakman, W., Maria, V. C., van den Berg, A., and van Hinsbergen, D. J. J. (2018). Puzzling features of western Mediterranean tectonics explained by slab dragging. *Nat. Geosci.* 11, 211. doi:10.1038/s41561-018-0066-z

Spakman, W., and Wortel, R. (2004). "A tomographic view on western mediterranean geodynamics," in *The TRANSMED atlas: the Mediterranean*

region from crust to mantle. Editors W. Cavazza and F. M. Roure, Spakman, W., MStampfli, G., and , P. A.Ziegler (Berlin, Germany: Springer), 31–52.

Stich, D., Ammon, C. J., and Morales, J. (2003a). Moment tensor solutions for small and moderate earthquakes in the Ibero-Maghreb region. *J. Geophys. Res.* 108, 2148. doi:10.1029/2002JB002057

Stich, D., Serpelloni, E., Mancilla, F. L., and Morales, J. (2006). Kinematics of the Iberia-Maghreb plate contact from seismic moment tensors and GPS observations. *Tectonophysics* 426, 295–317. doi:10.1016/j.tecto.2006.08.004

Stich, D., Mancilla, F. L., Baumont, D., and Morales, J. (2005). Source analysis of the M_w 6.3 2004 Al Hoceima earthquake (Morocco) using regional apparent source time functions. *J. Geophys. Res.* 110, B06306. doi:10.1029/2004JB003366

Stich, D., Batlló, J., Morales, J., Macià, R., and Dineva, S. (2003b). Source parameters of theM_w = 6.1 1910 Adra earthquake (southern Spain). *Geophys. J. Int.* 155, 539–546. doi:10.1046/j.1365-246x.2003.02059.x

Stich, D., Mancilla, F., and Morales, J. (2005). Crust-mantle coupling in the Gulf of Cadiz (SW-Iberia), geophysical research letters, 32. *Geophys. Res. Lett.* 32, L13306. doi:10.1029/2005GL023098

Stich, D., Martínez-Solares, J. M., Custódio, S., Batlló, J., Martín, R., Teves-Costa, P., et al. (2019). "Seismicity of the Iberian Peninsula. In: Geology of Iberia: a geodynamic approach," in *Seismicity of the iberian peninsula*. Editors C. Quesada, and J. T. Oliveira (Cham, Switzerland: Springer), 11–32.

Thingbaijam, K. K. S., Mai, P. M., and Goda, K. (2017). New empirical earthquake source-scaling laws. *Bull. Seismol. Soc. Am.* 107, 2225–2246. doi:10.1785/0120170017

Torne, M., Fernàndez, M., Menchu, C., and Juan, I. S. (2000). Lithospheric structure beneath the Alboran Basin: results from 3D gravity modeling and tectonic relevance. *J. Geophys. Res.* 105, 3209–3228. doi:10.1029/1999jb900281

Ulrich, T., Gabriel, A., Ampuero, J., and Xu, W. (2019). Dynamic viability of the 2016 M_w 7.8 Kaikōura earthquake cascade on weak crustal faults. *Nat. Commun.* 10, 1213. doi:10.1038/s41467-019-09125-w

Vallée, M., Charléty, J., Ferreira, A. M. G., Delouis, B., and Vergoz, J. (2011). SCARDEC: a new technique for the rapid determination of seismic moment magnitude, focal mechanism and source time functions for large earthquakes using body-wave deconvolution. *Geophys. J. Int.* 184, 338–358. doi:10.1111/j.1365-246x.2010.04836.x

van der Woerd, J., Anne-Sophie, M., Yann, K., Ryerson, F. J., Gaudemer, Y., and Tapponnier, P. (2002). The 14 november 2001, M_w = 7.8 Kokoxili earthquake in northern Tibet (qinghai province, China). *Seismol Res. Lett.* 73 (2), 125–135. doi:10.1785/gssrl.73.2.125

van der Woerd, J., Dorbath, C., Ousadou, F., Dorbath, L., Delouis, B., Eric, J., et al. (2014). The Al Hoceima M_w 6.4 earthquake of 24 February 2004 and its aftershocks sequence. *J. Geodyn.* 77, 89–109. doi:10.1016/j.jog.2013.12.004

van Hinsbergen, D. J. J., Vissers, R. L. M., Spakman, W. (2014). Origin and consequences of western Mediterranean subduction, rollback, and slab segmentation. *Tectonics* 33, 393–419. doi:10.1002/2013tc003349

Vergés, J., and Fernàndez, M. (2012). Tethys-Atlantic interaction along the Iberia-Africa plate boundary: the Betic-Rif orogenic system. *Tectonophysics* 579, 144–172. doi:10.1016/j.tecto.2012.08.032

Vernant, P., Fadil, A., Mourabit, T., Ouazar, D., Koulali, A., Davila, J. M., et al. (2010). Geodetic constraints on active tectonics of the Western Mediterranean: implications for the kinematics and dynamics of the Nubia-Eurasia plate boundary zone. *J. Geodyn.* 49 (3), 123–129. doi:10.1016/j.jog.2009.10.007

Wenzheng, Y., and Hauksson, E. (2011). Evidence for vertical partitioning of strike-slip and compressional tectonics from seismicity, focal mechanisms, and stress drops in the east Los Angeles basin area, California. *Bull. Seismol. Soc. Am.* 101, 964–974. doi:10.1785/0120100216

Xu, W., Feng, G., Meng, L., Zhang, A., Ampuero, J. P., Bürgmann, R., et al. (2018). Transpressional rupture cascade of the 2016 M_w 7.8 Kaikoura earthquake, New Zealand. *J. Geophys. Res. Solid Earth* 123, 2396–2409. doi:10.1002/2017jb015168

Yamini-Fard, F., Hatzfeld, D., Tatar, M., and Mokhtari, M. (2006). Microearthquake seismicity at the intersection between the Kazerun fault and the main recent fault (Zagros, Iran). *Bar Int.* 166, 186–196. doi:10.1111/j.1365-246x.2006.02891.x

Yu, G., Wesnousky, S. G., and Ekström, G. (1993). Slip partitioning along major convergent plate boundaries. *Pure Appl. Geophys.* 140, 183–210. doi:10.1007/bf00879405

Conflict of Interest: The authors declare that the research was conducted in the absence of any commercial or financial relationships that could be construed as a potential conflict of interest.

frontiers in Earth Science

ORIGINAL RESEARCH
published: 09 December 2020
doi: 10.3389/feart.2020.579398

Fault System-Based Probabilistic Seismic Hazard Assessment of a Moderate Seismicity Region: The Eastern Betics Shear Zone (SE Spain)

Octavi Gómez-Novell[1], Julián García-Mayordomo[2], María Ortuño[1], Eulàlia Masana[1] and Thomas Chartier[3]*

[1]RISKNAT Group, Geomodels Research Institute, Departament de Dinàmica de La Terra I de L'Oceà, Facultat de Ciències de La Terra, Universitat de Barcelona, Barcelona, Spain, [2]Departamento de Riesgos Geológicos, Instituto Geológico y Minero de España, Tres Cantos, Spain, [3]Hazard Team, Global Earthquake Model Foundation, Pavia, Italy

Including faults as seismogenic sources in probabilistic seismic hazard assessments (PSHA) has turned into a common practice as knowledge of active faults is improving. Moreover, the occurrence of earthquakes in multi-fault ruptures has evidenced the need to understand faults as interacting systems rather than independent sources. We present a PSHA for the Southeastern Spain obtained by including the faults of a moderate seismicity region, the Eastern Betics Shear Zone (EBSZ) in SE Spain, as the main seismogenic sources in two separate source models, one considering background seismicity. In contrast with previous studies in Spain, earthquake occurrence of the EBSZ system is modeled considering different hypotheses of multi-fault ruptures at the whole fault system scale and weighted in a logic tree. We compare the hazard levels with those from an area source PSHA and a previous fault-based approach. The results show a clear control of the EBSZ faults in the seismic hazard for all return periods, increasing drastically the hazard levels in the regions close to the fault traces and influencing up to 20 km farther with respect to the area source PSHA. The seismic hazard is dependent on the fault slip rates as peak ground accelerations and territorial extension of the fault influence appear higher around the Alhama de Murcia and Carboneras faults, while lower slip rate faults (Palomares Fault) show minor contribution to the hazard. For the return period of 475 years and near-fault locations, our models are more consistent with the ground motion values reached in the 2011 Mw 5.2 Lorca event than the building code or national seismic hazard map, which suggest that our fault system-based model performs more accurate estimations for this return period. Fault data, mainly slip rates, and its uncertainties have a clear impact on the seismic hazard and, for some faults, the lack of detailed paleoseismic studies can compromise the reliability of the hazard estimations. This, together with epistemic uncertainties concerning the background seismicity, are key discussion points in the present study, having an impact on further research and aiming to serve as a case example for other low-to-moderate seismicity regions worldwide.

Keywords: seismic hazard assessment, source modelling, fault system, peak ground acceleration, near-fault, moderate magnitude earthquakes, paleoseismology, Eastern Betics Shear Zone

OPEN ACCESS

Edited by:
Jorge Miguel Gaspar-Escribano, Polytechnic University of Madrid, Spain

Reviewed by:
Chong Xu, National Institute of Natural Hazards, China
Sergio Molina-Palacios, University of Alicante, Spain

****Correspondence:***
Octavi Gómez-Novell
octgomez@ub.edu

Specialty section:
This article was submitted to Geohazards and Georisks, a section of the journal Frontiers in Earth Science

Received: *02 July 2020*
Accepted: *27 October 2020*
Published: *09 December 2020*

Citation:
Gómez-Novell O, García-Mayordomo J, Ortuño M, Masana E and Chartier T (2020) Fault System-Based Probabilistic Seismic Hazard Assessment of a Moderate Seismicity Region: The Eastern Betics Shear Zone (SE Spain). Front. Earth Sci. 8:579398. doi: 10.3389/feart.2020.579398

INTRODUCTION

The use of geological data in probabilistic seismic hazard assessment (PSHA) has become increasingly important, since seismic catalogs do not usually extend for more than a few centuries. This is a very short time window for characterizing the occurrence of major events in regions of moderate seismic activity, even in areas where the catalogs extend for more than 1,000 years such as SE Spain or Portugal (García-Mayordomo, 2005; Vilanova and Fonseca, 2007, respectively). Traditionally, geological data and fault data have been used to characterize the occurrence of major, maximum or characteristic events (Wesnousky, 1986; Schwartz and Coppersmith, 1984). Maximum events usually have a very low impact in seismic hazard for the return periods considered in conventional building (e.g., 475 years) and so this type of fault-based PSHA has been regarded in studies interested in long return periods (e.g., critical infrastructures). However, there is increasing awareness of the fact that low-to-moderate magnitude events (Mw 4.0–6.0) are also able to produce significant damage, especially at sites located on top or very close to fault sources (e.g., 2011 Mw 5.2 Lorca earthquake in SE Spain; Alguacil et al., 2014). In this context, the identification and characterization of active faults as seismogenic sources able to produce all the range of earthquake magnitudes become critical tasks in the PSHA of moderate active regions.

For this reason, in accordance with the increasing availability and refinement of paleoseismic and geological studies, the incorporation of fault data in PSHA has become an important part of the source modeling aiming to estimate earthquake activity beyond the coverage of seismic catalogs. The use of faults in PSHA is a well-established practice worldwide (Frankel, 1995; WGCEP, 2003; Stirling et al., 2012; Woessner et al., 2015). In most of these cases, faults are modeled as independent sources following a characteristic earthquake model (Youngs and Coppersmith, 1985; Wesnousky, 1986) or a Gutenberg-Richter distribution (Gutenberg and Richter, 1945; Bungum, 2007).

During earthquakes, faults can rupture in very complex configurations involving several structures simultaneously and even with contrasting kinematics or geometries. Earthquakes such as the 2010 Mw 7.2 Cucapah (Fletcher et al., 2014), the 2012 Mw 8.6 Sumatra (Zhang et al., 2012) or the 2016 Mw 7.8 Kaikoura (Little et al., 2018) are good examples. Accordingly, in the recent years seismic hazard modelers and practitioners have developed new approaches for modeling faults as complex and interacting sources in seismic hazard. Including this complexity has demonstrated to be a turning point to model fault processes in PSHA. Approaches like UCERF-3 (Field et al., 2014) or the recent SHERIFS (Chartier et al., 2019) are emerging methodologies whose principle is modeling earthquake occurrence considering scenarios of multi-fault ruptures for source characterization in PSHA. In both cases fault rupturing is treated as an aleatory variable, whose occurrence is assumed to be linked to the randomness of the seismic process.

Most fault-based PSHA approaches are usually carried out in high seismicity regions with advanced paleoseismic fault knowledge to perform such studies (e.g., Stirling et al., 2012; Field et al., 2014 for New Zealand and California, respectively). Conversely, the scarcity of paleoseismic and geological slip rate data on faults has been one of the major challenges faced by PSHA analysts in low-to-moderate seismicity regions, such as Western Europe (e.g., Spain). In Spain, PSHA has been classically modeled using area sources following Cornell (1968) and McGuire (1976) methodology, as it is the case of the latest national seismic hazard map (IGN-UPM, 2013). In that work, fault information has been included as a complementary criterion for defining area sources and, particularly, the fault length, which is used to set the upper bound of the magnitude-frequency distribution in each one. In this map, faults have not been included as seismogenic sources in the calculations due to the incompleteness of the fault data across the country. However, that is not the case of SE Spain, the most seismically active area in the country (García-Mayordomo et al., 2007) and where one of the longest active fault systems is located: the Eastern Betics Shear Zone (EBSZ).

The EBSZ is a ~400 km long transpressive tectonic corridor of mainly reverse and left-lateral strike-slip kinematics with a characteristic NE-SW sigmoidal trend (Bousquet, 1979; De Larouzière et al., 1988; Silva et al., 1993) (**Figure 1B**). It absorbs most part of the NW-SE convergence from the Eurasian and Nubian plates in Iberia (4–6 mm/yr; DeMets et al., 2015). Although it is a moderate seismicity region with rates lower than other European regions (e.g., Italy or Greece), many destructive earthquakes with intensities up to IX-X (I_{EMS98}) have affected this region since historical times (e.g., 1518 VIII-IX Vera, 1522 VIII-IX Almería, 1674 VIII Lorca, 1804 VIII-IX Dalías-Berja, 1829 IX-X Torrevieja; Silva et al., 2014) (**Figure 1B**). More recently, moderate magnitude earthquakes have taken place (e.g., 1993–1994 Adra seismic series; the 1999 Mw 4.8 Mula, 2002 Mw 5.0 Bullas; the 2005 Mw 4.8 La Paca seismic series; Rodríguez-Escudero et al., 2014), including the damaging 2011 Mw 5.2 Lorca earthquake (e.g., Martínez-Díaz et al., 2012a).

Over the last two decades, the EBSZ tectonic context has motivated many geological, geodetic and paleoseismic studies, especially since the 2011 Lorca earthquake (e.g., Moreno, 2011; Ortuño et al., 2012; Echeverria et al., 2013; Insua-Arévalo et al., 2015; Martín-Banda et al., 2015; Ferrater, 2016; Martínez-Díaz et al., 2018; Masana et al., 2018). Accordingly, PSHA studies focused here have successfully incorporated faults as independent sources either considering a characteristic earthquake or Gutenberg-Richter model (García-Mayordomo, 2005; García-Mayordomo et al., 2007; Rivas-Medina et al., 2018). However, no PSHA study has yet modeled fault sources from the perspective of multi-fault ruptures, so the present constitutes the first one in this matter. The incorporation of this variable representing fault behaviors widely observed in nature is seen as a step toward more realistic approximations of fault modeling and seismic hazard in the EBSZ.

The aim of our paper is to explore a fault-based PSHA in a moderate seismicity region as it is the EBSZ in SE Spain, using a state-of-the-art fault source modeling approach that implements fault data as inputs, considers multi-fault rupture possibilities at the whole fault system scale and treats them as aleatory

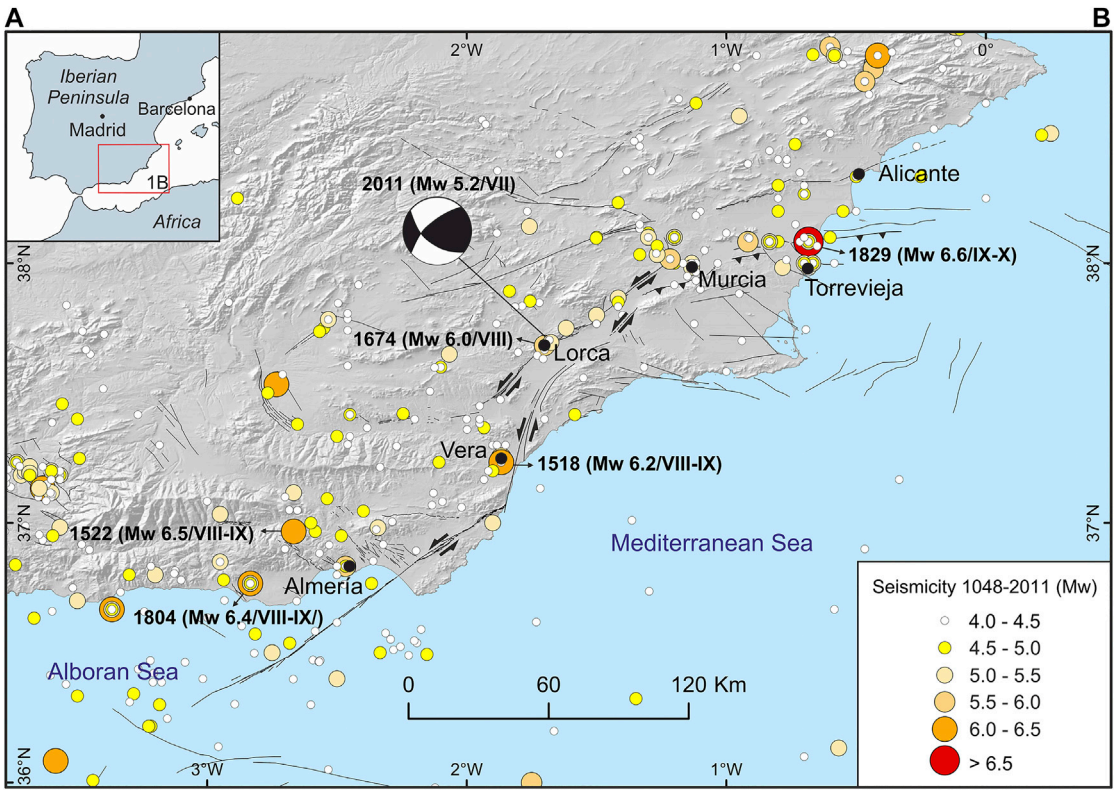

FIGURE 1 | (A) Location of the study region within the Iberian Peninsula; **(B)** Seismotectonic context of SE Spain with the seismicity of Mw ≥ 4.0 from the 1048–2011 period (IGN-UPM, 2013), including the most damaging historical earthquakes of the region pointed with an arrow. The focal mechanism of the 2011 Mw 5.2 Lorca earthquake is extracted from the Instituto Geográfico Nacional agency (IGN, 2011). Intensity scale is European Macroseismic Scale (EMS98). The main traces of the Quaternary active faults are extracted from QAFI v.3. Database (IGME, 2015a; García-Mayordomo et al., 2017).

uncertainty. We use the source models computed and published in a previous article (Gómez-Novell et al., 2020). There, an emergent methodology (SHERIFS; Chartier et al., 2019) is applied to perform a source modeling of the EBSZ by computing magnitude-frequency distributions (MFDs) at the scale of the whole EBSZ fault system considering different scenarios of fault ruptures. The adequacy of the models is evaluated and ranked in terms of their agreement with the regional seismic catalog and paleoseismic data. For the present study, we adapt and re-compute these models, weight them in a logic tree and use them as inputs for the hazard calculations. We compute seismic hazard using the OpenQuake engine (Pagani et al., 2014), evaluate the influence of the selected fault source models on the seismic hazard and compare them with previous PSHA approaches in SE Spain. We also place the interest of our study for other low-to-moderate seismicity regions worldwide.

GEOLOGICAL SETTING

The EBSZ is a main active fault system in SE Spain. The faults affect Quaternary sedimentary deposits and generate geomorphological and morphotectonic features (e.g., fluvial channel offsets, fault scarps) along a left-lateral transpressive corridor, evidencing tectonic activity during the recent Quaternary (De Larouzière et al., 1988; Silva et al., 1993). The onset of the neotectonic activity under the nowadays compressional transpressive regime in the Eastern Betics occurred during the Late Miocene (e.g., Rodríguez-Fernández et al., 2012). From SW to NE these faults are (**Figure 2A**): Carboneras Fault (CF), Palomares Fault (PF), Alhama de Murcia Fault (AMF), Los Tollos Fault (LTF), Carrascoy Fault (CAF) and Bajo Segura Fault (BSF) (Bousquet, 1979; Silva et al., 1993). Characterizing the role and activity degree of these faults during the Quaternary has been the aim of many geomorphological, paleoseismic and geodetic studies in the last two decades, making the EBSZ one of the most studied fault systems in the Iberian Peninsula so far.

The EBSZ is one of the most seismically active regions of the Western Mediterranean and it has hosted many damaging earthquakes since the historical period. Most damaging earthquakes in the area have been attributed to the main faults forming the EBSZ. Important examples are the 1518 Vera earthquake, attributed to PF (e.g., García-Mayordomo, 2005), the 1522 Almería earthquake to CF (e.g., Reicherter and Hübscher, 2007), the 1674 Lorca earthquake to AMF (Martínez-Díaz et al., 2018), the 1829 Torrevieja earthquake to BSF (e.g., Alfaro et al., 2012) or, in recent times, the 2011 Lorca

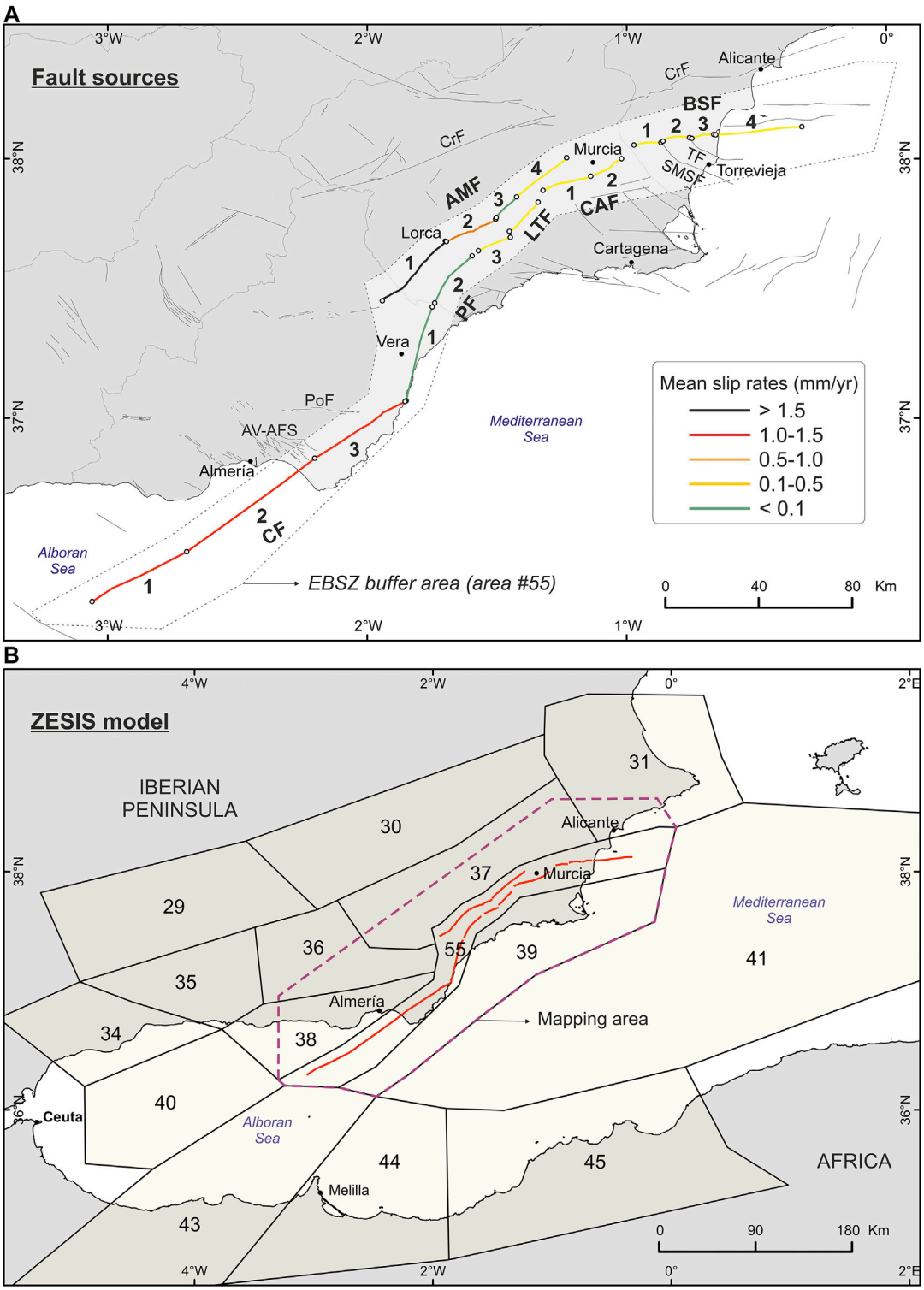

FIGURE 2 | (A) Simplified traces of the major faults of the EBSZ considered in the fault source modeling of this study. Each fault is marked by an abbreviation and each section of the respective fault has a number assigned (ID). The parameters of each fault ID are indicated in **Table 1**. CF: Carboneras Fault; PF: Palomares Fault; LTF: Los Tollos Fault; CAF: Carrascoy Fault; BSF: Bajo Segura Fault; AMF: Alhama de Murcia Fault. The fault traces are presented following a colored scale according to their estimated mean slip rate values (**Table 1**). Other relevant secondary faults not included in the fault source modeling are also indicated. CrF: Crevillente Fault; SMSF: San Miguel de Salinas Fault; TF: Torrevieja Fault; AV-AFS: Andarax Valley and El Alquián Fault System; PoF: Polopos Fault. The buffer area of the EBSZ is indicated around the faults by a dotted line; **(B)** Seismogenic area sources considered in this study from the ZESIS model (IGME, 2015b; García-Mayordomo, 2015), whose parameters are indicated in **Table 3**. A dashed purple line delineates the mapping area where the seismic hazard is computed. The location of the main faults of the EBSZ from **Figure 2A** within its buffer area (#55) are indicated.

earthquake to AMF (Martínez-Díaz et al., 2012a) (**Figure 1B**). Some of these historical earthquakes are known to have ruptured the surface, as recently unveiled for the 1674 Lorca earthquake (Martínez-Díaz et al., 2018). Importantly, most of the instrumental seismicity in the EBSZ occurs relatively at shallow depths and focal mechanisms are consistent with the strike-slip and reverse character of the main faults (Stich et al., 2007, Stich et al., 2010).

Paleoseismic trenching and detailed geomorphological studies have demonstrated the capability of the system to generate large magnitude earthquakes (Mw > 6.0) and allowed to constrain critical seismic parameters (slip rate) in several of the main faults: AMF, CF, CAF or LTF (**Table 1**). The slip rate ranges between 1.0 and 1.7 mm/yr for AMF, according to estimates from Ferrater et al. 2017; 1.0 and 1.3 mm/yr for CF (Moreno, 2011); 0.37 ± 0.08 mm/yr for CAF (Martín-Banda et al., 2015) and 0.12–0.17 mm/yr for LTF (Insua-Arévalo et al., 2015). Conversely, PF, BSF and the northern termination of AMF have not been studied using detailed paleoseismic trenching analysis and their slip rate estimations are based mainly on long-term displacements of geological markers (e.g., Herrero-Barbero et al., 2020), which may be affected by larger uncertainties.

Continued tectonic activity in the EBSZ is also inferred from the current geodetic data. The obtained velocities of AMF-PF combined (1.5 ± 0.3; Echeverria et al., 2013) are consistent with the paleoseismic and geomorphologic slip rates of AMF, suggesting a main role of this fault into the deformation. Similarly, geodetic velocities of CF are in agreement with its geological slip rates (1.3 ± 0.2 mm/yr; Echeverria et al., 2015). In the NE end of the EBSZ GPS data indicates a partitioning of the deformation into lateral and reverse components, and compatibility with the kinematics of CAF and BSF, respectively (Borque et al., 2019).

DATA AND METHODS FOR THE HAZARD ASSESSMENT

Source Modeling

In this work, we consider two types of seismogenic sources that are combined: faults and area sources (**Figure 2**). Fault sources are modeled within the EBSZ and area sources are modeled outside of it. The resulting composite source models are not a classical hybrid approach where faults accommodate earthquakes from a cutoff magnitude and area sources accommodate background seismicity (e.g., García-Mayordomo et al., 2007); instead, in our models both fault and area sources are modeled following a Gutenberg-Richter (GR) MFD for all the magnitude range (Mw ≥ 4.0), as we explain in the following sections.

Fault Sources

Fault sources are modeled exclusively for the EBSZ. The source modeling performed is based on the SHERIFS methodology as published in Gómez-Novell et al., 2020, where the first step of a source modeling for PSHA is performed at the EBSZ: the feasibility of multi-fault rupture scenarios is analyzed and earthquake occurrence on faults is modeled at the whole fault system scale following a GR distribution.

SHERIFS (Chartier et al., 2019) is a method of fault source modeling that uses geological fault data as inputs to calculate fault earthquake rates. Among its advantages, 1) it allows to model earthquake occurrence in fault systems as a whole and considering sets of multi-fault ruptures; 2) is well adapted for regions, such as the EBSZ, where geological data is the prime source of information for characterizing faults. In this sense, SHERIFS requires: i) a 3D geometry of the fault system, ii) slip rate of each fault source, iii) a target shape MFD of the fault system (e.g., GR) which is based on published studies or seismic databases and iv) a scaling relationship to estimate the upper bound of the MFD distribution (Mmax). The slip rate of each fault is treated as a budget and it is consumed following an iterative process to fit the target MFD, in which the different rupture scenarios are computed separately until the budget of the limiting faults is exhausted. The resulting MFDs are representative of the whole fault system and are weighted in a logic tree according to their consistency with data from the regional seismic catalog and paleoseismic studies (see Gómez-Novell et al., 2020 for details on how SHERIFS is applied to compute and weight the fault system MFDs).

Only the faults of the EBSZ have been considered for the SHERIFS modeling, because they are the ones absorbing most of the plate convergence motion in SE Spain (Bousquet, 1979; Silva et al., 1993) and because they show the best geological and paleoseismic data available in the region for seismogenic source modeling. The main fault sources are shown in **Figure 2A**. Faults outside of the EBSZ or secondary faults have not been considered mainly due to lack of enough quality data (e.g., Crevillente Fault, Torrevieja Fault, San Miguel de Salinas Fault, El Andarax Valley Fault, El Alquián Fault System, among others; **Figure 2A**).

For the fault source modeling we adopted the fault data and characteristics used in Gómez-Novell et al., 2020, obtained from available and mainly published data. Faults are sectioned (**Figure 2A**) according to segmentation in literature based on their geometry, geomorphic expression, seismicity, kinematics and activity evidence. Offshore segmentation of CF is adopted from Moreno (2011), onshore CF and PF from García-Mayordomo, 2005. Segmentation of CAF is based on Martín-Banda et al., 2015, BSF on Alfaro et al., 2012 and AMF on Martínez-Díaz et al., 2012b. These sections are then linked to create multi-fault rupture scenarios of the different fault rupture hypothesis explored in this study (see **Table 2**). Fault traces are simplified with respect to the ones depicted in the Quaternary Active Faults database of Iberia (QAFI v.3) (IGME, 2015a; García-Mayordomo et al., 2017) for the purposes of this study and multi-branch sections are simplified to a single one. This is consistent with studies that suggest that fault traces likely link at depth (e.g., CF: Moreno, 2011; AMF: Martínez-Díaz et al., 2012b). Dip, kinematics and seismogenic depths (**Table 1**) are extracted from the QAFI database, which compiles data from published studies on these faults. Fault slip rates are directly extracted from published works and, in selected cases, from unpublished data or expert opinion, as specified in **Table 1** (see also the Appendix in

TABLE 1 | Fault input data used to calculate the earthquake rates of the EBSZ fault system with the SHERIFS approach in the fault source modeling. The sources of information and references from where fault slip rate data are extracted are specified (see details in Gómez-Novell et al., 2020). Other fault parameters are extracted from the QAFI v.3. Database (IGME, 2015a; García-Mayordomo et al., 2017). See the map in **Figure 2A** for the location of each fault section mentioned in the table. Adapted from Gómez-Novell et al., 2020.

Fault name	Fault section ID	Dip (°)	Main kinematics	Seismogenic depth range (km)	Fault length (km)	Net slip rate (mm/yr)			Type of information used to infer slip rate (references) and time frame covered
						Min	Mean	Max	
Carboneras (CF)	CF–1	90	Strike-slip	0–11	39.1	1.1	1.2	1.3	Displaced fluvial channels, trench offsets and GPS data (Moreno, 2011; Echeverria et al., 2015); since Pliocene–Holocene
	CF–2	90	Strike-slip	0–11	59.6	1.1	1.2	1.3	
	CF–3	90	Strike-slip	0–11	39.5	1.1	1.2	1.3	
Palomares (PF)	PF–1	90	Strike-slip	0–8	41.1	0.01	0.04	0.08	Tectonic uplift of terraces and alluvial fans (García-Mayordomo, 2005 and references); since
	PF–2	90	Strike-slip	0–8	24.0	0.01	0.04	0.08	Lower-Middle Pleistocene
	PF-3	90	Strike-slip	0–8	12.0	0.04	0.1	0.16	Analogy with LTF and PF-2 (expert opinion)
Los Tollos (LTF)	LTF	85	Strike-slip	0–8	16.0	0.06	0.16	0.25	Recurrence intervals in paleoseismic trenches (Insua-Arévalo et al., 2015); since 12 kyr
Carrascoy (CAF)	CAF-1	70	Reverse	0–12	18.2	0.29	0.37	0.45	Restoration of deformed units, consistent with offsets in trenches (Martín-Banda et al., 2015); since 209.1 kyr
	CAF–2	85	Strike-slip	0–12	13.1	0.48	0.53	0.58	Tectonic uplift (unpublished research by Martín-Banda et al., 2015); since 160 kyr
Bajo Segura (BSF)	BSF–1	60	Reverse	1.0–12	11.6	0.25	0.33	0.41	Tectonic uplift (Alfaro et al., 2012); since 2–3 kyr
	BSF–2	60	Reverse	1.0–12	9.2	0.25	0.33	0.41	
	BSF–3	60	Reverse	1.0–12	7.7	0.12	0.2	0.3	
	BSF–4	60	Reverse	1.0–12	29.3	0.12	0.2	0.3	Assigned by analogy to BSF-3 section (expert opinion). Consistent with GPS data (Borque et al., 2019)
Alhama de Murcia (AMF)	AMF–1	70	Strike-slip	0–12	34.1	1.6	1.65	1.7	Displaced fluvial channels (Ferrater, 2016; Ferrater et al., 2017); since 200 kyr for AMF-1, 30 kyr for AMF-2
	AMF–2	70	Strike-slip	0–12	19.7	0.8	1.0	1.2	
	AMF–3	70	Strike-slip	0–12	11.3	0.01	0.07	0.1	Based on expert opinion from QAFI database (IGME, 2015a)
	AMF-4	45	Strike-slip	0–12	23.9	0.07	0.2	0.37	Tectonic uplift (Herrero-Barbero, 2016); since late Miocene-Pliocene

TABLE 2 | Fault sections involved in the maximum fault and multi-fault ruptures envisaged in each hypothesis of the fault source modeling. See **Figure 2A** for the location of the mentioned fault sections. The maximum magnitude ranges of each hypothesis of the FM and FM_bg models are indicated. These ranges result from the random sampling of different fault ruptures allowed within a same hypothesis by the SHERIFS methodology.

Hypothesis/fault rupture scenario	Maximum expected multi-fault ruptures	Maximum magnitude range (Mw)
1	Only single fault section ruptures are allowed	6.6–7.3
2	–CF–1 + CF–2 + CF–3 –PF–1 + PF–2 + PF–3 –LTF –CAF–1 + CAF–2 –BSF–1 + BSF–2 + BSF–3 + BSF–4 –AMF–1 + AMF–2 + AMF–3 + AMF–4	6.7–7.5
3	–CF-1 + CF–2 + CF–3 + PF–1 + PF–2 + PF–3 –LTF + CAF–1 + CAF–2 + BSF–1 + BSF–2 + BSF–3 + BSF–4 –AMF–1 + AMF–2 + AMF–3 + AMF–4	6.9–7.7
4	–CF–1 + CF–2 + CF–3 + PF–1 + PF–2 + PF–3 + LTF + CAF–1 + CAF–2 + BSF–1 + BSF–2 + BSF–3 + BSF–4 –AMF–1 + AMF–2 + AMF–3 + AMF–4	7.1–7.8

Gómez-Novell et al., 2020 for specific details on the criteria followed for slip rate selection, especially for unpublished work).

The fault-system source model considered is spatially constrained to the limits of area source #55 of the ZESIS national scale area source model (García-Mayordomo, 2015), available at the ZESIS database (IGME, 2015b), which was delineated as the envelope of the surface projection of the EBSZ fault planes and characterized by the seismic record within (IGN-UPM, 2013). In this present approach, earthquake occurrence in this area (hereinafter called EBSZ buffer area) is completely modeled on faults from the geological fault data shown in **Table 1**. However, we also consider the alternative possibility that a small portion of the seismic moment release in the EBSZ is due to unknown faults (e.g., blind, unmapped) different from the considered ones, by modeling background seismicity in one of our models. Although the EBSZ buffer area is a narrow area constrained to the surface projection of well-known faults, it cannot be precluded that some activity may occur on unknown active faults not considered in this study (**section 3.1.1.2**).

Therefore, two alternative fault source models are envisaged within the EBSZ buffer area, one exclusively considering the faults' activity (FM model) and another one considering a fraction of background seismic activity overlapped with the faults (FM_bg model).

Fault Sources: FM Model

For this model, earthquake rates in the EBSZ buffer area are modeled only on the EBSZ fault system, assuming that all seismicity over Mw 4.0 occurring within its limits is related to these faults. This fault-system source model is based on the results of the modeling performed in Gómez-Novell et al., 2020 without any additional modifications. Four scenarios or hypotheses of fault and multi-fault ruptures involving from single fault sections to nearly the whole system (hypothesis 1 to 4; **Table 2**) are modeled using SHERIFS and the fault data in **Table 1** to obtain different GR distributions for the whole EBSZ system. In order to incorporate the epistemic uncertainty in the input data, the GR of each scenario is composed by 20 GR curves resulting from 20 computations exploring random values of input parameters, i.e., fault slip rates, b-values and Mmax of GR distribution. Slip rates are explored within the ranges provided in **Table 1** and the b-values within the 0.8–1.2 range (**Figure 3**), whose mean (1.0) is in agreement with the one of the EBSZ in the ZESIS model (García-Mayordomo, 2015). The Mmax is set following Wells and Coppersmith, 1994 for rupture area and all kinematics. The resulting earthquake occurrences of each scenario (80 GR curves for all four scenarios) are expressed as the seismicity rates of each fault-rupture involved in that scenario (see Gómez-Novell et al., 2020 for details on the criteria applied to define the fault rupture scenarios, the input parameters used for the modeling with SHERIFS and the calculations). Furthermore, in the previous paper, the agreement of the resulting MFDs with the earthquake distribution from the catalog and paleoseismic record is analyzed and a qualitative ponderation of each hypothesis for PSHA is proposed, which we use here to set our logic tree weighting scheme (**section 3.3** and **Figure 3**). All these outputs are used to build the source models in hazard calculations.

Fault Sources Including Background Seismicity: FM_bg Model

We introduced, by means of a background ratio, a modification respect to the previous FM model in order to consider that part of the seismic moment release in the EBSZ could be due to unknown active faults apart from the main ones. The rest of the input parameters are the same as mentioned for the FM model.

The background ratio is a parameter from SHERIFS that allows sharing a fraction (percentage) of the seismicity rate of a given magnitude between the faults and the background or the area directly surrounding the faults. For instance, a background ratio of 70% for Mw 4.0 means that 70% of the total seismicity rate of Mw 4.0 is modeled on faults and 30% as background seismicity. Therefore, the occurrence rates of the selected magnitude range on the faults are lowered with respect to the FM model consistently with the ratio adopted, avoiding double-counting of seismicity and respecting the GR distribution (see Chartier et al., 2019 for details on the

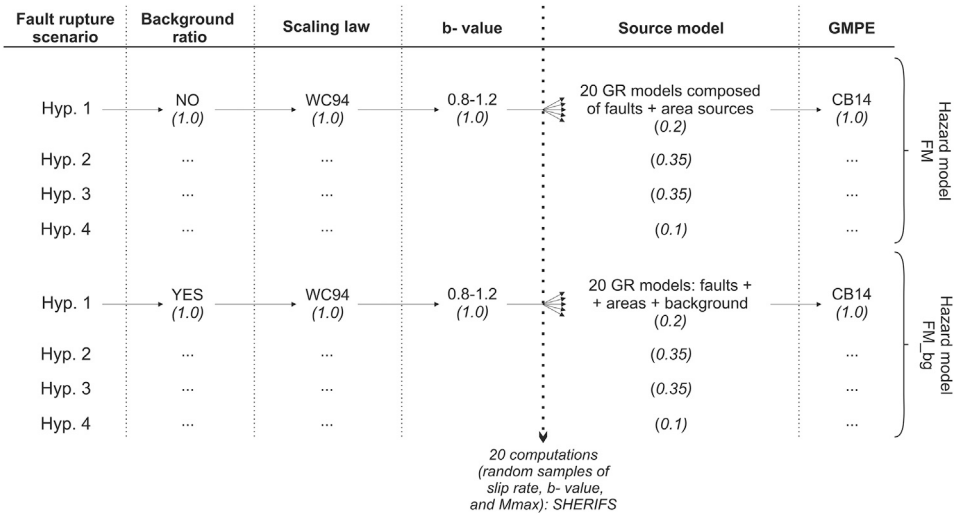

FIGURE 3 | Logic tree schemes followed in this study for both FM and FM_bg source models. The weights (over 1) of each branch in the logic tree are indicated in brackets. Hyp.: hypothesis; WC94: Wells and Coppersmith, 1994; CB14: Campbell and Bozorgnia, 2014.

background ratio). In our case, the background area corresponds to the EBSZ buffer area, whose seismic potential is then not only defined by the faults contained but also by the background seismicity as an area source.

Chartier et al., 2019 recognize that the user may rely on expert opinion to set this ratio due to its difficulty but propose to use the distance between earthquake epicenters and faults as possible criteria to set it. We cannot follow this approach due to large location errors at the EBSZ: 67% of the Mw ≥ 4.0 earthquakes are previous to year 1962 (IGN-UPM, 2013) and hence show epicentral errors larger than 10 km or even 20 km (García-Mayordomo, 2005). We then set the background ratios following expert opinion but based on criteria from seismicity data of the region as we explain below. These ratios are 70%, 80%, 90%, 95% for Mw 4.0, 4.5, 5.0, and 5.5, respectively, which represent the percentage of the total EBSZ seismic moment that is actually modeled on faults for each 0.5 magnitude bin. The remaining is modeled as background in the area of about 10 km around the faults.

The selected percentages are consistent with the fact that most of the instrumental earthquakes of Mw ≥ 4.0 in the EBSZ have occurred in the modeled faults. This is supported by the location of recent moderate earthquakes (e.g., 2011 Lorca seismic series related to AMF; Martínez-Díaz et al., 2012b) and by the fact that focal mechanisms of seismicity are in agreement with the main faults of the region (Stich et al., 2007, Stich et al., 2010). On the other hand, the GR distributions modeled with SHERIFS for the EBSZ in Gómez-Novell et al., 2020 predict good fits with the regional seismic catalog for most of the rupture scenarios in the Mw < 6.0 magnitude range. This supports that known faults might be responsible of most of the seismicity within the EBSZ. Consequently, we select ratios that do not modify significantly the GR distributions, hence that do not invalidate the proposed logic tree weighting in that study and comparison can be directly done with the FM model.

Only events in the range of Mw 4.0–5.5 are affected by the background ratio in our study, because earthquakes this size rarely cause surface rupture (Biasi and Weldon, 2006) and thus, they may occur in unrecognized faults and unadvertised by the paleoseismic studies. Mw > 6.0 earthquakes though, are considered to be produced in larger faults with geomorphic expression so they are modeled exclusively on the known EBSZ faults.

Area Sources

Outside the bounds of the EBSZ buffer area we consider the area sources of ZESIS model (García-Mayordomo, 2015). The area sources considered here are (**Figure 2B**): #29, #30, #31, #34, #35, #36, #37, #38, #39, #40, #41, #43, #44, #45 and, for the FM_bg model only, #55. These areas are all located within a radius of 50 km from the external boundary of the mapping area in order to account for the influence of seismogenic sources adjacent to the EBSZ buffer area (#55). The potential influence of farther sources is considered negligible for the purposes of this study. The earthquake occurrence in these areas is modeled according to GR distributions obtained in the frame of the project to update the national seismic hazard map of Spain (IGN-UPM, 2013), and their parameters (a and b-value, Mmin, Mmax; **Table 3**) are adopted here from the ZESIS database (IGME, 2015b). In the case of area #55, earthquake occurrence is controlled by the seismic moment assigned by the background ratios in each source model and following the target MFD of the faults (**section 3.1.1.2**). The area sources are added to the fault sources modeled with SHERIFS to build the different source models for the hazard calculations.

The characterization of the area sources is further completed defining a distribution of nodal planes and hypocentral depths in each area (OpenQuake manual v.3.7.1; GEM, 2019). The former controls the strike, dip and rake of earthquake ruptures inside the

TABLE 3 | Parameters of the area sources used for the area source model in this study. Mmin, Mmax (Mw range), a and b-values of the GR distribution are extracted from the ZESIS area source model (IGME, 2015b; García-Mayordomo, 2015). OpenQuake required parameters such as nodal planes are inferred from main fault orientations of the QAFI v.3. Database (IGME, 2015a; García-Mayordomo et al., 2017) or focal mechanisms of the studies indicated in the table. Seismogenic depths are based on fault data compiled in the QAFI database.

ZESIS parameters				OpenQuake parameters					
Area source	Mw range (Mw)	GR parameters		Seismogenic depth (km)	Hypocentral depths (km)		Nodal planes		
		a	b		Depth (km)	Probability	Dip/rake/strike (º)	Probability	References
29	4.0–6.6	3.36	1.02	20	a) 5 b) 10	a) 0.5 b) 0.5	a) 90/180/060	a) 1.0	Mean fault orientations inferred from the QAFI database (IGME, 2015a)
30	4.0–5.0	3.84	1.26	11	a) 5 b) 10	a) 0.5 b) 0.5	a) 85/−140/125 b) 90/−140/040	a) 0.5 b) 0.5	
31	4.0–6.6	2.99	0.89	15	a) 5 b) 10	a) 0.5 b) 0.5	a) 90/30/065 b) 60/−90/330	a) 0.5 b) 0.5	
34	4.0–6.6	3.30	1.0	8	a) 5 b) 8	a) 0.5 b) 0.5	a) 70/5/151 b) 85/160/060 c) 88/−170/243 d) 80/−2/152	a) 0.25 b) 0.25 c) 0.25 d) 0.25	Focal mechanisms by Stich et al. (2010)
35	4.0–6.8	4.24	1.12	9	a) 5 b) 9	a) 0.5 b) 0.5	a) 60/−90/150 b) 60/−90/330	a) 0.5 b) 0.5	Mean fault orientations (QAFI)
36	4.0–6.5	3.08	0.98	9	a) 5 b) 9	a) 0.5 b) 0.5	a) 60/−90/150 b) 60/−90/330	a) 0.5 b) 0.5	
37	4.0–6.8	4.23	1.16	11	a) 5 b) 10	a) 0.5 b) 0.5	a) 90/30/240 b) 90/−135/325	a) 0.5 b) 0.5	
38	4.0–6.7	3.34	0.96	8	a) 5 b) 8	a) 0.5 b) 0.5	a) 60/−135/150	a) 1.0	
39	4.0–6.7	4.29	1.34	8	a) 5 b) 8	a) 0.5 b) 0.5	a) 90/180/100 b) 60/−90/140	a) 0.5 b) 0.5	
40	4.0–6.5	2.88	0.94	10	a) 5 b) 10	a) 0.5 b) 0.5	a) 23/135/120 b) 85/5/214	a) 0.5 b) 0.5	Fault orientations from QAFI database and focal mechanisms by Gràcia et al. (2019)
41	4.0–6.5	4.5	1.35	8	a) 5 b) 8	a) 0.5 b) 0.5	a) 90/180/120 b) 90/0/014	a) 0.5 b) 0.5	Mean fault orientations (QAFI)
43	4.0–7.0	4.23	1.07	11	a) 5 b) 10	a) 0.5 b) 0.5	a) 85/5/214 b) 84/175/124 c) 90/0/210 d) 45/85/070	a) 0.25 b) 0.25 c) 0.25 d) 0.25	Focal mechanisms by Stich et al. (2010) and Gràcia et al. (2019)
44	4.0–6.4	3.08	0.9	11	a) 5 b) 10	a) 0.5 b) 0.5	a) 90/170/104 b) 90/170/001	a) 0.5 b) 0.5	Mean fault orientations (QAFI)
45	4.0–7.3	2.96	0.8	11	a) 5 b) 10	a) 0.5 b) 0.5	a) 18/102/59 b) 73/86/226	a) 0.5 b) 0.5	Focal mechanisms by Stich et al. (2010)
55	Earthquake occurrence is modeled with SHERIFS for Mw 4.0–5.5 considering the seismic rates assigned by the background ratios and following the target MFD shape (b-value) of the EBSZ faults			12	a) 5 b) 8	a) 0.5 b) 0.5	a) 90/20/050 b) 60/90/080	a) 0.5 b) 0.5	Mean fault orientations (QAFI)

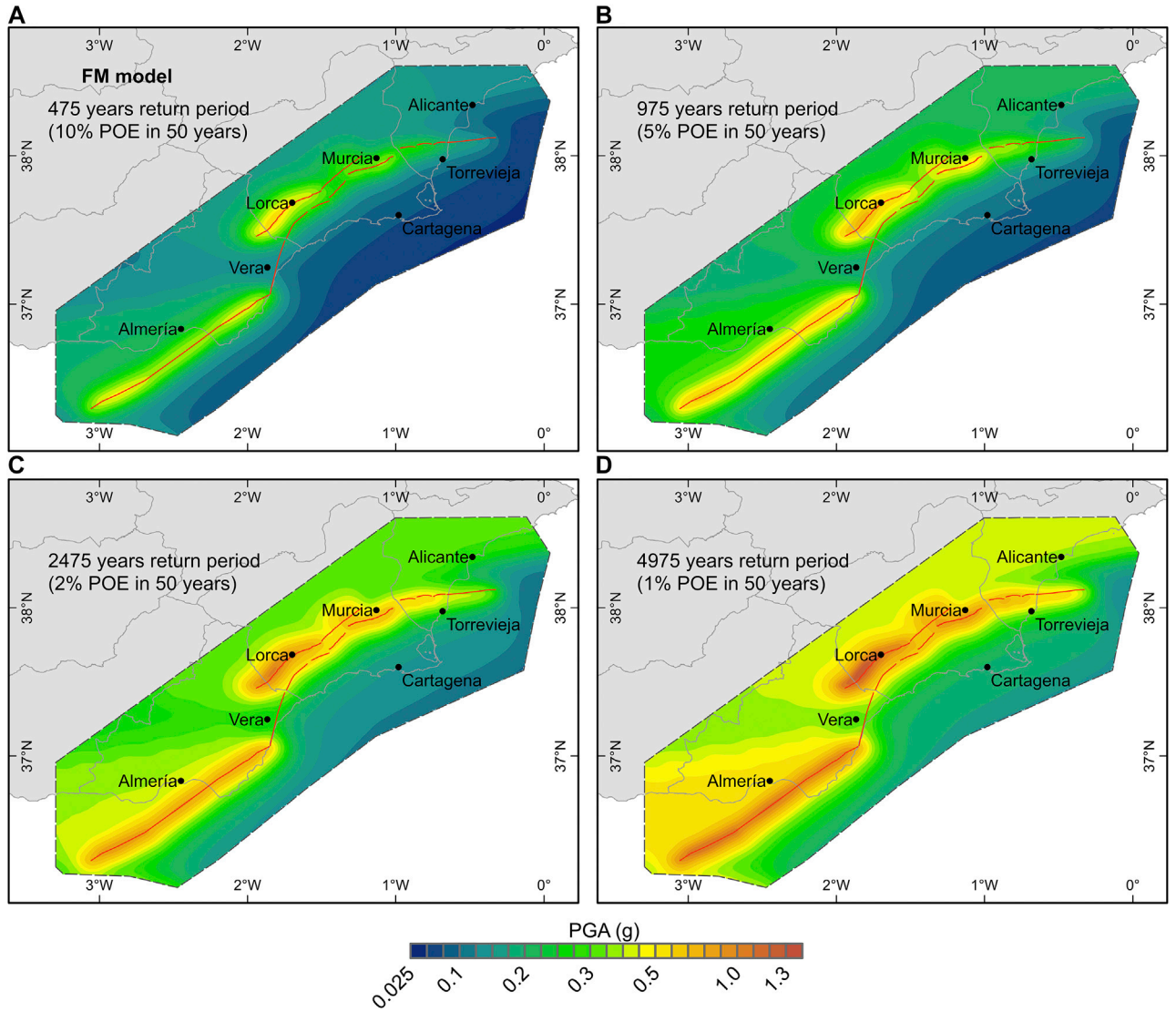

FIGURE 4 | (A) Mean hazard maps for PGA (g) of the FM model for the respective return periods (RPs) of 475 years; **(B)** 975 years; **(C)** 2,475 years and; **(D)** 4,975 years, equivalent to the probabilities of exceedance (POE) of 10%, 5%, 2%, and 1%, respectively. A common color scale is set for all return periods. The main cities in the region and the traces of the EBSZ faults considered are depicted in red. See **Figure 2A** for the names of each fault.

zone, while the latter controls the depth of the center of the ruptures. Nodal planes in each area are defined based on the predominant fault orientations from the QAFI v.3 database (IGME, 2015a), as well as by the distribution of focal mechanisms available in SE Spain and North-Africa (Stich et al., 2010), and the Alboran Sea (Gràcia et al., 2019) (**Table 3**). Eventually, a set of different nodal planes is defined for each area source representing each one the same probability of occurrence. Similarly, two equally probable hypocentral depths are defined for each source area (**Table 3**): the upper is set at 5 km and the lower between 8 and 10 km depending on the minimum common seismogenic depth of all faults contained in the area. The maximum seismogenic depth of the faults in the QAFI database defines the seismogenic depth for each area source.

Final Composite Seismogenic Source Models for Hazard Calculations

Two resulting composite source models are used for the calculations: FM + area sources and FM_bg + area sources. The "composite" term is used here to remark that each source model is composed by a fault source model and an area source model (**Figure 3**). The former sets the occurrence rates of all the fault ruptures envisaged in each fault rupture hypothesis modeled with SHERIFS within the EBSZ buffer area. The latter sets the occurrence rates of the different area sources considered outside the EBSZ buffer area and the background seismicity in the case of FM_bg model. The final models are referred by the distinctive fault source model name henceforth (i.e., FM and FM_bg). Because each of the four multi-fault rupture scenarios is composed of 20 different GR curves, a total of 80 input source

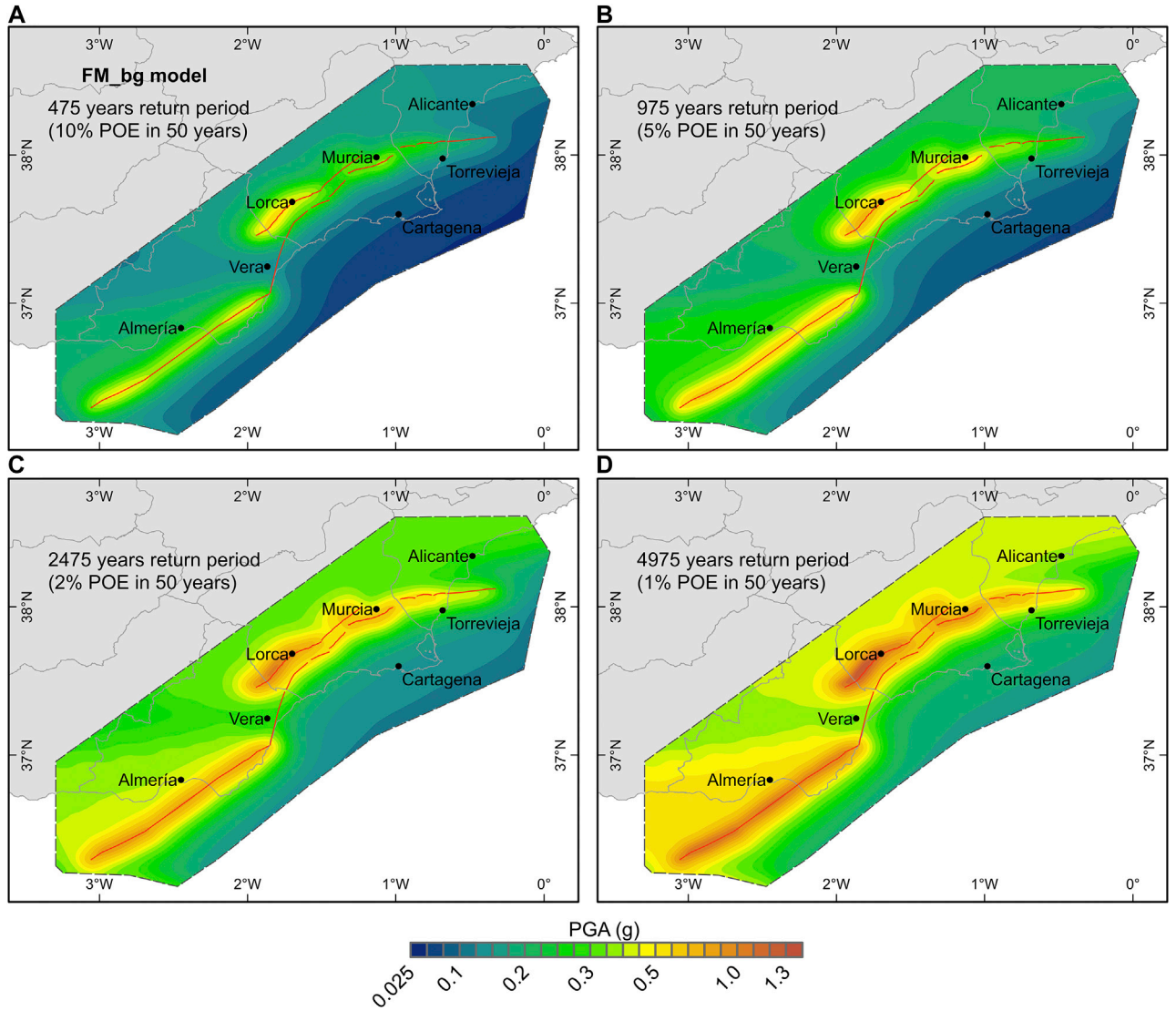

FIGURE 5 | (A) Mean hazard maps for PGA (g) of the FM_bg model for the return periods (RPs) of 475 years; **(B)** 975 years; **(C)** 2,475 years and; **(D)** 4,975 years, equivalent to the probabilities of exceedance (POE) of 10%, 5%, 2%, and 1%, respectively. A common color scale is set for all return periods. The main cities in the region and the traces of the EBSZ faults considered are depicted in red. See **Figure 2A** for the names of each fault.

models for OpenQuake compose both FM and FM_bg source models (**Figure 3**). The fault source part (e.g., earthquake rates, Mmax) is different for each 80 models because it depends on a) on the rupture scenario considered and b) the values of the input parameters explored randomly during the SHERIFS calculation. Each FM and FM_bg are computed separately in a different hazard calculation in order to better test and highlight the influence of including a background ratio, and to compare results more directly.

Ground Motion Prediction Equation

We selected the ground motion prediction equation (GMPE) derived by Campbell and Bozorgnia, 2014 from the PEER NGA project (Power et al., 2008). This equation is well adapted for fault-based PSHAs since it accounts for near-fault features such as fault geometry, style of faulting, depth of rupture and hanging wall effects. For the fault-based approach that we propose, this equation is then suitable to show the sensibility of the seismic hazard results to the fault source models. Additionally this equation is the one that Rivas-Medina et al., 2018 selected for a fault-based PSHA in SE Spain after an analysis of several GMPEs. According to the authors, this equation allowed better estimations of the expected accelerations in the study region considering the characteristics of the sources and the available data.

We acknowledge that considering a set of GMPEs is a normal practice in the attempt to capture the epistemic uncertainty related to ground motion. However, we consider just one GMPE to facilitate the detection of the impact of fault incorporation into PSHA and to be able to perform direct comparisons with

previous studies. In order to quantify the influence of the GMPE on the results related to the fault source model and compared to other GMPEs not sensible to near-fault effects, we perform a sensibility analysis to the FM model by using the Akkar et al., 2014 equation. This is the latest GMPE derived from pan-European databases and does not include fault parameters in its functional form apart from style of faulting as a dummy variable. The implications of this analysis are discussed in **section 5.3**.

Logic Trees Explored

Each source model is computed separately. Thus, two logic trees are explored in this study as depicted in **Figure 3**. For each logic tree, the four different hypotheses of multi-fault ruptures are considered in order to incorporate the epistemic uncertainty of earthquake occurrence on faults. Each rupture hypothesis constitutes a branch of the logic tree, weighted based on the analysis of the agreement with the seismic catalog and paleoseismic data performed in Gómez-Novell et al., 2020. That study concluded that hypotheses 2 and 3 were the ones with better agreement with the regional seismic catalog and paleoseismic data, followed by hypothesis 1 and lastly, hypothesis. 4. A better agreement implies a more suitable hypothesis for the study region. Accordingly, we assigned a weight of 35% to both hyp. 2 and 3, 20% to hyp. 1 and 10% to hyp. 4. Each hypothesis is composed by 20 GR curves, hence 20 input source models for OpenQuake that include a fault source model and an area sources model. The weight of each of the 20 branches or models that form a hypothesis equals 1/20 of the weight of the whole branch (**Figure 3**).

Hazard Calculations

Hazard calculations are performed using the OpenQuake engine (Pagani et al., 2014). We compute a set of mean hazard maps in terms of PGA as function of probabilities of exceedance of 10, 5, 2 and 1% in a time window of 50 years, which correspond to return periods (RPs) of 475-, 975-, 2,475- and 4,975-years, respectively (**Figures 4**, **5**). The region considered is depicted in **Figure 2B** and follows a 2 × 2 km grid, accounting for a total of 10,556 calculation points for each return period. This region is defined to comprise completely the EBSZ buffer area and include important cities of the region (Murcia, Lorca, Almería, Vera, Torrevieja, Alicante and Cartagena). To analyze fault influence, in the cities adjacent to the EBSZ faults (Murcia, Lorca, Almería, Vera, Torrevieja) we produce mean hazard curves in terms of PGA (**Figure 6**) and hazard disaggregation for distance-magnitude (**Figure 7** and **Supplementary material**). Soil conditions are always considered to be rock or hard soil (Vs30 = 760 m/s). The maximum distance considered for the hazard calculations is 100 km in order to better reproduce the near-fault related hazard of the EBSZ and because farther sources have negligible impact in the study area (see disaggregation results in **section 4.1**). Source input files of the hazard calculations including source models, GMPE, logic tree and calculation specifications are included in the **Supplementary material** of the article.

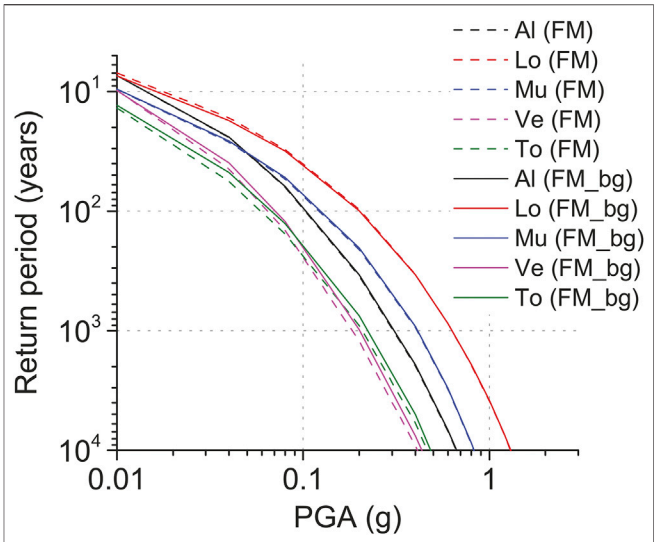

FIGURE 6 | Mean hazard curves for PGA (g) of the FM and FM_bg models in the cities of Almería (Al), Lorca (Lo), Murcia (Mu), Vera (Ve) and Torrevieja (To). Their location is indicated in the maps from **Figures 4**, **5**.

RESULTS

The results of the calculations are presented in mean hazard maps (**Figures 4**, **5**) and mean hazard curves for five cities of the region (**Figures 6**). Maps were obtained after interpolation using the natural neighbor approach from the OpenQuake outputs. A common colored scale has been set for all maps to facilitate comparison. Mean hazard curves for the cities of Murcia, Lorca, Almería, Vera, Torrevieja are also depicted in terms of PGA on rock (**Figure 6**). To test the influence of the different fault sources and the seismic background on the hazard, we computed hazard disaggregation of the FM_bg model for the magnitude-distance relationship. In **Figure 7**, we depict representative disaggregation results in three cities and for two RPs (475 and 2,475 years). For complete disaggregation, figures of all the cities considered in **Figure 6** and all four RPs are available the **Supplementary material**.

The results show a clear control of the EBSZ fault over the seismic hazard of SE Spain for all RPs, especially in the vicinity of faults (10–20 km). Slip rate values directly affect fault influence into the hazard because highest accelerations are located around faults with higher slip rates of the system, while lower slip rate faults have much less influence. The impact of the background into the models is very limited given the similarity of results from both FM and FM_bg.

Mean Hazard Maps and Disaggregation

Fault Influence

The mean hazard maps from both FM and FM_bg models (**Figures 4**, **5**) produce very similar results in terms of absolute hazard levels and distribution and increments between them are very low (**Figure 8**). The modeled EBSZ fault system exerts a clear control into the seismic hazard of SE Spain for all RPs, especially

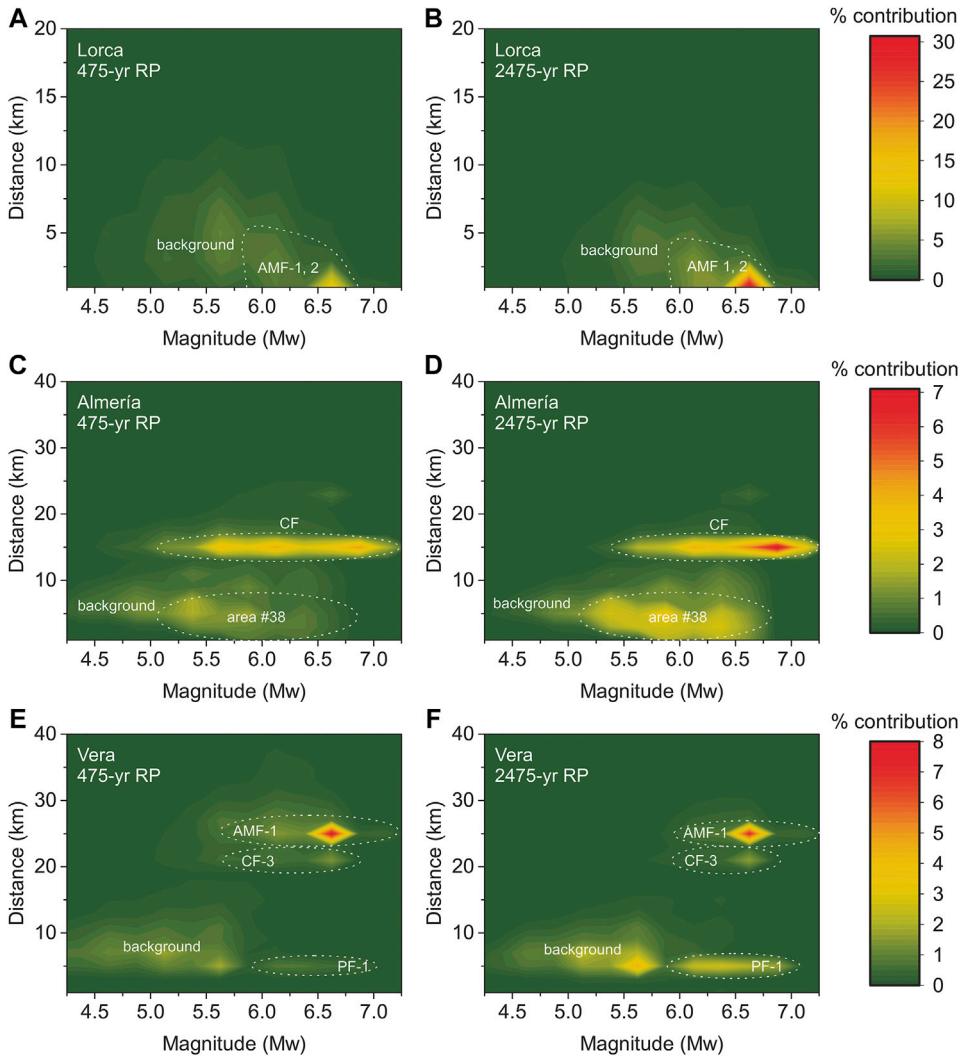

FIGURE 7 | (A) Hazard disaggregation for the magnitude-distance relationship of the FM_bg model in the cities of Lorca for the return periods of 475 years and; **(B)** 2,475 years; **(C)** Almería for 475 years and; **(D)** 2,475 years; **(E)** Vera for 475 years and; **(F)** 2,475 years. A common color scale is set for the two return periods representing each city. The main sources contributing to the hazard of each city and return period are highlighted. For disaggregation figures of all the cities in **Figure 6** and for the four return periods of 475, 975, 2,475, and 4,975 years, see the Supplementary Material of this paper.

noticeable in the near-fault regions, where maximum PGA values are located.

In both models, the maximum acceleration values range from 0.5–0.6 g for the 475 years RP to 1.2–1.3 g for the 4,975 years RP (**Figures 4**, **5**) and are located along the faults with higher slip rates. That is the case of the Southwestern termination of AMF, near Lorca (AMF-1 and 2) or CF near Almería, which have the highest slip rates of the system (>1.0 mm/yr; **Table 1** and **Figure 2A**). On the other hand, lower slip rate faults have minor influence in the hazard levels for all RPs, also depending on their slip rates. Mean hazard maps from both FM and FM_bg models (**Figures 4**, **5**, respectively) show that PF is the fault with less footprint on the hazard for all RPs, which is consistent with its slip rate being the lowest of all the system according to the available estimations (<0.1 mm/yr; **Table 1**). Other faults such as the Eastern termination of BSF (BSF-3 and 4), AMF-4 or LTF, have higher slip rates (~0.1–0.4 mm/yr; **Table 1**) but their influence to the hazard is limited compared to AMF-1, 2 or CF (**Figures 4**, **5**).

The hazard disaggregation of the FM_bg model (**Figure 7**) shows that all the contributions to the seismic hazard in a specific site are from sources located within a 20–30 km radius, suggesting that farther sources do not influence the hazard. Higher slip rate faults contribute the most to the seismic hazard values of the closer zones, while lower slip rate faults have very small contributions, even in the sites in their closest vicinity. In the cities of Lorca and Almería (**Figures 7A–D**), the magnitude-distance relationships that influence most the hazard coincide with the location of AMF-1 and 2, and CF-3, respectively, which are the fault sections with higher slip rates in the system (**Table 1**).

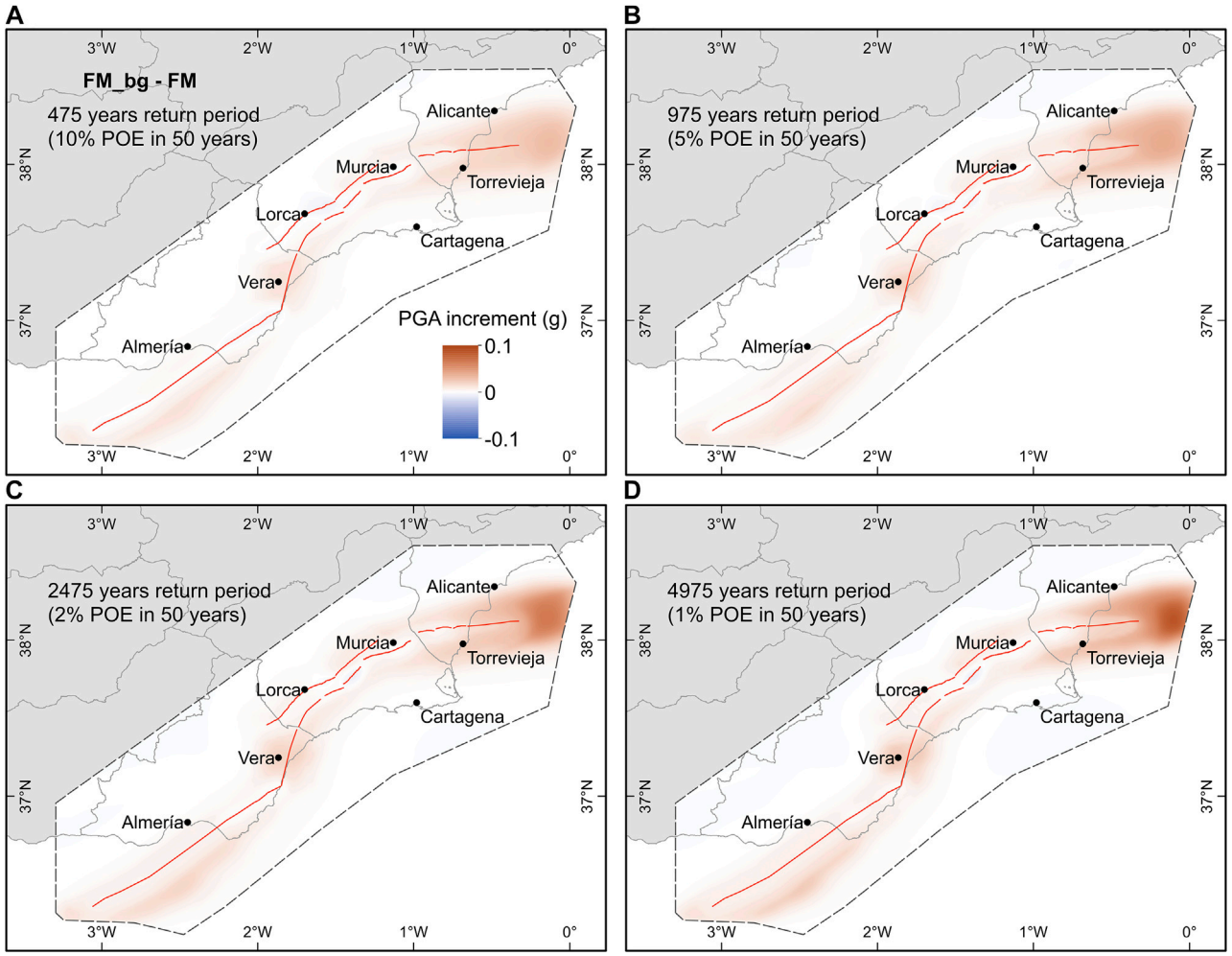

FIGURE 8 | (A) Difference (in g) of the mean hazard maps from the FM_bg model (**Figure 5**) respective to the FM model (**Figure 4**) for the return periods of 475 years; **(B)** 975 years; **(C)** 2,475 years, and; **(D)** 4,975 years. A common color scale is set for all return periods. The traces of the EBSZ faults considered are depicted in red.

Lorca is located <1 km from AMF in the limit between AMF-1 and 2, which explains the maximum influence from sources located between 1–5 km. These maximum AMF-1 and 2 contributions are in a tight Mw 6.5–6.75 range for both RPs (**Figures 7A**, **B**), which might suggest the controlling earthquakes in this city. Almería is located at ~15 km from CF-3, consistent with the distance of the source's maximum contribution. The higher distance of the fault from the city causes its contribution to be considerably lower than AMF-1 and hence other non-fault sources influence the hazard as well (**Figures 7C**, D). The contributions of CF-3 comprise a wider magnitude range (Mw 5.0–7.0) in the 475 years RP (**Figure 7C**), while they concentrate around Mw 6.5–7.0 in the 2,475 years RP (**Figure 7D**). Conversely, in zones such as Vera, located next to very low slip rate faults (i.e. PF), the main contributions to the seismic hazard are not from the closer faults, but from other farther faults (**Figures 7E**, F). In this city AMF-1 is the main contribution despite this fault being ~25 km farther, while PF is the least even for long RPs (**Figure 7F**).

A hanging wall effect can be observed in non-vertical dipping faults such as AMF, CAF or BSF (**Figures 4**, **5**). Such near-fault effect is more visible at longer RPs (i.e., 2,475 and 4,975 years), where PGAs for two selected sites at the same distance of a fault trace but on opposite sides, are higher on the hanging wall. A clear example is the transect perpendicular to AMF near the city of Lorca (**Figure 9E**). This is a significant observation for seismic hazard assessment in near-fault zones as we discuss in **section 5.1.1**.

Background Influence

The similarities between the mean hazard maps from the FM and FM_bg models suggest that adding a seismic activity background ratio in the FG_bg model produces minor changes to the final hazard results within the EBSZ buffer for any RP (**Figure 8**). In general, the background contributes to raise the hazard values with respect to the FM model, while the decreases are depreciable. PGA increments, especially for

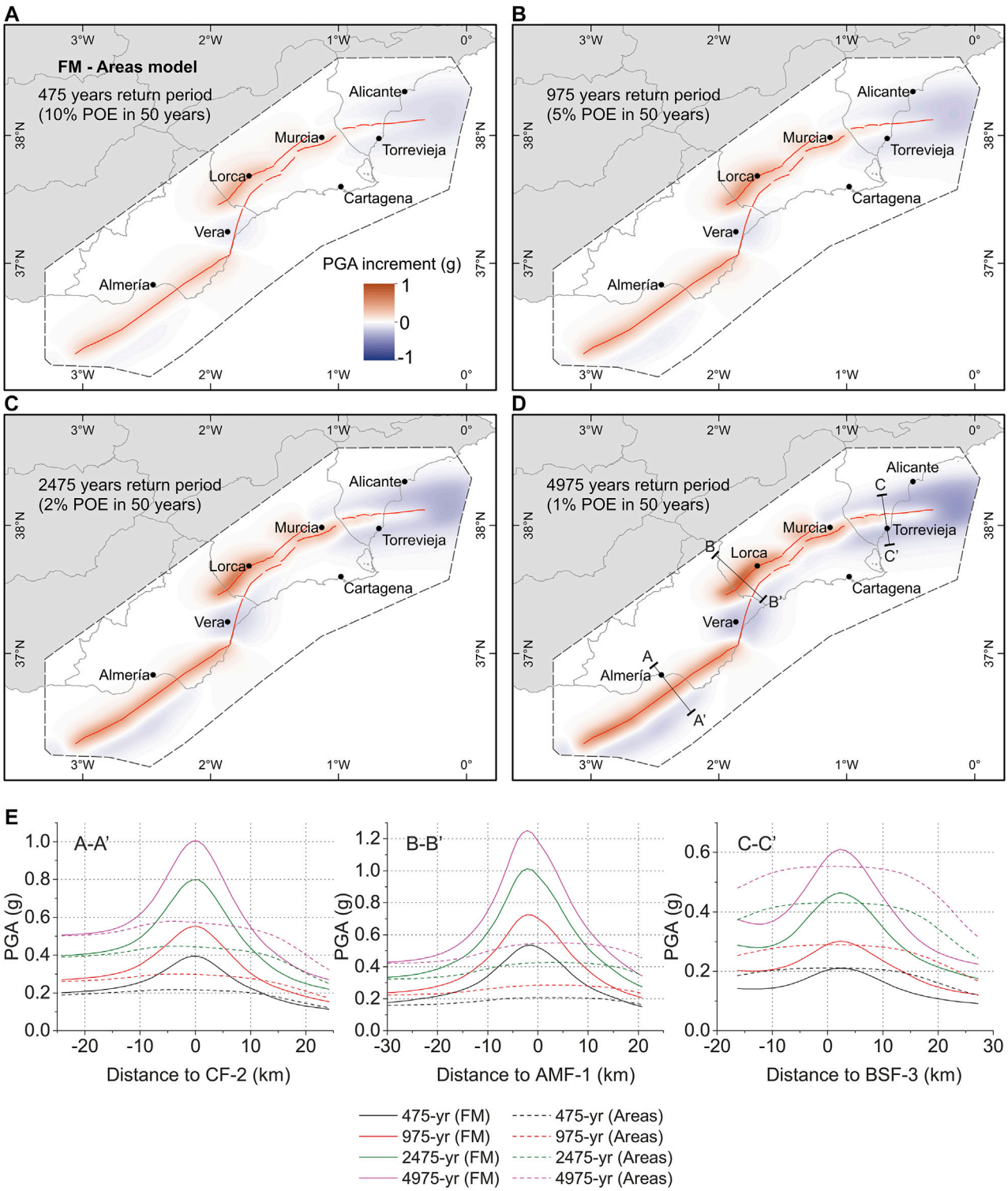

FIGURE 9 | (A) Difference (in g) of the mean hazard map from the FM model (**Figure 4**) respective to the mean hazard map using exclusively the ZESIS area source model (Areas model) and for the return periods of 475 years; **(B)** 975 years; **(C)** 2,475 years, and; **(D)** 4,975 years. The traces of the EBSZ faults considered are depicted in red. A common color scale is set for all return periods; **(E)** Cross sections representing PGA values of both FM model (solid line) and Areas model (dashed line) as a function of distance to the surface fault trace and for the same return periods as the maps. The locations of the cross sections are depicted in **Figure 9D**.

the shorter RPs, are mild (**Figures 8A–C**), but for the 4,975 years RP the hazard values are incremented up to a maximum of ~0.1 g in some zones (e.g., E of BSF; **Figure 8D**). For the faults, PGA values remain practically identical for all RPs, which means that earthquake occurrence on most faults is higher than the one generated by the background. However, the background contributes to slightly increment the hazard within the EBSZ buffer area in the zones farther from the traces and influence of the faults (e.g., E of BSF-4) or next to faults with slip rates much lower than the average of the system (~0.5 mm/yr; based on the mean values in **Table 1**); mainly PF. In these zones, the poor influence of faults allows the background of the FM_bg model to overcome the occurrence rates (i.e., probabilities of exceedance) of the hazard from the FM model, thus higher values are found in the FM_bg model within a same RP.

The maximum hazard increments caused by the background take place E of BSF-4 (**Figure 8**), where the Bajo Segura fault-system terminates. This is because fault-related seismic hazard influence is larger and wider in the transversal sections across faults rather than in their longitudinal ends, as it can be seen in CF or the Southwestern termination of AMF (**Figures 4**, **5**). In addition, BSF-4 has a lower slip rate (~0.2 mm/yr; **Table 1**) than the average of the faults in the system and the closest area sources in this zone, i.e., #31, #39 and especially #41 (**Figure 2B**), have very low activity rates (IGME, 2015b). This particular situation causes low occurrence rates of the hazard from the FM model in this zone and allows the background (FM_bg) to overcome such rates more remarkably than any other zone.

These observations are consistent with the disaggregation results of the FM_bg model as in general the background shows low contributions on the hazard, especially where faults dominate the hazard (**Figure 7** and **Supplementary material**). Only in the case of Vera, the seismic background has a significant contribution due to the lower slip rates, hence activity rates, of the PF (**Figures 7E**,**F**). This causes the background to overcome the contribution of PF in the Mw 4.0–5.5 range and to contribute significantly to the seismic hazard levels of the city, especially in longer RPs (**Figure 7F**).

Area Sources Influence

From the mean hazard maps of both FM and FM_bg models it can be observed that the area sources have a much minor footprint in the seismic hazard distribution of the EBSZ than the faults. This is mainly because the activity rates of the area sources modeled are either very low (#31, #36, #39 or #41; IGME, 2015b) or are located too far (>100 km) to have a significant impact in the hazard of the mapped region, such as the North-African source areas (#43, #44 and #45) (**Figure 2B**). Nevertheless, area sources such as #37 and #38 have a recognizable influence on the hazard results as their shapes can be recognized in the hazard maps especially for the 2,475 and 4,975 years RPs (**Figures 4**, **5**). These area sources have high activity rates comparable to the EBSZ buffer area (IGME, 2015b) and contain faults known to be capable of producing Mw > 5.0 earthquakes, such as the Crevillente Fault or the Andarax Valley and El Alquián fault systems (#37 and #38, respectively; **Figure 2**).

The hazard disaggregation shows the contribution of area source #38 on the hazard of Almería for RPs of 2,475-years RP (**Figure 7D**) as the city is located inside this area source. Contrarily, neither Lorca or Vera have contribution of area sources into their hazard (**Figures 7A–F**, respectively) as they are located ~8–9 km from the closest area source limit. Although these areas are at relatively close distances, the higher proximity of AMF-1 in Lorca and the low activity rates of the closer area #36 in Vera prevent them to contribute to the hazard in these cities.

Mean Hazard Curves

Figure 6 shows the mean hazard curves obtained for five cities located close to the EBSZ faults (Almería, Lorca, Murcia, Vera and Torrevieja) for both the FM and FM_bg models. It is clear that setting a background ratio for the EBSZ buffer area does not imply dramatic changes in the hazard curves of these cities, which are all very close to active faults. In the case of the Almería, Lorca and Murcia, the respective hazard curves of both models predict practically identical PGA values for any RP. Conversely, in Torrevieja and, especially, in Vera, the FM_bg model predicts higher PGAs than the FM model, although these differences are very small: less than <0.1 g for the ~10,000 years RP. The reason for these differences between models is the lower slip rates of the BSF and PF, respectively for Torrevieja and Vera, compared to the other faults close to the other studied cities.

DISCUSSION

Comparison With Previous Probabilistic Seismic Hazard Assessment in SE Spain: Implications of the Modeling

The results presented in this study highlight a clear influence of the faults of the EBSZ in the seismic hazard values of SE Spain, as shown in **Figures 4–7**. Both of the FM and FM_bg source models applied for the hazard calculations show very similar results, meaning that the application of a background ratio has minor influence on the hazard, especially in those zones closer to faults (**Figure 8**). Hence, for the comparison analysis that follows we will focus on results of the FM model, though practically all the observations are also applicable to the FM_bg model results. In the same way and due to the low impact of the background on the hazard, the fault influence observations from the disaggregation of the FM_bg model (**Figure 7**) are valid for the FM model. We compare our results with a PSHA produced only considering the ZESIS area sources model, as well as with a recent fault-based PSHA done in SE Spain (Rivas-Medina et al., 2018).

Comparison With a Probabilistic Seismic Hazard Assessment Using the ZESIS Area Source Model

The PSHA results of our FM model are compared with a PSHA reached here by using exclusively the area sources of the ZESIS model (**Figure 2B**) and the same GMPE as our calculations (Campbell and Bozorgnia, 2014). Significant changes in PGA

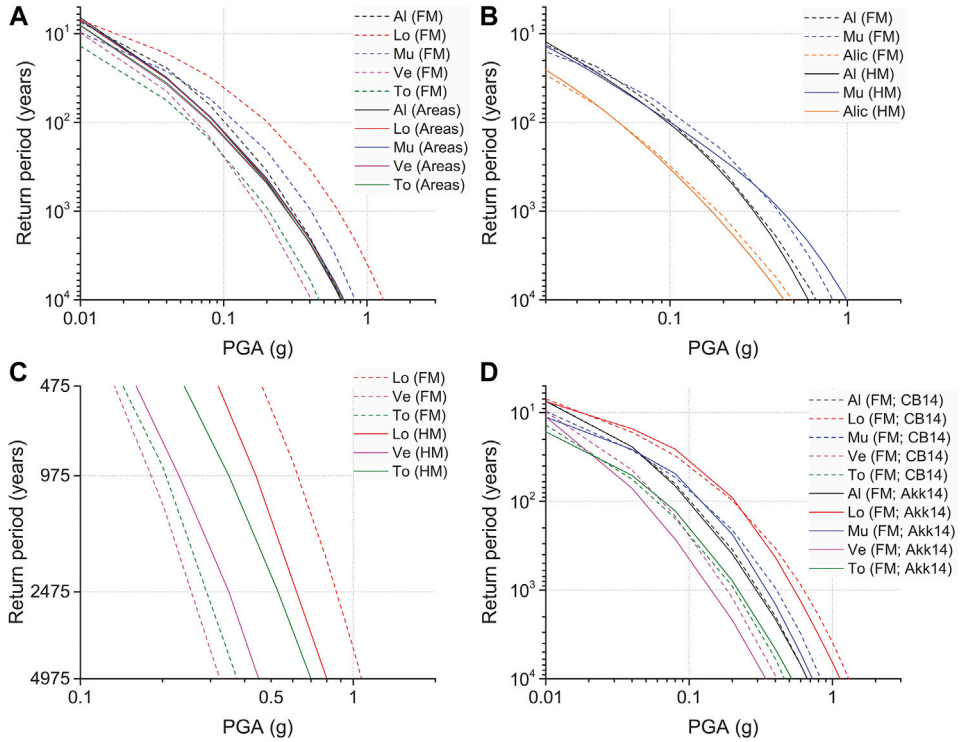

FIGURE 10 | (A) Mean hazard curves for PGA (g) of the FM model plotted with the ones of the ZESIS areas model for the cities of Almería (Al), Lorca (Lo), Murcia (Mu), Vera (Ve) and Torrevieja (To); **(B)** Mean hazard curves for PGA (g) of the FM model and the HM model from Rivas-Medina et al., 2018 for the cities of Almería, Alicante (Alic) and Murcia and **(C)** for the cities of Lorca, Vera and Torrevieja. In these last three cities, the results are visually inferred from pixels of the maps from this publication, hence the curves are exclusively plotted for the return periods of 475, 975, 2,475, and 4,975 years **(D)** Mean hazard curves for PGA (g) of the FM model using the CB14 (Campbell and Bozorgnia, 2014) and Akk14 (Akkar et al., 2014) GMPEs and for the same cities as **Figures 6**, **10A**.

are found between both models within the limits of the EBSZ, where the faults are modeled (**Figures 9A–D**); outside these limits, the hazard values do not experience any change since all use the same area sources model. The FM model increases the PGA with respect to the areas approach in the zones strictly around the faults. Hence, faults concentrate the hazard highlighting the controlling effect of the faults on the hazard levels. The curves in **Figure 10A** depict this effect as Lorca, which is located nearly on top of AMF (**Figure 2A**), shows the highest increment in the FM model. Next, Murcia and Almería show progressively lower PGA increments with respect to the areas model as the distance to the fault increases. These hazard increments in the near-fault zones are achieved by reducing the hazard in the zones farther from the faults with respect to the areas approach and are more visible in longer RPs (975 years RP or larger; **Figures 9B–D**), where the faults have more influence.

The influence of faults on the hazard (net PGA and areal extension) respect to the areas approach, strongly depend on the fault slip rates. The cross sections A-A′ and B-B’ (**Figure 9E**), show that higher slip rate faults in the system such as CF or AMF-1, respectively (1–2 mm/yr; **Table 1**) influence the hazard up to 10–20 km far from the fault trace for all return periods. This causes significant increments in the PGA values within 20–40 km-wide influence zones of ~70–80% for all RPs in CF-3 and ~130–150% for all RPs in AMF-1 (**Figure 9E**). Such increments are slip rate dependent, thus higher for AMF-1 because it has the highest slip rate. Despite this, the disaggregation results of the FM_bg model show that faults can control the hazard in regions farther than the influence zone of the faults up to 20–30 km from its traces, as it is the case of AMF-1 in Vera (**Figures 7E,F**). Farther than this distance limit however, no source has significant influence in any part of the studied area. Fault influence zones are also dependent on the dip direction in non-vertical dipping faults (AMF, BSF), wider in the hanging wall (**Figure 9E**), implying a hanging wall effect.

Contrarily, lower slip rate faults have much less impact on the hazard with respect to the areas approach. Although no exhaustive slip rate analysis has been performed, it can be observed that the faults that have slip rates <0.1 mm/yr do not increase the seismic hazard and it is overcome by the areas approach, as it is the clear case of PF (**Figures 9**, **10A** in Vera). Even so, faults with slightly higher slip rates (~0.1–0.4 mm/yr; AMF-4, LTF or BSF) do influence the hazard, but their impact is more limited than AMF-1, 2 or CF, even for long RPs (**Figure 9D**). The cross section in BSF-3 (C-C’; **Figure 9E**) depicts one of these latter examples. This fault section has a slip rate range 4–14 times smaller than AMF-1 and CF (0.12–0.3 mm/yr; **Table 1**), which causes its influence zone to be over 2–3 times smaller (<10 km wide). In this case the near-

fault PGA increments are negligible for short RPs of 475- and 975-years and very small (<0.1 g) for longer RPs (**Figure 9E**). The small influence of the fault causes the FM's PGA values to be overcome by the ones of the areas approach in less than 5 km from the peak of maximum fault influence. This is also depicted by the Torrevieja curves (**Figure 10A**) and the maps of **Figure 9**. The implications of lower slip rate faults on the hazard are discussed in **section 5.2**.

The consideration of near-fault hazard in zones in the vicinity of the EBSZ faults as both FM and FM_bg models do, including effects such as the hanging wall, provides more realistic estimations of the seismic hazard. This is relevant because during earthquakes, zones close to active faults are exposed to higher accelerations than farther zones due to these near-source effects (e.g., 2011 Lorca earthquake; Alguacil et al., 2014). Their location respect to the dip direction of the fault is also relevant for the ground motion, usually higher in the hanging wall (e.g., Yu and Gao, 2001). Conversely, area source approaches do not reproduce these effects, but uniform PGA distributions within an area, as depicted by the nearly identical mean hazard curves of the cities within the EBSZ buffer area (**Figure 10A**). A detailed and representative analysis of the relationship between PGA, distance to the fault and influence of fault slip rate is a necessary step to be taken in further hazard studies in the region, as it could be useful to define amplification coefficients in earthquake resistant provisions to account for near-fault effects at sites located next to active faults.

Comparison With Rivas-Medina et al., 2018 Fault-Based Approach

We compare the results from the FM model with the fault-based study of Rivas-Medina, 2014, recently published in Rivas-Medina et al., 2018. In that study a PSHA of Southern Spain is performed considering faults as independent, non-interacting sources, following a hybrid methodology (HM model) that avoids setting an arbitrary cutoff magnitude for modeling seismicity in the background (see details in Rivas-Medina et al., 2018). The PSHA was performed for a larger territory of SE Spain than the present study and for all the active faults of the region as compiled in the old QAFI v.2 database back in 2012. The areal model for this study (GM10) is different from the ZESIS model (aka GM12; IGN-UPM, 2013) as it does not identify the EBSZ buffer area (area #55; **Figure 2B**). The GMPE used is the same as in our study. We compare the mean hazard curves of the FM model with the HM model, including Alicante (**Figures 10B**, **10C**). The hazard curves for the cities of Lorca, Vera and Torrevieja were not computed specifically by the authors, hence we inferred visually the PGA values at these cities from pixel screening of the hazard maps for each of the four RPs calculated (475, 975, 2,475 and 4,975 years; **Figure 10C**).

The main contribution of our work with respect to Rivas-Medina et al., 2018 is the consideration of multi-fault ruptures in the source modeling, which causes differences in the hazard estimations mainly for long RPs. Regarding the EBSZ as a whole in PSHA is a novelty in Spain and might constitute a more realistic approach to model the seismic hazard. The main point is that multi-fault ruptures are regarded as a frequent phenomenon, demonstrated by numerous morphogenetic earthquakes in the last decades (e.g., Choi et al., 2012; Hamling et al., 2017; Villani et al., 2018).

In general, the study by Rivas-Medina et al., 2018 provides hazard levels in the range of the ones obtained by the FM model, however there are noteworthy differences. These are mainly due to 1) the consideration of multi-fault ruptures in the FM model, 2) differences in the fault data used in each source modeling, 3) the background seismicity of the HM model and 4) the number of faults considered. The FM model treats the fault system as a whole by allowing the possibility for faults to rupture simultaneously in multi-fault ruptures including large rupturing scenarios. This consideration allows a larger number of fault rupture possibilities to host a certain magnitude and therefore hazard values are generally higher for this model, as shown by the curves of Lorca, Almería and Alicante (**Figures 10B**,**C**). These differences are more notable in RPs over ~1,000 years because multi-fault ruptures produce higher magnitudes that control the longer RPs. Moreover, the discrepancies in the slip rate values and segmentation between both FM and HM models are also responsible for the hazard differences. For instance, the higher values of the FM in Lorca are because updated slip rate data for AMF-1 and AMF-2 are used (1.65 and 1.0 mm/yr, respectively; **Table 1**), contrary to the HM model (0.3 and 0.5 mm/yr). The higher values in Almería, on the other hand, are because CF is divided in three segments with a mean slip rate of 1.1 mm/yr (**Table 1**) in the FM model, while in the HM it is divided in two segments, one of which uses an outdated slip rate (0.04 mm/yr).

In the cities of Murcia, Vera and Torrevieja, the curves of the HM model predict higher values than the FM model (**Figures 10B**,**C**). In Murcia this is only for RPs over ~500 years, as for lower RPs the tendency is the same as the mentioned for Almería and Lorca. We attribute this to the fact that CAF, which controls the hazard of this city (see disaggregation in the **Supplementary material**), is considered as a single-segment fault in the HM model (CAF; 0.54 mm/yr), while in the FM as two segments with different and lower mean slip rates (0.37 and 0.53 mm/yr for CAF-1 and 2, respectively; **Table 1**). In RPs over 500 years this implies that probably a big part of the magnitudes that in the HM model are achieved independently by CAF, in the FM model are achieved by multi-fault ruptures involving CAF-1 and 2. As the slip rates of CAF-1 are lower than CAF-2, the occurrence rates of these multi-fault ruptures are limited by the former (see slip rate treatment in SHERIFS on **section 3.1.1**) and hence are lower than the HM model in this area. On the other hand, the fact that the fault is divided in two segments increases the earthquake rates of lower magnitudes and consequently the PGA values for low RPs (<500 years) in this city with respect to the HM model (**Figure 10B**). As such, linked ruptures between segments, i.e., higher magnitudes, are less frequent in low RPs.

In Vera and especially Torrevieja the higher values of the HM model are visible in all four RPs represented (**Figure 10C**). In the former, the hazard is not controlled by the nearest faults due to the low activity rates of PF, so the background seismicity of the HM model overcomes the ones from the FM. Remarkably, performing this comparison with the curves from the FM_bg model would produce practically the same results, as the

background seismicity of the HM model is modeled for a larger magnitude range (Mw 4.0–6.9) and implies higher seismicity rates. In the latter, the higher HM values are because in this area, additional fault sources apart from the BSF are considered in the modeling (Torrevieja and San Miguel de Salinas faults; **Figure 2A**). While the incorporation of more fault sources on the hazard might suggest that the results from the HM model in the Torrevieja zone are more accurate than the FM, it should be noted that including more faults on the hazard does not necessarily imply more accurate results. These additional faults are not included in our models because are secondary faults to the BSF system (Alfaro et al., 2012) and hence are not part of the main structures in the EBSZ. Moreover, neither their relationship with the EBSZ system and their geological parameters have been studied in detail. The inclusion of such faults on the hazard should account for these uncertainties as they could imply misguided hazard estimations.

Implications for Moderate Magnitude Earthquakes

The hazard results from the disaggregation show that moderate magnitudes in the Mw 4.5–6.0 range, although not being the most remarkable, have a non-depreciable contribution to the final hazard in the selected studied sites even in long RPs (e.g., Almería and Vera; **Figures 7D,F**, respectively). Moreover, according to Gaspar-Escribano et al., 2008, in SE Spain, low-to-moderate magnitude earthquakes between Mw 4.0 and 5.5 control seismic hazard for the 475 years RP. Such kind of earthquakes are relatively frequent in SE Spain and have demonstrated to be quite destructive. The 1999 Mw 4.8 Mula, 2002 Mw 5.0 Bullas and 2005 Mw 4.8 La Paca earthquake series are some recent examples (Benito et al., 2007), being the 2011 Mw 5.2 Lorca earthquake the latest one (Martínez-Díaz et al., 2012a).

The near-source effects of the 2011 Mw 5.2 Lorca earthquake produced exceptionally high accelerations around 0.37 g in the city of Lorca (Cabañas et al., 2011) due to: 1) the proximity of the epicenter to the city, 2) the shallow depth of the earthquake and 3) the directivity of the rupture propagation toward Lorca (Alguacil et al., 2014). The hazard map of the current Spanish Building Code (NCSE-02, 2002) for the 500 years RP and the updated national seismic hazard map for the 475 years RP (IGN-UPM, 2013) predict PGA values in Lorca (0.12 and 0.19 g, respectively) that underestimate the PGA reached in the Lorca earthquake. Conversely, the results of the FM model, but also FM_bg, predict values that differ less than 0.1 g from the ones reached in the 2011 Lorca earthquake: ~0.45 g for the 475 years RP. Rivas-Medina et al., 2018 predict slightly lower values of 0.3 g in Lorca for the same RP, but that are also close to the measured ones.

The fact that fault-based PSHAs in SE Spain predict PGA values for the 475 years RP coherent to the ones of the Lorca earthquake, whose moderate magnitude produced severe damage, may suggest that fault-based approaches perform more realistic hazard predictions than classical area source approaches, particularly for sites located on top of faults or in their vicinity. The PSHA such as the one presented in this study or the one from Rivas-Medina et al., 2018 approximate better the hazard for short RPs due to the effect of faults. However, other site effects such as topography, directivity and changes in soil properties should be incorporated for a more accurate hazard estimation, especially in seismic microzonation.

Implications of the Fault Slip Rates

Slip rate data of faults is a controlling factor in the hazard values obtained in this study as it has a direct impact on the probabilities of exceedance in a given observational period. Higher slip rate faults (e.g., AMF-1 and 2 or CF) imply higher PGA values and influence than lower slip rate faults, some of which have slip rate values so low (<0.1 mm/yr; PF) that are not able to influence significantly the hazard at any RP. This is also observable in the slip rate values used by the source models that compose each branch of the logic tree in relationship with the resulting PGA for each model (**Figure 11**). Each source model is built by picking a random slip rate value from the fault uncertainty ranges provided as inputs (**Table 1**). Thus, aside from the fault rupture hypotheses considered, the models that use higher slip rate values within the uncertainty range show an overall tendency to produce higher PGA estimations at closer sites within the same hypothesis (e.g., AMF-1 in Lorca; **Figures 11A**,**B**). Nevertheless, the data in the plots from **Figure 11** show high dispersion, which suggests that the slip rate uncertainty is not the only parameter affecting seismic hazard variability. In fact, the proximity of the analyzed site to the fault, the rupture hypothesis in question or the RP might control the slope of the mentioned tendency for each hypothesis. Closer sites, i.e., Lorca, result in steeper slopes, similarly to higher RPs (**Figures 11A**,**B**).

PGA variations as a function of slip rate uncertainty are more remarkable in higher slip rate faults (**Figures 11A**,**B**), despite their uncertainties being smaller than for lower slip rate faults (**Figures 11C,D**). AMF-1 has an uncertainty that represents only the ~3% of the mean, while it is ~100% for PF-1 (**Table 1**), however the hazard variations linked to the slip rate variations are considerably higher for the former in Lorca than the latter in Vera. This is because lower slip rates have less impact on the return periods studied than higher slip rate faults, which is consistent with the low influence of PF in our hazard calculations (**Figures 7E,F**).

The identification of the method and source of information upon which slip rate data is based on for each individual fault (**Table 1**) is a crucial step, as it affects the reliability of such data and ultimately the hazard results. At the EBSZ, this is one of the main challenges today as most paleoseismic studies focus only on specific fault sections or single strands of faults with multiple branches, while others remain poorly studied. The faults that concentrate most part of these studies and thus have a better characterization are AMF-1 and 2, CAF and CF. Although most of these focus only on the major fault branches, their slip rate estimations are robust and consistent with overall geodetic data (see **section 2** and references of **Table 1**). Conversely, PF, AMF-3 and 4 or BSF have not been object of detailed paleoseismic research to date and fault data is inferred based on qualitative geomorphological indicators and from geodetic data. These less studied faults at the EBSZ are the ones that have lower slip rate estimations (**Table 1**) and contribute poorly to the hazard, which could imply a bias of such hazard towards well-studied faults.

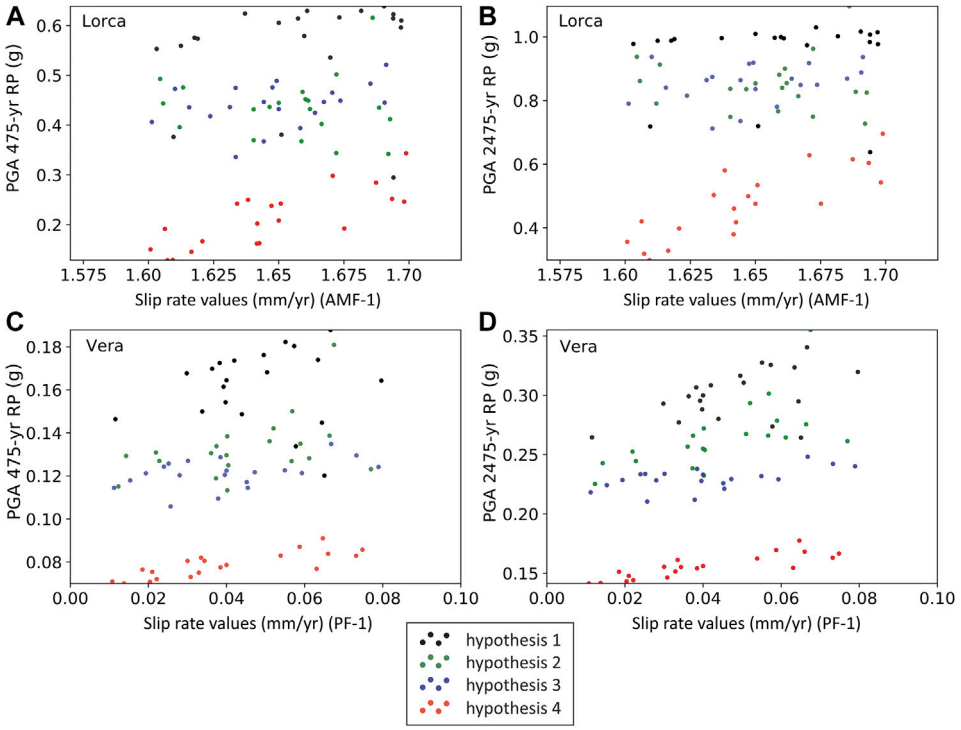

FIGURE 11 | (A) Relationship between the slip rate values of AMF-1 used in each 80 source models that compose the logic tree of this study and the respective PGA (g) values obtained in the city of Lorca for the return periods of 475 years and; **(B)** 2,475 years; **(C)** Same relationship for PF-1 and the PGA (g) obtained in the city of Vera for the return periods of 475 years and; **(D)** 2,475 years. Note that the faults considered are the closest to the cities analyzed and so that can highlight a better effect. The source models belonging to each fault rupture hypotheses that compose the logic tree of this study are depicted in different colors.

Considering the clear sensitivity of the seismic hazard to the fault slip rates, the acquisition of new data in the less studied faults is critical to increase the quality and reliability of the current available data compared to other faults in the EBSZ. Updated parameters can have important implications in the hazard results around them, especially PF. On the other hand, in the zones farther from the mentioned faults and controlled by faults with more paleoseismic research, seismic hazard estimations are more reliable and critical seismic parameters are well constrained (see references in **Table 1**).

Implications of the Ground Motion Prediction Equation Selection

The selection of GMPEs for PSHA is also a difficult task as it has a great influence on the hazard results obtained for a particular study region and sometimes can mask or exaggerate the influence of a seismic source. In this study, we selected a NGA GMPE that is well adapted for fault-based PSHA (Campbell and Bozorgnia, 2014; **section 3.2**) as it is sensitive to near-fault effects. Therefore, the strong contribution of the faults into our hazard models could be seen as a result of applying such equation. In order to test the sensitivity of the hazard models to the GMPEs we performed the hazard calculation of the FM model using the equation by Akkar et al., 2014 (henceforth Akk14). We used this equation because is not as specifically designed for near-fault effects as the one by Campbell and Bozorgnia, 2014 (henceforth CB14) and the source characteristics of earthquakes are exclusively represented by magnitude and style of faulting. The mean hazard maps of the FM model using Akk14 are shown in **Figures 12A**,**B** for the 475- and 4,975-years RPs. The differences with the CB14 equation are depicted in the maps of **Figures 12C** and **12D** and the cross sections of **Figure 12E** for the same RPs. Only these two extreme RPs are shown in order to point out the maximum variations with the CB14 equation.

The sensitivity test performed with the Akk14 equation evidences that the influence of the EBSZ faults on the hazard results performed in this paper is independent of the GMPE used. Therefore, the marked influence of the faults into the PSHA is not a consequence of the GMPE. The resulting mean hazard maps of Akk14 (**Figures 12A**,**B**) are very similar to the ones obtained with the CB14 equation (**Figure 4**) showing a similar hazard distribution. Faults have a clear influence on the hazard for both RPs explored in the near-fault zones and the highest PGA values are found along the traces of the faults, especially the most active according to their slip rates (e.g., AMF-1 and CF). Hanging wall effects are also recognized in the map using Akk14 for non-vertical dipping faults (AMF, CAF and BSF; **Figures 12A** and **12B**).

Despite this, due to its less sensitivity to near-fault hazard estimations, Akk14 computes a more diffuse hazard estimation around the faults, with lower PGA values in general and lower

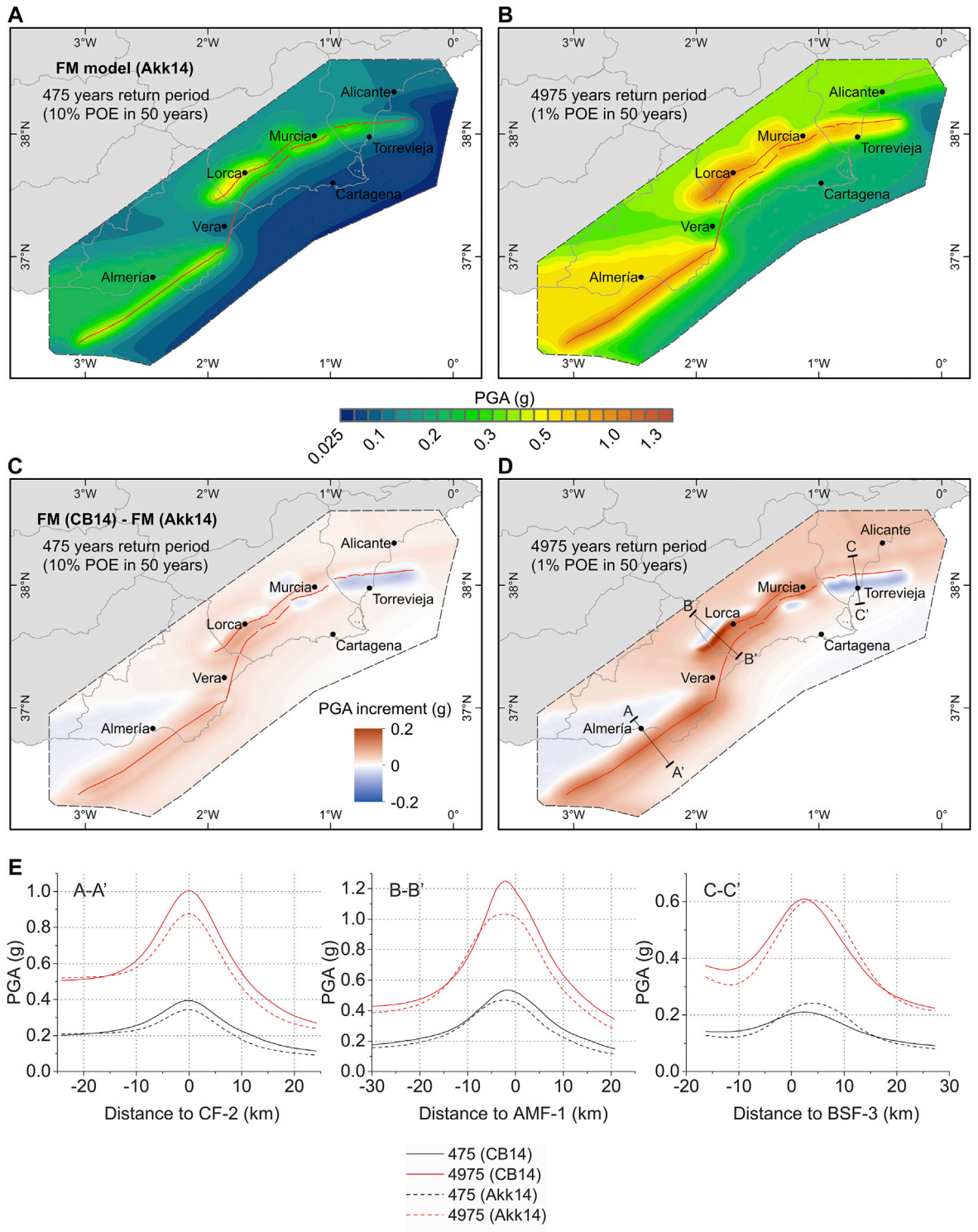

FIGURE 12 | (A) Mean hazard maps for PGA (g) of the FM model using the Akk14 GMPE (Akkar et al., 2014) for the return periods of 475 years and; **(B)** 4,975 years. The color scale is common for both return periods; **(C)** Difference (in g) of the mean hazard maps from the FM model using the CB14 equation with respect to using Akk14 for the return periods of 475 years and; **(D)** 4,975 years. The color scale is common for both return periods. The traces of the EBSZ faults considered are depicted in red in all panels; **(E)** Cross sections representing PGA (g) values of the FM model using the CB14 (solid line) and Akk14 (dashed line) GMPEs as a function of distance to the surface fault trace and for the same return periods as the maps. The locations of the cross sections are indicated in **Figure 12D**.

PGA increments as a function of distance to the fault trace (**Figure 12E**). Therefore, CB14 produces higher PGA values than Akk14 for most of the mapped area and especially around faults, accentuating near-fault effects on the hazard levels. Maximum variations are located close to the traces of faults with higher slip rates, importantly around CF or AMF-1, where these are up to 0.1 and 0.2 g, respectively for the 4,975 years RP and <0.1 g for the 475 years RP (A-A′ and B-B′, respectively; **Figure 12E**). The mean hazard curves from Lorca, Almería, Murcia and Vera also depict PGA increments for the CB14 equation in RPs over ~100 years (**Figure 10D**). In other lower slip rate faults such as BSF, the use of different GMPEs implies practically negligible PGA variations for all RPs (C-C′ cross section along BSF-3; **Figure 12E**). In this case, for the 475 years RP, the use of Akk14 provides slightly higher PGA values (~0.05 g) due to the less sensitivity of the equation to the fault slip rates, up to one order of magnitude lower than AMF-1 or CF (**Table 1**).

In non-vertical dipping faults, hanging wall effects are more accentuated with the CB14 equation (**Figures 12C–E**). In the zones further away from the fault trace on the hanging wall, hazard decreases more abruptly with CB14 with respect to Akk14, especially in long RPs. The higher PGA gradient around the fault trace causes a rapid drop on the hazard values with respect to the lower gradient of Akk14 as distance to the fault increases. AMF, CAF and BSF are clear examples of this effect and, in particular, BSF is the one affected by highest reductions on the hanging wall for all RPs, because the surface projection of its fault plane is larger (**Figures 12C**,**D**). The curve of Torrevieja represents this effect related to the BSF (**Figure 10D**).

Overview: Limitations and Perspectives

The high hazard values in the near-fault zones, the high contribution of faults on the sites hazard and the agreement of the 475 years RP PGA values with the 2011 Lorca earthquake represent more coherent results with the observed values than classical area source methods. Examples of these classical methods are the current Spanish Building Code (NCSE, 2002) and the updated national seismic hazard map (IGN-UPM, 2013). The inclusion of multi-fault ruptures into fault-based PSHA is a novelty for Spain and yet unusual in other low-to-moderate seismicity regions worldwide. Generally, the lack of fault data prevents such kind of analysis in these regions, but as seen, it can imply very important hazard (PGA) changes respect to classical approaches. Moreover, considering multi-fault ruptures is a step forward towards a more realistic seismic hazard assessment, as the occurrence of multi-fault ruptures in nature is becoming an increasingly identified phenomena (e.g., Langridge et al., 2018; Quigley et al., 2019). We therefore aim that our study could serve as a case example for other studies focused in low-to-moderate seismicity regions, such as the EBSZ.

Nevertheless, it is necessary to assess the uncertainties of our study that affect the results presented and need to be considered when interpreting them. One remarkable topic is the background ratio selection of our study. The ratios modeled are an assumption that is established following expert opinion, based on available geological and seismological data from earthquakes in the region. This means that the ratios are not necessarily defining of the study area, but an approximation. The option selected here considers that a big part of the earthquakes in the Mw 4.0–5.5 range are related to the faults modeled because it is consistent with observations (**section 3.1.1.2**). However, we acknowledge the existent implicit epistemic uncertainties within this assumption, as exemplified by the main shocks of the 2019 Ridgecrest sequence (Mw 6.4 and 7.1), which developed in non-previously mapped faults (Ross et al., 2019). In this sense, other background ratios could and should be explored in a logic tree in further research to account for the epistemic uncertainty of earthquakes happening outside of the known faults. In the line of Chartier et al., 2019, we also recognize the difficulty of setting this parameter and encourage the discussion among researchers on what parameters could help its determination. This is a key issue in SE Spain considering the aforementioned large uncertainties affecting the seismicity epicenter locations of most Mw ≥ 4.0 earthquakes.

Another limitation of our results is the fact that the present hazard calculations may be underestimating the contribution of other fault sources in SE Spain outside of the EBSZ fault system. There are many Quaternary-active faults within the mapping area selected in our study that have not been considered in the source modeling mainly because of a lack of quality data, contrary to the faults within the EBSZ. Fault systems such as El Alquián and Andarax Valley, Polopos or San Miguel de Salinas (**Figure 2A**) are some examples of active faults in the area with evidence of related seismicity (QAFI database; IGME, 2015a). These faults could also contribute to the seismic hazard, especially outside the EBSZ buffer area, although none of them have the dimensions (length) of the ones in the EBSZ considered in our study and thus their contribution should not be expected to be that relevant.

Further research is then encouraged to focus on incorporating such uncertainties in the light of a more complete and accurate PSHA analysis. As such, in the zones where there is a lack of paleoseismological studies, obtaining well-constrained and updated fault parameters, especially slip rate values, is critical because they can compromise the reliability or bias of the hazard results. This is not only important for the EBSZ faults but also for the ones outside of it and not included in this study. Updated paleoseismic and geodetic data on faults and the inclusion of more faults as sources would necessarily lead to a reassessment of the source modeling and the hazard in the region. In the meanwhile and given the need of updated and more realistic hazard assessments, it would be useful to consider the near-fault hazard estimations in our models as they could help to set near-fault amplification coefficients to be applied at sites located on top of active faults or in close vicinity. Further research should also focus on exploring the use of other parameters rather than PGA to quantify the seismic hazard such as the spectral acceleration or peak ground velocity and displacement. These parameters are more indicative of the damage generated by an earthquake than PGA as they highlight possible amplification effects in buildings and structures at a given site that ultimately are of interest for seismic engineering purposes. In this sense, and additionally to the use of GMPEs, exploring approaches of spatially correlated ground motion intensity measures (e.g., Park et al., 2007) could be

interesting for further research in order to better characterize expected ground motion, damage and loss estimates for seismic hazard and risk assessment.

CONCLUSIONS

This paper presents a fault system-based PSHA of SE Spain in which earthquake occurrence in the EBSZ is modeled at the scale of the whole fault system and using geological fault data. We devised two alternative models for characterizing the seismicity in the EBSZ, one assuming that all seismic activity is due to known faults of the EBSZ (FM) and another in which part of the seismicity (Mw 4.0–5.5) also occurs as background, related to unknown active faults (FM_bg).

The main conclusion is that, for both models analyzed, faults dominate the seismic hazard in the areas located around faults up to 20–30 km from them, even for short return periods of 475 years. This is remarkable for SE Spain as most of the important cities or towns in this area are commonly found on top or very close to Quaternary active faults (e.g., Lorca, Murcia, Totana, Alhama de Murcia, etc.). Fault effects increase PGA values compared to previous PSHAs based on classical area source methods, but their influence zone is strongly dependent on their slip rates. Around the faults with the higher slip rates of the system, such as the Carboneras Fault or the southwestern end of the Alhama de Murcia Fault (>1 mm/yr), the PGA values are increased up to 150% respect to area source methods for all return periods and the fault influence extends up to 10–20 km from the fault traces. On the other hand, lower slip rate faults such as Bajo Segura Fault (~0.2 mm/yr) produce minor PGA increments, only significant for long return periods, and their influence zones extend up to 5 km from the trace. Around non-vertical dipping faults (e.g., Alhama de Murcia and Bajo Segura faults), the higher hazard values are found in the hanging wall, implying hanging wall effects. Lastly, the faults with the lowest estimated slip rates of the system such as Palomares Fault (<0.1 mm/yr) have no significant impact in the hazard whatsoever. The very similar results from both models evidence that modeling a small portion of the Mw 4.0–5.5 seismicity rate as background (FM_bg) has a minor impact on the seismic hazard of the EBSZ, because fault activity generally overcomes the rates of the background.

The fault-based approach presented seems to provide more accurate hazard estimations than classical area source approaches in sites located close to the faults, at least for the return period of 475 years typically dominated by moderate-magnitude earthquakes. Our hazard results in Lorca for this return period appear to be more consistent with the instrumental PGA values recorded during the 2011 Mw 5.2 earthquake than the ones predicted in the Spanish Building Code or in the updated national seismic hazard map. Also, the consideration of multi-fault ruptures in the source modeling causes significant differences with previous fault-based PSHA in SE Spain and it is a step forward to account for the complexity observed in nature. This kind of approach is a novelty in Spain and might serve as a case example for other low-to-moderate seismicity regions worldwide.

Fault slip rate and its uncertainties have an important influence on the seismic hazard, especially in higher slip rate faults that have more impact in the studied return periods. However, the lack of detailed paleoseismic studies in some lower slip rate faults of the EBSZ (Palomares Fault, Bajo Segura Fault and northeastern termination of Alhama de Murcia Fault) compromises the reliability of the hazard in their surroundings. We identify thus that further research should focus primarily on the obtention of new data to characterize these faults. In the meanwhile, we suggest the use of a near-fault amplification coefficients to be applied to the basic design acceleration provided in the current seismic code for the buildings near Quaternary active faults in this region.

DATA AVAILABILITY STATEMENT

The original contributions presented in the study are included in the article/**Supplementary Material**, further inquiries can be directed to the corresponding author.

AUTHOR CONTRIBUTIONS

OGN and JGM conceived the original idea of the paper, prepared the input data and performed the hazard calculations. OGN, JGM and TC contributed to the interpretation of the results. All authors contributed to the discussions and preparation of the manuscript.

FUNDING

This work was funded by the PREVENT project (CGL2015-66263-R) and FPI predoctoral grant of Octavi Gómez-Novell (BES-2016-077048) from the Spanish Ministry of Science, Innovation and Universities. Open access fees were partially funded by the Vice-rectorate for Ph.D. and Research Promotion of the University of Barcelona.

ACKNOWLEDGMENTS

The authors want to thank Alicia Rivas-Medina for providing files for the comparison performed in the present paper and the ESC Fault2SHA working group for the discussions on the main topics of fault data as inputs for PSHA. We also want to thank Chong Xu, Sergio Molina-Palacios and an anonymous reviewer for their comments and suggestions that contributed to improve this paper.

SUPPLEMENTARY MATERIAL

The Supplementary Material for this article can be found online at: https://www.frontiersin.org/articles/10.3389/feart.2020.579398/full#supplementary-material.

REFERENCES

Akkar, S., Sandıkkaya, M. A., and Bommer, J. J. (2014). Empirical ground-motion models for point- and extended-source crustal earthquake scenarios in Europe and the Middle East. *Bull. Earthq. Eng.* 12, 359–387. doi:10.1007/s10518-013-9461-4

Alfaro, P., Bartolomé, R., Borque, M. J., Estévez, A., García-Mayordomo, J., García-Tortosa, F. J., et al. (2012). The Bajo Segura fault zone: active blind thrusting in the eastern betic cordillera (SE Spain). *J. Iber. Geol.* 38, 287–300. doi:10.5209/rev_JIGE.2012.v38.n1.39217

Benito, B., Capote, R., Murphy, P., Gaspar-Escribano, J. M., Martínez-Díaz, J. J., Tsige, M., et al. (2007). An overview of the damaging and low magnitude Mw 4.8 La Paca earthquake on 29 January 2005: context, seismotectonics, and seismic risk implications for southeast Spain. *Bull. Seismol. Soc. Am.* 97, 671–690. doi:10.1785/0120050150

Borque, M. J., Sánchez-Alzola, A., Martin-Rojas, I., Alfaro, P., Molina, S., Rosa-Cintas, S., et al. (2019). How much nubia-eurasia convergence is accommodated by the NE end of the eastern betic shear zone (SE Spain)? constraints from GPS velocities. *Tectonics* 38, 1824–1839. doi:10.1029/2018TC004970

Bousquet, J.-C. (1979). Quaternary strike-slip faults in southeastern Spain. *Dev. Geotectonics.* 13, 277–286. doi:10.1016/B978-0-444-41783-1.50044-1

Bungum, H. (2007). Numerical modelling of fault activities. *Comput. Geosci.* 33, 808–820. doi:10.1016/j.cageo.2006.10.011

Cabañas, L., Carreño-Herrero, E., Izquierdo-Álvarez, A., Martínez-Solares, J. M., Capote, R., Martínez-Díaz, J. J., et al. (2011). *Informe del sismo de Lorca del 11 de Mayo de 2011*, Madrid, Spain, Available at: http://hdl.handle.net/10261/62381 (Accessed Febuary 20, 2011).

Campbell, K. W., and Bozorgnia, Y. (2014). NGA-West2 ground motion model for the average horizontal components of PGA, PGV, and 5% damped linear acceleration response spectra. *Earthq. Spectra.* 30, 1087–1114. doi:10.1193/062913EQS175M

Chartier, T., Scotti, O., and Lyon-Caen, H. (2019). SHERIFS: open-source code for computing earthquake rates in fault systems and constructing hazard models. *Seismol Res. Lett.* 90, 1678–1688. doi:10.1785/0220180332

Choi, J.-H., Jin, K., Enkhbayar, D., Davvasambuu, B., Bayasgalan, A., and Kim, Y.-S. (2012). Rupture propagation inferred from damage patterns, slip distribution, and segmentation of the 1957 MW8.1 Gobi-Altay earthquake rupture along the Bogd fault, Mongolia. *J. Geophys. Res.* 117, a–n. doi:10.1029/2011JB008676

Cornell, C. A. (1968). Engineering seismic risk analysis. *Bull. Seismol. Soci. Am.* 58, 1583–1606.

De Larouzière, F. D., Bolze, J., Bordet, P., Hernandez, J., Montenat, C., and Ott d'Estevou, P. (1988). The Betic segment of the lithospheric Trans-Alboran shear zone during the Late Miocene. *Tectonophysics* 152, 41–52. doi:10.1016/0040-1951(88)90028-5

DeMets, C., Iaffaldano, G., and Merkouriev, S. (2015). High-resolution neogene and quaternary estimates of nubia-eurasia-north America plate motion. *Geophys. J. Int.* 203, 416–427. doi:10.1093/gji/ggv277

Echeverria, A., Khazaradze, G., Asensio, E., Gárate, J., Dávila, J. M., and Suriñach, E. (2013). Crustal deformation in eastern Betics from CuaTeNeo GPS network. *Tectonophysics* 608, 600–612. doi:10.1016/j.tecto.2013.08.020

Echeverria, A., Khazaradze, G., Asensio, E., and Masana, E. (2015). Geodetic evidence for continuing tectonic activity of the carboneras fault (SE Spain). *Tectonophysics* 663, 302–309. doi:10.1016/J.TECTO.2015.08.009

Ferrater, M., Ortuño, M., Masana, E., Martínez-Díaz, J. J., Pallàs, R., Perea, H., et al. (2017). Lateral slip rate of Alhama de Murcia fault (SE Iberian Peninsula) based on a morphotectonic analysis: comparison with paleoseismological data. *Quat. Int.* 451, 87–100. doi:10.1016/j.quaint.2017.02.018

Field, E. H., Biasi, G. P., Bird, P., Dawson, T. E., Felzer, K. R., Jackson, D. D., et al. (2014). Uniform California earthquake rupture forecast, version 3 (UCERF3): the time-independentmodel. *Bull. Seismol. Soc. Am.* 3, 1122–1180. doi:10.3133/ofr20131165

Fletcher, J. M., Teran, O. J., Rockwell, T. K., Oskin, M. E., Hudnut, K. W., Mueller, K. J., et al. (2014). Assembly of a large earthquake from a complex fault system: surface rupture kinematics of the 4 April 2010 El Mayor-Cucapah (Mexico) Mw 7.2 earthquake. *Geosphere* 10, 797–827. doi:10.1130/GES00933.1

Frankel, A. (1995). Mapping seismic hazard in the central and eastern United States. *Seismol Res. Lett.* 66, 8–21. doi:10.1785/gssrl.66.4.8

Ferrater, M. (2016). *Velocitat de desplaçament de la falla d'Alhama de Murcia (Bètiques Orientals); implicacions en el seu potencial sísmic*. Dissertation thesis. Barcelona (Spain): Universitat de Barcelona.

García-Mayordomo, J. (2005). *Caracterización y analisis de la peligrosidad sismica en el sureste de España*. Dissertation thesis. Madrid (Spain): Universidad Complutense de Madrid.

García-Mayordomo, J. (2015). *Creación de un modelo de zonas sismogénicas para el cálculo del mapa de peligrosidad sísmica de España*. Dissertation thesis. Madrid (Spain): Instituto Geológico y Minero de España.

García-Mayordomo, J., Gaspar-Escribano, J. M., and Benito, B. (2007). Seismic hazard assessment of the Province of Murcia (SE Spain): analysis of source contribution to hazard. *J. Seismol.* 11, 453–471. doi:10.1007/s10950-007-9064-0

García-Mayordomo, J., Martín-Banda, R., Insua-Arévalo, J. M., Álvarez-Gómez, J. A., Martínez-Díaz, J. J., and Cabral, J. (2017). Active fault databases: building a bridge between earthquake geologists and seismic hazard practitioners, the case of the QAFI v.3 database. *Nat. Hazards Earth Syst. Sci.* 17, 1447–1459. doi:10.5194/nhess-17-1447-2017

Gaspar-Escribano, J. M., Benito, B., and García-Mayordomo, J. (2008). Hazard-consistent response spectra in the Region of Murcia (Southeast Spain): comparison to earthquake-resistant provisions. *Bull. Earthq. Eng.* 6, 179–196. doi:10.1007/s10518-007-9051-4

Gil, G., Vidal, F., Navarro, M., García-Jerez, A., and Pérez-Muelas, J. (2014). Characterization of earthquake shaking severity in the town of Lorca during the May 11, 2011 event. *Bull. Earthq. Eng.* 12, 1889–1908. doi:10.1007/s10518-013-9475-y

Global Earthquake Model (GEM) (2019). The OpenQuake-engine user manual. Global earthquake model (GEM) open–quake manual for engine version 3.7.1. doi:10.13117/GEM/OPENQUAKE.MANENGINE.3.7.1

Gómez-Novell, O., Chartier, T., García-Mayordomo, J., Ortuño, M., Masana, E., Insua-Arévalo, J. M., et al. (2020). Modelling earthquake rupture rates in fault systems for seismic hazard assessment: the eastern betics shear zone. *Eng. Geol.* 265 105452. doi:10.1016/j.enggeo.2019.105452

Gràcia, E., Grevemeyer, I., Bartolomé, R., Perea, H., Martínez-Loriente, S., Gómez de la Peña, L., et al. (2019). Earthquake crisis unveils the growth of an incipient continental fault system. *Nat. Commun.* 10, 1–12. doi:10.1038/s41467-019-11064-5

Hamling, I. J., Hreinsdóttir, S., Clark, K., Elliott, J., Liang, C., Fielding, E., et al. (2017). Complex multifault rupture during the 2016Mw7.8 Kaikōura earthquake, New Zealand. *Science* 356, eaam7194. doi:10.1126/science.aam7194

Herrero-Barbero, P. (2016). *Análisis estructural del segmento Alhama–alcantarilla de la Falla de Alhama de Murcia y sus implicaciones en el Riesgo Sísmico*. Master's thesis Madrid (Spain): Universidad Complutense de Madrid.

Herrero-Barbero, P., Álvarez-Gómez, J. A., Martínez-Díaz, J. J., and Klimowitz, J. (2020). Neogene basin inversion and recent slip rate distribution of the northern termination of the Alhama de Murcia fault (eastern betic shear zone, SE Spain). *Tectonics* 39, 1–25. doi:10.1029/2019TC005750

Instituto Geográfico Nacional–Universidad Politécnica de Madrid Working Group (IGN-UPM) (2013). *Actualización de mapas de peligrosidad sísmica de España 2012*. Madrid, Spain: Centro Nacional de Información Geográfica, Instituto Geográfico Nacional.

Instituto Geológico y Minero de España (IGME) (2015a). QAFI v.3: quaternary active faults database of Iberia. Available at: http://info.igme.es/qafi (Accessed March 9, 2020).

Instituto Geológico y Minero de España (IGME) (2015b). ZESIS: base de Datos de Zonas Sismogénicas de la Península Ibérica y territorios de influencia para el cálculo de la peligrosidad sísmica en España. Available at: http://info.igme.es/zesis (Accessed March 9, 2020).

Instituto Geográfico Nacional (2011). Serie terremoto NE Lorca (Murcia). Available at: http://www.ign.es (Accessed May 11, 2020).

Insua-Arévalo, J. M., García-Mayordomo, J., Salazar, A. E., Rodríguez-Escudero, E., Martín-Banda, R., Álvarez-Gómez, J. A., et al. (2015). Paleoseismological evidence of holocene activity on Los Tollos Fault (Murcia, SE Spain): a lately formed quaternary tectonic feature of the eastern betic shear zone. *J. Iber. Geol.* 41, 333–350. doi:10.5209/rev_JIGE.2015.v41.n3.49948

Langridge, R. M., Rowland, J., Villamor, P., Mountjoy, J., Townsend, D. B., Nissen, E., et al. (2018). Coseismic rupture and preliminary slip estimates for the papatea fault and its role in the 2016 Mw 7.8 kaikōura, New Zealand, earthquake. *Bull. Seismol. Soc. Am.* 108, 1596–1622. doi:10.1785/0120170336

Little, T. A., van Dissen, R., Kearse, J., Norton, K., Benson, A., and Wang, N. (2018). Kekerengu fault, New Zealand: timing and size of late holocene surface ruptures. *Bull. Seismol. Soc. Am.* 108, 1556–1572. doi:10.1785/0120170152

Martín-Banda, R., García-Mayordomo, J., Insua-Arévalo, J. M., Salazar, Á. E., Rodríguez-Escudero, E., Álvarez-Gómez, J. A., et al. (2016). New insights on the seismogenic potential of the eastern betic shear zone (SE Iberia): quaternary activity and paleoseismicity of the SW segment of the Carrascoy Fault zone. *Tectonics* 35, 55–75. doi:10.1002/2015TC003997

Martínez-Díaz, J. J., Bejar-Pizarro, M., Álvarez-Gómez, J. A., Mancilla, F. d. L., Stich, D., Herrera, G., et al. (2012a). Tectonic and seismic implications of an intersegment rupture. *Tectonophysics* 546–547, 28–Q17 37. doi:10.1016/j.tecto.2012.04.010

Martínez-Díaz, J. J., Masana, E., and Ortuño, M. (2012b). Active tectonics of the Alhama de Murcia fault, betic cordillera, Spain. *J. Iber. Geol.* 38, 253–270. doi:10.5209/rev_JIGE.2012.v38.n1.39218

Masana, E., Moreno, X., Gràcia, E., Pallàs, R., Ortuño, M., López, R., et al. (2018). First evidence of paleoearthquakes along the Carboneras fault zone (SE iberian Peninsula): Los trances site. *Geol. Acta*. 16, 461–476. doi:10.1344/GeologicaActa2018.16.4.8

McGuire, R. K. (1976). USGS Open-File Report 76-67. *FORTRAN computer program for seismic risk analysis*. Available at: https://pubs.usgs.gov/of/1976/0067/report.pdf. (Accessed January 26, 1976).

Medialdea, J. J., Alonso-Henar, J., Insua-Arévalo, J. M., Canora, C., García-Mayordomo, J., Rodríguez-Escudero, E., et al. (2018). Geological evidences of surface rupture related to a seventeenth century destructive earthquake in Betic Cordillera (SE Spain): constraining the seismic hazard of the Alhama de Murcia fault. *J. Iber. Geol.* 45, 73. doi:10.1007/s41513-018-0082-2

Moreno, X. (2011). *Neotectonic and paleoseismic onshore-offshore integrated study of the Carboneras fault (eastern Betics, SE Iberia)*. Dissertation thesis. Barcelona (Spain): Universitat de Barcelona.

Norma de la Construcción Sismorresistente Española (NCSE-02) (2002). Real Decreto 997/2002, de 27 de septiembre, por el que se aprueba la norma de construcción sismorresistente: parte general y edificación (NCSR-02). *Boletín Oficial del Estado*. 244, 35898–35967.

Ortuño, M., Masana, E., García-Meléndez, E., Martínez-Díaz, J., Stepancikova, P., Cunha, P. P., et al. (2012). An exceptionally long paleoseismic record of a slow-moving fault: the Alhama de Murcia fault (Eastern Betic shear zone, Spain). *Geol. Soc. Am. Bull.* 124, 1474–1494. doi:10.1130/B30558.1

Pagani, M., Monelli, D., Weatherill, G. A., and Garcia, J. (2014). Global earthquake model (GEM) technical report 2014-08. *The OpenQuake-engine book: hazard*. 67. doi:10.13117/-GEM.OPENQUAKE.TR2014.08

Park, J., Bazzurrro, P., and Baker, J. (2007). "Modeling spatial correlation of ground motion Intensity Measures for regional seismic hazard and portfolio loss estimation," in *Applications of Statistics and Probability in civil engineering*. editors T. Kanda and Furuta (London, UK: Taylor and Francis Group), 579.

Power, M., Chiou, B., Abrahamson, N., Bozorgnia, Y., Shantz, T., and Roblee, C. (2008). An overview of the NGA project. *Earthq. Spectra*. 24, 3–21. doi:10.1193/1.2894833

Quigley, M. C., Jiménez, A., Duffy, B., and King, T. R. (2019). Physical and statistical behavior of multifault earthquakes: darfield earthquake case study, New Zealand. *J. Geophys. Res. Solid Earth.* 124, 4788–4810. doi:10.1029/2019JB017508

Reicherter, K., and Hübscher, C. (2007). Evidence for a seafloor rupture of the Carboneras fault zone (southern Spain): relation to the 1522 Almería earthquake? *J. Seismol.* 11, 15–26. doi:10.1007/s10950-006-9024-0

Rivas-Medina, A., Benito, B., and Gaspar-Escribano, J. M. (2018). Approach for combining fault and area sources in seismic hazard assessment: application in south-eastern Spain. *Nat. Hazards Earth Syst. Sci.* 18, 2809–2823. doi:10.5194/nhess-18-2809-2018

Rivas-Medina, A. (2014). *Contribución metodológica para incorporar fallas activas en la modelización de la fuente dirigida a estimaciones de peligrosidad sísmicaAplicación al sur de España*. PhD thesis. Madrid (Spain)]: Universidad Politécnica de Madrid.

Rodríguez-Escudero, E., Martínez-Díaz, J. J., Álvarez-Gómez, J. A., Insua-Arévalo, J. M., and Capote del Villar, R. (2014). Tectonic setting of the recent damaging seismic series in the Southeastern Betic Cordillera, Spain. *Bull. Earthq. Eng.* 12, 1831–1854. doi:10.1007/s10518-013-9551-3

Rodríguez-Fernández, J., Miguel Azañón, J., and Azor, A. (2012). "The betic intramontane basins (SE Spain): stratigraphy, subsidence, and tectonic history," in *Tectonics of sedimentary basins: recent advances*. editors C. Busby and A. Azor (Hoboken: Blackwell Publishing Ltd.), 461–479.

Ross, Z. E., Idini, B., Jia, Z., Stephenson, O. L., Zhong, M., Wang, X., et al. (2019). Hierarchical interlocked orthogonal faulting in the 2019 Ridgecrest earthquake sequence. *Science* 366, 346–351. doi:10.1126/science.aaz0109

Schwartz, D. P. and Coppersmith, K. J. (1984). Fault behavior and characteristic earthquakes: examples from the Wasatch and San Andreas fault zones. *J. Geophys. Res.* 89, 5681–5698. doi:http://dx.doi.org/10.1029/JB089iB07p05681

Silva, P. G., Goy, J. L., Somoza, L., Zazo, C., and Bardají, T. (1993). Landscape response to strike-slip faulting linked to collisional settings: Quaternary tectonics and basin formation in the Eastern Betics, southeastern Spain. *Tectonophysics* 224, 289–303. doi:10.1016/0040-1951(93)90034-H

Silva, P. G., Rodríguez-Pascua, M. A., Giner-Robles, J. L., Perez-Lopez, R., Gomez Lario, J., Perucha Atienza, M., et al. (2014). *Catálogo de los efectos geológicos de los terremotos en España*. Available at: http://igmepublicaciones.blogspot.com.es/ (Accessed April 6, 2015).

Stich, D., Martín, J. B., and Morales, J. (2007). Deformación sísmica y asísmica en la zona Béticas-Rif-Alborán. *Rev. Soc. Geol. Espana*. 20, 311–320.

Stich, D., Martín, R., and Morales, J. (2010). Moment tensor inversion for Iberia-Maghreb earthquakes 2005-2008. *Tectonophysics* 483, 390–398. doi:10.1016/j.tecto.2009.11.006

Stich, G. P., and Weldon, R. J. (2006). Estimating surface rupture length and magnitude of paleoearthquakes from point measurements of rupture displacement. *Bull. Seismol. Soc. Am.* 96, 1612–1623. doi:10.1785/0120040172

Stirling, M., McVerry, G., Gerstenberger, M., Litchfield, N., Van Dissen, R., Berryman, K., et al. (2012). National seismic hazard model for New Zealand: 2010 update. *Bull. Seismol. Soc. Am.* 102, 1514–1542. doi:10.1785/0120110170

Vilanova, S. P., and Fonseca, J. F. B. D. (2007). Probabilistic seismic-hazard assessment for Portugal. *Bull. Seismol. Soc. Am.* 97, 1702–1717. doi:10.1785/0120050198

Villani, F., Pucci, S., Civico, R., De Martini, P. M., Cinti, F. R., and Pantosti, D. (2018). Surface faulting of the 30 october 2016 Mw 6.5 Central Italy earthquake: detailed analysis of a complex coseismic rupture. *Tectonics* 37, 3378–3410. doi:10.1029/2018TC005175

Villaseñor, B., and Richter, C. F. (1945). Frequency of earthquakes in California. *Nature* 156, 371. doi:10.1038/156371a0

Wells, D. L., and Coppersmith, K. J. (1994). New empirical relationships among magnitude, rupture length, rupture width, rupture area, and surface displacement. *Bull. Seismol. Soc. Am.* 84, 974–1002.

Wesnousky, S. G. (1986). Earthquakes, quaternary faults, and seismic hazard in California. *J. Geophys. Res.* 91 (12), 12587–12631. doi:10.1029/JB091iB12p12587

Woessner, J., Laurentiu, D., Laurentiu, D., Giardini, D., Crowley, H., Cotton, F., et al. (2015). The 2013 European Seismic Hazard Model: key components and results. *Bull. Earthq. Eng.* 13, 3553–3596. doi:10.1007/s10518-015-9795-1

Working Group on California Earthquake Probability (WGCEP) (2003). USGS Open-File Report 03-214. *Earthquake probabilities in the san francisco bay Region : 2002-2031*.

Youngs, R. R., and Coppersmith, K. J. (1985). Implications of fault slip rates and earthquake recurrence models to probabilistic seismic hazard estimates. *Int. J. Rock Mech. Min. Sci. Geomech. Abstr.* 23, 125. doi:10.1016/0148-9062(86)90651-0

Yu, Y.-X., and Gao, M.-T. (2001). Effects of the hanging wall and footwall on peak acceleration during the Jiji (Chi-Chi), Taiwan Province, earthquake. *Acta Seimol. Sin.* 14, 654–659. doi:10.1007/BF02718076

Zhang, H., Chen, J., and Ge, Z. (2012). Multi-fault rupture and successive triggering during the 2012 Mw 8.6 Sumatra offshore earthquake. *Geophys. Res. Lett.* 39, a–n. doi:10.1029/2012GL053805

Conflict of Interest: The authors declare that the research was conducted in the absence of any commercial or financial relationships that could be construed as a potential conflict of interest.

frontiers in Earth Science

ORIGINAL RESEARCH
published: 22 December 2020
doi: 10.3389/feart.2020.567939

Earthquake Source Characteristics and S-Wave Propagation Attenuation in the Junction of the Northwest Tarim Basin and Kepingtage Fold-and-Thrust Zone

Hongwei Wang[1,2] *and Ruizhi Wen*[1,2]*

[1]*Institute of Engineering Mechanics, China Earthquake Administration, Harbin, China,* [2]*Key Laboratory of Earthquake Engineering and Engineering Vibration of China Earthquake Administration, Harbin, China*

We separated the propagation path attenuation and source spectra from the S-wave Fourier amplitude spectra of the observed ground motions recorded during 46 small-to-moderate earthquakes in the junction of the northwest Tarim Basin and Kepingtage fold-and-thrust zone, mainly composed of two Jiashi seismic sequences in 2020 and 2018. Slow seismic wave decay was observed as the distance increased, while the quality factor regressed as 60.066 $f^{0.988}$ for frequency f = 0.254–30 Hz reflects the strong anelastic attenuation in the study region. We estimated the stress drops for the 46 earthquakes under investigation from the preferred corner frequencies and seismic moments by fitting the inverted source spectra and the theoretical ω-square model. The relationship between seismic moment and corner frequency and the dependence of the stress drop on the moment magnitude reveal the breakdown of earthquake self-similar scaling for the events in this study. The temporal variation in stress drops indicates that the mainshock plays a short-term role in the source characteristics of the surrounding earthquakes. Aftershocks immediately following the mainshock show a low stress release and then gradually recover in a short time. The healing process for the fractured fault in the mainshock may be one reason for the stress drop recovery of the aftershock. The foreshock with the low stress release occurring in the high-heterogeneity fault zone may motivate the following occurrence of the largest magnitude mainshock with a high stress drop. We inferred that the foreshock-mainshock behavior, including several moderate events, may be predisposed to occur in our study region characterized by an inhomogeneous crust.

Keywords: seismic ground motion, spectral inversion, propagation path attenuation, source spectra, stress drop

OPEN ACCESS

Edited by:
Pier Paolo Bruno,
University of Naples Federico II, Italy

Reviewed by:
Shuang Li,
Harbin Institute of Technology, China
R. B. S. Yadav,
Kurukshetra University, India

***Correspondence:**
Ruizhi Wen
ruizhi@iem.ac.cn

Specialty section:
This article was submitted to Solid Earth Geophysics, a section of the journal Frontiers in Earth Science

Received: *31 May 2020*
Accepted: *22 October 2020*
Published: *22 December 2020*

Citation:
Wang H and Wen R (2020) Earthquake Source Characteristics and S-Wave Propagation Attenuation in the Junction of the Northwest Tarim Basin and Kepingtage Fold-and-Thrust Zone. Front. Earth Sci. 8:567939. doi: 10.3389/feart.2020.567939

INTRODUCTION

A moderate earthquake of M_s 5.4 abruptly shook the Jiashi county of the Xinjiang region in northwest China on January 18, 2020, at 00:05 Beijing time (**Figure 1**), arousing the 2020 Jiashi seismic sequence. This sequence rapidly reached its climax on the following night as the largest magnitude mainshock, measured as M_s 6.4, occurred ~2.5 km to the east of the M_s 5.4 foreshock, and a great number of aftershocks followed immediately, including the largest one measured as M_s 5.2 about 22 km to the east of the mainshock. However, the M_s 5.4 foreshock and M_s 6.4 mainshock did

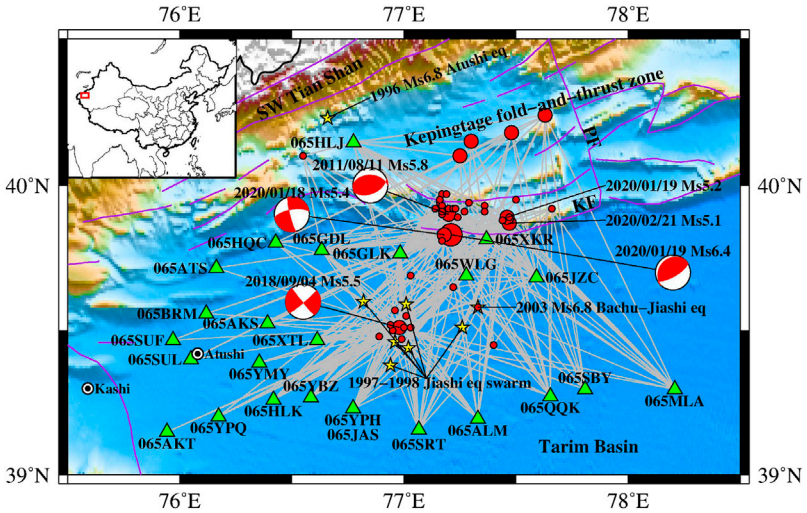

FIGURE 1 | Locations of earthquakes (circles) and stations (triangles) considered in the spectral inversion analysis. The stars represent the major historical earthquakes in the proximity of the seismogenic area. The ray paths from the epicenter to the station are depicted by the gray lines. The focal mechanisms were derived from the United States Geology Survey. Purple lines indicate the active faults, and KF and PF represent the Kepingtage thrust fault and the Piqiang fault, respectively. Insert in the top left corner shows the location of the study region (rectangle).

not share similar rupture mechanisms according to the fault plane solutions reported by the United States Geology Survey, strike slip for the former, and low-angle reverse dip slip for the latter (**Figure 1**). On February 21, 2020, another moderate earthquake of M_s 5.1 adjacent to the M_s 5.2 largest aftershock occurred at the easternmost end of this sequence (**Figure 1**). Up until March 1, 2020, this sequence consisted of 26 events of $M_s \geq 3.0$ [derived from China Earthquake Network Center (CENC), www.ceic.ac.cn/history], primarily assembled in a narrow belt in a nearly east-west orientation and nucleated in the upper crust mostly at a depth of 15–20 km.

The 2020 Jiashi seismic sequence occurred on the western segment of the frontal Kepingtage thrust fault, which is exposed west of the north-northwest to south-southeast trending Piqiang fault (**Figure 1**). The Kepingtage thrust fault is the southernmost margin of the Kepingtage fold-and-thrust zone, Cenozoic compressive structures neoformed above a Paleozoic basal decollement level at a depth of 4–6 km, predominantly thrusting toward the interior of the northwest Tarim Basin to the south (Allen and Vincent, 1999; Turner et al., 2010; Yang et al., 2018; Laborde et al., 2019). Much deeper focal depths implied that this sequence was more likely to occur in the basement structures below the decollement level, rather than the thrust sheets that grew above the decollement level (Gao et al., 2013; Laborde et al., 2019).

The high seismic activity in the junction of the northwest Tarim Basin and Kepingtage fold-and-thrust zone was majorly driven by the compressive stresses transmitted by the undeformed rigid Tarim block far to the north from the continental collision of the Indian and Eurasian plates (Buslov et al., 2007; Laborde et al., 2019). Consequently, this region has suffered frequently from moderate-to-large earthquakes, e.g., the 1996 M_s 6.9 Atushi earthquake, the 1997–1998 Jiashi earthquake swarm, the 2003 M_s 6.8 Bachu-Jiashi earthquake, the 2011 M_s 5.8 Atushi earthquake, and the 2018 M_s 5.5 Jiashi earthquake (highlighted by stars in **Figure 1**). This region is thus persistently exposed to a relatively high seismic hazard. The seismic accelerations reached up to 0.20 and 0.30 g (g, gravitational acceleration) in this region according to the latest generation of seismic ground motion parameter zonation maps of China (GB 18306, 2015).

Studies associated with the earthquake source were of decisive importance for a deep understanding of the seismic source physics and reliable prediction of future ground motions and seismic hazards. The observed ground motion recordings have been commonly utilized in a number of established methods (e.g., empirical Green's function-based method and large-scale stacking and generalized inversion techniques) aimed at revealing the earthquake source characteristics, e.g., the earthquake source scaling (Allmann and Shearer, 2009; Viegas et al., 2010; Baruah et al., 2016; Trugmann and Shearer, 2017; Baltay et al., 2019) and the source rupture directivity (Abercrombie et al., 2017; Calderoni et al., 2017; Wang et al., 2018). The source characteristics have important implications for explaining the earthquake nucleation and growth (e.g., Moyer et al., 2018).

A dense strong ground motion observation network composed of 48 stations has been constructed and continuously operated since 2007 to monitor the seismic activity in the junction of the southwest Tian Shan and the northwest Tarim Basin. During the 2020 Jiashi seismic sequence, the strong ground motion observation network was progressively triggered by 24 earthquakes and collected a total of over 200 three-component (i.e., east-west, north-south, and up-down) ground motion acceleration recordings. Before this sequence, the observation network had accumulated ~300

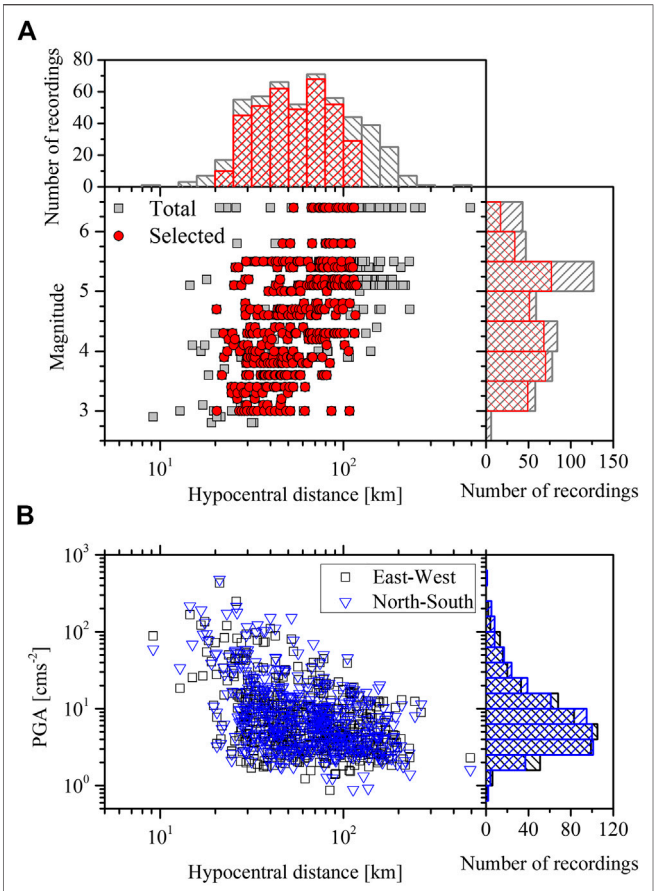

FIGURE 2 | (A) Hypocentral distance vs. magnitude for the total recordings collected in this region (squares) and the recordings selected for the spectral inversion analysis (circles). The histograms of the hypocentral distance and the magnitude of the total recordings and selected recordings are also plotted. **(B)** Peak ground accelerations (PGAs) of both horizontal components (east-west and north-south) for total recordings and the histograms of the horizontal PGAs.

recordings from ~40 earthquakes, including the 2018 Jiashi seismic sequence, which mainly occurred on the buried faults in the northwest Tarim Basin (Song et al., 2019) and the Kepingtage thrust fault. The buried faults have been verified to be the seismogenic structures of the 1997–1998 Jiashi earthquake swarm (Liu et al., 2000; Li et al., 2002). The Jiashi seismic sequences in both 2020 and 2018 were characterized by the foreshock-mainshock behavior.

In this study, the nonparametric spectral inversion analysis of the S-wave Fourier amplitude spectra of the observed ground motions was performed to isolate the path attenuation and the source spectra for 46 earthquakes considered in this region, including 20 events from the 2020 Jiashi seismic sequence. The source parameters were derived from the inverted source spectra according to the grid-searching method. The resultant stress drop estimates provided the crucial evidence for the source scaling, and the temporal variation in stress drop was further analyzed and used to explain the occurrence of multiple moderate events in the Jiashi seismic sequence.

DATASET

For the spectral inversion analysis, we first collected a total of 502 three-component acceleration waveforms well recorded at 48 strong-motion observation stations from 59 M 2.8 to 6.4 earthquakes occurring in proximity to the seismogenic area of the 2020 Jiashi seismic sequence since 2007. As shown in **Figure 2**, the hypocentral distances (R) of recordings were mainly in the range of 20–200 km, and the horizontal peak ground accelerations (PGAs) were not greater than 50 cm/s^2 for most recordings. These recordings were uniformly processed by the baseline correction, appending zero pads to the beginning and end, and a Butterworth bandpass filter. The high-cut corner frequency was uniformly set to 30 Hz, while the low-cut corner frequency (f_{lc}) was preliminarily estimated by two empirical relations and further adjusted and determined after manual inspection. Both empirical relations include the lower boundary (f_{lb}) for the usable frequency band associated with the moment magnitude (M_w) imposed by Yenier and Atkinson (2015) based on the minimum usable frequencies reported in the Next Generation Attenuation-West2 (NGA-West2) database and f_{lc} associated with f_{lb}, i.e., $f_{lb} = 1.25f_{lc}$ (Abrahamson and Silva, 1997). Here, the magnitudes (surface magnitude M_s or local magnitude M_L) released by CENC were approximately regarded as M_w for the preliminary estimate of f_{lc}. The determined f_{lc} values were in the range of 0.10–0.95 Hz. In order to avoid the nonlinear soil behavior potentially occurring under strong ground shaking (Beresnev and Wen, 1996; Wu et al., 2010) and reduce the contamination of the surface wave and/or Lg wave to the applied S-wave as much as possible (McNamara et al., 2012; Sedaghati et al., 2019), recordings with R > 120 km or PGA > 100 cm/s^2 were first eliminated. Moreover, to ensure data redundancy, we adopted a minimum three-recording criterion requiring each selected earthquake to be recorded by at least three selected stations, each of which recorded at least three selected earthquakes. Following these parameters, 116 recordings were eliminated, and we retained 386 ones recorded at 25 stations in 52 M 2.8–6.4 earthquakes.

We manually picked the P- and S-wave onsets and identified the S-wave end time according to the distance-dependent percentage of the seismic wave energy, i.e., 90% for R < 25 km, 80% for R = 25–50 km, and 70% for R > 50 km (Pacor et al., 2016). In order to guarantee an acceptable spectral resolution, the minimum length of the S-wave window was imposed as 1.0/(1.25 f_{lc}). The cosine tapers at the beginning and end of the extracted S-wave were applied to avoid truncation effects, and the length of each taper was 10% of the length of the S-wave window. The Fourier amplitude spectra of the cosine-tapered and zero-padded S-waves were calculated and smoothed using the window function of Konno and Ohmachi (1998) with smoothing parameter b equal to 20. The spectral amplitudes at 300 frequencies uniformly spaced on the logarithmic scale from 0.25 to 30 Hz were obtained by linear interpolation in log-log space. The root square average of the spectral amplitude at both horizontal components was regarded as the horizontal ground motion in the frequency domain.

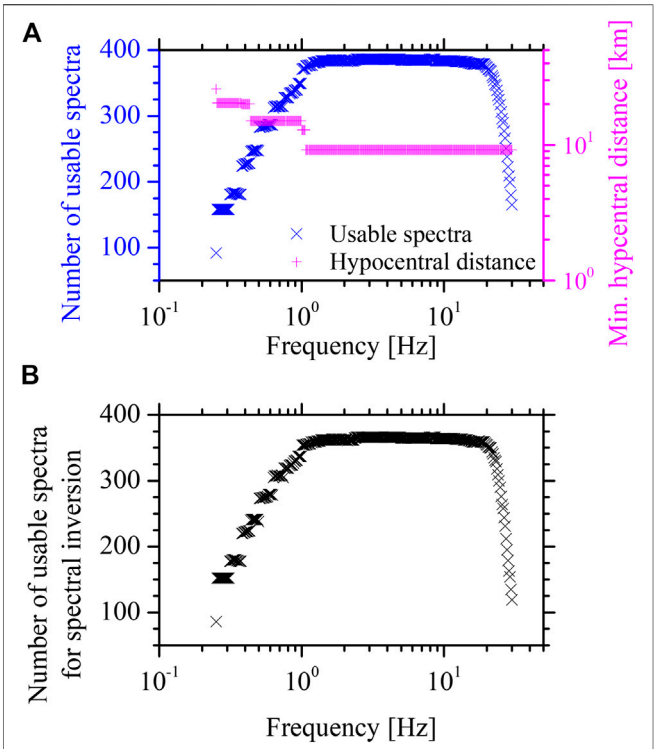

FIGURE 3 | (A) The number of usable spectra and minimum hypocentral distance of usable spectra varied with the frequency. **(B)** The number of usable spectra at each frequency for the recordings selected for the spectral inversion analysis.

The pre-P-wave noise window, sharing the same length of the S-wave window, was extracted and processed, and its Fourier amplitude spectrum was calculated and smoothed for the following calculation of the signal-to-noise ratio (SNR). An SNR threshold of five and f_{lc} were simultaneously considered to distinguish the usable frequency band of the S-wave spectra. **Figure 3A** plots the number of usable spectra and the minimum hypocentral distance (R_0) of the usable spectra against frequency. It was clearly observed that the number of usable spectra increases gradually at frequencies of 0.25–1.0 Hz and then approximately keeps constant at frequencies of 1.0–20.0 Hz before a decreasing tendency appears with frequencies over 20.0 Hz. The R_0 of the usable spectra also varied with the frequency, which showed smaller values at higher frequencies, i.e., 25.75 km at 0.25 Hz, 20.33 km at 0.254–0.373 Hz, 20.01 km at 0.379–0.431 Hz, 15.02 km at 0.434–0.991 Hz, 12.86 km at 1.007–1.056 Hz, and 9.17 km at 1.073–30 Hz. In order to balance R_0 and the lowest usable frequency, R_0 = 20.33 km was used. and eight recordings with $R < R_0$ were eliminated. The minimum three-recording criterion was then performed for usable spectra at each frequency to reconstruct the spectra used for the following spectral inversion analysis, and the numbers of usable spectra against frequency are shown in **Figure 3B**. Finally, 366 recordings recorded at 25 stations in 46 M 3.0–6.4 earthquakes were applied for spectral inversion analysis. Earthquakes and stations considered, as well as the ray paths from earthquake to station, are plotted in **Figure 1**. The magnitude-hypocentral distance distribution for recordings under consideration is plotted in **Figure 2A**.

METHODOLOGY

The two-step nonparametric spectral inversion method (Castro et al., 1990; Oth et al., 2008; Oth et al., 2009) was applied to isolate the Fourier amplitude spectra of the S-waves into the source spectra, site response functions, and propagation path attenuation term.

In the first step, the dependence of the spectral amplitudes at frequency f_m on the hypocentral distance is modeled by

$$O_{ij}\left(f_m, R_{ij}\right) = M_i\left(f_m\right)A_{ij}\left(f_m, R_{ij}\right), \quad (1)$$

where O_{ij} (f_m, R_{ij}) is the spectral amplitude observed at the jth station resulting from the ith earthquake, R_{ij} is the hypocentral distance between the jth station and the ith earthquake, M_i (f_m) is a scalar dependent on the size of the ith earthquake, and A_{ij} (f_m, R_{ij}) accounts for seismic wave attenuation (geometrical spreading, anelastic attenuation and scattering attenuation, refracted arrivals, etc.) along the travel path from the ith earthquake to the jth station. The path attenuation term is not supposed to have any predefined parametric functional form and is constrained to be a smooth distance function with a value of one at the reference distance R_0 = 20.33 km, which is the smallest hypocentral distance for recordings considered in our study. In practice, the hypocentral distance of the usable spectra at frequency f_m was divided into $N_{D,m}$ bins with 5 km width, and A_k (f_m, $R_{k,m}$) instead of A_{ij} (f_m, R_{ij}) was computed, where $R_{k,m}$ represents the average hypocentral distance of the usable spectra at frequency f_m lying within the kth distance bin. After taking the logarithm for linearization and adding constraints for path attenuation term, **Eq. 1** can be solved for each frequency separately using the singular value decomposition (SVD) method.

In the second step, the spectral amplitudes corrected for propagation path attenuation are divided into source spectra and site response:

$$O_{ij}\left(f_m, R_{ij}\right)\Big/A_k\left(f_m, R_{k,m}\right) = S_i\left(f_m\right)G_j\left(f_m\right), \quad (2)$$

where G_j (f_m) is the site response function at the jth station and S_i (f_m) is the source spectrum of the ith earthquake.

In order to resolve a remaining degree of freedom coming from the trade-offs between source and site terms, the constraining condition for either the source or the site should be fixed beforehand. The most commonly used method was to set the site response of an ideal outcrop bedrock site to be equal to unity irrespective of frequency (Wang et al., 2018), or to set the average site response of a set of rock sites to be equal to unity (Oth et al., 2009; Oth and Kaiser, 2014; Pacor et al., 2016) or the horizontal-to-vertical (H/V) spectral ratio of body waves (Bindi et al., 2004; Wang et al., 2018). The site conditions for the 25 strong-motion stations considered in this study were classified into three classes defined in the Code for Seismic Design of Buildings in China (GB 50011, 2010) according to

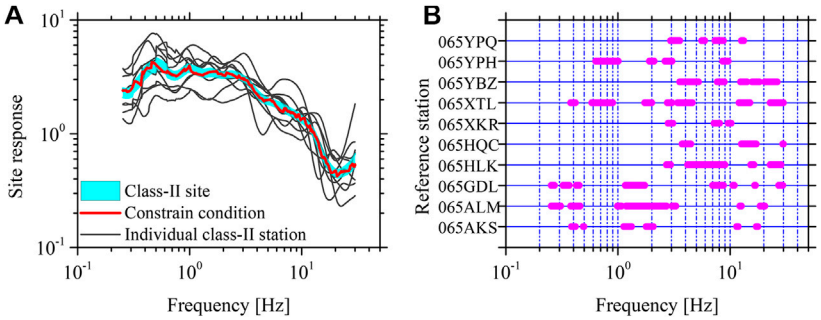

FIGURE 4 | (A) The site responses for 10 class II stations (thin gray lines) were represented by the average of the S-wave horizontal-to-vertical spectral ratios of ground motion recordings with peak ground acceleration not greater than 100 cm/s^2. A range of the average plus and minus 0.25 SD on the base-10 logarithmic scale over the 10 stations (shaded area) represents the site response of the class II site. At each frequency, stations with site responses falling into the range of the site response of the class II site were selected, and their average site response was used as the constraining condition (thick red line). **(B)** The selected stations for the constraining condition varied with frequency.

the terrain-based metrics (Shi, 2009), 16 for class II (medium-stiff soil), eight for class III (medium soft soil), and one for class IV (soft soil); thus, no one can be approximately regarded as a rock site.

As reported by Lermo and Chavez-Garcia (1993), the H/V spectral ratio of the body waves was largely controlled by the site response. Further studies from Atkinson and Cassidy (2000) and Atkinson (2004) found that the amount of amplification observed or calculated from the shear-wave velocity gradient approximately matches the H/V spectral ratio for both the rock and the soil sites. Kanbur et al. (2020) evaluated the local site effects according to the H/V spectral ratios. Bindi et al. (2004) defined the site response for station ASSI to be the H/V spectral ratio for the spectral inversion. In this study, the H/V spectral ratio was also treated as the site response. The S-wave H/V spectral ratio for each class II site was computed based on the ground motion recordings with PGA $\leq$ 100 cm/s^2, and the average over at least five H/V spectral ratios was approximately regarded as the site response. Finally, the site responses for 10 out of 16 stations were retrieved and plotted in **Figure 4A**. The site response of the class II site was simply depicted by a range of the average plus and minus 0.25 SD over the 10 stations, shown with the shaded area in **Figure 4A**. At each frequency, stations with site responses falling into the range of the site response of the class II site were selected as shown in **Figure 4B**, and the average site response over the selected stations was used as the constraining condition.

RESULTS AND DISCUSSION

Propagation Path Attenuation

Path attenuation curves for frequencies ranging from 0.254 to 30 Hz were obtained from the solutions of **Eq. 1** and plotted in **Figure 5A**. They continuously decrease with increasing distance up to 120 km for all frequencies considered. The slow decay is obviously expressed by the inverted path attenuation, which is generally between $(R_0/R)^{0.5}$ and $(R_0/R)^{1.0}$. For simplicity, the frequency-independent geometrical spreading as a function of distance and the anelastic attenuation as a function of frequency-dependent quality factor (Q) were commonly adopted as substitutes for the complex path attenuation in practice, e.g., the ground motion prediction (e.g., Boore, 2003; Bora et al., 2015) and regional attenuation investigation (e.g., Pavel and Vacareanu, 2018). In addition to the linear function of R, the more complicated geometrical spreading functional forms were widely proposed to represent the particular geologic and tectonic setting, e.g., the hinged bilinear and trilinear models (Atkinson and Boore, 1995; Atkinson, 2004). Studies, e.g., Mahani and Atkinson (2012), verified that various geometrical spreading models have similar effects on fitting the data. Atkinson and Mereu (1992) proposed the typical hinged trilinear model. In this model, the transition distances were related to the crustal thickness. Considering a crustal thickness of ~50 km (Gao et al., 2013), the second transition distance was about 125 km, greater than the maximum hypocentral distance (i.e., 120 km). In this study, the hinged bilinear geometrical spreading model was used, and the inverted path attenuation curve was modeled by

$$\ln A(f_m, R_{k,m}) = n_1 \ln(R_0/R_{k,m}) + [f_m/Q(f_m)] \quad [-\pi(R_0 - R_{k,m})/\beta] \quad \text{for} \quad R_{k,m} \leq R_1, \text{and}$$

$$\ln A(f_m, R_{k,m}) = n_1 \ln(R_0/R_1) + n_2 \ln(R_1/R_{k,m}) + [f_m/Q(f_m)] \quad [-\pi(R_0 - R_{k,m})/\beta] \text{for} \quad R_{k,m} > R_1, \tag{3}$$

where β is the shear-wave velocity set to 3.60 km/s at depths of 15–20 km near the source (Zhao et al., 2008), R_1 is the transition distance, and n_1 and n_2 represent the decay rates at the first and second segmentation, respectively. The SVD method was applied to solve **Eq. 3** for optimum n_1, n_2, and Q values by taking different values of transition distance R_1 = 50, 55, 60, and 65 km, respectively. Note that the strong trade-off between the geometrical spreading and anelastic attenuation was not constrained before the solution. Therefore, the specified combination of geometrical spreading and anelastic attenuation obtained in this study should be used simultaneously.

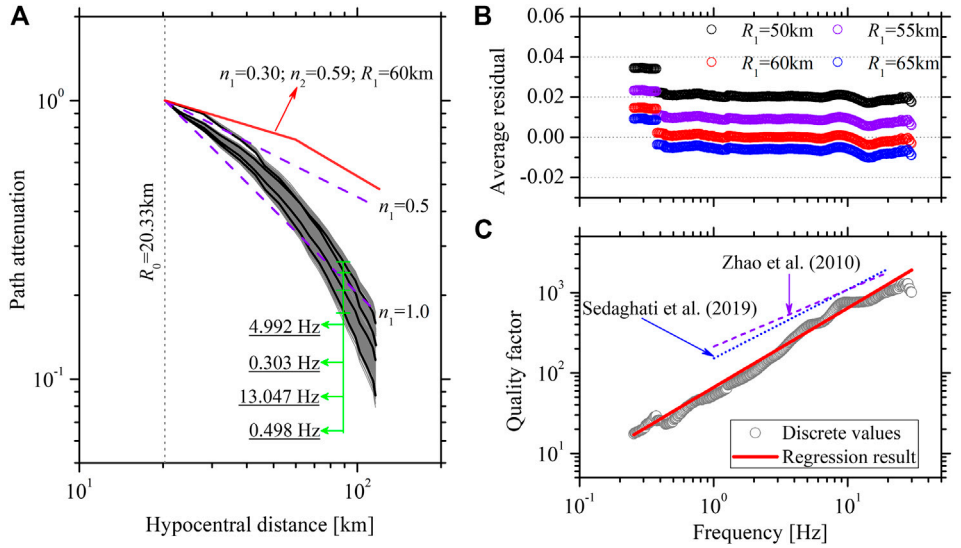

FIGURE 5 | (A) The path attenuation curves derived for frequencies at 0.254–30 Hz. The hinged bilinear geometrical spreading model with the transition distance R_1 = 60 km provided in this study is plotted and compared with the geometrical spreading models expressed as $(R_0/R)^{0.5}$ and $(R_0/R)^{1.0}$. **(B)** The average residual between the inverted and the modeled path attenuations over all distances for each frequency with transition distances of R_1 = 50, 55, 60, and 65 km, respectively. **(C)** Calculated Q values (circles) and the regressed Q model (solid line) in our study. The Q models for the northwest Tarim Basin proposed by Zhao et al. (2011) and the Tajikistan-Kyrgyzstan region west and northwest of our study region proposed by Sedaghati et al. (2019) are also plotted.

The residuals between the inverted and modeled path attenuations, i.e., $\log_{10}$ $(A_{\text{inverted}}/A_{\text{modeled}})$, were calculated to explain whether the inverted path attenuation was well fitted with respect to the parametric functions. The average residual over all distances was obtained for each frequency, as shown in **Figure 5B**. The minimum average residual, fluctuating around zero, occurs at frequencies over ~0.3 Hz for the case of R_1 = 60 km. The parametric functions for R_1 = 50 and 55 km generally provide a faster decay than the inverted path attenuations at frequencies over ~0.3 Hz, as indicated by the positive average residuals, while slower decay was provided by the parametric functions for R_1 = 65 km. Allowing for the good representation of the inverted attenuation curve, R_1 = 60 km was recommended in this study. Correspondingly, n_1 and n_2 are, respectively, equal to 0.30 and 0.59. The derived hinged bilinear geometrical model was slightly larger than the linear geometrical spreading expressed by $(R_0/R)^{0.5}$ (**Figure 5A**). The frequency-dependent Q model, following a power-law equation expressed as $Q_0 f^{\eta}$, was used to fit the derived Q values at frequencies of 0.254–30 Hz, and the Q model was regressed as $60.066\ f^{0.988}$, as shown in **Figure 5C**. The low Q_0 and high-frequency-dependent power η can be explained by the seismically active region considered in this study (Xu et al., 2010; Singh et al., 2019). Our results are slightly lower than the S-wave quality factor $Q = 212.6\ f^{0.71}$ at frequencies of 1–20 Hz obtained by Zhao et al. (2011) for the northwest Tarim Basin using the hinged trilinear geometrical spreading model proposed by Atkinson and Mereu (1992). After defining a geometrical spreading function as R^{-1}, Sedaghati et al. (2019) also demonstrated strong anelastic attenuation for the Tajikistan-Kyrgyzstan region in Central Asia, west and northwest of our study region, according to the S-wave quality factor $Q = 152\ f^{0.856}$ at frequencies of 1–20 Hz determined by the multiple-station coda normalization method. The much stronger anelastic attenuation (low Q) verified in our study may be majorly attributed to the enormous scattering from the prominent interaction of seismic wave propagation with the highly inhomogeneous crust. The high heterogeneity in the crust beneath the junction of the southwest Tian Shan and the Tarim Basin has been globally recognized, e.g., the well-developed imbricate structures and complex tectonic activity (Allen and Vincent, 1999; Gao et al., 2013; Laborde et al., 2019).

Source Characteristics

The acceleration source spectra for the 46 earthquakes derived from the second-step inversion were plotted in log-log space in **Figure 6A**. The bootstrap analysis was first adopted to evaluate the stability of the inverted source spectra (Oth et al., 2009; Wang et al., 2018). At each frequency, we performed 100 bootstrap inversions and calculated the inverted source spectra, as shown in **Figure 6B** for five typical events. The small deviations to the source spectra obtained using the whole dataset indicated the inverted source spectra are stable and well constrained. We generally observed that the source spectra approximately increase proportional to the square of frequency at low frequencies and then display a plateau at moderate frequencies generally less than ~10 Hz. However, the rapid decay with increasing frequency occurs at high frequencies generally over ~10 Hz, as has also been observed in other studies, e.g., Oth et al. (2011), Oth and Kaiser (2014), and Nakano et al. (2015). The well-known ω-square source model proposed by Brune (1970) matches well with the spectral shape below the high-end cutoff frequency ($f_{\max}$). The high-frequency

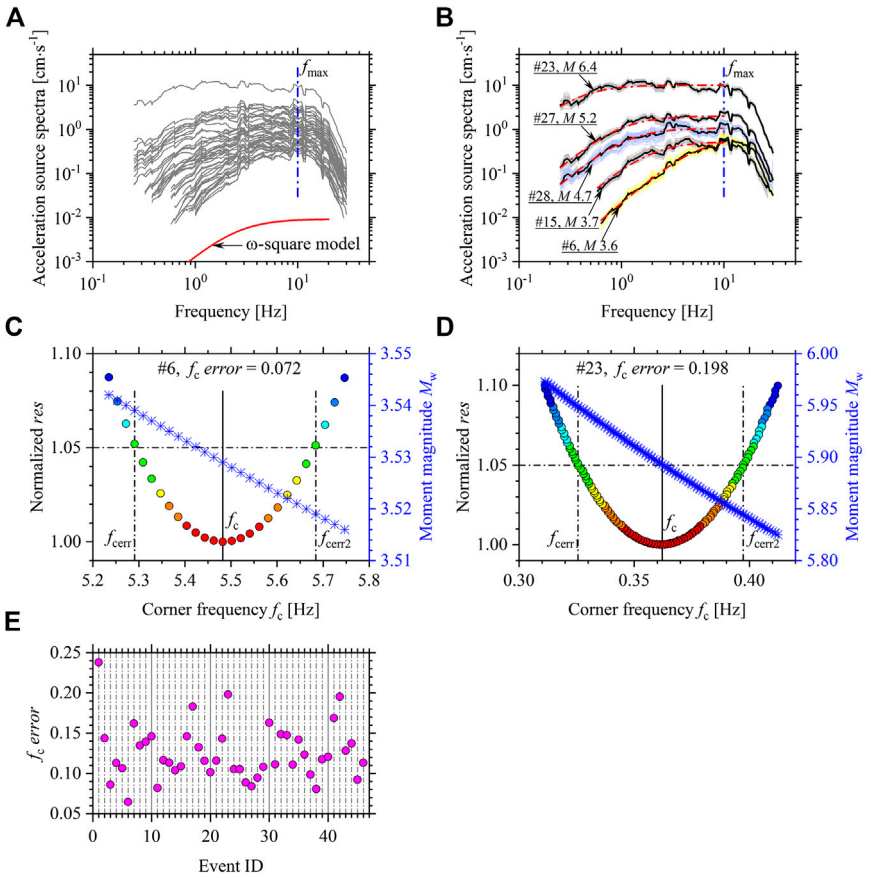

FIGURE 6 | (A) Inverted acceleration source spectra for the earthquakes considered; **(B)** the inverted source spectra from 100 bootstrap inversions (gray, lightblue, and light yellow lines) and the best-fitted theoretical source spectra (red dashed-dotted lines) at frequencies below 10 Hz for five typical events (#10, 20, 27, 40, and 41). The dark lines represent the inverted source spectra using the whole dataset; **(C,D)** the parabola shapes for the *res* normalized by the minimum *res* corresponding to the preferred f_c against the possible corner frequencies for #10 and 40 events, respectively. Frequencies at which *res* exceeds 5% of the minimum *res* are regarded as f_c uncertainty bounds (f_{cerr1} and f_{cerr2}) to provide f_c *error* for quantitatively evaluating the parabola shape. The estimated M_w-f_c pairs (crosses) for the possible f_c are also provided; **(E)** f_c *error* values for the considered events. Event ID is listed in **Table 1**.

spectral decay observed above f_{max} is universally considered to be path- and site-dependent at present (Campbell, 2009; Ktenidou et al., 2013; Lai et al., 2016) and modeled by exp $(-\pi f\kappa)$ where κ indicates the high-frequency decay parameter. A hinged model, single ω-square source model below f_{max}, and combining model of the ω-square source model below f_{max} and the high-frequency decay model above f_{max} can be adopted to describe the inverted source spectra. Our study did not focus on the high-frequency spectral decay beyond the scope of the present work. Following the ω-square source model (Brune, 1970), the inverted source spectra at frequencies below f_{max} = 10 Hz were expressed theoretically by

$$S(f) = (2\pi f)^2 \frac{R_{\Theta\Phi} VF}{4\pi\rho\beta^3} \frac{M_0}{1 + (f/f_c)^2}, \quad (4)$$

where M_0 and f_c are the seismic moment and corner frequency, respectively. $R_{\Theta\Phi}$ is the average radiation pattern over a suitable range of azimuths and take-off angles [set to 0.55 according to Boore and Boatwright (1984)], $V = 1/\sqrt{2}$ represents the partitioning of the total S-wave energy into horizontal components, $F = 2$ accounts for the free surface amplification effect, and ρ is the density in the vicinity of the source (set to 2,600 kg/m^3 according to Zhao et al. (2008)).

The grid-searching method was applied to provide the preferred M_0 and f_c estimates for individual events that minimize the function $res = \sum_{m=1}^{N} [\log_{10} S_{inverted}(f_m) - \log_{10} S_{theoretical}(f_m)]^2$, in which N is the frequency number, and $S_{inverted}$ and $S_{theoretical}$ represent the inverted and theoretical source spectra, respectively. Any values of M_0 and f_c from a grid of all possible values of M_0 and f_c were paired to generate the theoretical source spectra, and the pair that yields the minimum *res* was regarded as the preferred M_0 and f_c estimates. The estimates of M_0 and f_c are listed in **Table 1** for all earthquakes under investigation. Moment magnitude (M_W) was obtained from the spectrally derived M_0 according to the relationship proposed by Hanks and Kanamori (1979), $\log_{10}(M_0) = 1.5(M_W + 10.7)$, where M_0 is in dynecm. **Figure 6B** plots the inverted and best-fitted theoretical spectra for five typical events, and their good agreements were obviously observed.

In order to examine the reliability for estimates by grid searching, we further tested the *res* against possible f_c values

TABLE 1 | Basic information for earthquakes under investigation and source parameter estimates.

Event ID	Date (yyyy/mm/dd)	Time (hh:mm:ss)	No. of recordings	Longitude (°E)	Latitude (°N)	Depth (km)	M	M_w	M_w SD	M_0 (Nm)	log10 (M_0) SD	f_c (Hz)	log10 (f_c) SD	$\Delta\sigma$ (MPa)	log10 ($\Delta\sigma$) SD
1	2007/7/25	18:06:11	10	77.22	39.65	38	4.2	4.257	0.027	2.73E+15	0.04	1.511	0.036	1.708	0.101
2	2007/7/27	13:18:11	8	77.33	39.58	18	4.3	4.19	0.026	2.16E+15	0.039	2.097	0.037	3.621	0.081
3	2007/12/21	8:45:03	5	77.03	39.69	31	3.9	3.929	0.087	8.78E+14	0.131	3.132	0.056	4.897	0.067
4	2012/8/7	17:43:25	7	77.4	39.45	12	4.4	4.432	0.031	4.99E+15	0.047	1.54	0.03	3.309	0.062
5	2015/1/30	9:49:46	4	76.96	39.57	5	3.4	3.589	0.031	2.71E+14	0.046	6.939	0.018	16.455	0.069
6	2018/6/23	16:38:18	12	76.94	39.52	24	3.6	3.529	0.026	2.21E+14	0.039	5.482	0.023	6.597	0.055
7	2018/9/4	5:51:44	16	77	39.51	7	4.9	4.586	0.026	8.49E+15	0.039	1.167	0.02	2.452	0.025
8	2018/9/4	5:52:56	23	76.98	39.51	8	5.5	4.95	0.03	2.99E+16	0.045	1.023	0.02	5.801	0.029
9	2018/9/4	6:24:28	7	77	39.51	5	3	3.449	0.027	1.67E+14	0.04	5.008	0.034	3.815	0.072
10	2018/9/4	7:20:39	5	77.03	39.51	6	3.2	3.631	0.028	3.14E+14	0.042	3.892	0.034	3.357	0.067
11	2018/9/4	8:25:24	9	77.03	39.51	7	3.8	3.964	0.018	9.91E+14	0.027	2.417	0.016	2.541	0.035
12	2018/9/4	10:51:24	17	76.89	39.48	17	4.4	4.353	0.017	3.80E+15	0.026	1.291	0.016	1.483	0.037
13	2018/9/4	21:57:57	6	76.95	39.5	25	3.4	3.672	0.021	3.61E+14	0.031	3.48	0.022	2.766	0.051
14	2018/9/5	2:44:08	9	76.99	39.47	18	3.6	3.706	0.018	4.06E+14	0.028	3.639	0.017	3.557	0.031
15	2018/9/5	11:15:21	12	77.01	39.55	22	3.7	4.088	0.027	1.52E+15	0.04	1.878	0.023	1.828	0.053
16	2011/8/11	18:06:29	11	77.2	39.9	10	5.8	5.093	0.047	4.89E+16	0.071	0.794	0.023	4.443	0.028
17	2012/4/18	22:47:59	3	77.16	39.94	7	4.2	4.429	0.039	4.94E+15	0.058	1.808	0.054	5.296	0.116
18	2012/4/18	22:49:34	3	77.17	39.97	7	4.1	4.151	0.06	1.89E+15	0.09	2.922	0.127	8.562	0.303
19	2013/1/26	23:41:14	4	77.36	39.93	12	4.1	4.309	0.035	3.26E+15	0.053	2.653	0.028	11.059	0.126
20	2018/8/29	15:59:49	6	77.5	39.95	38	3	3.445	0.022	1.65E+14	0.032	5.994	0.044	6.45	0.113
21	2020/1/18	0:05:00	20	77.18	39.83	20	5.4	5.189	0.027	6.82E+16	0.04	0.58	0.022	2.42	0.029
22	2020/1/18	0:09:20	7	77.17	39.81	25	3.9	4.262	0.039	2.77E+15	0.058	1.324	0.024	1.168	0.07
23	2020/1/19	21:27:00	17	77.21	39.83	16	6.4	5.893	0.042	7.75E+17	0.063	0.362	0.031	6.684	0.036
24	2020/1/19	21:39:32	4	77.17	39.91	16	3.4	3.879	0.057	7.39E+14	0.086	2.545	0.062	2.21	0.133
25	2020/1/19	21:48:40	4	77.19	39.97	17	3.3	3.854	0.039	6.78E+14	0.058	2.864	0.036	2.89	0.117
26	2020/1/19	21:51:52	6	77.27	39.91	19	4	4.247	0.038	2.63E+15	0.057	1.665	0.038	2.206	0.073
27	2020/1/19	22:23:01	16	77.46	39.89	14	5.2	4.87	0.023	2.27E+16	0.034	0.945	0.021	3.474	0.033
28	2020/1/19	22:55:10	9	77.44	39.88	18	4.7	4.613	0.036	9.32E+15	0.055	1.074	0.017	2.097	0.045
29	2020/1/19	23:49:31	13	77.47	39.89	16	4.3	4.24	0.019	2.57E+15	0.028	1.976	0.015	3.599	0.034
30	2020/1/20	3:56:10	3	77.24	39.89	15	3	3.59	0.03	2.72E+14	0.045	4.853	0.037	5.65	0.083
31	2020/1/20	5:15:17	3	77.14	39.92	16	3	3.547	0.047	2.35E+14	0.07	4.484	0.062	3.842	0.119
32	2020/1/20	11:17:16	5	77.36	39.91	15	3.6	3.812	0.043	5.86E+14	0.065	4.608	0.067	10.414	0.149
33	2020/1/20	12:45:26	3	77.22	39.92	20	3.2	3.753	0.042	4.78E+14	0.062	4.5	0.027	7.909	0.079
34	2020/1/20	15:33:31	5	77.29	39.94	19	3.4	3.726	0.036	4.36E+14	0.054	4.845	0.031	8.993	0.094
35	2020/1/21	0:15:31	3	77.23	39.92	14	3.6	4.067	0.024	1.41E+15	0.036	1.788	0.043	1.469	0.153
36	2020/1/26	3:49:35	4	77.2	39.92	20	4	4.291	0.03	3.07E+15	0.045	2.771	0.041	11.836	0.09
37	2020/1/29	18:13:58	4	77.16	39.95	21	3.9	4.094	0.035	1.55E+15	0.052	2.861	0.019	6.6	0.069
38	2020/1/31	13:45:31	4	77.17	39.93	24	4.3	4.164	0.047	1.98E+15	0.071	2.619	0.043	6.45	0.077
39	2020/1/31	13:51:17	3	77.17	39.9	15	3.3	3.577	0.079	2.60E+14	0.119	3.985	0.044	2.991	0.055
40	2020/2/21	23:39:14	15	77.47	39.87	10	5.1	4.8	0.02	1.78E+16	0.029	0.925	0.021	2.552	0.042
41	2009/4/22	17:26:09	4	77.25	40.1	25	5	5.024	0.065	3.86E+16	0.098	0.695	0.043	2.353	0.098
42	2010/4/15	8:55:52	6	76.55	40.1	15	4.3	4.23	0.042	2.48E+15	0.063	2.748	0.057	9.351	0.112
43	2013/3/11	11:01:37	7	77.48	40.18	10	5.1	4.906	0.031	2.56E+16	0.047	1.145	0.018	6.982	0.037
44	2015/1/10	14:50:57	5	77.3	40.15	10	5	4.814	0.042	1.87E+16	0.062	0.693	0.037	1.126	0.071
45	2018/11/4	5:36:19	10	77.63	40.24	22	5.1	4.956	0.021	3.05E+16	0.032	1.01	0.015	5.703	0.027
46	2019/1/7	0:22:30	9	77.66	39.92	10	4.8	4.929	0.037	2.78E+16	0.055	0.745	0.04	2.087	0.083

for a parabola shape with a clear minimum at the preferred f_c. Following Viegas et al. (2010), Abercrombie (2014), and Ruhl et al. (2017), we used frequencies at which the *res* exceeds 5% of the minimum *res* as an estimate of the f_c uncertainty bounds f_{cerr1} and f_{cerr2}, and f_c *error*, defined as the frequency-normalized ratio $|f_{cerr1} - f_{cerr2}|/f_c$, must be not greater than two to guarantee the parabola shape with a clear minimum. **Figures 6C,D** provide two events (#10 and #40 with small and large f_c *error* values, respectively) to illustrate the robust estimates for M_0 and f_c. As shown in **Figure 6E**, the parabola shapes were verified for all events by the small f_c *error* values, mainly in the range 0.1–0.2. The uncertainty estimates for M_0 and f_c, provided in **Table 1**, were represented by the SDs over their estimated values from the inverted source spectra based on 100 bootstrap-resampled datasets.

Seismic moments for the earthquakes considered range from 1.650×10^{14} to 7.754×10^{17} Nm, corresponding to M_W = 3.445–5.893. We obtained corner frequencies from 0.362 to 6.940 Hz for these events. Approximately constant earthquake stress drops over a wide range of earthquake sizes and the well-known scaling relation $M_0 \propto f_c^{-3}$ reveal earthquake self-similar scaling, first proposed by Aki (1967).

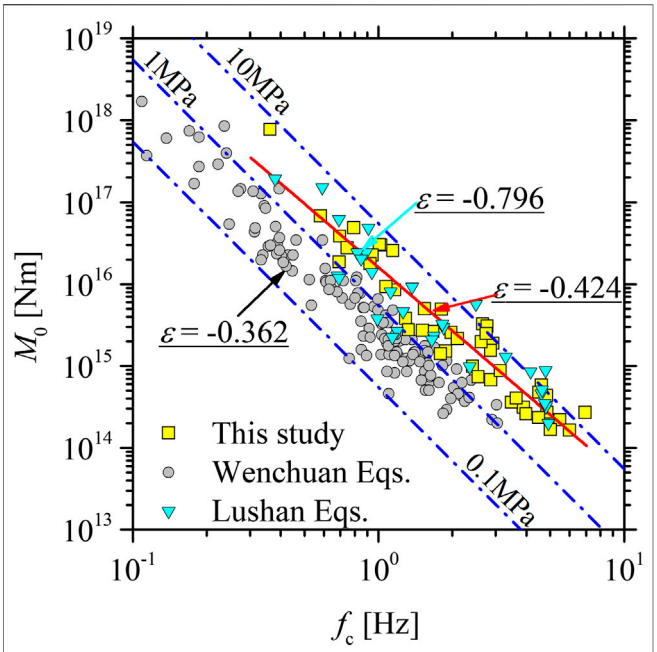

FIGURE 7 | Seismic moment (M_0) vs. corner frequency (f_c). Squares, circles, and triangles represent the earthquakes considered in this study, the 2008 Wenchuan (Wang et al., 2018), and the 2013 Lushan (Wen et al., 2015) seismic sequences, respectively. The $M_0 \propto f_c^{-3}$ scaling relation corresponding to constant stress drops 0.1, 1.0, and 10.0 MPa, respectively, following the theoretical model of Brune (1970), is represented by the dotted-dashed lines.

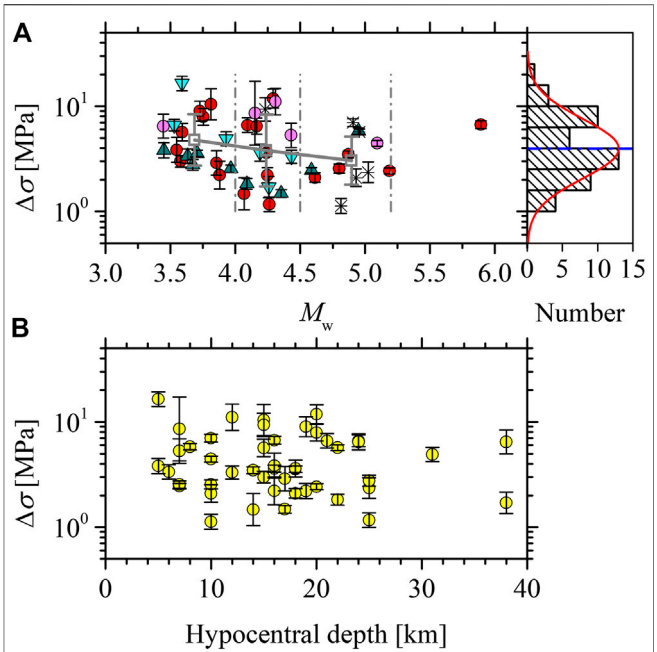

FIGURE 8 | Stress drop ($\Delta\sigma$) as a function of moment magnitude (M_w) **(A)** and hypocentral depth **(B)**. Red circles and dark cyan triangles represent earthquakes in the 2020 and 2018 Jiashi seismic sequences, respectively. Light magenta circles and light cyan triangles represent earthquakes that formerly occurred in proximity to the seismogenic regions of the 2020 and 2018 sequences, respectively. Other earthquakes considered are marked by crosses. The lognormally distributed $\Delta\sigma$ values are found from the histogram.

The self-similar scaling has crucial implications for seismic hazard assessment and understanding of the scale dependence of the earthquake rupture process. The self-similarity has been widely reported by many studies (e.g., Allmann and Shearer, 2009; Oth et al., 2010; Oth and Kaiser, 2014; Boyd et al., 2017; Moyer et al., 2018), while other studies have provided evidence for the significant breakdown of self-similarity (e.g., Drouet et al., 2011; Pacor et al., 2016; Baruah et al., 2016; Trugmann and Shearer, 2018). The plots of M_0 vs. f_c for earthquakes considered in this study intuitively depart from the scaling relation, as shown in **Figure 7**. Moreover, we applied a so-called parameter ε proposed by Kanamori and Rivera (2004) from the scaling relation $M_0 \propto f_c^{-(3+\varepsilon)}$ to quantify the deviation from the self-similarity. When $\varepsilon = 0$, it indicates perfect self-similar scaling. We found $\varepsilon = -0.424 \pm 0.122$ according to the least-squares regression, which indicates the decrease of stress drop on average with the increasing magnitude size. Similar ε values have also been observed in the 2008 Wenchuan and 2013 Lushan seismic sequences (Wen et al., 2015; Wang et al., 2018), even if the estimated stress drops showed differences (**Figure 7**).

According to the circular source model (Eshelby, 1957; Brune, 1970), the stress drop $\Delta\sigma$ can be obtained from the following formulas:

$$\Delta\sigma = 7M_0/16r^3, \quad (5)$$

$$r = (k\beta)/f_c, \quad (6)$$

where r is the fault radius and k is a numerical factor that depends on the specific theoretical model (Brune, 1970; Madariaga, 1976; Kaneko and Shearer, 2014; Kaneko and Shearer, 2015). The selection of the theoretical model predominantly controls the absolute values of $\Delta\sigma$. For example, the two most commonly adopted models proposed by Brune (1970) and by Madariaga (1976) yield a difference for the computed stress drops with a factor of ~5.5. However, the relative values and the variations in $\Delta\sigma$ are not influenced by the model selection. In this study, k = 0.37 was used for S-waves according to the theoretical model of Brune (1970). The combination of M_0 and f_c yields $\Delta\sigma$ values between 1.126 and 16.455 MPa, as shown in **Figure 8A**. Computed stress drops exhibit large scatter and approximately show a lognormal distribution with an average value of 3.942 MPa and an SD for the stress drop on the base-10 logarithmic scale equal to 0.284. The average stress drop is similar to the global averages for tectonic earthquakes, ~1–10 MPa (Allmann and Shearer, 2009; Oth et al., 2010; Trugmann and Shearer, 2017; Baltay et al., 2019). Median stress drops show a mild decreasing tendency as a function of moment magnitude over a range M_w = 3.445–5.189, which indicates that self-similar scaling breaks for these earthquakes under investigation. However, there is no dependence of stress drop on the hypocentral depth (**Figure 8B**). As shown in

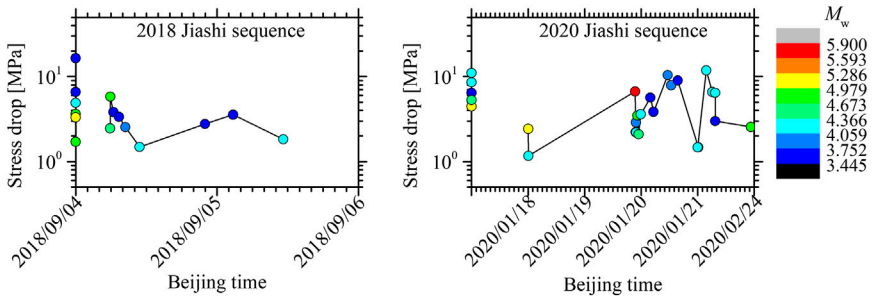

FIGURE 9 | Temporal variation of stress drops for the 2018 and 2020 Jiashi seismic sequences. Earthquakes previously occurring close to the seismogenic region are plotted in the vertical axis; #1–#6 and #16–#20 represent the 2018 and 2020 sequences, respectively.

Figure 8A, except for some events in the 2020 sequence with relatively higher stress drops, earthquakes with similar moment magnitudes from the Jiashi seismic sequences in both 2020 and 2018 generally share a similar level of stress drop (~1–6 MPa), and stress drops first decrease and then increase with the increasing moment magnitude.

Earthquakes considered in this study mainly consist of the 2020 Jiashi seismic sequence (#21–#40) on the Kepingtage thrust fault and the 2018 Jiashi seismic sequence (#7–#15) on the buried fault in the northwest Tarim Basin. Similar to the 2020 sequence, an M_s 4.9 foreshock immediately followed by the M_s 5.5 mainshock aroused the 2018 sequence. **Figure 9** provides the temporal variation of stress drop estimates for both sequences. In or close to the seismogenic regions of both sequences, some sporadic small earthquakes occurred months to years before the sequence with relatively higher stress drops compared with aftershocks with a similar moment magnitude (**Figures 8A**, **9**), while the foreshocks minutes to days before the mainshock released much lower stress, consistent with the observations from other earthquake sequences (e.g., Moyer et al., 2018). After the stress drop returned to the higher level during the adjoining mainshock, aftershocks immediately following in close proximity to the mainshock showed depressing stress drops in both sequences, which furnishes a potential clue of the continuous rerupture of the already fractured and not fully healed portion by the mainshock (Shaw et al., 2015). Aftershocks with stress drops much smaller than the mainshock have also been commonly reported for both tectonic and induced seismic sequences (e.g., Boyd et al., 2017; Trugman et al., 2017; Moyer et al., 2018; Trugmann and Shearer, 2018; Baltay et al., 2019) and used to account for the reduced ground motion of aftershocks (Abrahamson et al., 2014). The stress drops of the aftershocks appeared to recover gradually as time increased, which was also observed in the induced seismic sequences (e.g., Trugman et al., 2017; Yenier et al., 2017). Such temporal recovery of the stress drop may be indicative of an increase of fault strength with the increase in healing time. Finally, the released stress was elevated to a rather high level, even over 10 MPa for partial aftershocks, which subsequently occurred 10 h to days later in the 2020 sequence, which hints to potential ruptures for the isolated, small-scale patches with high strength concentrating substantial stress levels in the damaged fault zone (Dreger et al., 2007; Oth and Kaiser, 2014). The changes of the fault strength across the seismogenic fault caused by the mainshock play short-term roles on sources of the surrounding earthquakes.

In both sequences, the strong foreshock did not ultimately expand to be the largest mainshock. In view of the low stress drop of the foreshock and the high stress release in the adjoining mainshock, we presumed that the adjoining high-strength patch eventually ruptured by the mainshock may cease the continuous expansion of the fractured low-strength patch by the foreshock. Moreover, the initiating fracture of the low-strength patch may play an effective role in accelerating the concentration of stress at the edge of the high-strength patch (Oth and Kaiser, 2014), until the high-strength patch broke to account for the mainshock. As concluded by Ben-Zion and Zhu (2002), large earthquakes grow in a relatively homogeneous stress field and average out the remaining short-scale fluctuations over their (large) rupture areas. We thus inferred that the foreshock-mainshock behavior may be likely to occur in the high heterogeneous fault zone.

CONCLUSION

We performed the nonparametric spectral inversion to isolate the propagation path attenuation and source spectra from the S-wave Fourier amplitude spectra of the observed ground motions from 46 earthquakes in the junction of the northwest Tarim Basin and Kepingtage fold-and-thrust zone, mainly composed of two Jiashi seismic sequences in 2020 and 2018. Nonparametric path attenuation curves indicate slow seismic wave decay with increasing hypocentral distance. The path attenuation was simply modeled by the combination of the hinged bilinear geometrical model and the anelastic attenuation model as a function of the quality factor. The combination derived in this study can be directly used for predicting ground motions in this region. The transition distance R_1 = 60 km, n_1 = 0.30, and n_2 = 0.59 defined the preferred hinged bilinear geometrical model in the study region. The strong anelastic attenuation in the study

region, represented by $Q = 60.066\ f^{0.988}$ at frequencies of 0.254–30 Hz, may be ascribed to enormous scattering resulting from the prominent interaction of seismic wave propagating with the high inhomogeneous crust.

The inverted source spectra at frequencies below f_{max} = ~10 Hz are found in good agreement with the ω-square model; the source parameters were thus estimated by fitting the inverted spectra with the theoretical ω-square model. The obvious deviation of M_0-f_c plots to the $M_0 \propto f_c^{-3}$ scaling relation and the dependence of the stress drop on the moment magnitude provide crucial evidence for the breakdown of earthquake self-similar scaling for the events considered in this study. The stress drops for earthquakes from the Jiashi seismic sequences in both 2020 and 2018 appear to first decrease and then increase as the moment magnitude increased. The average stress drop for these earthquakes was 3.942 MPa. The temporal variation of the stress drops indicates the short-term effects of the mainshock on the source characteristics of the adjoining earthquakes before and after the mainshock. After the great stress release during the mainshock, the stress drops fell to a low level for aftershocks immediately following and then gradually recovered in a short time, which reveals the gradual healing of the fractured fault by the mainshock. The much higher stress drops for some aftershocks in the damaged fault zone may also be related to the potential ruptures for small-scale patches with high strength. The foreshock with a low stress release occurring in the high-heterogeneity fault zone may motivate the following occurrence of the largest magnitude mainshock with a high stress release. We inferred that the foreshock-mainshock behavior may be inclined to occur in the inhomogeneous fault zone, e.g., the junction of the northwest Tarim Basin and Kepingtage fold-and-thrust zone.

DATA AVAILABLITY STATEMENT

Publicly available datasets were analyzed in this study. This data can be found here: Ground motion recordings for this study were provided by China Strong Motion Network Centre at Institute of Engineering Mechanics, China Earthquake Administration, contacting the email csmnc@iem.ac.cn for data application (last accessed March 2020). Basin information for earthquakes mentioned in this study was obtained from China Earthquake Network Center at the website of http://news.ceic.ac.cn/ (last accessed March 2020). The focal mechanisms for some earthquakes in this study were derived from the United States Geology Survey at the website of www.usgs.gov/ (last accessed February 2020).

AUTHOR CONTRIBUTIONS

HW and RW worked together for this manuscript. They jointly collected and processed the strong ground motion recordings for the observed S-wave spectra. HW performed the nonparametric spectral inversion for isolating the propagation path attenuation and the source spectra. HW and RW estimated the source parameters and evaluated their reliability and uncertainty. They analyzed the temporal variation of stress drop and drew some interesting conclusions. They together wrote this article.

FUNDING

This work was supported by the National Natural Science Foundation of China (nos. 51808514; 51878632) and the Science Foundation of the Institute of Engineering Mechanics, China Earthquake Administration (no. 2018B03).

REFERENCES

Abercrombie, R. E. (2014). Stress drops of repeating earthquakes on the San Andreas fault at Parkfield. *Geophys. Res. Lett.* 41, 8784–8791. doi:10.1002/2014GL062079

Abercrombie, R. E., Bannister, S., Ristau, J., and Doser, D. (2017). Variability of earthquake stress drop in a subduction setting, the Hikurangi margin, New Zealand. *Geophys. J. Int.* 208, 306–320. doi:10.1093/gji/ggw393

Abrahamson, N. A., and Silva, W. J. (1997). Empirical response spectral attenuation relations for shallow crustal earthquakes. *Seismol Res. Lett.* 68 (1), 94–127. doi:10.1785/gssrl.68.1.94

Abrahamson, N. A., Silva, W. J., and Kamai, R. (2014). Summary of the ASK14 ground-motion relation for active crustal regions. *Earthquake Spectra* 30 (3), 1025–1055. doi:10.1193/070913EQS198M

Aki, K. (1967). Scaling law of seismic spectrum. *J. Geophys. Res.* 72 (4), 1217–1231. doi:10.1029/JZ072i004p01217

Allen, M. B., and Vincent, S. J. (1999). Late Cenozoic tectonics of the Kepingtage thrust zone: interactions of the Tien Shan and Tarim Basin, northwest China. *Tectonics* 18 (4), 639–645. doi:10.1029/1999TC900019

Allmann, B. P., and Shearer, P. M. (2009). Global variations of stress drop for moderate to large earthquakes. *J. Geophys. Res.* 114, B01310. doi:10.1029/2008JB005821

Atkinson, G. M. (2004). Empirical attenuation of ground-motion spectral amplitudes in southeastern Canada and the northeastern United States. *Bull. Seismol. Soc. Am.* 94 (3), 1079–1095. doi:10.1785/0120040161

Atkinson, G. M., and Boore, D. M. (1995). Ground-motion relation for eastern North America. *Bull. Seismol. Soc. Am.* 85 (1), 17 –30.

Atkinson, G. M., and Cassidy, J. F. (2000). Integrated use of seismography and strong-motion data to determine soil amplification: response of the Fraser River Delta to the Duvall and Georgia Strait earthquakes. *Bull. Seismol. Soc. Am.* 90 (4), 1028–1040. doi:10.1785/0119990098

Atkinson, G. M., and Mereu, R. F. (1992). The shape of ground motion attenuation curves in southeastern Canada. *Bull. Seismol. Soc. Am.* 82 (5), 2014–2031.

Baltay, A. S., Hanks, T. C., and Abrahamson, N. A. (2019). Earthquake stress drop and Arias intensity. *J. Geophys. Res. Solid Earth* 124, 3838–3852. doi:10.1029/2018JB016753

Baruah, B., Kumar, P., Kumar, M. R., and Ganguli, S. S. (2016). Stress-drop variations and source scaling relations of moderate earthquakes of the Indian tectonic plate. *Bull. Seismol. Soc. Am.* 106 (6), 2640–2652. doi:10.1785/0120150106

Ben-Zion, Y., and Zhu, L. (2002). Potency–magnitude scaling relations for southern California earthquakes with 1.0 < ML < 7.0. *Geophys. J. Int.* 148, F1–F5. doi:10.1046/j.1365-246X.2002.01637.x

Beresnev, I. A., and Wen, K.-L. (1996). Nonlinear soil response—a reality. *Bull. Seismol. Soc. Am.* 86 (6), 1964–1978.

Bindi, D., Castro, R. R., Franceschina, G., Luzi, L., and Pacor, F. (2004). The 1997–1998 Umbria–Marche sequence (Central Italy): source, path, and site effects estimated from strong motion data recorded in the epicentral area. *J. Geophys. Res.* 109, B04312. doi:10.1029/2003JB002857

Boore, D. M. (2003). Simulation of ground motion using the stochastic method. *Pure Appl. Geophys.* 163, 635–676.

Boore, D. M., and Boatwright, J. (1984). Average body-wave radiation coefficients. *Bull. Seismol. Soc. Am.* 74 (5), 1615–1621.

Bora, S. S., Scherbaum, F., Kuehn, N., Stafford, P., and Edwards, B. (2015). Development of a response spectral ground-motion prediction equation (GMPE) for seismic-hazard analysis from empirical Fourier spectra and duration models. *Bull. Seismol. Soc. Am.* 105 (4), 2192–2218. doi:10.1785/0120140297

Boyd, O. S., McNamara, D. E., Hartzell, S., and Choy, G. (2017). Influence of lithostatic stress on earthquake stress drops in North America. *Bull. Seismol. Soc. Am.* 107 (2), 856–868. doi:10.1785/0120160219

Brune, J. N. (1970). Tectonic stress and the spectra of seismic shear waves from earthquakes. *J. Geophys. Res.* 75 (26), 4997–5009. doi:10.1029/JB075i026p04997

Buslov, M. M., Grave, J. D., Bataleva, E. A. V., and Batalev, V. Y. (2007). Cenozoic tectonic and geodynamic evolution of the Kyrgyz Tien Shan Mountains: a review of geological, thermochronological, and geophysical data. *J. Asian Earth Sci.* 29, 205–214. doi:10.1016/j.jseaes.2006.07.001

Calderoni, G., Rovelli, A., and Giovambattista, R. D. (2017). Rupture directivity of the strongest 2016–2017 central Italy earthquakes. *J. Geophys. Res. Solid Earth* 122 (11), 9118–9131. doi:10.1002/2017JB014118

Campbell, K. W. (2009). Estimates of shear-wave Q and κ_0 for unconsolidated and semiconsolidated sediments in eastern North America. *Bull. Seismol. Soc. Am.* 99 (4), 2365–2392. doi:10.1785/0120080116

Castro, R. R., Anderson, J. G., and Singh, S. K. (1990). Site response, attenuation and source spectra of S waves along the Guerrero, Mexica, subduction zone. *Bull. Seismol. Soc. Am.* 80 (6), 1481–1503.

Dreger, D., Nadeau, R. M., and Chung, A. (2007). Repeating earthquakes finite source models: strong asperities revealed on the San Andreas fault. *Geophys. Res. Lett.* 34, L23302. doi:10.1029/2007gl031353

Drouet, S., Bouin, M.-P., and Cotton, F. (2011). New moment magnitude scale, evidence of stress drop magnitude scaling and stochastic ground motion model for the French West Indies. *Geophys. J. Int.* 187, 1625–1644. doi:10.1111/j.1365-246X.2011.05219.x

Eshelby, J. D. (1957). The determination of the elastic field of an ellipsoidal inclusion, and related problems. *Proc. R. Soc. Lond.* 241 (1226), 376–396. doi:10.1098/rspa.1957.0133

Gao, R., Hou, H., Cai, X., Hnapp, J. H., He, R., Liu, J., et al. (2013). Fine crustal structure beneath the junction of the southwest Tian Shan and Tarim Basin, NW China. *Lithosphere* 5, 382–392. doi:10.1130/L248.1

Hanks, T. C., and Kanamori, H. (1979). A moment magnitude scale. *J. Geophys. Res.* 84, 2348–2350. doi:10.1029/JB084iB05p02348

Kanamori, H., and Rivera, L. (2004). Static and dynamic scaling relations for earthquakes and their implications for rupture speed and stress drop. *Bull. Seismol. Soc. Am.* 94 (1), 314–319. doi:10.1785/0120030159

Kanbur, M. Z., Silahtar, A., and Aktan, G. (2020). Local site effects evaluation by surface wave and H/V survey methods in Senirkent (Isparta) region, southwestern Turkey. *Earthq. Eng. Eng. Vib.* 19, 321–333. doi:10.1007/s11803-020-0564-z

Kaneko, Y., and Shearer, P. M. (2014). Seismic source spectra and estimated stress drop derived from cohesive-zone models of circular subshear rupture. *Geophys. J. Int.* 197, 1002–1015. doi:10.1093/gji/ggu030

Kaneko, Y., and Shearer, P. M. (2015). Variability of seismic source spectra, estimated stress drop, and radiated energy, derived from cohesive-zone models of symmetrical and asymmetrical circular and elliptical ruptures. *J. Geophys. Res. Solid Earth* 120, 1053–1079. doi:10.1002/2014JB011642

Konno, K., and Ohmachi, T. (1998). Ground-motion characteristics estimated from ratio between horizontal and vertical components of microtremor. *Bull. Seismol. Soc. Am.* 88 (1), 228–241.

Ktenidou, O.-J., Gélis, C., and Bonilla, L.-F. (2013). A study on the variability of kappa (κ) in a borehole: implications of the computation process. *Bull. Seismol. Soc. Am.* 103 (2A), 1048–1068. doi:10.1785/0120120093

Laborde, A., Barrier, L., Simoes, M., Li, H., Coudroy, T., Woerd, J. V. D., et al. (2019). Cenozoic deformation of the Tarim Basin and surrounding ranges (Xinjiang, China): a regional overview. *Earth Sci. Rev.* 197, 102891. doi:10.1016/j.earscirev.2019.102891

Lai, T.-S., Mittal, H., Chao, W.-A., and Wu, Y.-M. (2016). A study on kappa value in Taiwan using borehole and surface seismic array. *Bull. Seismol. Soc. Am.* 106 (4), 1509–1517. doi:10.1785/0120160004

Lermo, J., and Chavez-Garcia, F. (1993). Site effect evaluation using spectral ratios with only one station. *Bull. Seismol. Soc. Am.* 83, 1574–1594.

Li, S., Zhang, X., Mooney, W. D., and Lai, X. (2002). A preliminary study on the structures of Jiashi earthquake region and earthquake generating fault. *Chin. J. Geophys.* 45 (1), 76–82 [in Chinese, with English summary].

Liu, Q., Chen, J., Li, S., and Guo, B. (2000). Passive seismic experiment in Xinjiang-Jiashi strong earthquake region and discussion on its seismic genesis. *Chin. J. Geophys.* 43 (3), 356–365 [in Chinese, with English summary]. doi:10.1002/cjg2.48

Madariaga, R. (1976). Dynamics of an expanding circular fault. *Bull. Seismol. Soc. Am.* 66 (3), 639–666.

Mahani, A. B., and Atkinson, G. M. (2012). Evaluation of functional forms for the attenuation of small-to-moderate earthquake response spectral amplitudes in North America. *Bull. Seismol. Soc. Am.* 102 (6), 2714–2726. doi:10.1785/0120120050

McNamara, D., Meremonte, M., Maharrey, J. Z., Mildore, S.-L., Altidore, J. R., Anglade, D., et al. (2012). Freqeuncy-dependent seismic attenuation within the Hispaniola Island region of the Caribbean sea. *Bull. Seismol. Soc. Am.* 102 (2), 773–782. doi:10.1785/0120110137

Moyer, P. A., Boettcher, M. S., McGuire, J. J., and Collins, J. A. (2018). Spatial and temporal variations in earthquake stress drop on Gofar transform fault, east Pacific Rise: implications for fault strength. *J. Geophys. Res. Solid Earth* 123, 7722–7740. doi:10.1029/2018jb015942

Nakano, K., Matsushima, S., and Kawase, H. (2015). Statistical properties of stromg ground motions from the generalized spectral inversion of data observed by K-NET, KiK-net and the JMA Shindokei Network in Japan. *Bull. Seismol. Soc. Am.* 105 (5), 2662–2680. doi:10.1785/0120140349

Oth, A., Bindi, D., Parolai, S., and Giacomo, D. D. (2011). Spectral analysis of K-NET and KiK-net data in Japan, Part II: on attenuation characteristics, source spectra, and site response of borehole and surface stations. *Bull. Seismol. Soc. Am.* 102 (2), 667–687. doi:10.1785/0120100135

Oth, A., Bindi, D., Parolao, S., and Giacomo, D. D. (2010). Earthquake scaling characteristics and the scale-(in)dependence of seismic energy-to-moment ratio: insights from KiK-net data in Japan. *Geophys. Res. Lett.* 37 (19), 470–479. doi:10.1029/2010GL044572

Oth, A., Bindi, D., Parolai, S., and Wenzel, F. (2008). S-wave attenuation characteristics beneath the Vrancea region in Romania: new insights from the inversion of ground-motion spectra. *Bull. Seismol. Soc. Am.* 98 (5), 2482–2497. doi:10.1785/0120080106

Oth, A., and Kaiser, A. E. (2014). Stress release and source scaling of the 2010–2011 Canterbury, New Zealand earthquake sequence from spectral inversion of ground motion data. *Pure Appl. Geophys.* 171, 2767–2782. doi:10.1007/s00024-013-0751-1

Oth, A., Parolai, S., Bindi, D., and Wenzel, F. (2009). Source spectra and site response from S waves of intermediate-depth Vrancea, Romania, earthquakes. *Bull. Seismol. Soc. Am.* 99 (1), 235–254. doi:10.1785/0120080059

Pacor, F., Spallarossa, D., Oth, A., Luzi, L., Puglia, R., Cantore, L., et al. (2016). Spectral models for ground motion prediction in the L'Aquila region (central Italy): evidence for stress-drop dependence on magnitude and depth. *Geophys. J. Int.* 204, 697–718. doi:10.1093/gji/ggv448

Pavel, F., and Vacareanu, R. (2018). Investigation on regional attenuation of Vrancea (Romania) intermediate-depth earthquakes. *Earthq. Eng. Eng. Vib.* 17, 501–509. doi:10.1007/s11803-018-0458-5

Ruhl, C. J., Abercrombie, R. E., and Smith, K. D. (2017). Spatiotemporal variation of stress drop during the 2008 Mogul, Nevada earthquake swarm. *J. Geophys. Res. Solid Earth* 122 (1), 8163–8180. doi:10.1002/2017JB014601

Sedaghati, F., Nazemi, N., Pezeshk, S., Ansari, A., Daneshvaran, S., and Zare, M. (2019). Investigation of coda and body wave attenuation functions in Central Asia. *J. Seismol.*, 23, 1047–1070. doi:10.1007/s10950-019-09854-x

Shaw, B. E., Richards-Dinger, K., and Dieterich, J. H. (2015). Deterministic model of earthquake clustering shows reduced stress drops for nearby aftershocks. *Geophys. Res. Lett.* 42, 9231–9238. doi:10.1002/2015GL066082

Shi, D. (2009). Study on new methods of site classification based on GIS. Master's thesis. Harbin (China): China Earthquake Administration.

Singh, C., Biswas, R., Jaiswal, N., and Kumar, M. R. (2019). Spatial variations of coda wave attenuation in Andaman-Nicobar subduction zone. *Geophys. J. Int.* 217 (3), 1515–1523. doi:10.1093/gji/ggz098

Song, C., Gao, R., Liu, J., Liu, P., Guo, Y., and Wen, S. (2019). Discussion on earthquake sequence and seismogenic structure for the Jiashi M_s5.5 earthquake on September 4, 2018, Xinjiang. *Earthq. Res. China* 35 (2), 256–268 [in Chinese, with English summary].

Trugmann, D. T., and Shearer, P. M. (2017). Application of an improved spectral decomposition method to examine earthquake source scaling in southern California. *J. Geophys. Res. Solid Earth* 122 (4), 2890–2910. doi:10.1002/2017JB013971

Trugmann, D. T., and Shearer, P. M. (2018). Strong correlation between stress drop and peak ground acceleration for M 1-4 earthquakes in the San Francisco Bay area. *Bull. Seismol. Soc. Am.* 108 (2), 929–945. doi:10.1785/0120170245

Trugman, D. T., Dougherty, S. L., Cochran, E. S., and Shearer, P. M. (2017). Source spectral properties of small-to-moderate earthquakes in southern Kansas. *J. Geophys. Res. Solid Earth* 122 (10), 8021–8034. doi:10.1002/2017JB014649

Turner, S. A., Cosgrove, J. W., and Liu, J. G. (2010). Controls on lateral structural variability along the Keping Shan Thrust belt, SW Tien Shan Foreland, China. *Geol. Soc. Spec. Publ.* 348, 71–85. doi:10.1144/SP348.5

Viegas, G., Abercrombie, R. E., and Kim, W.-Y. (2010). The 2002 M5 Au Sable Forks, NY, earthquake sequence: source scaling relationships and energy budget. *J. Geophys. Res. Solid Earth* 115, B07310. doi:10.1029/2009JB006799

Wang, H., Ren, Y., and Wen, R. (2018). Source parameters, path attenuation and site effects from strong-motion recordings of the Wenchuan aftershocks (2008–2013) using a non-parametric generalized inversion technique. *Geophys. J. Int.* 212, 872–890. doi:10.1093/gji/ggx447

Wen, R., Wang, H., and Ren, Y. (2015). Estimation of source parameters and quality factor based on the generalized inversion method in Lushan earthquake. *J. Harbin Inst. Technol.* 47 (4), 58–63. doi:10.11918/j.issn.0367-6234.2015.04.010

Wu, C., Peng, Z., and Ben-Zion, Y. (2010). Refined thresholds for non-linear ground motion and temporal changes of site response associated with medium-size earthquakes. *Geophys. J. Int.* 182, 1567–1576. doi:10.1111/j.1365-246X.2010.04704.x

Xu, Y., Herrmann, R. B., Wang, C.-Y., and Cai, S. (2010). Preliminary high-frequency ground-motion scaling in Yunnan and southern Sichuan, China. *Bull. Seismol. Soc. Am.* 100 (5B), 2508–2517. doi:10.1785/0120090196

Yang, Y., Yao, W. Q., Yan, J. J., Guo, Y., and Xie, D. Q. (2018). Mesozoic and Cenzoic structural deformation in the NW Tarim Basin, China: a case study of the Piqiang-Selibuya fault. *Int. Geol. Rev.* 60 (7), 929–943. doi:10.1080/00206814.2017.1360803

Yenier, E., and Atkinson, G. M. (2015). An equivalent point-source model for stochastic simulation of earthquake ground motions in California. *Bull. Seismol. Soc. Am.* 105 (3), 1435–1455. doi:10.1785/0120140254

Yenier, E., Atkinson, G. M., and Sumy, D. F. (2017). Ground motions for induced earthquakes in Oklahoma. *Bull. Seismol. Soc. Am.* 107 (1). doi:10.1785/0120160114

Zhao, C., Chen, Z., Hua, W., Wang, Q., Li, Z., and Zheng, S. (2011). Study on source parameters of small to moderate earthquakes in the main seismic active regions, China mainland. *Chin. J. Geophys.* 54 (6), 1478–1489. doi:10.3969/j.issn.0001-5733.2011.06.007

Zhao, C., Chen, Z., Zheng, S., and Zhang, Z. (2008). Moment inversion of moderate earthquakes and the locally perturbed stress field in the Jiashi source region. *Chin. J. Geophys.* 51 (3), 782–792. doi:10.1002/cjg2.1246

Conflict of Interest: The authors declare that the research was conducted in the absence of any commercial or financial relationships that could be construed as a potential conflict of interest.

frontiers in Earth Science

ORIGINAL RESEARCH
published: 12 February 2021
doi: 10.3389/feart.2021.618400

Strong-Motions From Damaging Moderate Magnitude (5.9 ≥ Mw) Earthquakes in Japan Recorded by K-NET and KiK-net

Yadab P. Dhakal *

National Research Institute for Earth Science and Disaster Resilience, Tsukuba, Japan

Strong-motions from 79 moderate magnitude (5.9 ≥ Mw) earthquakes that caused various degrees of impact on humans and built-environment in Japan between 1996 and 2019, after the start of K-NET and KiK-net, are presented. As such, most of the earthquakes occurred beneath the land, and agencies had reported damages from events as small as Mw 4.1. Together, large peak ground accelerations exceeding 500 cm/s^2 were recorded during 15 earthquakes, reaching approximately 1128 cm/s^2 during one event. Similarly, large peak ground velocities exceeding 30 cm/s were recorded during ten earthquakes, reaching about 76 cm/s to the maximum. Most of the large values aforementioned were recorded within a hypocentral distance of approximately 30 km and on soil site conditions. Intermediate to long-period ground motions are of growing concerns in urban areas located on sedimentary basins with mid-rise and high-rise buildings. The threshold magnitude for the large ground motions at the periods of about 2–5 s is not well understood. In March 2013, the Japan Meteorological Agency introduced four levels of long-period ground motion intensity (LPGMI) based on absolute velocity response spectra (AVRS) between 1.6 and 7.8 s. In the present data set, LPGMI of level 3 (AVRS 50–100 cm/s) and level 4 (AVRS >100 cm/s) were observed each at a single site from shallow-focus earthquakes of Mw 5.8 and 5.9 at distances of approximately 12 and 15 km, respectively. However, the peak response periods were relatively short (1.6–1.8 s). The data showed that LPGM from moderate earthquakes is of lower concern regarding earthquake early warning at distances beyond 200 km. The 2018 Mw 5.5 North Osaka earthquake, despite the moderate magnitude, caused the loss of six human lives and brought significant damage to buildings and lifelines. Comparing the data with the ground motion prediction equations (GMPEs) and other events suggested that the North Osaka earthquake was probably a higher stress drop event. These moderate earthquakes' observations hinted that the commonly used GMPEs in Japan may not sufficiently grasp these earthquakes' hazards.

Keywords: strong-motions, source effect, site amplification, moderate earthquakes, the 2018 North Osaka earthquake, PGA and PGV, JMA seismic intensity scale, long-period ground motions

OPEN ACCESS

Edited by:
Nicola Alessandro Pino, National Institute of Geophysics and Volcanology (INGV), Italy

Reviewed by:
Luca Moratto, National Institute of Oceanography and Applied Geophysics (Italy), Italy
Nitin Sharma, National Geophysical Research Institute (CSIR), India

***Correspondence:**
Yadab P. Dhakal
ydhakal@bosai.go.jp

Specialty section:
This article was submitted to Solid Earth Geophysics, a section of the journal Frontiers in Earth Science

Received: *16 October 2020*
Accepted: *11 January 2021*
Published: *12 February 2021*

Citation:
Dhakal YP (2021) Strong-Motions From Damaging Moderate Magnitude (5.9 ≥ Mw) Earthquakes in Japan Recorded by K-NET and KiK-net. Front. Earth Sci. 9:618400. doi: 10.3389/feart.2021.618400

INTRODUCTION

Big earthquakes are generally well reported and investigated in detail for disaster prevention measures for future earthquakes. It is well known that strong-earthquakes of magnitudes over about six can cause damage to broad areas crossing town and city borders, sometimes resulting in many fatalities: for example, the 2009 Mw 6.3 L'Aquila earthquake that caused fatalities of over 300 people and left more than 65,000 homeless (e.g., Alexander, 2010), the 2011 Mw 6.2 Christchurch earthquake that caused 181 deaths and widespread damages (e.g., Kaiser et al., 2012). On the other hand, damages from moderate magnitude events (moment magnitude Mw ≤ 5.9) are confined relatively to small areas and recorded by relatively few strong-motion sensors mainly due to sparse network operations. However, as the major cities and population centers in Japan are prone to large magnitude earthquakes due to the active plate tectonics in the region (e.g., Hashimoto and Jackson, 1993; Matsu'ura, 2017), dense strong-motion observation networks have been in operation throughout Japan, especially after the Kobe earthquake of 1995 (e.g., Okada et al., 2004; Aoi et al., 2020a). In the present study, I collected and analyzed more than 10,000 strong-motion records observed by K-NET and KiK-net (NIED, 2019a) from the moderate magnitude events (4.1 ≤ Mw ≤ 5.9) during the years 1996–2019. Altogether, 79 events of the aforementioned magnitudes were selected from the list of damaging earthquakes provided by the Japan Meteorological Agency (JMA, 2020a). The moderate earthquakes' effects ranged from an injury to a person without reported damages to built-structures for some events to fatalities of six people, the destruction of several buildings, damages to lifelines and national treasures and cultural assets, disruption to social services, etc. by the Mw 5.5 North Osaka earthquake in 2018 (e.g., Hirata and Kimura, 2018; Koshiyama, 2019). Examples of notable damaging moderate magnitude earthquakes recorded by modern instrumentation are the 2012 northern Italy earthquakes of Mw values between 5.5 and 6.0 (e.g., Mucciarelli and Liberatore, 2014; Meroni et al., 2017), the 2011 Mw 5.1 Lorca earthquake in southeastern Spain (e.g., Lopez-Comino et al., 2012; Gordo-Monso' and Miranda, 2018), and so on.

This paper has mainly two objectives. The first is to introduce the peak ground motions from the damaging moderate magnitude events in terms of the peak ground accelerations (PGAs), peak ground velocities (PGVs), JMA instrumental intensities, and the absolute velocity response spectra (AVRS) at selected periods, and to discuss the factors that contributed to the generation of the larger values. Nationwide earthquake early warning (EEW) has been implemented in Japan since October 2007 (Hoshiba et al., 2008). The AVRS in the period range of 1.6–7.8 s has been used to provide the information on long-period ground motion intensity (LPGMI) by JMA since March 2013 (Aizawa et al., 2013; Nakamura 2013). Experimental EEW and real-time information on LPGMI has been operated in Japan (e.g., Aoi et al., 2020b). The threshold magnitudes and distance ranges for the large long-period ground motions are not known sufficiently because the sedimentary basins can remarkably amplify the long-period ground motions. For example, Dhakal et al. (2015) constructed ground motion prediction equations (GMPEs) for AVRS in the period range of 1–10 s with an objective of EEW of LPGMI using events of Mw ≥ 6.5. Analysis of data from the moderate earthquakes may also contribute to understanding the threshold magnitudes and distance ranges for EEW of short-period (conventional seismic intensity) and the long-period ground motions. Recently, a large-scale ocean bottom seismograph network, named as S-net (Aoi et al., 2020b), has been operated in the Japan Trench area with the objectives of enhanced EEW and tsunami warnings. Preliminary ground motion analysis at the S-net sites revealed that the PGVs were much larger at the ocean bottom sites while the PGAs were similar to those recorded at the land sites (Dhakal et al., 2020). An analysis of the ground motions from the damaging moderate magnitude earthquakes is an integral part of understanding the ground motions at the ocean bottom sites because the S-net data are expected to contribute to EEW. The 2018, Mw 5.5, North Osaka earthquake caused damages to wide areas despite the moderate magnitude, as mentioned above. PGA, PGV, and acceleration response spectra (ARS) for the North Osaka earthquake were compared with the GMPEs and data from similar magnitude events. The analysis indicated that the ground motions were significantly larger during the North Osaka earthquake. Therefore, another objective in this paper is to discuss the main features and generation mechanism of the strong-motions recorded during the 2018 Mw 5.5, North Osaka earthquake.

DATA AND PROCESSING

The list of damaging earthquakes analyzed in this study are given in **Table 1**. The epicenters of the earthquakes are shown in **Figure 1**. The list was prepared from the list of damaging earthquakes reported online by JMA (JMA, 2020a), by selecting events that occurred after the start of K-NET and KiK-net and had moment magnitude (Mw) values between 4.1 and 5.9. The original list by JMA contained the information on the JMA magnitude of the events, but not the Mw values. For uniformity, the moment magnitudes of the analyzed events were taken from F-net, NIED (NIED, 2019b), except for the first and second events (see **Table 1**), which occurred in 1996. The F-net moment tensor solutions were not available in 1996. For the first event, the Mw value was taken from the GCMT catalog (Dziewonski et al., 1981), and for the second event, the value was taken from the JMA CMT catalog (see the data availability). The hypocenter information of all events were taken from the unified hypocenter catalog of JMA (see the data availability section).

Visual inspection of original accelerograms, velocity seismograms obtained by integrating accelerograms, and their Fourier spectra were carried out. Recordings were selected if both P- and S-onsets were present, and pre-event window of length 7 s was available. The corresponding mean acceleration of the pre-event window was reduced from the

TABLE 1 | List of damaging moderate magnitude earthquakes in Japan.

SN	Date (JST)	Japan Meteorological Agency				F-net	Reported maximum intensity	Calculated maximum intensity	Remark
		Lon	Lat	Depth	Mj	Mw			
1	1996/09/09, 13:34	130.96	30.4893	22	5.8	5.7[a]	4	5+	Near Sea of Tanegashima
2	1996/12/21, 10:28	139.86	36.095	53	5.6	5.4[b]	5-	6-	Southwest Ibaraki Prefecture
3	1997/03/16, 14:51	137.5252	34.9282	39	5.9	5.6	5+	5+	Northeast Aichi Prefecture
4	1997/06/25, 18:50	131.6662	34.4415	8	6.6	5.8	5+	5-	Yamaguchi Prefecture
5	1998/02/21, 09:55	138.7707	37.288	21	5.2	5	4	5-	Mid Niigata Prefecture
6	1998/04/22, 20:32	136.57	35.165	10	5.5	5.2	4	5-	Shiga Gifu Border Region
7	1998/09/03, 16:58	140.9097	39.7957	10	6.2	5.9	6-	4	Northern Iwate Prefecture
8	1998/09/15, 16:24	140.7655	38.2782	13	5.2	5	4	5-	Southern Miyagi Prefecture
9	1998/11/08, 21:40	140.0538	35.61	78	4.7	4.7	4	3	Central Chiba Prefecture
10	1999/03/26, 08:31	140.6162	36.4552	58	5	5.1	4	5-	Northern Ibaraki Prefecture
11	1999/07/16, 02:59	133.1958	34.4247	20	4.5	4.2	4	4	Eastern Hiroshima Prefecture
12	1999/09/13, 07:56	140.1595	35.5663	77	5.1	5.3	4	3	Central Chiba Prefecture
13	2000/06/08, 09:32	130.7562	32.6953	10	5	4.9	5-	5-	Southern Kumamoto Prefecture
14	2000/10/31, 01:42	136.3485	34.2808	43	5.7	5.5	5-	5-	Shima Peninsula Region
15	2001/01/04, 13:18	138.7617	36.959	14	5.3	5.2	5-	5+	Mid Niigata Prefecture
16	2001/04/03, 23:57	138.1087	34.9958	33	5.3	5.2	5+	4	Central Shizuoka Prefecture
17	2001/08/25, 22:21	135.6608	35.1472	10	5.4	4.9	4	4	Mid Kyoto Prefecture
18	2002/03/25, 22:58	132.6175	33.8213	46	4.7	4.7	4	4	Akinada Setonaikai
19	2002/06/14, 11:42	139.9803	36.2132	57	5.1	4.9	4	5+	Southwest Ibaraki Prefecture
20	2002/11/17, 13:47	136.6765	36.2988	8	4.7	4.5	4	5-	Ishikawa Prefecture
21	2003/05/12, 00:57	140.089	35.8657	47	5.3	5.2	4	4	Southern Ibaraki Prefecture
22	2003/09/20, 12:54	140.3037	35.2155	70	5.8	5.7	4	4	Kujukuri Coast Boso Peninsula
23	2003/10/15, 16:30	140.0532	35.6103	74	5.1	5.1	4	4	Central Chiba Prefecture
24	2004/10/06, 23:40	140.0932	35.9857	66	5.7	5.7	5-	5-	Southern Ibaraki Prefecture
25	2004/12/14, 14:56	141.7033	44.0743	9	6.1	5.7	5+	6-	Rumor Region
26	2005/01/09, 18:59	136.854	35.3085	13	4.7	4.4	4	4	Central Aichi Prefecture
27	2005/01/18, 21:50	139.0002	37.3677	8	4.7	4.5	4	5-	Mid Niigata Prefecture
28	2005/02/16, 04:46	139.8963	36.036	45	5.3	5.4	5-	5-	Southwest Ibaraki Prefecture
29	2005/04/23, 00:23	138.2965	36.662	4	4.1	4.1	4	3	Northern Nagano Prefecture
30	2005/06/03, 04:16	130.5478	32.4955	11	4.8	4.6	5-	4	Amasa Region
31	2005/06/20, 01:15	140.6947	35.7338	51	5.6	5.7	4	4	Near Choshi City
32	2005/07/23, 16:34	140.1385	35.5817	73	6	5.9	5+	5-	Central Chiba Prefecture
33	2005/07/28, 19:15	139.8463	36.1262	51	5	4.9	4	4	Southwest Ibaraki Prefecture
34	2005/08/07, 01:05	140.1148	35.5595	73	4.7	4.7	4	3	Central Chiba Prefecture
35	2005/10/16, 16:05	139.9375	36.0393	47	5.1	5	4	4	Southwest Ibaraki Prefecture
36	2005/12/24, 11:01	136.8402	35.2307	43	4.8	4.7	4	4	Central Aichi Prefecture
37	2006/05/15, 01:42	135.221	34.2243	3	4.5	4.3	4	4	Northwest Wakayama Prefecture
38	2007/04/15, 12:19	136.4077	34.7912	16	5.4	5	5+	5+	Northern Mie Prefecture
39	2007/06/06, 23:42	131.4952	33.3338	11	4.9	4.7	4	4	Northern Oita Prefecture
40	2007/08/18, 04:14	140.36	35.3495	23	4.8	4.9	5-	4	Kujukuri Coast Boso Peninsula
41	2007/10/01, 02:21	139.1185	35.2255	14	4.9	4.7	5+	5-	Hakone Region
42	2008/03/08, 01:54	140.6117	36.4525	57	5.2	5.1	4	4	Northern Ibaraki Prefecture
43	2008/06/13, 11:21	137.7033	35.9115	13	4.7	4.3	4	4	Western Nagano Prefecture
44	2009/12/17, 23:45	139.1365	34.9588	4	5	4.8	5+	6-	East Off Izu Peninsula
45	2009/12/18, 08:45	139.1293	34.9612	5	5.1	4.9	5+	6-	East Off Izu Peninsula
46	2010/03/13, 21:46	141.4717	37.6142	78	5.5	5.5	4	4	East Off Fukushima Prefecture
47	2010/05/01, 18:20	139.1912	37.5592	9	4.9	4.6	4	4	Northeast Niigata Prefecture
48	2010/07/04, 04:33	140.9128	39.0247	7	5.2	5	4	4	Southern Iwate Prefecture
49	2011/03/15, 22:31	138.7145	35.3095	14	6.4	5.9	6+	6+	Mt. Fuji Region
50	2011/04/01, 19:49	140.364	40.2568	12	5	4.9	5+	5-	Northern Akita Prefecture
51	2011/04/16, 11:19	139.9455	36.3408	79	5.9	5.8	5+	5+	Southwest Ibaraki Prefecture
52	2011/06/30, 08:16	137.9547	36.1885	4	5.4	5	5+	4	Central Nagano Prefecture
53	2011/08/01, 23:58	138.5477	34.7085	23	6.2	5.8	5-	5-	Southern Suruga Bay Region
54	2011/11/20, 10:23	140.5882	36.7107	9	5.3	5	5+	5-	Northern Ibaraki Prefecture
55	2011/11/21, 19:16	132.8937	34.8717	12	5.4	5.2	5-	5+	Shimane Hiroshima Border
56	2011/12/14, 13:01	137.2443	35.3555	49	5.1	5.1	4	4	Southeast Gifu Prefecture
57	2012/01/28, 07:43	138.977	35.4892	18	5.4	5.2	5-	4	Eastern Yamanashi Prefecture
58	2012/07/10, 12:48	138.3883	36.8315	9	5.2	5.1	5-	4	Northern Nagano Prefecture
59	2013/04/13, 05:33	134.829	34.4188	15	6.3	5.8	6-	5+	Awajishima Island Region
60	2013/04/17, 17:57	139.353	34.0473	9	6.2	5.8	5+	5+	Near Miyakejima Island
61	2013/09/20, 02:25	140.6953	37.0513	17	5.9	5.4	5+	5+	Eastern Fukushima Prefecture
62	2014/07/08, 18:05	141.267	42.6498	3	5.6	5.4	5-	5-	Iburi Region
63	2014/09/16, 12:28	139.864	36.0937	47	5.6	5.5	5-	5-	Southwest Ibaraki Prefecture

(Continued on following page)

TABLE 1 | (*Continued*) List of damaging moderate magnitude earthquakes in Japan.

SN	Date (JST)	Japan Meteorological Agency				F-net	Reported maximum intensity	Calculated maximum intensity	Remark
		Lon	Lat	Depth	Mj	Mw			
64	2015/05/25, 14:28	139.6387	36.0543	56	5.5	5.2	5-	5-	Eastern Saitama Prefecture
65	2015/07/10, 03:32	141.5598	40.354	88	5.7	5.6	5-	5-	Northern Iwate Prefecture
66	2015/07/13, 02:52	131.8552	32.9927	58	5.7	5.5	5+	4	Southern Oita Prefecture
67	2015/09/12, 05:49	139.8292	35.5545	57	5.2	5	5-	4	Tokyo Bay Region
68	2016/05/16, 21:23	139.8868	36.034	42	5.5	5.4	5-	5-	Southwest Ibaraki Prefecture
69	2016/06/16, 14:21	140.987	41.9485	11	5.3	5.2	6-	6-	Uchiura Bay Region
70	2016/12/28, 21:38	140.5742	36.7202	11	6.3	5.9	6-	6-	Northern Ibaraki Prefecture
71	2017/06/25, 07:02	137.5865	35.868	7	5.6	5.2	5+	5+	Western Nagano Prefecture
72	2017/07/01, 23:45	141.859	42.7877	27	5.1	5	5-	5-	Ishikari Depression
73	2017/07/11, 11:56	130.62	31.384	10	5.3	5.3	5+	5+	Satsuma Peninsula Region
74	2017/10/06, 23:56	141.1557	37.0875	53	5.9	5.7	5-	5-	East Off Fukushima Prefecture
75	2018/04/09, 01:32	132.5867	35.1847	12	6.1	5.6	5+	6-	Shimane Hiroshima Border
76	2018/06/18, 07:58	135.6217	34.8443	13	6.1	5.5	6-	6-	Kyoto Osaka Border Region
77	2019/01/03, 18:10	130.5543	33.0273	10	5.1	4.9	6-	4	Northern Ariakekai Region
78	2019/02/21, 21:22	142.0033	42.7662	33	5.8	5.5	6-	6-	Ishikari Depression
79	2019/05/25, 15:20	140.29	35.3568	38	5.1	4.9	5-	4	Kujukuri Coast Boso Peninsula

[a]*Note: The Mw value was taken from GCMT catalog.*
[b]*The Mw value was taken from JMA CMT catalog. See the main text for the explanation.*

accelerograms to obtain peak ground motion parameters. Then, low cut filtering was applied at a corner frequency of 0.1 Hz for most of the recordings. However, for some recordings, the corner frequency for low-cut filtering was increased up to 0.5 Hz, based on the presence of noise. Cosine tapering was applied for a window of 5 s at both ends of the recordings. The ARS and AVRS were calculated for 5%-damping ratios using the method of Nigam and Jennings (1969). The sums of relative velocity responses and the corresponding velocity seismograms obtained by integration of filtered accelerograms give the absolute velocity responses, which were computed for each horizontal component. Finally, we calculated the vector sum of the two horizontal component absolute velocity responses and obtained the maximum value of all the time steps as the value of AVRS for each natural period.

Similarly, the ARS represents the peak vector of two horizontal component acceleration response time histories. The PGA and PGV values reported in this paper are larger ones of the PGAs and PGVs, respectively, of the two horizontal components. The definitions of PGA and PGV are different in some GMPEs, and they are defined at appropriate sections when they appear in this paper. An example plot of the acceleration and velocity seismograms is given in **Figure 2** for two sites. The seismograms are discussed in the next section. The JMA instrumental intensity was computed following the procedure explained in JMA (2020b). A comparison of the JMA instrumental intensity scale with the Modified Mercalli Intensity (MMI) scale and the computation procedure of JMA instrumental intensity can also be found in Shabestari and Yamazaki (2001). Hoshiba et al. (2010) provide the relationship between the JMA intensity, JMA instrumental intensity, and MMI scale according to which JMA intensity of 4, 5L or 5−, 5U or 5+, 6L or 6−, 6U or 6+, and 7 correspond to MMI scale of 6-7, 7-8, 8-9, 9-10, 10-11, and 12, respectively.

GENERAL FEATURES OF STRONG-MOTIONS

PGA and PGV

The PGAs and PGVs from all the earthquakes used in this study are plotted in **Figures 3A,B**, respectively. **Figure 3A** shows the PGAs (larger of two horizontal components) plotted as a function of hypocentral distance and magnitudes. The PGA values are colored by the magnitudes divided into four groups: 4.1–4.4, 4.5–4.9, 5.0–5.4, and 5.5–5.9. Out of the 79 earthquakes, 40 earthquakes had focal depths lower than 20 km. The median focal depth was about 23 km of all earthquakes. The minimum and maximum depths were approximately 3 and 88 km. The median prediction curves for Mw = 4.0, 4.5, 5.0, 5.5, and 6.0 are also shown in the figures for crustal type earthquake, focal depth of 20 km, and soil site condition using the equations in Si and Midorikawa (1999), Si and Midorikawa (2000). Similarly, the median prediction curves for interplate and intraslab earthquakes of Mw = 5.5 and 6 are drawn in the figures for two focal depths (30 km for interplate earthquake and 30 and 70 km for intraslab earthquake). The paper, Si and Midorikawa (1999), is, hereafter, referred to as SM 1999. The GMPEs in SM 1999 were constructed using events of Mw ≥ 5.8. However, the GMPEs are used here as reference GMPEs for PGA and PGV because of their widespread use in Japan. For example, the GMPEs for PGV in SM 1999 have been used by the Headquarters for Earthquake Research Promotion (HERP, 2018) in producing the national seismic hazard maps for Japan. For PGA, soil site condition means the site has Vs30 values (average S-wave velocity in the top 30 m of the soil column) lower than 620 m/s. For the PGV, the prediction curves are drawn for the Vs30 value of 300 m/s because this value is roughly the average site condition for the strong-motion stations (e.g., Kanno et al., 2006).

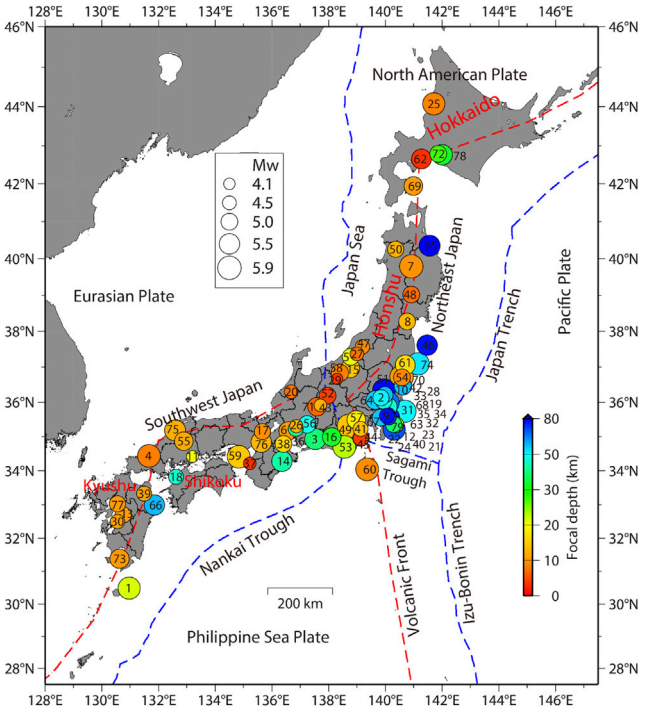

FIGURE 1 | Location of the damaging moderate magnitude earthquakes (5.9 ≥ Mw) in Japan from 1996 to 2019. Circles denote the epicenters of the earthquakes. Numbers attached or close to the circles indicate the serial numbers of the events listed in **Table 1**.

Magnitude and distance are the two most commonly employed parameters in the GMPEs. **Figures 3A,B** show that the PGAs and PGVs generally depend on the magnitude and the distance. The values increase with the increase of magnitudes and decrease with the increase of distances, on average. These trends are generally captured well by the prediction curves plotted in the figures. However, a significant proportion of the data between the magnitude groups overlap. The amplitude and frequency content of ground motions are strongly modified by the local site conditions, propagation path, and source factors such as focal mechanisms, stress drops, rupture directivity effects and so on (e.g., Campbell, 2003). To see the variation of the PGA and PGV values with respect to the magnitude, focal depth, and site condition clearly, the PGA and PGVs are shown repeatedly in **Figure 4** by selecting the data over 100 cm/s^2. The log-scales used in **Figure 3** for the horizontal axes are changed to linear scales, and the ranges of vertical and horizontal scales are narrowed down in **Figure 4**. **Figures 4A,B** show that the PGA values for the deeper events are larger than those for the shallower events. In **Figure 4C**, PGVs are plotted as a function of distance, and the values are colored by magnitudes. Even though the largest PGVs seen over wider distance bins are from large magnitude events, the PGVs from three magnitude bins (4.5–4.9, 5.0–5.4, 5.5–5.9) noticeably overlap within 10–30 km. The PGVs are color-coded by Vs30 values in **Figure 4D**. The PGV values at sites where Vs30 were not available are shown by open circles. The open circle data are from the K-NET stations. K-NET stations had PS-loggings down to the depth of 20 m. In this study, the Vs30 values for the K-NET stations were obtained using the correlation formula between the Vs20 and Vs30 in Kanno et al. (2006) for the sites where Vs20 was available. But many stations had PS-loggings down to the depth of 10 m. The open circles in **Figure 4D** are the sites lacking measured Vs20. It can be seen in **Figure 4D** that the PGVs are generally larger for sites with smaller Vs30 values. These figures showed that the PGAs and PGVs are generally larger for the deeper earthquakes and at sites with lower Vs30 values.

Here I discuss the plots of residuals for PGAs and PGVs against the different variables used in the GMPEs and against the predicted and observed values. The residuals in base-10 log-scale are plotted in **Figure 5** for the PGAs from hypocentral distances smaller than 200 km. The residuals were grouped into different bins, and the binned mean values with plus-minus one standard deviation are also indicated in the figure. The binned mean residuals against the Mw values plotted in **Figure 5A** are positive, and the values decrease with the increase of magnitude. The mean values ranged between approximately 0.06 and 0.16. Similarly, the residuals against the hypocentral distance are plotted in **Figure 5B**. The plot shows that the binned mean residuals gradually decrease from short to long distances. In the construction of GMPEs in SM 1999, fault distance was used as a measure of source-to-site distance. I used the hypocentral distance as a measure of distance because the fault models of the events were not available except for few events. A mismatch

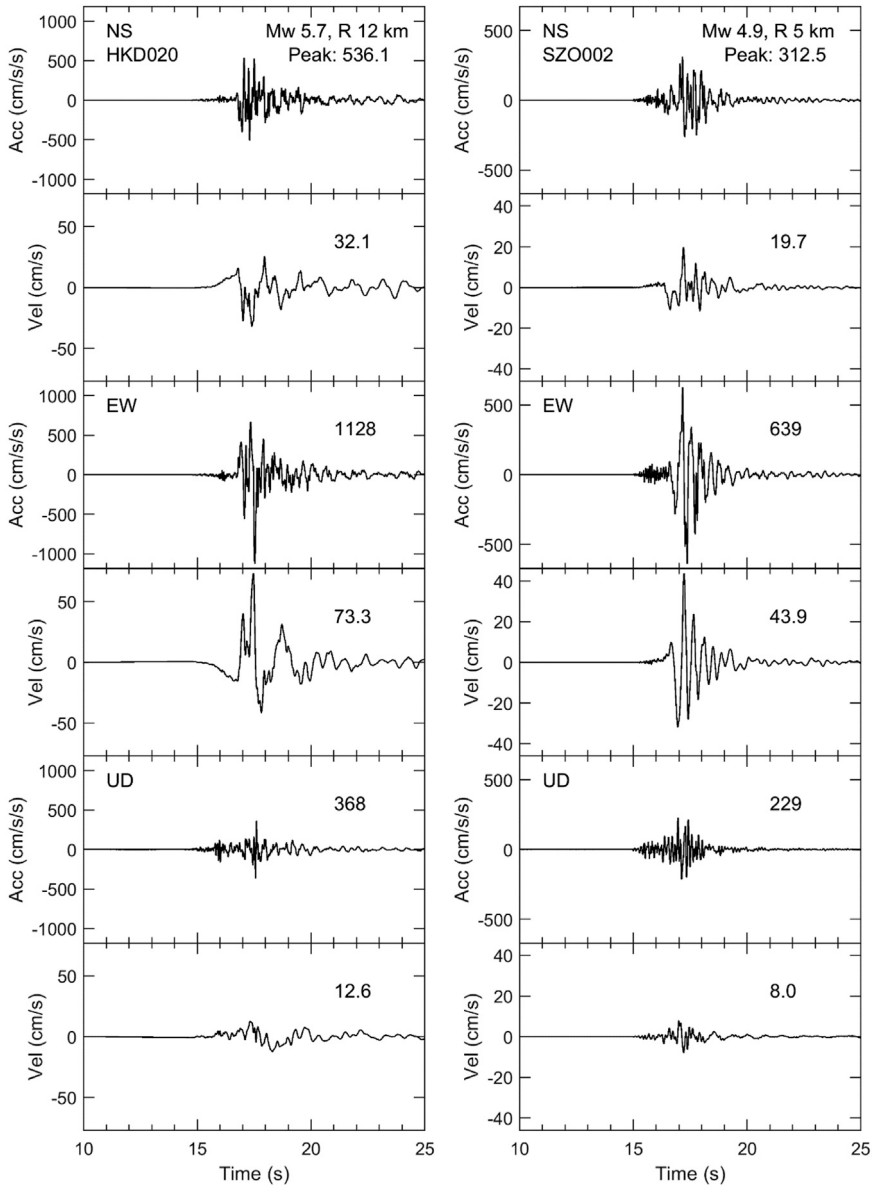

FIGURE 2 | Plots of acceleration and velocity seismograms at HKD020 site for an Mw 5.7 event **(left panel)** and SZO002 site for an Mw 4.9 event **(right panel)**. R denotes the hypocentral distance rounded to the closest integer. The peak values of the seismograms are written above the corresponding traces. Note the difference between the vertical scales in the left and right panels.

between the fault distance and hypocentral distance may have resulted in the relatively larger residual values at the short distances. However, most of the recordings were from Mw values smaller than 5.5 for data points at short distances, and hence the difference between the fault and hypocentral distance may be small (see the **Supplementary Material** for the magnitude versus distance distribution of data). The residuals against the focal depth plotted in **Figure 5C** do not show a definite trend. The binned mean residuals plotted against the Vs30 values in **Figure 5D** show positive values for Vs30 values smaller than 600 m/s. For larger Vs30 values, the binned means are negative. The residuals against the predicted values and observed values are plotted in **Figures 5E,F**, respectively. The binned mean residuals for predicted PGAs >50 cm/s^2 are relatively larger. The residuals plotted against the observed values show a linear trend in **Figure 5F**. The binned mean residuals for the observed PGAs >100 cm/s^2 are larger than 0.6, which is larger than twice the standard deviation reported in SM 1999. The amount of data at small distances is fewer and the use of hypocentral distance is different from the fault distance used in the GMPEs. Therefore,

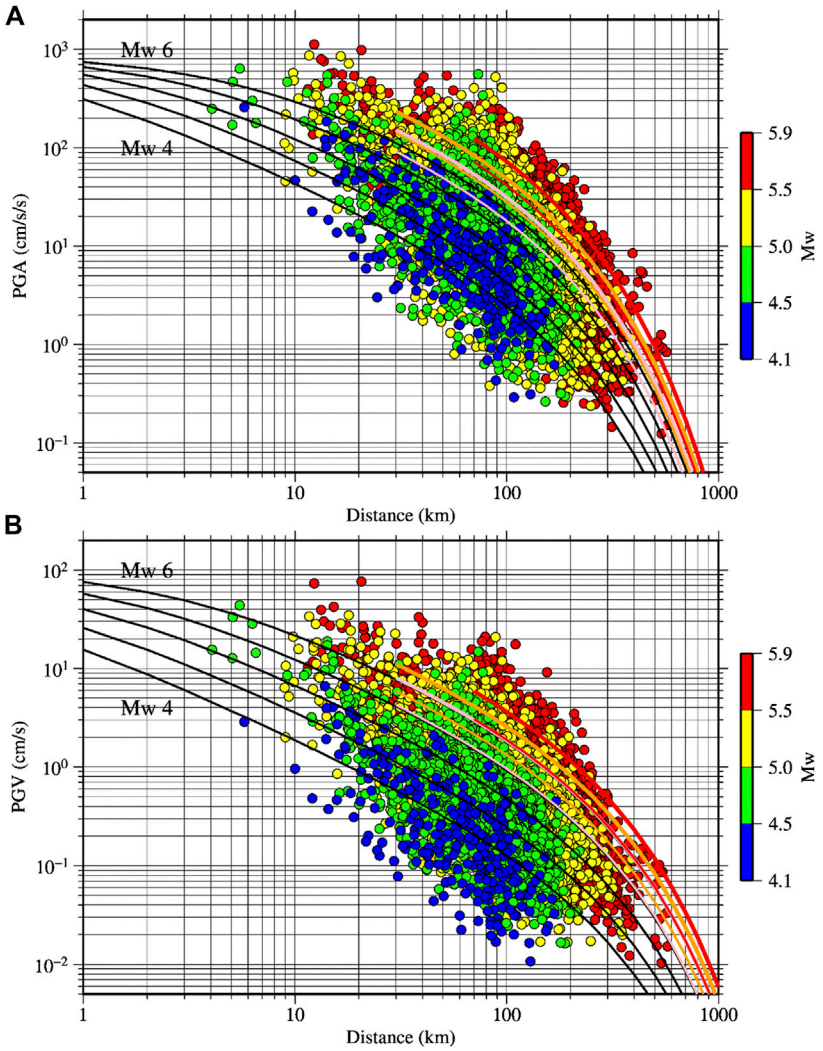

FIGURE 3 | Plot of PGAs **(A)** and PGVs **(B)** as a function of hypocentral distance. The black curved lines denote the median prediction curves for crustal earthquakes for soil site conditions in **(A)** and Vs30 = 300 m/s in (**B**) for Mw = 4.0, 4.5, 5.0, 5.5, and 6.0, respectively, using the GMPEs in Si and Midorikawa (1999). The thin and thick pink (orange) lines denote the median prediction curves for interplate (intraslab) earthquakes of Mw = 5.5 and 6.0, respectively (focal depth = 30 km). Similarly, the thin and thick red lines denote the median prediction curves for intraslab earthquakes of Mw = 5.5 and 6.0, respectively, for focal depth = 70 km.

the absolute value of residuals at short distances may not be accurate. However, the systematic difference of residual values between the soil and rock sites separated by Vs30 value of 620 m/s may indicate that the classification of sites into soil and rock based on the Vs30 value of 620 m/s may not be sufficient.

The distributions of residuals for PGVs against the Mw, hypocentral distance, focal depth, Vs30, predicted PGV, and observed PGV are shown in **Figures 6A–F**, respectively. Different from the results for PGAs discussed above, the binned mean residuals tended to be lower for the PGVs. A gentle trend with Vs30 is seen; this is different from that for the PGAs, and may be due to that the Vs30 was used as continuous variable in the GMPEs for PGVs than just soil and rock sites for the PGAs. The binned mean residuals at small distances were relatively larger than at longer distances. The binned mean residuals for the observed PGVs > than 10 cm/s were larger than twice the standard deviation for PGV in SM 1999.

The largest PGA was approximately 1,128 cm/s^2, which was recorded at HKD020 (see **Figure 2**) during an Mw 5.7 event that occurred on December 14, 2004, at 14:56 JST in Rumoi, Hokkaido (see **Figure 1** for the location of the epicenter, Event no. 25). The maximum value of the PGV for the event was about 73 cm/s, which was also recorded at HKD020 (see **Figure 2**). The largest PGV of approximately 76 cm/s was observed at the SZO011 site during an Mw 5.9 event (Event no. 49, see **Figure 1** for the event location); the observed PGA was ~981 cm/s^2 at the site during the event. The instrumental intensities at the HKD020 and SZO011 sites were approximately 5.9 and 6.4, respectively. These values translate to 6− and 6+ intensities in the conventional JMA

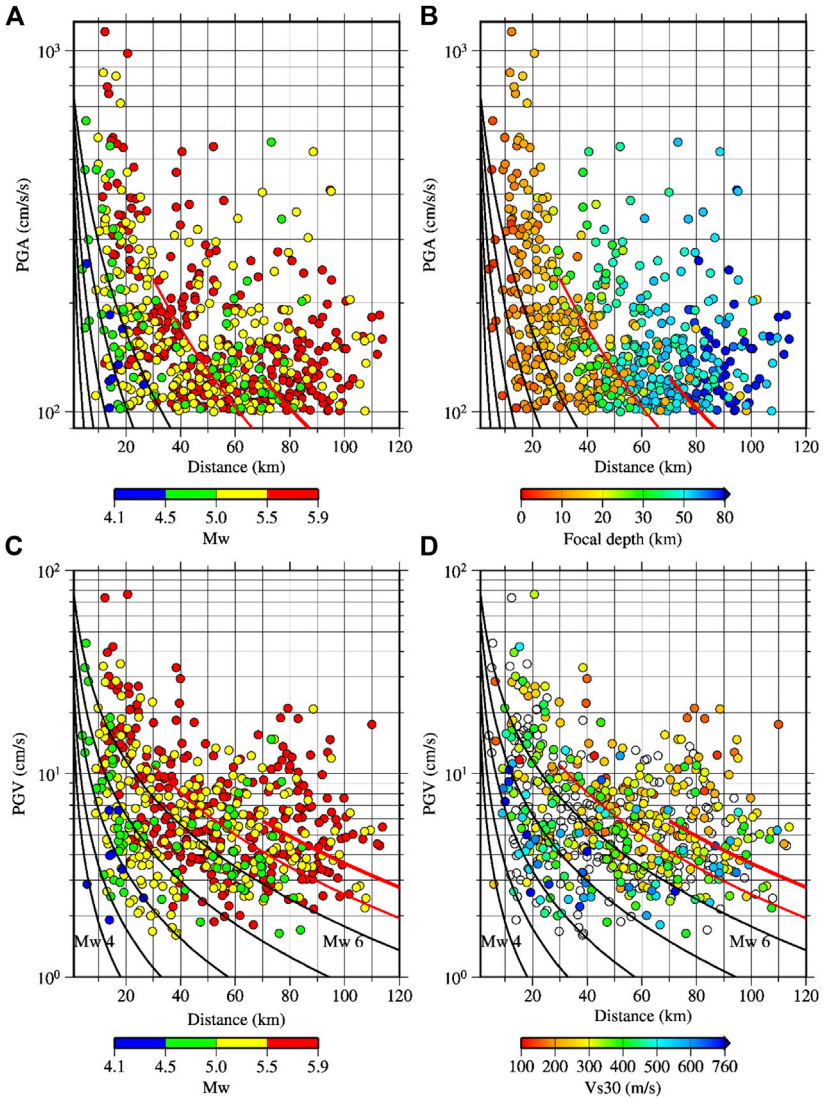

FIGURE 4 | (A,B): same plot as in **Figure 3A**, but the PGA values smaller than 100 cm/s/s are not shown, and the hypocentral distance is limited to 120 km. The data in **(A)** are color-coded by magnitude while data in b by focal depths. **(C,D)**: similar to **(A,B)**, but for the PGVs. The data are color-coded by magnitudes in **(C)** and by Vs30 in **(D)**. Open circles show data lacking Vs30 values. The black curved lines denote the prediction curves in the same order, as plotted in **Figure 3**. The red thin and thick lines denote the median prediction curves for intraslab earthquakes of focal depths 30 and 70 km, respectively, for Mw = 6. The prediction curves were obtained using the GMPEs in Si and Midorikawa (1999).

intensity scale and are identical to the reported maximum intensities for the two earthquakes (see **Table 1**).

Here I briefly discuss the mechanisms for the large PGA and PGV at the HKD020 site during the Mw 5.7, Hokkaido Rumoi earthquake, based on available literature. The site's location, the epicenter of the event, and the F-net focal mechanism solution are given in a **Supplementary Material**. The site had S-wave velocity profiles known down to the depth of 10 m based on PS-logging, and the Vs10 was approximately 398 m/s. Based on empirical H/V spectral analysis and theoretical amplification models based on available shallow and deep velocity models, Maeda and Sasatani (2009) reported that the site amplification was not sufficient to explain the large PGA, PGV, and pseudo-velocity response spectrum exceeding 100 cm/s at frequencies of about 0.5–1.5 Hz at the site. Using empirical Green's function method, Maeda and Sasatani (2009) constructed a source model for the earthquake. Based on the used parameters and agreement between the observed and synthetic waveforms, they concluded that the earthquake was a typical crustal earthquake, and the large PGA and PGV were due to the source effect (close to the strong motion generation area and forward rupture directivity). Later on, Sato et al. (2013) conducted detailed geophysical borehole loggings and estimated input motions at a depth of 41 m that corresponded to Vs layer of 700 m/s. They showed that input PGA was approximately 50% smaller than the surface PGA, but the

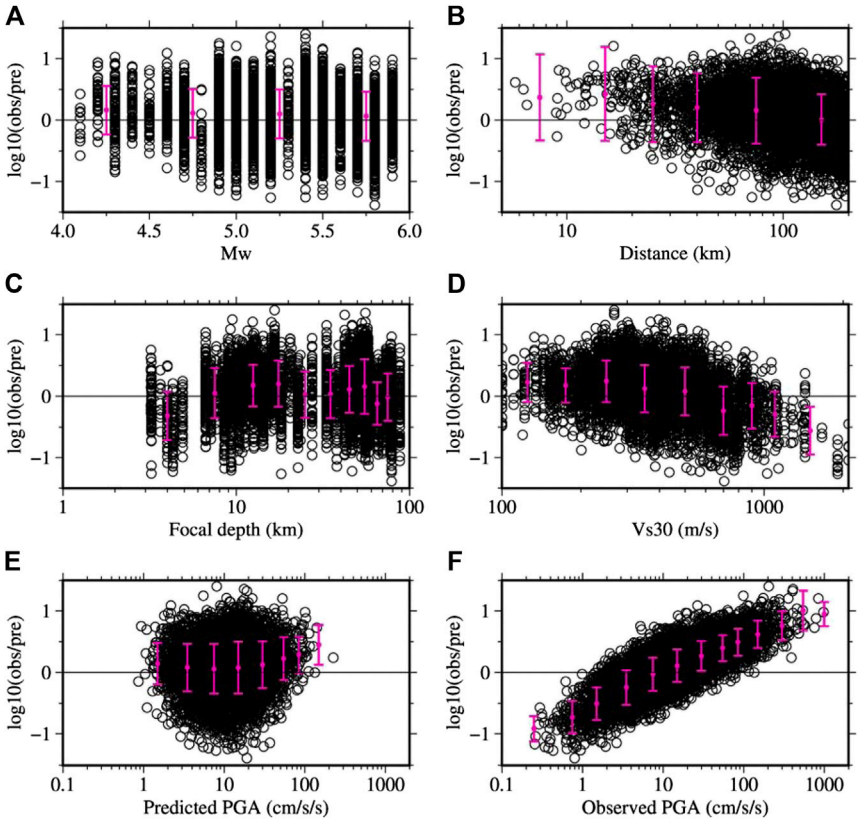

FIGURE 5 | Plots of residuals for PGA data plotted in **Figure 3A** for hypocentral distances smaller than 200 km. The **(A–F)** show the distribution of residuals against the Mw, hypocentral distance, focal depth, Vs30, predicted PGA, and observed PGA, respectively. The vertical bars denote the mean values with plus-minus one standard deviation of the binned residuals.

PGV was only around 20% smaller. They showed that 3–13 Hz ground motions were amplified by the soil layers above, while higher than 13 Hz were reduced by nonlinearity. I examined the PGV ratios at different frequency bands between the NS and EW components and found that the difference was the largest between 0.5 and 3 Hz (larger than a factor of two, 56 cm/s vs. 21 cm/s, between the two components). I found that the contribution to the PGV by the frequency band between 3 and 13 Hz was small, which is generally an expected result because the PGV better represents the intermediate period ground motions. On the other hand, the PGA of this frequency band was approximately 644 cm/s^2, and for the lower frequencies between 0.5 and 3 Hz, it was 560 cm/s^2, suggesting that the PGA was governed by broad frequency ranges between about 0.3 and 13 Hz. As shown in **Figure 2**, the EW-component had the PGV approximately 2.3 times the NS-component (73 cm/s versus 32 cm/s approximately). The site was located up-dip in the rupture propagation direction of a reverse fault, and the EW-component roughly coincides with the fault-normal component. Thus, the geometry between the fault and site and the large amplitude difference between the two horizontal components suggested that the cause of the large PGA and PGV was most probably the forward rupture directivity effect (Sommerville et al., 1997), and the aggravation by site amplification including the nonlinear one (e.g., Sato et al., 2013; Garini et al., 2017; Dhakal et al., 2019).

Even though the dominating values of PGAs and PGVs were mostly from the large magnitude events, the color scale in **Figures 3**, **4** shows that relatively large PGAs and PGVs are possible from smaller magnitude events (Mw < 5) at short distances (<7 km). The PGAs and PGVs at these small distances were between 170 and 639 cm/s^2, and 3–44 cm/s, respectively; the largest PGA and PGV were from an Mw 4.9 event recorded at the SZO002 site. Though it is beyond the scope of this paper to discuss each event, the above-mentioned Mw 4.9 event is briefly discussed here. The event occurred on December 18, 2009, at 08:45 JST (Event no. 45 located near the west end of the Sagami Trough; see **Figure 1** for the location of the event and **Table 1** for the other information about the event). The acceleration and velocity seismograms at the SZO002 site are plotted in **Figure 2** (right panels). The S-wave profile at the site was available up to 12 m, and the Vs10 at the site was 232 m/s. **Figure 2B** shows that the PGV on the EW-component is approximately 2.2 times the PGV on the NS-component. Available literature (HERP, 2010) did not uniquely identify the causative fault's geometry for this earthquake. The earthquake's focal mechanism based on F-net, NIED, moment tensor solution is given in a **Supplementary**

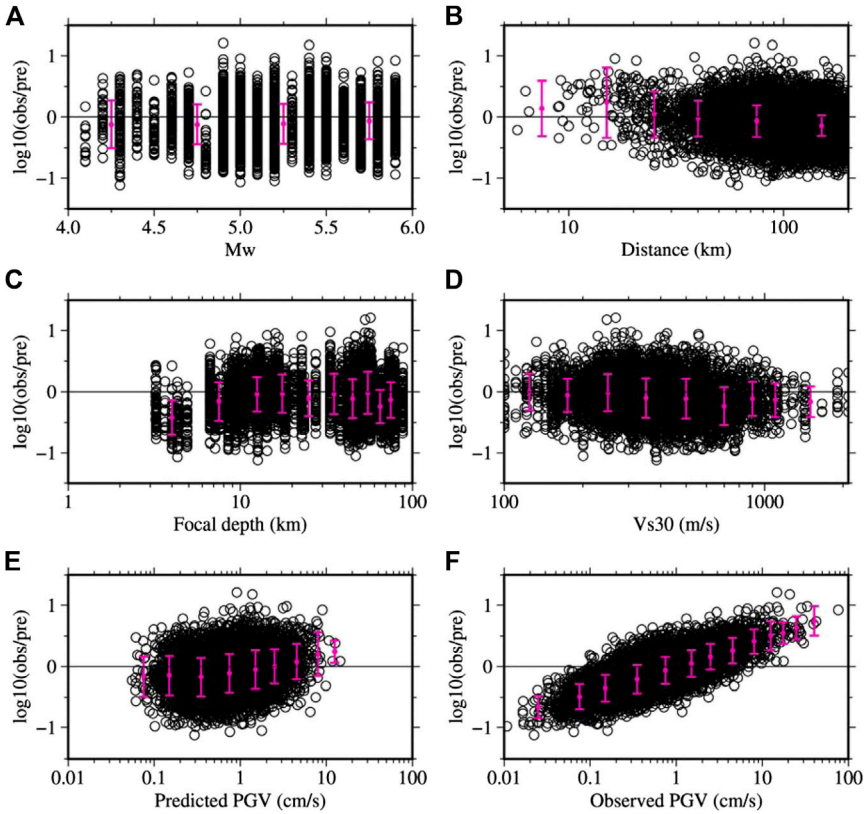

FIGURE 6 | Plots of residuals for PGV data plotted in **Figure 3B** for hypocentral distances smaller than 200 km. The **(A–F)** show the distribution of residuals against the Mw, hypocentral distance, focal depth, Vs30, predicted PGA, and observed PGA, respectively. The vertical bars denote the mean values with plus-minus one standard deviation of the binned residuals.

Material. The mechanisms suggest steeply dipping roughly east-west fault or north-south strike-slip fault. The site was located roughly west of the epicenter. The strike-slip mechanism can produce large amplitude normal to the strike, in this case the EW-component at the SZO002 site. Based on the F-net solution and the observed PGVs on the two components, a strong source radiation effect can be suspected at the site. The reported maximum intensity for this event was 5+. The computed instrumental intensity in this study is 5.65, which translates to 6- based on the intensity class divisions (5.0–5.4: 5+; 5.5–5.9: 6-) (JMA 2020b). In **Figure 3**, it can be seen that the PGAs and PGVs within the distance of 7 km are larger than those indicated by the median prediction curves for their magnitude values.

Instrumental Intensity

The instrumental intensities for all the events analyzed in this study are plotted in **Figure 7A**. The values are color-coded by the magnitudes. Median prediction curves for the instrumental intensities are also plotted based on the equations in Morikawa and Fujiwara (2013) for crustal earthquakes (Mw = 4, 4.5, 5, 5.5, and 6), interplate earthquakes (Mw = 5.5 and 6), and intraslab earthquakes (Mw = 5.5 and 6). Hereafter, the paper, Morikawa and Fujiwara (2013), is referred to as MF 2013. Similar to the PGAs and PGVs, the intensities also are larger for larger magnitudes, on average, and the prediction curves clearly capture the trends. Instrumental intensities larger than five were observed from events having Mw < 5 at short distances and up to approximately 100 km. An instrumental intensity of over five was recorded at the TCG009 site located at the hypocentral distance of approximately 90 km during an Mw 5.4 event; the focal depth of the event was 53 km (Event no. 2, southwest Ibaraki Prefecture earthquake, see **Table 1**; **Figure 1** for event location). The Vs30 value at the TCG009 site was approximately 247 m/s. However, instrumental intestines of 5 and over were mostly within smaller than 50 km. At short distances of 10–20 km, larger intensity values were most probably governed by magnitudes and rupture directivity effects for these moderate magnitude earthquakes as discussed in the previous section, while at the longer distances, the intensity values near five were observed at sites having lower Vs30 values.

Figures 7B,G shows the plots of residuals (observed instrumental intensity–predicted instrumental intensity) based on the GMPEs for instrumental intensity in MF 2013. The binned mean residuals against the Mw values and hypocentral distances are positive, and their trends are similar to those plotted in

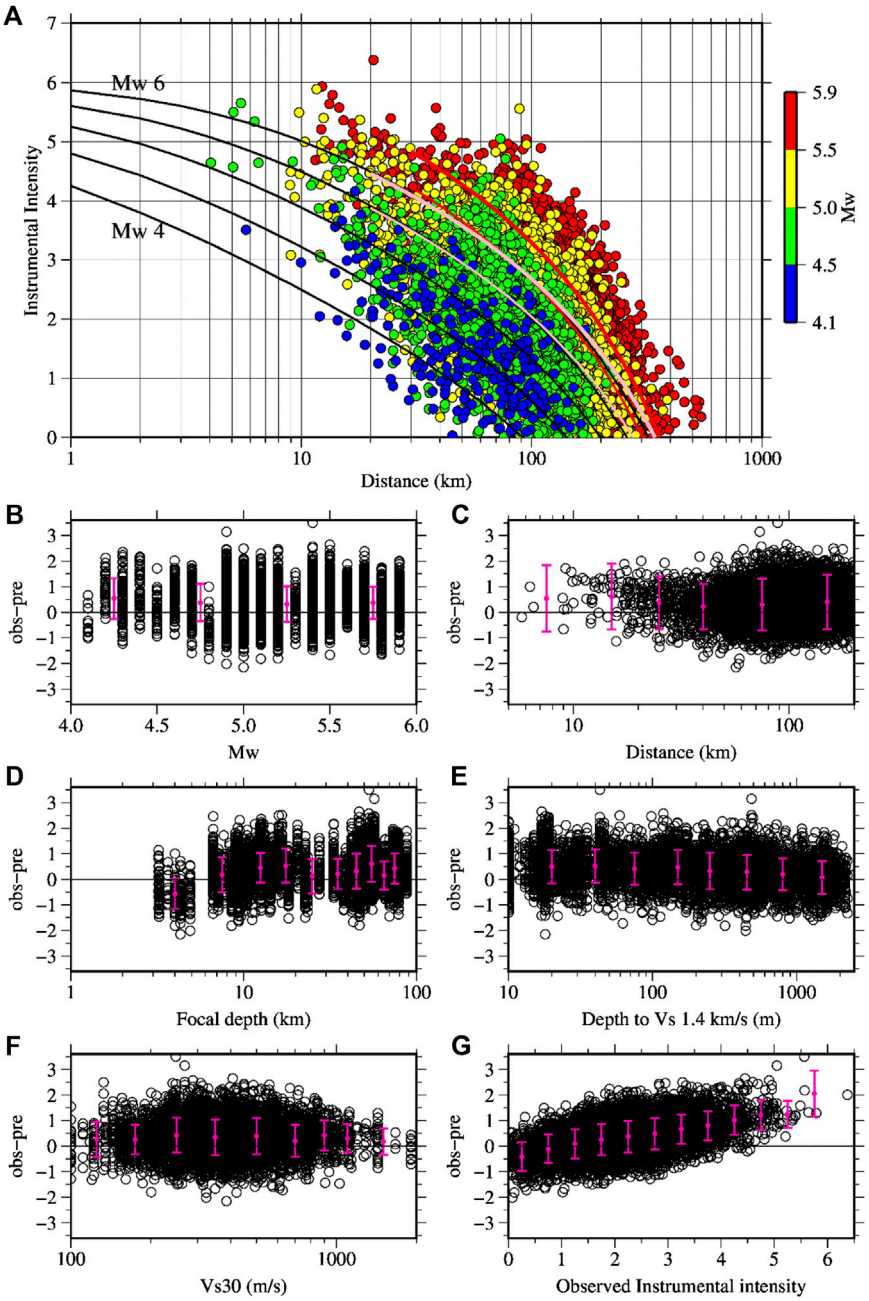

FIGURE 7 | (A) JMA instrumental intensities for the same set of data plotted in **Figure 3**. The black lines denote the median prediction curves for crustal earthquakes of Mw = 4, 4.5, 5, 5.5, and 6, respectively, using the GMPEs in Morikawa and Fujiwara (2013). The thin and thick pink (red) lines denote the median prediction curves for Mw = 5.5 and 6, respectively, for the interplate (intraslab) earthquakes. **(B–G)** show the distribution of residuals against the Mw, hypocentral distance, focal depth, depth to Vs 1.4 km/s, Vs30, and observed instrumental intensity, respectively. The vertical bars denote the mean values with plus-minus one standard deviation of the binned residuals.

Figures 5A,B for the residuals for PGAs. The binned means are relatively larger for smaller magnitude events and at short distances. In MF 2013, two different parameters were used for site corrections. They are the depth to Vs 1.4 km/s for the effect of deep sediments and Vs30 for the effect of shallow sediments. The depths to Vs 1.4 km/s were taken from the J-SHIS (Japan Seismic Hazard Information Station) subsurface velocity model (Fujiwara et al., 2009) (see the Data Availability Statements). The binned mean residuals decrease with the increase of sediment thickness (**Figure 7E**), and the binned mean residuals do not show a definite trend with the Vs30 (**Figure 7F**). The binned mean residuals plotted against the observed instrumental intensities in **Figure 7G** show that the binned mean residual values range approximately between 0.5 and 2 for observed intensities larger

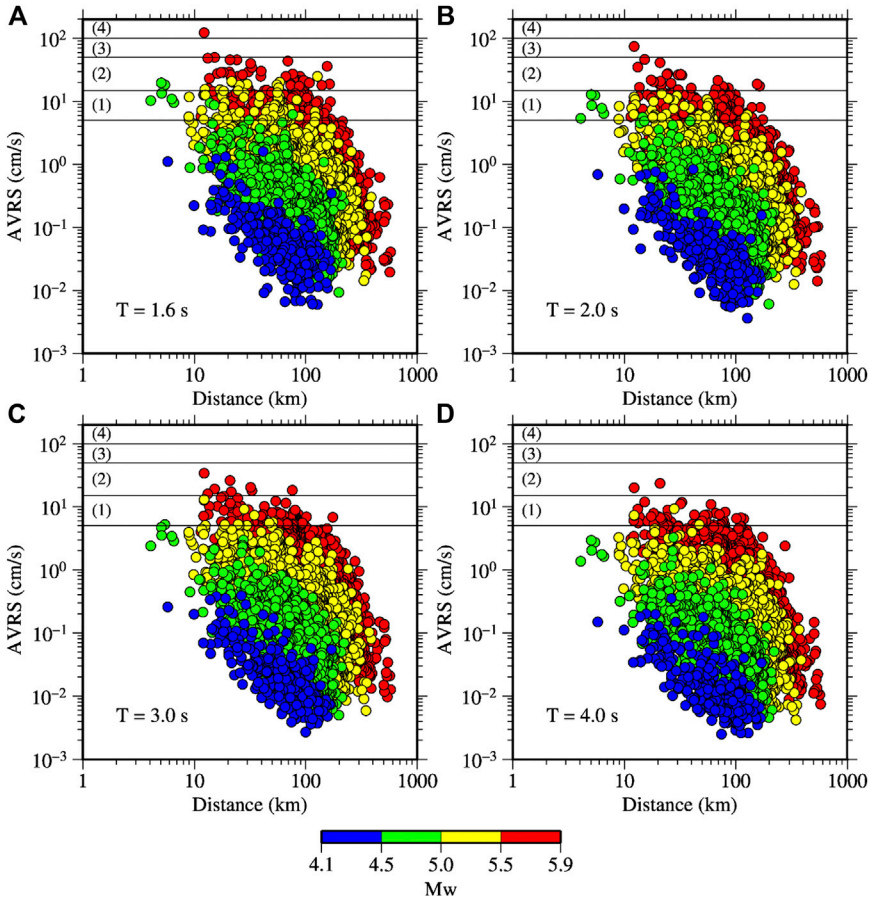

FIGURE 8 | Absolute velocity response spectra (AVRS) at the periods of 1.6, 2.0, 3.0, and 4.0 s plotted against the hypocentral distance in **A**, **B**, **C**, **D**, respectively. The horizontal lines across the AVRS of 5, 15, 50, and 100 cm/s mark the threshold values for JMA long-period ground motion intensities of 1, 2, 3, and 4, respectively.

than 4. Most probably, the damages from these small to moderate earthquakes were related to the large ground motions, which are underpredicted considerably by the GMPEs employed in the present study.

AVRS

The AVRS at the periods of 1.6, 2.0, 3.0, and 4.0 s are plotted as a function of hypocentral distance and colored by magnitudes in **Figure 8**. As briefly described in the introduction section, long-period ground motion intensities (LPGMIs) are calculated from the AVRS in the period band of 1.6–7.8 s. The maximum value determines the level of intensity. The intensity levels are as follows: class 1 (5–15 cm/s), class 2 (>15–50 cm/s), class 3 (>50–100 cm/s), and class 4 (>100 cm/s). These intensity levels are indicated in **Figure 8**. Out of the 79 earthquakes, 47 earthquakes produced LPGMI of 1 or over, totaling 489 recordings. The dominant peak period was 1.6 s within the band of 1.6–7.8 s from 346 recordings. The number of recordings with the dominant peak period of 1.8 s was 59, the second-largest number. Similarly, the number of recordings with dominant peak periods between 2 and 2.8 s was 62, between 3 and 3.8 s was 13, and between 4 and 5 s was 9. The dominant peak periods >3 s were mostly from the Kanto basin area and were not from shallow events, but with focal depths between 20 and 40 km and magnitudes between 5.4 and 5.7. In **Figure 1**, it can be seen that most of the events have larger focal depths in the Kanto area, north of the Sagami Trough. However, the maximum intensity from these longer periods was 2. During the June 18, 2018, 07:58, North Osaka earthquake, LPGMI of level 2 was observed at ten sites, and the peak periods from the band of 1.6–7.8 s were mostly 1.6 s. It can be clearly seen in **Figure 8** that the number of recordings with intensity 2 is only two at the period of 4 s. Also, from the plots in **Figure 8**, it may be inferred that the moderate earthquakes are of not serious concern at distances beyond 200 km. The distribution of peak spectral periods from the period band of 1–10 s against the Mw, hypocentral distance, focal depth and depth to Vs 1.4 km/s are provided in the **Supplementary Material**. In the **Supplementary Material**, the peak spectral

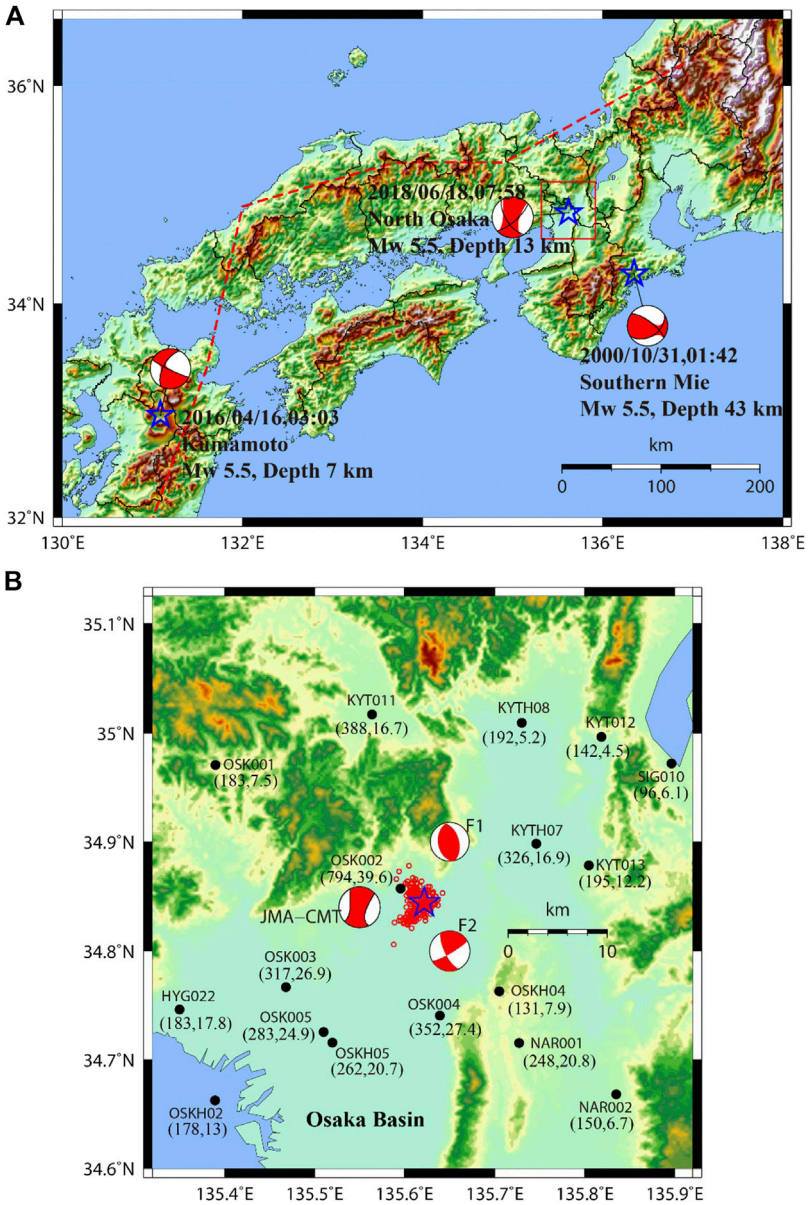

FIGURE 9 | (A) Stars denote epicenters of three Mw 5.5 earthquakes in North Osaka, Southern Mie, and Aso Kumamoto regions, as depicted in the figure. The rectangle around the epicenter is the enlarged area in **(B)**. The red dashed line represents the volcanic front. The F1 and F2 written near the focal mechanism plots in **(B)** are the double couple mechanisms proposed by Kato and Ueda (2019) for the two subevents of the North Osaka mainshock. The small red circles denote the aftershocks having JMA magnitude >1 recorded within 24 h after the mainshock. The black filled circles represent the strong-motion observation stations. The site codes and the recorded larger PGA and PGV of the two horizontal components are given within parenthesis near the observation stations.

periods are shown only for the records for which the maximum AVRS was >1 cm/s in the period band of 1–10 s. The peak periods increased generally with the increase of magnitude, hypocentral distance, and sediment thickness, while they decreased with the increase of focal depths. However, the peak periods scattered largely suggesting that multiple parameters can influence the spectral values and hence the peak periods.

NORTH OSAKA EARTHQUAKE

Strong-Motions

The epicenter of the 2018 North Osaka earthquake is shown in **Figures 9A,B**. The larger values of the two horizontal components' PGAs and PGVs observed at small distances are depicted along with the site codes in **Figure 9B**. Within an epicentral distance of 20 km, ten strong-motion stations of K-NET and KiK-net recorded

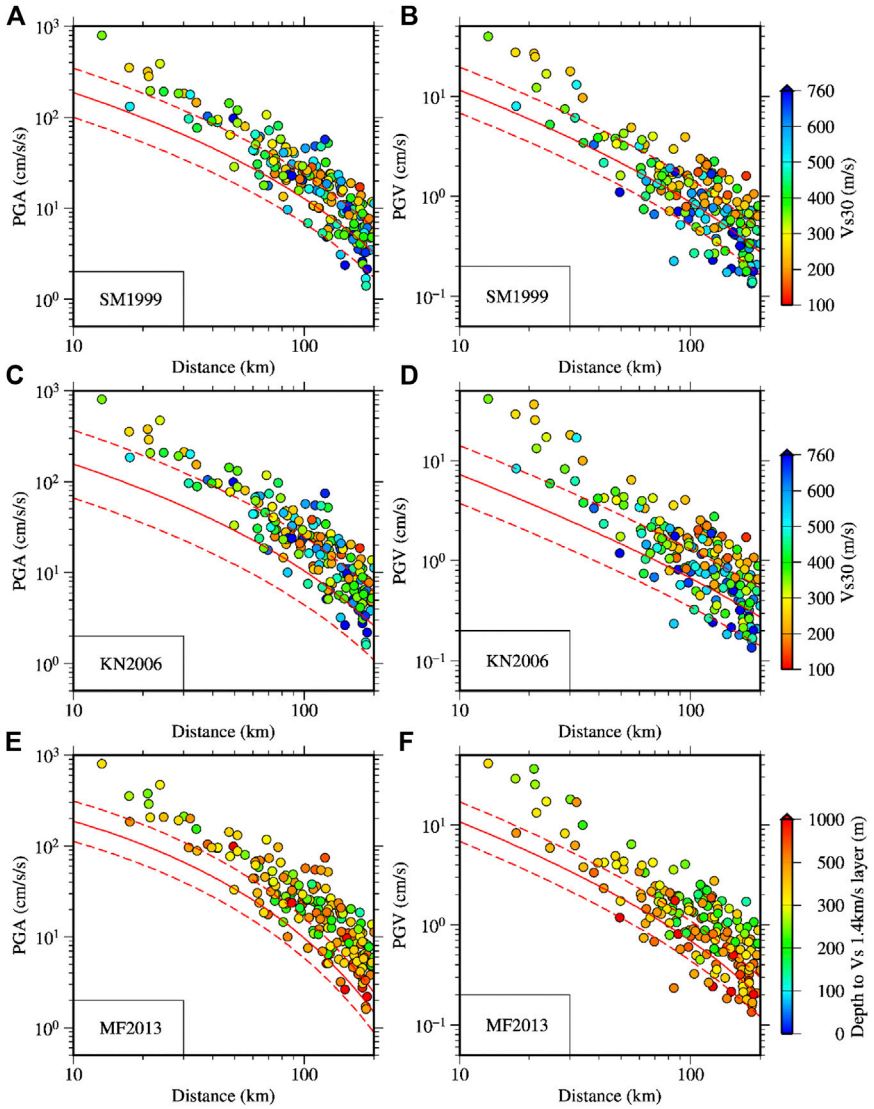

FIGURE 10 | Comparison of the observed PGAs and PGVs during the Mw 5.5 North Osaka earthquake with the ground motion prediction curves. The horizontal axes denote the hypocentral distance. The data points in panels **(A–D)** are color-coded by Vs30 values while the data in **(E,F)** are by depth to Vs 1.4 km/s. The used prediction equations are indicated in each panel by alphanumeric codes. The codes SM 199, KN 2006, and MF 2013 mean the prediction equations in Si and Midorikawa (1999), Kanno et al. (2006), and Morikawa and Fujiwara (2013), respectively.

the ground motions. Out of the ten stations, eight stations recorded PGAs >200 cm/s^2 and PGVs >15 cm/s. The maximum PGA and PGV were approximately 794 cm/s^2 and 40 cm/s, respectively, recorded at an epicentral distance of approximately 2.7 km at the same site (OSK002, Takatsuki). It was shown by several studies that the North Osaka earthquake occurred on two different faults closely separated in space almost simultaneously (Kato and Ueda, 2019; Hallo et al., 2019). As shown in **Figure 9B**, one of the events was a reverse fault (F1 in the figure), and the other was a strike-slip fault (F2 in the figure). The start of slips on fault F2 was about 0.3 s after the start of slips on the fault F1 (Kato and Ueda, 2019). The plots of aftershocks and fault models by Kato and Ueda (2019) (see **Figure 2** in Kato and Ueda, 2019) showed that the OSK002 site was located on the footwall of the north-south striking east-dipping reverse fault, and in the direction of the rupture propagation (see **Figure 9B** for the site location). The large PGV was observed on the EW-component, which is roughly perpendicular to the strike of the reverse fault. This observation also supports that the forward rupture directivity contributed to the generation of the large PGV on the EW-component. **Figure 10** shows a comparison of the observed PGAs and PGVs with the median prediction curves for three different GMPEs: **Figures 10A,B** SM 1999, **Figures 10C,D** Kanno et al. (2006), and **Figures 10E,F** MF 2013. Hereafter, the equations in Kanno et al. (2006) are abbreviated as KN 2006. The Mw value for the North Osaka earthquake estimated by Kato and Ueda (2019) and Hallo et al. (2019) was 5.6. In the present study, I used the F-net (NIED) Mw value of 5.5 for the median prediction curve for

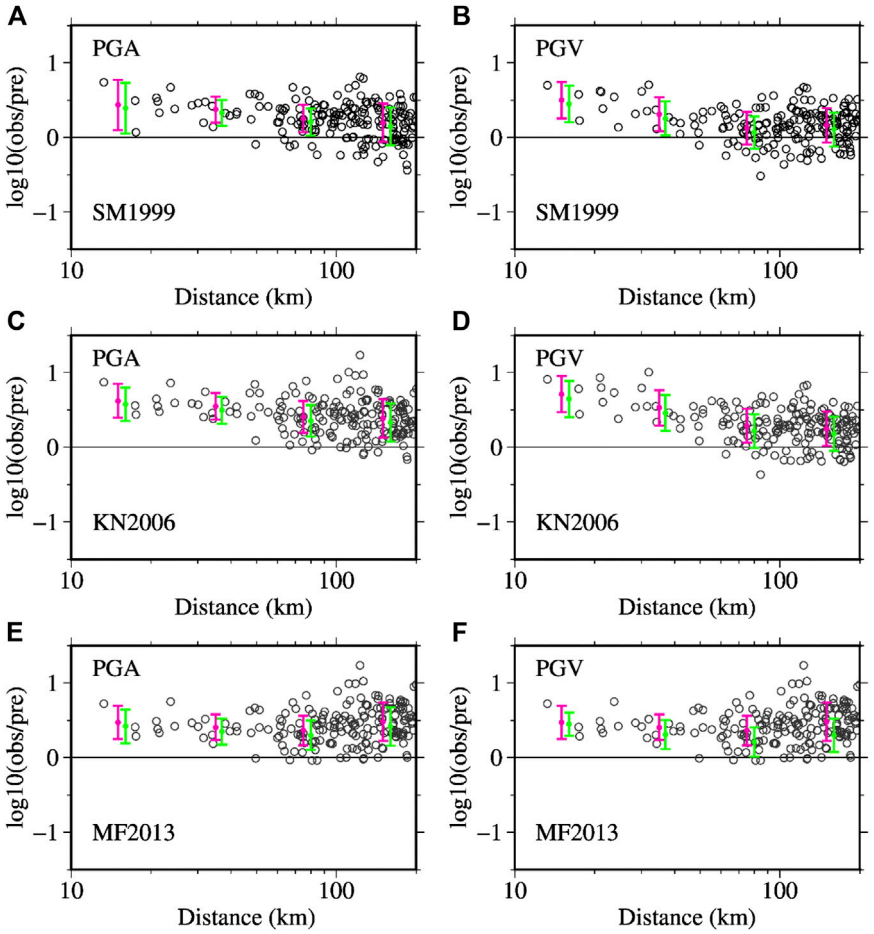

FIGURE 11 | Plots of residuals as a function of hypocentral distance after the site corrections for the data plotted in **Figure 10** for the PGAs and PGVs. The figure parts **A-F** correspond to the figure parts in **Figure 10**. The residual values shown in the plots were obtained for the Mw value of 5.5. The magenta-colored vertical bars represent the error bars for binned data with mean error and plus-minus one standard deviation. The green-colored vertical bars show the error bars for comparison for the Mw value of 5.6.

uniformity with the Mw values used in this paper for other earthquakes and in KN2006 and MF 2013. However, the mean errors using the Mw value of 5.6 are also plotted in **Figure 11** for the comparison. The observed values are colored to the Vs30 values in **Figures 10A–D**, while the values in **Figures 10E,F** are colored to the depth of Vs layer of 1.4 km/s. This is because SM 1999 and KN2006 used Vs30 values for site corrections, while the MF 2013 used both the Vs30 and depth of Vs layer of 1.4 km/s. It is expected that the color scales provide a general view of the site profiles.

In **Figure 10**, it can be seen that the PGAs and PGVs at distances smaller than about 50 and 40 km, respectively, are larger than the median values on average. **Figure 11** shows the plots of residuals after the site corrections. The binned mean errors for two magnitude values (Mw = 5.5 and 5.6) are also plotted as a function of distance. The mean errors suggest a distance dependence of the residuals for PGAs and PGVs for the SM 1999 and KN 2006. On the other hand, the mean residuals are generally uniformly distributed for the MF 2013. The mean residuals give that the PGA data are larger by a factor of about 2.7, 2.3, and 1.8 than the values from the median prediction curve at distances smaller than 20 km, between 20 and 50 km, and between 50 and 100 km, respectively, on average, for the SM 1999.

Similarly, the PGV data are larger by a factor of about 3.2, 2.0, and 1.3 at the above distance ranges, respectively, for the SM 1999. The results for the KN2006 are also similar: the PGA data are larger by factors of about 4.2, 3.5, and 2.6, while the PGV data are larger by factors of about 5, 3.3, and 1.9. The results for the MF 2013 are also similar: for the PGA, the data are larger by factors of about 3, 2.5, and 2.3, respectively, and for the PGV, the data are larger by factors of about 3.2, 2.3, and 1.9, respectively. The binned mean errors for the case of Mw = 5.6 are slightly smaller than the values for the case of Mw = 5.5. Based on the above results, it may be said that SM 1999, which has been used in the seismic hazard estimation for Japan by HERP (2018), gives the smallest error for the North Osaka earthquake. In general, all the equations used underpredicted the PGAs and PGVs for the North Osaka earthquake.

Figure 12 shows the residual plots for acceleration response spectra at the periods of 0.1, 0.5, 1, 2, 5, and 7 s after the site corrections, using the prediction equations in MF 2013. At periods up to 2 s, the results are similar to those discussed

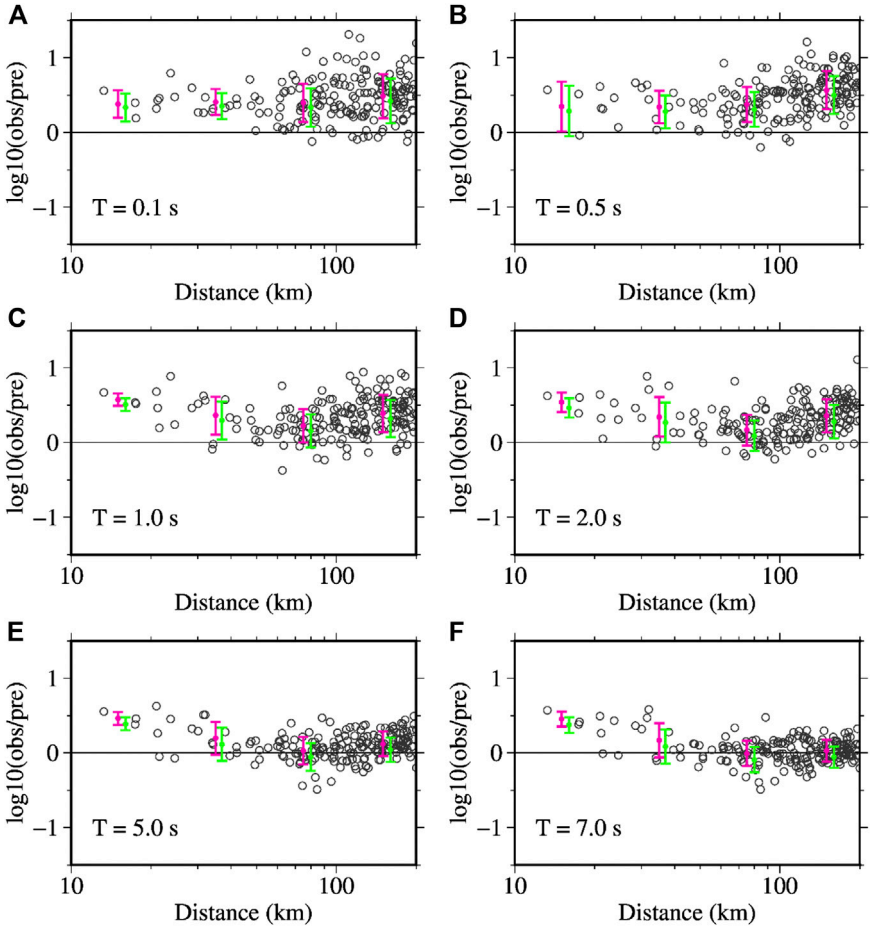

FIGURE 12 | Plots of residuals as a function of hypocentral distance after the site corrections for the acceleration response spectra (ARS) at the periods of 0.1, 0.5, 1, 2, 5, and 7 s in panels, **A-F**, respectively, using the prediction equations in Morikawa and Fujiwara (2013). The residual values shown in the plots were obtained for the Mw value of 5.5. The magenta-colored vertical bars denote the error bars for binned data with mean error and plus-minus one standard deviation. The green-colored vertical bars show the error bars for comparison for the Mw value of 5.6. See the supplementary file for the plots of ARS values as a function of hypocentral distance.

above for PGA and PGV. However, at the periods of 5 and 7 s, the residuals were generally within the expected range of errors at longer distances, while the data were noticeably underpredicted at distances smaller than about 40 km. The plots of the observed data as a function of distance for the above periods are shown in a **Supplementary Material**.

Comparison With Other Events

Here, the PGAs and PGVs from the North Osaka earthquake are compared with those from the other two earthquakes of identical Mw values of 5.5 but differing focal depths. One of the earthquakes occurred as a shallow crustal event beneath the northeast Kumamoto Prefecture at a focal depth of 7 km on April 16, 2016, at 03:03 local time, and the other as an intraslab earthquake in the subducting Philippine Sea Plate at the focal depth of 43 km on October 31, 2000, at 01:42 local time (Event no. 14 in **Table 1**). The first event may be an aftershock of the Mw 7.1 Kumamoto earthquake (e.g., Hashimoto et al., 2017). This Mw 5.5 Kumamoto event is, however, not available in the list of events in **Table 1** because this event was not listed in the list of damaging events. If any damage occurred from this event, the reports were perhaps combined with the mainshock event, which occurred less than two hours before this small event. The epicenters of the earthquakes used here are depicted in **Figure 9A**. In **Figures 13A,B**, the PGAs and PGVs, after adjusting for the site corrections, are plotted, respectively, as a function of distance for the North Osaka and northeast Kumamoto earthquakes, together with the prediction curves by MF 2013. It can be seen that the data for the shallow focus northeast Kumamoto earthquake are generally described well by the prediction curves for both PGAs and PGVs. On the other hand, the difference is considerable between the observed data and the median prediction curves for the North Osaka Earthquake, as discussed previously.

Similarly, the data from the relatively deep focus (43 km) southern Mie Prefecture earthquake and the North Osaka earthquake are plotted together for PGAs in **Figure 13C** and for PGVs in **Figure 13D**, after adjusting for the site corrections. The prediction curves drawn in **Figures 13C,D** are for the intraslab earthquake

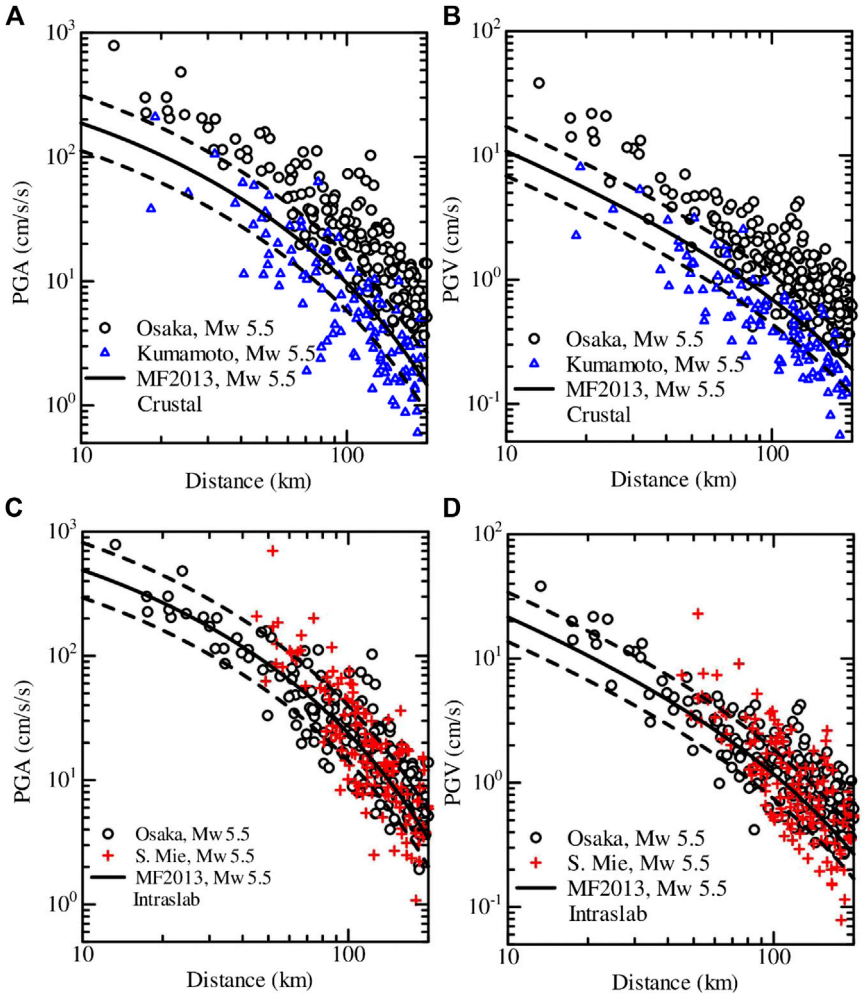

FIGURE 13 | Comparison of the PGAs and PGVs between three events having identical Mw value of 5.5 (F-net, NIED). **A-B**: between the North Osaka and northeast Kumamoto Prefecture earthquakes. **C-D**: between the North Osaka and southern Mie Prefecture earthquakes. The horizontal axes denote the hypocentral distance. The circles, cross marks, and triangles denote the adjusted values by site corrections using equations in Morikawa and Fujiwara (2013) for the events indicated in each panel. See **Figure 9(a)** for the location of the events. See the text for further explanation.

category in MF 2013. It can be seen that the data for the southern Mie Prefecture earthquake and the North Osaka earthquakes are generally described well by the prediction curves.

It has been known that the static stress drop generally increases with the increase of focal depths for inland crustal earthquakes (e.g., Asano and Iwata 2011), and the stress drop is larger for the intraslab earthquakes (e.g., Morikawa and Sasatani, 2004). The difference in the focal depth between the North Osaka earthquake (13 km) and the Kumamoto earthquake (7 km) is not large. This difference may only partially explain the observed difference of the PGAs and PGVs between the two earthquakes. The mean event residual computed from the data within 200 km for the northeast Kumamoto earthquake after the site corrections was approximately −0.14 for PGA in the base-10 log-scale. Although the error is within the range of estimation errors, the negative value suggests that the median prediction curve tends to overestimate the northeast Kumamoto earthquake data. This observation is in line with that the aftershocks tend to have a lower level of stress drops than the mainshocks, at least for smaller aftershocks (e.g., Nakano et al., 2015; Bindi et al., 2018), resulting in lower high-frequency ground motions. In the volcanic region in Japan, it has been shown that the low Q mantle wedge can cause considerable attenuation of short-period ground motions in the back-arc (BA) regions than in the fore-arc (FA) regions (Kanno et al., 2006; Morikawa and Fujiwara 2013; Dhakal et al., 2010). The PGAs and PGVs for the northeast Kumamoto earthquake were grouped into the FA, and BA regions separated by the volcanic-front and are shown in **Figure 14**. The plots do not indicate a noticeable effect of the low Q mantle wedge. The observed general similarities of the PGAs and PGVs between the north Osaka and the relatively deep focus southern Mie Prefecture earthquake mentioned above also augmented the possibility that the North Osaka earthquake was a higher stress drop event. Thus, one of the reasons for the discrepancy between the observed values and the prediction curves for the moderate events discussed here is likely due to the variability of stress drops among the

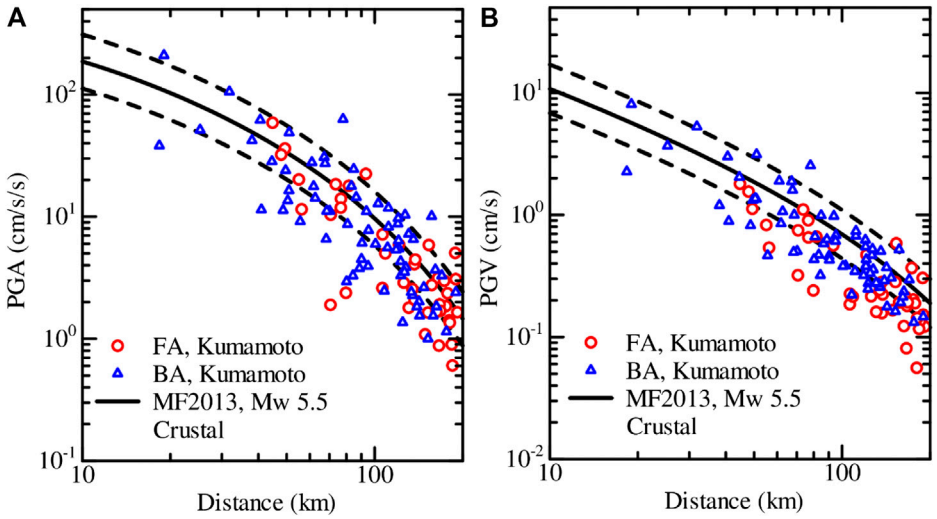

FIGURE 14 | Same as in **Figures 13A,B** for the northeast Kumamoto earthquake, but here the data are grouped into the fore-arc (FA) and back-arc (BA) regions. See the text for further explanation.

events (e.g., Baltay et al., 2013; Oth et al., 2017; Bindi et al., 2018). It is also likely that the almost concurrent fault movements on two closely located faults with different orientations but with comparable magnitudes caused the larger ground motions during the North Osaka earthquake.

CONCLUSION

PGA, PGV, JMA instrumental intensity and AVRS from 79 damaging moderate magnitude earthquakes were analyzed and presented. It was found that the focal depth and site Vs30 values were significant contributing factors for large values at longer hypocentral distances. At smaller distances (<30 km), considerable overlap was seen between the differing magnitudes producing similar PGA, PGV, and intensities. This overlap exists due to the contributions of both sources and sites. Based on the available literature and the analyzed data, source effects, mostly forward rupture directivity effect was found to produce the large velocity pulses even for the Mw 4 class events. Moderate earthquakes of Mw 4 class can generate an instrumental intensity of 4 or larger at short distances and up to about 80 km from the hypocenter of deeper earthquakes of focal depths 50–60 km. The instrumental intensities were smaller than 4 at distances > about 120 km from these moderate magnitude events. The analysis of residuals for the PGA, PGV, and instrumental intensities based on the GMPEs suggested that the observed values at the small distances are somewhat underestimated by the GMPEs. All the GMPEs used in the analysis were constructed using data from events of Mw ≥ 5.5. The large ground motions reported in the paper for smaller events indicated that it is important to evaluate the ground motion hazards from these smaller events. The long-period ground motions (AVRS) at the periods of 1.6 s–7.8 s are found to be of lower concern at distances over 200 km from the viewpoint of EEW for these moderate magnitude earthquakes. However, at intermediate periods of 1.6–2 s, large AVRS leading to LPGMI of level 4 may be observed at short distances. Comparing the observed data from the North Osaka earthquake with GMPEs and other events suggested that the North Osaka earthquake was probably a higher stress drop event. Also, the complex faulting resulting in double earthquakes very closely separated in time and space resulted in large input motions in wide areas. The sediments further caused amplification leading to the large ground motions in the basin areas.

DATA AVAILABILITY STATEMENT

The strong-motion records and PS-logging data were obtained from http://www.kyoshin.bosai.go.jp/. The hypocenter information of the events were taken from https://www.data.jma.go.jp/svd/eqev/data/bulletin/hypo_e.html. The moment magnitude for the first event was taken from https://www.globalcmt.org/, and, for the second event, the moment magnitude was taken from https://www.data.jma.go.jp/svd/eqev/data/bulletin/cmt_e.html. For all the other events, the moment magnitudes were taken from http://www.fnet.bosai.go.jp/event/joho.php?LANG=en. The J-SHIS deep subsurface model was obtained from http://www.j-shis.bosai.go.jp/map/JSHIS2/download.html?lang=en. The list of damaging events was obtained from https://www.data.jma.go.jp/svd/eqev/data/higai/higai1996-new.html. The original contributions presented in the study are included in the article/**Supplementary Material**, further inquiries can be directed to the corresponding author.

AUTHOR CONTRIBUTIONS

The author confirms being the sole contributor of this work and has approved it for publication.

FUNDING

This study was supported by "Advanced Earthquake and Tsunami Forecasting Technologies Project" of NIED and JSPS KAKENHI Grant Number JP20K05055.

ACKNOWLEDGMENTS

I would like to thank the Japan Meteorological Agency for providing us with hypocenter information for the earthquakes used in this study. I would also like to thank Wessel and Smith (1998) for providing us with Generic Mapping Tools, which were used to make some figures in the manuscript. I would like to thank the Editor Nicola Alessandro Pino for arranging review of this manuscript and two reviewers for their constructive and helpful comments.

SUPPLEMENTARY MATERIAL

The Supplementary Material for this article can be found online at: https://www.frontiersin.org/articles/10.3389/feart.2021.618400/full#supplementary-material.

REFERENCES

Aizawa, K., Kawazoe, Y., Uratani, J., Sakihara, H., and Nakamura, M. (2013). "Japan meteorological agency information on long-period ground motion," in American Geophysical Union, Fall Meeting. Abstract ID: S41A-2410, San Francisco, December 9–13.

Alexander, D. E. (2010). The L'Aquila earthquake of April 6 2009 and Italian government policy on disaster response. *J. Nat. Resour. Pol. Res.* 2 (4), 325–342. doi:10.1080/19390459.2010.511450

Aoi, S., Asano, Y., Kunugi, T., Kimura, T., Uehira, K., Takahashi, N., et al. (2020a). MOWLAS: NIED observation network for earthquake, tsunami and volcano. *Earth Planets Space* 72, 126. doi:10.1186/s40623-020-01250-x

Aoi, S., Kimura, T., Kunugi, T., Suzuki, T., Dhakal, Y., and Koja, N. (2020b). Real-time long-period ground-motion prediction system and experimental demonstration for its practical usage. Proceedings: 17th world conference on earthquake engineering, 17WCEE, Paper ID 1e-0004, Sendai, September 27–October 2, 2021.

Asano, K., and Iwata, T. (2011). Characterization of stress drops on asperities estimated from the heterogeneous kinematic slip model for strong motion prediction for inland crustal earthquakes in Japan. *Pure Appl. Geophys.* 168, 105–116. doi:10.1007/s00024-010-0116-y

Baltay, A. S., Hanks, T. C., and Beroza, G. C. (2013). Stable stress-drop measurements and their variability: implications for ground-motion prediction. *Bull. Seismol. Soc. Am.* 103 (1), 211–222. doi:10.1785/0120120161

Bindi, D., Spallarossa, D., Picozzi, M., Scafidi, D., and Cotton, F. (2018). Impact of magnitude selection on aleatory variability associated with ground-motion prediction equations: part I—local, energy, and moment magnitude calibration and stress-drop variability in central Italy. *Bull. Seismol. Soc. Am.* 108 (3A), 1427–1442. doi:10.1785/0120170356

Campbell, K. W. (2003). "Strong-motion attenuation relations," in *International handbook of earthquake & engineering seismology*. Editors W. Lee, H. Kanamori, P. Jennings, and C. Kisslinger, Vol. 81B, 1003–1012.

Dhakal, Y. P., Kunugi, T., Kimura, T., Wataru, S., and Aoi, S. (2019). Peak ground motions and characteristics of nonlinear site response during the 2018 Mw 6.6 Hokkaido eastern Iburi earthquake. *Earth Planets Space* 71, 56. doi:10.1186/s40623-019-1038-2

Dhakal, Y. P., Kunugi, T., Suzuki, W., Kimura, T., Morikawa, N., and Aoi, S. (2020). Comparison of PGA, PGV, and acceleration response spectra between the K-NET, KIK-net, and S-net strong-motion sites. Annual meeting of Seismological Society of Japan, October 29–31, S15-P12.

Dhakal, Y. P., Takai, N., and Sasatani, T. (2010). Empirical analysis of path effects on prediction equations of pseudo-velocity response spectra in northern Japan. *Earthq. Eng. Struct. Dynam.* 39, 443–461. doi:10.1002/eqe.952

Dhakal, Y. P., Wataru, S., Kunugi, T., and Aoi, S. (2015). Ground motion prediction equations for absolute velocity response spectra (1-10 s) in Japan for earthquake early warning. *J. Jpn. Assoc. Earthquake Eng.* 15, 91–111. doi:10.5610/jaee.15.6_91

Dziewonski, A. M., Chou, T.-A., and Woodhouse, J. H. (1981). Determination of earthquake source parameters from waveform data for studies of global and regional seismicity. *J. Geophys. Res.* 86, 2825–2852. doi:10.1029/JB086iB04p02825

Fujiwara, H., Kawai, S., Aoi, S., Morikawa, N., Senna, S., Kudo, N., et al. (2009). A study on subsurface structure model for deep sedimentary layers of Japan for strong-motion evaluation. No, 337. Technical Note of the National Research Institute for Earth Science and Disaster Prevention. (in Japanese).

Garini, E., Gazetas, G., and Anastasopoulos, I. (2017). Evidence of significant forward rupture directivity aggravated by soil response in an Mw6 earthquake and the effects on monuments. *Earthq. Eng. Struct. Dynam.* 46, 2103–2120. doi:10.1002/eqe.2895

Gordo-Monsó, C., and Miranda, E. (2018). Significance of directivity effects during the 2011 Lorca earthquake in Spain. *Bull. Earthq. Eng.* 16, 2711–2728. doi:10.1007/s10518-017-0301-9

Hallo, M., Opršal, I., Asano, K., and Gallovič, F. (2019). Seismotectonic of the 2018 northern Osaka M6.1 earthquake and its aftershocks: joint movements on strike-slip and reverse faults in inland Japan. *Earth Planets Space* 71, 34. doi:10.1186/s40623-019-1016-8

Hashimoto, M., and Jackson, D. D. (1993). Plate tectonics and crustal deformation around the Japanese Islands. *J. Geophys. Res.* 98 (B9), 16149–16166. doi:10.1029/93JB00444

Hashimoto, M., Savage, M., Nishimura, T., Horikawa, H., and Tsutsumi, H. (2017). Special issue "2016 Kumamoto earthquake sequence and its impact on earthquake science and hazard assessment". *Earth Planets Space* 69, 98. doi:10.1186/s40623-017-0682-7

HERP (Headquarters for Earthquake Research Promotion) (2010). Seismic activity off-shore east of the izu peninsula. Available at: https://www.jishin.go.jp/main/chousa/10jan_izu/index-e.htm (Accessed August 24, 2020).

HERP (Headquarters for Earthquake Research Promotion) (2018). Report: national seismic hazard maps for Japan (2009). Available at: https://www.jishin.go.jp/main/index-e.html (Accessed September 5, 2020).

Hirata, N., and Kimura, R. (2018). The earthquake in Ōsaka-Fu Hokubu on June 18 2018 and its ensuing disaster. *J. Disaster Res.* 13 (4), 813–816. doi:10.20965/jdr.2018.p0813

Hoshiba, M., Kamigaichi, O., Saito, M., Tsukada, S., and Hamada, N. (2008). Earthquake early warning starts nationwide in Japan. *Eos, Transact., Am. Geophy. Uni.* 89 (8), 73–80. doi:10.1029/2008EO080001

Hoshiba, M., Ohtake, K., Iwakiri, K., Tamotsu Aketagawa, T., Nakamura, H., and Yamamoto, S. (2010). How precisely can we anticipate seismic intensities? A study of uncertainty of anticipated seismic intensities for the earthquake early warning method in Japan. *Earth Planets Space* 62, 611–620. doi:10.5047/eps.2010.07.013

JMA (Japan Meteorological Agency) (2020a). Major damaging earthquakes near Japan. Available at: https://www.data.jma.go.jp/svd/eqev/data/higai/higai1996-new.html, (in Japanese), Accessed March 28, 2020.

JMA (Japan Meteorological Agency) (2020b). Calculation method of measured seismic intensity (In Japanese). Available at: http://www.data.jma.go.jp/svd/eqev/data/kyoshin/kaisetsu/calc_sindo.htm (Accessed April 2, 2020).

Kaiser, A., Holden, C., Beavan, J., Beetham, D., Benites, R., Celentano, A., et al. (2012). The Mw 6.2 Christchurch earthquake of February 2011: preliminary report. *N. Z. J. Geol. Geophys.* 55 (1), 67–90. doi:10.1080/00288306.2011.641182

Kanno, T., Narita, A., Morikawa, N., Fujiwara, H., and Fukushima, Y. (2006). A new attenuation relation for strong ground motion in Japan based on recorded data. *Bull. Seismol. Soc. Am.* 96, 879–897. doi:10.1785/0120050138

Kato, A., and Ueda, T. (2019). Source fault model of the 2018 Mw 5.6 northern Osaka earthquake, Japan, inferred from the aftershock sequence. *Earth Planets Space* 71, 11. doi:10.1186/s40623-019-0995-9

Koshiyama, K. (2019). Damage characteristics of 2018 northern Osaka earthquake. *Saf. Sci. Rev.* 9, 69–72. Available at: https://kansai-u.repo.nii.ac.jp/ (Accessed August 12, 2020).

Lopez-Comino, J. A., Mancilla, F., Morales, J., and Stich, D. (2012). Rupture directivity of the 2011, Mw 5.2 Lorca earthquake (Spain). *Geophys. Res. Lett.* 39 (3), L03301. doi:10.1029/2011GL050498

Maeda, T., and Sasatani, T. (2009). Strong ground motions from an Mj 6.1 inland crustal earthquake in Hokkaido, Japan: the 2004 Rumor earthquake. *Earth Planets Space* 61, 689–701. doi:10.1186/BF03353177

Matsu'ura, R. S. (2017). A short history of Japanese historical seismology: past and the present. *Geosci. Lett.* 4, 3. doi:10.1186/s40562-017-0069-4

Meroni, F., Squarcina, T., Pessina, V., Locati, M., Modica, M., and Zoboli, R. (2017). A damage scenario for the 2012 northern Italy earthquakes and estimation of the economic losses to residential buildings. *Int. J. Disaster Risk Sci.* 8, 326–341. doi:10.1007/s13753-017-0142-9

Morikawa, N., and Fujiwara, H. (2013). A new ground motion prediction equation for Japan applicable up to M9 mega-earthquake. *J. Disaster Res.* 8, 878–888. doi:10.20965/jdr.2013.p0878

Morikawa, N., and Sasatani, T. (2004). Source models of two large intraslab earthquakes from broadband strong ground motions. *Bull. Seismol. Soc. Am.* 94 (3), 803–817. doi:10.1785/0120030033

Mucciarelli, M., and Liberatore, D. (2014). Guest editorial: the Emilia 2012 earthquakes. *Italy. Bull. Earthquake Eng.* 12, 2111–2116. doi:10.1007/s10518-014-9629-6

Nakamura, M. (2013). Information on long-period ground motion of the Japan meteorological agency. Proceedings 10th International Workshop on Seismic Microzoning and Risk Reduction, Paper ID 12. September 25, Tokyo.

Nakano, K., Matsushima, S., and Kawase, H. (2015). Statistical properties of strong ground motions from the generalized spectral inversion of data observed by K-NET, KiK-net, and the JMA Shindokei network in Japan. *Bull. Seismol. Soc. Am.* 105 (5), 2662–2680. doi:10.1785/0120140349

NIED (2019a). NIED K-net, KiK-net. Tsukuba: National Research Institute for Earth Science and Disaster Resilience. doi:10.17598/NIED.0004

NIED (2019b). NIED F-net. Tsukuba: National Research Institute for Earth Science and Disaster Resilience. doi:10.17598/nied.0005

Nigam, N. C., and Jennings, P. C. (1969). Calculation of response spectra from strong motion earthquake records. *Bull. Seism. Soc. Am.* 59, 909–922.

Okada, Y., Kasahara, K., Hori, S., Obara, K., Sekiguchi, S., Fujiwara, H., et al. (2004). Recent progress of seismic observation networks in Japan —hi-net, F-net, K-NET and KiK-net—. *Earth Planets Space* 56, 15–58. doi:10.1186/BF03353076

Oth, A., Miyake, H., and Bindi, D. (2017). On the relation of earthquake stress drop and ground motion variability. *J. Geophys. Res.* 122, 5474–5492. doi:10.1002/2017JB014026

Sato, H., Shiba, Y., Higashi, S., Kunugi, T., Maeda, T., and Fujiwara, H. (2013). *Estimation of basement earthquake motion and site characteristics at HKD020 during the 2004 rumor earthquake based on geophysical exploration and laboratory test*. Central Research Institute of Electric Power Industry (CRIEPI), Tokyo, Civil Engineering Research Laboratory Rep. No. N13007.

Shabestari, K. T., and Yamazaki, F. (2001). A proposal of instrumental seismic intensity scale compatible with MMI evaluated from three-component acceleration records. *Earthq. Spectra* 17 (4), 711–723. doi:10.1193/1.1425814

Si, H., and Midorikawa, S. (1999). New attenuation relations for peak ground acceleration and velocity considering effects of fault type and site condition. *J. Struc. Construc. Eng. Transact. AIJ* 523, 63–70. doi:10.3130/aijs.64.63_2 (in Japanese with English abstract).

Si, H., and Midorikawa, S. (2000). New attenuation relations for peak ground acceleration and velocity considering effects of fault type and site condition. Proceedings of the 12th world conference on earthquake engineering, Auckland, New Zealand, January 30 - February 4, 2000, paper no. 0532.

Sommerville, P. G., Smith, N. F., Graves, R. W., and Abrahamson, N. A. (1997). Modification of empirical attenuation relations to include the amplitude and duration effects of rupture directivity. *Seismol Res. Lett.* 70, 59–80. doi:10.1785/gssrl.68.1.199

Wessel, P., and Smith, W. H. F. (1998). New, improved version of generic mapping tools released. *Eos, Transact., American Geophysical Union* 79, 579. doi:10.1029/98EO00426

Conflict of Interest: The author declares that the research was conducted in the absence of any commercial or financial relationships that could be construed as a potential conflict of interest.

frontiers in Earth Science

ORIGINAL RESEARCH
published: 11 March 2021
doi: 10.3389/feart.2020.617794

On the Source Parameters and Genesis of the 2017, M_w 4 Montesano Earthquake in the Outer Border of the Val d'Agri Oilfield (Italy)

José Ángel López-Comino[1,2,3]*, *Thomas Braun*[4], *Torsten Dahm*[3,5], *Simone Cesca*[5] and *Stefania Danesi*[6]

[1]Instituto Andaluz de Geofísica, Universidad de Granada, Granada, Spain, [2]Departamento de Física Teórica y del Cosmos, Universidad de Granada, Granada, Spain, [3]Institute of Geosciences, University of Potsdam, Potsdam-Golm, Germany, [4]Istituto Nazionale di Geofisica e Vulcanologia, Arezzo, Italy, [5]GFZ German Research Centre for Geosciences, Potsdam, Germany, [6]Istituto Nazionale di Geofisica e Vulcanologia, Bologna, Italy

On October 27, 2017, an M_w 4 earthquake occurred close to the municipality of Montesano sulla Marcellana, less than 10 km external to the concession of the largest European onshore hydrocarbon reservoir—the Val d'Agri oilfield (Southern Italy). Being a weak event located outside the extended monitoring domain of the industrial concession, the relevance of this earthquake and the possible links with the hydrocarbon exploitation were not extensively discussed. Actually, the analysis of shallow seismic events close to subsurface exploitation domains plays a significant role in the definition of key parameters in order to discriminate between natural, triggered, and induced seismicity, especially in tectonically active regions. The study of weak-to-moderate earthquakes can improve the characterization of the potentially destructive seismic hazard of this particular area, already struck by M > 6.5 episodes in the past. In this work, we analyze the source parameters of this M_w 4 earthquake by applying advanced seismological techniques to estimate the uncertainties derived from the moment tensor inversion and identify plausible directivity effects. The moment tensor is dominated by a NW–SE oriented normal faulting with a centroid depth of 14 km. A single M_L 2.1 aftershock was recorded and used as the empirical Green's function to calculate the apparent source time function for the mainshock. Apparent durations (in the range 0.11–0.21 s, obtained from S-waves) define an azimuthal pattern, which reveals an asymmetric bilateral rupture with 70% of the rupture propagation in the N310°W direction, suggesting a rupture plane dipping to the SW. Our results tally with the activation of a deeper fault segment associated with the Eastern Agri Fault System close to the basement as the origin of the Montesano earthquake. Finally, the Coulomb stress rate induced by depletion of the oilfield is calculated to quantify the trigger potential estimated for the Montesano earthquake yielding relatively low probabilities below 10%. Our analyses point toward the conclusion that the M_w 4 event was more likely due to the local natural tectonic stress, rather than induced or triggered by the long-term hydrocarbon extraction in the Val d'Agri oilfield.

Keywords: earthquake source, induced seismicity, directivity, triggered earthquake, Val d'Agri oilfield

OPEN ACCESS

Edited by:
Jorge Miguel Gaspar-Escribano, Polytechnic University of Madrid, Spain

Reviewed by:
Sebastiano D'Amico, University of Malta, Malta
Hamoud Beldjoudi, Centre de Recherche en Astronomie Astrophysique et Géophysique, Algeria

***Correspondence:**
José Ángel López-Comino
jalopezcomino@ugr.es

Specialty section:
This article was submitted to Solid Earth Geophysics, a section of the journal Frontiers in Earth Science

Received: *15 October 2020*
Accepted: *28 December 2020*
Published: *11 March 2021*

Citation:
López-Comino JÁ, Braun T, Dahm T, Cesca S and Danesi S (2021) On the Source Parameters and Genesis of the 2017, Mw 4 Montesano Earthquake in the Outer Border of the Val d'Agri Oilfield (Italy). Front. Earth Sci. 8:617794. doi: 10.3389/feart.2020.617794

INTRODUCTION

Induced seismicity can nowadays be considered as a relevant and pressing problem of increasing interest for the general public. Underground operations such as shale gas and oil exploitation, mining, and other energy technologies could generate seismic activity (McGarr et al., 2002; Grigoli et al., 2017; Braun et al., 2018; Foulger et al., 2018). Some directly induced earthquakes reached moderate moment magnitude (e.g., $M_w > 5$) and were strong enough to cause damages, and even casualties (Grigoli et al., 2018). In some cases, moderate-to-strong earthquakes may also be triggered at distances larger than 10 km from the underground operations (Keranen et al., 2014; Goebel et al., 2017), with an impact on the regional seismic hazard related to such activities. Usually, a well-constrained hypocentral location with small uncertainties as well as the temporal correlation between geotechnical activities and seismicity patterns play an important role in distinguishing the origin of seismic events (Healy et al., 1968; Raleigh et al., 1976). However, a detailed and robust analysis about the seismic source of potentially induced events could reveal and clarify the discrimination between induced, triggered, or natural earthquakes. Generally, the term "induced seismicity" is referred to anthropogenic seismic events in a wide sense encompassing both pure induced and triggered seismicity; however, different specific definitions have been given for these two seismic processes. According to McGarr and Simpson (1997), induced earthquakes are events where most of the stress changes release during the rupture produced by human action, while triggered events release a substantial amount of tectonic stress. More precisely, according to Dahm et al. (2015), an induced event is when the rupture is driven by the induced stress over the full rupture plane, whereas for triggered events only the rupture initiation is caused by the stress rate at the hypocenter. In other words, induced seismic events are entirely controlled by stress changes caused by human operations and would not have occurred without anthropic intervention; on the other hand, in triggered seismicity, the tectonic stress plays a primary role, with a stress variation on favorably oriented faults in agreement with the existing regional or local background stress field and geological structure.

In the particular case of Italy, a framework for the management of the geophysical monitoring associated with hydrocarbon reservoir exploitation and gas storage was established in 2014 by the publication of the "Guidelines for Monitoring Seismicity, Ground Deformation and Pore Pressure in Subsurface Industrial Activities" (ILG, Dialuce et al., 2014). The ILGs are currently experimentally applied for selected pilot sites (Braun et al., 2020), including the largest European onshore hydrocarbon reservoir, the Val d'Agri (VA) oilfield (Southern Italy), which will be the focus of our study (**Figure 1**). With the purpose of distinguishing between natural seismicity from possibly induced or triggered one, the ILGs define limits, domains, and technical requirements intended to localize the seismicity in a volume surrounding the area where human activities take place. More specifically, the ILGs define: (i) the Internal Monitoring Domain (DI) as the volume that includes the mineralized zone (oilfield) extended by an additional 5 km wide volume and (ii) the Extended Monitoring Domain (DE) beyond the DI to a neighborhood of 5–10 km (**Figure 1b**). Moreover, the ILGs also recommend the application of a Traffic Light System (TLS) protocol as guidance for the seismic surveillance management (Bommer et al., 2006; Bosman et al., 2016), which is based on the estimation of seismic parameters (hypocenter, magnitude, peak ground velocity, and peak ground acceleration) for events occurring within the DI close to operational reinjection wells (Dialuce et al., 2014; Braun et al., 2020).

The present-time tectonics of the VA is mainly characterized by NE–SW extension, which is accommodated by two main quaternary fault structures, the Monti della Maddalena (MMFS) and the Eastern Agri Fault System (EAFS), bounding the VA on the SW edge and the NE edge, respectively (Maschio et al., 2005). This active deformation is expressed seismically through mostly high-angle, normal-faulting earthquakes that occur on the two main NW–SE-trending fault systems. The occurrence of sparse background seismicity is well known, moderate seismic events in VA are significant, and historical seismicity suggests that large and destructive events can occur (**Figure 1A**). The most destructive earthquake, with an equivalent magnitude M_w 7.0, occurred on December 16th, 1857, causing extreme damage (I_{max} = XI, EMS-98) and accounting for more than 11,000 victims (Guidoboni et al., 2019; Rovida et al., 2019; Rovida et al., 2020). A conclusive characterization of the event source is still under debate: Benedetti et al. (1998), Cello et al. (2003), and Barchi et al. (2006) ascribe the main 1857 M7 event to the EAFS; more recently, Burrato and Valensise (2008) indicate a ~40 km-long complex rupture of at least two segments of the MMFS (**Figure 1A**). Comprehensive and historical reports about the effects of the 1857 M7 earthquake were performed by Mallet (1862) and later re-edited by Guidoboni and Ferrari (1987). While the building damage and number of victims due to the 1857 M7 event were definitely higher in VA, Mallet (1862) reported significant surface effects for adjacent areas; for example, in the area of Montesano sulla Marcellana (Vallo del Diano), located in the western part of the MMFS, Mallet (1862) reports, "real surface ruptures in old rock layers for an extension of 200 feet". Even if our study does not investigate the hypocenter of the "great Neapolitan earthquake" (Mallet, 1862), it is however important to keep in mind that the exact location of the 1857 M7 event is still discussed.

According to the earthquake bulletins of ENI (the Italian governmental energy company assigned to the VA concession) and INGV (Istituto Nazionale di Geofisica e Vulcanologia), since 1990 in VA only few seismic events with a magnitude of $M > 3$ have been reported (Improta and Piccinini, 2015). Note that two significant clusters linked to anthropogenic operations have been well-described in previous works (**Figure 1A**). The main swarm (depth range between 1 and 5 km and magnitudes smaller than Ml 3) occurred a few kilometers SW of the artificial Pertusillo lake in the southern termination of the MMFS and was interpreted as water reservoir-induced seismicity, due to an increased impoundment during the late winter/spring rainfalls (Valoroso et al., 2009; Valoroso et al., 2011; Stabile et al., 2014). Another

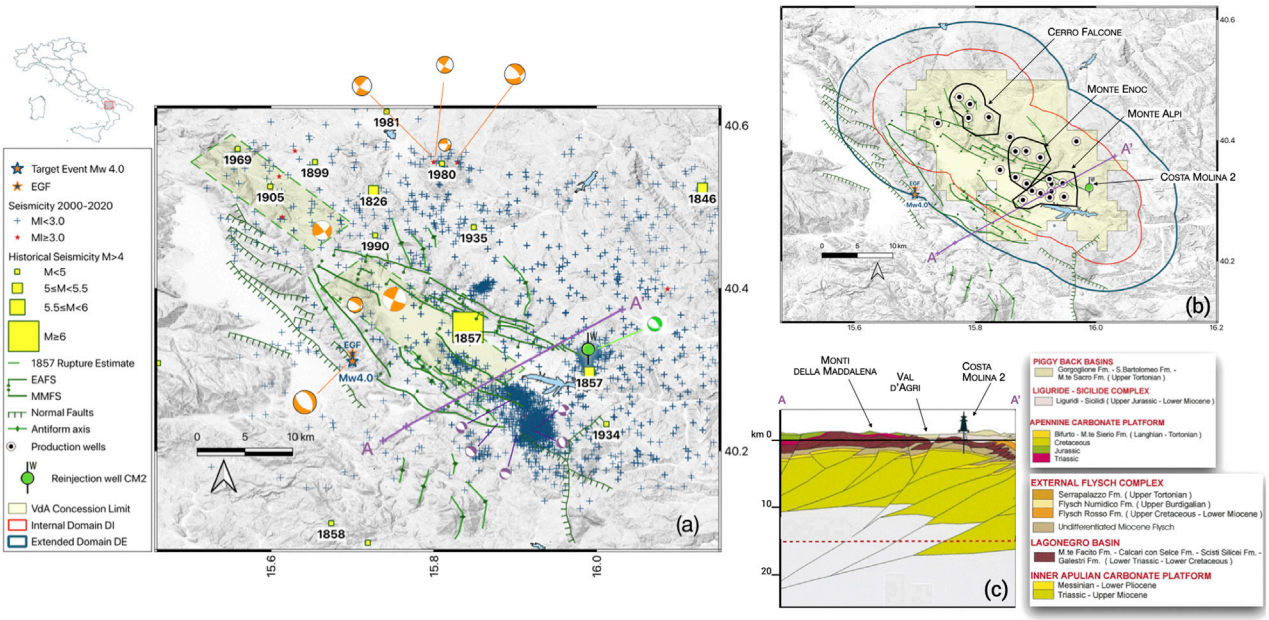

FIGURE 1 | General information and reference map of the study area. **(A)** The large orange star indicates the target event and the smaller star (inverted colors) indicates the single aftershock used as the empirical Green's function (EGF); the corresponding orange beachball represents the moment tensor (MT) solution released by INGV. Other orange beach balls show regional MT (Cucci et al., 2004); purple beach balls show the MT of a few Ml~2 events (Improta et al., 2017); the green beachball is a representative MT of the seismicity linked to the Costa Molina 2 (CM2) reinjection well. Geological features are in accordance with Valoroso et al. (2011, and references therein: the Eastern Agri Fault System (EAFS) and the Monti della Maddalena Fault System (MMFS). Blue crosses show the recorded seismicity in the timespan 2001–2020, red stars are Ml > 3 events. The main historical events (yellow squares) are extracted from CPTI15 (Rovida et al., 2019; Rovida et al., 2020); green dashed boxes indicate the potential causative sources of the 1857M~7 Earthquake (after Burrato and Valensise, 2008) **(B)** The yellow shaded area represents the Val d'Agri (VA) industrial concession; circled black dots mark the production wells. The red and blue boundaries indicate the internal and extended monitoring domains, respectively. CM2 is represented as in **(A)**. The profile AA′ follows Menardi Noguera and Rea (2000) **(C)** Schematic geologic cross-section across the VA basin was modified after Menardi Noguera and Rea (2000). The red dashed line represents the approximate limit of seismic data images.

intense swarm-like seismic activity (Ml_{max} 2.2), starting from 2006, was recorded in the SE area of a reduced volume (5 × 5 × 5 km) around the 3 km deep injection point of the wastewater disposal well, Costa Molina (CM2) (Improta et al., 2015); this is actually the only confirmed case of waste-water induced seismicity in Italy.

In this study, we investigate the source parameters and genesis of a weak-to-moderate earthquake that occurred at 22:38 UTC on October 26th, 2017, and was located 4 kmN of the municipality of Montesano sulla Marcellana (hereon referred to as Montesano earthquake). Its magnitude of M_w 3.8 makes this event the largest earthquake in the Monti della Maddalena since the last 2 decades. Being located in the proximity of the external margin of the VA oilfield's extended monitoring domain, it is generally of interest to investigate whether the seismic source of this event may be natural, induced, or triggered. Due to the hypocentral depth of more than 10 km (10.9 and 14 km from ENI and INGV catalogues, respectively), the national monitoring service classified it as a natural tectonic event, excluding any anthropogenic origin. Taking advantage of a wide coverage of seismic stations deployed in the VA region, we describe a detailed and robust analysis of the source parameters for the Montesano earthquake in order to decipher its genesis and apply a probabilistic approach to address the question of discriminating between natural, triggered, and induced origin. A combination of advanced seismological techniques is applied to estimate the uncertainties derived from the moment tensor inversion and identify plausible directivity effects from Apparent Source Time Functions (ASTFs), revealing preferred rupture directions and potential asymmetries in the rupture propagation as well as to resolve the fault plane ambiguities. Finally, we analyze the origin of the source of the Montesano earthquake through a probabilistic approach based on the modeling of depletion-induced stress changes and the previously calculated seismological source parameters.

Geological Setting, Val d'Agri Oilfield and Seismic Monitoring

The formation of the hydrocarbon reservoir in VA is the result of a succession of complex multiple tectonic phases. Below the Quaternary deposits of the VA Basin, upper Messinian and/or Pliocene terrigenous marine deposits are found (Doglioni et al., 1999; Scrocca et al., 2005), underlain by 6–7 km thick allochthonous units of Mesozoic-early Tertiary carbonate sequence, which form the Apulian Platform (AP) and the Lagonegro units (LU) (e.g., Cello and Mazzoli, 1999). The collision of the African and the Eurasian Plates, which started in the late Cretaceous, caused a shortening in anti-Apenninic direction, which was accommodated by a series of thrust and reverse faults. This process led to a displacement of the LU and

the overlying Apennine platform toward the east, overriding thus the AP (D'Argenio et al., 1975; Cello and Mazzoli, 1999; Mazzoli et al., 2001; Butler et al., 2004; Valoroso et al., 2009). The internal deformation of the AP by thrust faults and related folds, sealed on top by the marine deposits, formed the main structural traps for the oilfields in the region (e.g., Mazzoli et al., 2001; Butler et al., 2004; Shiner et al., 2004).

The giant deposit of VA, discovered in 1988, is actually the most productive oilfield onshore in Europe. The structural trap is represented by a large-scale pop-up bounded by high-angle reverse faults oriented in the NW–SE Apennine direction (Bertello et al., 2011) hosted in the extensional homonym Quaternary basin. The reservoir rocks for the oil/gas production are hosted inside the Cretaceous to Miocene limestone and dolostone of the Apulian Platform. The carbonate reservoirs include vuggy intervals, as well as extensively developed fracture systems, which provide flow rates in the range of 500–2000 Sm^3/day (Standard cubic meters per day) from oil columns that vary in thickness from 600 to 1000 m. The entire producing complex is sealed by the overlying Neogene sequences (Wavrek and Mosca, 2004). Depending on the type of depositional facies, the hydrocarbon column of the VA reservoir shows significant lateral heterogeneities in density (in the range of 835–1013 kg/m^3), in petrophysical characteristics and in compositional grading (Wavrek and Mosca, 2004). The reservoir includes three main productive regions corresponding to the three geographical culminations named Cerro Falcone (CF), Monte Enoc (ME), and Monte Alpi (MA) (**Figure 1B**). After a long initial test period, production started at MA in 1996. Subsequently, the number of production wells increased to the current number of 24 (ranging from a depth of 1.8–3.5 km below sea level), the crude oil treatment lines were improved, the CM2 wastewater disposal well came into operation, and the entire VA field achieved full production in 2010. The wastewater reinjection well CM2 was initially drilled for exploitation purposes in 1982–83; due to its limited production potential, it was converted into a reinjection well and became operational in 2006.

ENI has continuously operated a seismic network in the VA domain since 2001 (Eni Spa, 2001), when the first eight seismic stations were installed, providing a significant refinement in the location capacity and sensitivity of the national seismic monitoring system for the area. Schorlemmer et al. (2010) estimated that by 2008, in the broader VA region including Lake Pertusillo, the magnitude of completeness for the INGV network was between $1.5 \leq M_C \leq 2.0$. In 2012, the local ENI seismic network was upgraded to 15 stations (Braun et al., 2020). For the southern sector of the oilfield, this new configuration led to a lowering of the detection threshold of local seismic events to $1.0 \leq M_C \leq 1.2$ (Improta and Piccinini, 2015). In the framework of specific research projects that focused on the observation of the microseismicity potentially induced by the CM2-well and the Lake Pertusillo, between 2005 and 2012, temporary seismic stations were deployed in the VA area to complement the permanent ENI and INGV networks, thus providing a significant improvement for the integration of local seismic catalogs (Valoroso et al., 2009; Stabile et al., 2014).

MOMENT TENSOR INVERSION

We performed a deviatoric moment tensor inversion for the mainshock based on broadband seismological data using the probabilistic seismic source inversion algorithm Grond (Heimann et al., 2018; Kühn et al., 2020). Grond allows for simultaneously fitting the available seismic data in different frequency ranges, using different velocity models, and implementing different misfit definitions, both in the time and frequency domains. The inversion algorithm optimization starts with a random search of the parameter space and then progressively scans the parameter space closer to a range of best-fitting solutions. Parameter uncertainties are estimated by a bootstrap approach, simulating many different data configurations.

Here, we chose to simultaneously model full waveforms and amplitude spectra using data from the permanent INGV network (IV, INGV Seismological Data Centre 2006) and the local network (VA, Eni Spa, 2001). For near stations, located within 30 km from the epicenter, we build synthetic seismograms using the local 1D velocity model of Improta et al. (2017), while for stations at distances of 30–200 km we use a regional model from the Crust 2.0 database (Bassin et al., 2000). Both models are provided in the **Supplementary Material S1**. The inversion is setup to simultaneously fit different datasets, using in all cases 3-components data, as follows: 1) full waveform (60 s time windows) amplitude spectra in the frequency band 0.04–0.20 Hz for near stations, 2) full waveform (180 s time windows) amplitude spectra in the frequency band 0.04–0.08 Hz for far stations, 3) full waveform (60 s time windows) displacement traces in the frequency band 0.04–0.20 Hz for near stations, 4) cross-correlation of body wave displacement signals (from 2 s before P phases to 4 s after S phases) in the frequency band 0.5–2.0 Hz for near stations, and 5) cross-correlation of full waveform (180 s time windows) displacements in the frequency band 0.04–0.08 Hz for far stations. The choice of the frequency bands has been based on a number of considerations. At regional distances, modeling full waveforms can only be successfully achieved for relatively low frequencies, as high frequency waveforms cannot be reproduced at these distances with a simplified 1D model; below 0.04 Hz, however, the signal-to-noise ratio becomes too low, due to the moderate magnitude of the earthquake. At local distances, and when modeling body wave pulses, the seismic signals can be well reproduced to higher frequencies using the local velocity model. Results (**Figure 2** and **Table 1**) show a moment tensor dominated by a NW–SE oriented normal faulting, plus an additional negative compensated linear vector dipole (CLVD) component, the presence of which is not robustly resolved (see uncertainties in **Supplementary Figure S2**). The resolved focal mechanism is in a good agreement with the INGV solution, but we estimate a slightly larger moment magnitude of M_w 4.0 ± 0.2 and a slightly deeper depth of 14.0 ± 2.8 km (see **Table 1**).

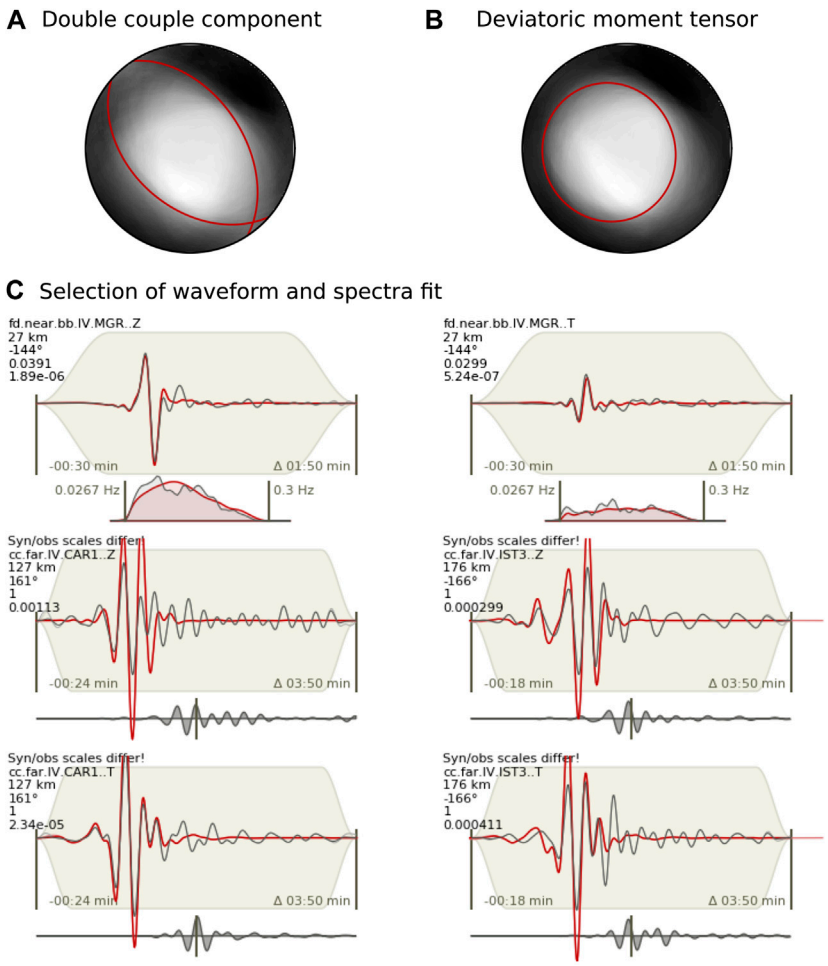

FIGURE 2 | Focal spheres for the moment tensor result, showing the overlay of the ensemble of pure double couple **(A)** and deviatoric moment tensors **(B)** out of the Grond bootstrap analysis, where a read line denotes the focal sphere of the best solutions. Panel **(C)** shows a selection of data fit (synthetic waveforms and spectra in red, observations in black), illustrating different fitting procedures and stations located at different distances and azimuths (the main information is reported in each subplot).

TABLE 1 | Summary of the best solution for the deviatoric and double couple (DC) moment tensor inversion, reporting mean and standard deviation according to the DC solutions. Centroid time is defined with respect to the assumed origin time, October 26, 2017 22:38:35.3.

Parameter	Best MT deviatoric	Best MT DC	Mean value	Standard deviation
Time (s)	1.1	0.9	0.5	0.7
Centroid latitude (°)	40.3187	40.3331	40.3331	0.0171
Centroid longitude (°)	15.7205	15.7358	15.7326	0.0153
Depth (km)	14.7	16.0	14.0	2.8
Mw magnitude	4.1	4.0	4.0	0.2
Strike 1	153	131	121	55
Dip 1	29	43	45	15
Rake 1	–95	–102	–75	48
Strike 2	339	327	287	49
Dip 2	61	48	55	14
Rake 2	–87	–79	–96	37
CLVD (%)	–93	0	0	0

ASTFs and Rupture Directivity Analysis

Earthquake sources can be isolated from seismograms applying empirical Green's functions (EGFs) techniques (Hartzell, 1978). For this purpose, a detailed knowledge of the earth structure between the target earthquake and receivers through which the waves propagated is required. Waveforms of fore- and aftershocks, sharing a common path with the mainshock, are then used as EGFs to accurately model these propagation effects. A point source representing a delta function is assumed for the EGFs (typically, one to two magnitude units smaller than the mainshock), which must also show similar hypocentral locations and focal mechanism implying similar waveforms with the mainshock. Under these conditions, ASTFs can be retrieved through a deconvolution procedure revealing the relative moment rate functions of the target event observed at different receivers (e.g., López-Comino et al., 2016; Abercrombie et al., 2017; Stich et al., 2020). The shape and duration of these ASTFs can be then modeled providing constraints to identify preferred rupture directions and source complexities (e.g., López-Comino and Cesca, 2018; Wu et al., 2019).

Following the M_w four Montesano earthquake, a single M_L 2.1 aftershock was recorded 13 days later at 09:51 UTC on November 8th, 2017, located less than 2 km from the mainshock at a depth of 15 km (Bolletino Sismico Italiano, INGV), with a similar hypocentral location (just 1 km deeper than the mainshock). Both events show similar polarities in the P-wave arrivals (**Supplementary Figure S3**) as well as similar waveforms (**Figure 3**) revealing a common focal mechanism (**Supplementary Figure S4**); therefore, we use this aftershock as an EGF to calculate the ASTFs of the Montesano earthquake. We perform the deconvolution in the frequency domain through spectral division using the seismic recordings of the mainshock and the EGF (López-Comino et al., 2012). To avoid numerical instabilities derived from the deconvolution procedure, a Gaussian low pass with a pulse width of ~0.075 s and a water level of 0.01 of the maximum spectral amplitude are used. Successful deconvolution results are obtained for S-wave windows (length of 6 s starting 1 s before the S-wave arrival) using the horizontal components (**Figure 3**). The resulting ASTF at each station is obtained by stacking both components (east–west and north–south), reaching a good azimuthal coverage for 21 near-regional and local stations up to a distance of 41 km (**Supplementary Figure S5**). ASTFs are normalized to unit area according to the total seismic moment of the mainshock and negative values derived from the deconvolution procedure are removed. Apparent durations are identified manually by picking onset and end of each ASTF at the intersection of the initial and final slopes with the baseline assuming uncertainties of about 0.01s. One single and consistent pulse can be clearly identified for the Montesano earthquake with slightly shorter apparent durations at NW azimuths, and slightly larger durations for stations located at the opposite directions (**Figure 4**). Apparent durations range from 0.11 up to 0.21 s.

Assuming a line source after Haskell (1964), theoretical predictions for unilateral and asymmetric bilateral ruptures are considered to adjust the azimuthal pattern of the apparent durations identified by the ASTFs (for technical details, see Cesca et al., 2011a and López-Comino et al., 2016). Some fixed parameters are considered to solve the nonlinear functions: local S-wave velocity of 3.2 km/s (from Improta et al., 2017) and a rise time of 0.09 s. Our results reveal an asymmetric bilateral rupture with 69 ± 8% of the rupture propagation toward N310°W ± 12°, rupture duration of 0.16 ± 0.03 s and rupture length of 0.29 ± 0.12 km (**Figure 4C** and **Table 2**). This model yields lower L1 misfit of 0.01 s in comparison with pure unilateral rupture. The largest uncertainties are observed for the rupture velocity because intrinsic trade-offs among rise time, rupture length, and velocity remain in these inversions; and, we obtain a reasonable value of 2.9 km/s, corresponding to 90% of the local S-wave velocity. Resolving the fault plane ambiguities in a normal faulting focal mechanism is challenging due to the similar strike values in both planes and its uncertainties around 50° estimated from the moment tensor analysis (**Table 2**). However, the directivity direction is well constrained from this analysis and small differences in the strike values are observed from the best solution of the DC moment tensor (strike1 = 131° (311°); strike2 = 327°), which could allow to identify the plane dipping to the SW as our preferred solution (**Figure 4C**).

PROBABILISTIC DISCRIMINATION

The discrimination problem between a natural, triggered, or induced event is addressed through a probabilistic scheme to quantify the likelihood of a correlation with the depletion-induced stress perturbations (Dahm et al., 2015). This methodology based on physical-statistical seismicity models considers an earthquake occurring close to an oil- or gas-field, that has continuously produced over a period of several years and is depleted; this is the case of the Montesano earthquake. The result of this analysis is the probability that the target event has been triggered by the stressing rate induced by the depletion of the oilfield. The scheme can account for the target event source parameters and their uncertainties, which were addressed above.

In a first step, the steady-state tectonic stress rate is estimated from the background seismicity before the production started, using (Hainzl et al., 2010; Dahm et al., 2015):

$$\dot{\tau}^T = 10^{a+9.1}\frac{b}{1.5-b}\frac{10^{(1.5-b)M_{\max}}}{AD}. \quad (1)$$

Variables in this equation are the a and b values of the Gutenberg Richter frequency-magnitude distribution, the maximum observed magnitude (M_{max}), the area of the seismogenic zone (A), and the seismogenic width (D). These parameters are considered for the seismogenic zone 927 defined in the ZS9 model proposed by Meletti et al. (2008), which contains our study region. Assuming the same seismogenic zone, slightly different M_{min}, M_{max}, N (annual earthquake rate

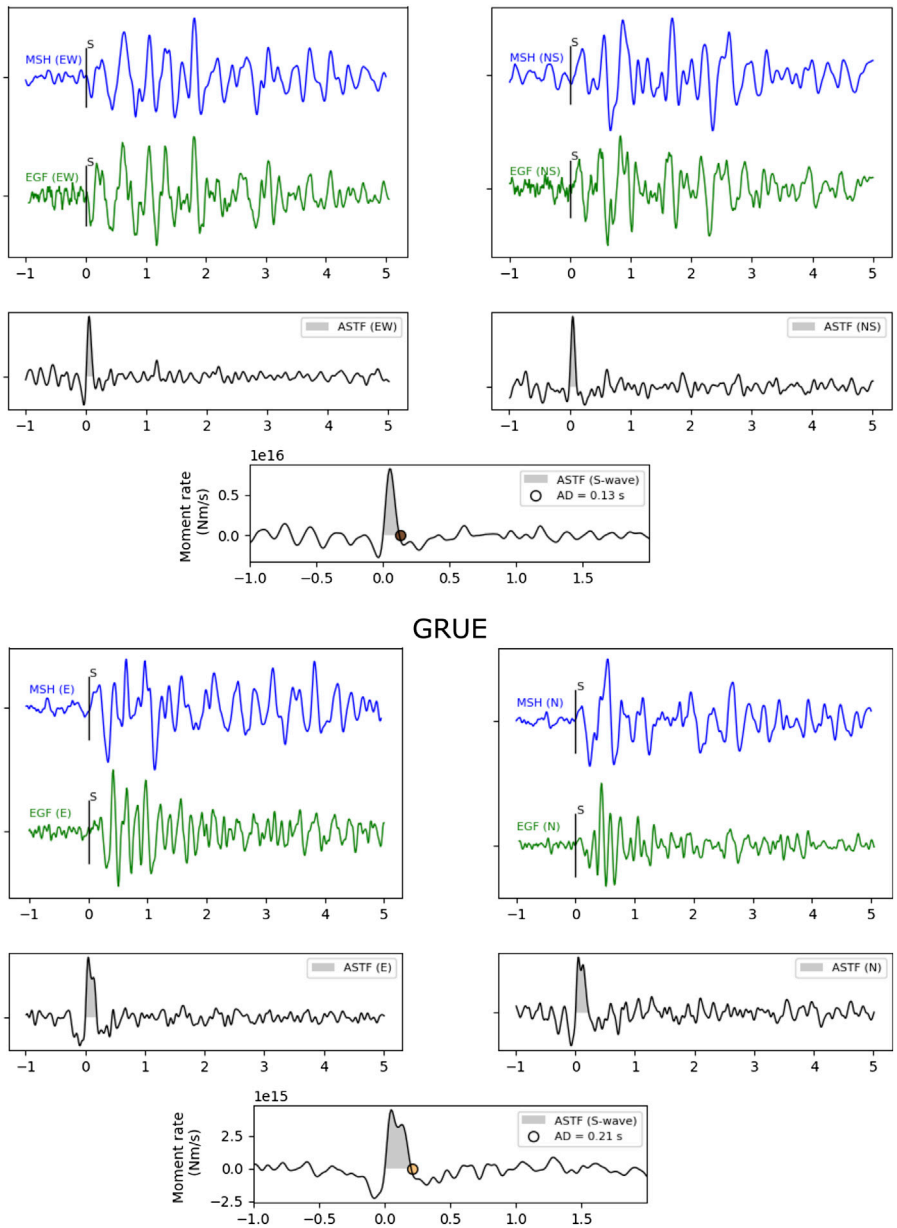

FIGURE 3 | Frequency-domain deconvolution results for the seismic stations TITE (top panel) and GRUE (bottom panel) using S-wave windows for the East (E) component **(left side)** and North (N) component **(right side)**. Each panel shows original seismograms from the mainshock (MSH, blue lines), the empirical Green's function (EGF, green lines); the calculated Apparent Source Time Function (ASTF), with a water level value of 0.01 (black lines). Final ASTF from stacking of the results from E and N components are shown in the lower center of each panel, indicating the apparent duration (AP, circles) and moment rate (grey area). S-phase is indicated by vertical bars in the original seismograms. Horizontal axis is in seconds.

of $M \geq M_{min}$), and *b* values were reported by different authors (Convertito et al., 2009; Iervolino et al., 2011). Then, two plausible values of tectonic stress rate of 6.1 and 2.3 kPa/yr are estimated for the VA region (**Table 3**). These results show a much higher level of background seismicity compared to other studied areas in Italy, such as the Po Plain Adriatic front in the region of Emilia earthquake (Dahm et al., 2015) and the Central Apennines graben system in the region of Aquila (Catalli et al., 2008), where values around 0.7 kPa/yr were calculated.

In a second step, the stress rate induced from the depletion of the oilfield is estimated. The cumulative annual production in the VA oilfield has reached an almost constant value since 2001. Before this date, it was relatively minor. Often, the pore pressure reduction, and thus the depletion of the reservoir layer, correlates more or less linearly with the production (Cesca et al., 2011b). The VA oilfield is more complex, as the reservoir is extremely thick and variable in vertical length, and the porosity and permeability are unusually small. Pore pressure and oil flow is

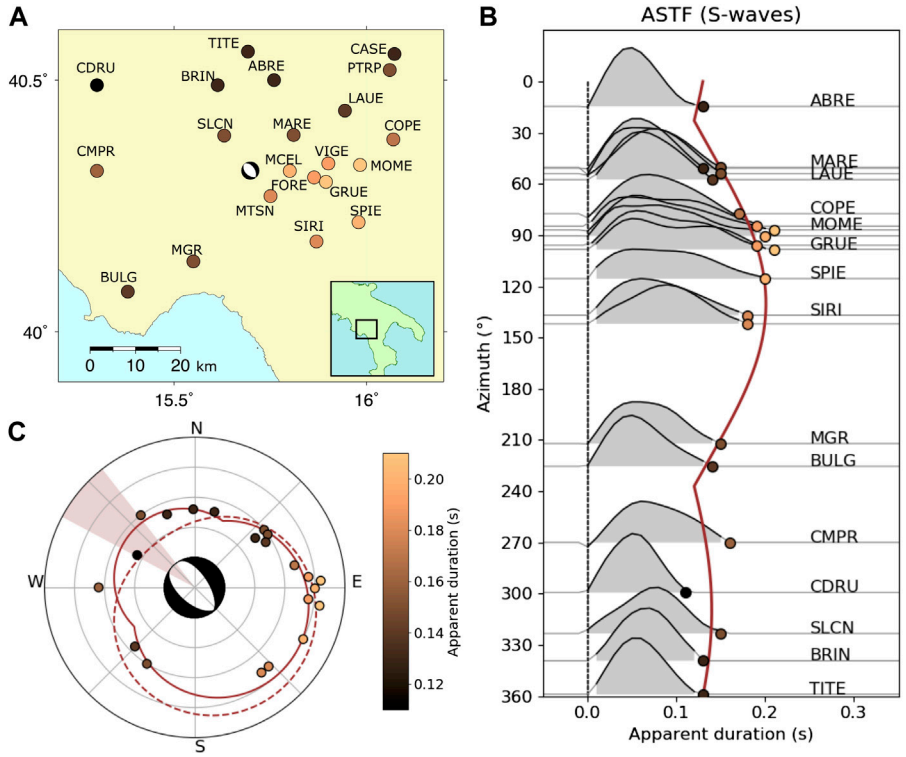

FIGURE 4 | Directivity analysis from the Apparent Source Time Functions (ASTFs) for the 2017 Mw 4 Montesano earthquake, Southern Italy. **(A)** Map of near-regional seismic stations used (circles) showing the apparent durations (color bar in c) and the moment tensor mechanism for the Montesano earthquake. **(B)** ASTFs are plotted according to station azimuth showing the apparent duration (circles) and moment rate (grey area) for each seismic station (see labels in traces) and the resulting asymmetric bilateral rupture model (solid line). **(C)** Apparent durations (circles) identified in **(B)** along with the synthetic predictions for the resulting asymmetric bilateral rupture model (solid line), represented in a polar plot; predicted rupture directivity and their uncertainties (brown area) are also shown together with the best solution from the moment tensor analysis. Dashed line indicates the solution applying a unilateral rupture model.

TABLE 2 | Inversion of apparent durations for the Mw 4 Montesano earthquake using a trust-region algorithm considering a pure unilateral rupture model and an asymmetric bilateral rupture model.

	Pure unilateral rupture	Asymmetric bilateral rupture
Directivity (°)	324 ± 18	310 ± 12
Bilateral percentage (%)	100	69 ± 8
Rupture length (km)	0.20 ± 0.06	0.29 ± 0.12
Rupture velocity (km/s)	3.01 ± 1.14	2.90 ± 2.33
Total rupture time (s)	0.16 ± 0.01	0.16 ± 0.03
L1 - misfit (s)	0.0209	0.0116

mainly controlled by localized individual fractures rather than a distributed pore space. The permeability can change with varying pore pressure in the fractures. In addition, structural compartments between the CF, ME, and MA are present. Possibly because of this complexity, the measured pore pressure reduction varies between different wells, and the correlation with cumulative production is not strictly linear. Direct measures of the bottom-hole pressure since the beginning of production (late 1990s) are protected by proprietary rights; nevertheless, Improta et al. (2017) stated that a cumulative depletion of about 3MPa involved the southern productive region of the VA oilfield until 2017. The variation of the pressure depletion can be large for thick reservoirs with structural compartments. For a conservative estimate, and to simplify the problem, we assume a pressure drop in the range between 4.5 and 18 MPa (5% and 95% percentiles) through a time span of 16 years over the whole field. The uncertainties of the tectonic stress were taken in the range $\dot{\tau}^T$ = [0.2 kPa/yr, 0.6 kPa/yr]. The induced stress from field pressure depletion is estimated using the nucleus of the strain approach, implemented in a 3D boundary element method (see Dahm et al., 2015). The outline of the field is adapted to the water–oil contact isoline, and the simplified model field was associated with a depth of 3 km, where a regular gridding of 2 km was used. Other parameters used for modeling were a reservoir thickness of 800 m, a Biot's constant of 0.1, and a Poisson ratio of 0.25. The strike, dip, and rake of our target source mechanism were taken from the best MT DC solution (**Table 1**). A friction coefficient of 0.6 was used to calculate Coulomb stress changes, which is at the lower range of typical sedimentary rocks under high confining stress (e.g., Byerlee, 1978). The Coulomb stress rate is calculated on a grid between 4 and 17 km depth with 1 km spacing. **Figure 5A** shows the simulated stress rate induced by depletion for a target fault 14

TABLE 3 | Source parameters and resulting tectonic stress rate for the VA region considering two different parameter sets taken from different references.

Study region	Source zone	A (km^2)	D (km)	M_{min}	M_{max}	N ($M \geq M_{min}$/year)	*a*	*b*	$\dot{\tau}^T$(Pa/year)
Val d'Agri	ZS9 (927)[a]	8354[a]	10[a]	4.3[b] 4.0[c]	7.3[b] 7.06[c]	0.362[b] 0.69[c]	1.95 2.72	0.557[b] 0.72[c]	6,125.9 2,338.9

[a]*Meletti et al. (2008);*
[b]*Iervolino et al. (2011);*
[c]*Convertito et al. (2009).*
a-values are calculated by a = *log*(N)+bM_{min}.

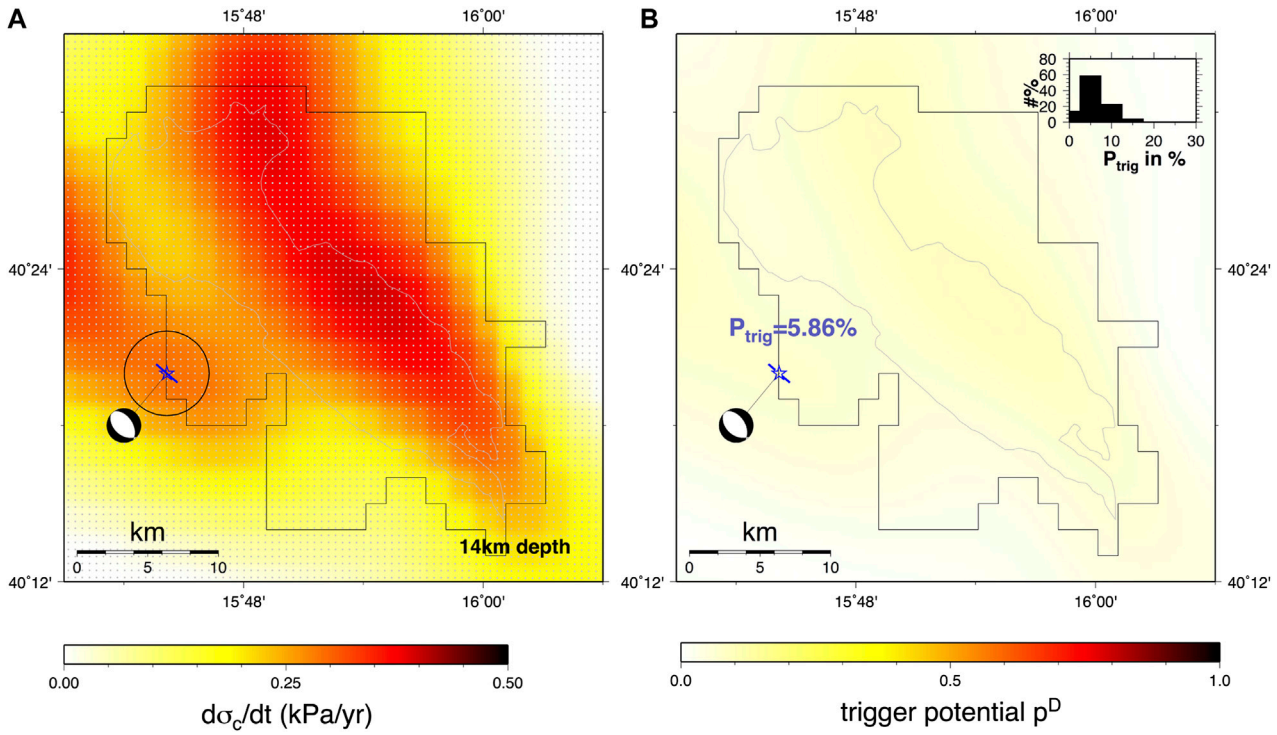

FIGURE 5 | (A) Coulomb stress rate model and **(B)** trigger potential at a depth of 14 km from the depletion of the Val d'Agri oilfield. Centroid location (star), best double couple moment tensor and preferred plane dipping to SW identified from the directivity analysis (blue line) are shown. Epicenter location uncertainties following Garcia-Aristizabal et al. (2020) (black open circle) are shown in **(A)**. Val d'Agri concession and the outline of the water oil contact are indicated with black and grey lines, respectively.

km depth. At this depth, the largest stress changes induced by the field depletion are expected below the center of the field. The Montesano earthquake is located just at the border of the high stress rate. If the target depth is smaller and closer to the field, the Coulomb stress change increases and the pattern becomes more complex. In any case, the estimated stressing at the hypocenter of the Montesano is in the range of only $\dot{\tau}^D \sim$ 0.25 kPa/yr.

The trigger potential (p^D) for an earthquake at a given location, that is, the probability that the rupture nucleation was triggered by field depletion, is described by (see Dahm et al., 2015, Eq. 4):

$$p^D = \frac{H(\dot{\tau}^D)\dot{\tau}^D}{H(\dot{\tau}^D)\dot{\tau}^D + \dot{\tau}^T}. \quad (2)$$

H is the Heaviside function. Values for p^D can vary in the range [0,1] with 0 meaning pure tectonic trigger potential and one meaning pure induced trigger potential. The estimated trigger potential for the target event, calculated at a depth of 14 km, is shown in **Figure 5B**, where we follow the procedure described in Dahm et al. (2015). The pattern shows a smooth field, with diffuse small potential below 0.2. The probability that the Montesano earthquake was triggered by the depletion of the VA oilfield is most likely only ~6%, where the uncertainties of the tectonic stressing, pore pressure depletion, and earthquake location have been bootstrapped. If the auxiliary plane is assumed to have ruptured, the trigger probability is similar. Note a slight increase in the trigger probability is observed if we consider a shallower earthquake in the same epicentral location of our target event; still, low probabilities are reached, for instance, values around 15% at a depth of 4 km (**Supplementary Figure S6**).

DISCUSSION AND CONCLUSION

Standard procedures of location and magnitude calculation are carried out automatically by different seismological institutions, at the local or national scale as well as the global scale, including also moment tensor inversion for the largest events (e.g., M_w > 4.0). Rupture processes for smaller events are typically neglected and a point source approximation is assumed. However, designed near-regional and local seismic networks, providing important datasets of microseismicity and weak earthquakes, can also reveal important information about the earthquake rupture. The dense network of permanent and temporal seismic stations in the VA region provides us a great opportunity to decipher the genesis of weak events, such as the 2017, M_w 4 Montesano earthquake located outside the outer border of the DE. Other than the natural seismicity that is expected in this area, induced seismicity has also been well reported, which was previously associated with variations in the water level of the Lake Pertusillo and derived from wastewater reinjection operations in the disposal well CM2. Moment tensor solutions from natural and induced earthquakes do not reveal significant differences to discriminate the source origin. Typically, the main pattern of normal faulting and some strike-slip focal mechanisms are identified (**Figure 1A**), which are associated with the main tectonic regime of NE–SW extension accommodated in the MMFS and EAFS fault systems. Therefore, further seismological and modeling analyses must be conducted to discriminate the rupture plane and assess cases of natural, triggered, or induced seismicity.

Generally, an accurate relocation of aftershocks showing some alignments helps to identify the fault plane activated by the mainshock. However, we cannot proceed with this analysis for the Montesano earthquake because only one aftershock was observed. Despite this, rupture directivity has been inferred for the mainshock using this single aftershock as the EGF. Apparent durations, ranging from 0.11 to 0.21 s, have been obtained from S-waves and define an azimuthal pattern, which reveals an asymmetric bilateral rupture with 70% of the rupture propagation in the NW direction and a fault length of ~0.3 km. The rupture directivity of N310°W is well constrained with small uncertainties and matches the N311°W strike of the fault plane identified in the best double couple of the moment tensor solution, suggesting the rupture plane dipping to the SW. A possible continuation of the EAFS NE–SW dipping normal faults below the allochthone down to the Apulia Platform is still debated (Maschio et al., 2005; Buttinelli et al., 2016 and references therein). Nevertheless, our results could exclude an activation of the MMFS dipping to the NE, and reveal the EAFS as the plausible structure hosting the Montesano earthquake. Further support comes from the observation that the hypocentral location of the target event at ~14 km depth is consistent with the activation of a deep fault segment associated with the EAFS, which would extend to the basement as reported in previous geological profiles (Menardi Noguera and Rea, 2000; Candela et al., 2015; **Figure 1C**).

Although hydrocarbon extraction is performed at a shallower layer around 1.8–3.5 km depth, stress perturbation and pore pressure changes may induce or trigger deeper events on preexisting faults previously identified in our seismological analysis. In fact, potential destructive events with an M_w larger than 6.5 that occurred in the past (Burrato and Valensise, 2008) could be reactivated by anthropogenic activities, increasing the seismic hazard of the VA region. We have calculated the Coulomb stress rate induced by the depletion of the oilfield to quantify the trigger potential estimated for the Montesano earthquake; our results yield relatively low probabilities below 10%. Note that our analysis does not include the role of the fluids in the reservoir and the surrounding rocks due to the reinjection of water in CM2, which would require specific modeling beyond the scope of the present paper; in particular, hydraulic connections with the VA oilfield should be considered. For instance, some extreme cases in Oklahoma reported triggering mechanisms for earthquakes in the far-field at distances larger than 40 km attributable to fluid disposal wells (Goebel et al., 2017); however, a larger number of injection wells, as well as larger injection volumes, and shallower earthquakes were involved in comparison with our study area. Therefore, we conclude that it is highly unlikely that our target event had originated from the depletion-induced stress rate of the VA oilfield and, rather, a natural cause controlled by the tectonic stress on preexisting faults can be assumed.

On the other hand, we can also apply other qualitative discrimination approaches based on a series of YES–NO questions (Davis and Frohlich, 1993; Davis et al., 1995; Frohlich et al., 2016), which remain used today and have been recently improved (Verdon et al., 2019). A new framework has been proposed including numerical scores to each question considering also some uncertainties, where positive and negative points are assigned depending on whether the answers indicate an induced or a natural cause. Following this scheme (Verdon et al., 2019), we obtain an induced assessment ratio (IAR) of +1.8%, which quantifies whether the overall assessment indicates a natural (−100%) or an induced cause (+100%), considering an evidence strength ratio (ESR) of 98.2% (ranging between 0 and 100%) describing quality and quantity of information used in the assessment (**Supplementary Figure S7 and S8**). Our seismological analysis allows for reaching a high ESR and evidences a very low IAR score; this suggests that we are unlikely to discriminate whether the Montesano earthquake was originated by an induced or a natural cause. In such a case, the probabilistic discrimination approach described in the present study has more relevance and brings us closer to a better understanding of the genesis of such seismic sources.

In conclusion, we describe a detailed seismological procedure to discriminate between induced, triggered, and natural earthquakes in the VA oilfield, which should be applied together with the previous TLS protocol proposed by the ILG. The relatively large magnitude (M_w 4) of the Montesano earthquake and its location close to the external margin of the DE should require the automatic implementation of such an advanced seismological analysis in order to clarify and identify the activation of preexisting or unknown faults. Our results conclude that the Montesano

earthquake activated a deeper fault segment associated with the EAFS close to the basement. The relative low trigger potential based on depletion-induced stress changes discards an induced or triggered event due to the long-term hydrocarbon extraction in the VA oilfield, and it rather suggests a natural cause due to the local tectonic stress.

DATA AVAILABILITY STATEMENT

The raw data supporting the conclusion of this article will be made available by the authors, without undue reservation.

AUTHOR CONTRIBUTIONS

JL-C has realized the rupture directivity analysis. TB and SD compiled the data, and framed the geological and monitoring context. TD has realized the probabilistic discrimination analysis. SC has realized the moment tensor analysis. JL-C prepared the initial draft, with contributions and editing from all authors. All authors have contributed to the interpretation and discussion.

FUNDING

This research has been funded by the European Union's Horizon 2020 research and innovation programme under the Marie Skłodowska-Curie grant agreement No 754446 and UGR Research and Knowledge Transfer Found—Athenea3i, and by the Deutsche Forschungsgemeinschaft (DFG, German Research Foundation)—Projektnummer (407141557). In the framework of ILGs experimentation, this work is co-funded by the Progetto di Monitoraggio Val d'Agri (INGV).

ACKNOWLEDGMENTS

For this study, we use seismic data from stations operated by the INGV and ENI.

SUPPLEMENTARY MATERIAL

The Supplementary Material for this article can be found online at: https://www.frontiersin.org/articles/10.3389/feart.2020.617794/full#supplementary-material.

REFERENCES

Abercrombie, R. E., Poli, P., and Bannister, S. (2017). Earthquake directivity, orientation, and stress drop within the subducting plate at the Hikurangi margin, New Zealand. *J. Geophys. Res. Solid Earth* 122 (10), 188. doi:10.1002/2017JB014935

Barchi, M., Amato, A., Cippitelli, G., Merlini, S., and Montone, P. (2006). "*Extensional tectonics and seismicity in the axial zone of the Southern Apennines*," in *CROP-04*. A. Mazzotti, E. Patacca, and P. Scandone (New York: Boll. Soc. Geol. It.Spec. Issue), 47–56.

Bassin, C., Laske, G., and Masters, G. (2000). The current limits of resolution for surface wave tomography in north America. *EOS Trans. AGU* 81, F897.

Benedetti, L., Tapponier, P., King, G. C. P., and Piccardi, L. (1998). Surface rupture due to the 1857 southern Italian earthquake. *Terra. Nova* 10 (4), 206–210.

Bertello, F., Fantoni, R., Franciosi, R., Gatti, V., Ghielmi, M., and Pugliese, A. (2011). "*From thrust-and-fold belt to foreland: hydrocarbon occurrences in Italy*", in Petroleum Geology Conference series 2010, 113–126. doi:10.1144/0070113

Bommer, J. J., Oates, S., Cepeda, J. M., Lindholm, C., Bird, J., Torres, R., et al. (2006). Control of hazard due to seismicity induced by a hot fractured rock geothermal project. *Eng. Geol.* 83 (4), 287–306. doi:10.1016/j.enggeo.2005.11.002

Bosman, K., Baig, A., Viegas, G., and Urbancic, T. (2016). Towards an improved understanding of induced seismicity associated with hydraulic fracturing. *First Break* 34, 61–66. doi:10.1038/s41598-018-26970-9

Braun, T., Cesca, S., Kühn, D., Martirosian-Janssen, A., and Dahm, T. (2018). Anthropogenic seismicity in Italy and its relation to tectonics: state of the art and perspectives. *Anthropocene* 21, 80–94. doi:10.1016/j.ancene.2018.02.001

Braun, T., Danesi, S., and Morelli, A. (2020). Application of monitoring guidelines to induced seismicity in Italy. *J. Seismol.* 9, 1–91. doi:10.1007/s10950-019-09901-7

Burrato, P., and Valensise, G. (2008). Rise and fall of a hypothesized seismic gap: source complexity in the Mw 7.0 16 december 1857 southern Italy earthquake. *Bull. Seism. Soc. Am.* 98 (1), 139–148. doi:10.1785/0120070094

Butler, R. W. H., Mazzoli, S., Corrado, S., De Donatis, M., Di Bucci, D., Gambini, R., et al. (2004). "*Applying thick-skinned tectonic.model to the Apennine thrust-belt of Italy: limitations and implications*," in *Thrust tectonic and hydrocarbon system: American association of petroleum geologists memoir*. Editor K. R. McClay, 647–667.

Buttinelli, M., Improta, L., Bagh, S., and Chiarabba, C. (2016). Inversion of inherited thrusts by wastewater injection induced seismicity at the Val d'Agri oilfield (Italy). *Sci. Rep.* 6, 37165. doi:10.1038/srep37165

Byerlee (1978). Friction of rocks. *Pure Appl. Geophys.* 116, 615–626.

Candela, S., Mazzoli, S., Megna, A., and Santini, S. (2015). Finite element modelling of stress field perturbations and interseismic crustal deformation in the Val d'Agri region, southern Apennines, Italy. *Tectonophysics* 657, 245–259. doi:10.1016/j.tecto.2015.07.011

Catalli, F., Cocco, M., Console, R., and Chiaraluce, L. (2008). Modeling seismicity rate changes during the 1997 Umbria-Marche sequence (central Italy) through rate- and state-dependent model. *J. Geophys. Res.* 113, B11301. doi:10.1029/2007JB005356

Cello, G., and Mazzoli, S. (1999). Apennine tectonics in southern Italy: a review. *J. Geodyn.* 27, 191–211.

Cello, G., Tondi, E., Micarelli, L., and Mattioni, L. (2003). Active tectonics and earthquake sources in the epicentral area of the 1857 Basilicata earthquake (Southern Italy). *J. Geodyn.* 36, 37–50. doi:10.1016/S0264-3707(03)00037-1

Cesca, S., Dahm, T., Juretzek, K., and Kühn, D. (2011b). Rupture process of the 7 may 2011, Mw 4.2, ekofisk induced earthquake. *Geophys. J. Int.* 187, 407–413. doi:10.1111/j.1365-246X.2011.05151.x

Cesca, S., Heimann, S., and Dahm, T. (2011a). Rapid directivity detection by azimuthal amplitude spectra inversion. *J. Seismol.* 15, 147–164. doi:10.1007/s10950-010-9217

Convertito, V., Iervolino, I., and Herrero, A. (2009). *Design earthquakes' map: an additional tool for engineering seismic risk analysis. Application to southern Apennines (Italy). XIII Convegno Anidis . June 28–July 2. Bologna, I.*

Cucci, L., Pondrelli, S., Frepoli, A., Mariucci, M. T., and Moro, M. (2004). Local pattern of stress field and seismogenic sources in Melandro Pergola basin and in Agri valley (Southern Italy). *Geophys. J. Int.* 156, 575–583.

Dahm, T., Cesca, S., Hainzl, S., Braun, T., and Krüger, F. (2015). Discrimination between induced, triggered, and natural earthquakes close to hydrocarbon reservoirs: a probabilistic approach based on the modeling of depletion-induced stress changes and seismological source parameters. *J. Geophys. Res.* 120 (4), 2491–2509. doi:10.1002/2014JB011778

Davis, S. D., and Frohlich, C. (1993). Did (or will) fluid injection cause earthquakes?. *Criteria for a rational assessment, Seismol. Res. Lett.* 64, 207–224.

Davis, S. D., Nyffenegger, P. A., and Frohlich, C. (1995). The 9 April 1993 earthquake in south-central Texas: was it induced by fluid withdrawal?. *Bull. Seismol. Soc. Am.* 85, 285.

Dialuce, G., Chiarabba, C., Di Bucci, D., Doglioni, C., Gasparini, P., Lanari, R., et al. (2014). Guidelines for monitoring seismicity, ground deformation and pore pressure in subsurface industrial activities. available at https://unmig.mise.gov.it/images/docs/151_238.pdf . Accessed Oct 2020.

Doglioni, C., Harabaglia, P., Merlini, S., Mongelli, F., Peccerillo, A., and Piromallo, C. (1999). Orogens and slabs vs. their direction of subduction. *Earth Sci. Rev.* 45, 167–208.

D'Argenio, B., Pescatore, T., and Scandone, P. (1975). Structural pattern of the campania-lucania Apennines, le scienze. *Front. Earth Sci.* 90, 313–327.

Eni Spa (2001). *International federation of digital seismograph networks*. doi:10.7914/SN/VA

Foulger, G. R., Wilson, M. P., Gluyas, J. G., Julian, B. R., and Davies, R. J. (2018). Global review of human-induced earthquakes. *Earth Sci. Rev.* 178, 438–514. doi:10.1016/j.earscirev.2017.07.008

Frohlich, C., DeShon, H., Stump, B., Hayward, C., Hornbach, M., and Walter, J. I. (2016). A historical review of induced earthquakes in Texas. *Seismol Res. Lett.* 87, 1022–1038. doi:10.1002/2017JB014460

Garcia-Aristizabal, A., Danesi, S., Braun, T., Anselmi, M., Zaccarelli, L., Famiani, D., et al. (2020). Epistemic uncertainties in local earthquake locations and implications for managing induced seismicity. *Bull. Seismol. Soc. Am.* 100, 202. doi:10.1785/0120200100

Goebel, T. H. W., Weingarten, M., Chen, X., Haffener, J., and Brodsky, E. E. (2017). The 2016 Mw5.1 Fairview, Oklahoma earthquakes: evidence for long-range poroelastic triggering at >40 km from fluid disposal wells. *Earth Planet Sci. Lett.* 472, 50–61. doi:10.1016/j.epsl.2017.05.011

Grigoli, F., Cesca, S., Rinaldi, A. P., Manconi, A., López-Comino, J. A., Clinton, J. F., et al. (2018). The November 2017 Mw 5.5 Pohang earthquake: a possible case of induced seismicity in South Korea. *Science* 360, 1003. doi:10.1126/science.aat2010

Grigoli, F., Cesca, S., Priolo, E., Rinaldi, A. P., Clinton, J. F., Stabile, T. A., et al. (2017). Current challenges in monitoring, discrimination, and management of induced seismicity related to underground industrial activities: a European perspective. *Rev. Geophys.* 55 (2), 310–340. doi:10.1002/2016RG000542

Guidoboni, E., Ferrari, G., Tarabusi, G., Sgattoni, G., Comastri, A., Mariotti, D., et al. (2019). CFTI5Med, the new release of the catalogue of strong earthquakes in Italy and in the Mediterranean area. *Sci. Data* 6, 80. doi:10.1038/s41597-019-0091-9

Guidoboni, E., and Ferrari, G. (1987). "The earthquake of December 16th 1857," in *Mallet's macroseismic survey on the Neapolitan earthquake of 16th December 1857*. Editors E. Guidoboni and G. Ferrari (Bologna (Italy): ING-SGA), 101–147.

Hainzl, S., Brietzke, G., and Zoeller, G. (2010). Quantitative earthquake forecasts resulting from static stress triggering. *J. Geophys. Res.* 115, B11311. doi:10.1029/2010JB007473

Hartzell, S. H. (1978). Earthquake aftershocks as Green's functions. *Geophys. Res. Lett.* 5, 1–4.

Haskell, N. A. (1964). Total energy and energy spectra density of elastic waves from propagating faults. *Bull. Seismol. Soc. Am.* 54, 1811–1841.

Healy, J., Rubey, W., Griggs, D., and Raleigh, C. (1968). The Denver earthquakes. *Science* 161, 1301–1310.doi:10.1126/science.161.3848.1301

Heimann, S., Isken, M., Kühn, D., Sudhaus, H., Steinberg, A., Vasyura-Bathke, H., et al. (2018). Grond - a probabilistic earthquake source inversion framework. Potsdam (Germany): *GFZ Data Services*. doi:10.5880/GFZ.2.1.2018.003

Iervolino, I., Chioccarelli, E., and Convertito, V. (2011). Engineering design earthquakes from multimodal hazard disaggregation. *Soil Dynam. Earthq. Eng.* 31 (9), 1212–1231. doi:10.1016/j.soildyn.2011.05.001

Improta, L., Bagh, S., De Gori, P., Valoroso, L., Pastori, M., Piccinini, D., et al. (2017). Reservoir structure and wastewater induced seismicity at the Val d'Agri oilfield (Italy) shown by three-dimensional Vp and Vp/Vs local earthquakes tomography. *J. Geophys. Res. Solid Earth*. 14, 725. doi:10.1002/2017JB014725

Improta, L., and Piccinini, D. (2015). *INGV report on the analysis of the val d'Agri natural and induced seismicity with reference to the area involved in the produced water reinjection (Costa Molina 2 well)*.

Improta, L., Valoroso, L., Piccinini, D., and Chiarabba, C. (2015). A detailed analysis of wastewater-induced seismicity in the Val d'Agri oilfield (Italy). *Geophys. Res. Lett.* 42, 2682–2690. doi:10.1002/2015GL063369

Keranen, K., Weingarten, M., Abers, G., Bekins, B. A., and Ge, S. 2014). Induced earthquakes. Sharp increase in central Oklahoma seismicity since 2008 induced by massive wastewater injection. *Science* 345, 448–451. http://www.sciencemag.org/content/345/6195/448.short. doi:10.1126/science.1255802

Kühn, D., Heimann, S., Isken, M., Ruigrok, E., and Dost, B. (2020). Probabilistic moment tensor inversion for hydrocarbon-induced seismicity in the Groningen gas field, The Netherlands, part 1: testing, *Bull. Seismol. Soc. Am.* 19, 185. doi:10.1785/0120200099

López-Comino, J. A., and Cesca, S. (2018). Source complexity of an injection induced event: the 2016 Mw 5.1 Fairview, Oklahoma earthquake. *Geophys. Res. Lett.* 45, 4025–4032. doi:10.1029/2018GL077631

López-Comino, J. A., Mancilla, F., Morales, J., and Stich, D. (2012). Rupture directivity of the 2011, Mw 5.2 lorca earthquake (Spain). *Geophys. Res. Lett.* 39, L03301. doi:10.1029/2011GL050498

López-Comino, J. A., Stich, D., Morales, J., and Ferreira, A. M. G. (2016). Resolution of rupture directivity in weak events: 1-D versus 2-D source parameterizations for the 2011, Mw 4.6 and 5.2 Lorca earthquakes, Spain. *J. Geophys. Res. Solid Earth* 121, 6608–6626. doi:10.1002/2016JB013227

Mallet, R. (1862). *Great Neapolitan earthquake of 1857—the principles of observational seismology*. London: Chapman & Hall.

Maschio, L., Ferranti, L., and Burrato, P. (2005). Active extension in Val d'Agri area, Southern Apennines, Italy: implications for the geometry of seismogenic belt. *Geophys. J. Int.* 162, 591–609. doi:10.1111/j.1365-246X.2005.02597.x

Mazzoli, S., Barkham, S., Cello, G., Gambini, R., Mattioni, L., Shiner, P., et al. (2001). Reconstruction of continental margin architecture deformed by the contraction of the Lagonegro Basin, Southern Italy. *J. Geol. Soc.* 158, 309–319. doi:10.1144/jgs.158.2.309

McGarr, A., and Simpson, D. (1997). "Keynote lecture: a broad look at induced and triggered seismicity," in *Rockbursts and seismicity in mines*. Editors S. J. Gibowitz and S. Lasocki (Rotterdam: Balkema), 948–970.

McGarr, A., Simpson, D., and Seeber, L. (2002). 40 Case histories of induced and triggered seismicity. *Int. Geophys.* 81A, 647–661. doi:10.1016/S0074-6142(02)80243-1

Meletti, C., Galadini, F., Valensise, G., Stucchi, M., Basili, R., Barba, S., et al. (2008). A seismic source zone model for the seismic hazard assessment of the Italian territory. *Tectonophysics* 450, 85–108. doi:10.1007/s12517-017-3325-1

Menardi Noguera, A., and Rea, G. (2000). Deep structure of the campanian-lucanian arc (southern apennine, Italy). *Tectonophysics* 324, 239–265. doi:10.1016/S0040-1951(00)00137-2

Raleigh, C., Healy, J., and Bredehoeft, J. (1976). An experiment in earthquake control at rangely, Colorado. *Science* 191, 1230–1237. doi:10.1126/science.191.4233.1230

Rovida, A., Locati, M., Camassi, R., Lolli, B., and Gasperini, P. (2019). *Italian parametric earthquake catalogue (CPTI15)*. Italy: (Istituto Nazionale di Geofisica e Vulcanologia (INGV)). doi:10.13127/CPTI/CPTI15.2

Rovida, A., Locati, M., Camassi, R., Lolli, B., and Gasperini, P. (2020). The Italian earthquake catalogue CPTI15. *Bull. Earthq. Eng.* 18 (7), 2953–2984. doi:10.1007/s10518-020-00818-y

Schorlemmer, D., Mele, F., and Marzocchi, W. (2010). A completeness analysis of the national seismic network of Italy. *J. Geophys. Res.* 115, B04308. doi:10.1029/2008JB006097

Scrocca, D., Carminati, E., and Doglioni, C. (2005). Deep structure of the southern Apennines, Italy: thin-skinned or thick-skinned?. *Tectonics 24*, doi:10.1029/2004TC001634, 2005

Shiner, P., Beccaccini, A., and Mazzoli, S. (2004). Thin-skinned versus thick-skinned structural models for Apulian carbonate reservoirs: constraints from the Val d'Agri Fields, *S. Apennines*, Italy. *Mar. Petrol. Geol.* 21, 805–827. doi:10.1016/j.jsg.2006.07.002

Stabile, T. A., Giocoli, A., Lapenna, V., Perrone, A., Piscitelli, S., and Telesca, L. (2014). Evidence of low-magnitude continued reservoir-induced seismicity associated with the Pertusillo artificial lake (southern Italy). *Bull. Seismol. Soc. Am.* 104, 1820–1828. doi:10.1785/0120130333

Stich, D., Martin, R., Morales, J., López-Comino, J. A., and Mancilla, F. (2020). Slip partitioning in the 2016 alboran sea earthquake sequence (western mediterranean). *Front. Earth Sci.* 8, 587356. doi:10.3389/feart.2020.587356

Valoroso, L., Improta, L., Chiaraluce, L., Stefano, R. D., Ferranti, L., Govoni, A., et al. (2009). Active faults and induced seismicity in the Val d'Agri area (Southern Apennines, Italy). *Geophys. J. Int.* 178, 488–502. doi:10.1111/j.1365-246x.2009.04166.x

Valoroso, L., Improta, L., De Gori, P., and Chiarabba, C. (2011). Upper crustal structure, seismicity and pore pressure varia0ons in an extensional seismic belt through 3-D and 4-D VP and VP/VS models: the example of the Val d'Agri area (southern Italy). *J. Geophys. Res.* 116, B07303. doi:10.1029/2010JB007661

Verdon, J. P., Baptie, B. J., and Bommer, J. J. (2019). An improved framework for discriminating seismicity induced by industrial activities from natural earthquakes. *Seismol Res. Lett.* 90 (4), 1592–1611. doi:10.1785/0220190030

Wavrek, D. A., and Mosca, F. (2004). "*Compositional grading in the oil column: advances from a mass balance and quantitative molecular analysis*", in *Understanding petroleum reservoirs: towards an integrated reservoir engineering and geochemical approach*. (London (UK): The Geological Society of London), 207–220.

Wu, Q., Chen, X., and Abercrombie, R. E. (2019). Source complexity of the 2015 Mw 4.0 Guthrie, Oklahoma earthquake. *Geophys. Res. Lett.* 46. doi:10.1029/2019GL082690

Conflict of Interest: The authors declare that the research was conducted in the absence of any commercial or financial relationships that could be construed as a potential conflict of interest.

frontiers in Earth Science

ORIGINAL RESEARCH
published: 22 March 2021
doi: 10.3389/feart.2021.642721

Centroid Moment Tensor of the 2019 M_W 5.7 Changning Earthquake Refined Using 3D Green's Functions Considering Surface Topography

Yuanhang Huo[1,2], *Wei Zhang*[2]* *and Jie Zhang*[1]

[1]School of Earth and Space Sciences, University of Science and Technology of China, Hefei, China, [2]Department of Earth and Space Sciences, Southern University of Science and Technology, Shenzhen, China

The M_W 5.7 Changning earthquake occurred in southern Sichuan basin on 17 June 2019 and was the largest event ever recorded in this region. There are still some arguments existing about the causes of the earthquake and its possible links with water injections. Many studies on this earthquake have been performed, but the event depths obtained among them are significantly different and the source mechanisms also exhibit variations. In this study, we design an inversion scheme and use 3D Green's functions considering the rugged topography of this region to determine the event location and moment tensor of the Changning earthquake based on waveform fittings. The 3D model can reduce the uncertainty due to the approximation of 1D model and better constrain the solutions. The latitude and the longitude of event location are 28.34°N and 104.82°E respectively and the depth is 3.14 km. The nodal plane solutions are strike 295°/dip 88°/rake 14° and strike 204°/dip 76°/rake 178°. The percentages of DC, CLVD and ISO components are 10, −83, and −7%, respectively. The good waveform fittings at 17 broadband stations indicate the reliability of the source mechanism in this study.

Keywords: changning earthquake, source mechanism, seismic location, 3D strain Green's tensors, topography

OPEN ACCESS

Edited by:
Nicola Alessandro Pino, Vesuvius Observatory, National Institute of Geophysics and Volcanology (INGV), Italy

Reviewed by:
Wenbo Wu, California Institute of Technology, United States
Xin Wang, California Institute of Technology, United States
Jiri Zahradnik, Charles University, Czechia

***Correspondence:**
Wei Zhang
zhangwei@sustech.edu.cn

Specialty section:
This article was submitted to Solid Earth Geophysics, a section of the journal Frontiers in Earth Science

Received: *16 December 2020*
Accepted: *04 February 2021*
Published: *22 March 2021*

Citation:
Huo Y, Zhang W and Zhang J (2021) Centroid Moment Tensor of the 2019 M_W 5.7 Changning Earthquake Refined Using 3D Green's Functions Considering Surface Topography. Front. Earth Sci. 9:642721. doi: 10.3389/feart.2021.642721

INTRODUCTION

Sichuan basin is a highly productive field of oil and shale gas in China, which exhibits rather stable geological settings with a very small tectonic shear strain rate of $(0.5–7) \times 10^{-9}$/yr (Gan et al., 2007; Ma, 2017; Wang and Shen, 2020). The historical seismicity is low in this region although there are two neighboring seismically active blocks to the southwest and northwest (Lei et al., 2020). However, the number of earthquakes occurring in Sichuan basin dramatically increases since 2015, including several moderate to large damaging events (Lei et al., 2017; Meng et al., 2019; Lei et al., 2020). The industrial activities, including the disposal of wastewater and the water injections for hydraulic fracturing and salt mining, are active in this region recent years. Possible links between the induced or triggered earthquakes and the fluid injections were discussed and debated in many studies (Ellsworth, 2013; Clarke et al., 2014; Goebel and Brodsky, 2018; Grigoli et al., 2018; Lei et al., 2019; Tan et al., 2020; Wang et al., 2020).

On June 17, 2019, a M_W 5.7 earthquake struck Changning in southern Sichuan basin of China, which is the largest destructive earthquake recorded there since 1,600 and caused a huge

economic loss and 13 deaths (Yi et al., 2019). After the mainshock of the Changning earthquake, a number of events with magnitudes up to 5.6 followed subsequently within very short period (Zhang et al., 2020). The hypocenter of the Changning earthquake is close to the salt mine with water injection well at the depth of 2.7–3 km, which belongs to Changning anticline fold system with no active faults existing (Lei et al., 2019; Jiang et al., 2020).

There have been many studies on the location and source mechanism of the Changning earthquake. Regional 1D layered velocity models are commonly employed to locate the hypocenter (Lei et al., 2019; Yi et al., 2019; Liu and Zahradník, 2020). Besides, the development of dense arrays makes it possible to obtain the three-dimensional (3D) model. Long et al. (2020) and Zuo et al. (2020) applied double-difference tomography method to invert the 3D velocity structure of Changning-Gongxian and Changning-Xingwen area respectively and relocated the Changning earthquake sequences. But for the determination of source mechanism for the Changning earthquake, previous results are still limited to the utilization of the 1D model. For instance, Yi et al. (2019) simulated the synthetic waveforms at 50 stations in the local 1D model and used the CAP method (Zhao and Helmberger, 1994; Zhu and Helmberger, 1996) to demonstrate that the earthquake is a thrust event with some strike components. Liu and Zahradník (2020) provided a new explanation in terms of the shallow doublet of two different subevents, initial thrust fault followed by a strike-slip, both estimated in 1D model of Zhao and Zhang (1987). In addition, the calculation of the rupture directivity for the Changning earthquake was also based on the 1D crustal velocity model (Li et al., 2020). The 3D model can improve the event location and reduce the error due to the simplicity of 1D model (Johnson and Vincent, 2002; Myers et al., 2015; Zhou et al., 2016). Zhu and Zhou (2016) and Wang and Zhan (2019) highlighted that the accuracy of source mechanism can be significantly improved when the appropriate 3D model is used.

In this study, we determine the centroid location and source mechanism of the Changning earthquake using 3D strain Green's tensors (SGTs) considering the rugged-topography model of this region. The SGTs are accurately synthetized by the curvilinear-grid finite-difference method (Zhang and Chen, 2006; Zhang et al., 2012) to avoid the simulation errors caused by the staircase approximation of the irregular surface. The horizontal centroid location is obtained by minimizing the traveltime misfits of P- and surface waves in the 3D grid volume, and the full moment tensors and event depth are determined similar to the CAP approach but using the 3D SGTs at this horizontal location.

INVERSION WORKFLOW

In this section, we will describe the inversion workflow of the Changning earthquake in 3D velocity model with rugged topography (**Figure 1**).

Raw Data Processing

The continuous waveform data of the Changning earthquake can be downloaded from the China Seismic Experimental Site (CSES) website[1] and we use 17 local broadband stations surrounding the epicenter to determine the source parameters in the study. These stations are distributed in Sichuan basin and four provinces of China with a good azimuth coverage and epicenter distances from 70 km to 370 km (**Figure 2**). After removing the mean, trend and instrumental responses, the displacement seismograms are cut to 400 s starting from the origin time, resampled with an interval of 0.04 s after lowpass filtering with corner frequency of 12.5 Hz, and then bandpass filtered to two period ranges (0.04–0.2 Hz and 0.03–0.1 Hz) respectively. The 2nd-order Butterworth filter with the same parameters is used for the seismograms and synthetic data.

3D SGTs Construction

3D Model and Topography

Compared with averaged 1D layered models, a 3D velocity model shows more advantages in the estimation of the source parameters to obtain the more reliable solution, especially the light to moderate earthquakes (Johnson and Vincent, 2002; Hejrani et al., 2017; Nayak and Dreger, 2018; Wang and Zhan, 2019). In this study, we use the 3D P- and S-wave velocity model of the crust and uppermost mantle in the southwest China (SWChinaCVM-1.0, doi: 10.12093/02md.02.2019.01.v1) to compute the synthetics. The 3D model is obtained by the joint body and surface wave traveltime tomography, which involves 390,000 P-wave and 370,000 S-wave first-arrival traveltimes from more than 230 permanent stations and 8,100 dispersion curves of surface-wave phase velocity (5–50 s) extracted from the ambient noise data (Fang et al., 2016; Liu et al., 2020). The horizontal resolution of the model is about 50 km and the depth ranges from the surface to 70 km with an interval of 5 km. We extend the 3D model to 100 km in depth using the velocity at the depth of 70 km. **Figures 3**, **4** show the map view and two profiles of the P-wave velocity and S-wave velocity across the event location in the study area.

The Changning earthquake occurs in the south of Sichuan basin and the east of the Tibetan plateau. The elevation in the study area rises from about 200 m in the south of Sichuan basin to over 4,000 m of Longmenshan Mountain within a very short distance (**Figure 2**). In order to accurately calculate the SGTs database, we should consider and handle the effect of the topography on the results. We utilize the topography data with a spatial resolution of approximately 90 m from CGIAR-CSI SRTM website[2] and perform the down sampling of 500 m as the preparation of the next step.

Numerical Simulation by Curvilinear-Grid Finite-Difference

The traditional finite-difference methods commonly apply the strategy of grid refinement to fit the surface shape as much as possible, but it cannot avoid the artifacts due to the staircase approximation. We use the curvilinear-grid finite-difference approach with the Traction

[1]http://124.17.4.85/wp-content/uploads/2019/06/wave_6.1.rar
[2]https://srtm.csi.cgiar.org/srtmdata/

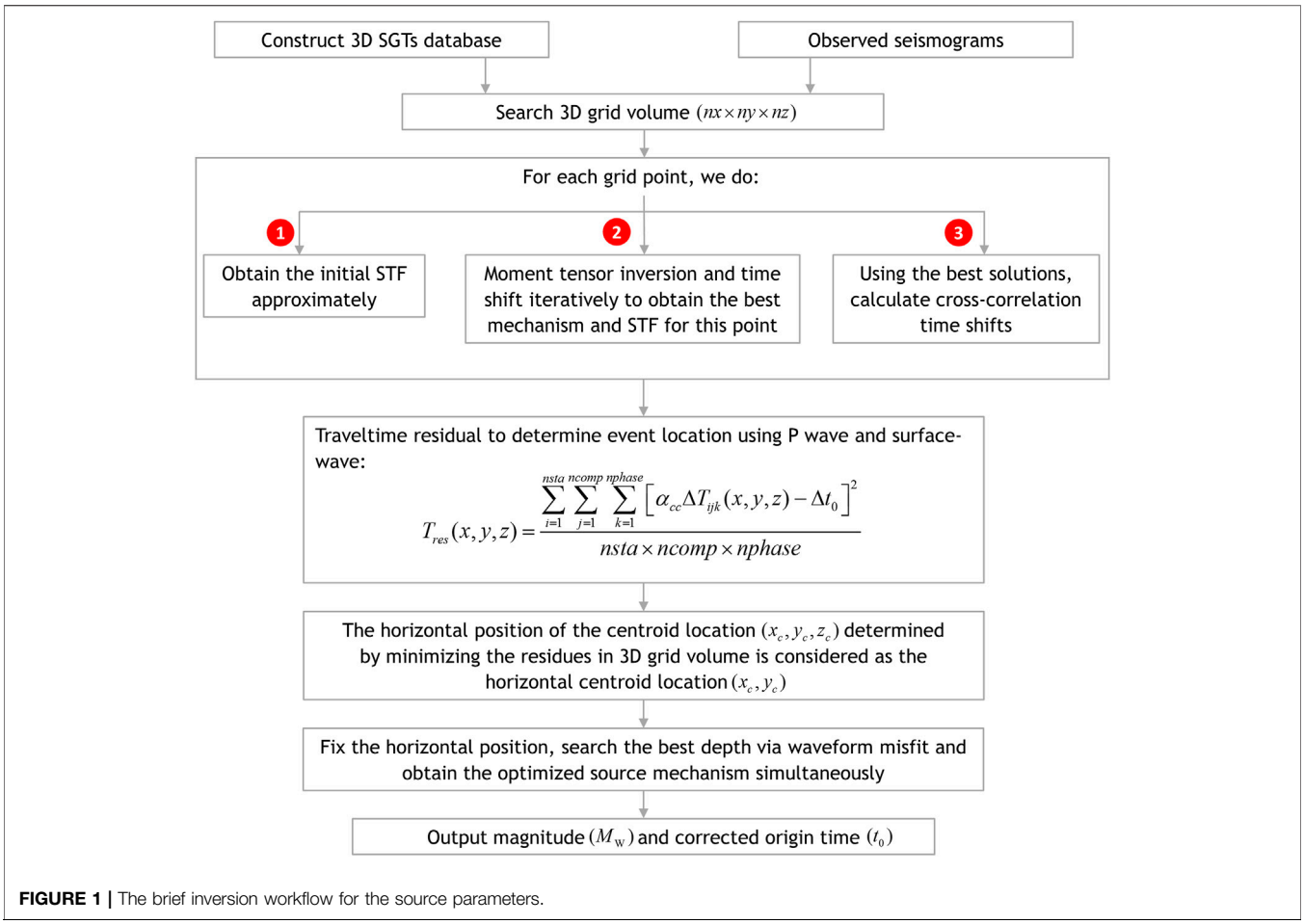

FIGURE 1 | The brief inversion workflow for the source parameters.

Image free surface boundary implementation (Zhang and Chen, 2006; Zhang et al., 2012) to construct the SGTs database in the 3D model with the rugged topography of this region. **Figure 5** shows the partial curvilinear grids along one vertical profile (XOZ) as marked with dashed line in **Figure 2**.

Generally, the number of forward modeling is proportional to the total number of potential source points, which seems not feasible for the large 3D grid volume. Fortunately, we can adopt the reciprocity theorem and calculate the SGTs from each station to all source points instead of computing the Green's functions source by source (Eisner and Clayton, 2001; Zhao et al., 2006). In this way, the number of the simulations is reduced to the three times of the total number of stations when the three-component data are needed, which dramatically saves the computational costs. Using the SGTs, the calculated displacements at the station $\mathbf{x_r}$ from the source $\mathbf{x_s}$ can be represented as (the Einstein summation convention is used):

$$\begin{aligned} u_n(\mathbf{x_r}, t; \mathbf{x_s}) &= \frac{1}{2}\left[G_{in,j}(\mathbf{x_s}, t; \mathbf{x_r}) + G_{jn,i}(\mathbf{x_s}, t; \mathbf{x_r})\right] M_{ij} * S_b(t) \\ &= E^n_{ij}(\mathbf{x_s}, t; \mathbf{x_r}) M_{ij} * S_b(t) \end{aligned} \quad (1)$$

where $E^n_{ij}(\mathbf{x_s}, t; \mathbf{x_r})$ is the SGT at location $\mathbf{x_s}$ when the n-direction force acts at location $\mathbf{x_r}$, t is time, $S_b(t)$ is the bell function as the source time function (STF) and M_{ij} denotes the moment tensor component with $i, j = 1, 2, 3$ (Zhao et al., 2006). Advantage of the direct finite-difference calculation is that the SGTs used in this study can be easily obtained in our codes and we can avoid the numerical differentiation of Green's tensor presented on the first line of **Eq. 1**.

The geographical coordinates are projected to the Cartesian coordinates with the reference origin point (25.0°N, 102.5°E). The computational model size in the study area is 480 km × 550 km × 100 km with a horizontal grid spacing of 500 m. We employ the complex-frequency-shifted perfectly matched layer based on auxiliary differential equations (ADE CFS-PML) technique and configure 12 layers as the non-reflecting boundaries in the forwarding modeling (Zhang and Shen, 2010). For accurately simulating the surface wave in the presence of the rugged topography, we set the vertical grid spacing to 200 m. Thus, the number of grid points for three dimensions becomes 960 × 1,100 × 500. The simulated maximum frequency reaches 0.5 Hz and the sampling interval is set to 0.02 s derived from the minimum grid spacing and the maximum velocity. The recording time length is 400 s along with a total number of time steps of 20,000. The calculation of SGTs for 17 stations totally costs about 160 thousand CPU hours. We save the SGTs of a 3D grid volume (200 × 200 × 140) in the neighborhood of the

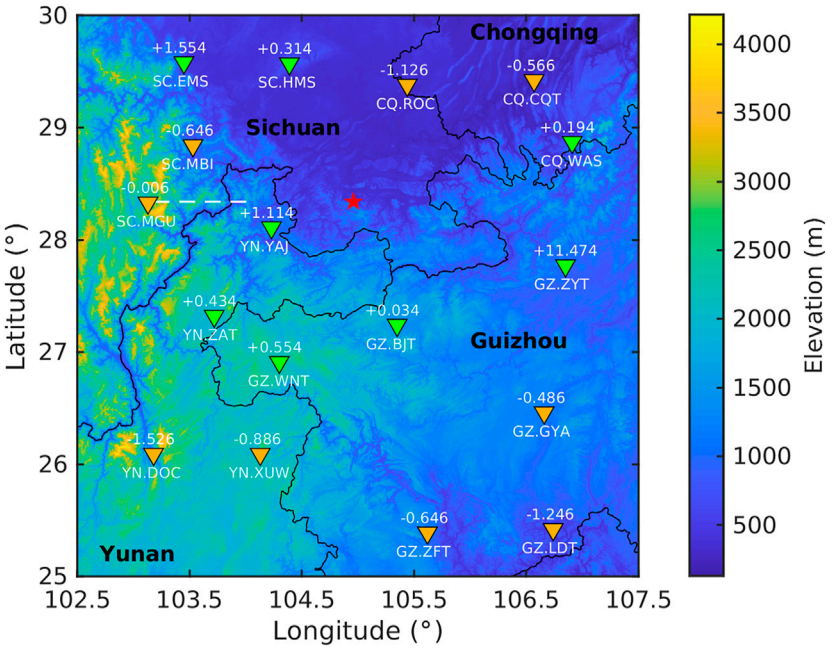

FIGURE 2 | The topography in the study along with the centroid location of the Changning earthquake (red star) and 17 broadband stations (triangles) in the four provinces (black texts) of China. The white numbers above the triangles are the z-component time shifts of surface wave at stations (positive in green and negative in yellow) in **Figure 10**. The white texts below the triangles denote the names of seismic network and stations and the white dashed line marks the location of grid profile in **Figure 5**.

epicenter from CENC with a mesh of 500 m × 500 m × 200 m and an interval of 0.04 s, resulting about 95 TB of total storage for the 17 broadband stations. We use the cubic-spline interpolation approach to retrieve the SGTs at the finer grids (200 m × 200 m × 10 m) near the event to improve the resolution of location and depth.

Source Mechanism Estimation in Each Trial Point

In this step, we optimize the source mechanism in each trial source point of 3D grid volume in terms of the initial solutions from Global CMT. With the representation of the synthetics using **Eq. 1**, the moment tensors can be linearly inversed by solving the normal equation:

$$(\mathbf{G}^T\mathbf{G})\mathbf{m} = \mathbf{G}^T\mathbf{d} \tag{2}$$

and $\mathbf{G}$ and $\mathbf{d}$ are represented as:

$$\mathbf{G} = \begin{bmatrix} \alpha_p \alpha_d^i \mathbf{E}_p^{ij} \\ \sqrt{\alpha_d^i}\mathbf{E}_{surf}^{ij} \end{bmatrix} \tag{3}$$

$$\mathbf{d} = \begin{bmatrix} \alpha_p \alpha_d^i \mathbf{d}_p^{ij} \\ \sqrt{\alpha_d^i}\mathbf{d}_{surf}^{ij} \end{bmatrix} \tag{4}$$

where $\mathbf{m}$ denotes the model parameters including six independent moment tensor components, $\mathbf{d}_p^{ij}$ and $\mathbf{d}_{surf}^{ij}$ are the P- and surface-wave observed displacement data of the jth component at the ith station after alignment by waveform cross-correlation with the synthetics, $\mathbf{E}_p^{ij}$ and $\mathbf{E}_{surf}^{ij}$ are the P- and surface-wave SGTs with the same definitions of subscripts, α_p is the scale factor of P wave relative to surface wave and α_d^i represents the weighting to consider the geometrical spreading effects of the ith station. In this study, α_p is set as 1.5 and the frequency bands we use for P wave and surface wave are 0.04–0.2 Hz and 0.03–0.1 Hz, respectively.

The frequency bands in the inversion are relatively low, so we can use a simple function to approximate the complex real STF and ignore the high-frequency variations. We choose the bell function as the form of the STF (moment-rate function). The source duration T_{dur} can be derived from an empirical relationship (Ekström and Engdahl, 1989; Ekström et al., 2012):

$$T_{dur} = 2.1 \times 10^{-8} M_0^{1/3} \tag{5}$$

where M_0 is the scalar moment measured in dyne-cm. And M_0 is calculated by:

$$M_0 = \sqrt{\sum_{ij} M_{ij}^2} \Big/ \sqrt{2} \tag{6}$$

Specifically, the optimal moment tensors and STF in each trial source point are determined by the following procedures. We first use the source mechanism from Global CMT as the initial approximated solution to calculate the synthetics. Then we cross-correlate the observed and the synthetic waveforms to obtain the time shifts for each component of P- and surface waves. After aligning the SGTs with the corresponding time

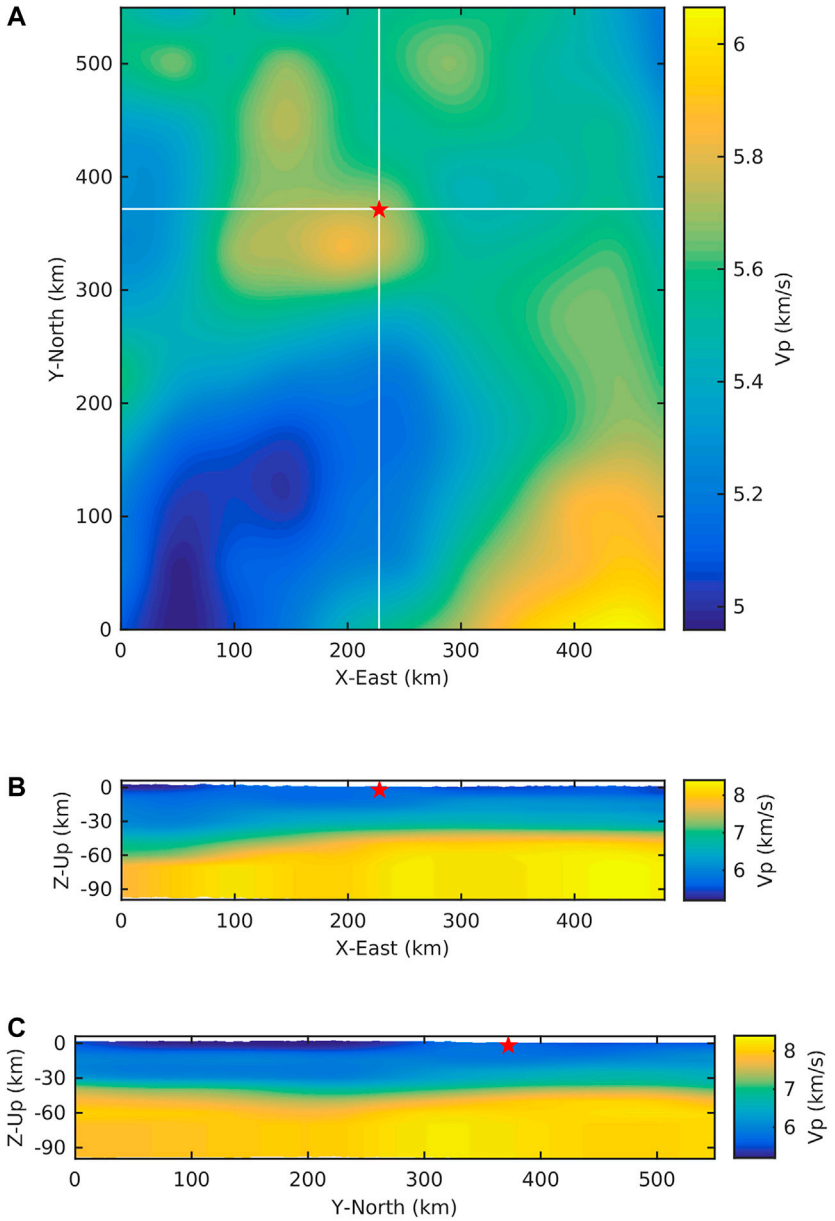

FIGURE 3 | The map view and two profiles of the 3D P-wave velocity model across the event location (red star). The horizontal and vertical white lines in map view **(A)** show the location of XOZ profile **(B)** and YOZ profile **(C)** respectively.

shifts, we can solve the **Eq. 2** to determine the moment tensors. Subsequently, the calculated moment tensors are considered as the new initial source mechanism to the next inversion. The inversion procedures can be carried out repeatedly until both of moment tensors and STF become stable for each trial point.

Horizontal Position Locating

For each trial source point in 3D grid volume, we obtain the optimal source mechanism and STF at this point that can best fit the observed seismograms in *Source Mechanism Estimation in Each Trial Point*. Then, the time shifts of the P wave and surface wave are derived by cross-correlating the observation and the synthetics for all stations. The traveltime residual T_{res} in each trial source point (x, y, z) is defined as:

$$T_{res}(x,y,z) = \frac{\sum_{i=1}^{nsta}\sum_{j=1}^{ncomp}\sum_{k=1}^{nphase}\left[\alpha_{cc}\Delta T_{ijk}(x,y,z) - \Delta t_0(x,y,z)\right]^2}{nsta \times ncomp \times nphase} \tag{7}$$

where ΔT_{ijk} represents the time shift of the kth phase for jth component at the ith station, α_{cc} is the cross-correlation coefficient between the aligned observation and the synthetics, *nsta*, *ncomp*, *nphase* are the total number of the stations,

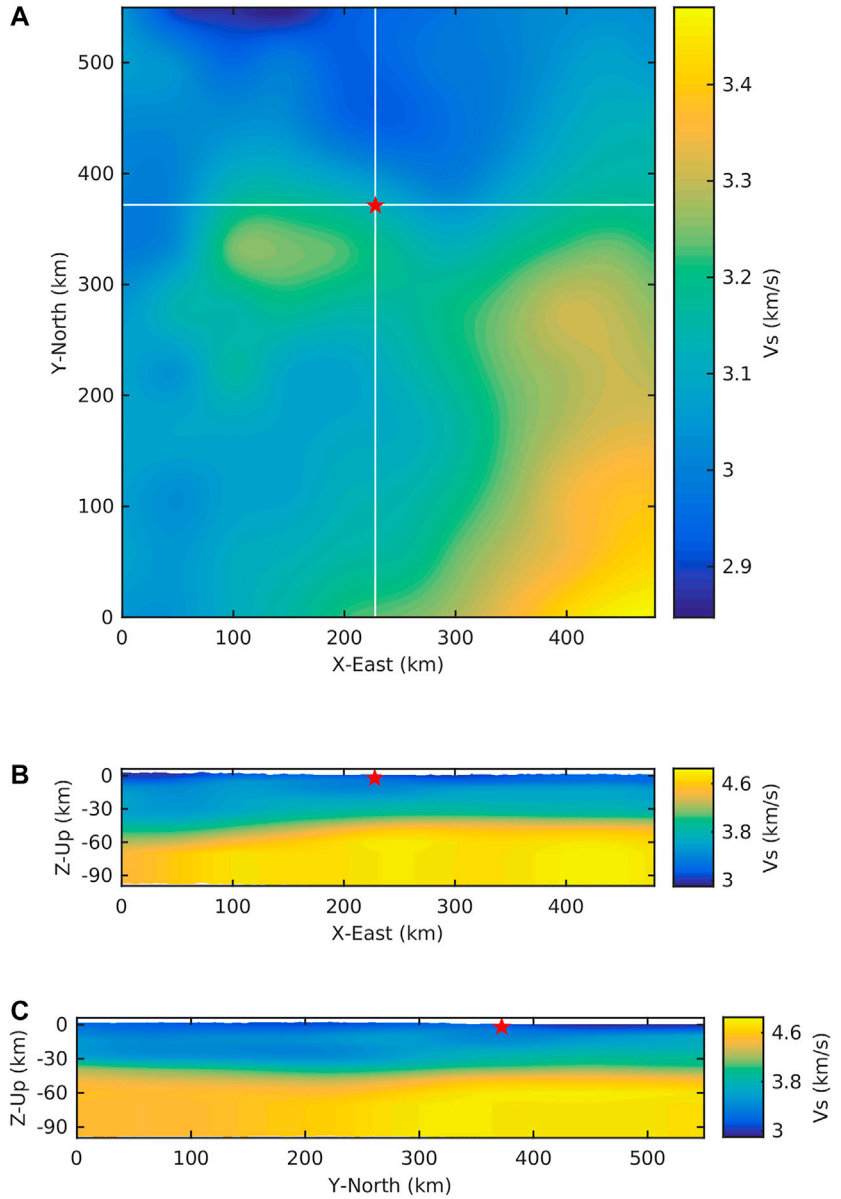

FIGURE 4 | As in **Figure 3**, but for S-wave velocity.

components and phases respectively, and Δt_0 denotes the correction term of origin time that can be averaged directly with all time shifts:

$$\Delta t_0(x,y,z) = \frac{\sum_{i=1}^{nsta}\sum_{j=1}^{ncomp}\sum_{k=1}^{nphase}\alpha_{cc}\Delta T_{ijk}(x,y,z)}{nsta \times ncomp \times nphase} \quad (8)$$

The weighting factor of α_{cc} can ensure more contributions of the segments with better waveform fit to the residual. Applying the grid search method, the candidate source point with the minimum traveltime misfit in 3D grid volume indicates the located event position (x_c, y_c, z_c), i.e., the earthquake centroid. As the investigated earthquake is not big ($M_W < 6$), we do not distinguish the centroid and hypocenter in the following text. Meanwhile, the horizontal coordinates of the located event are considered as the horizontal centroid location (x_c, y_c).

Figure 6 shows the map of the traveltime misfit with a grid size of 1 km × 1 km at the event depth (3.14 km) of Changning earthquake which is determined later by minimizing the waveform misfit in *Event Depth Determination*. The coordinates of initial location are 235.1 km (X) and 371.8 km (Y). The searching X-coordinate ranges from 199.5 km to 298.5 km and the Y-coordinate ranges from 324.5 km to

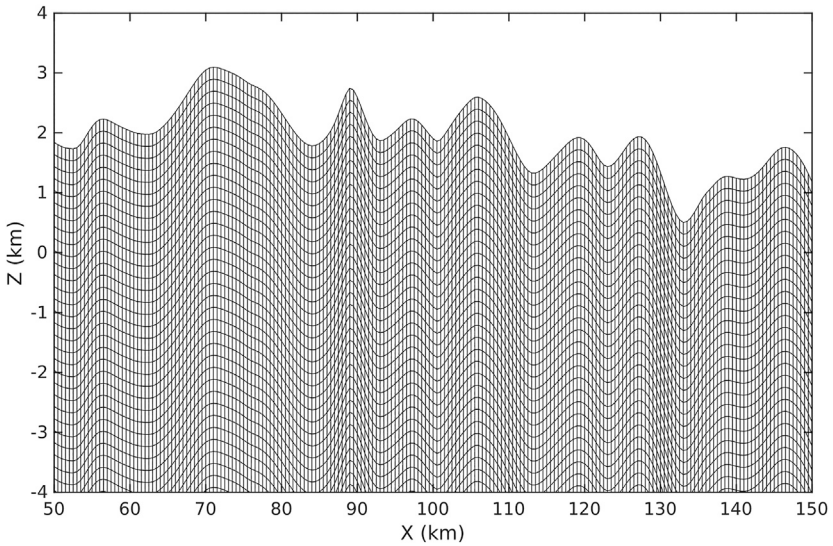

FIGURE 5 | The curvilinear grids along one vertical profile (white dashed line in **Figure 2**) in the presence of the topography of the region.

423.5 km. A nest grid search strategy and a local finer searching with the grid size of 200 m is applied to accelerate the locating process and refine the centroid location. The map illustrates the reasonable characteristics of the misfit value increasing gradually with the grid far away the true location. In addition, the three contours near the event show that the error distribution does not exhibit apparently directional pattern.

Besides, we also plot the traveltime misfit maps with a coarse grid size of 6 km × 6 km at the various depths from 1.2 km to 27.7 km (**Figure 7**). From the top to the bottom, the patterns of the misfit distribution exhibit generally consistent except for some little anomalies probably caused by model complexities.

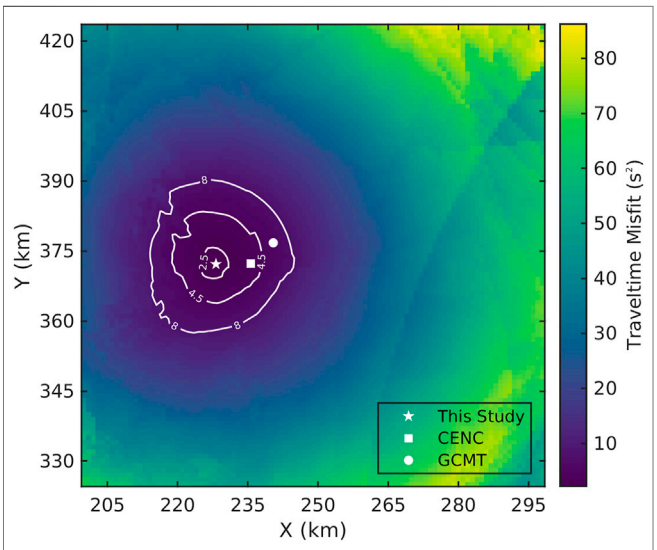

FIGURE 6 | The traveltime misfit map along with three contours (white lines), the centroid location in this study (white star), epicenter location by CENC (white square) and centroid location by Global CMT (white dot) at the event depth (3.14 km).

Event Depth Determination

The traveltime information has a better constraint on the horizontal position of the event, but it is not suitable for the estimation of the event depth unless the epicenter distances are short enough relative to the depth. Nevertheless, the waveform misfits in terms of L2 norm between the observation and the synthetics are sensitive to the variation of hypothetical depth. As a consequence, we minimize the waveform misfits at different depths to find the optimal event depth while the horizontal location is fixed for each calculation. The corresponding source mechanism and STF in the optimal depth are accepted as the final solution. As the **Figure 8** shows, the waveform misfit reaches a minimum when the trial depth is 3.14 km.

The moment magnitude can be easily derived from the source mechanism by **Eq. 6** and the formulas proposed by Hanks and Kanamori (1979). Based on the event location from *Horizontal Position Locating and Event Depth Determination*, the origin time is also updated with the correction item from **Eq. 8**.

RESULTS

Table 1 summarizes the source parameters of the Changning earthquake in this study, Global CMT, Liu and Zahradník (2020), and CENC. The origin time (2019-06-17 14:55:45.0 GMT) in this study is about 2 s earlier than Global CMT and 2 s behind CENC. The magnitude results are almost the same among these reports excluding that of CENC in M_S. The horizontal centroid position in our research (28.34°N, 104.82°E) is located on the west of the others and has a maximum distance deviation of about 15 km with respect to Global CMT, which is possibly caused by the effects of the local 3D model we used. With the optimization of

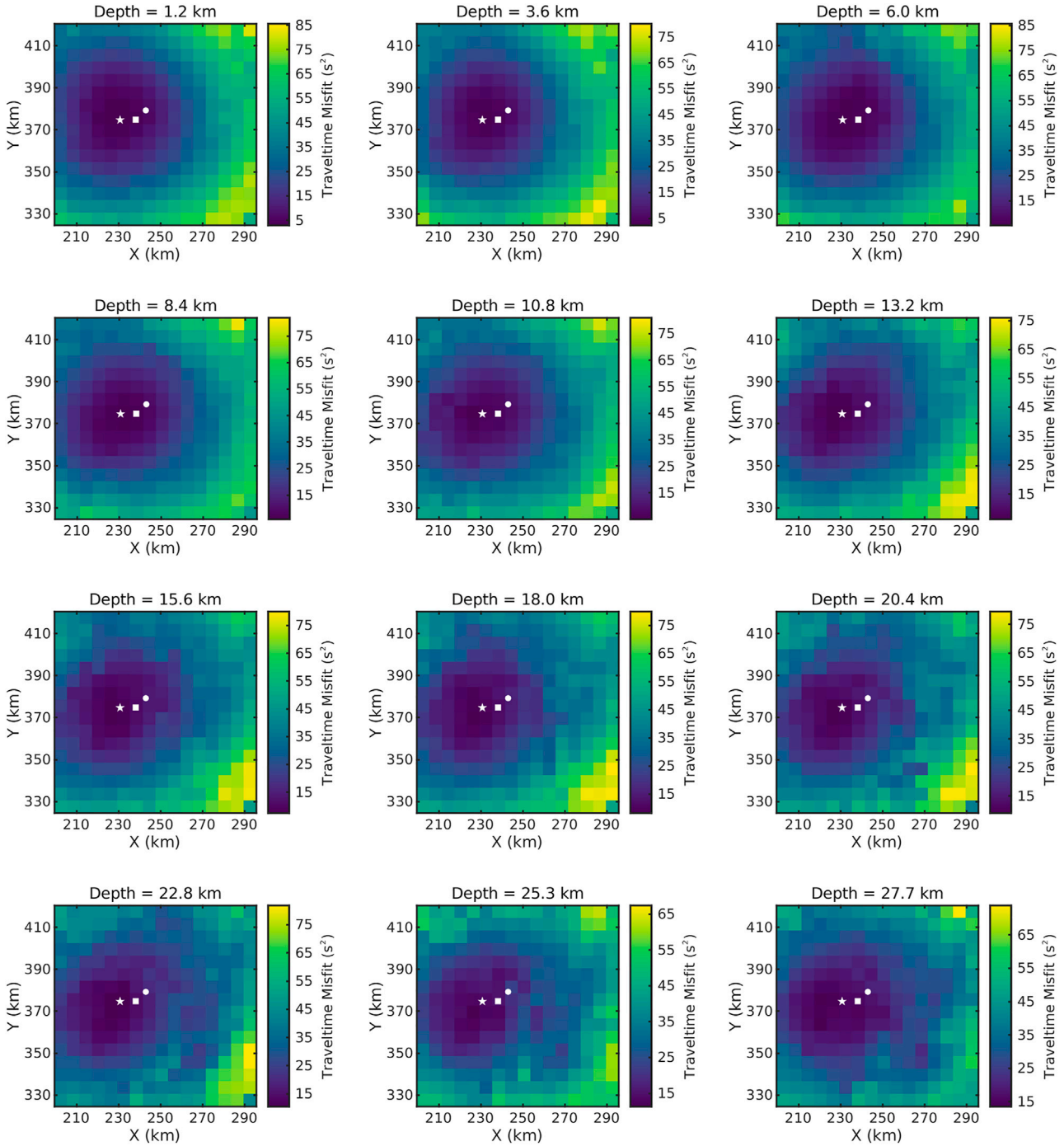

FIGURE 7 | Traveltime misfit maps along with the centroid location in this study (white star), epicenter location by CENC (white square) and centroid location by Global CMT (white dot) at various depth from 1.2 km to 27.7 km.

waveform misfit along depth, we find the final event depth is 3.14 km which is the shallowest among all the results and very close to the operation geological layer of shale gas in Sichuan basin. The two nodal planes are strike 295°/dip 88°/rake 14° and strike 204°/dip 76°/rake 178°. The moment tensors are decomposed to DC, CLVD and ISO components using the method proposed by Knopoff and Randall (1970), with the percentages of 10, −83 and −7% respectively. The optimum duration of STF is 3.48 s. The comparison of beachballs between this study and the other two agencies is shown as **Figure 9**. The shaded areas among the three beachballs are similar and nodal planes of the DC part of the moment tensor

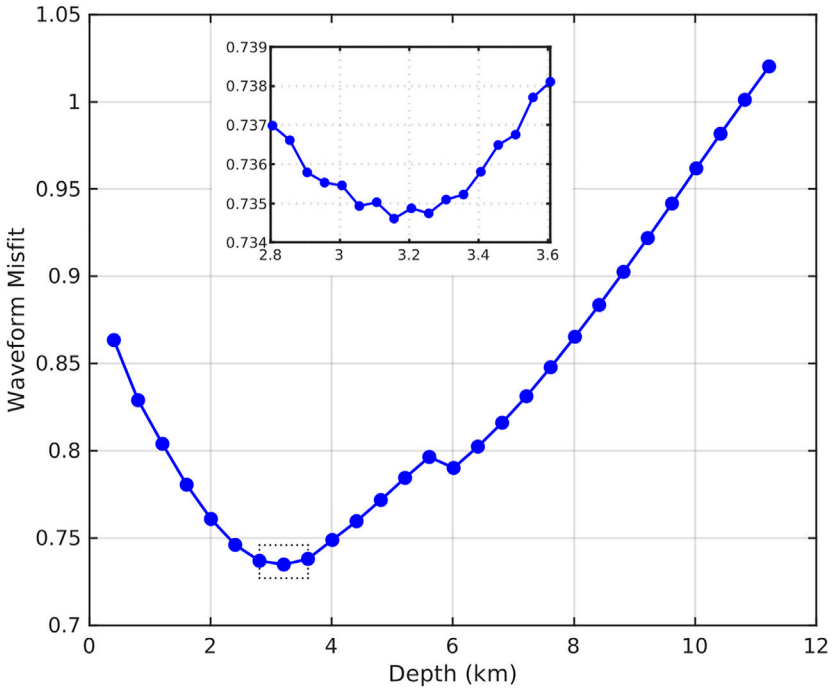

FIGURE 8 | The curve of waveform misfits vs. trial event depths with the horizontal location fixed. The middle solid rectangle is a partial enlarged drawing for local smaller grid-searching size (50 m) from 2.8 km and 3.6 km depth.

TABLE 1 | The source parameters of Changning earthquake from different affiliations.

Parameters	This study	Global CMT	Liu and Zahradník	CENC
Origin time (GMT)	2019–06-17 14:55:45.0	2019–06-17 14:55:47.1	2019–06-17 14:55:43.0	2019–06-17 14:55:43.0
Magnitude	M_W 5.7	M_W 5.7	M_W 5.74	M_S 6.0
Latitude (N)	28.34°	28.38°	28.37°	28.34°
Longitude (E)	104.82°	104.95°	104.88°	104.90°
Depth (km)	3.14	12.0	4.0	16.0
Moment Tensor ($\times 10^{17}$ Nm)	$\begin{bmatrix} 1.78 & -0.49 & 0.98 \\ -0.49 & 1.40 & 2.66 \\ 0.98 & 2.66 & -4.42 \end{bmatrix}$	$\begin{bmatrix} 3.14 & -0.17 & 0.53 \\ -0.17 & 2.35 & 2.90 \\ 0.53 & 2.90 & -5.49 \end{bmatrix}$	$\begin{bmatrix} 1.27 & -0.10 & 0.42 \\ -0.10 & 1.38 & 2.78 \\ 0.42 & 2.78 & -4.70 \end{bmatrix}$	-

CENC, China Earthquake Networks Center.

are not the same which could be explained by the low DC percentage. Overall, our results are in agreement with the other two agencies.

The reliability of our results in **Table 1** can be evaluated by comparing the observed seismograms and the synthetic waveforms. **Figure 10** shows the waveform fitting of six segments from three-component P waves (0.04–0.2 Hz) and surface waves (0.03–0.1 Hz) at all stations. The waveforms in each segment are aligned with the cross-correlation time shifts. In the determination of the event location, these time shifts with large deviations relative to the other two components for the same phase are abandoned directly, which is possibly caused by the insufficiency of the used 3D model. Specifically, they are E components of surface wave at BJT and HMS station, Z component of surface wave at ZYT station as marked with red rectangles in **Figure 10**. In addition, the corresponding time shifts in these segments with bad quality ($\alpha_{cc} < 0.5$) are also removed in the calculation of traveltime residuals.

Apart from the analysis of waveform fitting segment by segment, we also plot the whole observed seismograms and synthetics without the artificial time alignment at each station in **Figure 11**, **12**. The seismograms at all stations are starting from the same origin time in **Table 1** and then bandpass filtered with 0.03–0.06 Hz (**Figure 11**) and 0.03–0.1 Hz (**Figure 12**) as well as the synthetics. We can observe the waveforms at most of stations fit very well except for the ZYT and HMS station which could be caused by the possible error in absolute timing at ZYT station and in sensor orientation at HMS station.

While the horizontal centroid location is fixed, the uncertainties of the event depth and moment tensors for the

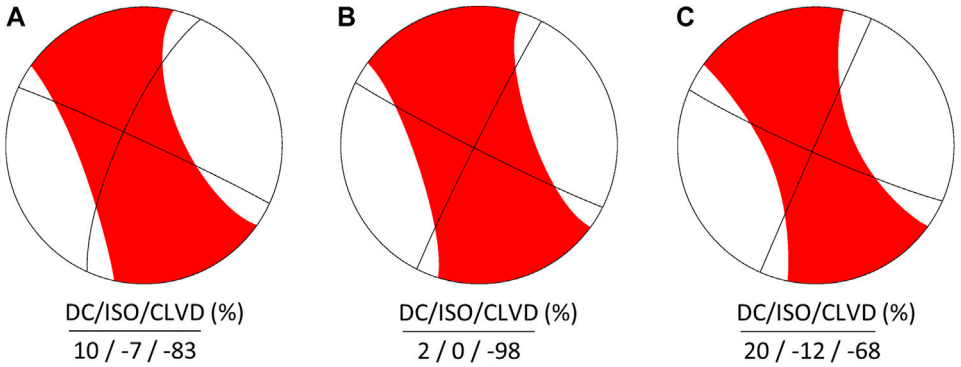

FIGURE 9 | The beachballs along with the fault plane solutions and the percentages of DC, ISO and CLVD components at the bottom of each panel **(A)** This study **(B)** Global GMT **(C)** Liu and Zahradnik (2020).

Changning earthquake are estimated by the bootstrapping method (Efron and Tibshirani, 1991; Zhan et al., 2012) with 17 stations resampled independently for 1,000 times totally. The bootstrapping results show that the percentages of DC and ISO components do not have very small uncertainties with standard deviations (STD) of 10.5% and 8.1% respectively, which are possibly caused by their low percentages in moment tensor (**Supplementary Figure S1A,B** in **Supplementary Material**). The CLVD exhibits a little bit larger STD of 15.0% but with about 65% of the statistics more than 70%, indicating the confident existence of the large CLVD component (**Supplementary Figure S1C**). The Kagan angle (K-angle) is defined as the minimum rotation angle between two focal mechanisms, which can be employed to transfer one focal mechanism to the other (Kagan, 1991). The focal mechanisms are regarded as similar with K-angle among them less than 30° and significantly different for larger than 40° (Zahradník and Custódio, 2012; Dias et al., 2016). The average K-angle with respect to the presented fault-plane solution in *Results* is 26.3°, indicating good consistency between our results and those in the bootstrapping test (**Supplementary Figure S1D**). The small STD (0.4 km) shown as **Supplementary Figure S1E** illustrates the event depth is well constrained in this study. Similarly, the centroid location is relocated many times with the same configuration of bootstrapping but using moment tensor and depth in **Table 1**. The local refinement of grid (200 m × 200 m) in the locating step is not applied but with overall grid size of 1 km × 1 km for efficiency. The estimated STDs of X- and Y-coordinate are 2.7 km and 1.6 km respectively (**Supplementary Figure S1F,G**). The azimuth gaps of the current seismic network possibly become large in some directions if several stations are removed in the resampling of bootstrap, which could affect the uncertainty estimate. From our perspective, more stations used with better coverage will reduce the uncertainty of the Changning earthquake and other local events in the further study.

DISCUSSIONS

The attenuation factors are not incorporated in the construction of SGTs database by curvilinear-grid finite-difference simulation in this study. We estimate the average quality factors of P- and surface waves ($Q_P \approx 500$ and $Q_S \approx 500$) at the depth of 5 km in this region from Dai et al. (2020). The distances from the Changning earthquake to 17 broadband stations range from 70 km to 370 km. In terms of the used frequency bands, the amplitudes with attenuation for P- and surface waves at the farthest station decrease to about 96% of the simulated amplitudes without attenuation by approximately multiplying an exponential term. The effects of attenuation on the determination of source parameters would be very small.

Besides, in order to evaluate the effects of topography and 3D complexities on the centroid location and moment tensors, we perform another two tests for 3D non-topography model (**Supplementary Figures S3, S4**) and 1D model in **Supplementary Material**. The 1D model is extracted from the 3D model at the horizontal centroid location from the surface to the bottom (**Supplementary Figure S8**). The comparisons of the source parameters of Changning earthquake are summarized in **Supplementary Table S1**. Compared with results in 3D model with topography, the event latitude and depth for 3D non-topography model have a difference of 1.4 km and 60 m respectively. The results for 1D model show larger difference of 3.0 km in latitude, 0.8 km in longitude and 160 m in depth. **Supplementary Figure S2** shows the beachballs along with nodal plane and the percentages of the decomposed DC, ISO and CLVD components for the three models. The pattern of nodal planes for 1D model exhibits large variances with 3D model and 3D non-topography model. Although K-angle of the mechanism found in the 1D solution with respect to the 3D solution with topography is about 35°, it is still within 95% confidence region of the K-angle bootstrap variation in **Supplementary Figure S1D**. Using the source parameters in **Supplementary Table S1**, we plot the waveform fit for 3D non-topography model (**Supplementary Figure S5–S7**) and 1D model (**Supplementary Figure S9–S11**), respectively. Because the frequency bands we used are relatively low, the consideration of topography has no significant improvement on the waveform comparison. If we move to the higher frequency in the inversion, the distortion of waveform due to the topography will play a more important

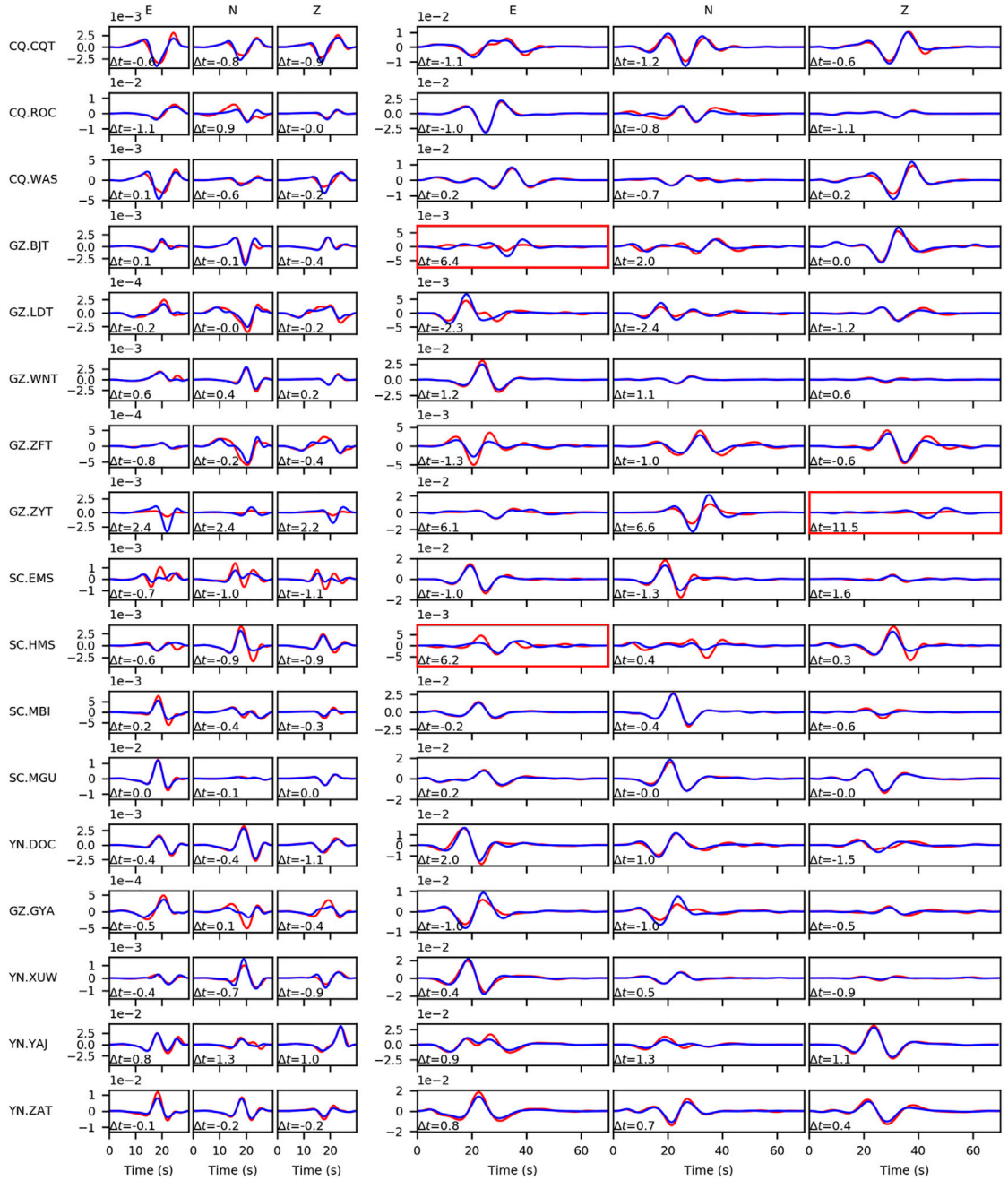

FIGURE 10 | The waveform fitting of the three-component (ENZ) P wave (left three columns, 0.04–0.2 Hz) and the surface wave (right three columns, 0.03–0.1 Hz) at all stations utilized for inversion. The leftmost texts in each row mark the seismic network and station names. The red and blue solid lines indicate the observation and the synthetic data using the optimum source position and mechanism respectively along with the time shift below each waveform. The red rectangles mark the segments in which the time shifts are not used in the calculation of traveltime residuals.

role in the results analysis. Although the waveform fit is very similar between **Figures 10–12** and **Supplementary Figure S5–S7**, the moment tensor components and its decomposition change indeed when the topography is ignored. **Supplementary Figure S9–S11** show an overall good fit except for the shifts on some stations, indicating the 1D model extracted in this way is a feasible and reliable approximation of 3D model.

CONCLUSION

The 2019 M_W 5.7 Changning earthquake caused huge economic losses and casualties, which is the largest earthquake recorded in southern Sichuan basin. There are many studies reporting this event, but the location, depth and source mechanism of them are different each other. In this study, we use 3D SGTs to obtain

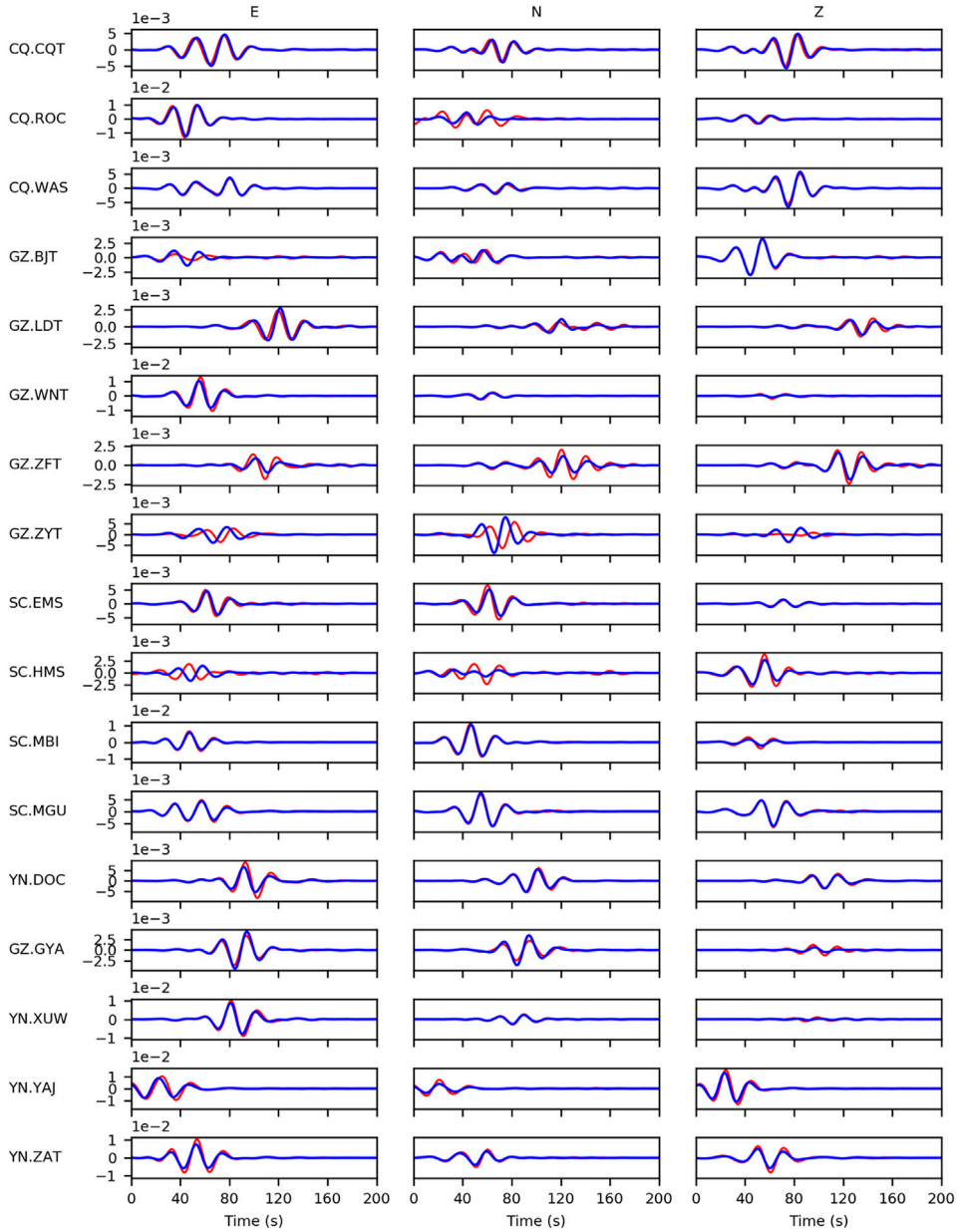

FIGURE 11 | The waveform fittings (0.03–0.06 Hz) of the whole three-component data at all stations with the origin time of **Table 1**. The red and blue solid lines indicate the observation and the synthetic data using the optimum source position and mechanism, respectively. Here, the artificial time shifts are not applied. The leftmost texts in each row mark the seismic network and station names.

centroid location, moment tensors and other source parameters of the Changning earthquake. The 3D SGTs are calculated by curvilinear-grid finite-difference method with the 3D model of southwest China considering the rugged topography of this region. The event location is derived by minimizing the traveltime residuals of P wave and surface wave in the candidate 3D grid volume and the depth is determined by the minimum waveform misfit along trial depths between the observations and the synthetics when the horizontal location is fixed. Based on the waveform inversion, we refine the event location to (28.34°N, 104.82°E) and the optimized depth is 3.14 km. The strike, dip and rake angles for the nodal planes are 295°/88°/14° and 204°/76°/178°. The moment tensors can be decomposed to DC, CLVD and ISO components with the percentages of 10, −83, and −7% respectively. The waveform fit for the corrected origin time (2019-06-17 14:55:45.0 GMT) is good, and it indicates the reliability of the results.

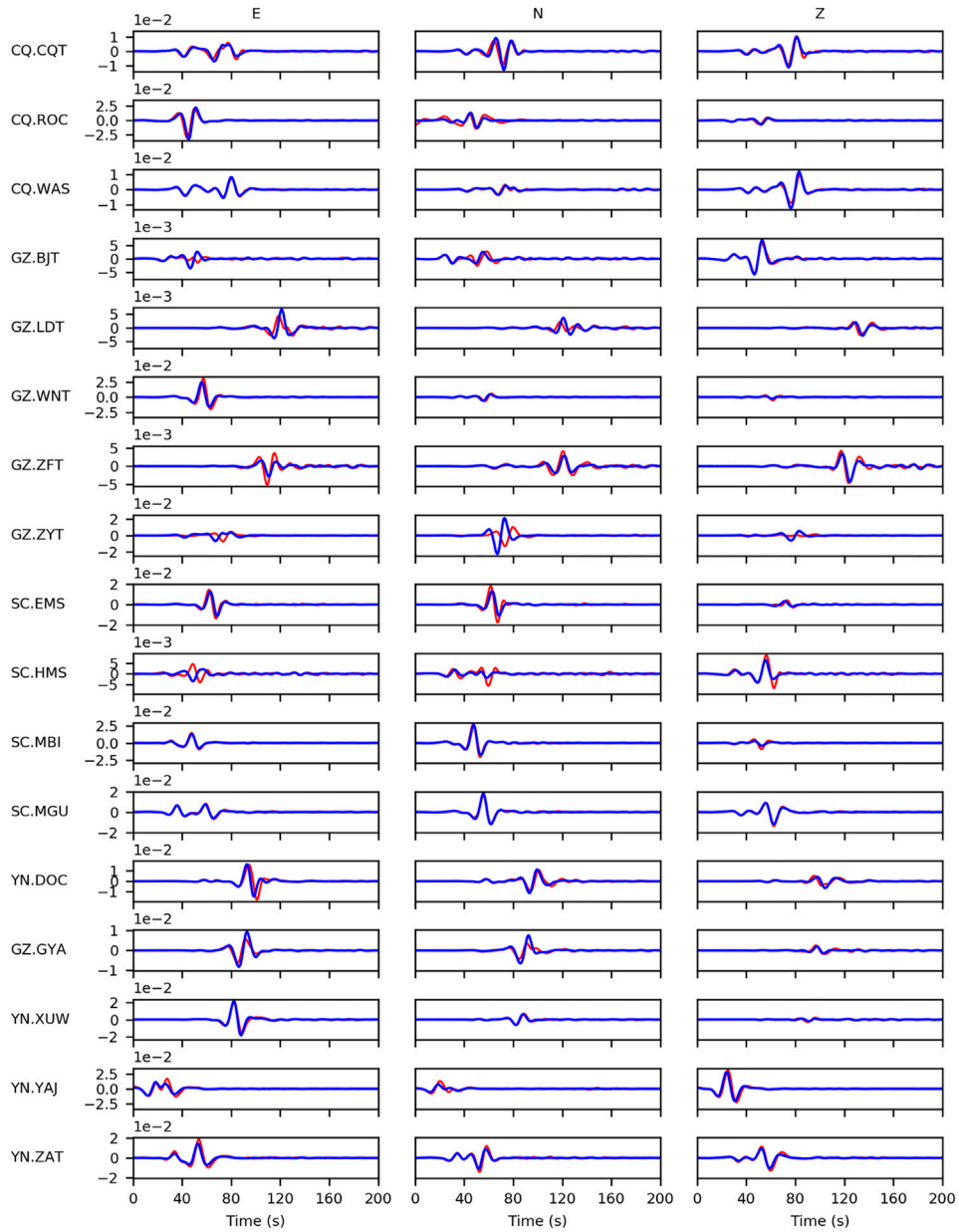

FIGURE 12 | As in **Figure 11**, but for frequency range of 0.03–0.1 Hz.

DATA AVAILABILITY STATEMENT

Publicly available datasets were analyzed in this study. This data can be found here: China Seismic Experimental Site (CSES) website (http://124.17.4.85/wp-content/uploads/2019/06/wave_6.1.rar).

AUTHOR CONTRIBUTIONS

YH accomplishes the processing of raw data, the programming of the inversion codes and the writing of the manuscript. WZ proposes the main ideas of the study and participates in the writing of the manuscript. The curvilinear-grid finite-difference codes were written by WZ in 2006 and continuously developed by our research group. JZ helps discuss the results and provides many useful instructions and suggestions. All authors contribute the revisions and the editing before submission.

FUNDING

The project is supported by the China Earthquake Science Experiment Project of the China Earthquake Administration (Grant No.

2018CSES0101), the National Natural Science Foundation of China (Grant No. U1901602) and Shenzhen Science and Technology Program (Grant No. KQTD20170810111725321).

ACKNOWLEDGMENTS

We thank the three reviewers for their insightful comments which greatly improve the manuscript. The continuous waveform data of the Changning earthquake are downloaded from the repository of the China Seismic Experiment Site (Wave 6.1. CSES Scientific Products, doi: 10.12093/01db.01.2019.03.v1). The instrumental responses are obtained from the Seismic Data Management Center of China (http://www.seisdmc.ac.cn/). The topography data are download from the CDIAR-CSI SRTM website (https://srtm.csi.cgiar.org/srtmdata/). Figures in this study are partly created using the GMT (http://gmt.soest.hawaii.edu/home).

SUPPLEMENTARY MATERIAL

The Supplementary Material for this article can be found online at: https://www.frontiersin.org/articles/10.3389/feart.2021.642721/full#supplementary-material.

REFERENCES

Clarke, H., Eisner, L., Styles, P., and Turner, P. (2014). Felt seismicity associated with shale gas hydraulic fracturing: the first documented example in Europe. *Geophys. Res. Lett.* 41 (23), 8308–8314. doi:10.1002/2014GL062047

Dai, A., Tang, C.-C., Liu, L., and Xu, R. (2020). Seismic attenuation tomography in southwestern China: insight into the evolution of crustal flow in the Tibetan Plateau. *Tectonophysics* 792, 228589. doi:10.1016/j.tecto.2020.228589

Dias, F., Zahradník, J., and Assumpção, M. (2016). Path-specific, dispersion-based velocity models and moment tensors of moderate events recorded at few distant stations: examples from Brazil and Greece. *J. South Am. Earth Sci.* 71, 344–358. doi:10.1016/j.jsames.2016.07.004

Efron, B., and Tibshirani, R. (1991). Statistical data analysis in the computer age. *Science* 253 (5018), 390–395. doi:10.1126/science.253.5018.390

Eisner, L., and Clayton, R. W. (2001). A reciprocity method for multiple-source simulations. *Bull. Seismological Soc. America* 91 (3), 553–560. doi:10.1785/0120000222

Ekström, G., and Engdahl, E. R. (1989). Earthquake source parameters and stress distribution in the Adak Island region of the central Aleutian Islands, Alaska. *J. Geophys. Res.* 94 (B11), 15499–15519. doi:10.1029/JB094iB11p15499

Ekström, G., Nettles, M., and Dziewoński, A. M. (2012). The global CMT project 2004-2010: centroid-moment tensors for 13,017 earthquakes. *Phys. Earth Planet. Interiors* 200-201, 1–9. doi:10.1016/j.pepi.2012.04.002

Ellsworth, W. L. (2013). Injection-induced earthquakes. *Science* 341 (6142), 1225942. doi:10.1126/science.1225942

Fang, H., Zhang, H., Yao, H., Allam, A., Zigone, D., Ben-Zion, Y., et al. (2016). A new algorithm for three-dimensional joint inversion of body wave and surface wave data and its application to the Southern California plate boundary region. *J. Geophys. Res. Solid Earth* 121 (5), 3557–3569. doi:10.1002/2015JB012702

Gan, W., Zhang, P., Shen, Z.-K., Niu, Z., Wang, M., Wan, Y., et al. (2007). Present-day crustal motion within the Tibetan Plateau inferred from GPS measurements. *J. Geophys. Res.* 112 (B8), B08416. doi:10.1029/2005JB004120

Goebel, T. H. W., and Brodsky, E. E. (2018). The spatial footprint of injection wells in a global compilation of induced earthquake sequences. *Science* 361 (6405), 899–904. doi:10.1126/science.aat5449

Grigoli, F., Cesca, S., Rinaldi, A. P., Manconi, A., López-Comino, J. A., Clinton, J. F., et al. (2018). The November 2017 MW 5.5 Pohang earthquake: a possible case of induced seismicity in South Korea. *Science* 360 (6392), 1003–1006. doi:10.1126/scienceaat201010.1126/science.aat2010

Hanks, T. C., and Kanamori, H. (1979). A moment magnitude scale. *J. Geophys. Res.* 84 (B5), 2348–2340. doi:10.1029/JB084iB05p02348

Hejrani, B., Tkalčić, H., and Fichtner, A. (2017). Centroid moment tensor catalogue using a 3-D continental scale Earth model: application to earthquakes in Papua New Guinea and the Solomon Islands. *J. Geophys. Res. Solid Earth* 122 (7), 5517–5543. doi:10.1002/2017JB014230

Jiang, D., Zhang, S., and Ding, R. (2020). Surface deformation and tectonic background of the 2019 Ms 6.0 Changning earthquake, Sichuan basin, SW China. *J. Asian Earth Sci.* 200, 104493. doi:10.1016/j.jseaes.2020.104493

Johnson, M., and Vincent, C. (2002). Development and testing of a 3D velocity model for improved event location: a case study for the India-Pakistan region. *Bull. Seismological Soc. America* 92 (8), 2893–2910. doi:10.1785/0120010111

Kagan, Y. Y. (1991). 3-D rotation of double-couple earthquake sources. *Geophys. J. Int.* 106 (3), 709–716. doi:10.1111/j.1365-246X.1991.tb06343.x

Knopoff, L., and Randall, M. J. (1970). The compensated linear-vector dipole: a possible mechanism for deep earthquakes. *J. Geophys. Res.* 75 (26), 4957–4963. doi:10.1029/JB075i026p04957

Lei, X., Huang, D., Su, J., Jiang, G., Wang, X., Wang, H., et al. (2017). Fault reactivation and earthquakes with magnitudes of up to Mw4.7 induced by shale-gas hydraulic fracturing in Sichuan Basin, China. *Sci. Rep.* 7, 7971. doi:10.1038/s41598-017-08557-y

Lei, X., Su, J., and Wang, Z. (2020). Growing seismicity in the Sichuan Basin and its association with industrial activities. *Sci. China Earth Sci.* 63, 1633–1660. doi:10.1007/s11430-020-9646-x

Lei, X., Wang, Z., Wang, Z., and Su, J. (2019). Possible link between long-term and short-term water injections and earthquakes in salt mine and shale gas site in Changning, south Sichuan Basin, China. *Earth Planet. Phys.* 3 (6), 510–525. doi:10.26464/epp2019052

Li, W., Ni, S., Zang, C., and Chu, R. (2020). Rupture directivity of the 2019 Mw 5.8 changning, sichuan, China, earthquake and implication for induced seismicity. *Bull. Seismological Soc. America* 110 (5), 2138–2153. doi:10.1785/0120200013

Liu, J., and Zahradník, J. (2020). The 2019 M W 5.7 changning earthquake, Sichuan basin, China: a shallow doublet with different faulting styles. *Geophys. Res. Lett.* 47 (4), e2019GL085408. doi:10.1029/2019GL085408

Liu, Y., Yao, H., Zhang, H., and Fang, H. (2020). The Community Velocity Model V1.0 of southwest China, constructed from joint body- and surface-wave traveltime tomography. *Seismological Res. Lett.* in press.

Long, F., Zhang, Z., Zhang, Z., Qi, Y., Liang, M., Ruan, X., et al. (2020). Three dimensional velocity structure and accurate earthquake location in Changning-Gongxian area of southeast Sichuan. *Earth Planet. Phys.* 4 (2), 1–15. doi:10.26464/epp2020022

Ma, X. (2017). A golden era for natural gas development in the Sichuan Basin. *Nat. Gas Industry B* 4 (3), 163–173. doi:10.1016/j.ngib.2017.08.001

Meng, L., McGarr, A., Zhou, L., and Zang, Y. (2019). An investigation of seismicity induced by hydraulic fracturing in the Sichuan basin of China based on data from a temporary seismic network. *Bull. Seismological Soc. America* 109 (1), 348–357. doi:10.1785/0120180310

Myers, S. C., Simmons, N. A., Johannesson, G., and Matzel, E. (2015). Improved regional and TeleseismicP-wave travel-time prediction and event location using a global 3D velocity model. *Bull. Seismological Soc. America* 105 (3), 1642–1660. doi:10.1785/0120140272

Nayak, A., and Dreger, D. S. (2018). Source inversion of seismic events associated with the sinkhole at napoleonville salt dome, Louisiana using a 3D velocity model. *Geophys. J. Int.* 214 (3), 1808–1829. doi:10.1093/gji/ggy202

Tan, Y., Hu, J., Zhang, H., Chen, Y., Qian, J., Wang, Q., et al. (2020). Hydraulic fracturing induced seismicity in the southern Sichuan Basin due to fluid diffusion inferred from seismic and injection data analysis. *Geophys. Res. Lett.* 47 (4), e2019GL084885. doi:10.1029/2019GL084885

Wang, M., and Shen, Z. K. (2020). Present-Day crustal deformation of continental China derived from GPS and its tectonic implications. *J. Geophys. Res. Solid Earth* 125 (2), e2019JB018774. doi:10.1029/2019JB018774

Wang, S., Jiang, G., Weingarten, M., and Niu, Y. (2020). InSAR evidence indicates a link between fluid injection for salt mining and the 2019 Changning (China) earthquake sequence. *Geophys. Res. Lett.* 47 (16), e2020GL087603. doi:10.1029/2020GL087603

Wang, X., and Zhan, Z. (2019). Moving from 1-D to 3-D velocity model: automated waveform-based earthquake moment tensor inversion in the Los Angeles region. *Geophys. J. Int.* 220 (1), 218–234. doi:10.1111/j.1365-246X.2012.05472.x10.1093/gji/ggz435

Yi, G., Long, F., Liang, M., Zhao, M., Wang, S., Gong, Y., et al. (2019). Focal mechanism solutions and seismogenic structure of the 17 June 2019 M_S 6.0 Sichuan Changning earthquake sequence. *Chin. J. Geophys. (in Chinese)* 62 (9), 3432–3447. doi:10.6038/cjg2019N0297

Zahradník, J., and Custódio, S. (2012). Moment tensor resolvability: application to Southwest Iberia. *Bull. Seismological Soc. America* 102 (3), 1235–1254. doi:10.1785/0120110216

Zhan, Z., Helmberger, D., Simons, M., Kanamori, H., Wu, W., Cubas, N., et al. (2012). Anomalously steep dips of earthquakes in the 2011 Tohoku-Oki source region and possible explanations. *Earth Planet. Sci. Lett.* 353-354, 121–133. doi:10.1016/j.epsl.2012.07.038

Zhang, B., Lei, J., and Zhang, G. (2020). Seismic evidence for influences of deep fluids on the 2019 Changning Ms 6.0 earthquake, Sichuan basin, SW China. *J. Asian Earth Sci.* 200, 104492. doi:10.1016/j.jseaes.2020.104492

Zhang, W., and Chen, X. (2006). Traction image method for irregular free surface boundaries in finite difference seismic wave simulation. *Geophys. J. Int.* 167 (1), 337–353. doi:10.1111/j.1365-246X.2006.03113.x

Zhang, W., and Shen, Y. (2010). Unsplit complex frequency-shifted PML implementation using auxiliary differential equations for seismic wave modeling. *Geophysics* 75 (4), T141–T154. doi:10.1190/1.34634310.1190/1.3463431

Zhang, W., Zhang, Z., and Chen, X. (2012). Three-dimensional elastic wave numerical modelling in the presence of surface topography by a collocated-grid finite-difference method on curvilinear grids. *Geophys. J. Int.* 190 (1), 358–378. doi:10.1111/j.1365-246X.2012.05472.x

Zhao, L., Chen, P., and Jordan, T. H. (2006). Strain green's tensors, reciprocity, and their applications to seismic source and structure studies. *Bull. Seismological Soc. America* 96 (5), 1753–1763. doi:10.1785/0120050253

Zhao, L., and Helmberger, D. V. (1994). Source estimation from broadband regional seismograms. *Bull. Seismological Soc. America* 84 (1), 91–104.

Zhao, Z., and Zhang, R. (1987). Primary study of crustal and upper mantle velocity structure of Sichuan Province. *Acta Seismologica Sinica* 9 (2), 154–166.

Zhou, L., Zhang, W., Shen, Y., Chen, X., and Zhang, J. (2016). Location and moment tensor inversion of small earthquakes using 3D Green's functions in models with rugged topography: application to the Longmenshan fault zone. *Earthq Sci.* 29 (3), 139–151. doi:10.1007/s11589-016-0156-1

Zhu, L., and Helmberger, D. V. (1996). Advancement in source estimation techniques using broadband regional seismograms. *Bull. Seismological Soc. America* 86 (5), 1634–1641.

Zhu, L., and Zhou, X. (2016). Seismic moment tensor inversion using 3D velocity model and its application to the 2013 Lushan earthquake sequence. *Phys. Chem. Earth, Parts A/B/C* 95, 10–18. doi:10.1016/j.pce.2016.01.002

Zuo, K., Zhao, C., and Zhang, H. (2020). 3D crustal structure and seismicity characteristics of Changning-Xingwen area in the southwestern Sichuan basin, China. *Bull. Seismological Soc. America* 110 (5), 2154–2167. doi:10.1785/0120200085

Conflict of Interest: The authors declare that the research was conducted in the absence of any commercial or financial relationships that could be construed as a potential conflict of interest.

frontiers in Earth Science

ORIGINAL RESEARCH
published: 08 April 2021
doi: 10.3389/feart.2021.629736

The Seismicity of Ischia Island, Italy: An Integrated Earthquake Catalogue From 8th Century BC to 2019 and Its Statistical Properties

Jacopo Selva[1], Raffaele Azzaro[2], Matteo Taroni[3], Anna Tramelli[4], Giuliana Alessio[4], Mario Castellano[4], Cecilia Ciuccarelli[1], Elena Cubellis[4], Domenico Lo Bascio[4], Sabina Porfido[4,5], Patrizia Ricciolino[4] and Andrea Rovida[6]*

[1] *Istituto Nazionale di Geofisica e Vulcanologia, Sezione di Bologna, Bologna, Italy,* [2] *Istituto Nazionale di Geofisica e Vulcanologia, Osservatorio Etneo, Catania, Italy,* [3] *Istituto Nazionale di Geofisica e Vulcanologia, Sezione di Roma 1, Rome, Italy,* [4] *Istituto Nazionale di Geofisica e Vulcanologia, Sezione Osservatorio Vesuviano, Naples, Italy,* [5] *Consiglio Nazionale delle Ricerche, CNR-ISA, Avellino, Italy,* [6] *Istituto Nazionale di Geofisica e Vulcanologia, Sezione di Milano, Milan, Italy*

OPEN ACCESS

Edited by:
Jorge Miguel Gaspar-Escribano, Polytechnic University of Madrid, Spain

Reviewed by:
Álvaro González, German Research Centre for Geosciences, Helmholtz Centre Potsdam, Germany
Tim Greenfield, University of Cambridge, United Kingdom

***Correspondence:**
Jacopo Selva
jacopo.selva@ingv.it

Specialty section:
This article was submitted to Volcanology, a section of the journal Frontiers in Earth Science

Received: *15 November 2020*
Accepted: *05 March 2021*
Published: *08 April 2021*

Citation:
Selva J, Azzaro R, Taroni M, Tramelli A, Alessio G, Castellano M, Ciuccarelli C, Cubellis E, Lo Bascio D, Porfido S, Ricciolino P and Rovida A (2021) The Seismicity of Ischia Island, Italy: An Integrated Earthquake Catalogue From 8th Century BC to 2019 and Its Statistical Properties. Front. Earth Sci. 9:629736. doi: 10.3389/feart.2021.629736

Ischia is a densely inhabited and touristic volcanic island located in the northern sector of the Gulf of Naples (Italy). In 2017, the M_W 3.9 Casamicciola earthquake occurred after more than one century of seismic quiescence characterized only by minor seismicity, which followed a century with three destructive earthquakes (in 1828, 1881, and 1883). These events, despite their moderate magnitude ($M_W < 5.5$), lead to dreadful effects on buildings and population. However, an integrated catalogue systematically covering historical and instrumental seismicity of Ischia has been still lacking since many years. Here, we review and systematically re-analyse all the available data on the historical and instrumental seismicity, to build an integrated earthquake catalogue for Ischia with a robust characterization of existing uncertainties. Supported by new or updated macroseismic datasets, we significantly enriched existing catalogues, as the Italian Parametric Earthquake Catalogue (CPTI15) that, with this analysis, passed from 12 to 57 earthquakes with macroseismic parametrization. We also extended back by 6 years the coverage of the instrumental catalogue, homogenizing the estimated seismic parameters. The obtained catalogue will not only represent a solid base for future local hazard quantifications, but also it provides the unique opportunity of characterizing the evolution of the Ischia seismicity over centuries. To this end, we analyse the spatial, temporal, and magnitude distributions of Ischia seismicity, revealing for example that, also in the present long-lasting period of volcanic quiescence, is significantly non-stationary and characterized by a b-value larger than 1.

Keywords: Ischia, volcano seismicity, seismic catalogue, completeness analysis, ensemble modelling, frequency size distribution, Poisson process

INTRODUCTION

The characterization of the seismic activity and of the consequent hazard is largely based on the knowledge that we can gain from past activity, that is, from seismic catalogues. To allow a robust characterization of the seismicity, such catalogues should systematically collect all the known seismic events, as well as characterize at best the completeness of the record in the different periods

and the existing uncertainty about seismic parametrization. Especially for historical times and for light to moderate magnitudes (M < 6), this is often very challenging.

Ischia is a volcanic island within the Neapolitan volcanic system. It is located to the southwest of the Campi Flegrei caldera and, along with the volcanic islands of Procida and Vivara, they form the Phlegraean volcanic district (**Figure 1**). The volcano-tectonic framework of Ischia is rather complex: it represents the emerged part of an active volcanic field, which rises more than 1,000 m above the seafloor along the margin of an E-W trending scarp bordering to the south the Phlegraean volcanic district (Orsi et al., 1999). Seismic hazard is just one of the possible hazards related to the local volcanic system, responsible in the past for landslides, tsunamis, hydrothermal explosions, and volcanic eruptions (see Selva et al., 2019 for a review). Ischia has a long record of eruptions also in historical times, the last one being the 1302 AD Arso lava flow (Vezzoli, 1988; Iacono, 1996), after which it began a long period of volcanic quiescence that nowadays has been lasting for more than 7 centuries. Ischia has been affected by a significant intra-calderic resurgence of approximately 1000 m (Orsi et al., 1991; Acocella and Funiciello, 1999). Seismicity is mainly concentrated on the E-W structures that limit to the north the resurgent block of Mt. Epomeo (Carlino et al., 2006; Cubellis and Luongo, 2018; Trasatti et al., 2019; Cubellis et al., 2020; Carlino et al., 2021; Nappi et al., 2021; and references therein). Local seismicity may be connected to a relevant seismic hazard (Cubellis et al., 2004; Selva et al., 2019) and, in a multi-hazard view, it can be seen as one of the possible events in a multi-hazard chain that may include other phenomena like landslides or tsunami (e.g., Violante et al., 2003; Della Seta et al., 2012; Paparo and Tinti, 2017; Selva et al., 2019).

On the evening of the 21st August 2017, a M_w 3.9 earthquake struck the island of Ischia, causing 2 casualties, many injuries, and extensive damage in the village of Casamicciola, on the northern coast of the island (Azzaro et al., 2017). The earthquake was very shallow (depth <1 km), with a source striking E-W in the northern sector of Ischia revealed by ground deformation and surface fracturing (e.g., Gruppo di Lavoro INGV, 2017; Braun et al., 2018; De Novellis et al., 2018; Nappi et al., 2018, 2019; Calderoni et al., 2019; Ricco et al., 2019). Different solutions of the source geometry have been proposed from the joint interpretations of seismic and geodetic data, or field geological data alone, differing in the dip-angle and the fault plane geometry at depth, and its generation mechanism (Braun et al., 2018; De Novellis et al., 2018; Devoti et al., 2018; Calderoni et al., 2019; Cubellis et al., 2020).

The 2017 strong earthquake struck Ischia after tens of years of very low seismicity (D'Auria et al., 2018). However, the same area was strongly hit by a series of heavily damaging earthquakes in the XIX century (Cubellis and Luongo, 2018; Guidoboni et al., 2018; Cubellis et al., 2020), the most devastating of which occurred on July 28 1883, causing more than 2000 casualties and heavy destruction in a large part of the island and following by only two years another destructive event occurred in 1881 (Cubellis, 1985; Alessio et al., 1996; Cubellis and Luongo, 1998, 2018; Cubellis et al., 2004, 2020; Luongo et al., 2006; Guidoboni et al., 2018). Therefore, the 2017 event renewed the attention on the evaluation of the seismic hazard and related risk at Ischia (e.g., Avvisati et al., 2019; De Natale et al., 2019; Nappi et al., 2021), considering that this small island (less than 50 km^2) is densely inhabited with more than 60,000 steady inhabitants, incremented by tourists during the summer season.

The interpretation of the genesis of the seismicity at Ischia and the relationship with its volcanic activity is still debated (e.g., Martinelli and Dadomo, 2017; Cubellis and Luongo, 2018; Calderoni et al., 2019; Selva et al., 2019; Trasatti et al., 2019; Cubellis et al., 2020). The existence of a high-temperature gradient hampering brittle behaviour of the medium limits the seismogenic volume to the first 2–3 km (Carlino et al., 2006; Castaldo et al., 2017; Cubellis et al., 2020). In any case, the existence of long periods of seismic quiescence with very low seismicity rates and of sequences of destructive earthquakes such as the one that occurred in the XIX century shows the complexity of the processes that generate the earthquakes at Ischia.

A unified, extended earthquake catalogue for Ischia does not exist yet. Given the complex character of the seismicity at Ischia, a homogeneous characterization of both historical and instrumental seismicity is fundamental for quantitatively addressing scientific analyses about its spatio-temporal evolution, to better constrain its origin and quantify the seismic hazard and the related risk. Indeed, most of the literature studies have been focused on the main historical events (Cubellis, 1985; Luongo et al., 1987, 2006; Alessio et al., 1996; Cubellis and Luongo, 1998; Cubellis et al., 2004; Carlino et al., 2010), and only some macroseismic datasets (Guidoboni et al., 2007, 2018) were used to compile the Italian parametric earthquake catalogue (hereinafter CPTI15[1]; Rovida et al., 2016, 2019, 2020). In this frame, the magnitude estimates are controversial, while a systematic collection of the minor seismicity is missing. On the other hand, the instrumental seismicity presented by D'Auria et al. (2018) results limited to the most recent period, with duration magnitude estimations (M_d) incompatible to CPTI15. Therefore the existing catalogues are, in their present form, inappropriate to characterize the seismicity of Ischia due to the very low number of events reported, as well as earthquake parameters not directly comparable to each other and uniform through time.

In this paper, we systematically revise the historical and instrumental seismicity in order to produce the first integrated catalogue of the earthquakes that can be attributed to the local volcano-tectonic activity of Ischia. The analysis of the historical macroseismic records (Section "Macroseismic Catalogue: 8th Century BC – 2019") consisted of: (i) scrutinizing the literature data to include all the earthquakes caused by local sources in the island; (ii) homogenizing intensity data; (iii) re-parametrizing the collected data with a standardized procedure that takes into account the relevant uncertainty; (iv) evaluating the completeness of the catalogue from the historical standpoint. As for the recent instrumental seismicity (Section "Instrumental Catalogue: 1993–2019"), we: (i) discuss the evolution of the local instrumental network; (ii) revise the data and the parameter estimations, extending the analysis as far back as the 1990s; (iii) evaluate the completeness of the catalogue. The resulting

[1]https://emidius.mi.ingv.it/CPTI15-DBMI15/index_en.htm

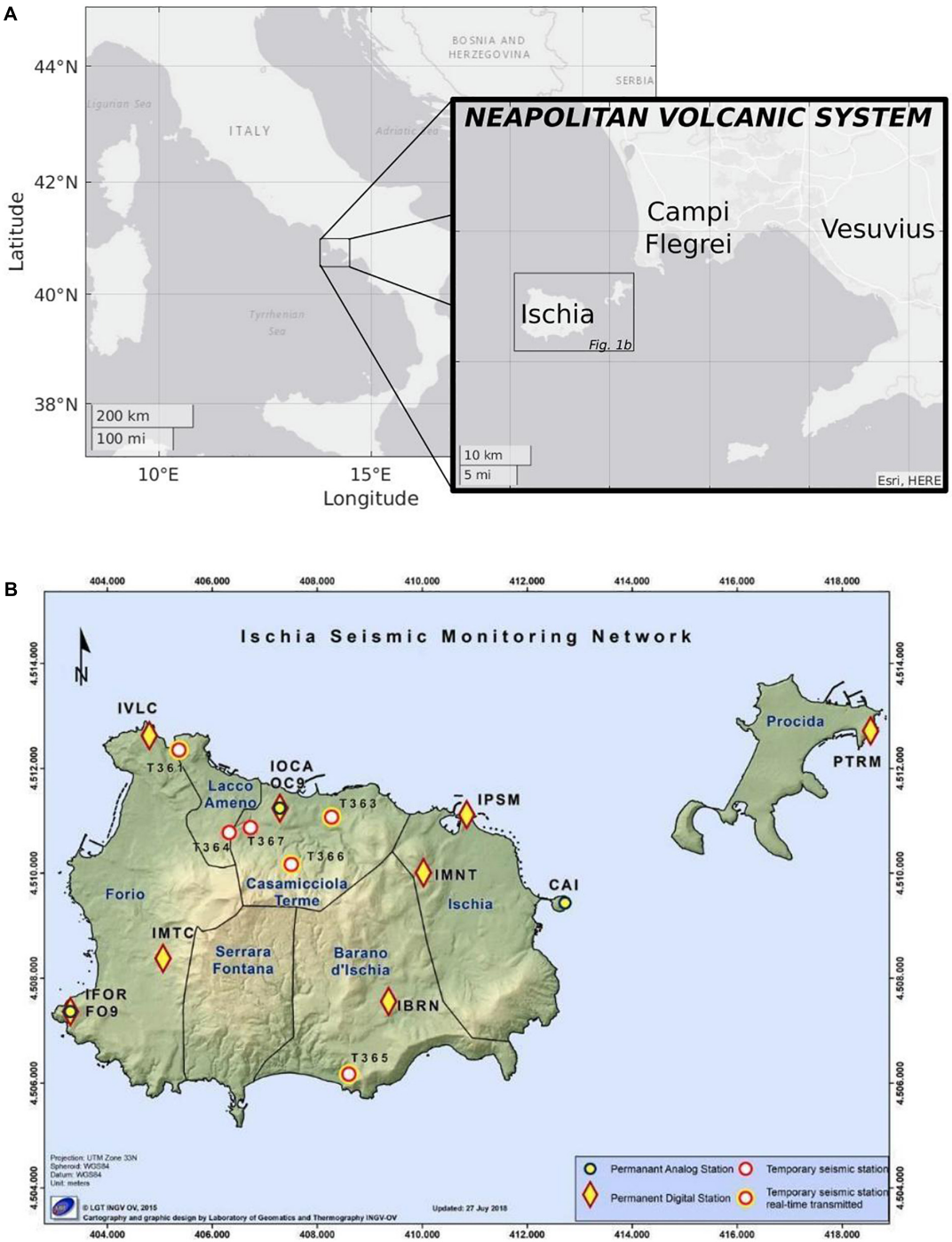

FIGURE 1 | Ischia and the Neapolitan volcanic district. **(A)** Location of the Neapolitan volcanic district and of Vesuvius, Campi Flegrei, and Ischia. **(B)** Map of the island of Ischia and its present-day seismic network of the Island of Ischia and Procida.

integrated catalogue (macroseismic plus instrumental records) is then statistically analysed (Section "Statistical Characterization of the Seismicity") through: (i) the characterization of the frequency-size distribution and related uncertainty; (ii) the characterization of the occurrence model of the seismicity, by testing the hypothesis of stationarity in time utilizing a statistical test; and iii) the characterization of the spatial distribution and related uncertainty. The result is an earthquake catalogue spanning over ten centuries, which represents the primary dataset for investigating the long-term behaviour of the volcano seismicity of Ischia and assessing the related seismic hazard at local scale.

MACROSEISMIC CATALOGUE: 8TH CENTURY BC – 2019

The long-term seismicity is described in the historical earthquake catalogues by macroseismic intensity data, which are parameterized in terms of epicentral location and magnitude. For Ischia, the CPTI15 catalogue reports the main events above the damage threshold (corresponding to epicentral intensity I_0 > V-VI MCS). However, many studies investigated other minor damaging earthquakes as well as simply felt events. Therefore, there is the possibility to increase the number of records of the historical catalogue taking into account all the results available in the literature. In doing this, we also revised the whole procedure to parametrize earthquakes, that is, the Macroseismic Data Points (MDPs) production, the intensity-magnitude relationship, and the epicentral determinations. This is crucial to produce reliable and homogeneous information through time. Note that, at the present state, there is a large variability of the parameters in the literature even for the most studied events: for example, the magnitude estimations for the largest known event (1883) range in literature from 4.3 to 5.2 (CPTI15, Rovida et al., 2019, 2020; Cubellis and Luongo, 1998; Cubellis et al., 2020; Carlino et al., 2021).

In the following, we describe the procedure adopted to produce the new revised macroseismic catalogue for Ischia through three main steps: (i) producing a comprehensive inventory of the known earthquakes; (ii) homogenising geographically the macroseismic intensity data; and (iii) parametrizing with a standardized procedure the events to determine their magnitude and location, accounting for uncertainties.

The revised catalogue, covering the time-span from the 8th century BC to 2019, is reported as **Supplementary Dataset 1**.

Step 1: Inventory of the Earthquakes

We collected all the information available in the literature into a comprehensive inventory. The starting point is represented by the events included in the Italian Archive of Historical Earthquake Data (hereinafter ASMI;[2] Rovida et al., 2017) – the basic tool for collecting, homogenizing, and validating macroseismic data in Italy – updated to 2017 and from which CPTI15 is compiled.

Before the present work, ASMI provided a list of 13 earthquakes for Ischia, known through 18 different studies and catalogues. We integrated this list with a large number of events reported in other studies (for example, Cubellis, 1985; Luongo et al., 1987, 2006; Alessio et al., 1996; Cubellis and Luongo, 2018), and in the CFTI5Med catalogue (Guidoboni et al., 2018), as well as some other unpublished research data. The resulting inventory is reported as **Supplementary Dataset 2**. It contains a list of 245 studies referred to 102 earthquakes with related parameters and also the primary sources. For each event, we also evaluated the state of knowledge through the critical analysis of data and sources.

[2]https://emidius.mi.ingv.it/ASMI/index_en.htm

This process mainly focused on the evaluation of the reliability of the primary sources – direct or indirect, coeval or later, local or external to the island etc. – and on the existence of explicit references to the earthquake effects at Ischia. In the inventory, we tracked any specific doubt or issue that emerged, for future investigations. As a result, we distilled the content of the inventory by removing fake and doubtful events potentially generated by other phenomena, and those generated by seismic sources located outside the volcanic system of Ischia. The analysis allowed eliminating 24 events. Among these, it is worth mentioning some events which derived from the misinterpretation of historical sources (e.g., 28–29 July 1762, 1852) and the events of the 1880 seismic sequence located near the Pontine islands (80 km NW of Ischia). The same occurred for more recent earthquakes, such as the 1980 one, now relocated by instrumental data in the Tyrrhenian Sea, and the 1983 event relocated in the Campi Flegrei area.

For several other events, the review of the basic information posed significant doubts about their origin. The most evident situation is when the occurrence of an earthquake is not explicitly reported in the original documents, but it derives from the interpretation of other phenomena to which it could be potentially associated. For example, large landslides may be interpreted as triggered by a strong earthquake (e.g., the one that occurred in 1228), and volcanic eruptions are potentially associated with earthquake swarms. Detailed discussions about these events can be found in Buchner (1986), Civetta et al. (1999), Polara and De Vivo (2011), Guidoboni and Comastri (2005), Gialanella (2013), de Vita et al. (2013), Cubellis and Luongo (2018), and Cubellis et al. (2020). In these cases, we indicated a record in the catalogue reporting "questionable" in the column "Notes".

In a few cases, we also found groups of events not distinguished in terms of time and intensity (e.g., 1883/07/28 or 1932/02/12). In these cases, we indicated a record in the catalogue reporting the information about multiple events in the column "Notes".

In conclusion, the inventory of the historical earthquakes referring to Ischia consists of 102 events, 24 fake ones, and 5 doubtful ones.

Step 2: Homogenization of Intensity Data

The rich bibliography available for the historical earthquakes of Ischia includes studies based on different geographic positioning of the localities therein analysed; this makes original intensity data (both values and distribution) not directly comparable to each other. In order to overcome this problem, we applied a homogenization procedure to univocally define a locality and, hence, to produce comparable seismic histories as well as earthquake parameters (see next section).

As a first step, we adopted the same national geographic gazetteer used in DBMI15 (Locati et al., 2019), which grants the unequivocal association of a place name with a pair of geographical coordinates (lat, long, ID, place name and other geographical and administrative information). The intensity data available in the literature have been therefore assigned to this geographic reference, which includes municipalities and main

inhabited localities. Because of the dense urbanization of the area and the strong decay of intensity in very short distances, we also added new points to the gazetteer in order to better sample the macroseismic effects in the several minor settlements spread in the territory. Details on the implementation of the gazetteer's localities for Ischia are provided in **Supplementary Appendices**.

The above operation has been accompanied by the homogenization of the MDPs available in the literature. For the best-documented earthquakes (namely 1828, 1881, and 1883), we generally grouped the great number of original MDPs into the reference localities, but we also did the reverse, i.e., we ungrouped information referred to a locality into new sites if adequately supported by the historical sources. When available, alternative studies about the same earthquake were considered. For 49 minor events, the historical information has been instead reviewed and new MDPs were produced. Details of this revision are reported in **Supplementary Appendices**. The adopted intensity scale is MCS (Cancani, 1904; Sieberg, 1912).

In total, we obtained new (revised or produced ex-novo) MDPs distributions for 54 earthquakes, which significantly improved the ASMI database. The MDPs for the largest known earthquakes in Ischia (1828, 1881, 1883, and 2017) are reported in **Figure 2**.

Step 3: Parameterization of Historical Earthquakes

The seismotectonic features of Ischia required specific procedures for defining the epicentral parameters of the historical events from intensity data, particularly regarding the epicentral location and the magnitude determination. As for the latter, it is widely recognized that the use of regional intensity-magnitude relationships is inappropriate in volcanic areas (for Italy, see for example the Etna case in Azzaro et al., 2011) that are typically characterized by extremely shallow hypocentres like Ischia (depth = 1–2 km; e.g., Cubellis et al., 2020). On the other hand, the low number of events recorded in recent times (D'Auria et al., 2018) prevents the formulation of specific relationships. To better interpret spatio-temporal variations and characterize the seismic hazard and risk, it is critical to homogenize the parameters from different data sources, characterizing as much as possible the existing uncertainty. In the following, we shortly describe how this was achieved for Ischia.

Epicentral Location

The epicentral location from intensity data is routinely calculated in the CPTI15 catalogue through the latest version of the "Boxer" code (4.0; Gasperini et al., 2010). Also for Ischia, we applied the simplest technique for the determination of the epicentre – the so-called "Method 0" – that is calculated as the centre of gravity (truncated average of their coordinates) of the sites with highest intensities, since it proved to be robust in case of poor intensity datasets and provided reliable results at Etna, where the macroseismic features are similarly characterized by high-intensity attenuation and the extreme concentration of damage in small zones.

The results of the location estimation are reported in **Figures 3A,B**; note that the areas represent only the uncertainty of the epicentres and do not indicate any source geometry.

Given the dense urbanization of Ischia, an estimation of location uncertainty is of primary importance. To this end, we first defined a reliability index for the location of the earthquakes, based on the number of data available: VL (Very Low) for 1 MDP; L (Low) for 2–5 MDPs; H (High) for MDPs >5. For events labelled as VL, we did not provide an estimation of the epicentre while for those labelled as L we calculated only the epicentre, since data are considered not suitable for quantifying the related uncertainty. Finally, epicentre and related uncertainty are reported for all the events classified as H. To do this, we exploited the bootstrap method implemented in Boxer 4.0: the code fits a 2D Gaussian distribution, quantifying its 2×2 covariance matrix.

For the earthquakes documented by multiple studies (1828 and 1883), discarding any "unconventional" operation of average among the different intensity values available for a given locality, the solution usually adopted in literature is to reassess intensity starting from the reanalysis of the historical sources and to produce an unified set of MDPs for each earthquake from which an epicentral solution was calculated anew. This approach requires bringing together the authors of all the existing historical studies overcoming the different macroseismic interpretations, to reduce existing epistemic uncertainty. Here, given the purpose of the present paper, we prefer to adopt a different strategy that aims at quantifying the uncertainty arising from alternative interpretations, in order to evaluate its impact on the definition of earthquakes' parameters. Starting from the epicentral solutions and related uncertainty from the geographically homogenized data of the multiple studies, we integrated them with an ensemble model (Marzocchi et al., 2015). Ensemble modelling consists of fitting a parent distribution to the available alternative models to quantify the emerging epistemic uncertainty, weighting each alternative by their credibility. Ensemble modelling represents an evolution of the Logic Tree technique usually adopted in seismic hazard quantification, and provides more robust results when few alternatives are available (for more details, see discussion in Marzocchi et al., 2015 and reference therein). In doing this, we assigned the same weight to the available solutions, merging the best guess location and the related uncertainty. The ensemble model is obtained by fitting a Gaussian distribution through the Maximum Likelihood Estimation using a sample of locations obtained combining two samples with equal size from the individual input uncertainty distributions (Selva et al., 2014, 2018).

The results of the ensemble models are shown in **Figure 2**, together with the individual Boxer solutions. The two datasets for the 1828 event (see **Supplementary Appendices**) provide slightly different epicentral estimations, the one revising Alessio et al. (1996, see **Supplementary Appendices, section 2.1.1**) covering almost entirely the uncertainty area associated with the solution revising Guidoboni et al. (2018; see **Supplementary Appendices, section 2.1.2**, Ciuccarelli et al., 2018). Thus, the ensemble model extends to almost the larger entire area

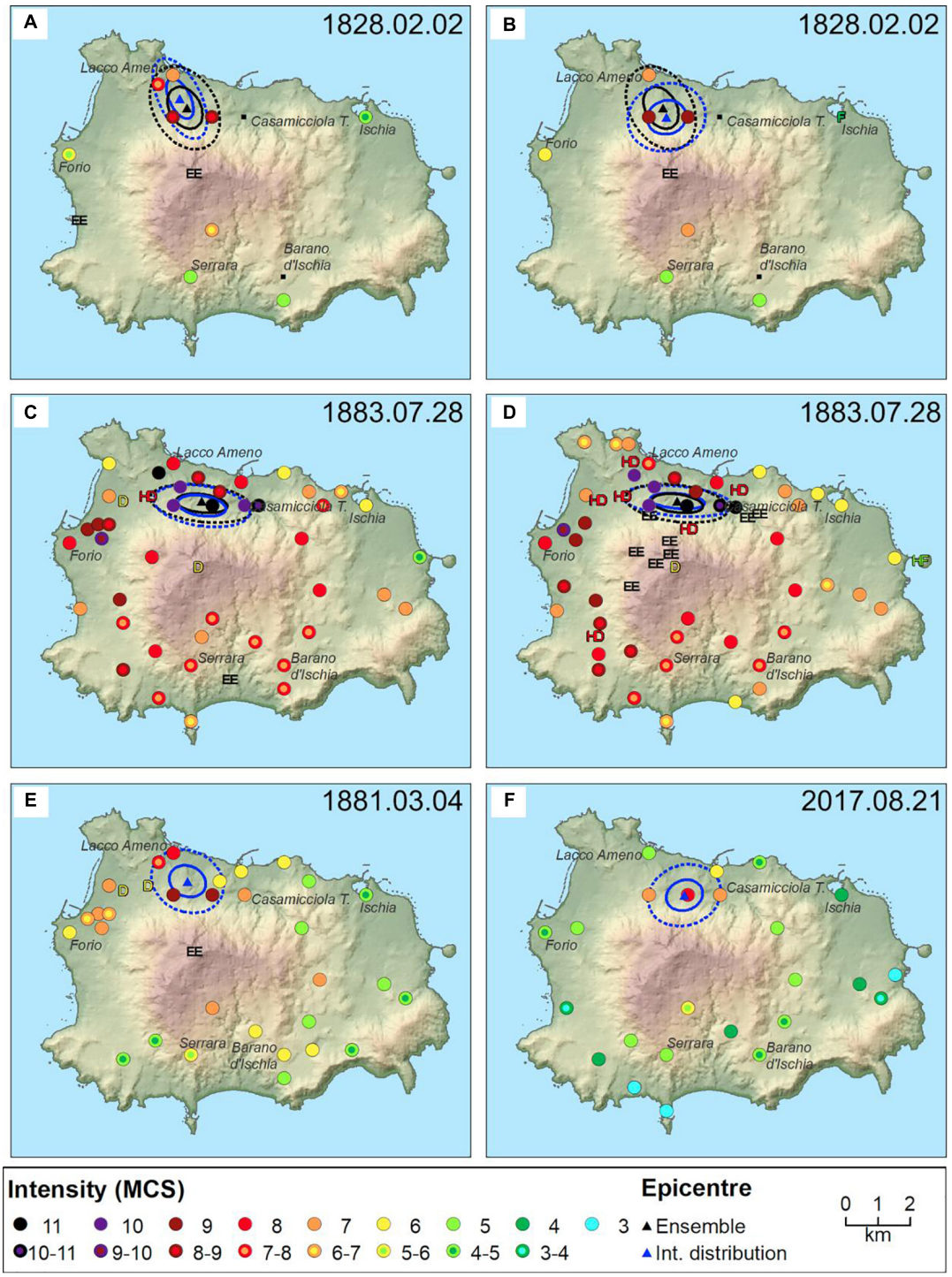

FIGURE 2 | Intensity maps of the largest earthquake of Ischia. Coloured circles are MDPs; blue triangles, solid and dashed lines represent the location uncertainty distribution (best guess; 1 and 2 σ areas, respectively) for all the earthquakes. When multiple studies are available for the 1828 **(A,B)** and 1883 **(C,D)** events, the location uncertainty distribution represents also the ensemble of the available models (in black, see text for details). When only one study is available [1881 in panel **(E)**; 2017 in panel **(F)]**, the ensemble and the study results coincide. EE stands for Environmental Effects.

of uncertainty, with the highest probability in the area in common to the two individual studies. As for the 1883 earthquake, the two studies available (Cubellis and Luongo, 1998; Ciuccarelli et al., 2018; see **Supplementary Appendices**) produce similar locations, so the ensemble model does not differ much from either individual study, with the zone

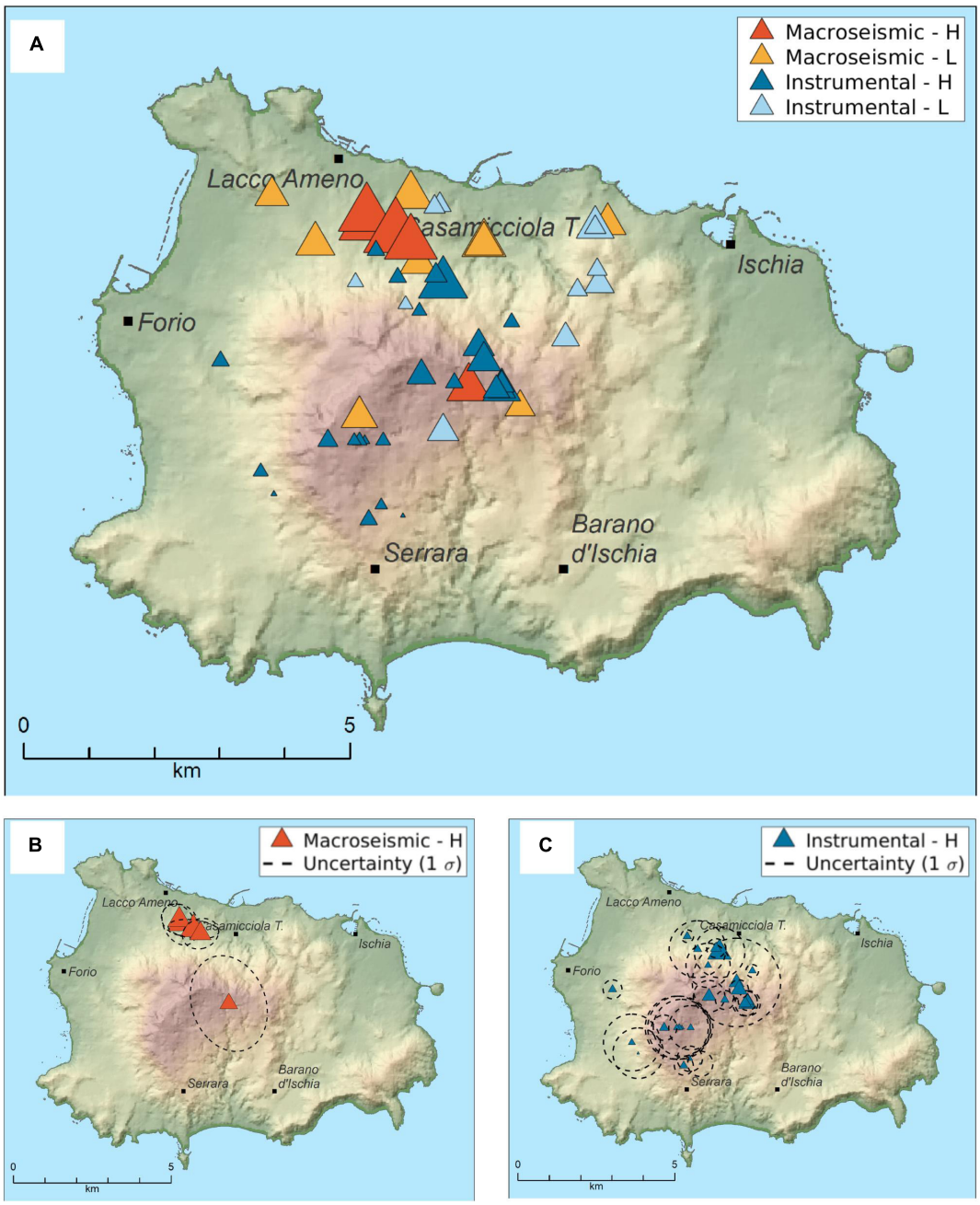

FIGURE 3 | Location of earthquakes. **(A)** Location map of the earthquakes included in the macroseismic and instrumental catalogues. The size of the symbols is proportional to the magnitude, while H and L indicate high and low-quality solutions, respectively. **(B)** Location uncertainty for the macroseismic catalogue (only class 'H' event). **(C)** Location uncertainty for the instrumental catalogue.

of highest probability (1 sigma) substantially covering the maximum damage area.

Magnitude

Because of the lack of a specific intensity-magnitude relationship (hereinafter IMR) for the seismicity of Ischia, we built ensemble models taking into account alternative IMRs produced for other Italian volcanic areas, namely Campi Flegrei and Etna, where high values of epicentral intensity are associated to low to moderate magnitude, similarly to Ischia. Given that the reference magnitude for the CPTI15 catalogue is the moment magnitude M_w, while for the instrumental magnitude is traditionally M_d (see Section "Magnitude"), we produced ensemble models for both the magnitude scales. Considering that CPTI15, in analogy to Etna, estimated the magnitude M_w for the Neapolitan volcanoes using first an IMR to estimate M_L (Richter, 1935; Gasperini, 2002) from

the intensity (Azzaro et al., 2011) and then converted M_L to M_w, we also considered procedures to quantify M_w passing through the estimation of M_L.

For Campi Flegrei, Marturano et al. (1988) proposed two IMRs (linear and logarithmic, hereafter MAR88lin and MAR88log, respectively) obtained from few macroseismic data of the bradiseismic crisis of 1982–1984, calibrated on the duration magnitude M_d (Branno et al., 1984; Marturano et al., 1988). Since neither model reports uncertainty in the model parameters, we reconstructed the input data to reproduce the best-guess linear and logarithmic IMRs (see Figure 9 in Marturano et al., 1988) with the same methodology adopted in the original paper (standard least-square). We obtained a standard deviation of residuals equal to 0.51 and 0.49, respectively.

A M_d-M_w relationship has been produced by Petrosino et al. (2008; hereinafter PET08; **Figure 4A**), calibrated on the instrumental magnitude range 0–4 through a standard least-square procedure. Adopting the fit of Petrosino et al. (2008), the uncertainty on M_w evaluation from M_d results 0.30 (1 standard deviation, evaluated from the original data). With a similar procedure, PET08 produced a $M_L - M_w$ relationship, with uncertainty on M_w evaluation of 0.13.

For Etna, a large set of instrumental and macroseismic data was used by Azzaro et al. (2011; hereinafter AZZ11) to derive the IMRs for M_d and M_L, adopting a standard least-square procedure. The authors indicate the standard deviation of the residuals as 0.12 for M_d and 0.36 for M_L. The conversion from M_L to M_w can be then obtained through the relationship by Saraò et al. (2016; hereinafter SAR16), calibrated on a large set of instrumental data (magnitude range 2.1–4.8) adopting an orthogonal least-square relationship, with a reported uncertainty on M_w of 0.2 (Saraò et al., 2016).

Here we considered the available IMRs to define 3 alternative procedures for estimating M_d (models D1 to D3) and 5 for M_w (models W1 to W5), as reported in **Table 1**. Note that AZZ11 combined with SAR16 (model W5) and PET08 (model W1) was previously adopted in CPTI15 for estimating M_w at Etna and Neapolitan volcanoes, respectively. To account for the uncertainty of each of these procedures, the ensemble takes in input not only best-guess estimates, but also sets sampling the existing uncertainty. Notably, all the models are accompanied by the quantification of uncertainty on the final magnitude, for which we assume a normal distribution with a standard deviation equal to the uncertainty declared in the original study. To propagate the uncertainty also in the models that consider the sequential application of two relationships (namely the ones to obtain M_w: models W1 to W5), we applied a sequential sampling procedure. We first sampled the first uncertainty distribution and then, for each sampled value (M_L for W1 and W5, M_d for W2, W3 and W5), we applied the second relationship to obtain Mw, sampling also its uncertainty. In this way, we obtained samples of M_w that propagate the uncertainty of both models.

These 3 + 5 models represent all the possible procedures, but they cannot be considered equally credible. In particular, MAR88lin and MAR88log models derive from similar data and mainly differ for large magnitudes, which are outside the

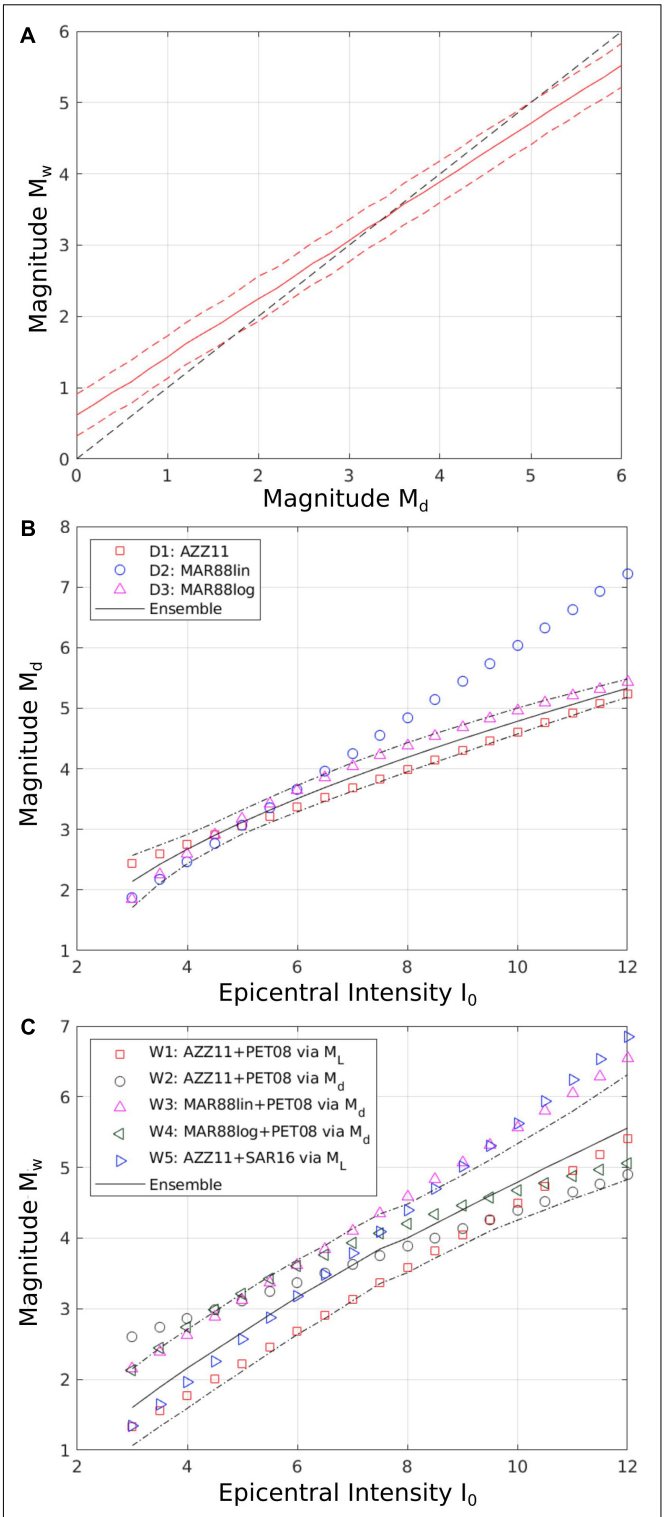

FIGURE 4 | Relationships among magnitudes and intensity. **(A)** M_d to M_w relationship from Petrosino et al. (2008). Solid and dashed lines refer to the best guess model and uncertainty bounds (+/–1 sigma, red dashed lines), respectively. The relationship is compared with a 1: 1 relationship (black dashed line). **(B)** The ensemble model (mean and +/–1 σ) compared with the ensemble members for the IMR of M_d. All the alternative methods are defined in **Table 1**. **(C)** Same as panel (B), but for M_w.

TABLE 1 | Alternative methods adopted to estimate M_d and M_w.

Target magnitude	ID	Label of Figure 4	Description
M_d	Method D1	AZZ11	Based on Etna data
	Method D2	MAR88lin	Based on Campi Flegrei data, with a linear regression
	Method D3	MARlog	Based on Campi Flegrei data, with a logarithmic regression
M_w	Method W1	AZZ11+PET08 via M_L	M_L from AZZ11 combined with the $M_w - M_L$ relationship of PET08
	Method W2	AZZ11+PET08 via M_d	from AZZ11 combined with the $M_w - M_d$ relationship of PET08 (IMR currently implemented in CPTI15 for earthquakes in the volcanic area of Naples)
	Method W3	MAR88lin+PET08 via M_d	M_d from MAR88lin combined with the $M_w - M_d$ relationship of PET08
	Method W4	MAR88log+PET08 via M_d	from MAR88log combined with the $M_w - M_d$ relationship of PET08
	Method W5	AZZ11+SAR16 via M_L	M_L from AZZ11 combined with the $M_w - M_L$ relationship of SAR16 (IMR currently implemented in CPTI15 for earthquakes in the Etna region)

magnitude range of the original calibration. Given that MAR88lin calculates unrealistically high magnitudes, which for the largest intensities would require too large fault sources for the size of the island and its seismogenic sources, we prefer not to include in the ensemble the models performed with this relationship (Model D2 and W3 for M_w). For M_d, the remaining models (D1 and D3) were weighted equally for all intensities. For M_w we adopted a more elaborate strategy. Model W2 provides a slope markedly different from the other models, leading to relatively large magnitudes for low intensities and vice versa, and therefore we decided to remove it from the ensemble. The remaining models (W1, W4, and W5) were differently weighted for low ($I_0 <$ VIII) and high ($I_0 \geq$ VIII) epicentral intensities. Considering that Campi Flegrei may be considered a volcano-tectonic environment more similar to Ischia, but high intensity and magnitude values are available only for Etna, we defined the following weights: for $I_0 <$ VIII, a weight of 2 is given to models including PET08 relationship (Models W1 and W4), and a weight of 1 to the remaining model (Model W5); for $I_0 \geq$ VIII, equal weight is assigned to all the models (W1, W4, and W5).

The ensemble models are then obtained as in Section "Epicentral Location", by fitting a Gaussian distribution through the Maximum Likelihood Estimation using a sample of potential values of M_d and M_w obtained by combining different samples related to the single models, whose size was proportional to the credibility weight of each model (Selva et al., 2014, 2018). The results are shown in **Figures 4B,C**, while the numerical results are reported in **Table 2**.

In general, the ensemble models show a good coherence with the dimensions of seismic sources in such a volcano-tectonic setting, that is, high intensities can be reached with relatively low magnitudes, given that the earthquake hypocentres are very shallow. The seismic cut-off is located at about 2 km depth due to the high geothermal gradient (150–220°C/km) while causative faults display short lengths because of the extreme fracturing of the shallow crust. These structural conditions limit the maximum possible magnitude estimated between 5.3 and 5.8, considering different assumptions (Carlino et al., 2006; Luongo et al., 2006; Castaldo et al., 2017; Cubellis and Luongo, 2018; Nappi et al., 2018; Cubellis et al., 2020). In **Figure 5**, we report the magnitude estimations for all the earthquakes in the macroseismic catalogue.

In order to verify the ensemble IMRs, we compared the ensemble models with the instrumental magnitudes of the two earthquakes for which both instrumental and macroseismic intensity estimations are available. This comparison is blind, since these data have not been used for setting up the models. The 2017 earthquake had an epicentral intensity I_0 = VIII (Azzaro et al., 2017) and several magnitude estimations in the literature. In **Figure 6A**, we compare these data with the probability distributions for an intensity I_0 = VIII; both ensemble models (for M_w and M_d) are in good agreement with the instrumental estimates. In **Figure 6B**, we report the comparison for the 2008 earthquake, with I_0 = V (Cubellis and Marturano, 2009). In this case, even if the ensemble model for M_w appears compatible with data, the one for M_d appears significantly biased toward higher magnitudes, also considering an uncertainty of 0.3 on the instrumental M_d. We note, however, that both the ensembles would be compatible considering a lower epicentral intensity (I_0 = IV).

While for the 1883 earthquake the alternative studies (Cubellis and Luongo, 1998; Ciuccarelli et al., 2018; see **Supplementary Appendices**) indicate the same epicentral intensity (I_0 = XI), for the 1828 earthquake the two available studies provide two slightly different intensities (I_0 = VIII-IX and IX, respectively). As made in Section "Epicentral Location", we fitted a 1D Gaussian ensemble model with the Maximum Likelihood Estimation from a sample of potential input magnitudes from both models. As expected, the obtained ensemble in **Figure 5C** shows a distribution centred at an intermediate level, slightly

TABLE 2 | Numerical values for the obtained IMRs for M_w and M_d.

Epicentral intensity I_0	M_w		M_d	
	μ	σ	μ	σ
IV	2.2	0.6	2.7	0.2
V	2.7	0.6	3.1	0.2
VI	3.2	0.5	3.5	0.2
VII	3.6	0.5	3.9	0.2
VIII	4.0	0.5	4.2	0.2
IX	4.4	0.5	4.5	0.2
X	4.8	0.5	4.8	0.2
XI	5.2	0.8	5.1	0.2

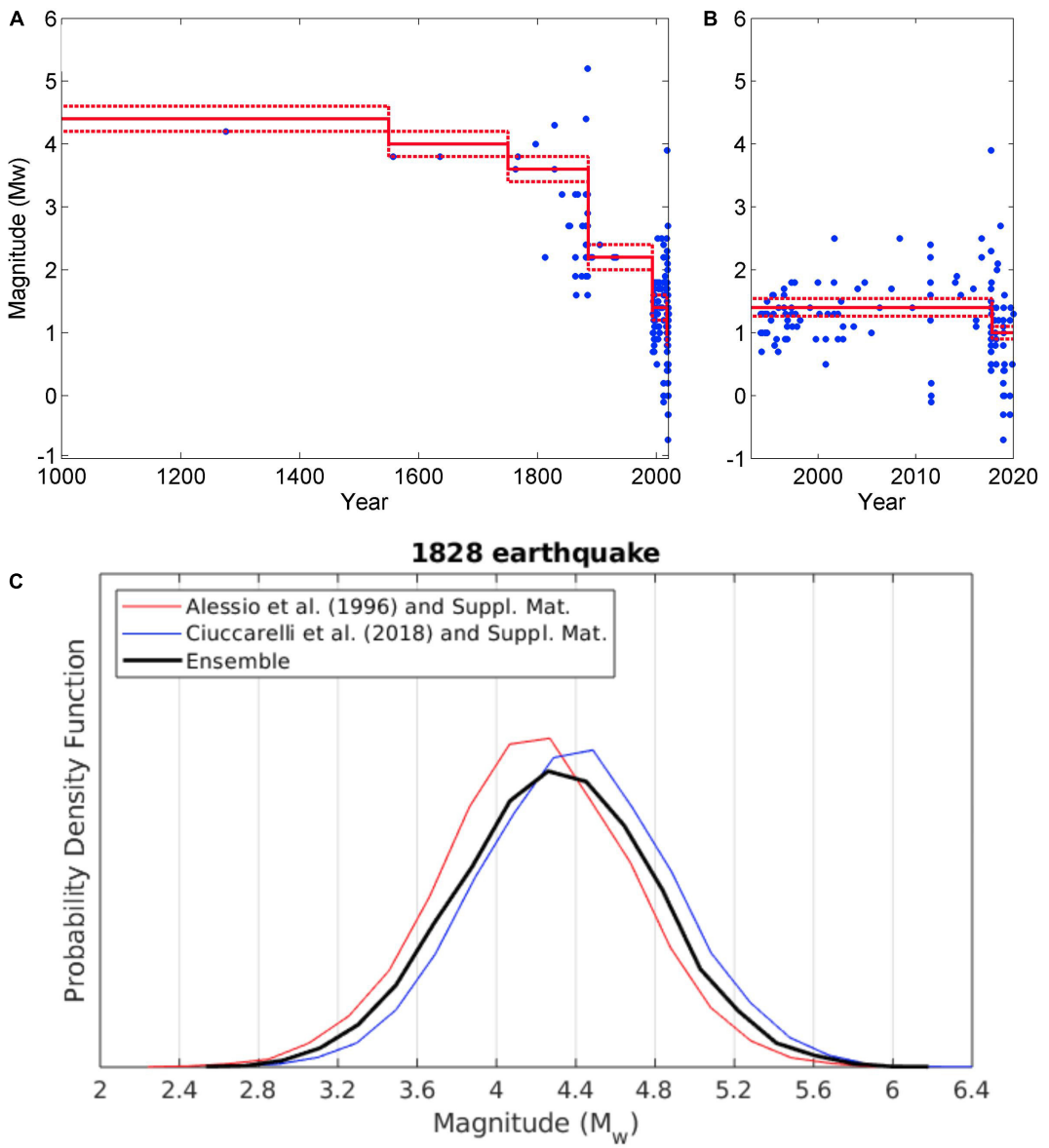

FIGURE 5 | Magnitude (M_w) vs time and completeness, as estimated in Sections "Historical Completeness" and "The Sensitivity of the Instrumental Network and Completeness": **(A)** time-span 1000–2019; **(B)** time-span 1993–2019. The red lines indicate the best guess value for the completeness magnitude (defined in Section "Magnitude-Frequency Distribution", based on the results of Sections "Historical Completeness" and "The Sensitivity of the Instrumental Network and Completeness" for the historical and the instrumental catalogues, respectively); the dotted red lines report the assumed uncertainty bounds (+/– 0.2 M_w) for the completeness magnitude used to check the stability of parameters of the magnitude-frequency distribution (more details in Section "Magnitude-Frequency Distribution"). **(C)** Ensemble magnitude estimation for the 1828 earthquake compared with ensemble's members (more details in Section "Magnitude").

more dispersed than the original distributions. Noteworthy, the uncertainty of I_0 derived from the alternative MDPs is significantly smaller than the one resulting from the IMR.

Historical Completeness

The long-term seismicity of Ischia appears rather discontinuous and fragmentary, mainly for the most ancient periods. In general, the lack of events in a given historical period does not necessarily indicate a seismicity gap but rather a break in the continuity of information from the contemporary sources (Valensise and Guidoboni, 1995; Stucchi et al., 2004; Cubellis and Luongo, 2018). This situation may depend on several reasons related to both the territory and the social or political context. As for the Neapolitan region and Ischia, a detailed description of the historical situation from Antiquity to recent times is reported in **Supplementary Appendices**. In the following, we shortly recall the main facts referred to Ischia to evaluate the degree of completeness of its seismic history.

During the Greek and Roman periods (VIII BC – V century AD), Ischia was populated mainly along the coast

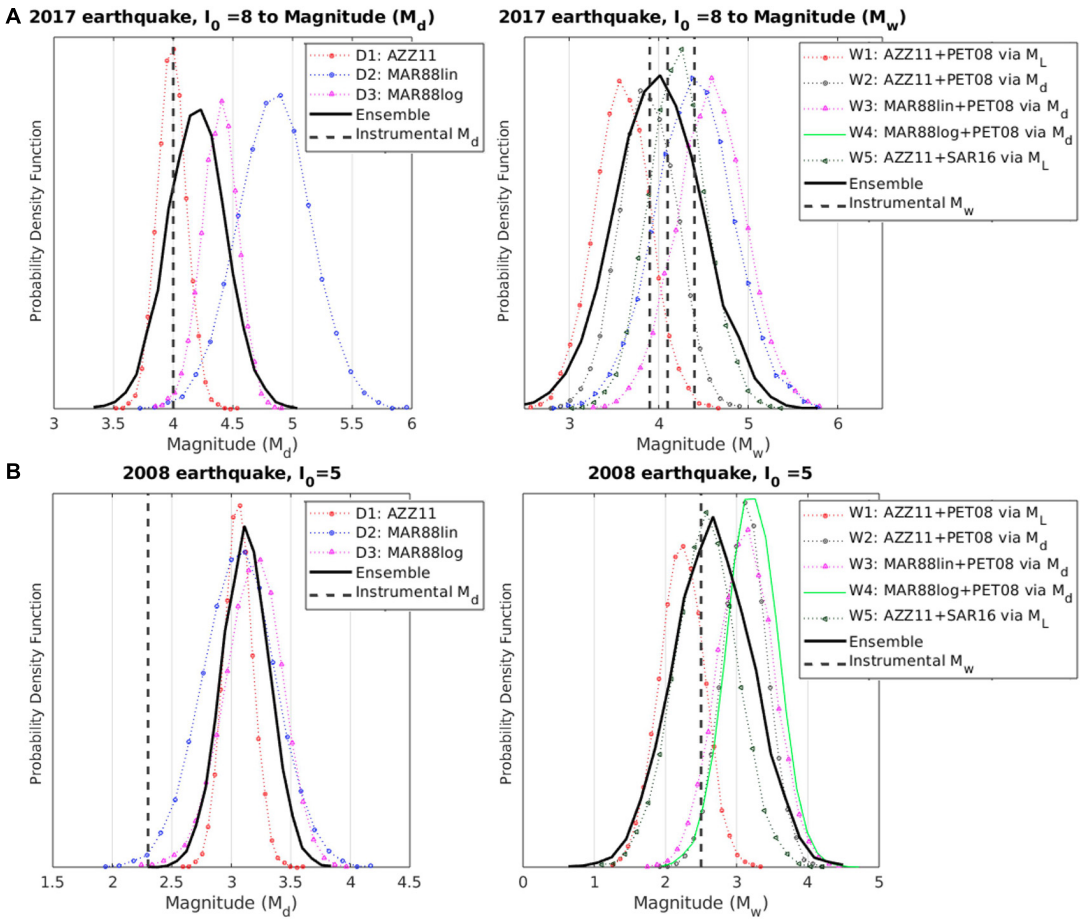

FIGURE 6 | Comparison between instrumental estimations and ensemble Magnitudes estimations: **(A)** for the August 21, 2017 Casamicciola earthquake (I_0 = VIII, Azzaro et al., 2017; M_w 3.9 in Osservatorio Nazionale Terremoti (ONT; http://cnt.rm.ingv.it/en/event/16796811); M_w 4.1 in De Novellis et al. (2018); M_w 4.1/3.9 in Braun et al. (2018), considering/not considering CLVD component); M_w 4.4 in Montuori et al. (2018), considering the entire deformation, therefore potentially overestimated); M_d = 4.0 in D'Auria et al. (2018); M_B = 4.3 for EMSC; M_B = 4.1 for USGS); **(B)** for the April 5, 2008 event (I_0 = V; Cubellis and Marturano, 2009).

(Delizia, 1987). The available sources for this period have recorded only earthquakes associated with eruptions, which dramatically impacted the inhabitants. In the early Middle Ages (VI-X century AD), Ischia was scarcely inhabited (Buchner Niola, 1965; Cundari, 1998) and no information is available about local seismic activity. Starting from the XI-XII centuries, the island began to be part of a wider economic and administrative context for the extraction of alum but, unfortunately, the relevant administrative documents were lost during the Second World War bombardments in Naples. In the XIII century, some contemporary sources recorded two natural events of significant impact for the island, a landslide in 1228, and an earthquake in 1275.

The 1302 eruption caused a serious impact on mining, agricultural, and fishing activities, determining a depopulation of Ischia until the second half of the XVI century. As a consequence, in the time-span XIV-mid-XV century, there is a substantial lack of information about facts and events of the island, and probably the apparent lack of seismic events cannot exclude the occurrence of moderate earthquakes (I_0 < VIII MCS), having left no traces in the few written sources of that time. Starting from the late-XV century, the role of thermal baths became increasingly important for Ischia: the settlements grew and the thermal treatments became the main activity, mostly at Casamicciola. Thus in the XVIII-XIX centuries, thanks to the proximity to the Neapolitan area, the island represented an elite destination for Italian and European tourism, so for this period it is very likely that also traces of events of lower intensity should have been reported. This condition of cultural interest for the "geological" events occurring in Ischia was strengthened by the foundation of the Osservatorio Vesuviano in Naples in 1841 and, lastly, of the Osservatorio Geodinamico in Casamicciola in 1885.

In conclusion, the results of the analysis of the historical completeness reported in **Table 3** show that the catalogue can be considered complete starting from the mid-XVIII century as regards events of moderate intensity ($I_0 \geq$ VII MCS), while the completeness for low intensity earthquakes ($I_0 \geq$ IV MCS) significantly jumps to 1885, when the first local seismic monitoring system was installed at Ischia (Luongo et al., 2012).

TABLE 3 | Completeness of the macroseismic and instrumental catalogues of Ischia, based on historical considerations and network sensitivity tests, respectively.

	Period	Comment	Original threshold	M_w threshold
Macroseismic catalogue	VIII BC – V century AD	Only earthquakes connected to eruptions large enough to force the abandonment of the island	–	–
	VI – X century AD	No information	–	–
	XI– first half of XVI century AD	Likely completeness for destructive earthquakes	$I_0 \geq$ IX MCS	4.4
	Second half of XVI– first half of XVIII century AD	Complete for destructive earthquakes	$I_0 \geq$ VIII MCS	4.0
	Second half of XVIII century AD – 1885	Complete for moderately damaging earthquakes	$I_0 \geq$ VII MCS	3.6
	1885 – today	Complete for earthquakes felt from people	$I_0 \geq$ IV MCS	2.2
Instrumental catalogue	1993 – Oct 2017	Before updating the network in 2017	$M_d \geq 1.0$	1.4
	Nov. 2017 – present	After the end of the updating phase, at the end of October 2017	$M_d \geq 0.5$	1.0

INSTRUMENTAL CATALOGUE: 1993–2019

The first seismic sensor deployed on the island of Ischia dates back to 1885, when G. Grablovitz installed a seismic tank in the newly founded Casamicciola observatory (Grablovitz, 1901; Grablovitz, 1902-1903; Ferrari, 2009; Luongo et al., 2012). The first modern seismic station was installed in the same location by the Osservatorio Vesuviano (hereinafter INGV-OV) (station OC9) in 1993. Since then, the seismic network has been regularly improved up to the present state.

The current network is the result of a first set of three analogue stations integrated over the years with digital ones (D'Auria et al., 2018). Since 2015 the network counted 4 sites instrumented with 3 analogue velocimeters (OC9, FO9, and CAI), 3 digital velocimeters (IOCA, IMTC, and IFOR), and 1 accelerometer (IOCA). After the 2017 earthquake, the network was upgraded with 5 sites instrumented with velocimeters and/or accelerometers of the permanent seismic network and up to 6 seismic stations of the temporary network (Galluzzo et al., 2019). The configuration of the seismic network since late July 2018 until present is reported in **Figure 1B**, while the complete list of stations, time of installation, and sensor type is reported in **Table 4**.

The most recent instrumental seismic catalogue of Ischia, presented by D'Auria et al. (2018), contains earthquakes located or detected from January 1999 until February 2018. Instrumental earthquake data are routinely produced by INGV-OV and periodically updated, and made available on the web (the Ischia instrumental online catalogue)[3]. The catalogue includes origin time, duration magnitude, and, when possible, location estimation. In some cases, in order to save information on the occurrence area of a seismic event, the catalogue is integrated with the indications of the felt area.

As detailed in the next subsections, to enlarge the instrumental dataset and make it comparable with the macroseismic catalogue, we revised the published instrumental catalogue (D'Auria et al., 2018) by (i) extending its time to the pre-1999 period, (ii) better characterizing location uncertainties, iii) enriching magnitude estimation by adding a derived M_w to the usually estimated M_d, and reporting also the estimation uncertainty. Then, we evaluated the completeness of the revised catalogue.

The revised catalogue, updated for the time-span from 1991 to 2019, is reported as **Supplementary Dataset 3**.

Revision of the Instrumental Seismic Catalogue

Extension to the Pre-1999 Period

The revision of the instrumental seismic catalogue was carried out to reconstruct a robust catalogue of pre-1999 seismicity, since the first modern seismic station was installed in 1993.

The first step was the recovery of the information present in the "Reports on the Surveillance Activity," periodically prepared by INGV-OV and addressed to the Italian Civil Protection Department.

From a first comparison between the Reports and information reported in the paper archives, we found discrepancies requiring a deeper analysis. As a consequence, the archived seismic traces have been visually verified, when still available. This painstaking analysis allowed us to distinguish between local earthquakes and other transient signals such as anthropic events (explosions by abusive fishermen), atmospheric events (thunders), or regional earthquakes.

The re-examination led to the identification of 42 seismic events dated between 1993 and 1998. The maximum magnitude is M_d 1.5 in 1997, recorded by the 3 seismic stations working on the island. Other events of low magnitude were recorded by one or two stations (mainly by FO9; **Table 4**) and therefore not located. Close to FO9, in the south-western sector of the island, some very low energy shallow earthquakes were identified in a small seismogenic area characterized also by a strong geothermal activity (Selva et al., 2019), in the same area where some events were recently located in 2018, after the improvement of the seismic network.

[3]http://sismolab.ov.ingv.it/sismo/index.php?PAGE~=~SISMO/last&area~=~Ischia&rmenu~=~on

TABLE 4 | Seismic stations at Ischia and Procida operated by the INGV Osservatorio Vesuviano.

	Name	Coordinates	Location	Installation	Sensor	Data logger	sps
Permanent network	OC9	0.7468N 13.9014E 123 m	Casamicciola Observatory	1993	MarkL4-3C	Analog	100
	FO9	40.7115N 13.8551E 234 m	Forio Punta Imperatore	1995	MarkL4-3C	Analog	100
	CAI	40.7322N 13.9655E 103 m	Aragonese Castle	1996	MarkL4-3C	Analog	100
	IFOR	40.7115N 13.8551E 234 m	Forio Punta Imperatore	11/2009	Guralp CMG-40T 60s	Digital – GILDA	100
	IOCA	40.7468N 13.9014E 123 m	Casamicciola Observatory	9/2/2011	Guralp CMG-40T 60s Episensor ES-T	GILDA	100200
	IMTC	40.7209N 13.8758E 209 m	Monte Corvo	17/4/2015	Guralp CMG-40T 60s	GILDA	100
	PTMR	40.7614N 13.0349E 100 m	Procida Terra Murata	18/06/2018	Guralp CMG-40T 30s Episensor ES-T	Guralp DM24	100200
	IPSM	40.7462N 13.9439E 10 m	Ischia Porto	2/07/2018	Guralp CMG-40T 30s Episensor ES-T	Guralp DM24	100200
	IVLC	40.7591N 13.8721E 70 m	Villa la Colombaia	27/07/2018	Guralp CMG-40T 60s Episensor ES-T	Guralp DM24	100200
	IBRN	40.7140N 13.9268E 150 m	Barano	26/07/2018	Guralp CMG-40T 30s	Guralp DM24	100
	IMNT	40.7361N 13.9346E 180 m	Montagnone	26/07/2018	Guralp CMG-40T 30s	Guralp DM24	100
Mobile network	T1361	40.7567N 13.8789E 7 m	Lacco Ameno Negombo	26/08/2017	Lennartz LE-3Dlite	Nanometrics Taurus	100
	T1362	40.7346N 13.9100E 303 m	Casamicciola T. Via Pera di Basso	26/08/2017 disinstalled 03/10/2017	Lennartz LE-3Dlite Episensor ES-T	Nanometrics Taurus+Trident	100100
	T1363	40.7455N 13.9135E 50 m	Casamicciola T. Via Cretaio	31/08/2017	Lennartz LE-3Dlite	Lennartz MARSlite	125
	T1364	40.7426N 13.8905E 129 m	Lacco Ameno Hotel Grazia	31/08/2017	Lennartz LE-3Dlite	Nanometrics Taurus	100
	T1365	40.7014N 13.9181E 130 m	Barano Hotel Villa a Mare	18/09/2017	Lennartz LE-3Dlite	Gilda	100
	T1366	40.7373N 13.9046E 213 m	Casamicciola T. Via S. Barbara	03/10/2017	Lennartz LE-3Dlite Episensor ES-T	Nanometrics Taurus	100100
	T1367	70.7435N 13.8952E 81 m	Casamicciola T. Hotel V.Janto	23/10/2017	Lennartz LE-3D/5s	Gilda	100

Epicentral Location

Many events cannot be located, because of their low magnitude and the scarce number of seismic stations deployed on the island. The first located event was a M_d 1.3 earthquake that occurred in 2007. The situation slightly improved in 2015, when the network passed from three to four seismic stations, and further

improved in 2018, when the present-day monitoring network became available (**Figure 1** and **Table 4**).

The fairly low seismicity rate recorded in recent times in Ischia prevented also the development of detailed tomographic images by using local earthquake recordings. Three velocity models are currently used to locate earthquakes on the island (**Figures 7A–C**):

A. The 1D velocity model of the Campi Flegrei;
B. The 1D velocity model of Ischia, described in Capuano et al. (2015);
C. The 3D velocity model described in D'Auria et al. (2008).

The 1D crustal models (model A in green and B in blue) are very similar (model A resulting slightly faster than B) while model C shows the greatest differences. Models B and C were obtained by using data from the SERAPIS tomographic experiment (Judenherc and Zollo, 2004), aimed at defining the velocity model of Campi Flegrei. Therefore, despite the presence of some seismic stations on the islands of Ischia and Procida, the number of seismic rays crossing the crust below Ischia is relatively low, not allowing a detailed tomography. As a consequence, model C has a resolution of 250 m in the Campi Flegrei area which increases up to 1 km for Ischia (whose size is approximately 9 km × 6 km). Model C is characterized by a strong velocity contrast between Campi Flegrei and Ischia, which, in the discretized velocity model, results in a highly heterogeneous vertical layer.

Model A is the one adopted for the locations reported in the instrumental catalogue (see **Figures 3A,C**, **7C**). Locations are performed using the Hypo71 program (Lee and Lahr, 1972). The epicentral errors, ERH, are estimated through the square root of the sum of the estimated latitude and longitude variance while the vertical error, ERZ, can be interpreted as a 68% confidence interval, assuming a chi-squared value of 1.00 (Boyd and Snoke, 1984; Husen and Hardebeck, 2010). As for the macroseismic catalogue, we classified each event in terms of quality. In particular, we assigned a high-quality class when location error is smaller than the island size (5 km) and a low-quality class when it is larger. When the horizontal and vertical errors were not present in the catalogue we reported the lower limit estimate of 10 km, which is already a relatively large value considering the size of the island and its seismogenic structures (Selva et al., 2019; Trasatti et al., 2019). When the estimation of the location was impossible, we assigned a quality class Null (N).

Notably, this estimation does not account for the uncertainty on the velocity model, which can potentially lead to an important underestimation of the effective uncertainty (Husen and Hardebeck, 2010; Garcia-Aristizabal et al., 2020).

An indication of the impact of the uncertainty of the velocity model on the location is provided in **Figures 7C,D**, where the largest earthquakes ($M_d \geq 0.9$) of the 2014–2018 period are located with the A and B velocity models. Note that model B, characterized by higher velocities, tends to spread the epicentres.

To further deepen into the uncertainties introduced by the velocity model and by the use of a small number of stations, we compared the locations obtained with each of the available velocity models for the 3 strongest earthquakes recorded from 2008 to 2018. The analysis, reported in **Supplementary Appendices**, indicates that whether the uncertainty estimation provided by the location algorithm is often small (<0.5 km), the uncertainty due to the velocity models can be very significant. In addition, the possibility of using more stations is critical to reduce location uncertainty. This is indeed particularly important for Ischia, considering its small size and the complex 3D structure (Selva et al., 2019 and references therein).

Magnitude

The magnitude reported in the catalogue is the duration magnitude M_d, based on coda duration, that allows rapid estimates even when the seismic traces are saturated or the signal to noise level is low (Petrosino et al., 2008). M_d is still used to compile the seismic catalogue of Ischia because the magnitude of the recorded earthquakes is usually very low (<2.5) and the seismic stations very noisy. In these cases the M_L often cannot be estimated.

Duration magnitude is estimated using the relationship derived for the Campi Flegrei caldera (D'Auria et al., 2018) and the duration is estimated through the visual analysis of the seismograms. Before 2017, the seismicity of Ischia was characterized by small and shallow events, most of which were detectable only in Casamicciola Terme; therefore it was not possible to define a magnitude-duration relationship. Thus, the scale created for the Campi Flegrei was adopted also for Ischia on the basis of the similar geological and seismological features of the two volcanoes. The duration-magnitude empirical relation can be found in Orsi et al. (2004).

Based on experience, we consider an uncertainty of 0.3 associated with low M_d values. For the events with the highest magnitude ($M_d \gtrsim 4.0$), where the experience cannot be invoked, the uncertainty quantified in the macroseismic catalogue is probably more appropriate (Section "Step 3: Parameterization of Historical Earthquakes").

In order to allow the comparison between the instrumental and macroseismic local and national datasets, we added the estimate of M_d and M_w to both catalogues. For the instrumental one, following the same approach made for the macroseismic part (Section "Magnitude"), we used the $M_d - M_w$ relationship defined by PET08 shown in **Figure 4A**. The uncertainty was estimated by combining the uncertainty of M_d (assuming a normal distribution with $\sigma = 0.3$) with the one of the $M_d - M_w$ relationship (normal distribution with $\sigma = 0.3$, see Subsection "Magnitude" in Section "Step 3: Parameterization of Historical Earthquakes"), that is, similarly to the procedure adopted for the macroseismic catalogue, we sampled both the uncertainty distribution of M_d and, sequentially, the one from the $M_d - M_w$ relationship for each sampled M_d. The M_w uncertainty reported in the instrumental catalogue corresponds to 1 σ.

The Sensitivity of the Instrumental Network and Completeness

Considering the low number of events in the instrumental catalogue of Ischia and the potential nonstationarities of local seismicity (Selva et al., 2019; further discussed in Section "Statistical Characterization of the Seismicity"), we evaluated the

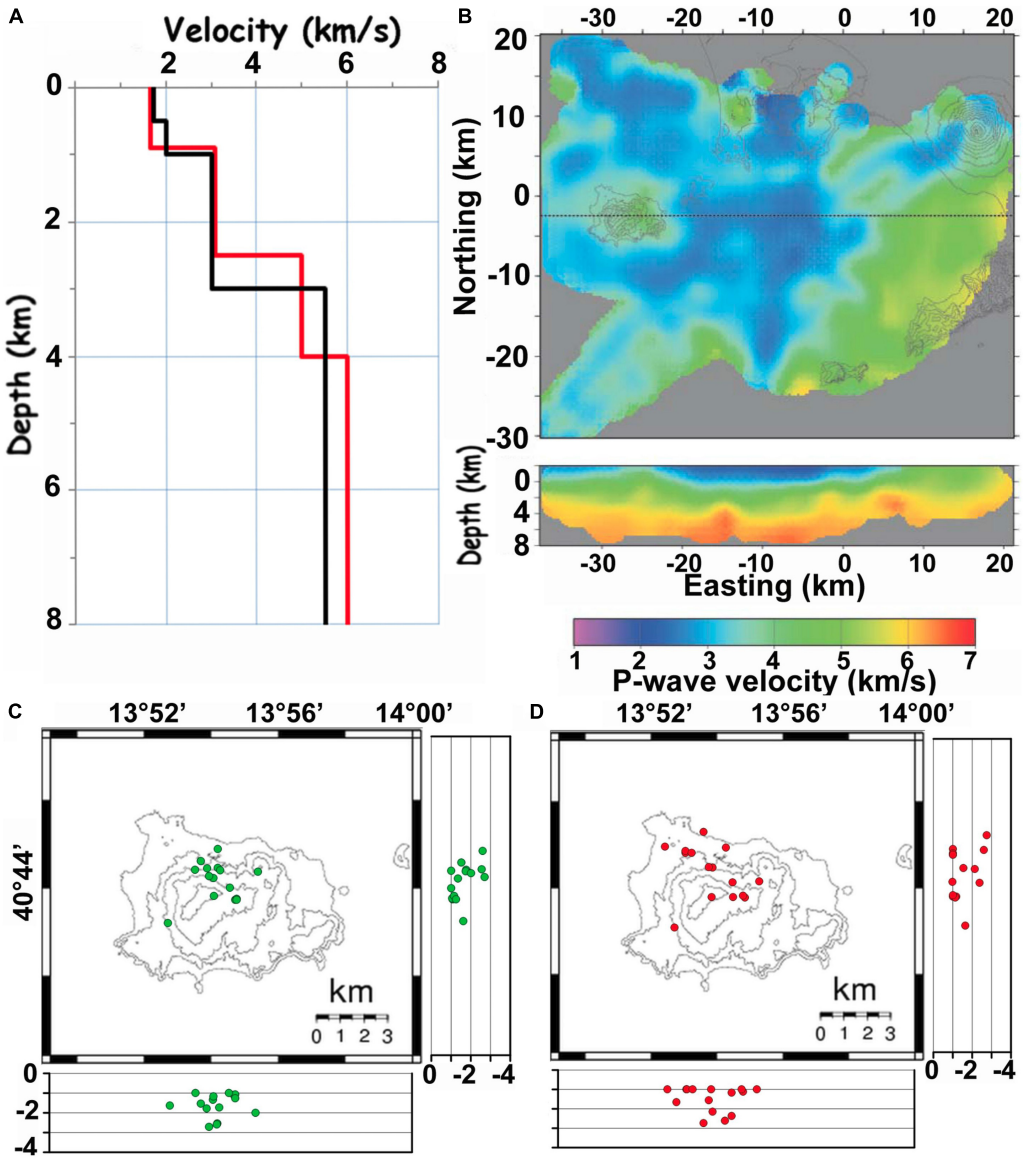

FIGURE 7 | Available velocity models and instrumental locations. **(A)** 1D Velocity models for Campi Flegrei (black, model A in the text) and Ischia (red, model B). **(B)** 3D velocity model for P waves (model C) for the Neapolitan volcanic district (modified from D'Auria et al., 2008). **(C)** Hypocentral location adopting the 1D (model A). **(D)** Same as panel **(C)**, but by the 1D model (model B).

completeness by analysing the sensibility of the seismic networks operating through time, rather than performing statistical analyses (e.g., Schorlemmer and Woessner, 2008; Tramelli et al., 2013a,b). To this end, we applied the SENSI code (Orazi et al., 2013)[4] to the network composed of 4 seismic stations (as it was on August 21, 2017), to the current permanent seismic network (9 stations), and to the integrated seismic network given by the union of the mobile and permanent seismic networks (14 stations).

The simulation of the detection and location threshold was carried out down to a hypocentral depth of 1,500 m because the high thermal gradient determines the ductile-fragile transition at a depth of about 2 km (e.g., Carlino et al., 2006; Castaldo et al., 2017; Cubellis et al., 2020), inhibiting deeper seismicity.

In **Figure 8a–f** we show the minimum magnitude to identify an earthquake with a hypocentral depth of 500 m (panels a, b and c) or 1,500 m (panels d,e, and f) b.s.l. at least at one seismic station. Panels a, d display the detection threshold for a seismic network composed of 4 stations, b and e for the permanent seismic network (9 stations), and c and f for the permanent plus mobile networks (14 stations). As expected, the detection threshold decreases when approaching the stations themselves. The detection performance of the 4 stations seismic network was high (M_d = 0) in the northern area of the island, leaving the

[4]https://zenodo.org/record/4438122#.YAADxHZKiiQ

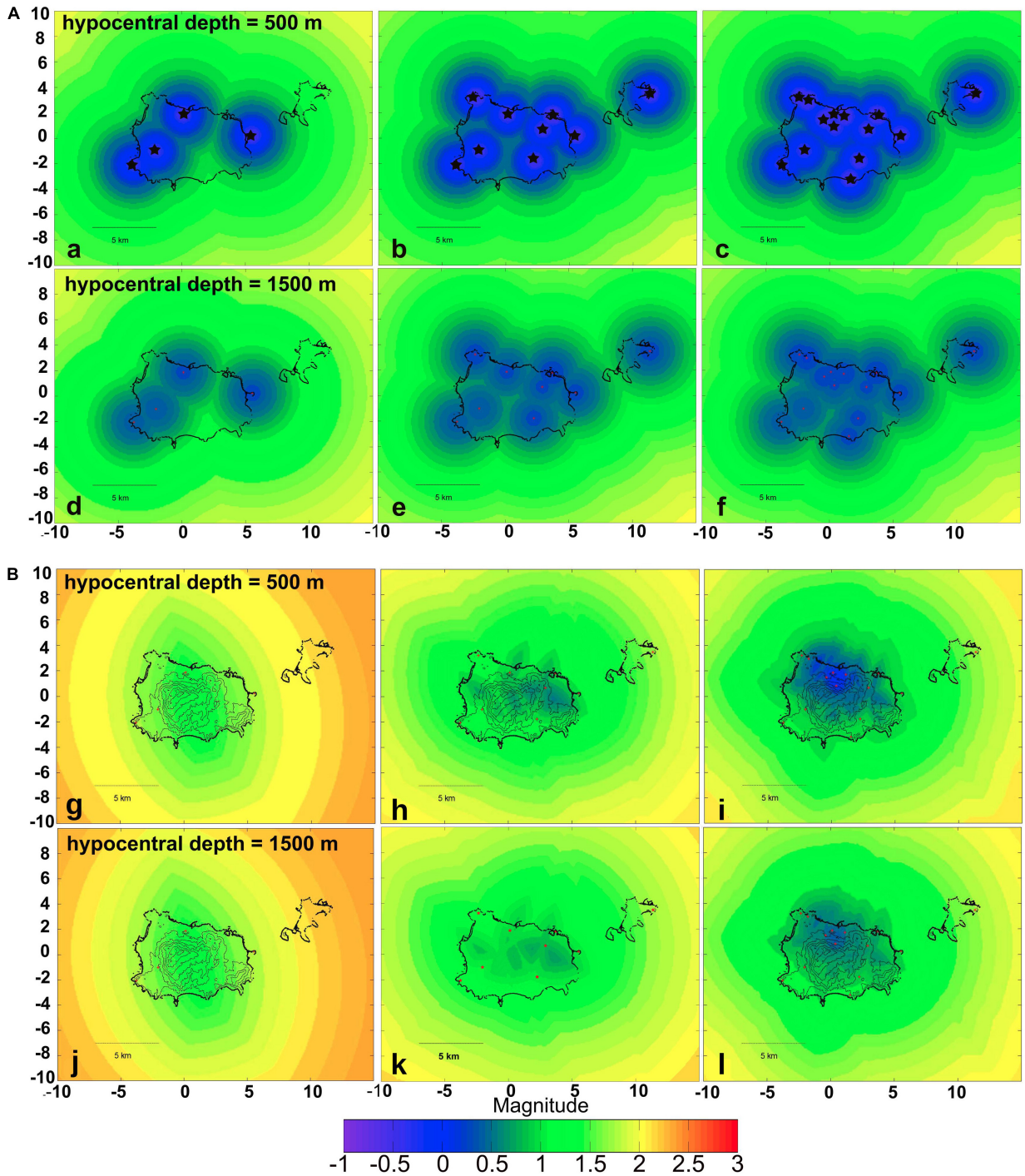

FIGURE 8 | Sensitivity of the instrumental network. **(A)** Detection threshold of the seismic network composed of 4 (left), 9 (centre), and 14 stations (right), for earthquakes with a hypocentral depth of 500 and 1,500 m. The stations' position is indicated with black stars in the top panels [a, b, and c in panel (A)].**(B)** Minimum magnitude for locating (4 recordings at least) events with a hypocentral depth between 500 and 1,500 m of depth, considering a network with 4 stations (left), 9 stations (centre), and 14 stations (right).

southern sector uncovered. Overall, considering that most of the seismicity is very shallow (closer to 500 m than to 1,500 m), an approximate completeness M_d = 1.0 can be assumed, in agreement with M_d 1.3 found in D'Auria et al. (2018).

The permanent seismic network, whose deployment terminated at the end of October 2017, is able to detect shallow earthquakes of magnitude $M_d > 0.5$ in the whole island (panels b, e); again, the best coverage remains in the northern

area (where the historical main seismicity is concentrated). Note that this network also includes a station on the island of Procida, not existing before. The integrated network (permanent plus mobile stations) has a very high coverage in the epicentral area of the 2017 Casamicciola earthquake in order to identify any aftershocks.

Figure 8g–l shows the minimum magnitude to locate an earthquake with a hypocentral depth of 500 m (panels g, h, and i) and 1500 m (panels j, k, and l) b.s.l., picked at 4 seismic stations at least, according to the different network configurations. The localization level of the current permanent seismic network is around $M_d = 1$, reaching $M_d = 0$–0.5 for very shallow earthquakes (depth 500 m) in the central-northern sector of the island. Before the upgrade of the network (concluded in 2018), the location threshold was higher than M_d 1.5 on the whole island.

STATISTICAL CHARACTERIZATION OF THE SEISMICITY

Merging the earthquakes of the macroseismic catalogue (up to 1992) with the ones of the instrumental catalogue (from 1993) leads to a unified catalogue of 252 earthquakes, covering the time-span from the 8th century BC to the end of 2019. Among them, 78 events are the ones above the completeness magnitudes. The merged catalogue is reported as **Supplementary Dataset 4**. This represents the most complete and extended catalogue available for Ischia to date.

With this catalogue, we can attempt to characterize the Ischia seismicity from a statistical point of view, analysing spatial and magnitude-frequency distributions of the earthquakes, and exploring the stationarity process of seismicity.

The completeness of the unified catalogue is defined according to the results of the historical completeness analysis for the macroseismic catalogue (Section "Historical Completeness") and the completeness based on network sensitivity (Section "The Sensitivity of the Instrumental Network and Completeness"), adopting for both the moment magnitude M_w (**Table 3**). In **Figures 5A,B**, the variation of completeness through time is compared with the magnitude estimations reported in the catalogue. Given the small number of events and the difficulty in robustly defining completeness, the impact of the uncertainty on the parameter estimations (b-value and annual rates) is investigated.

Magnitude-Frequency Distribution

First, we estimated the magnitude-frequency distribution of the earthquakes assuming a Gutenberg-Richter (GR) law (Gutenberg and Richter, 1944) with a taper for the strongest events. This tapered GR (Vere-Jones et al., 2001; Kagan, 2002) has a soft bound for the highest magnitude, differently from the hard bound of the classical truncated GR, which instead assumes a maximum magnitude that cannot be exceeded. From a statistical standpoint, we prefer the tapered version of the GR law because it is not possible to estimate the maximum magnitude value of the truncated version of the GR in a proper manner solely based on seismic data, even with a catalogue lasting centuries (Holschneider et al., 2011; Geist and Parsons, 2014).

The tapered GR distribution is described by the equation (Kagan, 2002):

$$F(M) = \left(\frac{M_t}{M}\right)^{\beta} exp\left(\frac{M_t - M}{M_{cm}}\right) \quad (1)$$

where $F(M)$ is the cumulative distribution function for the seismic moment M(F = 1-S, survivor function reported by Kagan, 2002); M_t is the minimum moment; β is the parameter controlling the slope of the distribution, and M_{cm} is the corner moment that rules the tapering of the right tail of the distribution. Since we adopt M_w in our catalogue, we convert the seismic moment in the previous equation using the Kanamori (1977) formula. Comparing with more commonly used parameters and definitions, M_t corresponds to the completeness magnitude, M_{cm} to a "corner magnitude" over which the magnitude-frequency distribution decays quicker than a GR, and β corresponds to 2/3 of the classical b-value. For simplicity, in the following we refer to the classical parameters in terms of magnitude and b-value.

To estimate these parameters, i.e., the cumulative annual rate of events (λ), the b-value, and the corner magnitude, in a catalogue with a time-varying magnitude of completeness, we used the method proposed by Taroni and Selva (2021). This approach couples the maximum likelihood estimation (MLE) proposed by Weichert (1980) and adapted for the tapered GR, with a Monte Carlo Markov Chains (MCMC) computation to properly explore and estimate the uncertainty associated with the parameters, allowing for a joint evaluation of potentially correlated parameters (Keller et al., 2014). The smallest explored magnitude (the minimum among completeness levels) is magnitude M_w = 1.0. Notably, this method allows accounting for time-variable magnitude completeness and it considers in input the annual rates observed in each magnitude bin (including no observations), evaluated according to the estimated completeness for this magnitude (longer time intervals are available for the larger magnitudes). Consequently, this method is less sensible than other ones (like the classical MLE) to the small magnitudes recorded only in the most recent part of the catalogue.

Figure 9A shows the observed and estimated annual rates of the events in the seismic catalogue, while **Figures 9B–D** display the uncertainty associated with these parameters using 10^4 sampling from the MCMC computation. **Figure 9E** represents the scatter plot of the joint estimation of the annual rate and the b-value, which are correlated to each other. Overall, the b-value is significantly larger than 1 and it can be constrained in the range 1.0–1.3, with the best guess value of 1.11. The annual rate λ of $M_w \geq 1.0$ is in the range 4–8 events per year, with the best guess of 5.54 /yr. The corner magnitude uncertainty distribution is almost flat, showing that it cannot be well constrained by the data and demonstrating that the parameter that describes the right tail of any GR distribution is difficult to constrain statistically (Holschneider et al., 2011).

Since several events are close to the magnitude of completeness, we verify the robustness of our results for

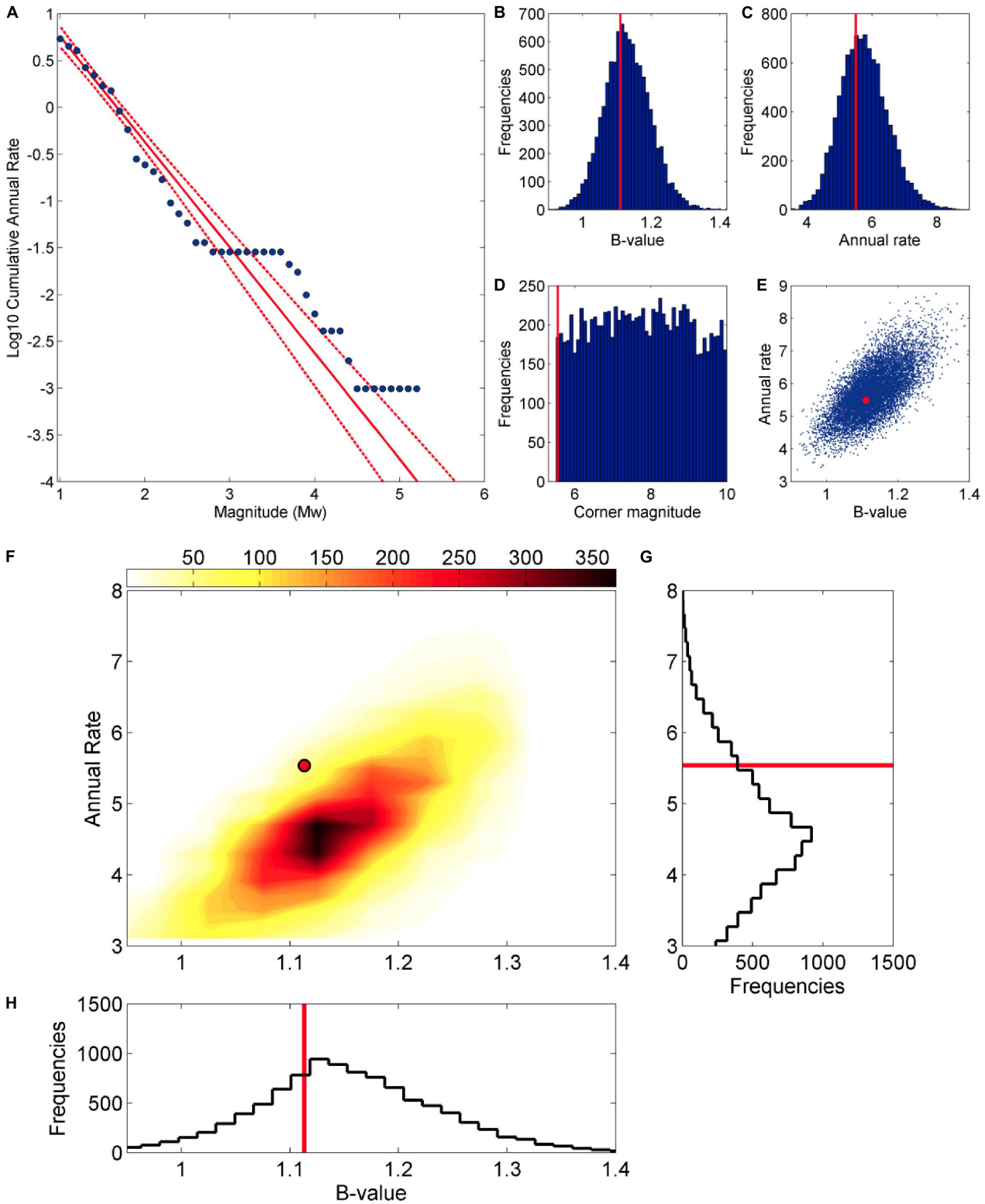

FIGURE 9 | Magnitude-frequency distribution of the Ischia seismicity. **(A)** Distribution: Blue dots, observed annual rate; red line, MLE of the tapered GR model; red dashed lines, 95% confidence interval of the model. **(B)** Uncertainty (blue histogram) and MLE (red line) for b-value estimation. **(C)** As panel **(B)**, but for annual rate estimation. **(D)** as panel **(B)**, but for the corner magnitude estimation. **(E)** Scatter plot (blue points) and MLE (red dot) of the joint estimation of b-value (*X*-axis) and annual rate (*Y*-axis). **(F)** 2D histogram of the joint estimation of the b-value (*X*-axis) and annual rate (*Y*-axis); the colour scale represents the density and the red dot the joint MLE. **(G)** Marginal distribution of the annual rate; the red line is the MLE. **(H)** Marginal distribution of the b-value; the red line is the MLE.

the uncertainty on its definition. To this end, we simulated 10^4 different sets of completeness, by adding a Gaussian random error with zero mean and a standard deviation of 0.2 (this value can be considered suitable to model the completeness uncertainty) as graphically shown in **Figures 5A,B** (dashed red lines correspond to +/− 1 standard deviation bounds). The results in **Figures 9F–H** show the 2D-histogram of the joint estimation of annual rate and b-value, as well as the marginal distribution (i.e., the 1D-histogram) of the annual rate and b-value. Comparing the different panels in **Figure 9**, we note that the uncertainties resulting from the parameter estimation with an MLE approach are comparable with the uncertainties considering a Gaussian error (with standard deviation of 0.2) on the evaluation of the magnitude of completeness. This means that the obtained results for the magnitude-frequency distribution are robust, being not critically dependent on the selected completeness magnitudes. The strong correlation between the parameters leads to a non-centred joint MLE with respect to the 2D-histogram, whereas the same MLE is compatible with both marginal distributions.

Given the strong correlation between a- and b-values and that the Poisson hypothesis used in Weichert (1980) approach may be challenging in Ischia (see next Section), we further check the stability of results by estimating the b-value also independently from the annual rate. To this end, we use the method described in Taroni (2021) that allows estimating the b-value with a time-varying magnitude of completeness, including the correction for the binning of the magnitudes (in our case 0.1) and the correction for an unbiased MLE (Marzocchi et al., 2020). We obtain a b-value = 1.18 +/−0.13, very similar to the one previously estimated.

Overall, the characterization of the magnitude-frequency distribution appears reliable, and the results, in particular the b-value > 1, appear in line with analogous analysis in other volcanic areas (Vilardo et al., 1991; D'Auria et al., 2013). This value differs from the one estimated by D'Auria et al. (2018). The difference is partially due to the adopted magnitude (M_d instead of M_w), whose conversion has a slope smaller than 1 (0.82, Petrosino et al., 2008; see **Figure 4A**). In addition, the quantification method (Ogata and Katsura, 1993) adopted in D'Auria et al. (2018) estimates, at the same time, the parameters describing both the complete and the incomplete part of the catalogue, fact that, in case of a catalogue with a low number of events (<100), can lead to unstable results. In any case, if we consider the b-value estimation and the associated uncertainty, 0.75+/−0.13, a larger b-value, e.g., 1.1, is still compatible with their findings (i.e., inside the 99% confidence interval). Considering that the largest earthquakes occurred in pre-instrumental times while most of small magnitude events are complete in instrumental times, only the future seismicity detectable by the updated seismic network operating since 2018 will give the possibility to further test our findings (e.g., b-value >1) with a more homogeneous dataset.

Notably, while quite large uncertainties exist in magnitude estimations, in this analysis we did not explore this uncertainty because most likely it has a quite complex structure that could influence the results. For example, the errors on magnitude are probably correlated in the macroseismic part of the catalogue but independent in the instrumental part. This complex uncertainty structure, if not satisfactory described, may bias the results, and may be the topic for future works.

Is the Ischian Seismicity a Stationary Poisson Process?

Since the catalogue shows periods with different seismicity rates, we also estimated the annual rate and the b-value of the tapered GR separately for the two sub-catalogues: the first one spans 1750–1884 and the second one 1885–2019, with a length of 135 years each. The goal is to understand if the higher seismic rate observed in the past (until the 1881–1883 earthquake sequence) is statistically compatible with the present low seismic rate associated with the development of the early seismic monitoring system to date (Luongo et al., 2012). In fact, the observed annual rate of the largest events (from M_w 3.6, complete from 1750) in the period 1750–1884 is 7 times higher with respect to the one in the period 1885–2019 (7 and 1 events, respectively).

Note that the 7 events that occurred during the time-span 1750–1884 are not all independent of each other: indeed, applying a classical declustering method to the catalogue (Gardner and Knopoff, 1974), one event is removed.

Assuming a stationary Poisson process, we computed the probability to observe 6 (or more) events in 135 years, i.e., the number of observed events in the first declustered sub-catalogue, using the annual rate and the b-value estimated in the second sub-catalogue ($\lambda = 6.85$ /year of $M_w \geq 1.0$, b-value = 1.34).

The computed probability corresponds to the p-value of a binomial test for the number of observed events (Taroni et al., 2017); we used 10^4 pairs of annual rate and b-value coming from the MCMC estimation in the second sub-catalogue in order to take into account the uncertainty in the parameter estimation. Since 3 over 6 events are near the completeness threshold (see **Figure 5A**), we also perform the binomial test using only 3 events, in order to check the robustness of our findings. The results are shown in **Figure 10A**. We obtained a large majority of low probabilities (<0.05), demonstrating that the Poisson hypothesis for the seismic events' distribution can be rejected, independently from the existing uncertainty on the GR parameters or the magnitudes. In practice, the seismicity of Ischia described by our integrated catalogue is a non-stationary process, and significant modulations in the seismogenic process should be invoked to justify the observed long-term oscillations of the seismicity rate.

While the non-stationarity process could not be a surprising feature in volcanic seismicity, it is not so obvious in a volcanic system that did not experience any eruption in the last 700 years (last eruption occurred in 1302 AD) as well as volcanic unrest episodes in recent times (Selva et al., 2019). On the other hand, this significant non-stationarity will challenge the assessment of seismic hazard, as the available data are sufficient to demonstrate that the Poisson hypothesis, commonly adopted in the long-term analyses, does not hold in Ischia.

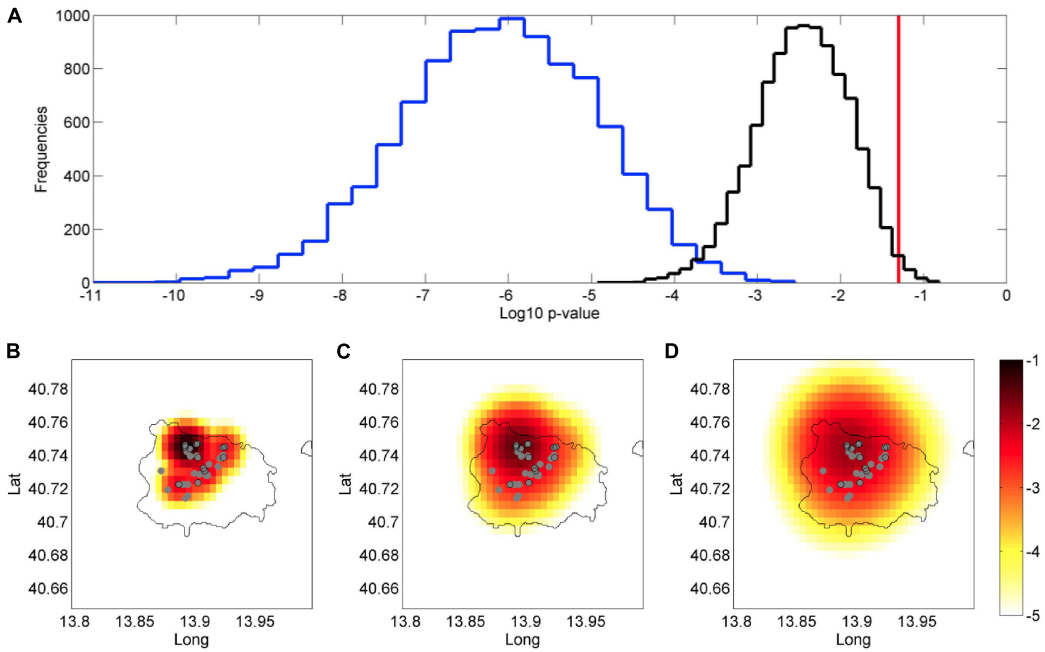

FIGURE 10 | (A) Histogram of the *p*-values (in a log10 scale) of the binomial test. The curves represent the *p*-value distribution for the test with 6 events (blue) and 3 events (black); the red vertical line indicates the 0.05 significance level. **(B)** spatial distribution of events (2D probability density function), applying smoothing seismicity models with σ of spatial kernel equal to 0.5 Km; **(C)** same as panel (B), with σ = 1 Km. **(D)** same as panel (B), with σ = 1.5 Km. The colour scale represents the spatial density of events (red higher, blue lower). White dots are reported for all the events in the catalogue, while black circles for events that are also mainshocks, according to the Gardner and Knopoff (1974) declustering method.

Spatial Distribution of the Seismicity

To analyse the spatial distribution of the earthquakes, we built a very high-resolution model of smoothed seismicity by using cells of 0.005° × 0.005°. Instead of Frankel's classic smoothed seismicity method (Frankel, 1995), we implemented the innovative method proposed by Hiemer et al. (2014), where the Gaussian smoothing kernel is multiplied by a function that gives more emphasis to the strong past events that occurred when the magnitude completeness of the catalogue was higher, to compensate the lack of low magnitude events in the catalogue. In this way, we can base the smoothed seismicity model catalogue using all the events in the catalogue, with a completeness that varies through time, instead of using the most recent seismicity only. This is particularly important for Ischia, due to the rather limited number of events in the catalogue.

The method uses the following Gaussian kernel:

$$K_{ij} = \frac{1}{2\pi\sigma^2} exp\left(-\frac{r_{ij}^2}{2\sigma^2}\right) \quad (2)$$

where K_{ij} is the contribution to the j-th spatial cell of the i-th earthquake in the catalogue; r_{ij} is the distance between the i-th event of the catalogue and the centre of the j-th spatial cell; and σ is the so-called correlation distance which regulates the smoothing. To obtain the total spatial rate of the j-th spatial cell, the contributions of all the N earthquakes in the catalogue must be summed: $K_j = \sum_{i=1}^{N} K_{ij}$.

Figures 10B–D show the spatial distributions obtained, adopting different σ (0.5, 1, and 1.5 km). We preferred to avoid any optimization procedure, since the total number of data in the catalogue is not large enough to produce a robust inversion of this parameter. The catalogue is declustered adopting the Gardner and Knopoff (1974) method, to avoid a fictitious concentration of the spatial rate where past sequences occurred. The maps, having the same logarithmic scale, represent the spatial probability density function of the events, i.e., the sum of the values in all the cells is 1.

These results show that the most widely adopted method to analyse the spatial distribution of earthquakes (smoothed seismicity with typical settings) recognizes the importance of the well known Casamicciola seismogenic source area, in the northern sector of Mt. Epomeo. Indeed, this small area generated almost all the largest magnitudes in the catalogue (1828, 1881, 1883, and 2017). This area is characterized by E-W faults limiting toward north the most uplifted part of the resurgent block of Mt. Epomeo (Vezzoli, 1988; Tibaldi and Vezzoli, 1998; Acocella and Funiciello, 1999, 2006; Trasatti et al., 2019), and these events seem to concentrate in the western part of this seismogenic area, possibly due to a more ductile behaviour of rocks in the eastern sector, where most of the volcanic activity took place (Cubellis and Luongo, 1998; Carlino et al., 2010; Selva et al., 2019; Cubellis et al., 2020). However, a non-negligible probability area extends further south, including the majority of the most uplifted part of the resurgent block of Mt. Epomeo (Selva et al., 2019; Trasatti et al., 2019),

TABLE 5 | Log file of the unified earthquake catalogue.

		N°	Notes
Macroseismic Catalogue	Total considered events	103	referred to Ischia in the literature
	Removed events	25	located outside Ischia
	Not parameterized events	21	multiple events (several earthquakes) or questionable (e.g., landslide)
	Parameterized events	57 (16*)	final list of events in the catalogue
Instrumental Catalogue	Recognized earthquakes	42	new entries in the period 1991–1998
	Parametrized events	39	parametrized events in the period 1991–1998
	Earthquakes in catalogue	176	Total number of events in the period 1991–2019
Merged Catalogue	Earthquakes in catalogue	252	The parameters of the 2008 e 2017 events are taken from the instrumental catalogue

*Over the damage threshold ($I_0 \geq$ V-VI).

especially in its western and the central sector. In this area is also located the 1863 event, the only large event showing rather constant intensity values throughout the island and, consequently, with a probable deeper origin. This means that this larger area cannot be completely neglected as a potential source of future seismicity.

Noteworthy, adopting the classical Frankel's (1995) method and/or not declustering, we obtain similar results, even if the classical approach – equal weight to all the events in the catalogue – creates a more homogeneous spatial distribution on the island and less emphasis to the stronger past events, mainly clustered in the north-western sector of Ischia.

CONCLUDING REMARKS

This manuscript describes the statistical characterization of seismicity occurring within the volcanic island of Ischia (Italy), based on the analysis of a newly developed and exceptionally long seismic catalogue of the seismicity generated within Ischia. This catalogue is based on an extensive screening of all the information available in the literature, from historical records to instrumental data. This work has been accompanied by a significant effort toward the quantification of existing uncertainty, as well as data completeness. The produced catalogue significantly extends the pre-existing catalogues, producing an unprecedented reach dataset covering several centuries, as summarized in **Table 5**. This allowed characterizing the statistical properties of the Ischia seismicity, revealing some peculiar properties like, for example, its significant non-stationarity also in a period of no eruptions or unrest episodes.

This study not only provides significant insights into the knowledge of the seismicity of Ischia and its related hazard, but also introduces significant novelties into the quantification and use of the uncertainties in the earthquake catalogues and their statistical characterization. This is particularly important whenever a limited number of earthquakes is available, as in the case of Ischia. The characterization and the management of uncertainty are based on the extensive use of the ensemble modelling, as well as on the developments of tests that quantify the robustness of the statistical characterization accounting for existing uncertainties.

More specifically, the main achievements of this study can be summarized as follows:

- Overall, the macroseismic data well describe the seismic history of Ischia and its seismic style, characterized by isolated events, small swarms with few low-energy events concentrated in few months, and sequences with a destructive mainshock accompanied by some minor fore- and aftershocks. The events which can be parameterized (location, magnitude) are 57, 16 of which above the damage threshold (I_0 > V-VI MCS). They are being included in the Historical Archive of Historical Earthquake Data (ASMI) and will be used to update the national earthquake catalogue CPTI15 (currently including only 12 events). The standardization of intensity data represents a methodological aspect of interest for future applications.
- The integration of results from different studies through ensemble models is also an innovative approach to quantify the epistemic uncertainty of parametric data, providing more realistic uncertainty bounds than any single individual procedure (Taroni et al., 2014; Garcia-Aristizabal et al., 2020). The application to Ischia to the 1828 and 1883 events highlights good compatibility of the results from alternative studies, especially for the 1883 event. Beyond the specific intensity estimates for a given site, we are now aware that the relative difference in the earthquake parameters due to subjective factors (selection of localities, interpretation of historical sources) or objective ones (the most important of which is the building vulnerability) are relatively minor. This is particularly important for the earthquakes having a strong impact on the seismic hazard at the local scale.
- The ensemble approach has been also adopted to merge a set of intensity-magnitude relationships, given the lack of data to derive a specific relationship for Ischia. The values of moment magnitude M_w obtained for the destructive earthquakes of 1881 and 1883 (epicentral intensity I_0 IX and XI, respectively) are now 4.4 and 5.2, significantly higher than the ones reported in CPTI15 (4.1 and 4.3, respectively). Overall, our results are consistent with the seismogenic volumes proposed for Ischia in the literature (Carlino et al., 2006, 2010; Castaldo et al., 2017; Cubellis and Luongo, 2018; Selva et al., 2019; Trasatti et al., 2019; Cubellis et al., 2020; Carlino et al., 2021).
- The extension of the instrumental catalogue as far back as 1991 confirms the very low rate seismicity in recent times. The uncertainty on the earthquake parameters, especially the location, is fairly large until October 2017,

when the improvement of the seismic network allowed a better definition of the parameters, although a decisive step would derive only from more constrained velocity models, potentially including the entire area Ischia-Procida-Campi Flegrei to take advantage also of the Campi Flegrei seismic network.

- By merging the historical and instrumental datasets, we obtained the most complete earthquake catalogue available for Ischia to date, representing a solid base to analyse the statistical features of seismicity and their temporal variations. Regarding the estimation of the parameters of the magnitude-frequency distribution, the best guess b-value obtained from the unified catalogue is 1.11, a value steadily larger than 1. This result is robust also considering the uncertainty in the MLE method or the completeness threshold. This in line with other volcanic zones in Italy and worldwide (Wyss et al., 1997; Murru et al., 1999), appearing also consistent with the high-temperature gradient beneath the seismogenic volume (Carlino et al., 2006; Castaldo et al., 2017; Trasatti et al., 2019; Cubellis et al., 2020), but different from what obtained for Ischia, using only instrumental seismicity, by D'Auria et al. (2018).
- The seismicity is not limited only to the well known seismogenic area of Casamicciola, but is extended to the central part of the island, especially along the faults surrounding the most uplifted part of the resurgent block of Mt. Epomeo (e.g., Selva et al., 2019; Trasatti et al., 2019), in particular in its western sector. While a decrease of the uncertainty in the location estimates may better constrain modulations in its spatial distribution, the extension beyond the Casamicciola area is confirmed beyond uncertainty from both the spatial distribution of the instrumental seismicity and the results of standard statistical analyses applied to the entire revised catalogue. Thus, this result is fairly stable and cannot be considered an artefact of the uncertainty on historical or instrumental locations.
- The intensity distributions of the largest events (1828, 1881, 1883, and 2017) show an elongated trend in the E-W direction and a rapid decrease with distance indicating a shallow sources. The E-W trend coincides with local fault system, probably indicating the potential contribution of source directivity effects in the spatial distribution of intensities (Vezzoli, 1988; Alessio et al., 1996; Acocella and Funiciello, 1999, 2006; Carlino et al., 2010; Nappi et al., 2018, 2021; Trasatti et al., 2019; Cubellis et al., 2020).
- The observed Ischian seismicity significantly deviates from a stationary process, also taking into account the uncertainty in data. The exceptional higher rates of earthquakes with $M_w \geq 3.6$ in the years 1750–1884 cannot be explained with the parameters estimated in the years 1885–2019; then a stationary Poisson process is not suitable to describe the Ischian seismicity independently from the application of declustering algorithms. Thus, observations suggest that significant modulations in the seismogenic process have occurred, leading to significant variations of the seismic rate through time.
- In this study, we have considered only events with local origin (within the island of Ischia). External sources may of course contribute to the local seismic hazard. The national seismic hazard map locates Ischia within a single volcanic source area that includes the entire Neapolitan volcanic district and extends to the Apennines, and it reports a relatively low seismic hazard (Selva et al., 2019). The main Apennines sources do not report damages in Ischia, as for example for the 1805 M_w 6.6 Matese earthquake or the 1980 M_w 6.9 Irpinia earthquakes (Intensities VI and V in Ischia, respectively; Esposito et al., 1987; Gaudiosi et al., 2020). Seismo-volcanic events at Vesuvius and Campi Flegrei are barely felt in Ischia, and mostly are not even felt (Branno et al., 1984; Cubellis et al., 2007).

DATA AVAILABILITY STATEMENT

The macroseismic data produced in this manuscript will be integrated in the same databases (ASMI, CPTI, and DBMI) in their next releases. The original contributions presented in the study are included in the article/**Supplementary Material**, further inquiries can be directed to the corresponding author.

AUTHOR CONTRIBUTIONS

JS coordinated the overall work, with the help of RA for the macroseismic catalogue, of AT for the instrumental catalogue, and MT for the statistical analyses. JS, RA, GA, CC, EC, SP, and AR developed the macroseismic catalogue of Section "Macroseismic Catalogue: 8th Century BC – 2019." JS, AT, MC, DL, and PR participated in the development of the instrumental catalogue of Section "Instrumental Catalogue: 1993–2019." JS, MT, and AT contributed to the development of the statistical analysis of Section "Statistical Characterization of the Seismicity." All the authors reviewed and approved the final manuscript.

FUNDING

This work benefited of the agreement between Istituto Nazionale di Geofisica e Vulcanologia and the Italian Presidenza del Consiglio dei Ministri, Dipartimento della Protezione Civile (DPC). This paper does not necessarily represent DPC official opinion and policies.

ACKNOWLEDGMENTS

The authors thank F. Mastino, G. Ferrari and the two reviewers for the fruitful discussions and constructive suggestions.

SUPPLEMENTARY MATERIAL

The Supplementary Material for this article can be found online at: https://www.frontiersin.org/articles/10.3389/feart.2021.629736/full#supplementary-material

REFERENCES

Acocella, V., and Funiciello, R. (1999). The interaction between regional and local tectonics during resurgent doming: the case of the island of Ischia, Italy. *J. Volcanol. Geother. Res.* 88, 109–123. doi: 10.1016/s0377-0273(98)00109-7

Acocella, V., and Funiciello, R. (2006). Transverse systems along the extensional Tyrrhenian margin of Central Italy and their influence on volcanism. *Tectonics* 2006:TC2003. doi: 10.1029/2005TC001845

Alessio, G., Esposito, E., Ferranti, L., Mastrolorenzo, G., and Porfido, S. (1996). Correlazione tra sismicità ed elementi strutturali nell'isola d'Ischia. *Il Quaternario* 9, 303–308.

Avvisati, G., Sessa, E. B., Colucci, O., Marfè, B., Marotta, E., Nave, R., et al. (2019). Perception of risk for natural hazards in Campania Region (Southern Italy). *Int. J. Disast. Risk Reduc.* 40:101164. doi: 10.1016/j.ijdrr.2019.101164

Azzaro, R., D'Amico, S., and Tuvè, T. (2011). Estimating the magnitude of historical earthquakes from macroseismic intensity data: new relationships for the volcanic region of Mount Etna (Italy). *Seism. Res. Lett.* 82, 520–531.

Azzaro, R., Del Mese, S., Graziani, L., Maramai, A., Martini, G., Paolini, S., et al. (2017). *QUEST – Rilievo macrosismico per il terremoto dell'isola di Ischia del 21 agosto 2017. Rapporto finale. Rapporto Interno INGV*. Napoli: INGV. doi: 10.5281/zenodo.886047

Boyd, T. M., and Snoke, J. A. (1984). Error estimates in some commonly used earthquake location programs. *Earthquake Notes* 55, 3–6. doi: 10.1785/gssrl.55.2.3

Branno, A., Esposito, E. G. I., Luongo, G., Marturano, A., Porfido, S., and Rinaldis, V. (1984). The October 4th, 1983 – Magnitude 4 earthquake in Phlegrean Fileds: macroseismic survey. *Bull. Volcnol.* 47, 233–238. doi: 10.1007/BF01961553

Braun, T., Famiani, D., and Cesca, S. (2018). Seismological constraints on the source mechanism of the damaging seismic event of 21 August 2017 on Ischia Island (Southern Italy). *Seismol. Res. Lett.* 89, 1741–1749. doi: 10.1785/0220170274

Buchner, G. (1986). "Eruzioni vulcaniche e fenomeni vulcano-tettonici di età preistorica e storica nell'isola d'Ischia," in *Tremblements de Terre, Éruptions Volcaniques et vie des Hommes Dans la Campanie Antique. Deuxième séries*, Vol. 7, (Napoli: Francais de Naples), 145–188. doi: 10.4000/books.pcjb.2455

Buchner Niola, D. (1965). *L'isola d'Ischia*. Napoli: Studio geografico.

Calderoni, G., Di Giovambattista, R., Pezzo, G., Albano, M., Atzori, S., Tolomei, C., et al. (2019). Seismic and geodetic evidences of a hydrothermal source in the Md 4.0, 2017, Ischia earthquake (Italy). *J. Geophys. Res. Solid Earth* 124, 5014–5029. doi: 10.1029/2018jb016431

Cancani, A. (1904). "Sur l'emploi d'une double échelle sismique des intensité, empirique et absolue," in *Proceedings of the C.R. des Séances de la deuxième Conference Seismologique Internationale réunie a Strasbourg, Leipzig 1903. Gerlands Beitrage zur Geophysik II*. (Strasbourg). 281–283.

Capuano, P., De Matteis, R., and Russo, G. (2015). The structural setting of the Ischia Island Caldera (Italy): first evidence from seismic and gravity data. *Bull. Volcanol.* 77:79.

Carlino, S., Cubellis, E., Luongo, G., and Obrizzo, F. (2006). "On the mechanics of caldera resurgence of Ischia Island (southern Italy)," in *Mechanisms of Activity and Unrest at Large Calderas, Geological Society*, Vol. 269, eds C. Troise, G. De Natale, and C. R. J. Kilburn (London: Special Publications), 181–193. doi: 10.1144/gsl.sp.2006.269.01.12

Carlino, S., Cubellis, E., and Marturano, A. (2010). The catastrophic 1883 earthquake at the island of Ischia (southern Italy): macroseismic data and the role of geological conditions. *Nat. Hazards* 52, 231–247. doi: 10.1007/s11069-009-9367-2

Carlino, S., Pino, N. A., Tramelli, A., De Novellis, V., and Convertito, V. (2021). A common source for the destructive earthquakes in the volcanic island of Ischia (Southern Italy): insights from historical and recent seismicity. *Nat. Hazards* doi: 10.1007/s11069-021-04675-z

Castaldo, R., Gola, G., Santilano, A., De Novellis, V., Pepe, S., Manzo, M., et al. (2017). The role of thermo-rheological properties of the crust beneath Ischia Island (Southern Italy) in the modulation of the ground deformation pattern. *J. Volcanol. Geother. Res.* 344, 154–173. doi: 10.1016/j.jvolgeores.2017.03.003

Ciuccarelli, C., Mariotti, D., and Comastri, A. (2018). *Revisione e Integrazione di Ricerca Riguardante i Forti Terremoti del 1828, 1881 e 1883 Avvenuti Nell'isola d'Ischi – Dati Macrosisici. Internal Report for the Catalogue of Strong Earthquakes in Italy (version CFTI6Med)*.

Civetta, L., de Vivo, A., Orsi, G., and Polara, G. (1999). *Il Vulcanismo a Ischia in etá Greco-Romana Secondo le Evidenze Geologiche e le Testimonianze Storicoletterarie. From: Vichiana, Rassegna di Studi Filologici e storici, 4_ serie, anno I, 1/1999.*. (Napoli: Loffredo Editore), 15–32.

Cubellis, E. (1985). Il terremoto di Casamicciola del 28 luglio 1883 : Analisi degli effetti, modellizzazione della sorgente ed implicazioni sulla dinamica in atto. *Boll. Soc. Nat. Napoli* 94, 157–186.

Cubellis, E., Carlino, S., Iannuzzi, R., Luongo, G., and Obrizzo, F. (2004). Management of historical seismic data using GIS: the island of Ischia (Southern Italy). *Nat. Hazards* 33, 379–393. doi: 10.1023/b:nhaz.0000048465.40413.17

Cubellis, E., and Luongo, G. (1998). "Il contesto fisico," in *AA.VV., Il Terremoto del 28 luglio 1883 a Casamicciola nell'isola d'Ischia*. Rome: Presidenza Consiglio dei Ministri, 49–123.

Cubellis, E., and Luongo, G. (2018). *History of Ischian Earthquakes. Pagine: 140 + XXVI tavv. f.t. Anno: 2017*. Napoli: Bibliopolis.

Cubellis, E., Luongo, G., and Marturano, A. (2007). Seismic hazard assessment at Mt. Vesuvius: maximum expected magnitude. *J. Volcanol. Geother. Res.* 162, 139–148. doi: 10.1016/j.jvolgeores.2007.03.003

Cubellis, E., Luongo, G., Obrizzo, F., Sepe, V., and Tammaro, U. (2020). Contribution to knowledge regarding the sources of earthquakes on the island of Ischia (Southern Italy). *Nat. Hazards* 100, 955–994. doi: 10.1007/s11069-019-03833-8

Cubellis, E., and Marturano, A. (2009). *Il terremoto del 5 aprile 2008 nell'isola d'Ischia: Studio Macrosismico. Open File Report 1*. Napoli: INGV.

Cundari, G. (1998). *Ambiente e Territorio. Lo Sviluppo Sostenibile Dalla Teoria alla Realtà*. Torino: Giappichelli.

D'Auria, L., Esposito, A. M., Bascio, D. L., Ricciolino, P., Giudicepietro, F., and Martini, M. (2013). The recent seismicity of Mt. Vesuvius: inference on seismogenic processes. *Ann. Geophys.* 56:0442.

D'Auria, L., Giudicepietro, F., Tramelli, A., Ricciolino, P., Lo Bastio, D., Orazi, M., et al. (2018). The seismicity of Ischia Island. *Seismol. Res. Lett.* 89:2018. doi: 10.1785/0220180084

D'Auria, L., Martini, M., Esposito, A., Ricciolino, P., and Giudicepietro, F. (2008). "A unified 3D velocity model for the Neapolitan volcanic areas," in *Conception, Verification and Application of Innovative Techniques to Study Active Volcanoes*, eds W. Marzocchi and A. Zollo (Napoli: INGV-DPC), 375–390.

De Natale, G., Petrazzuoli, S., Romanelli, F., Troise, C., Vaccari, F., Somma, R., et al. (2019). Seismic risk mitigation at Ischia island (Naples, Southern Italy): an innovative approach to mitigate catastrophic scenarios. *Eng. Geol.* 261:105285. doi: 10.1016/j.enggeo.2019.105285

De Novellis, V., Carlino, S., Castaldo, R., Tramelli, A., De Luca, C., Pino, N. A., et al. (2018). The 21st August 2017 Ischia (Italy) earthquake source model inferred from seismological, GPS and DInSAR measurements. *Geophys. Res. Lett.* 45, 2193–2202. doi: 10.1002/2017gl076336

de Vita, S., Di Vito, M. A., Gialanella, C., and Sansivero, F. (2013). The impact of the Ischia Porto Tephra eruption (Italy) on the Greek colony of Pithekoussai. *Quat. Int.* 303, 142–152. doi: 10.1016/j.quaint.2013.01.002

Delizia, I. (1987). *Ischia, l'identità Negata*. Napoli: Edizioni Scientifiche Italiane, 269.

Della Seta, M., Marotta, E., Orsi, G., De Vita, S., Sansivero, F., and Fredi, P. (2012). Slope instability induced by volcano-tectonics as an additional source of hazard in active volcanic areas: the case of Ischia island (Italy). *Bull. Volcanol.* 74, 79–106. doi: 10.1007/s00445-011-0501-0

Devoti, R., De Martino, P., Pietrantonio, G., and Dolce, M. (2018). Coseismic displacements on Ischia island, real-time GPS positioning constraints on earthquake source location. *Ann. Geophys.* 61:SE337. doi: 10.4401/ag-7656

Esposito, E., Luongo, G., Marturano, A., and Porfido, S. (1987). Il terremoto di S. Anna del 26 luglio 1805. *Mem. Soc. Geol. It.* 37, 171–191.

Ferrari, G. (2009). Giulio Grablovitz (1846-1928) and his scientific activity based on personal and institutional correspondence. *Ann. Geophys.* 52, 709–727. doi: 10.4401/ag-4627

Frankel, A. (1995). Mapping seismic hazard in the central and eastern United States. *Seismol. Res. Lett.* 66, 8–21. doi: 10.1785/gssrl.66.4.8

Galluzzo, D., Nardone, L., Carandente, A., Buonocunto, C., Scarpato, G., Marotta, E., et al. (2019). Le attività del gruppo operativo SISMIKO in occasione del

terremoto di Ischia Mw3.9 (MD4.0) del 21 Agosto 2017. *Quaderni di Geofisica* 154, 1–28.

Garcia-Aristizabal, A., Danesi, S., Braun, T., Anselmi, M., Zaccarelli, L., Famiani, D., et al. (2020). Epistemic uncertainties in local earthquake locations and implications for managing induced seismicity. *Bull. Seismol. Soc. Am.* 110, 2423–2440. doi: 10.1785/0120200100

Gardner, J. K., and Knopoff, L. (1974). Is the sequence of earthquakes in Southern California, with aftershocks removed, Poissonian? *Bull. Seismol. Soc. Am.* 64, 1363–1367.

Gasperini, P. (2002). Local magnitude revaluation for recent Italian earthqua kes (1981–1996). *J. Seismol.* 5, 503–524.

Gasperini, P., Vannucci, G., Tripone, D., and Boschi, E. (2010). The location and sizing of historical earthquakes using the attenuation of macroseismic intensity with distance. *Bull. Seismol. Soc. Am.* 100, 2035–2066. doi: 10.1785/0120090330

Gaudiosi, G., Alessio, G., Nappi, R., Noviello, V., Spiga, E., and Porfido, S. (2020). Evaluation of damages to the architectural heritage of naples as a result of the strongest earthquakes of the Southern Apennines. *Appl. Sci.* 10:6880. doi: 10.3390/app10196880

Geist, E. L., and Parsons, T. (2014). Undersampling power-law size distributions: effect on the assessment of extreme natural hazards. *Nat. Hazards* 72, 565–595. doi: 10.1007/s11069-013-1024-0

Gialanella, C. (2013). "Interazione tra attività vulcanica e vita dell'uomo: evidenze archeologiche nell'isola d'Ischia," in *Scuola Estiva AIQUA 2013, Miscellanea INGV, anno 2013*, (Napoli: INGV), 115–123.

Grablovitz, G. (1901). "Vasca sismica. Sonderabduck aus dem Bericht der I. Intern," in *Proceedings of the Sismologischen Konferenz, Estratto I Conferenza Internazionale di Sismologia di Strasburgo*, (Strasburgo).

Grablovitz, G. (1902-1903). Nuova vasca sismica. *Bollettino della Società Sismologica Italiana* VIII, 245–249.

Gruppo di Lavoro INGV (2017). *Rapporto di Sintesi Preliminare sul Terremoto dell'isola d'Ischia (Casamicciola) M4.0 del 21 agosto 2017 (6 settembre 2017)*. Genève: Zenodo, doi: 10.5281/zenodo.886045

Guidoboni, E., and Comastri, A. (2005). *Catalogue of earthquakes and tsunamis in the Mediterranean area from the 11th to the 15th century*. Bologna: INGV-SGA, 1037.

Guidoboni, E., Ferrari, G., Mariotti, D., Comastri, A., Tarabusi, G., Sgattoni, G., et al. (2018). *CFTI5Med, Catalogo dei Forti Terremoti in Italia (461 a.C.-1997) e nell'area Mediterranea (760 a.C.-1500)*. Napoli: Istituto Nazionale di Geofisica e Vulcanologia, doi: 10.6092/ingv.it-cfti5

Guidoboni, E., Ferrari, G., Mariotti, D., Comastri, A., Tarabusi, G., and Valensise, G. (2007). *CFTI4Med, Catalogue of Strong Earthquakes in Italy (461 B.C.-1997) and Mediterranean Area (760 B.C.-1500)*. Napoli: INGV-SGA.

Gutenberg, B., and Richter, C. F. (1944). Frequency of earthquakes in California. *Bull. Seismol. Soc. Am.* 34, 185–188.

Hiemer, S., Woessner, J., Basili, R., Danciu, L., Giardini, D., and Wiemer, S. (2014). A smoothed stochastic earthquake rate model considering seismicity and fault moment release for Europe. *Geophys. J. Int.* 198, 1159–1172. doi: 10.1093/gji/ggu186

Holschneider, M., Zöller, G., and Hainzl, S. (2011). Estimation of the maximum possible magnitude in the framework of a doubly truncated Gutenberg–Richter model. *Bull. Seismol. Soc. Am.* 101, 1649–1659. doi: 10.1785/0120100289

Husen, S., and Hardebeck, J. L. (2010). *Earthquake Location Accuracy. Community Online Resource for Statistical Seismicity Analysis (CORSSA)*. Available online at: http://www.corssa.org.

Iacono, A. (1996). La "Guerra d'Ischia" nel De Bello Neapolitano di G. Pontano. *Quaderni dell'Accademia Pontaniana* 19:91.

Judenherc, S., and Zollo, A. (2004). The Bay of Naples (southern Italy): Constraints on the volcanic structures inferred from a dense seismic survey. *J. Geophys. Res. Solid Earth* 109, B10312.

Kagan, Y. Y. (2002). Seismic moment distribution revisited: I. Statistical results. *Geophys. J. Int.* 148, 520–541. doi: 10.1046/j.1365-246x.2002.01594.x

Kanamori, H. (1977). The energy release in great earthquakes. *J. Geophys. Res.* 82, 2981–2987. doi: 10.1029/JB082i020p02981

Keller, M., Pasanisi, A., Marcilhac, M., Yalamas, T., Secanell, R., and Senfaute, G. (2014). A Bayesian methodology applied to the estimation of earthquake recurrence parameters for seismic hazard assessment. *Qual. Reliab. Eng. Int.* 30, 921–933. doi: 10.1002/qre.1735

Lee, W. H. K., and Lahr, J. C. (1972). *HYPO71: A Computer Program for Determining Hypocenter, Magnitude, and First Motion Pattern of Local Earthquakes*. Washington, DC: US Department of the Interior, 100.

Locati, M., Camassi, R., Rovida, A., Ercolani, E., Bernardini, F., Castelli, V., et al. (2019). *Database Macrosismico Italiano (DBMI15), versione 2.0*. Napoli: Istituto Nazionale di Geofisica e Vulcanologia, doi: 10.13127/DBMI/DBMI15.2

Luongo, G., Carlino, S., Cubellis, E., Delizia, I., Iannuzzi, R., and Obrizzo, F. (2006). *Il terremoto di Casamicciola del 1883 : Una ricostruzione mancata*. Napoli: Alfa Tipografia, 64.

Luongo, G., Carlino, S., Cubellis, E., Delizia, I., and Obrizzo, F. (2012). *Casamicciola 1883 Il sisma tra interpretazione scientifica e scelte politiche*. Napoli: Bibliopolis, 282.

Luongo, G., Cubellis, E., and Obrizzo, F. (1987). *Ischia Storia di un'isola Vulcanica*. Napoli: Liguori, 164.

Martinelli, G., and Dadomo, A. (2017). Factors constraining the geographic distribution of earthquake geochemical and fluid-related precursors. *Chem. Geol.* 469, 176–184. doi: 10.1016/j.chemgeo.2017.01.006

Marturano, A., Esposito, E., Porfido, S., and Luongo, G. (1988). Il terremoto del 4 ottobre 1983 (Pozzuoli). Attenuazione dell'intensità con la distanza e relazione magnitudo-intensità. Zonazione della città di Napoli. *Mem. Soc. Geol. It.* 41, 941–948.

Marzocchi, W., Spassiani, I., Stallone, A., and Taroni, M. (2020). How to be fooled searching for significant variations of the b-value. *Geophys. J. Int.* 220, 1845–1856. doi: 10.1093/gji/ggz541

Marzocchi, W., Taroni, M., and Selva, J. (2015). Accounting for epistemic uncertainty in PSHA: logic tree and ensemble modeling. *Bull. Seismol. Soc. Am.* 105, 2151–2159. doi: 10.1785/0120140131

Montuori, A., Albanoi, M., Polcari, M., and Atzori, S. (2018). "Using multi-frequency Insar data to constrain ground deformation of Ischia Earthquake," in *Proceedings of the IGARSS 2018 - 2018 IEEE International Geoscience and Remote Sensing Symposium*, (Valencia: IEEE), doi: 10.1109/IGARSS.2018.8519372

Murru, M., Montuori, C., Wyss, M., and Privitera, E. (1999). The locations of magma chambers at Mt. Etna, Italy, mapped by b-values. *Geophys. Res. Lett.* 26, 2553–2556. doi: 10.1029/1999gl900568

Nappi, R., Alessio, G., Gaudiosi, G., Nave, R., Marotta, E., Siniscalchi, V., et al. (2018). The 21 August 2017 MD 4.0 Casamicciola earthquake: First evidence of coseismic normal surface faulting at the Ischia volcanic island. *Seismol. Res. Lett* 89, 1323–1334. doi: 10.1785/0220180063

Nappi, R., Alessio, G., Gaudiosi, G., Nave, R., Marotta, E., Siniscalchi, V., et al. (2019). Emergeo Working Group, A photographic collection of the coseismic geological effects induced by the 21 August 2017, M=4, Casamicciola earthquake (Ischia island, Italy). *Misc. INGV* 49, 1-94.

Nappi, R., Porfido, S., Paganini, E., Vezzoli, L., Ferrario, M. F., Gaudiosi, G., et al. (2021). The 2017, MD = 4.0, Casamicciola earthquake:ESI-07 scale evaluation and implications for the source model. *Geosciences* 11:44. doi: 10.3390/geosciences11020044

Ogata, Y., and Katsura, K. (1993). Analysis of temporal and spatial heterogeneity of magnitude frequency distribution inferred from earthquake catalogues. *Geophys. J. Int.* 113, 727–738. doi: 10.1111/j.1365-246x.1993.tb04663.x

Orazi, M., D'Auria, L., Tramelli, A., Buonocunto, C., Capello, M., Caputo, A., et al. (2013). The seismic monitoring network of Mt. Vesuvius. *Ann. Geophys.* 56:0450.

Orsi, G., Civetta, L., Del Gaudio, C., de Vita, S., Di Vito, M., Isaia, R., et al. (2004). Short-term ground deformations and seismicity in the resurgent campi flegrei caldera (italy): an example of active block-resurgence in a densely populated area. *J. Volcanol. Geoth. Res.* 91, 415–451. doi: 10.1016/s0377-0273(99)00050-5

Orsi, G., Gallo, G., and Zanchi, A. (1991). Simple-shearing block resurgence in caldera depressions. A model from Pantelleria and Ischia. *J. Volcanol. Geother. Res.* 47, 1–11. doi: 10.1016/0377-0273(91)90097-j

Orsi, G., Patella, D., Piochi, M., and Tramacere, A. (1999). Magnetic modelling of the Phlegrean volcanic district with extension to the Ponza archipelago, Italy. *J. Volcanol. Geotherm. Res.* 91, 345–360. doi: 10.1016/s0377-0273(99)00043-8

Paparo, M. A., and Tinti, S. (2017). Analysis of seismic-driven instability of Mt. Nuovo in the Ischia Island, Italy. *Bull. Seismol. Soc. Am.* 107, 750–759. doi: 10.1785/0120160139

Petrosino, S., De Siena, L., and Del Pezzo, E. (2008). Recalibration of the magnitude scales at Campi Flegrei, Italy, on the basis of measured path and site and transfer functions. *Bulletin of the Seismological Society of America* 98, 1964–1974. doi: 10.1785/0120070131

Polara, G., and De Vivo, A. (2011). *Aenaria - Pithecusa - Inarime. Il nome.I; Ischia nella storia antica.II. Bollettino di Studi Latini, Anno XLI, fascicolo II*. Napoli: Loffredo Editore, 495–511; 511–521.

Ricco, C., Alessio, G., Aquino, I., Brandi, G., Brunori, C. A., D'Errico, V., et al. (2019). High precision leveling survey following the Md 4.0 Casamicciola earthquake of August 21, 2017 (Ischia, Southern Italy): field data and preliminary interpretation. *Ann. Geophys.* 61:665. doi: 10.4401/ag-7769

Richter, C. F. (1935). An instrumental earthquake magnitude scale. *Bull. Seismol. Soc. Am.* 25, 1–32. doi: 10.1515/9781400884445-002

Rovida, A., Locati, M., Antonucci, A., and Camassi, R. (2017). *Archivio Storico Macrosismico Italiano (ASMI)*. Napoli: Istituto Nazionale di Geofisica e Vulcanologia, doi: 10.13127/asmi

Rovida, A., Locati, M., Camassi, R., Lolli, B., and Gasperini, P. (2016). *Catalogo Parametrico dei Terremoti Italiani (CPTI15)*. Napoli: Istituto Nazionale di Geofisica e Vulcanologia, doi: 10.6092/INGV.IT-CPTI15

Rovida, A., Locati, M., Camassi, R., Lolli, B., and Gasperini, P. (2019). *Italian Parametric Earthquake Catalogue (CPTI15), version 2.0*. Napoli: Istituto Nazionale di Geofisica e Vulcanologia, doi: 10.13127/CPTI/CPTI15.2

Rovida, A., Locati, M., Camassi, R., Lolli, B., and Gasperini, P. (2020). The Italian earthquake catalogue CPTI15. *Bull. Earthquake Eng.* 18, 2953–2984. doi: 10.1007/s10518-020-00818-y

Saraò, A., Cocina, O., Moratto, L., and Scarfì, L. (2016). "Earthquake features through the seismic moment tensor," in *Project V3: Multi-Disciplinary Analysis of the Relationships Between Tectonic Structures and Volcanic Activity (Etna, Vulcano-Lipari system) Final Report*, Vol. 29, eds R. Azzaro and R. De Rosa (Napoli: Miscellanea INGV), 98–101.

Schorlemmer, D., and Woessner, J. (2008). Probability of detecting an earthquake. *Bull. Seismol. Soc. Am.* 98, 2103–2117. doi: 10.1785/0120070105

Selva, J., Acocella, V., Bisson, M., Caliro, S., Costa, A., Della Seta, M., et al. (2019). Multiple natural hazards at volcanic islands: a review for the Ischia volcano (Italy). *J. Appl. Volcanol.* 8:5. doi: 10.1186/s13617-019-0086-4

Selva, J., Costa, A., De Natale, G., Di Vito, M. A., Isaia, R., and Macedonio, G. (2018). Sensitivity test and ensemble hazard assessment for tephra fallout at Campi Flegrei, Italy. *Volcanol. Geotherm. Res.* 351, 1–28. doi: 10.1016/j.jvolgeores.2017.11.024

Selva, J., Costa, A., Sandri, L., and Marzocchi, W. (2014). Probabilistic short-term volcanic hazard in phases of unrest: a case study for tephra fallout. *J. Geophys. Res.* 119, 8805–8826. doi: 10.1002/2014JB011252

Sieberg, A. (1912). Über die makroseismische Bestimmung der Erdbebenstärke. *Gerlands Beitr Geophys.* 11, 227–239.

Stucchi, M., Albini, P., Mirto, C., and Rebez, A. (2004). Assessing the completeness of Italian historical earthquake data. *Ann. Geophys.* 47, 659–674.

Taroni, M. (2021). Back to the future: old methods for new estimation and test of the Gutenberg-Richter b-value for catalogs with variable completeness. *Geophys. J. Int.* 224, 337–339. doi: 10.1093/gji/ggaa464

Taroni, M., Marzocchi, W., and Roselli, P. (2017). Assessing 'alarm-based CN' earthquake predictions in Italy. *Ann. Geophys.* 59:S0648.

Taroni, M., and Selva, J. (2021). GR_EST: an OCTAVE/MATLAB toolbox to estimate Gutenberg-Richter law parameters and their uncertainties. *Seismol. Res. Lett.* 92, 508–516. doi: 10.1785/0220200028

Taroni, M., Zechar, J. D., and Marzocchi, W. (2014). Assessing annual global M 6+ seismicity forecasts. *Geophys. J. Int.* 196, 422–431. doi: 10.1093/gji/ggt369

Tibaldi, A., and Vezzoli, L. (1998). The space problem of caldera resurgence: an example from Ischia Island, Italy. *Geol. Rundsch.* 1998, 53–66. doi: 10.1007/s005310050189

Tramelli, A., Troise, C., De Natale, G., and Orazi, M. (2013a). Testing and optimization of the seismic networks of Campi Flegrei (Southern Italy). *Adv. Geosci.* 36, 49–55. doi: 10.5194/adgeo-36-49-2013

Tramelli, A., Troise, C., De Natale, G., and Orazi, M. (2013b). A new method for optimization and testing of microseismic networks: an application to Campi Flegrei (Southern Italy). *Bull. Seismol. Soc. Am.* 103, 1679–1691. doi: 10.1785/0120120211

Trasatti, E., Acocella, V., Di Vito, M. A., Del Gaudio, C., Weber, G., Aquino, I., et al. (2019). Magma degassing as a source of long-term seismicity at volcanoes: the Ischia island (Italy) case. *Geophys. Res. Lett.* 46, 14421–14429. doi: 10.1029/2019gl085371

Valensise, G., and Guidoboni, E. (1995). "Verso nuove strategie di ricerca: zone sismogenetiche silenti o silenzio delle fonti?," in *Catalogo dei Forti Terremoti in Italia dal 461 a.C. al 1980*, eds E. Boschi, E. Ferrari, G. Gasperini, E. Guidoboni, P. Smriglio, and G. Valensise (Bologna: ING-SGA), 112–127.

Vere-Jones, D., Robinson, R., and Yang, W. Z. (2001). Remarks on the accelerated moment release model: problems of model formulation, simulation and estimation. *Geophys. J. Int.* 144, 517–531. doi: 10.1046/j.1365-246x.2001.01348.x

Vezzoli, L. (1988). *Island of Ischia*, Vol. 10. Rome: CNR, Quaderni de La Ricerca Scientifica, 114.

Vilardo, G., Alessio, G., and Luongo, G. (1991). Analysis of the magnitude-frequency distribution for the 1983–1984 earthquake activity of Campi Flegrei, Italy. *J. Volcanol. Geotherm. Res.* 48, 115–125. doi: 10.1016/0377-0273(91)90037-z

Violante, C., Budillon, F., Esposito, E., Porfido, S., and Vittori, E. (2003). "Submerged hummocky topographies and relations with landslides on the northwestern flank of Ischia Island, Southern Italy," in *Proceeding International Workshop on Occurrence and Mechanisms of Flow-like Landslides in Natural Slopes and Earthfills May 14–16*, ed. L. Piccarelli (Sorrento: Quarto Inferiore), 309–315.

Weichert, D. H. (1980). Estimation of the earthquake recurrence parameters for unequal observation periods for different magnitudes. *Bull. Seismol. Soc. Am.* 70, 1337–1346.

Wyss, M., Shimazaki, K., and Wiemer, S. (1997). Mapping active magma chambers by b values beneath the off-Ito volcano, Japan. *J Geophys. Research: Solid Earth* 102, 20413–20422. doi: 10.1029/97jb01074

Conflict of Interest: The authors declare that the research was conducted in the absence of any commercial or financial relationships that could be construed as a potential conflict of interest.

frontiers in Earth Science

ORIGINAL RESEARCH
published: 08 April 2021
doi: 10.3389/feart.2021.618293

The 2011–2014 Pollino Seismic Swarm: Complex Fault Systems Imaged by 1D Refined Location and Shear Wave Splitting Analysis at the Apennines–Calabrian Arc Boundary

Marina Pastori[1], Lucia Margheriti[1], Pasquale De Gori[1], Aladino Govoni[1], Francesco Pio Lucente[1], Milena Moretti[1], Alessandro Marchetti[1], Rita Di Giovambattista[1], Mario Anselmi[1], Paolo De Luca[1,2,3], Anna Nardi[1], Nicola Piana Agostinetti[4,5], Diana Latorre[1], Davide Piccinini[1], Luigi Passarelli[6] and Claudio Chiarabba[1]*

[1]Istituto Nazionale di Geofisica e Vulcanologia (INGV), Rome, Italy, [2]University of Perugia, Perugia, Italy, [3]Institute for Environmental Studies (IVM), Vrije Universiteit Amsterdam, Amsterdam, Netherlands, [4]Department of Earth and Environmental Sciences, Università di Milano Bicocca, Milano, Italy, [5]Department of Geodynamics and Sedimentology, University of Vienna, Vienna, Austria, [6]Department of Earth Sciences, University of Geneva, Geneva, Switzerland

OPEN ACCESS

Edited by:
Jorge Miguel Gaspar-Escribano, Polytechnic University of Madrid, Spain

Reviewed by:
Luca De Siena, Johannes Gutenberg University Mainz, Germany
Emily Warren-Smith, GNS Science, New Zealand

***Correspondence:**
Marina Pastori
marina.pastori@ingv.it

Specialty section:
This article was submitted to Solid Earth Geophysics, a section of the journal Frontiers in Earth Science

Received: *16 October 2020*
Accepted: *03 February 2021*
Published: *08 April 2021*

Citation:
Pastori M, Margheriti L, De Gori P, Govoni A, Lucente FP, Moretti M, Marchetti A, Di Giovambattista R, Anselmi M, De Luca P, Nardi A, Agostinetti NP, Latorre D, Piccinini D, Passarelli L and Chiarabba C (2021) The 2011–2014 Pollino Seismic Swarm: Complex Fault Systems Imaged by 1D Refined Location and Shear Wave Splitting Analysis at the Apennines–Calabrian Arc Boundary. Front. Earth Sci. 9:618293. doi: 10.3389/feart.2021.618293

In the years between 2011 and 2014, at the edge between the Apennines collapsing chain and the subducting Calabrian arc, intense seismic swarms occurred in the Pollino mountain belt. In this key region, <2.5 mm/yr of NE-trending extension is accommodated on an intricate network of normal faults, having almost the same direction as the mountain belt. The long-lasting seismic release consisted of different swarm episodes, where the strongest event coinciding with a M_L 5.0 shock occurred in October 2012. This latter comes after a M_L four nucleated in May 2012 and followed by aseismic slip episodes. In this study, we present accurate relocations for ~6,000 earthquakes and shear-wave splitting analysis for ~22,600 event-station pairs. The seismicity distribution delineates two main clusters around the major shocks: in the north-western area, where the M_L 5.0 occurred, the hypocenters are localized in a ball-shaped volume of seismicity without defining any planar distribution, whilst in the eastern area, where the M_L 4.3 nucleates, the hypocenters define several faults of a complex system of thrusts and back-thrusts. This different behavior is also imaged by the anisotropic parameters results: a strong variability of fast directions is observed in the western sector, while stable orientations are visible in the eastern cluster. This tectonic system possibly formed as a positive flower structure but as of today, it accommodates stress on normal faults. The deep structure imaged by refined locations is overall consistent with the complex fault system recently mapped at the surface and with patterns of crustal anisotropy depicting fractures alignment at depth. The possible reactivation of inherited structures supports the important role of the Pollino fault as a composite wrench fault system along which, in the lower Pleistocene, the southward retreat of the ionian slab was accommodated; in this contest, the inversion of the faults kinematics indicates a probable southward shift of the slab edge. This interpretation may help to comprehend the physical mechanisms behind the seismic swarms of the region

and defining the seismic hazard of the Pollino range: nowadays a region of high seismic hazard although no strong earthquakes are present in the historical record.

Keywords: seismic swarm, 1D and DD localizations, shear wave splitting, tectonics, geodynamics and seismicity

INTRODUCTION

In a long period between 2011 and 2014, intense seismic swarms developed at the edge between the Calabrian Arc and the Apennines (Govoni et al., 2013; Passarelli et al., 2015).

This area is a crucial node at the rim of the ionian subduction (Totaro et al., 2014; Chiarabba et al., 2016; Palano et al., 2017). Pollino massif has been retained as the major seismic gap (**Figure 1C**) of peninsular Italy (Locati et al., 2016). The lack of large events ($M_W \geq 6.5$) in historical catalogs for a 100 km-long section concurred with this hypothesis in a framework of a unique and continuous seismic belt first introduced by the pioneering intuition of Omori (1909). Therefore, seismic unrest of past years became a great concern for the management of short-term hazard.

According to the gap hypothesis, seismic catalogs did not report large earthquakes in historical time in the Pollino area, while they are present in the north and south confining regions (Tertulliani and Cucci, 2014; Rovida et al., 2016). Few seismic events with a magnitude of likely lower than six are documented, including the M_W 5.6 "Mercure" earthquake in 1998 (Brozzetti et al., 2009). Although historical earthquakes are not documented, the seismic hazard map reports a 10% chance of exceeding 0.225 g in the next 50 years (Gruppo di Lavoro 2004). In fact, despite some discordance on fault geometry, paleoseismological studies found evidence for slip occurring in the past 10 kyrs and consistent with $M > 6.0$ earthquakes (Michetti et al., 1997; Cinti et al., 2002; 1997). These findings suggested the Pollino (P) fault (**Figure 1B**) as an active source of major earthquakes and this strong potential allowed for it to be included as a "debated seismogenic source" in the database of Individual Seismogenic Sources (DISS Working Group 2018; DOI:10.6092/INGV.IT-DISS3.2.1). Recent studies (Passarelli et al., 2015; Cheloni et al., 2017), reporting mixed seismic/aseismic strain release for the 2012 seismicity in the Pollino gap, promote a long recurrence-time for strong magnitude earthquakes.

In this work, we produce accurate locations of seismic events that occurred during the swarm in the years between 2011 and 2014, because of the employ of a quite dense network composed of both temporary and permanent seismic stations. Later on, we discuss the main seismological features of the seismicity, focusing on its evolution in space and time, and provide refined earthquake locations to investigate the presence—and image the geometry—of the fault system in a 1D velocity model. To refine our knowledge of the geometry of the fracture field and the structure of the crust, we also compute crustal anisotropic parameters from the splitting of local S-waves.

Seismic anisotropy is manifested on a 3-component waveform through the shear wave splitting phenomenon.

Seismic shear wave energy, when it enters into an anisotropic medium, is divided into two components having orthogonal polarization directions traveling at different velocities.

Usually, the fast direction (φ) term is used to indicate the polarization direction of the fastest wave and delay time (δt) to identify the lag between the fast and slow components.

The main causes of crustal anisotropy are represented by highly foliated metamorphic rocks, layered bedding in sedimentary formations, or preferentially aligned fracture or microcracks.

Crustal anisotropy, induced by the alignment of vertical fluid-filled cracks, is often used to discriminate the state of stress in the rock volume since in many cases cracks are preferentially aligned by the local active horizontal stress field. Moreover, the δt value is proportional to the thickness of the sampled anisotropic volume and therefore the strength of the anisotropy. The above assumption well describes the theory of the Extensive Dilatancy Anisotropy (EDA) model proposed by Crampin (1993).

The Pollino area shows a wide range of geological units from sedimentary carbonatic to metamorphic rocks such as a complex structural setting. Generally, a totally sedimentary contest, characterized by horizontal layering interfaces, is explained with a vertical transverse isotropic (VTI) symmetry. Instead, the presence of near-vertical fractures aligned in a preferred orientation, as predicted by the EDA model, makes a change this symmetry into horizontal transverse isotropy (HTI) and makes the medium orthorhombic (Tsvankin, 2001; Watson and van Wijk, 2015).

S-wave splitting parameters are tightly related to the geometries and intensities of the fracture field in the area and the presence of fluids during swarm activities in the upper crust, above the earthquake clusters. We investigate the distribution in space of these parameters looking for the possible physical mechanisms behind the seismic swarm and for understanding how the prolonged seismic activity should be interpreted in evaluating the seismic hazard of the region.

GEOPHYSICAL AND GEOLOGIC OUTLINES

The study area is placed in the transition sector between the Apennines and Calabria arc (**Figure 1**), where one of the last fragments of the former Tethys Ocean is subducted at depth. Across the lineament, referred to as the "Pollino line" (Van Dijk et al., 2000, and references therein) the geological characteristics at the surface change rapidly from the carbonate platform units to the San Donato metamorphic core.

The subduction derives from the ionian oceanic plate sinking below the Calabrian Arc-Southern Tyrrhenian Sea and it represents a portion of the fragmented tectonic edge between

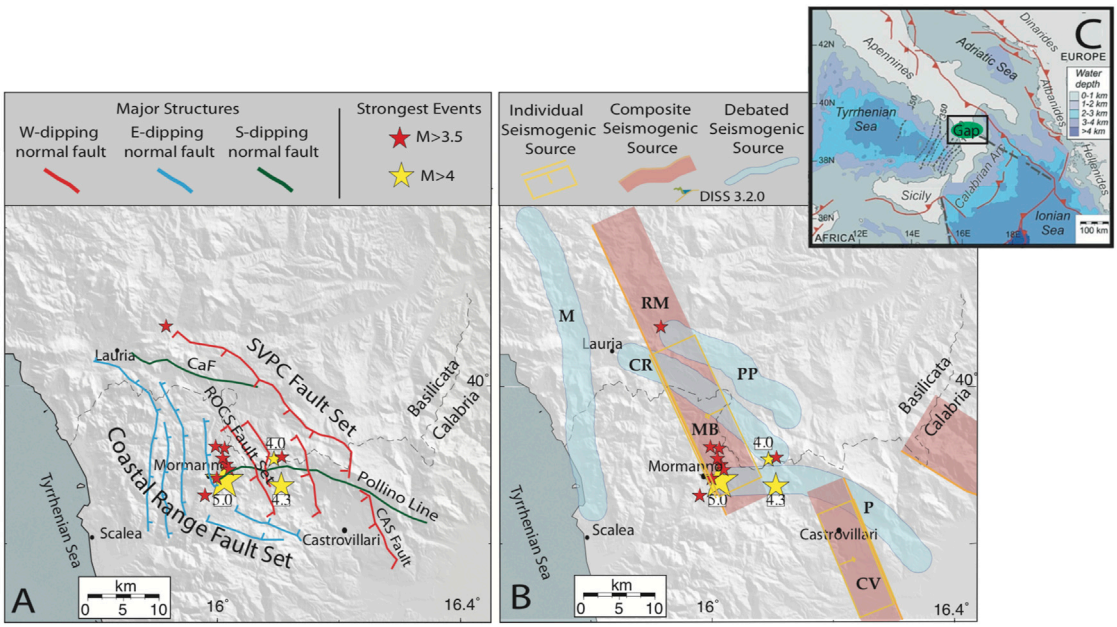

FIGURE 1 | (A) Detailed map of active faults, in the Calabria-Basilicata border region (modified after Brozzetti et al., 2017) and their interaction with Pollino 2010–2014 swarm strongest events. Major structures are represented by: Coastal Range Fault Set (CRFS); Castello Seluci-Viggianello-Piano di Pollino-Castrovillari Fault Set (SVPC); Castelluccio Fault (CaF); Rotonda-Campotenese Fault Set (ROCS); Castrovillari Fault (CAS); Pollino Line (P). **(B)** Main seismogenic sources reported in the Italian database of the Individual Seismogenic Sources, DISS version 3.2.0 (DISS Working Group 2018). According to DISS, Pollino seismicity is located between the Castrovillari (CV) seismogenic source to the South and the "Rimendiello–Mormanno" Mecure Basin (RM–MB) source to the North. Other major seismogenic sources, even if classified as debated, such as the Castelluccio–Rotonda (CR) fault, the Piana Perretti (PP) fault, and the Pollino (P) fault are also identified in the area. Yellow stars represent the strongest earthquakes recorded during the seismic sequence, M_L 5.0 on October 25th, 2102, M_L 4.3 in May 28th, 2012, and M_L4 on June 06th, 2014. Red stars represent events greater than M 3.5. **(C)** Geodynamic setting of the central Mediterranean, modified after Ferranti et al. (2014), is also reported.

two slowly converging macro-plates: Eurasia and Africa (Lucente et al., 2006, among many others, and references therein). Several seismological studies well document the lithospheric structure of the area (e.g., Piana Agostinetti et al., 2008, 2009; Di Stefano et al., 2009; Totaro et al., 2014), and the geometry of the subduction (Chiarabba et al., 2008, and references therein).

The Calabrian Arc-Southern Tyrrhenian Basin system is characterized by E–W extensional tectonics, despite the N-S slow convergence between Eurasia and Africa macro-plates. Since the late Miocene, the Calabrian Arc slab was subject to a quick rollback, moving at a rate of 5–6 cm/yr from E to SE, which is greater than the ~1–2 cm/yr rate of convergence between Europa and Africa (Faccenna et al., 2004). Despite this, in the late Pleistocene, subduction and rollback slowed down and are probably advancing at <1 cm/yr (D'Agostino and Selvaggi 2004). Seismicity and tomographic images of the slab may point out the southward lateral migration of the slab boundary, progressively following the subduction zone lateral reduction caused by the slab detachment process (Orecchio et al., 2015).

The study area structural setting (**Figure 1**) is indeed a consequence of the different tectonic phases. During the Middle Miocene-Late Pliocene, the Verbicaro and the Pollino Units compressional structures were dislocated by a set of WNW–ESE-oriented regional strike-slip faults characterized by left-lateral kinematics (Ghisetti and Vezzani 1982; Van Dijk et al., 2000). The presence of lateral step in these faults occasionally causes the formation of positive and negative flower structures in the region that, in certain conditions, could be reactivated.

Geodetic measurements show today a continuous extensional area that runs along the Southern Apennines ridge and reaches the Pollino region, which is subject to NE–SW extension (D'Agostino and Selvaggi, 2004); the extension rate seems to reduce from the Southern Apennines to the Calabria–Lucania boundary region (D'Agostino et al., 2013). These observations suggest that the Pollino area is affected by an increase of tectonic strain and deformation that results in a composite system of active normal faults mainly oriented near-parallel to the Apenninic chain (Brozzetti, 2011).

Recently Brozzetti et al. (2017) mapped in detail the active faults at the Calabria-Lucania border (**Figure 1A**) finding both NW-SE trending SW dipping and N–S striking E dipping normal fault sets. This complex fault system is located between two major normal tectonic structures, already known in this area as the "Rimendiello-Mormanno" Mercure Basin (RM–MB) fault system to the Northwest and the Castrovillari (CV) fault to the South (**Figure 1B**). These are cataloged as individual seismic sources in the Italian database of the Individual Seismogenic Sources (DISS Working Group 2018).

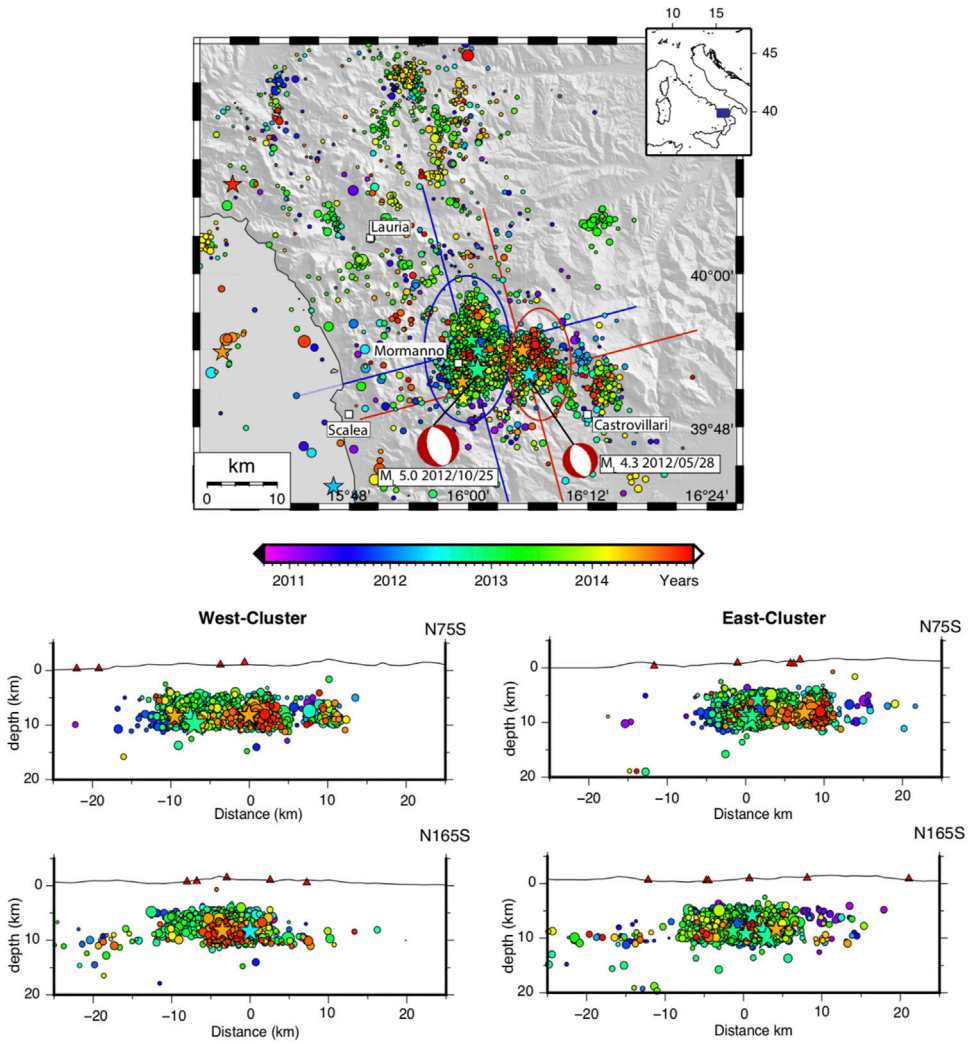

FIGURE 2 | Map and sections of the 2011–2014 seismic sequence/swarm from ISIDe Working Group (2016), https://doi.org/10.13127/ISIDE. The size of the epicenters is proportional to the magnitude and star symbols depict events having $M > 3.5$. The epicenters are divided into two main clusters: Western and Eastern, enhanced on the map by blue and red ellipses. The cross-sections of the Eastern and Western clusters are plotted to the bottom.

The 2011–2014 Pollino Seismic Sequence

Between 2011 and 2014 the Italian Seismic Network (INGV Seismological Data Center, 2006) recorded more than 6,000 earthquakes in the study area that spread over an area extending up to about 25 km in both the N–S and E–W directions (**Figure 2**). The whole distribution of earthquakes delineates two main clusters around the two major shocks: M_L 4.3 (M_W 4.2) and M_L 5.0 (M_W 5.2), the eastern smaller and the western larger, respectively (**Figure 2**). Between 2011 and early 2012, the earthquakes rate has been variable (data source: ISIDe working group 2016), with high and low phases and magnitudes not exceeding M_L 3.6 (**Figure 3**).

Preliminary hypocentral locations are concentrated at depths between 5 and 10 km during the entire swarm (data source: ISIDe working group 2016). The analysis of the Time Domain Moment Tensor (TDMT; http://cnt.rm.ingv.it/tdmt.html; Scognamiglio et al., 2009) recognized for the strongest events, two fault plane solutions consistent with normal faults striking ~N25°W and dipping at about 45°. On the whole, focal mechanisms are coherent with a NE–SW extension observed in the area (Totaro et al., 2013).

The seismicity mainly occurred near the Mormanno village (western larger dashed ellipse in **Figure 2**). On May 28th, 2012, at about 5 km eastward of the first main cluster of seismicity a shallow M_L 4.3 event occurred (**Figure 2**). The seismic activity remained concentrated in this area (eastern smaller dashed ellipse in **Figure 2**) until early August. Thereafter, seismicity moved again westward to the Mormanno activated area, where several events with a magnitude larger than 3.0 preceded the strongest earthquake (M_L 5.0) that occurred on October 25th, 2012. The seismicity rate persisted high for some months, but magnitudes did not exceed M_L 3.7. At the beginning of 2013, the seismic activity started to decrease (inset in **Figure 3**), remaining relatively low until June 2014, when a magnitude M_L four

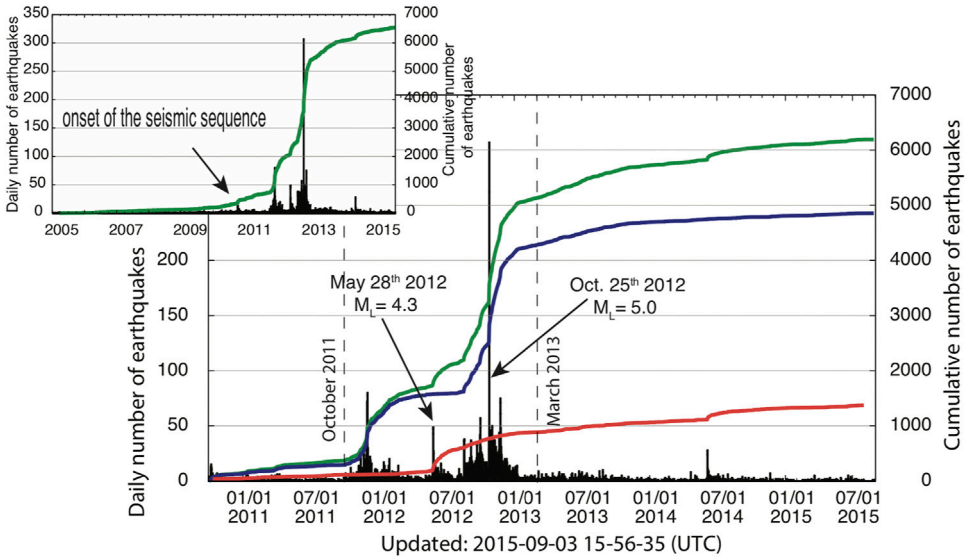

FIGURE 3 | Temporal evolution of the swarm: black histogram defines the daily number of events, the green line is the cumulative number of events in the whole region, the blue line and the red line are the cumulative number of events for the western and eastern cluster, respectively. Only the blue line trend seems to follow a mainshock–aftershock behavior.

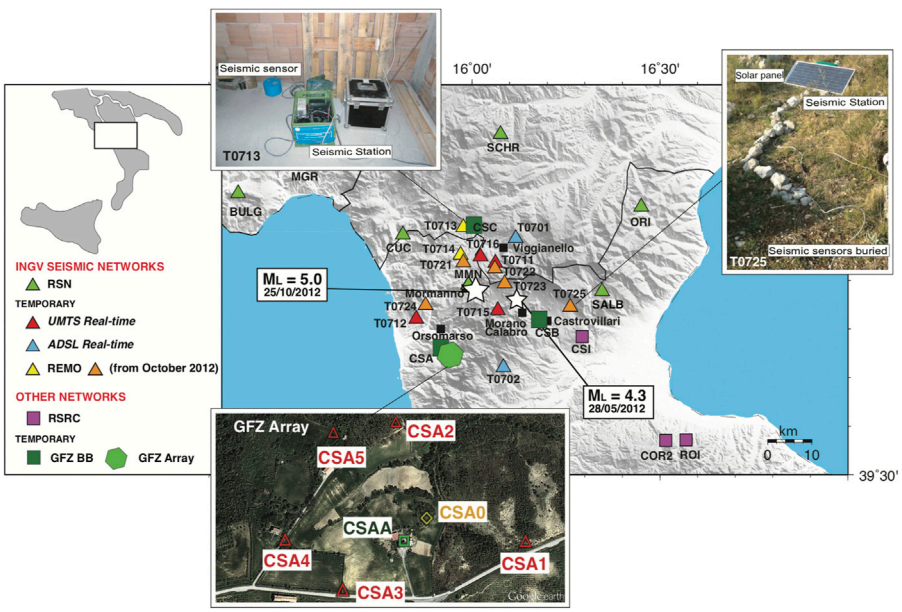

FIGURE 4 | Map of temporary and permanent seismic networks deployed in the area during the seismic activity. In the upper insets an example of installation is reported; in the lower panel is shown the GFZ seismic array configuration. In the map, the two main-shocks are also reported as white stars.

earthquake occurred in the eastern cluster, giving rise to a sudden increase of the seismic rate in the surrounding area. The seismicity rate kept decreasing during 2015, although remaining above the background seismicity threshold (inset in **Figure 3**).

There is evidence that this seismic sequence behaves as a swarm more than as a mainshock-aftershock seismic sequence, in fact, this preliminary hypothesis is supported by a more accurate and detailed analysis performed by Passarelli et al. (2015); they found that 75% of earthquakes may be related to a transient forcing and only 25% could be interpreted as aftershocks, We show in **Figure 3** the temporal evolution of the seismic sequence in term of seismicity rate to investigate different behaviors of the two clusters. The histograms of the daily number of events and the cumulative number of events for the whole area (green line in

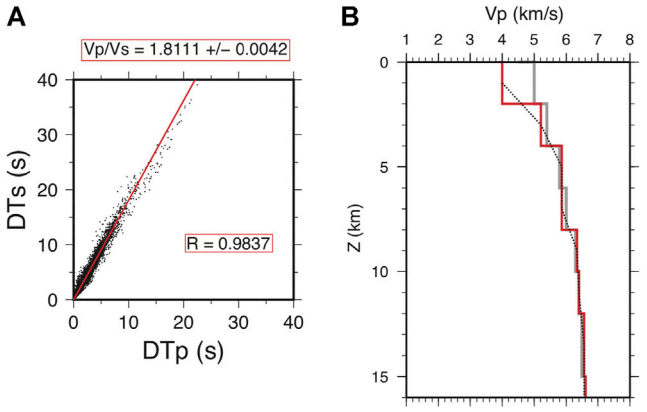

FIGURE 5 | (A) Wadati (1933) diagram computed on all the earthquakes with up-going ray-paths to the stations. For each event, DTp and DTs are the differences between P- and S-phase arrival times, respectively, at couples of stations. The *Vp/Vs* value is the slope of the straight red line, while *R* is the correlation coefficient of the linear regression **(B)** Starting (dark gray) and final (red) P-wave 1-D velocity model computed using the VELEST code (Kissling et al., 1994).

Figure 3) show an increase of the seismicity months before the mainshocks, with a seismic rate that increases and decreases at varying pace.

We also believe, when considered the two main clusters separately, that the events clustered inside the western area have swarm behavior (blue line in **Figure 3**); whilst the events occurred in the eastern region seem to follow a mainshock-aftershock trend (red line in **Figure 3**).

Temporary Seismic Network

During these four years of intense seismic activity, a group of temporary INGV seismic stations (INGV Seismological Data Center, 2006) and Deutsches Geo Forschungs Zentrum (GFZ) seismic stations and array (Passarelli et al., 2012) were installed, for the purpose of enhancing the earthquakes identification capability of the Italian National Seismic Network there in real-time (**Figure 4**, see also Govoni et al., 2013 for details) and to refine the accuracy of the locations using also off-line data. The temporary seismic network was composed of a variable number of seismic stations during the entire seismic sequence, from eight stations in late 2011 to about 20 stations in late 2012, in order to refine the hypocentral locations of small-magnitude earthquakes and ensure a lower magnitude detection threshold of the network (see also De Gori et al., 2014, for the timing of stations deployment). In May 2015 the temporary network deployed in the Pollino region was removed keeping only two stations to maintain a lower magnitude detection threshold in the area with respect to the regional standard.

REFINED EARTHQUAKES LOCATION

The analysis of the seismic sequence greatly benefited from data provided by the temporary seismic stations installed soon after the sequence started (**Figure 4**), many of which contributed to the real-time monitoring (Govoni et al., 2013). Earthquakes were originally located by analysts on seismic surveillance duty with the HYPOINVERSE-2000 code (Klein, 2002) using a 1D velocity model with two layers at 0–11 km (Vp = 5.0 km/s) and 11–38 km (Vp = 6.5 km/s) depth over a half-space at depth >38 km with Vp = 8.0 km/s. These locations (**Figure 2**), available in real time on the ISIDe website, were used as the initial dataset.

For this study, we carefully reprocessed the earthquakes reading P- and S-phases arrivals on the three-component digital recordings at local stations from October 2011 to March 2013. As the first step, we located all the earthquakes using the program Hypoellipse (Lahr, 1989) and a starting Vp model taken from Chiarabba et al., 2005, adopted for the whole Italian region.

The average Vp/Vs in the crustal volume where seismicity developed has been estimated through the modified Wadati method (Chatelain, 1978). Since seismicity mainly occurs at depths of 5–10 km, most of the observations consist of up-going ray-paths, thus the retrieved Vp/Vs (1.81, see **Figure 5A**) is strongly representative of the focal volume.

Locations With Minimum 1D Velocity Model

In order to improve earthquake locations, we computed an ad hoc 1D velocity model by applying the inversion scheme introduced by Kissling et al. (1994) and implemented in the code VELEST. To obtain a stable 1D reference model, we selected a subset of events that meet the following selection criteria: rms <0.5, azimuthal gap <200°, location errors within 2 km, and at least seven P- and 3 S-wave readings.

We then inverted P- and S-wave arrival times, from a subset of 808 selected earthquakes, to simultaneously compute hypocenter solutions and the minimum 1D velocity model parameterized by horizontal layers with Vp values varying with depth. The damping parameter was chosen by running different inversions as the best trade-off between data variance reduction and model complexity. The optimum model (**Figure 5B**) was achieved after 10 iterations, obtaining a final rms of 0.12s with a variance reduction of 48%.

Below a thin layer of sediments cover, with a thickness of 2 km and Vp of 4 km/s, the P-wave velocity (**Figure 5B**) displays values characteristic for consolidated sedimentary rocks like Mesozoic evaporites and carbonates, in agreement with the velocity values found by Improta et al. (2017), in an adjacent area.

The retrieved relatively high Vp/Vs values (1.8) is often observed in Mesozoic carbonate rocks of the Apennines and can be related to fracturing and fluid saturation (e.g., Improta et al., 2014).

Finally, we use this minimum 1D model to relocate the whole set of earthquakes through the Hypoellipse code (Lahr, 1989). We obtain a final set of 2,323 well located earthquakes; the performance of the adopted approach, in terms of rms and location errors can be evaluated in **Figure 6**.

Results of the analysis described above are shown in **Figure 7**, where map and cross section views of the seismic sequence are provided. The relocated earthquake catalog represents a sensible improvement with respect to that shown in **Figure 2** in terms of

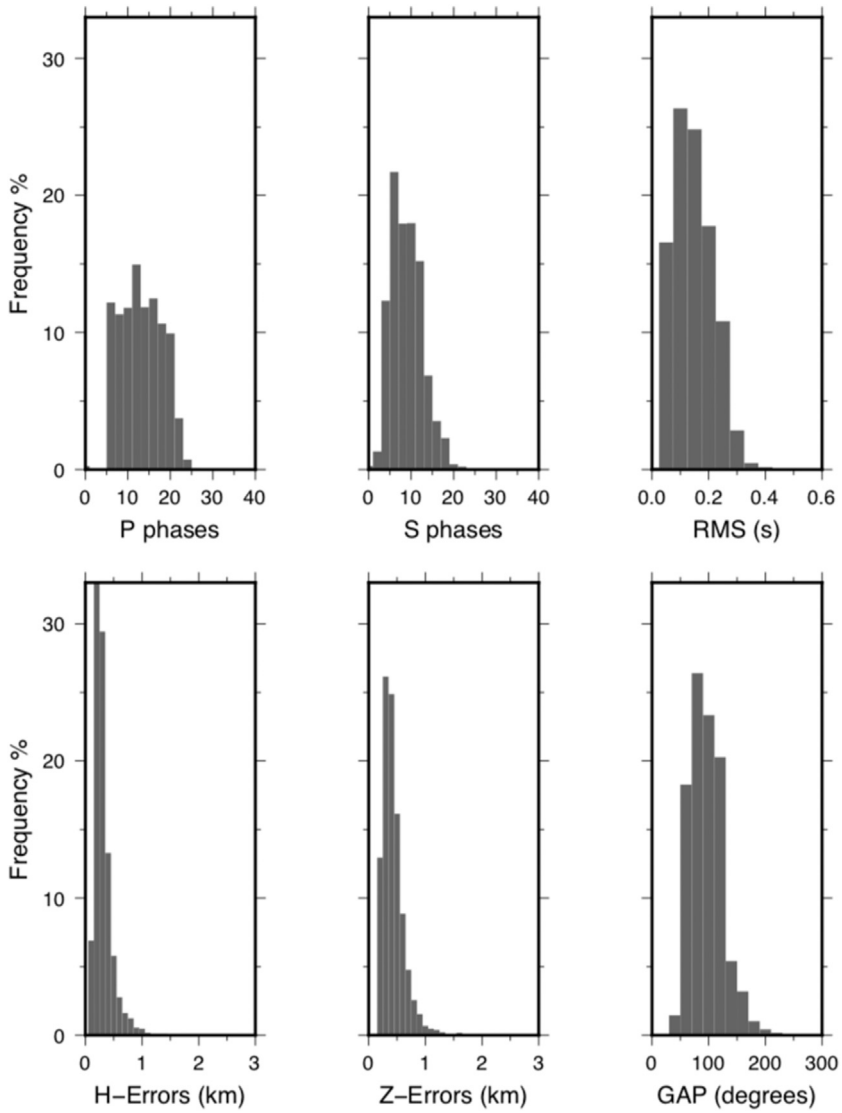

FIGURE 6 | Histograms summarizing the main outputs of the localization procedure, in terms of frequency of observations for each of the following parameters (from top left to bottom right): number of observations for P phases; number of observations for S phases; residual rms (s); horizontal location errors (km); vertical location errors (km); azimuthal gap between stations (°).

geometrical definition of the activated fault system, whose characteristics are here recognizable.

The analyzed earthquakes describe two main areas of seismicity: Western and Eastern clusters; in the first one, the M_L 5.0 is located instead in the second one the M_L 4.3 occurred. The cross-sections well delineate two different behaviors: in the northern cross-section (**Figure 7B**) the hypocenters define a ball-shaped volume without imaging any planar lineament. The distribution of the M_L >3.0 best-recorded events in the area (yellow stars in **Figure 7B**), also agrees with more diffuse seismicity rather than depicting a planar one.

On the contrary, in the southern cross-section (**Figure 7C**), hypocenters define at least three dipping fault planes. Those planes include the one potentially responsible for the M_L 5.0 event, which was imaged by the seismicity hypocenters also before the occurrence of such mainshock. This plane has been reconstructed with a similar geometry also by other recent studies (Brozzetti et al., 2017; Napolitano et al., 2021). But with respect to these latter works, thanks to the ~2,300 events analyzed and re-located, we were also able to depict an antithetic E-dipping fault plane located to the West of the main fault plane, and another NE-dipping, on the East, related to the M_L 4.3 event, possibly the source of this second mainshock.

Relative Locations With hypoDD

To further improve locations, we applied the double-difference (DD) relocation algorithm using the hypoDD code (Waldhauser and Ellsworth, 2000; Waldhauser, 2001). The algorithm

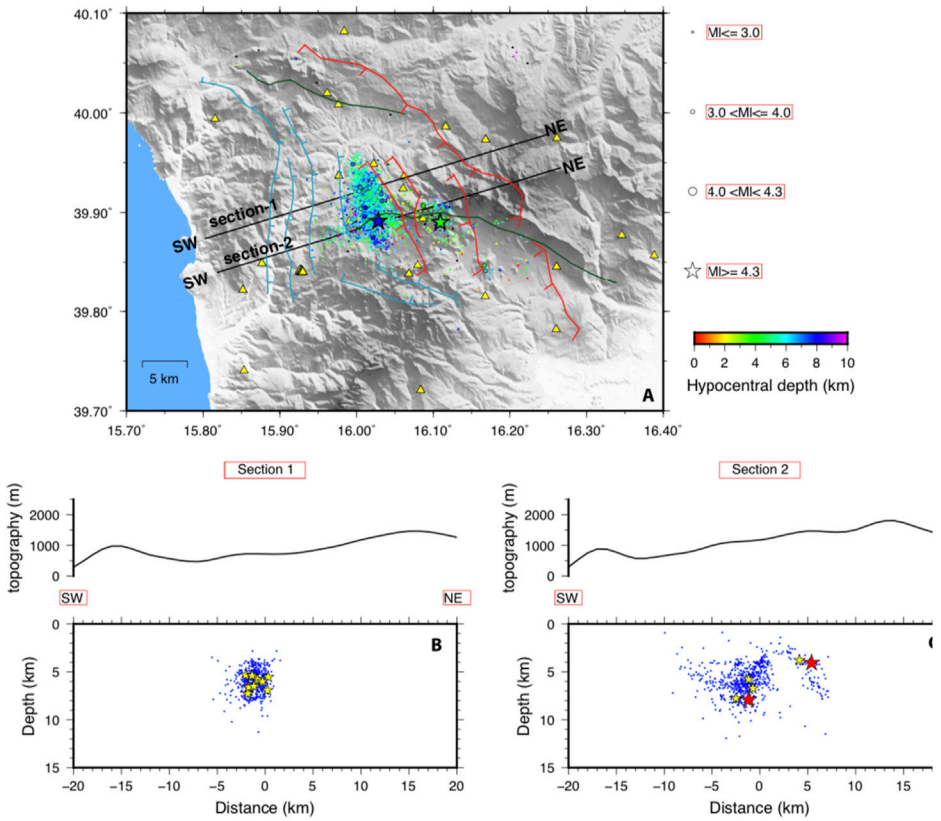

FIGURE 7 | Map and cross sections view of the earthquakes relocated using the minimum 1-D model **(A)** The top image shows a map of the epicenters, where earthquakes are sized by magnitude according to the symbols on the right of the map and color-coded by hypocentral depth according to the scale on bottom. The M_L 5.0 and M_L 4.3 mainshocks are represented by stars. Yellow triangles are permanent and temporary seismic stations. Black lines are the traces of the vertical cross-sections. See **Figure 1A** for major structures description. Two main clusters are recognized: the first one to the West and the other on the East, which include the M_L 5.0 and M_L 4.3 events, respectively **(B, C)** On the cross sections -1, and -2, we project all the events located within 1 km from the vertical plane. **(B)** The hypocenters, in section-1, in the northern part of the sequence, depict a ball-shaped seismogenic volume. **(C)** The hypocenters, in section-2, on the south, seem to delineate three seismogenic faults. On both the cross sections, the M_L 5.0 and M_L 4.3 mainshocks are represented by the red stars while the yellow stars identify epicenters with a magnitude larger than 3.0.

minimizes the residuals between observed and calculated travel-time differences for pairs of earthquakes at common stations by iteratively adjusting the difference between the hypocenters. This condition holds if the hypocentral distance between earthquakes is small compared to the source receiver separation.

We used P and S wave arrival times picked from three component seismograms, the starting locations derived above and the minimum 1D velocity model already described. Double-differences are generated to link each event to several neighbors, so that all the events are connected and the adjustment to hypocenter parameters is simultaneously determined. In our case, all the selected events are strongly linked to the others forming one main cluster. We performed 10 iterations optimizing the damping parameter to obtain good conditioning and convergence of the solution. The iterations were grouped into three sets for better control of the inversion procedure and to achieve a consistent convergence. The final adjustments are in the order of meters.

The DD locations show a seismicity distribution similar to that obtained with the minimum 1D model, but emphasizes some aspects of the geometry like the opposite dipping of the two main faults (**Figure 8**). The northern part of the main cluster still does not present a clear planar geometry.

SHEAR-WAVE SPLITTING

From ~6,000 events recorded at temporary (T07*) and permanent stations deployed in during the seismic sequence, we analyzed 22,623 event-station pairs looking for crustal anisotropy to evaluate the shear wave splitting parameters: fast direction polarization (φ) and delay time (δt). Seismicity used in the anisotropic analysis is mainly concentrated under Mormanno village between 5 and 10 km depth, with magnitudes ranging from 0.2 to 3.0. To avoid complications on the S-wave arrival, due to the P-wave coda of a strong events that could make difficult the splitting analysis, we decided to discard events with a magnitude greater than 3.0. We used Anisomat+ (Piccinini et al., 2013) a set of MatLab scripts able to retrieve automatically φ and δt from the seismic recording of local earthquakes. We tuned this code by

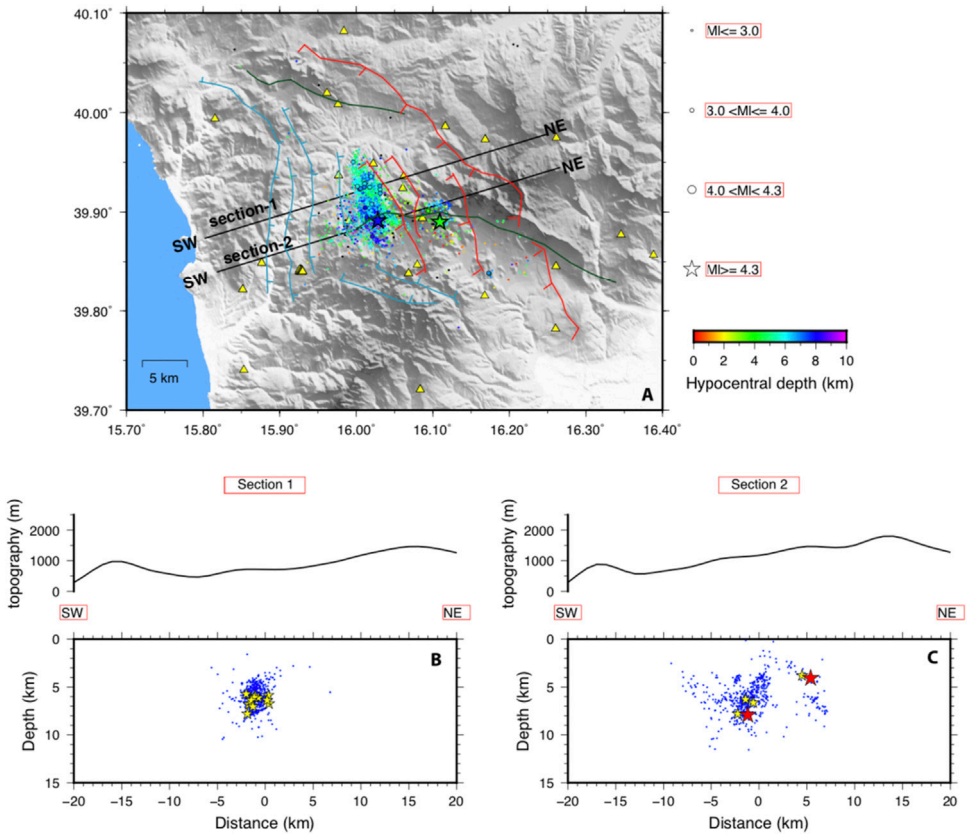

FIGURE 8 | Map and cross sections view of the earthquakes relocated using the hypoDD location. Layouts and symbols are the same as in **Figure 7**.

using a standard configuration for local earthquakes, already tested in other studies, such as in Pastori et al. (2019) for the Amatrice–Visso–Norcia seismic sequence and in Baccheschi et al. (2016) for the L'Aquila earthquake, applying the following values: (1) Corner frequencies of cf1 = 1 Hz and cf2 = 12 Hz of the four poles 2 pass Butterworth filter; (2) PRE variable set on 0.15 s time before the S-picking in which the analysis window starts; (3) DUR variable, representing the time after the S-picking, is computed using the formula DUR = C 1/cf2 where C is a coefficient, in this case set on 2.5 to ensure including at least a complete filtered shear wave cycle; (4) the total duration of the analyzed signal is 0.35 s (PRE + DUR) and encompass the S-wave arrival.

To ensure that the observed shear wave energy pertains only to the horizontal plane, the code performs a number of tests. In detail, the code evaluates i) the S-to-P ratio, the ratio between the amplitude of the horizontal components sum (RMSs) and the amplitude of the vertical component (RMSp) computed on the analysis window as RMSs/RMSp and it is set to be greater than four; ii) the geometrical incidence angle computed as ic = sin-1(Vs/Vp) is set to be lower than 45° (Booth and Crampin, 1985), where *Vs* and *Vp* are the velocities of S and P waves, respectively.

Following Bowman and Ando (1987) Anisomat + calculate the cross-correlation between the two horizontal components. This allows measuring the similarity of the pulse shape between the S-waves and their delay time (δt). These two time series in fact have similar shapes, mutually orthogonal oscillation directions, and travel with different velocities.

Horizontal components of the ground motion are then rotated (with steps of 1° from 0 to 180) and for each step, the cross-correlation function is stored. Finally, a two-dimensional matrix is obtained and after a grid search, the code estimates the couple of lag time and rotation angle which maximizes the cross-correlation coefficient.

These two quantities represent the delay time between the slow and fast shear wave (δt) and the polarization azimuth (φ) of the incoming fast shear wave.

Associated errors are defined by a criterion that reflects the shape of the cross-correlation matrix and how rapidly the matrix grows around the observed maximum value. In practice, the goodness of the estimation is related to the difference in delay time and in degrees between the cross-correlation maximum and 95% of the parameter values themselves. The mean errors for fast directions and delay times are 14.7° and 0.008 s, respectively (see **Table 1** for mean values at each station). At the end the code returns an ASCII output file composed by 21 fields described in the **Supplementary Material**. For further details, the reader should refer to Piccinini et al., 2013.

Seismicity used in the anisotropic analysis is mainly concentrated under Mormanno village between 5 and 10 km depth, with magnitudes ranging from 0.2 to 3.0. To avoid

TABLE 1 | Averaged anisotropic results and their associated errors obtained at each used station.

Station name	Event numbers	Mean fast direction (°)	Mean fast direction error (°)	Mean delay time (s)	Mean delay time error (s)
CET2	11	146	11.0	0.053	0.007
CSB	2	110	10.2	0.085	0.006
CSC	1	52	11.9	0.039	0.009
CUC	58	16	14.9	0.06	0.008
MGR	17	45	12.8	0.055	0.008
MMN	1,827	106	15.8	0.049	0.007
ORI	4	22	13.2	0.11	0.012
SALB	32	136	14.4	0.066	0.010
SCHR	32	94	14.6	0.062	0.009
SIRI	50	144	13.1	0.071	0.009
T0701	4	31	11.0	0.085	0.008
T0702	4	17	14.3	0.058	0.007
T0711	289	161	13.3	0.069	0.007
T0712	1	174	25.0	0.048	0.006
T0715	92	103	13.8	0.066	0.008
T0716	8	120	11.9	0.078	0.008
T0721	403	118	14.3	0.067	0.008
T0722	446	157	12.8	0.069	0.010
T0723	431	130	13.3	0.078	0.008
T0724	6	180	14.7	0.058	0.011
T0725	3	169	16.3	0.06	0.007
TDS	8	86	17.3	0.039	0.009
Total	3,727	124	14.7	0.06	0.008

complications on the S-wave arrival, due to the P-wave coda of a strong event that could make difficult the splitting analysis, we decided to discard events with a magnitude greater than 3.0.

After the Anisomat + analysis and its quality controls, in order to discuss a high-quality anisotropic dataset, we admitted only those results with a cross-correlation coefficient CC ≥ 0.75, which allowed us to obtain a total of 3,727 fast single measurements (δt > 0.02 s) and 2,040 null results ($\delta t \leq 0.02$ s). A measure is defined null when the S wave does not show splitting; this happens, in an anisotropic medium, when the initial S-wave polarization is coincident to the slow or the fast axis, and furthermore, nulls do not constrain the delay time.

We present the fast and null directions as interpolated values on a regular grid-box which nodes are 2-km spaced (see **Supplementary Figure S1** for details) evaluated with the Tomography Estimation of Shear wave splitting and Spatial Averaging (TESSA) program (Johnson et al., 2011). In each block, the rose diagram of fast values and the associate mean fast direction are displayed, providing i) the standard deviation is <30°, ii) the standard error is <10°, and iii) at least 10 rays pass through the grid-box. Furthermore, TESSA weights the data according to the fast errors estimated by means of Anisomat+ and to the weighting regime selected, in this case, we chose a 1/d regime, where d is the length in km between the grid-box and the station. The insets of **Figure 9**, the orange and green rose diagrams are frequency plots representing splitting fast and null measurements, respectively, for the whole area. Prevalent NW-SE fast directions are observed: the average fast direction is N124° (see **Table 1** for mean values at each station) while the null directions show two main peaks one strikes N127° (considered as the fast direction) and the other roughly orthogonal to it (considered as the slow direction).

In the crustal volume sampled by S-waves, the different mean fast directions observed lead us to suppose the presence of intense and complex anisotropic anomalies. The prevalent φ is both parallel to the major fault structures and consistent with the local stress field being parallel to the NW–SE S_{Hmax}, so the ambiguity on the probable crustal anisotropic source is not solved: structural anisotropy or aligned microfractures opened by the active stress field?

Fast orientations delineate three main areas North-East, West and South-East: 1) NNW–SSE mean direction (stable and coherent for fast and null measurements); 2) WNW-ESE mean direction (variable and not coincident for fast and null measurements) and 3) from NW-SE to E-W mean direction (stable and coherent for fast and null measurements), respectively.

In the north area of the activated fault system, the relocated hypocenters define a diffuse ball-shaped volume of seismicity instead of fault planes. This behavior could have influenced the anisotropic parameters, in fact, the strong variability of fast directions, noticed in the western area, can indicate the absence of dominant structures and the existence of a complex diffusivity system where fluids can flow. Instead, in the eastern part where the hypocenters delineate a main SW-dipping fault plane with an antithetic plane to the west and another dipping to NE on the east side (**Figures 7C**, **8C**), we observed stable and coherent φ with respect to the major structures, in this case, we can assume that anisotropy is structurally controlled as predicted by Zinke and Zoback (2000) structure-related model.

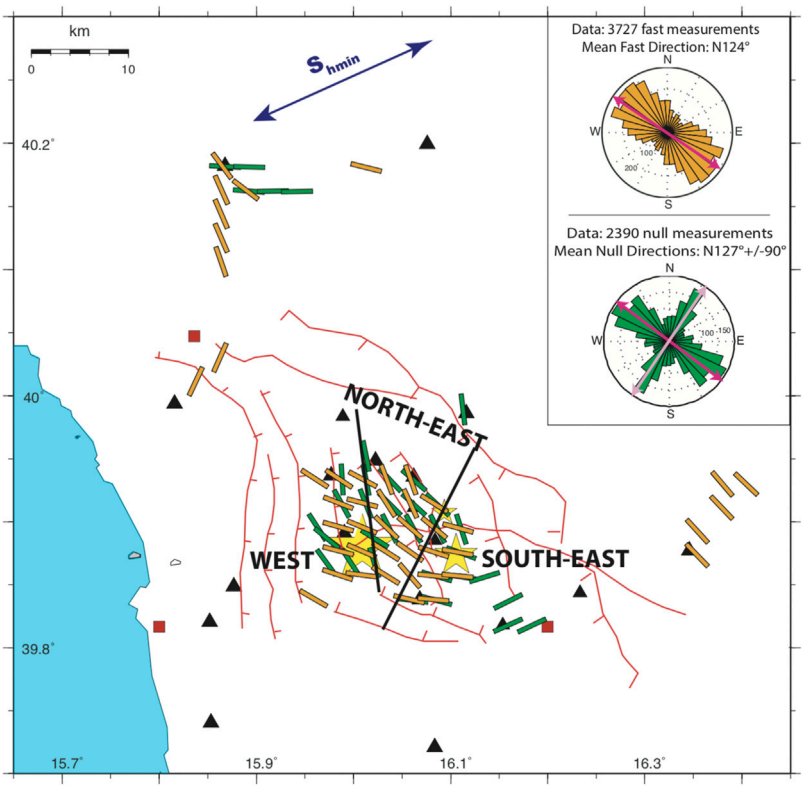

FIGURE 9 | Map of the spatial average for 3,727 fast (orange bars) and 2040 null (green bars) measurements. Three sectors are recognized: West) even if a WNW–ESE mean direction is observed, fast and null orientations are variables and not coincident; North-East) a NNW–SSE mean direction is visible, fast and null orientations are stables and coherent; South-East) a trend from NW–SE to E–W mean direction is delineated from both fast and nulls measurements. The upper right insets show the total rose diagrams for both fast and null measurements.

Delay time singular values oscillate between 0.024 up to 0.248 s (**Figure 10A**) with a total average value of 0.06 s (see **Table 1** for mean values at each station). These values agree with those found in other regions of Italy along the Apennine (Margheriti et al., 2006; Piccinini et al., 2006; Pastori et al., 2009; 2019), or in the crust of other regions in the world, as on the Karadere–Düzce fault (Peng and Ben-Zion, 2004). We will interpret the results in terms of delay time normalized for the hypocentral distance (δtn) because we suppose that the anisotropy measured at the station is just the sum of the anisotropic structures crossed by the seismic ray (e.g., Crampin, 1991; Zhang et al., 2007).

Normalized delay time values are represented in **Figure 10B** as the geographical distribution of interpolated single measurements on a 2-km spaced grid, similar to that used for the fast measurements averaging. The higher culmination of δtn (from 0.007 to 0.01 km/s) is visible in the Northeast sector that represents the hangingwall of the fault that generated the M 5.0 event. This value allows us to confirm that the principal source of crustal anisotropy, in this area, is represented by the structural control, as already seen by the φ pattern.

The lower values of δtn (from 0.003 to ~0.005 s/km) are visible in the external west and southeast areas. These values allow us to suppose the presence of a complex diffusivity fluid system where fluids can migrate along a relatively high-permeability hydraulic path but cannot be gathered. The existence of this network of fractures and/or porous fluid-filled is also invoked, i. e, by Della Vedova et al. (2001) to interpret the unusual low geothermal gradient of the region, by Barberi et al. (2004) and Totaro et al. (2014) to explain an high *Vp*/*Vs* value observed in the shallowest crust and by Napolitano et al. (2020) to justify the scatter and absorption anomalies.

DISCUSSION

The Pollino gap area is located at the edge of the southern Apennines where a broad strike-slip shear zone separates two lithospheric blocks (the Apennines and the Calabrian arc) with different evolution in the Plio-Pleistocene (Spina et al., 2009; Orecchio et al., 2015; Palano et al., 2017). This lithospheric discontinuity favored the retreat of the ionian slab during the lower Pleistocene and consists of a set of N120-trending faults, which comprises the Pollino fault and the Amendolara fault in the ionian off-shore (Ferranti et al., 2014).

In Late Pliocene-Quaternary the ancient thrust structures are crosscutting by extensional faults that forming intermountain basins along the Apennines axis (Ferranti et al., 2017), as well as

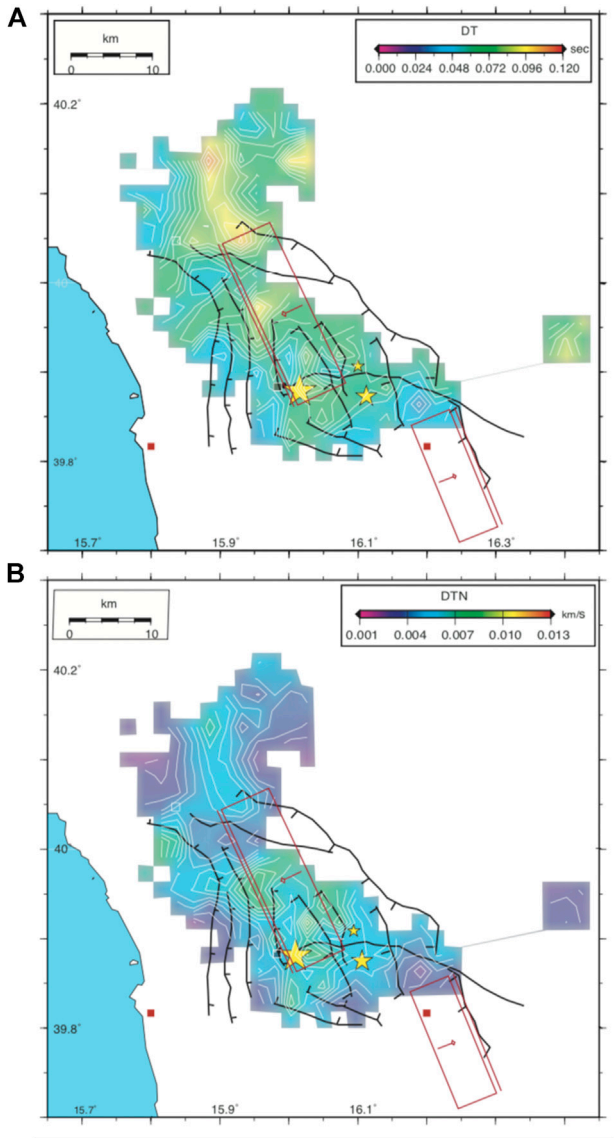

FIGURE 10 | Geographical distribution of **(A)** delay time and **(B)** normalized delay time values interpolated on a 2 km spaced grid, by means a nearest neighbor algorithm.

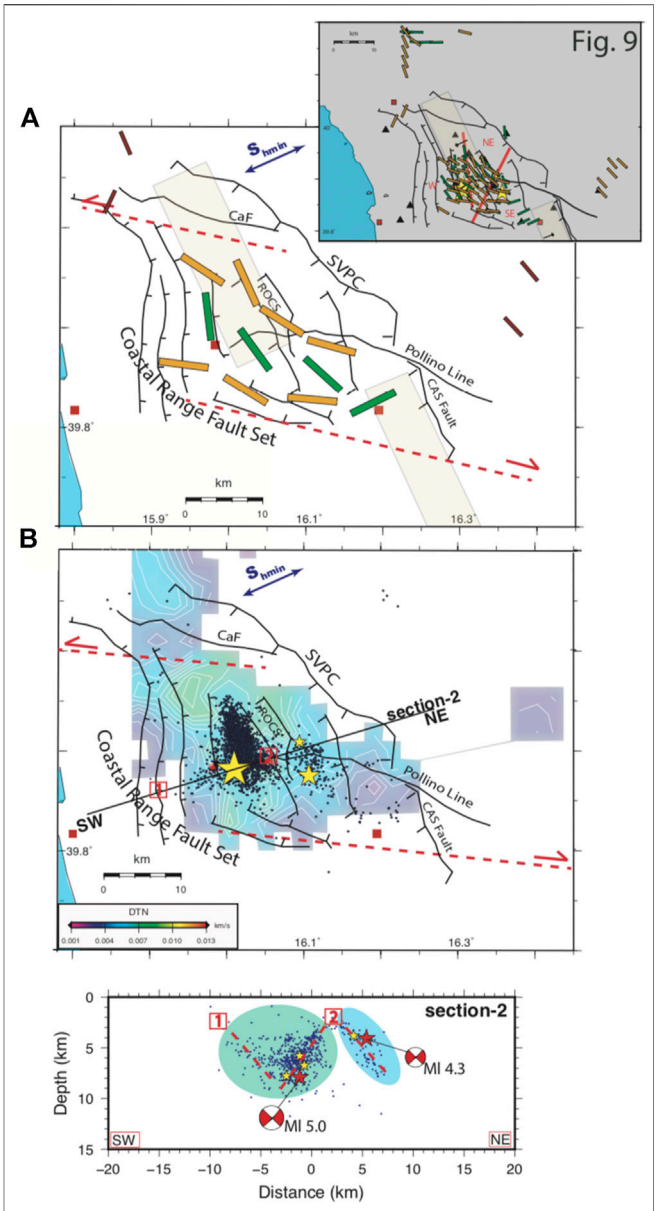

FIGURE 11 | (A) Sketch map of the identified three sectors with similar mean fast and null directions. In general, a rotation from roughly WNW–ESE to NNW–SSE and WNW–ESE is observed. These orientations are related to major active faults, such as CaF, ROCS, and Pollino line, respectively, except for the West sector where fast and null directions are not in agreement. **(B)** Map of interpolated values of δtn and the superimposed 1D relocated seismicity. **(C)** Southern cross-section of 1D accurate location; green and blue shadow are referred to as δtn values, and dashed lines define the activated fault systems. In **(B)–(C)**, 1 and two represent the top points of the probable fault planes projected in map. 1 falls into the CRFS area while two falls into the intersection between the ROCS area and the westernmost part of the Pollino line. In **(A)–(B)**, red dashed lines with arrows represent the regional scale strike-slip episodes related to geodynamic processes, yellow stars identify the strongest events, and the main fault systems are also reported.

the Mercure and the Crati basins respectively to the North and South of the Pollino fault.

Common tectonic models are based on the continuity of deformation between the southern Apennines and Calabrian arc (i.e., Valensise and Pantosti, 2001); lateral heterogeneities across the Pollino mountain range instead suggest that the strike-slip shear zone permits a kinematic decoupling between the extending Apennines and that retreating Calabrian block (Chiarabba et al., 2016), as also signaled by the imprint of toroidal flow at the ionian slab edge on GPS data (Palano et al., 2017).

The Quaternary normal active fault systems segmented by the tectonic structures inherited from the past and the complex interaction between the activated fault planes evidenced by the refined 1D and DD relocations can be considered as the cause of the great variability defined by the anisotropic pattern.

Recent studies tried to model the geometry of the activated fault system in this area. Napolitano et al. (2021) used a smaller portion of events (422 in 27 clusters) with respect to our dataset (~2,300 events). Their locations were concentrated mainly on the western cluster and depicted a structure, having a similar geometry to the one that we consider to be probably responsible for the M_L 5.0. On the contrary, they did not identify the antithetic fault, that we assume likely causing the M_L 4.3, because their data did not sample the eastern cluster.

Brozzetti et al. (2017) used both seismological and geological data to infer the geometry of activated faults. Their solutions agree with the geometry of the M_L 5.0 reconstructed by our data, on the other hand, to define the fault causative of the M_L 4.3, their locations showed an almost vertical alignment of earthquakes and considering the geological surface expressions they preferred a fault dip to the NE.

In our study, we compare refined 1D and DD locations and anisotropic results to better constrain the geometries of the activated fault system. The S-waves fast polarizations show a general rotation from roughly WNW–ESE (sub-parallel to CaF) to NNW–SSE (sub-parallel to the ROCS active extensional systems) to WNW–ESE (sub-parallel to the Pollino line) (orange bars in **Figure 11A**). Such orientations are also observed in null results, except for the Western area (green bars in **Figure 11A**); as previously explained we observe a null direction if the initial S-wave polarization is coincident to the source structures of the anisotropy. After these considerations, we can affirm that for the western sector, fast direction polarizations are probably more related to aligned microfractures opened by the active stress field, while nulls reflect major structure orientations confirming a structural control of anisotropy.

All these orientations well-delineate the regional scale structural complexities, such as the strike-slip episodes related to geodynamic processes and those at the small-scale represented by the local stress variations.

In general, the interaction between the irregular geometries of the fault systems could favor multisegment ruptures and/or the reactivation of inherited structures with the inversion of the kinematics due to the present stress regime. These segments take part in the generation of a complex diffusivity system where fluids can be channelized and carried toward heavily fractured rock volume where in some cases they can be gathered.

Overall, we found in the western sector, the volume where most of the seismicity occurs, a higher value of δtn. This crustal volume represents, under a structural point of view, the hangingwall of the main fault where the M 5 is supposed to be enucleated. Similarly, the 1D and DD accurate relocations depict a SW-dipping main fault plane but also an antithetic plane to the west. This area can be imaged as an ancient positive flower structure reactivated in the current extensional regime, as also considered by Totaro et al. (2015) to explained their focal mechanism solutions and high-precision locations using the DD method in the Mercure Basin.

The main faults, that border the flower structure, could play the role of a preferential pathway in which fluids are channelized and accumulated on the top of the heavily fractured rock volume and laterally confined by these structures (**Figures 11B,C**).

Instead, in the southeast sector, the 1D and DD relocation possibly represents a NE-dipping plane where the fewest seismicity occurs. In this area, the anisotropic pattern of fast directions recognizes a dominant WNW–WSW trend and lower value of δtn. These findings suggest that fluids migrate preferentially along hydraulic pathways having a high percentage of permeability, such as the hypothesized secondary fault, up to the free surface not allowing a constant pervading the crustal volume by fluids.

Seismogenesis

In the hangingwall of the activated fault systems (western sector), our anisotropic evidence and the excess rate of seismicity during the sequence are indicative of countless fluid-saturated cracks. Napolitano et al. (2020) through a study based on seismic scatter and absorption confirmed the presence of a highly fluid-filled micro-fractured seismogenic volume around the main activated structures during the swarm. Passarelli et al. (2015) established that the temporal and spatial behavior of seismicity in the western sector follows prevalently a swarm-like consistent with a transient, external forcing. Even Cheloni et al. (2017) evidenced a transient slip, around the mainshock, approximately 4 months before and gone on about one year.

Transient slip associated with a high percentage of fluid-filled fractures could have reduced the effective normal stress facilitating fault slip, partially inhibiting the development of large rupture (Cheloni et al., 2017; Yoshida and Hasegawa, 2018), increasing the rate of seismicity but limiting the maximum magnitude of events.

Furthermore, also lithology might affect the permanence of fluids, in fact, the carbonate rocks forming the hangingwall have an important function in both preserving and hosting the micro-fracture system responsible for the observed anisotropic pattern. This permanent presence of fluid could reduce the long-term fault strength, promoting aseismic fault slip and causing important weakening along the existing fault planes. In this contest, looking at the structures obtained by the 1D and DD relocations we can suggest the reactivation of an ancient positive flower structure in the actual stress regime.

We, therefore, explain the space-time-magnitude pattern of the seismic sequence, and the excess rate of seismicity, as governed by the preservation of the filled-fluid micro-fracture network in the seismogenic volume that followed transient slip.

Constraints to Hazard

Persistent swarms in the Pollino seismic gap area created repeated concerns in public and seismic risk stakeholders, for uncertainties on possible forecasting scenarios. Most of the concerns derived from the perception that the area was seismically silent for a long time and possibly prone to a large event. The analysis of the 2011–2014 swarm yields therefore precious information that might help to constrain hazard models.

The seismic gap idea, first expressed by Omori (1908), was motivated by the lack of large earthquakes since at least 10 Kyr (Rovida et al., 2016). In the continuous extensional fault system model (Valensise and Pantosti, 2001), a 60 km long gap encloses the Pollino mountain range and partially the upper Crati valley.

The faults studied by paleo-seismological trenches in the southern border of the Pollino area evidenced large slip earthquakes older than 1 Kyr (Galli et al., 2008; Cinti et al., 2002; Michetti et al., 1997), reinforcing the idea that large earthquakes are expectable.

The absence of large earthquakes in the historical catalog has been associated with a combination of low strain rate and mixed seismic/aseismic strain release that could increase the recurrence time of large magnitude events (Cheloni et al., 2017).

Under these circumstances, the persistence of a pervasive fluid system network in the pop-up structure accounted for increasing the stability of the faults, partially inhibiting the generation of large earthquakes. In any case, the reactivation of pre-existent thrusts and back-thrusts of the pop-up would promote the segmentation of the seismic gap in fragments with a maximum length of 10–12 km.

Although shear wave splitting analysis does not measure directly the activity of a fault, our results might help us to delineate the seismotectonic settings of the Pollino region.

In the western sector, where the highly fractured rock and the excess rate of seismicity are observed, we can suppose a reduction of shear-strength along CRFS and ROCS faults (**Figures 11B,C**), probably representing the boundaries of the flower structure. This reduction in turn can generate earthquakes also for a low level of stress accumulation.

In the eastern sector, instead, the lower values of δtn and fewer seismicity rates are concentrated; this area coincides with the upward continuation of the surface expression of CAS (Cinti et al., 2015). The absence of a strong pervasive fluid system network that reduces the effective normal stress facilitating fault slip, around the intersection between CAS fault might suggest that this eastern segment could be more prone to an unstable deformation and a large rupture.

Differences in Crustal Response to Slab Tearing Between Apennines and Calabria

Comparing **Figures 7B**,C, **8B**,C strikingly illustrates the different behavior in the release of seismic energy between the Northern half and the Southern half of the study area. While a more standard seismicity clustered along defined planes is present in the Southern half (**Figures 7C**, **8C**), diffuse seismicity is found in the North (**Figures 7B**, **8B**). Those two phenomena have been observed worldwide, but rarely in such close proximity. We speculate that such rapid spatial change in crustal behavior is caused by a different response of the Southern Apennines and the Calabrian block to the tearing of the ionian slab. Slab tearing is likely to generate diffuse deformation in the overriding plate (i.e., Maesano et al., 2020; Chiarabba and Palano, 2017; Gutscher et al., 2016). The Apennines slab has been torn in several places (Rosenbaum et al., 2008) and the tearing process has shown to affect the entire crustal volume (Bianchi et al., 2016). Such "crustal response" is likely to interest a wide area rather than a focalized rock volume on top of the tear fault (Rosenbaum et al., 2008), depending on the local rheological properties of the crust (Boncio et al., 2007; Polonia et al., 2011). Here the tearing of the ionian slab, revealed at depth by passive seismic (Rosenbaum et al., 2008; Orecchio et al., 2015), probably interested in different ways the juxtaposed two crustal domains, focusing a higher level of deformation on the Southern Apennines side, and, thus, weakening the entire crustal volume. This interpretation is supported by the distribution of earthquakes in a diffuse area (NW of Mormanno) indicating the inability of cumulating stress on relevant tectonic structures (i.e., km-scale planar faults) and corroborated by the misoriented fast polarization directions with respect to the major structures, given by the complex fluid-filled fracture network. Opposite observations in the Southern portion (planar faults, where main M_L 5.0 and M_L 4.3 events occurred) where fast directions reflect the strike of the major structures testifying to the different behavior of the crustal response to slab tearing, on the two sides of the boundary between Apennines and Calabria.

CONCLUSION

The seismic swarms occurred within the gap area, along the Pollino shear zone. Relocated earthquakes reveal that seismicity developed on two main NNW-trending and opposite dipping clusters with primary events being the M_L 4.3 and the M_L 5.0 on 28th May and 25th October 2012, respectively.

The geometry drawn by the refined 1D and DD locations delineates the activated fault system having the following characteristics: a) it is composed at least of three fault segments with a length <10 km; b) it is located in the shallower 10 km of the crust; c) it is oriented roughly NW-SE. The dip of the main fault segment, where most of the seismicity occurs such as the M_L 5.0 earthquake, is toward SW while, the two other minor segment faults dip toward NE. Although with a lower resolution also Totaro et al. (2014) pointed out a similar geometry of the main fault segment.

According to the data reported in DISS database, we could place the activated fault system between the two major seismogenic sources present in the area: the Rimendiello–Mormanno Mercure Basin fault system (RM-MB) and the Castrovillari Fault (CV). The geometry of the RM-MB, constrained by geological data, is about comparable with the trend of the recent seismicity, but its dip is to the NE. Instead, CV source has a similar orientation (N20W) and a western dip, as reported by the analyzed seismicity, but its northern border match to the southernmost epicentres. Finally, our results in terms of fault orientations delineated at depth by 1D and DD refined locations could be connected to the mapped fault systems reported by Brozzetti et al. (2017).

The reactivation of an ancient positive flower structure in the actual stress regime is supported by the fast direction polarization rotation from NNW–SSE in the middle of the extensional basin toward WNW–ESE in the area where the Pollino fault is supposed to be. As imaged by location earthquakes this structure is composed of a set of thrust and back-thrust strikes mainly NW–SE.

The interaction at a depth between these faults could generate a pathway for fluids and in certain conditions, i.e. in the presence of a structural barrier, reach the overpressure status. As observed from anisotropic results, the presence and mobility of channelized fluids in the crust promote multisegment ruptures

and/or the reactivation of inherited structures only if favorable oriented with the present-day stress regime.

Back thrust reactivation contributes to the segmentation of the 60 km long seismic gap in fragments with a maximum length of 10–12 km. In this vision, the subdivision could partially restrict the generation of large earthquakes in this area.

DATA AVAILABILITY STATEMENT

The data of used stations are from the Italian National Seismic Network (doi.org/10.13127/SD/X0FXnH7QfY). The waveform data of earthquakes used are available at EIDA database (European Integrated Data Archive http://eida.rm.ingv. it/).

AUTHOR CONTRIBUTIONS

MP wrote the manuscript, analyzed the data and evaluated the anisotropic parameters; LM coordinated the working group; PDG, AM and DL made picking analysis and 1D locations; AG installed the temporary stations in the field, made data available and helped in the discussions; FL, NA, DP and CC made picking analysis and discussed the results; MM coordinated the fieldwork and made picking analysis; PDL made picking analysis and evaluated anisotropic parameters; RDG, MA and AN made picking analysis; LP discussed the results.

FUNDING

This study has benefited from funding provided by the Italian Presidenza del Consiglio dei Ministri –Dipartimento della Protezione Civile (DPC). This paper does not necessarily represent DPC official opinion and policies.

ACKNOWLEDGMENTS

We would like to thank all operators who installed and serviced the temporary seismic stations managed by INGV. We would like to follow up by thanking all the INGV staff on shifts in the surveillance room in Rome for their work and the Bollettino Sismico Italiano working group (http://terremoti.ingv.it/bsi) for making available the files of the manually revised P- and S-phase pickings. We are grateful for the comments and suggestions of the Guest Associated Editor Jorge Gaspar-Escribano, Luca De Siena, and the reviewer, which helped us to improve the final version of the manuscript.

SUPPLEMENTARY MATERIAL

The Supplementary Material for this article can be found online at: https://www.frontiersin.org/articles/10.3389/feart.2021.618293/full#supplementary-material.

REFERENCES

Baccheschi, P., Pastori, M., Margheriti, L., and Piccinini, D. (2016). Shear wave splitting of the 2009 L'Aquila seismic sequence: Fluid satu- rated microcracks and crustal fractures in the Abruzzi region (central Apennines, Italy). *Geophys. J. Int.* 204 (3), 1531–1549. doi:10.1093/gji/ggv536

Barberi, G., Cosentino, M. T., Gervasi, A., Guerra, I., Neri, G., and Orecchio, B. (2004). Crustal seismic tomography in the Calabrian Arc region, south Italy. *Phys. Earth Planet. Inter.* 147 (4), 297–314. doi:10.1016/j.pepi.2004.04.005

Bianchi, I., Lucente, F. P., Di Bona, M., Govoni, A., and Piana Agostinetti, N. (2016). Crustal structure and deformation across a mature slab tear zone: the case of southern Tyrrhenian subduction (Italy). *Geophys. Res. Lett.* 43, 12380–12388. doi:10.1002/2016GL070978

Boncio, P., Mancini, T., Lavecchia, G., and Selvaggi, G. (2007). Seismotectonics of strike–slip earthquakes within the deep crust of southern Italy: geometry, kinematics, stress field and crustal rheology of the Potenza 1990–1991 seismic sequences (Mmax 5.7). *Tectonophysics* 445 (3–4). 281–300. doi:10.1016/j.tecto.2007.08.016

Booth, D. C., and Crampin, S. (1985). Shear-wave polarizations on a curved wavefront at anisotropic free surface. *Geophys. J. Roy. Astron. Soc.* 83, 31–45.

Bowman, J. R., and Ando, M. (1987). Shear-wave splitting in the upper-mantle wedge above the Tonga subduction zone. *Geophys. J. Int.* 88, 25–41. doi:10.1111/j.1365-246x.1987.tb01367.x

Brozzetti, F., Cirillo, D., de Nardis, R., Cardinali, M., Lavecchia, G., Orecchio, B., et al. (2017). Newly identified active faults in the Pollino seismic gap, southern Italy, and their seismotectonic significance. *J. Struct. Geol.* 94, 13–31. doi:10.1016/j.jsg.2016.10.005

Brozzetti, F., Lavecchia, MilanaG., G., Milana, G. G., and Cardinali, M. (2009). Analysis of the 9 september 1998 Mw 5.6 mercure earthquake sequence (southern Apennines, Italy): a multidisciplinary approach. *Tectonophysics* 476, 210–225. doi:10.1016/j.tecto.2008.12.007

Brozzetti, F. (2011). The Campania-Lucania Extensional Fault System, southern Italy: a suggestion for a uniform model of active extension in the Italian Apennines. *Tectonics* 30, 114. doi:10.1029/2010TC002794

Chatelain, J. L. (1978). *Etude fine de la sismicité en zone de collision continentale au moyen d'un réseau de stations portables: la région Hindu-Kush Pamir*. Thèse de doctorat de 3ème cycle Université scientifique et médicale de Grenoble. Berlin: Springer, 219.

Cheloni, D., D'Agostino, N., Selvaggi, G., Avallone, A., Fornaro, G., Giuliani, R., et al. (2017). Aseismic transient during the 2010-2014 seismic swarm: evidence for longer recurrence of M ≥ 6.5 earthquakes in the Pollino gap (Southern Italy)? *Sci. Rep.* 7 (576), 576. doi:10.1038/s41598-017-00649-z

Chiarabba, C., Agostinetti, N. P., and Bianchi, I. (2016). Lithospheric fault and kinematic decoupling of the Apennines system across the Pollino range. *Geophys. Res. Lett.* 43, 3201–3207. doi:10.1002/2015GL067610

Chiarabba, C., De Gori, P., and Speranza, F. (2008). The southern Tyrrhenian subduction zone: deep geometry, magmatism and PlioPleistocene evolution. *Earth Planet. Sci. Lett.* 268 (1–2), 408–423. doi:10.1016/j.epsl.2008.01.036

Chiarabba, C., Jovane, L., and DiStefano, R. (2005). A new view of Italian seismicity using 20 years of instrumental recordings. *Tectonophysics* 395, 251–268. doi:10.1016/j.tecto.2004.09.013

Chiarabba, C., and Palano, M. (2017). Progressive migration of slab break-off along the southern Tyrrhenian plate boundary: constraints for the present day kinematics. *J. Geodynamics* 105, 51–61. doi:10.1016/j.jog.2017.01.006

Cinti, F. R., Cucci, L., Pantosti, D., D'Addezio, G., and Meghraoui, M. (1997). A major seismogenic fault in a 'silent area': the Castrovillari fault (southern Apennines, Italy). *Geophys. J. Int.* 130, 595–605. doi:10.1111/j.1365-246x.1997.tb01855.x

Cinti, F. R., Moro, M., Pantosti, D., Cucci, L., and D'Addezio, G. (2002). New constraints on the seismic history of the Castrovillari fault in the Pollino gap (Calabria, southern Italy). *J. Seismol.* 6, 199–217. doi:10.1023/a:1015693127008

Cinti, F. R., Pauselli, C., Livio, F., Ercoli, M., Brunori, C. A., Ferrario, M. F., et al. (2015). Integrating multidisciplinary, multiscale geological and geophysical data to image the Castrovillari fault (Northern Calabria, Italy). *Geophys. J. Int.* 203 (3), 1847–1863. doi:10.1093/gji/ggv404

Crampin, S. (1993). Arguments for EDA. *Can. J. Explor. Geophys.* 29, 18–30.

Crampin, S. (1991). Wave propagation through fluid-filled inclusions of various shapes: interpretation of extensive-dilatancy anisotropy. *Geophys. J. Int.* 104 (3), 611–623. doi:10.1111/j.1365-246X.1991.tb05705.x

De Gori, P., Margheriti, L., Lucente, F. P., Govoni, A., Moretti, M., and Pastori, M. (2014). "Seismic activity images the activated fault system in the Pollino area, at the Apennines–Calabrian arc boundary region," in Proceedings of the 34th national conference of GNGTS, Bologna.

Della Vedova, B., Bellani, S., Pellis, G., and Squarci, P. (2001). *Deep temperatures and surface heat flow distribution, in anatomy of an orogen: the Apennines and adjacent mediterranean basins*. Editors F. Vai and I. P. Martini (Berlin: Springer), 65–76.

Di Stefano, R., Kissling, E., Chiarabba, C., Amato, A., and Giardini, D. (2009). Shallow subduction beneath Italy: three-dimensional images of the Adriatic-European-Tyrrhenian lithosphere system based on high-quality P wave arrival times. *J. Geophys. Res.* 114 (2009), 1–17. doi:10.1029/2008jb005641

DISS Working Group. (2018). Database of Individual Seismogenic Sources (DISS), in *Version 3.2.1: a compilation of potential sources for earthquakes larger than M 5.5 in Italy and surrounding areas*: Istituto Nazionale di Geofisica e Vulcanologia. Available at: http://diss.rm.ingv.it/diss/ doi:10.6092/INGV.IT-DISS3.2.1

D'Agostino, N., et al. (2013). GPS velocity and strain field in the Calabro–Lucania region. INGV-DPC, S1 project 2012-2013, Final Rep., 314–321.

D'Agostino, N., and Selvaggi, G. (2004). Crustal motion along the eurasia-nubia plate boundary in the Calabrian arc and sicily and active extension in the messina straits from GPS measurements. *J. Geophys. Res.* 109, B11402. doi:10.1029/2004JB002998

Faccenna, C., Piromallo, C., Crespo-Blanc, A., Jolivet, L., and Rossetti, F. (2004). Lateral slab deformation and the origin of the western Mediterranean arcs. *Tectonics* 23, 111. doi:10.1029/2002TC001488

Ferranti, L., Burrato, P., Pepe, F., Santoro, E., Mazzella, M. E., Morelli, D., et al. (2014). An active oblique-contractional belt at the transition between the southern Apennines and Calabrian arc: the Amendolara ridge, ionian Sea, Italy. *Tectonics* 33, 2169–2194. doi:10.1002/2014TC003624

Ferranti, L., Milano, G., and Pierro, M. (2017). Insights on the seismotectonics of the western part of northern Calabria (southern Italy) by integrated geological and geophysical data: coexistence of shallow extensional and deep strike-slip kinematics. *Tectonophysics* 721, 372–386. doi:10.1016/j.tecto.2017.09.020

Galli, P., Galadini, F., and Pantosti, D. (2008). Twenty years of paleoseismology in Italy. *Earth-Science Rev.* 88, 89–117. doi:10.1016/j.earscirev.2008.01.001

Ghisetti, F., and Vezzani, L. (1982). Strutture tensionali e compressive indotte da meccanismi profondi lungo la linea del Pollino (Appennino meridionale). *Boll. Soc. Geol. It* 101, 385e440.

Govoni, A., Passarelli, L., Braun, T., Maccaferri, F., Moretti, M., Lucente, F. P., et al. (2013). Investigating the origin of seismic swarms. *Eos Trans. AGU* 94 (41), 361–362. doi:10.1002/2013eo410001

Gruppo di Lavoro, M. P. S. (2004). Redazione della mappa di pericolosità sismica prevista dall'Ordinanza PCM 3274 del 20 marzo 2003. Rapporto Conclusivo per il Dipartimento della Protezione Civile., INGV, Milano-Roma. 65 pp. + 5 appendici.

Gutscher, M.-A., Dominguez, S., de Lepinay, B. M., M., B., Gallais, F., Babonneau, N., et al. (2016). Tectonic expression of an active slab tear from high-resolution seismic and bathymetric data offshore Sicily (Ionian Sea). *Tectonics* 35, 39–54. doi:10.1002/2015tc003898

Improta, L., Bagh, S., De Gori, P., Valoroso, L., Pastori, M., Piccinini,Buttinelli, D., et al. (2017). Reservoir structure and wastewater-induced seismicity at the Val d'Agri oilfield (Italy) shown by three-dimensional Vp and Vp/Vs local earthquake tomography. *J. Geophys. Res. Solid Earth* 122, 133. doi:10.1002/2017jb014725

Improta, L., De Gori, P., and Chiarabba, C. (2014). New insights into crustal structure, Cenozoic magmatism, CO2degassing, and seismogenesis in the southern Apennines and Irpinia region from local earthquake tomography. *J. Geophys. Res. Solid Earth* 119, 8283–8311. doi:10.1002/2013JB010890

INGV Seismological Data Centre. (2006). *Rete Sismica Nazionale (RSN)*. Italy: Istituto Nazionale di Geofisica e Vulcanologia (INGV). doi:10.13127/SD/X0FXNH7QFY

ISIDe Working Group. (2016). *Version 1.0.* Berlin: Springer. doi:10.13127/ISIDe

Kissling, E., Ellsworth, W. L., Eberhart-Phillips, D., and Kradolfer, U. (1994). Initial reference models in local earthquake tomographyInitial referent models in seismic tomography. *J. Geophys. Res.* 99 (B10), 19635–19646. doi:10.1029/93jb03138

Klein, F. W. (2002). User's guide to HYPOINVERSE-2000: a Fortran program to solve for earthquake locations and magnitudes. USGS Open File Rep. 02-171, 1–123. Version 1.0

Lahr, J. C. (1989). Hypoellipse/version 2.0: a computer program for determining local earthquake hypocentral parameters, magnitude and first motion pattern. U.S. Geological Survey Open-file Report, 89–116, 92 pp.

Locati, M., Camassi, R., Rovida, A., Ercolani, E., Bernardini, F., Castelli, V., et al. (2016). DBMI15, the 2015 version of the Italian macroseismic database. *Istituto Nazionale di Geofisica e Vulcanologia* 14, 114. doi:10.6092/INGV.IT-DBMI15

Lucente, F. P., Margheriti, L., Piromallo, C., and Barruol, G. (2006). Seismic anisotropy reveals the long route of the slab through the western-central Mediterranean mantle. *Earth Planet. Sci. Lett.* 241, 517–529. doi:10.1016/j.epsl.2005.10.041

Maesano, F. E., Tiberti, M. M., and Basili, R. (2020). Deformation and fault propagation at the lateral termination of a subduction zone: the alfeo fault system in the Calabrian arc, southern Italy. Front. *Earth Sci.* 8, 107. doi:10.3389/feart.2020.00107

Margheriti, L., Ferulano, M. F., and Di Bona, M. (2006). Seismic anisotropy and its relation with crust structure and stress field in the Reggio Emilia Region (Northern Italy). *Geophys. J. Int.* 167 (2), 1035–1043. doi:10.1111/j.1365-246X.2006.03168.x

Michetti, A. M., Ferreli, L., Serva, L., and Vittori, E. (1997). Geological evidence for strong historical earthquakes in an "aseismic" region: the Pollino case (southern Italy),. *J. Geodyn. 24, Nos* 1/4, 61–86.

Napolitano, F., De Siena, L., Gervasi, A., Guerra, I., Scarpa, R., and La Rocca, M. (2020). Scattering and absorption imaging of a highly fractured fluid-filled seismogenetic volume in a region of slow deformation. *Geosci. Front.* 11 (3), 989–998. doi:10.1016/j.gsf.2019.09.014

Napolitano, F., Galluzzo, D., Gervasi, A., Scarpa, R., and La Rocca, M. (2021). Fault imaging at Mt Pollino (Italy) from relative location of microearthquakes. *Geophys. J. Int.* 224 (1), 637–648. doi:10.1093/gji/ggaa407

Omori, F. (1908). (1909) preliminary report on the messina-reggio earthquake ofBull. Imperial earthquake invest. *Comm* 3–2, 37–46.

Orecchio, B., Presti, D., Totaro, C., D'Amico, S., and Neri, G. (2015). Investigating slab edge kinematics through seismological data: the northern boundary of the Ionian subduction system (south Italy). *J. Geodynamics* 88, 23–35. doi:10.1016/j.jog.2015.04.003

Palano, M., Piromallo, C., and Chiarabba, C. (2017). Surface imprint of toroidal flow at retreating slab edges: the first geodetic evidence in the Calabrian subduction system, Geophys. *Res. Lett.* 44, 121. doi:10.1002/2016GL071452

Passarelli, L., Hainzl, S., Cesca, S., Maccaferri, F., Mucciarelli, M., Roessler, D., et al. (2015). Aseismic transient driving the swarm-like seismic sequence in the Pollino range, Southern Italy. *Geophys. J. Int.* 201 (3), 1553–1567. doi:10.1093/gji/ggv111

Passarelli, L., Roessler, D., Aladino, G., Maccaferri, F., and Moretti, M. (2012). : Pollino seismic experiment (2012–2014). Deutsches GeoForschungsZentrum GFZ. Other/seismic network. doi:10.14470/9N904956

Pastori, M., Baccheschi, P., and Margheriti, L. (2019). Shear wave splitting evidence and relations with stress field and major faults from the "Amatrice-Visso-Norcia Seismic Sequence". *Tectonics* 38, 77. doi:10.1029/2018tc005478

Pastori, M., Piccinini, D., Margheriti, L., Improta, L., Valoroso, L., Chiaraluce, L., et al. (2009). Stress aligned cracks in the upper crust of the Val d'Agri region as revealed by shear wave splitting. *Geophys. J. Int.* 179 (1), 601–614. doi:10.1111/j.1365-246x.2009.04302.x

Peng, Z., and Ben-Zion, Y. (2004). Systematic analysis of crustal anisotropy along the Karadere-Düzce branch of the North Anatolian fault. *Geophys. J. Int.* 159 (1), 253–274. doi:10.1111/j.1365-246x.2004.02379.x

Piana Agostinetti, N., Park, J., and Lucente, F. P. (2008). Mantle wedge anisotropy in southern tyrrhenian subduction zone (Italy), from receiver function analysis. *Tectonophysics* 462 (1–4), 35–48. doi:10.1016/j.tecto.2008.03.020

Piana Agostinetti, N., Steckler, M., and Lucente, F. P. (2009). Imaging the subducted slab under the Calabrian Arc, Italy, from receiver function analysis. *Lithosphere* 1 (3), 1–8. doi:10.1130/L49.1

Piccinini, D., Margheriti, L., Chiaraluce, L., and Cocco, M. (2006). Space and time variations of crustal anisotropy during the 1997 Umbria-Marche, central Italy,

seismic sequence. *Geophys. J. Int.* 167, 1482–1490. doi:10.1111/j.1365-246X.2006.03112.x

Piccinini, D., Pastori, M., and Margheriti, L. (2013). ANISOMAT+: an automatic tool to retrieve seismic anisotropy from local earthquakes. *Comput. Geosciences* 56, 62–68. doi:10.1016/j.cageo.2013.01.012

Polonia, A., Torelli, L., Mussoni, P., Gasperini, L., Artoni, A., and Klaeschen, D. (2011). The Calabrian Arc subduction complex in the Ionian Sea: regional architecture, active deformation, and seismic hazard. *Tectonics* 30, TC5018. doi:10.1029/2010TC002821

Rosenbaum, G., Gasparon, M., Lucente, F. P., Peccerillo, A., and Miller, M. S. (2008). Kinematics of slab tear faults during subduction segmentation and implications for Italian magmatism. *Tectonics* 27, 119. doi:10.1029/2007TC002143

Rovida, A., Locati, M., Camassi, R., Lolli, B., and Gasperini, P. (2016). CPTI15, the 2015 version of the parametric catalogue of Italian earthquakes. *Istituto Nazionale di Geofisica e Vulcanologia* 7, 112. doi:10.6092/INGV.IT-CPTI15

Scognamiglio, L., Tinti, E., and Michelini, A. (2009). Real-time determination of seismic moment tensor for the Italian region. *Bull. Seismological Soc. America* 99 (4), 2223–2242. doi:10.1785/0120080104

Spina, V., Tondi, E., Galli, P., and Mazzoli, S. (2009). Fault propagation in a seismic gap area (northern Calabria, Italy): implications for seismic hazard. *Tectonophysics* 476 (1), 357–369. doi:10.1016/j.tecto.2009.02.001

Tertulliani, A., and Cucci, L. (2014). New insights on the strongest historical earthquake in the Pollino region (southern Italy). *Seismological Res. Lett.* 11, 39. doi:10.1785/0220130217

Totaro, C., Koulakov, I., Orecchio, B., and Presti, D. (2014). Detailed crustal structure in the area of southern Apennines-Calabrian Arc border from local earthquake tomography. *J. Geodyn.* 12, 94, doi:10.1016/j.jog.2014.07.004

Totaro, C., Presti, D., Billi, A., Gervasi, A., Orecchio, B., Guerra, I., et al. (2013). The ongoing seismic sequence at the Pollino mountains, Italy. *Seismological Res. Lett.* 84 (6), 955–962. doi:10.1785/0220120194

Totaro, C., Seeber, L., Waldhauser, F., Steckler, M., Gervasi, A., Guerra, I., et al. (2015). An intense earthquake swarm in the southernmost Apennines: fault architecture from high-resolution hypocenters and focal mechanisms. *Bull. Seismological Soc. America* 105 (6), 3121–3128. doi:10.1785/0120150074

Tsvankin, I. (2001). *Seismic signatures and analysis of reflection data in anisotropic media*. Cambridge: Elsevier Science.

Valensise, G., and Pantosti, D. (2001). Database of potential sources for earthquakes larger than M 5.5 in Italy (DISS version 2.0). Ann. *Geofis* 44 (Suppl. 1), 59. doi:10.4401/ag-3562

Van Dijk, J. P., Bello, M., Brancaleoni, G. P., Cantarella, G., Costa, V., Frixa, A., et al. (2000). A new structural model for the northern sector of the Calabrian Arc. *Tectonophysics* 324, 267e320. doi:10.1016/s0040-1951(00)00139-6

Wadati, K. (1933). On the travel time of earthquake waves. *Part. Geophys. Mag.* 7, 101–111.

Waldhauser, F. (2001). HypoDD: a computer program to compute double-difference earthquake locations. *U.S. Geol. Surv. Open File Rep.* 12, 01–113. doi:10.3133/ofr01113

Waldhauser, F., and Ellsworth, W. L. (2000). A double-difference earthquake location algorithm: method and application to the northern hayward fault, California. *Bull. Seismological Soc. America* 90, 1353–1368. doi:10.1785/0120000006

Watson, L., and van Wijk, K. (2015). Resonant ultrasound spectroscopy of horizontal transversely isotropic samples. *J. Geophys. Res. Solid Earth* 120, 4887–4897. doi:10.1002/2014JB011839

Yoshida, K., and Hasegawa, A. (2018). Hypocenter migration and seismicity pattern change in the yamagata-fukushima border, NE Japan, caused by fluid movement and pore pressure variation. *J. Geophys. Res. Solid Earth* 123, 5000–5017. doi:10.1029/2018jb015468

Zhang, H. J., Liu, Y. F., Thurber, C., and Roecker, S. (2007). Three-dimensional shear-wave splitting tomography in the Parkfield, California region. *Geophys. Res. Lett.* 34, L24308 doi:10.1029/2007GL03195

Zinke, J. C., and Zoback, M. D. (2000). Structure-related and stress-induced shear-wave velocity anisotropy: observations from microearthquakes near the Calaveras fault in central California. *Bull. Seismol. Soc. Am.* 90 (5), 1305–1312. doi:10.1785/0119990099

Conflict of Interest: The authors declare that the research was conducted in the absence of any commercial or financial relationships that could be construed as a potential conflict of interest.

frontiers in Earth Science

ORIGINAL RESEARCH
published: 10 May 2021
doi: 10.3389/feart.2021.629184

Applying Simulated Seismic Damage Scenarios in the Volcanic Region of Mount Etna (Sicily): A Case-Study From the M_W 4.9, 2018 Earthquake

Vera Pessina[1], Fabrizio Meroni[1], Raffaele Azzaro[2] and Salvatore D'Amico[2]*

[1] *Istituto Nazionale di Geofisica e Vulcanologia (INGV), Milan, Italy,* [2] *Istituto Nazionale di Geofisica e Vulcanologia (INGV), Catania, Italy*

An application for a quick earthquake damage scenario assessment is here presented as a potential tool for planning prevention actions or managing seismic emergencies in the volcanic region of Mt. Etna (Italy). As case-study, we considered the December 26, 2018 earthquake that, with a magnitude M_W 4.9, represents the largest event occurring in the area during the last 70 years. The QUEST working group (the INGV macroseismic team) carried out a detailed survey in the damage area, collecting data on the number of buildings in the different vulnerability classes and related damage, with the aim to assign intensity. The maximum intensity reached degree VIII EMS along a narrow strip extending for 5 km astride the Fiandaca fault. In this paper, we simulated the damage scenario in the most struck municipalities of the epicentral area by testing different methodological approaches proposed in the literature using the information of the ISTAT census data collected by the Italian Institute of Statistics. We evaluated the damage level of the residential buildings and we validated the results comparing with the real damage data recognized in the field. Our analysis highlighted the difficulty of applying methods calibrated for larger earthquakes in tectonic domains, to small magnitude events in volcanic zones, where some operating assumptions must be introduced. Despite this, the results confirm the potential of the simulations based on statistical damage assessment methods also in these peculiar conditions, opening the way to finalized plans of pre- and post-earthquake interventions.

Keywords: volcano seismicity, macroseismic survey, intensity data, seismic scenario, building vulnerability, damage scenario, Mt. Etna

OPEN ACCESS

Edited by:
Jorge Miguel Gaspar-Escribano, Polytechnic University of Madrid, Spain

Reviewed by:
Flora Faleschini, University of Padua, Italy
Giulio Zuccaro, University of Naples Federico II, Italy
Mario Andres Salgado-Gálvez, International Center for Numerical Methods in Engineering, Spain

****Correspondence:***
Vera Pessina
vera.pessina@ingv.it

Specialty section:
This article was submitted to Solid Earth Geophysics, a section of the journal Frontiers in Earth Science

Received: *13 November 2020*
Accepted: *09 April 2021*
Published: *10 May 2021*

Citation:
Pessina V, Meroni F, Azzaro R and D'Amico S (2021) Applying Simulated Seismic Damage Scenarios in the Volcanic Region of Mount Etna (Sicily): A Case-Study From the M_W 4.9, 2018 Earthquake. Front. Earth Sci. 9:629184. doi: 10.3389/feart.2021.629184

INTRODUCTION

Risk scenarios in volcanic areas are mostly referring to damage or disruption caused by lava flows, tephra fallout, or pyroclastic flows, i.e., in general to the eruption effects. This despite damage caused by volcano seismicity, whether or not related to an eruption, is a critical issue in these areas and often represents an under-studied aspect of the risk. In Italy, the analyses carried out at Vesuvius and Campi Flegrei are an example of the proper way to face the problem (Working Group, 2013) and are at the basis of the emergency plans issued by the Italian Department of Civil

Protection for the Neapolitan volcanic district. In the study by Zuccaro and De Gregorio (2019), for instance, the damage expected from pre-eruptive seismic activity is evaluated with a uniform seismic input on the whole area, but not considering the characteristics of the attenuation of ground shaking in a volcanic area. Luckily, the occurrence of strong volcano-tectonic earthquakes in the Neapolitan volcanic district is quite rare, and almost limited to the island of Ischia (De Natale et al., 2019; Selva et al., 2019). The situation is different at Mt. Etna, the largest active volcano in Europe, where the contribution of volcano-tectonic seismicity plays a more important role and significantly enhances the level of risk, since the earthquakes are frequent and often produce heavy damage (Azzaro et al., 2016).

Here, earthquake damage scenarios have been developed in the framework of the recent EU projects UPStrat-MAFA (Sigbjörnsson et al., 2016) and KnowRISK[1]. In these analyses, both the building vulnerability and the impact on network systems have been also considered (D'Amico et al., 2016; Meroni et al., 2016).

While the estimation of damage to residential buildings is a consolidated practice for "tectonic" earthquakes, its application on volcanoes requires *ad-hoc* approaches taking into account the characteristics of local seismicity, such as the small-moderate magnitude (M_{max} ∼5.3), the shallow depth of sources (<3 km), the high values of peak ground motion (PGM) parameters and the low-frequency content in the near field, and the strong attenuation of intensity in very short distances (Azzaro et al., 2006, 2017; Langer et al., 2016; Iervolino, 2018; Tusa et al., 2020). The main feature of the earthquake seismic scenarios at Etna is that the involved areas are relatively small (∼30 km^2) and characterized by a large variability of effects in a few kilometers (QUEST Working Group, 2019).

The problem is complicated by the fact that, for very shallow earthquakes, the geometrical spreading of the seismic intensity reflects the geometry of a linear source, i.e., the shape of the shaking area around the causative fault is elongated and not circular (Azzaro et al., 2013). Considering the anisotropic attenuation in earthquake scenarios, as illustrated below, introduces operative problems due to the wide variability of the shaking values also inside the same municipality, difficult to tackle for the statistical significance of vulnerability building data in an inhabited area. In general, data on residential buildings are indeed provided at a municipal scale, unless particular cases where strategical buildings (hospitals, fire stations, schools, etc.) are individually considered. The ISTAT National census collects data on dwellings or building every 10 years and releases them in an aggregated form for each municipality. The accuracy level of census data is an important aspect to obtain reliable earthquake scenarios.

In this paper we discuss some critical points about the damage models in the literature, in the light of the recent analyses for seismic risk at a national scale (Dolce et al., 2020). Notwithstanding damage estimation models have recently been harmonized (i.e., Lagomarsino et al., 2019; Zuccaro et al., 2020) to be integrated into the same platform (IRMA—Italian Risk Map, Dolce et al., 2020) and to obtain a comparison of results, in the present work, we use three damage models in their original form, based on macroseismic intensity as a input parameter and respecting the philosophy on which the models were created and validated. In this way we avoid resorting to intensity vs. acceleration conversion laws that are affected by significant uncertainties, and considering local amplification effects (where present), already included in the macroseismic parameter. The calibration of damage models on a local scale, as in the case of Mt. Etna, is a crucial point, characterized by the extremely rapid attenuation of intensity, and hence damage effects. An advantage in using macroseismic models is the immediate validation of the results with the data collected directly in terms of intensity.

Finally, the application to December 26, 2018, M_W 4.9 Fleri earthquake, the strongest event recorded in the last 70 years at Mt. Etna, allows verifying how damage models set for different seismotectonic contexts may depict the damage level caused by a volcanic earthquakes. To this end, the validation process is based on real damage data collected in a detailed macroseismic survey throughout the damage area (Azzaro et al., 2020).

THE DECEMBER 26, 2018 EARTHQUAKE: OBSERVED AND SIMULATED INTENSITY SCENARIOS

Macroseismic Survey and Intensity Data

Two days after the intense seismic swarm accompanying the December 24, 2018 eruption on the summit area of Mt. Etna (Alparone et al., 2020), a strong earthquake (M_L 4.8, M_W 4.9) hit, at 02:19 UTC, the lower southeastern flank of the volcano. Due to an extremely shallow hypocenter, located at a depth of ca. 1 km b.s.l., the event produced heavy damage in the area between the towns of Acireale and Zafferana (**Figure 1**), with more than 1,100 homeless, but luckily without causing victims (QUEST Working Group, 2019). As many other shallow shocks at Etna, the earthquake was accompanied by remarkable effects of surface faulting along the Fiandaca fault, the southernmost structure of the Timpe tectonic system (Civico et al., 2019; Cucci et al., 2019).

The severity of the effects prompted the QUEST Working Group—the INGV team devoted to the macroseismic survey—to undertake a detailed inspection in the localities of the epicentral area with the aim to assess intensity according to the European Macroseismic Scale EMS (Grünthal, 1998). Since the dense urbanization of the area and the rapid attenuation of seismic intensity moving out from the epicentral area, the survey was carried out, in some key zones, building by building in order to consider properly the variability of effects as well as the building vulnerability and the associated damage. As a result, an intensity map of 44 localities was produced by Azzaro et al. (2020), 24 of them reporting damage. Briefly, the intensity in the epicentral area reached degree 8 EMS—the most damaged zone is between the villages of Fleri and Pennisi along the Fiandaca fault—but the intensity distribution is strongly anisotropic, with a preferential

[1]https://knowriskproject.com/the-project/

FIGURE 1 | (A) Damage to reinforced concrete building at Mazzasette (*I* = 8 EMS) and **(B)** to masonry edifice at Testa di Vipera (*I* = 7–8 EMS).

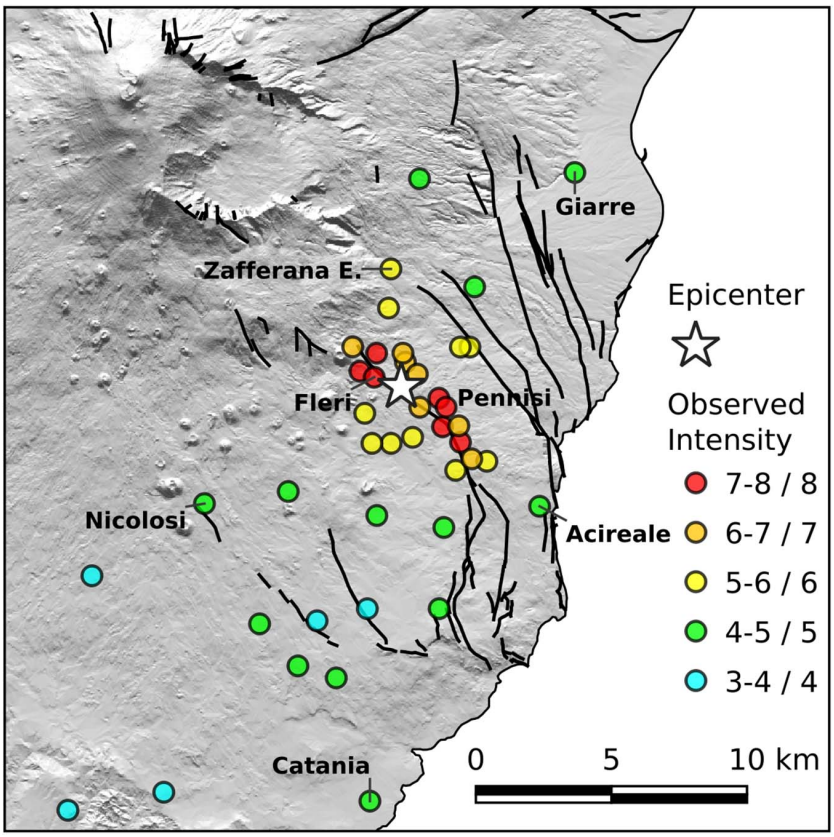

FIGURE 2 | Observed intensity of the December 26, 2018 earthquake (data from Azzaro et al., 2020).

propagation along the strike of the causative fault and a very strong attenuation in the orthogonal direction (**Figure 2**).

In the following, we refer to this data for the analysis of the damage scenario produced by the 2018 earthquake, basing particularly on the detailed forms compiled for surveyed localities.

Modeling Intensity Scenarios

As a first step for calibrating the damage scenarios, we simulated the intensity distribution of the December 26, 2018 earthquake by using a probabilistic approach based on the Bayesian statistics (Rotondi and Zonno, 2004). Briefly, the method calculates the decay of the macroseismic intensity conditioned on the epicentral intensity I_0 of the earthquake and the epicenter-site distance; as a result, it provides the probabilistic distribution of the intensity expected (I_{exp}) at a given site (Zonno et al., 2009). The intensity to be assumed as a reference value is given by the mode (the most frequent value) of the smoothed binomial distribution, whereas the uncertainty can be calculated by setting other probability thresholds (50, 75%, etc.). Being a probabilistic estimation, it does

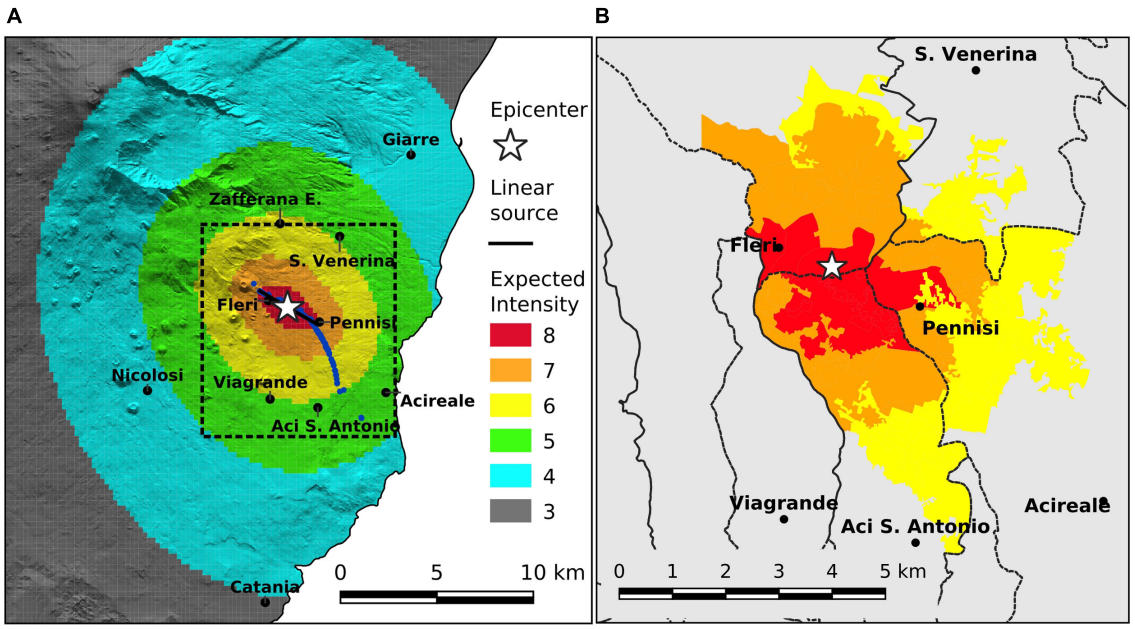

FIGURE 3 | (A) Seismic scenario of the December 26, 2018 earthquake. Dotted box represents the study area. **(B)** Detail of the same scenario applied at the urban scale of the census sections defined by ISTAT.

TABLE 1 | Typological parameters of the buildings, according to ISTAT census data.

Structural typology	Building age	Number of floors	Isolated or contiguous	*Maintenance status (*)*
Masonry	Before 1919	1 or 2	Isolated	*Good*
Reinforced concrete	From 1919 to 1945	from 3 to 5	Contiguous	*Bad*
Soft first floor building	From 1946 to 1960	more than 6		
Other typology	From 1961 to 1971			
No info	From 1972 to 1981			
	From 1982 to 1991			
	From 1992 to 2001			
	After 2001			

(*) indirect parameter deducted from ISTAT data.

not need applying other methods to calculate uncertainties, as for example a Monte Carlo approach.

The above procedure has been adapted to the Etna area by Azzaro et al. (2013) in order to take into account the particular features of attenuation of the volcano-tectonic earthquakes. For example, it is possible to consider both isotropic and anisotropic attenuation models, useful to represent point or linear sources, respectively.

The evident asymmetry in the distribution of the observed intensities (**Figure 2**) suggested us using the anisotropic attenuation model, in which the preferential direction of propagation of the seismic energy (i.e., minimum attenuation) corresponds to the causative fault, while the maximum attenuation is orthogonal. The decay of intensity along these two trends produces significant differences in terms of calculated intensities, reaching two intensity degrees at equal distances from the epicenter.

Concerning the fault model adopted for the simulation, we considered a linear source with a length of 4.5 km, that corresponds to the NW-SE trending segment of the Fiandaca fault (Civico et al., 2019) hosting the instrumental epicenter and the maximum intensity area ($I = 8$ EMS); the dip of the fault plane is considered vertical.

In **Figure 3A** the intensity scenario is represented on a grid with a resolution of 0.0025° (ca. 250 m), where the values of expected intensity I_{exp} represent the mode of the smoothed binomial distribution. To account for the uncertainty affecting the modeled scenario, we also calculated the intensities expected at probability 25, 50, and 75% (I_{ref25}, I_{ref50}, and I_{ref75}, respectively). I_{ref25} overestimates compared to I_{exp} by 1.5, while I_{ref50} and I_{ref75} overestimates and underestimate by 0.5, respectively. The mode, on average, corresponds to the value of 65 ± 8% of the probability, a percentage in which the uncertainties are confined between −0.5 and + 0.5 of intensity

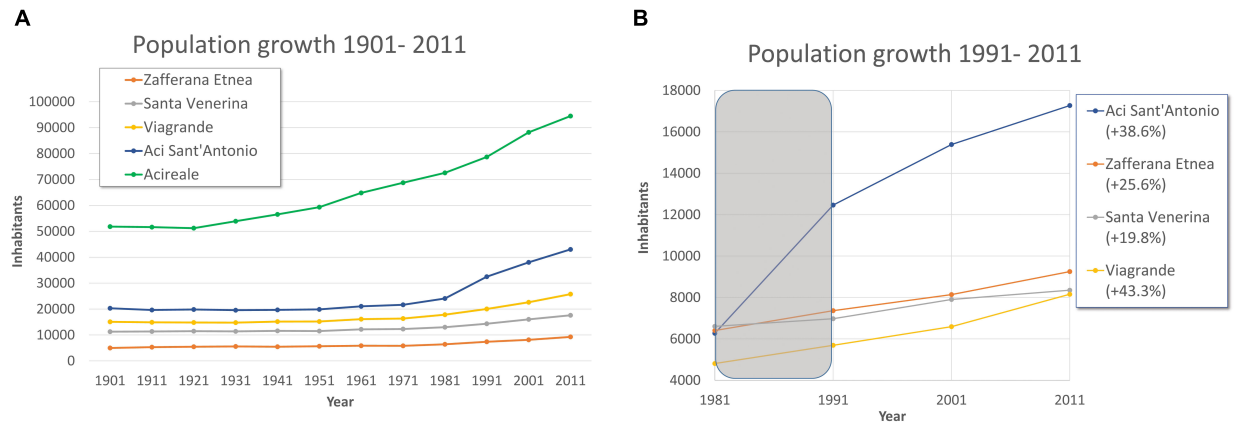

FIGURE 4 | Demographic trend in the municipalities: **(A)** from 1901, **(B)** in the last 20 years, population growth varies between +11.4% in Acireale and +43.3% at Viagrande.

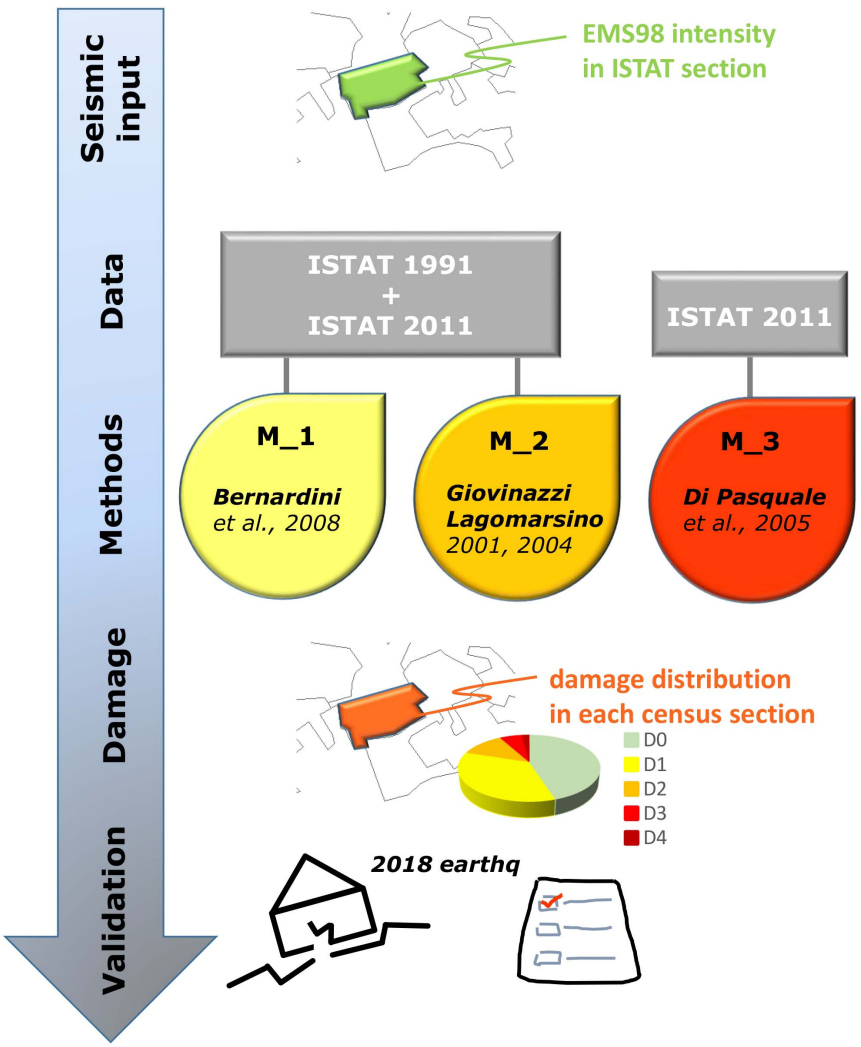

FIGURE 5 | Conceptual scheme of the procedure for damage scenario assessment by using census data on the building stocks.

TABLE 2 | Elements for the vulnerability assessment method based on the 1991 ISTAT data.

(A) Parameters for the classification of typological structures

k (Type)	1 Soft floor	2 Reinforced concrete	3 Masonry	4 Other	5 Unknown
$I_V{}^1{}_1$ (*k*)	50	45	60	55	52
Delta_i (*k*)	–20	–20	–25	–20	–22
Delta_j (*k*)	–10	–15	–15	–15	–15
Manut (*k*)	–10	–10	–10	–10	–10
Classif (*k*)	–10	–20	–10	–10	–15

(B) Parameters for the classifications of age of construction and typological factors

i	Age of construction	*j*	Typological factors	
			Aggregations	No. of storeys
1	<1919	1	2 (yes)	3 (>4)
2	1919–1945	2	2 (yes)	2 (3–4)
3	1946–1961	3	1 (no)	3 (>4)
4	1962–1971	4	2 (yes)	1 (1–2)
5	1972–1981	5	1 (no)	2 (3–4)
5, 4	1982–1984	6	1 (no)	1 (1–2)
6	1984–1991			

(C) Criterion of classification in the EMS vulnerability classes

EMS Class	A	B	C	D	E	F
I_V (mean)	$50 < I_V$	$30 < I_V \leq 50$	$10 < I_V \leq 30$	$-10 < I_V \leq 10$	$-30 < I_V \leq -10$	$I_V \leq -30$

(values commonly used in EMS to indicate, for example, intensity as "6–7," where the data can be interpreted in the same way as "6" or "7").

In order to estimate the overall reliability of this synthetic scenario, we used the deterministic criterion of validation of the absolute discrepancy *diff* to compare observed (I) and the calculated (I_{exp}) intensities at a site:

$$diff = \frac{1}{N}\sum_{n=1}^{N}\left|I^{(n)} - I_{exp}^{(n)}\right|$$

where N is the number of sites. For the whole scenario the result is 0.825, while for the study area (dashed box in **Figure 3A**) the value is 0.455, i.e., the difference between I and I_{exp} is comparable to the uncertainty often associated with the intensity estimate.

Given the aims of this study and the applications based on the ISTAT census data, we finally plotted the same scenario at an urban scale referring the expected intensities to the census sections (a subdivision of the municipality) considered in the following chapters. In **Figure 3B**, I_{exp} was calculated at the centroid of each polygon representing the sections. This approach reduces the resolution of the scenario, so that the extension of the areas characterized by a given value of I_{exp} is a bit different from the ones calculated in **Figure 3A**. Anyway, the result is sufficiently good, with a *diff* value between synthetic intensities obtained in the centroid of the sections with the observed intensities located inside a polygon, equal to 0.525.

THE ISTAT DATA

To assess the building vulnerability at an urban scale, we use the information for residential housing provided by the ISTAT census data, homogeneously collected every 10 years on the entire national territory. These data allow a reliable estimate of the total number of buildings and their corresponding volume. The number of buildings is published directly by ISTAT (2011), for each municipality and for each census section. On the contrary, in 1991, the number of buildings for the census section has to be inferred from the number of dwellings, using the average value of the item "No. of Dwellings per Building" associated with each record.

Edifices are described by multiple characteristics: structural typology, date of construction (or renovation), number of floors, position in the block, state of repair and quality of maintenance (**Table 1**). The last parameter is deduced indirectly from other ISTAT data such as the presence of efficient systems and the characteristics of installations[2]. This data allows a vulnerability classification of buildings when there is no other information collected specifically for the same purpose.

Until the 1991 census, the ISTAT data on residential buildings were provided at the resolution of census section in

[2]Installation and systems are: drinking water systems, plumbing systems, drainage systems, connections to the sewage system, bathtub and/or shower installations, domestic hot water supply, and fixed heating installations.

a disaggregated way, being so possible to correlate the relevant information (as for instance in Meroni et al., 2000).

From the 2001 census onwards, due to the introduction of more restrictive privacy rules, the ISTAT census information provides aggregated values only, reducing the vulnerability assessment to a rough estimation. There are no more disaggregated information at a census section scale neither at a municipal level, and few typological features on age, materials, and the other factors are available in a disaggregated form solely at a provincial level; in practice, they are not usable for detailed vulnerability analyses (Crowley et al., 2009).

Notwithstanding the most recent dataset (ISTAT, 2011) do not provides information suitable for setting the vulnerability model at a local scale, it well describe the recent urban development. Indeed, there are areas in the country with a scarce building development or even affected by the depopulation, for instance rural districts or mountain villages (e.g., in the Apennines). In these cases, data from the 1991 ISTAT census can still be considered representative. On the contrary, other areas of Italy are characterized by a considerable urban growth occurred in the last years, as in the case of the study area. The examined municipalities recorded a significant demographic growth (**Figure 4**) ranging from 11.4% in Acireale to 43.3% in Viagrande, resulting in a substantial increase in the number of buildings of approximately + 32% from 1991 up to 2011. Moreover, as often happens in case of a rapid urban development, the vulnerability level of the recent buildings is difficult to characterize because of the need to know the age of the buildings (i.e., year of construction) to be referred with the relevant technical rules.

The characterization at a municipal scale of buildings of the last 30 years is therefore a critical step in our analysis. For this reason, different methods for estimating vulnerability are examined in the following.

VULNERABILITY AND DAMAGE ASSESSMENT METHODS

From the methodological point of view, there is in Italy (but also in Europe) a tradition dating back 1980's of studies correlating damage to buildings vs. macroseismic intensity, based on data collected after strong earthquakes. This led structural engineers to derive robust fragility curves or vulnerability functions to be used for estimating local scenarios. Since then, this approach has been continuously improved both in the method and in the input data for calibration (e.g., Spence and Le Brun, 2006), with the increasing use of census data capable of providing better estimations. Several examples are represented by applications in European Risk projects such as in Spain, Portugal, France, Greece, Romania, Turkey, etc. (Lantada et al., 2010; Riedel et al., 2015; Kassaras et al., 2018; Mosoarca et al., 2019).

In general, the scarcity of instrumental ground motion data at a local scale as well as uncertainties associated with GMPEs, explains why in Italy/Europe the use of macroseismic intensity data is normally used for damage scenarios at an urban scale.

TABLE 3 | Vulnerability scores for masonry buildings.

(A) Mean vulnerability index *Vm(k)* based on typology and age				(B) Scores for behavior modifiers *Delta(i,k)*					
							Score modifiers		
(k)	**Building age**	**Typology**	$V_m(k)$	*(i)*	**ISTAT class**	**ISTAT class**	**<1919**	**1919–1945**	**1946–1971**	**>1971**
1	<1919	M1, M3, M5	50	1	Level of maintenance	Low maintenance	+6	+6	+6	–
2	1919–1945 urban area	M3, M4, M5	35	2	Number of floors	1 or 2 floors	–	–	–	–
	1919–1945 rural area	M1, M3, M5	45			3, 4, or 5 floors	+5	+5	+5	+5
3	1946–1971	M3, M5, M6	30			6 or more floors	+10	+10	+10	+10
4	>1971	M6	20	3	Context	Block of buildings	–	–	+6	+6

M1, Rubble stone, fieldstone; M3, Simple stone; M4, Massive stone; M5, Bricks, M6, Unreinforced masonry with reinforced concrete floors.

Among the methods available in the literature, we adopt the Bernardini et al. (2008, hereinafter M_1) and Giovinazzi and Lagomarsino (2001, hereinafter M_2) which allow to consider the whole information contained in the 1991 ISTAT census by providing a very detailed and precise vulnerability classification of both masonry and reinforced concrete buildings. Indeed, the accuracy of the input data makes the difference with the numerous methods able to group the buildings into vulnerability classes (Kassem et al., 2020). Even though the input data is very accurate, these methods cannot still provide information about the edifices of the last 20 years and need to be integrated (**Figure 5**).

Another method proposed by Di Pasquale et al. (2005, M_3) is directly applicable to the most recent ISTAT data (2011 census). This empirical approach is based on the relationships between structural types and age classes of the buildings and was widely tested by the technicians of the Department of Civil Protection (Di Pasquale et al., 2005).

For M_1 and M_2 methods, in order to characterize the vulnerability of the edifices built after 1991, we considered the 2011 ISTAT data, available as disaggregated variables at a provincial level only, by adapting them to the municipal scale. Naming Δ_P the number of buildings in the 1991–2011 period at provincial level and Δ_M the same number for each municipality here considered—Zafferana Etnea, Santa Venerina, Acireale, Aci Sant'Antonio, Viagrande—we calculated the vulnerability distribution of Δ_P, and added the normalized (Δ_P/Δ_M) values to the vulnerability distribution of each municipality, previously calculated on the 1991 ISTAT data. We assumed that the recent constructions over the last 20 years Δ_P follow the vulnerability distribution assessed at the province level. More details on this method can be found in the application to the 2012 Emilia-Romagna earthquake (Meroni et al., 2017).

With the exception of method M_3, these two methods also consider the year of seismic classification, after which the adoption of more restrictive seismic standards is conceivable. They include an additional parameter, namely the date of seismic classification of the territory, which defines a lower vulnerability for the buildings constructed with earthquake resistant design. Although the study-area was classified since 1914, with a revision in 1962, such an early classification does not guarantee an adequate vulnerability level compared to the present building seismic code.

Method M_1

The approach proposed by Bernardini et al. (2008) defines a score for homogeneous groups of buildings, consistent with a vulnerability assessment (Meroni et al., 2000) calibrated on more than 28.000 detailed buildings vulnerability forms collected during the main seismic crises occurred in Italy from 1983 to 2000 (GNDT database—National Group for the Defense Against Earthquakes).

The 1991 census (ISTAT, 1991) was taken as a starting point, since it provides disaggregated data at a resolution of the census section.

The mean vulnerability index I_v, for each group of buildings, is defined by the relation:

$$Iv\left(i,j,k\right) = Iv_1^1(k) + Delta\_i(k)\frac{(i-1)}{5} + Delta\_j(k)\frac{\left(j-1\right)}{5} +$$

$$Manut(k) + Classif(k)$$

where $i = 1 \div 6$ and $j = 1 \div 6$ (see **Table 2B**).

For a given k structural typology ($k = 1 \div 5$), the factors *Delta_i* and *Delta_j* (**Table 2A**) refer to the i ranges of the construction age (or total retrofitting) of the buildings and to the j typological factors, respectively (**Table 2B**). The factors *Manut* and *Classif* account for the state of building maintenance and the year of seismic classification of the municipality.

The corresponding EMS vulnerability class is determined according to the range of the vulnerability score shown in **Table 2C** (Bernardini et al., 2008). Vulnerability classes range from A (the weakest buildings, having the highest indices) to F (the most resistant ones, with the lowest scores).

The method proposed by Bernardini et al. (2007) uses macroseismic fragility curves to evaluate damage to residential

TABLE 4 | Vulnerability scores for reinforced concrete buildings.

(A) Mean vulnerability index *Vm (k)* based on typology and age

(k)	Building age	Typology	V_m *(k)*
5	Before seismic code	RC1, RC4	20
6	After seismic code	RC2, RC5	0
7		Soft floor	40

(B) Scores for the behavior modifiers *Delta (i,k)*

(i)	ISTAT class	ISTAT class	Score modifier
1	Building age	before 1971	+6
2	Number of floors	1 or 2 floors	–6
		3, 4, or 5 floors	–
		6 or more floors	+6
3	Adjacent buildings without ERD	Block of bldgs	+6*

RC1: Frame in reinforced concrete without ERD (Earthquake Resistant Design); RC2: Frame in reinforced concrete with moderate ERD; RC4, Concrete shear walls without ERD; RC5, Concrete shear walls with moderate ERD.

**Only for category k = 5–buildings built before the seismic code.*

TABLE 5 | (A) Vulnerability classes vs. horizontal and vertical structural elements. **(B)** Vulnerability classes vs. age for masonry buildings (modified from Di Pasquale and Orsini, 1998).

(A)					(B)			
Horizontal structure	**Vertical structure**				**Age**	**Vulnerability class [%]**		
	Masonry walls			**Reinforced concrete**		***A***	***B***	***C1***
	Field stone	***Hewn stone***	***Bricks***		<1919	74	23	3
Vaults	A	A	A	\	'19–'45	52	40	8
Wood	A	A	B	\	'46–'60	25	47	28
Steel and vaults	B	B	C1	\	'61–'71	4	31	65
Reinforced concrete	B	C1	C1	C2	'72–'91	2	19	79

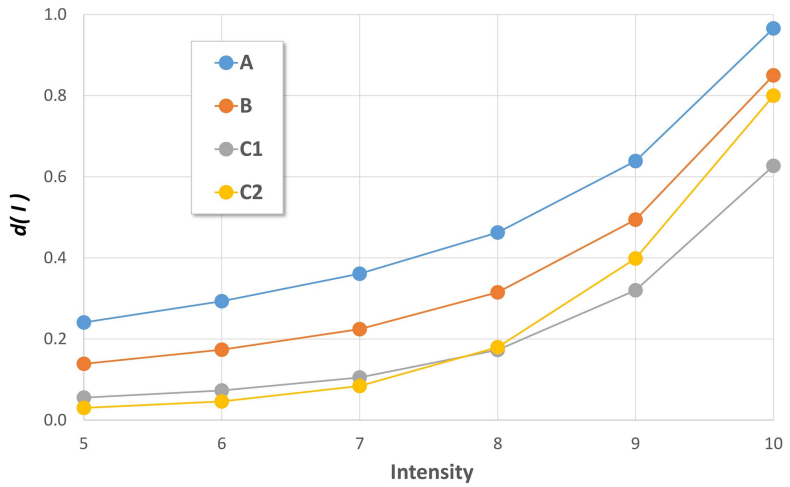

FIGURE 6 | Values of average damage *d(I)* of the binomial function p_k, for each vulnerability class and EMS intensity (Di Pasquale and Orsini, 1997, 1998; Di Pasquale et al., 2005)).

buildings, through the definition of five damage classes (D1 ÷ D5) according to EMS classification. The EMS adopts qualitative ratings to evaluate the frequencies of buildings with different degrees of damage, for each vulnerability class and intensity. For instance, the intensity degree VII is reached when "*Many buildings of vulnerability class A suffer damage of grade 3; a few of grade 4. Many buildings of vulnerability class B suffer damage of grade 2; a few of grade 3.A few buildings of vulnerability class C sustain damage of grade 2.A few buildings of vulnerability class D sustain damage of grade 1.*" (Grünthal, 1998).

According to this approach it is possible to estimate a damage grade μ_D following the equations:

$$\mu_D = 2.5 + 3\tanh\left(\frac{I + 6.25\,I_V - 12.7}{3}\right)\cdot f\,(I_V, I)$$

with $f\,(I_V, I)$ defined as:

$$f\,(I_V, I) = \begin{cases} e^{\left(\frac{I_V}{2}\cdot(I-7)\right)} & I \le 7 \\ 1 & I > 7 \end{cases}$$

where μ_D is the mean value of D, a random variable of damage grade; I is the intensity and I_V is the vulnerability index.

The fragility curves for damage distribution $P\left(D > d \mid I\right)$ are modeled according to a Beta distribution, with a probability density function given by:

$$p_\beta\,(d) = \frac{\Gamma\,(q)}{\Gamma\,(p)\cdot\Gamma\,(q-p)}\cdot d^{p-1}\,(5-d)^{q-p-1} \qquad 0 \le d \le 5$$

in which, Γ is the Gamma function, p and q are the parameters of the Beta distribution, defined as a function of the average value μ_D and the variance $\sigma_D{}^2$ from the relations:

$$q = \frac{\mu_D(5-\mu_D)}{\sigma_D^2} - 1 \qquad p = q\frac{\mu_D}{5}$$

Method M_2

Giovinazzi and Lagomarsino (2001, 2004) proposed a vulnerability assessment method based on EMS by identifying seven distinct categories of buildings. A mean vulnerability index $V_m(k)$ is given by the combination of the building age and the structural type: four classes are defined for masonry buildings (k = 1 ÷ 4) and three for reinforced concrete buildings (k = 5 ÷ 7), as shown in **Tables 3A**, **4A**.

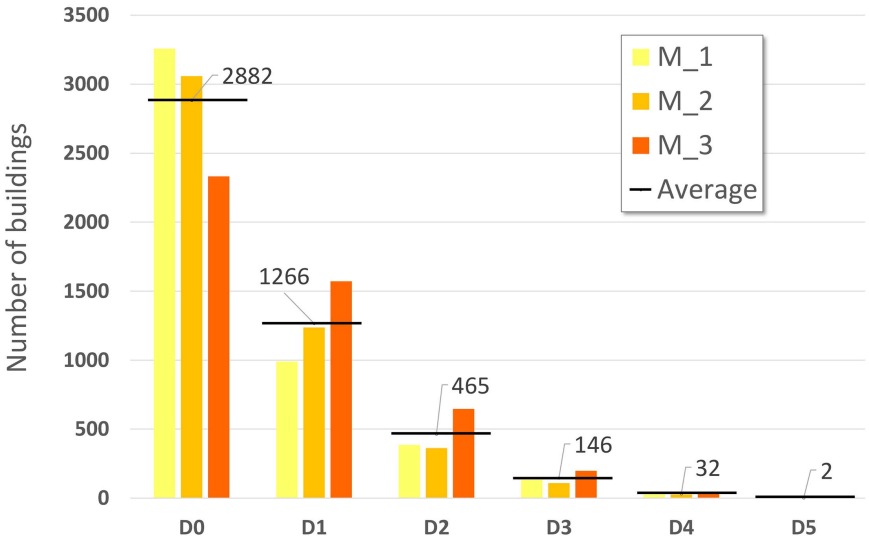

FIGURE 7 | Damage distribution obtained through the methods M_1 (Bernardini et al., 2007), M_2 (Lagomarsino and Giovinazzi, 2006), and M_3 (Di Pasquale et al., 2005). Black line indicates the average number of buildings in each damage class.

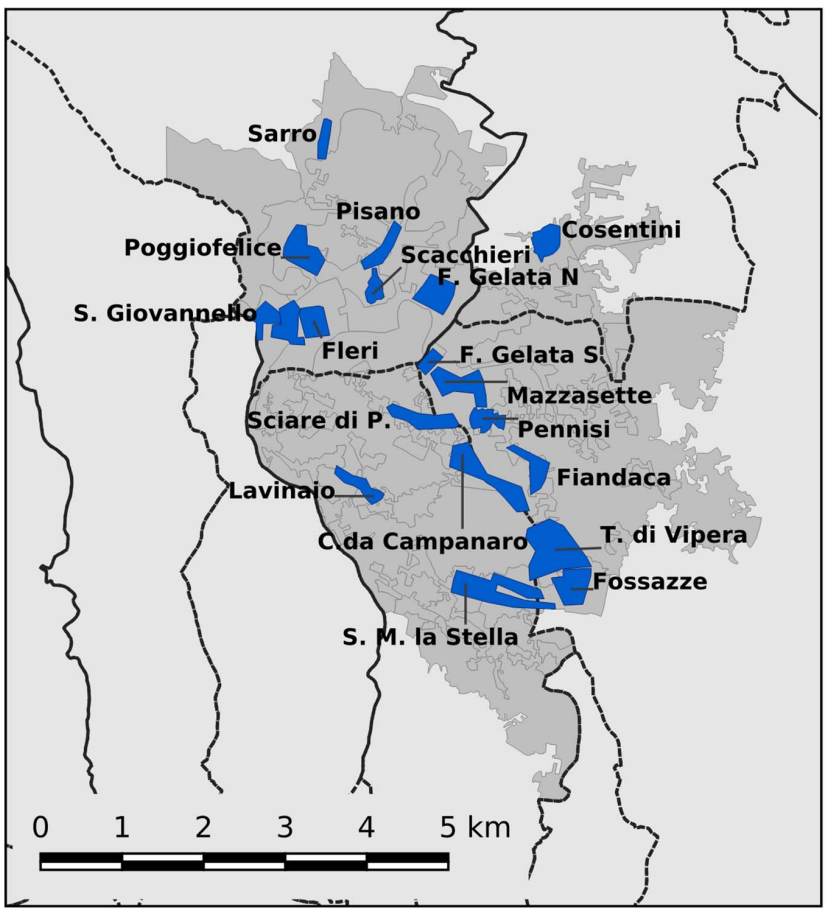

FIGURE 8 | Investigated area: ISTAT, 2011 census tracts (gray polygons) and target zones of the macroseismic survey (blue polygons). Black lines are the administrative boundaries of municipalities.

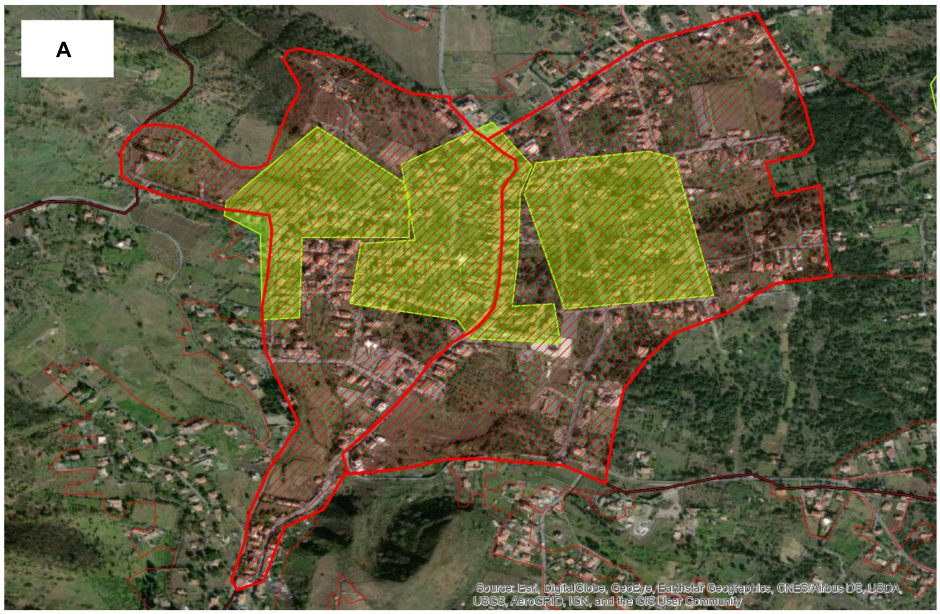

B

Fleri	A	B	C	D	Tot
D0		4	21	35	60
D1		14	39	18	71
D2		7	31	1	39
D3	2	1	21		24
D4	1	2	4		7
D5	4				4
Tot	7	28	116	54	205

C

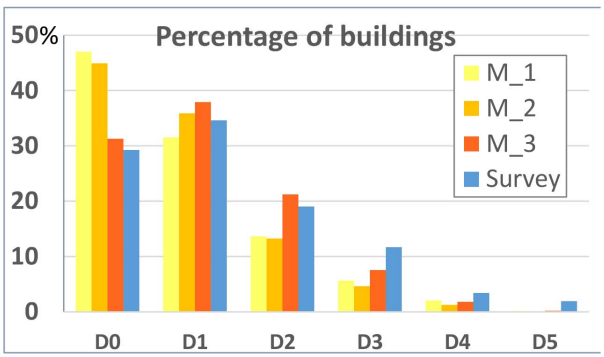

FIGURE 9 | Locality of Fleri: **(A)** coverage of the ISTAT census section (red polygons) and the surveyed areas (green polygons). **(B)** Number of surveyed building according to vulnerability (A÷D) and damage classes. **(C)** Comparison of damage estimation between the simulated distributions (M_1 ÷ M_3) and the one derived by the survey in the green areas.

The overall vulnerability index V is calculated from the typological score $V_m(k)$ and considering appropriate behavior modifiers derived from other ISTAT information (e.g., number of floors, structural context, maintenance status, see **Tables 3B**, **4B**):

$$V = V_m(k) + \sum_{i=1}^{3} Delta(i,k)$$

where $k = 1 \div 7$ refers to building structural typology. The $Delta(i,k)$ for $i = 1 \div 3$ score represents the behavior modifiers for masonry (**Table 3B**) and reinforced concrete buildings (**Table 4B**). They can either increase or decrease the initial value of the mean vulnerability index $V_m(k)$.

The damage model proposed by Lagomarsino and Giovinazzi (2006) is similar to the one adopted by the M_1 method. It classifies the building stock according to the vulnerability definition of the EMS and provides damage distributions, conditioned by the level of intensity, for each degree of damage of the EMS.

The fragility curves are modeled according to a Beta distribution, with a probability density function with the value μ_D calculated as:

$$\mu_D = 2.5 \cdot \left[1 + \tanh\left(\frac{I + 6.25 \cdot V - 13.1}{2.3}\right)\right]$$

μ_D is the mean damage grade of a random variable D, I is the intensity level and V is the vulnerability index (A ÷ F).

Applications of this method have been developed for Etna area (D'Amico et al., 2016) and Portugal (Zonno et al., 2010; Mota de Sá et al., 2016; Sousa and Campos Costa, 2016).

Method M_3

This method, adopted in the 2005 by the Department of Civil Protection for the assessments of seismic risk in

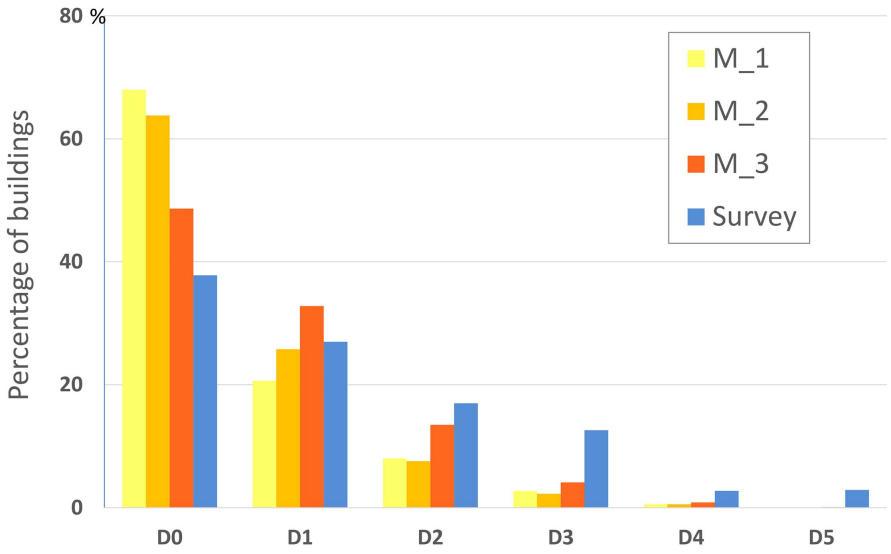

FIGURE 10 | Comparison of damage estimations between simulated (M_1 ÷ M_3) and surveyed distribution, in percentage, for the whole damaged area.

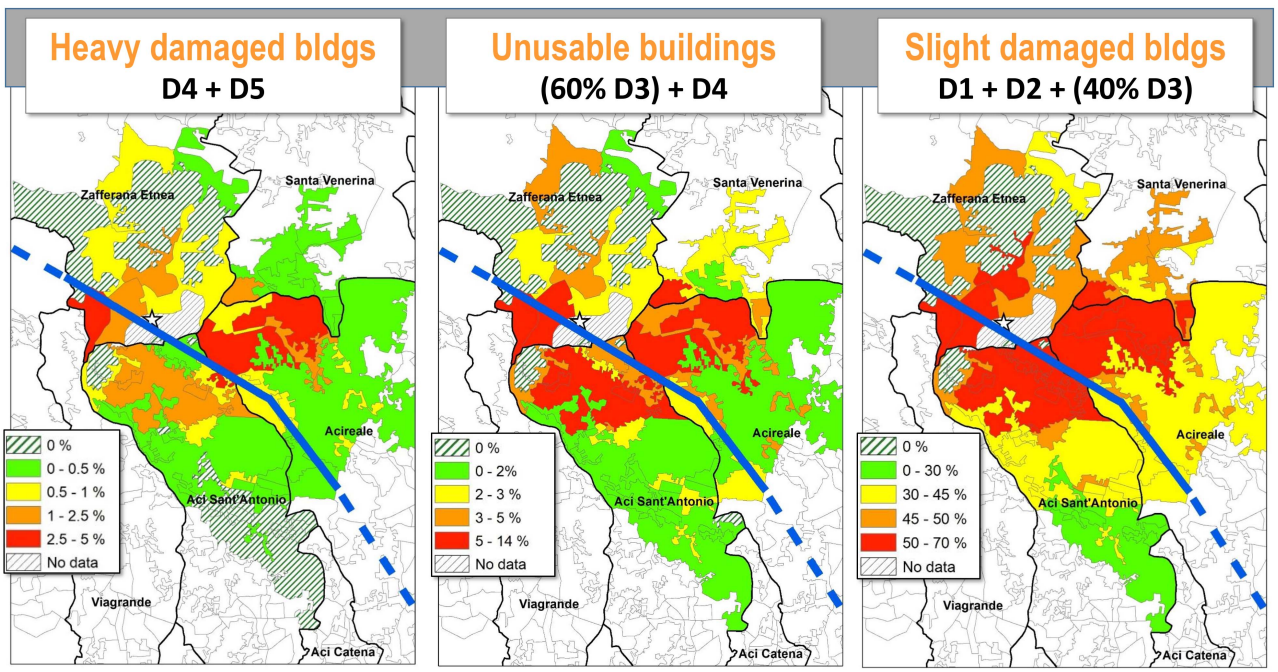

FIGURE 11 | Damage maps calculated with M_3 method with values shown in percentage for each census section. Results are presented in percentage for groups of damage levels. Star indicates the epicenter, blue dashed line is the Fiandaca fault.

Italy (Di Pasquale et al., 2005), subdivides the building stock into four vulnerability classes (A, B, C1, and C2) by means of a correlation between type of construction and age. The age classes are those of the ISTAT census, and therefore the method is immediately applicable to the 2011 data.

Table 5A lists the vulnerability class as a function of the horizontal and vertical structural elements (adapted from Braga et al., 1982). A correlation between vulnerability class and the age of masonry buildings has been obtained through a statistical study of a sample of about 50,000 dwellings after the 1980 Irpinia M_W 6.8 earthquake (**Table 5B**). The reinforced concrete buildings are classified into the C2 vulnerability class.

Damage scenarios are estimated by the Damage Probability Matrices (hereinafter DPM), that is a statistical correlation

among macroseismic intensity, vulnerability class and EMS damage grade (D0 ÷ D5). According to this approach, damage grade k ($k = 1 \div 5$) is evaluated through the ground shaking (expressed in terms of intensity) and the frequency of buildings in the vulnerability class. The scenario is obtained by adding in discrete terms the number of buildings in each vulnerability class (A, B, C1, and C2) given the intensity degree. The number of buildings is weighted by the probability p_k of the damage grade k given by the adopted DPM.

The DPM are described by a binomial distribution:

$$p_k = \frac{5!}{k!\ (5-k)!} d\,(I)^k \left(1 - d\,(I)\right)^{5-k}$$

where p_k is the damage probability of level k ($k = 1 \div 5$), for a given intensity degree I.

The binomial distribution is defined by the binomial coefficient (or "average damage") *d(I)*, ranging between 0 and 1. Technically, using the only average damage *d(I)* it is possible to describe the whole damage distribution for each vulnerability class and intensity grade. The values of p_k, for each intensity and vulnerability class, have been found through an error minimization procedure on the observed frequencies of damage level (observed DPM), relative to the same sample of structures surveyed after the 1980 Irpinia earthquake (Di Pasquale and Orsini, 1997, 1998). The assumed values of average damage *d(I)* are summarized in **Figure 6**.

ANALYSIS OF RESULTS AND COMPARISON WITH SURVEYED DATA

As described before, the intensity attenuation is characterized by a rapid variability at very short distances, and needs to be represented in detail when matched with the vulnerability data to produce reliable damage scenarios. The use of a single intensity value at a municipal scale is a rough approximation, while the ISTAT census section scale is a preferable option. Our analysis followed three main steps: (i) calculating the macroseismic intensity in the census section centroids by means of the specific attenuation model (see section The December 26, 2018 Earthquake: Observed and Simulated Intensity Scenarios), (ii) assessing the building vulnerability distribution for each census section according to the models M_1 to M_3, (iii) evaluating the damage distribution by means of macroseismic fragility curves and DPM.

Following the procedure used by Dolce et al. (2020) for the recent Italian risk maps we examined the estimations obtained by the M_1, M_2, and M_3 methods in terms of damage values that are comparable because are defined through the same EMS scale.

Figure 7 shows the damage distribution in five classes (D1 ÷ D5) for the residential buildings of the entire area. It is noteworthy that the methods M_1 and M_2 are more conservative than M_3. Largest differences exist in damage classes D2 and D3, where damage evaluated with M_3 is double than the ones calculated with M_1 and M_2. Furthermore, the M_2 method is the most conservative of all and it does not estimate any collapsed building (class D5).

In order to validate the methodological approaches here proposed, we compare the resulting damage assessments based on the ISTAT data with real data on individual buildings acquired during the macroseismic survey (Azzaro et al., 2020).

The main problem in applying the aforementioned methods is the different areal coverage to which data are referred, complicated by the fact that the study area is densely urbanized, in many places without a solution of continuity. In practice, while at the ISTAT scale the urban settlements are "viewed" through administrative boundaries (i.e., municipal limits and census sections), the extent of the macroseismic survey is focused on the "locality," that is a territorial unit significant from the statistical point of view of the macroseismic intensity (Grünthal, 1998). In these terms, a locality such as a town or village, typically consists of an historical center and more recent outskirts around them. The localities investigated in the survey are those reported in the national geographic gazetteer used in the Italian Macroseismic DataBase (DBMI15; Locati et al., 2019), which grants the unequivocal association of a locality with a pair of geographical coordinates. In this way all the intensity data available in the DBMI15 for a given geographic reference, are really representative of the seismic history of that locality.

As a result, there is only a partial correspondence between the data acquired on individual buildings during the macroseismic survey and the aggregated ones provided by ISTAT. This situation is shown in **Figure 8** where the surveyed areas (in blue) are overlapped on the census sections (in gray).

The macroseismic survey collected data out of 1,278 buildings in the localities damaged by the December 26, 2018 earthquake, distributed in four different municipalities (Azzaro et al., 2020). The focus on the historical centers has the effect of considering mostly the old buildings or the more vulnerable structures in general, whereas the new urbanized zones result "sampled" only for the nearest outskirts, while the residential areas with sparse and isolated buildings are not considered in the macroseismic survey practice.

Figure 9A illustrates the case of Fleri, a locality of the municipality of Zafferana Etnea which has been assigned an intensity $I = 8$ EMS. According to the 2011 ISTAT data, there are 453 buildings in the two census sections (red polygons) corresponding to this locality. During the macroseismic survey carried out in the areas marked by the green polygons, 205 buildings were inspected and classified in terms of vulnerability and damage (**Figure 9B**). The comparison between the simulated and surveyed damage distributions is shown in **Figure 9C**. Considering that no damage is expected in the recently urbanized areas with low vulnerability buildings, the surveyed damage distribution can be considered representative for the entire zone.

In this case, it is evident that the M_3 simulation provides values better approximating the observed data (**Figure 9C**). Further analyses on other localities show greater differences between the estimated and observed values, especially for the higher damage classes (D3 ÷ D5).

To quantify the comparison of the simulations with surveyed data, we calculated the index of the dispersion of the results by evaluating a sort of error err_D^j, defined as a sum of residuals, expressed in terms of numbers of buildings.

The error err_D^j for each *j-th* method (M_1 ÷ M_3) is:

$$err_D^j = \sqrt{\frac{1}{6}\sum_{D=D_0}^{D_5}\left(n_D^j - n_D^0\right)^2}$$

where n_D^j is the numbers of estimated buildings for the damage grade D (D0 ÷ D5) for the *j-th* method. The n_D^0 is the number of buildings surveyed during the macrosesmic campaign for the damage grades D.

The minimum value of sum of residuals err_D^j defines the method better approximating the real damage distribution.

For the final damage scenario, we considered the whole investigated area (gray polygons of **Figure 8**). In order to perform a comparison with the observed damage, we extrapolated the damage distribution of the 1,278 surveyed buildings to the 4,793 buildings associated to the relevant census sections, assuming that the damage in the investigated area is representative of the overall damage distribution.

The minimum value of err_D^j is obtained through the M_3 method (Di Pasquale et al., 2005). This method has a err_D^j values (307) half of the values of M_1 and M_2 (661 and 582, respectively) and therefore the M_3 method is the one better approximating the distribution observed by the survey.

The comparison of the damage distributions for the overall damage scenario is illustrated in **Figure 10**. The simulations provide damage distributions more conservative than the surveyed data: the damage degree from moderate to heavy damage (D3 ÷ D5) is not properly estimated. The largest differences are obtained for class D3, considering that discrepancies for classes D4 and D5 can be neglected because the sample is too small.

The presence of buildings with a level of vulnerability higher than the average level can explain this difference. Indeed, the survey highlights the presence of many reinforced concrete buildings built in the timespan 1970–90's that are particularly vulnerable. To simulate this condition, we forced the damage scenario by worsening the vulnerability of a part of the reinforced concrete buildings. In detail, 50% of the buildings of class C was classified as B. The downgrade of vulnerability is a practice suggested by the EMS guideline (Grünthal, 1998) in case of bad maintenance conditions or constructive defects, as in the case of reinforced concrete buildings without or with moderate level of resistant design. The new simulated distribution shows a minimum sum of residuals err_D^j equal to 231 (the minimum value of all simulations), a result confirming the robustness of the method as well as the need to calibrate the vulnerability assessment with local data.

The number of damaged buildings in each census section calculated with the M_3 method is illustrated in **Figure 11**. The first map shows the value of collapsed or very heavy damaged buildings (D5 + D4): the presence of victims (dead and injured) can be associated with this spatial distribution. The unusable buildings, calculated as the weighted sum of buildings with heavy and substantial damage (D4 + 60%D3) (Dolce et al., 2020), are illustrated in the central map of **Figure 11**; while the remaining part (D1 + D2 + 40%D3) represents the slightly damaged buildings that can be repaired but imply economic costs (Lucantoni et al., 2001; Di Pasquale et al., 2005).

In general, the spatial distributions of damaged buildings, illustrated in **Figure 11**, are mainly concentrated along the Fiandaca fault and damage decreases with distance from the fault, reproducing the attenuation effects of the seismic shaking.

CONCLUSIVE REMARKS

In this paper we compared the results of the earthquake damage scenarios obtained by theoretical vulnerability models and fragility curves with the real data collected through a macroseismic survey after a strong shock occurred at Etna volcano of the December 26, 2018 (M_W 4.9). We used three models available in the literature, used in the Italian territory and in Europe, to test if suitable in the case of volcano tectonic earthquakes. The application of these models point out a number of issues that has to be solved, the main ones being:

1. the macroseismic data are collected according to the consolidated procedure for assigning the intensity, that is referred to a well-defined locality and cannot be extended to a territory or, worse, to single buildings;
2. the organization of the ISTAT data is critical to perform correct vulnerability and damage assessments, and strongly influences the quality of the final estimates: the recent and updated (ISTAT, 2011) data are available only in an aggregated form, preventing their immediate use in sophisticated damage models.

Furthermore, the perimeter of the census sections in the study area has considerably changed in the last decades, making difficult to track the changes determined by the recent urban growth. Since the localities of the macroseismic survey are unevenly located compared to the administrative boundaries or the census sections, the geographical match with the ISTAT data is not immediate.

The analysis of this case-study highlights the following considerations:

1. the seismic damage assessment methods M_1 (Bernardini et al., 2008) and M_2 (Giovinazzi and Lagomarsino, 2001) can be applied to disaggregated ISTAT data; in Italy, this typology of data (ISTAT, 1991) fixes the situation dating back 1991. In general, these models can be used for settlements where the urban development in the last 30 years has being scarce (for example in the Apennines, Central Italy), but not in areas with recent urban expansion, such as the slopes of Etna. In these cases, the use of approximations for the characterization of the recent urbanized areas is necessary, but may lead to estimation errors;

2. the simpler vulnerability model M_3 (Di Pasquale et al., 2005) can be used with more recent data (ISTAT, 2011). Despite the limited number of ISTAT parameters and a rougher haracterization of the building vulnerability, this method produces reliable estimates when calibrated with real data collected through the macroseismic survey;
3. the considered vulnerability models are calibrated on data mainly collected in Central Italy and do not fully adapt to some typologies of residential buildings in the Etna region. In general, bad quality of materials, construction errors, poor observance of the rules, subsequent structural changes may contribute to increase the effective level of vulnerability, and deserve a correct calibration. Validation remains an open issue until more detailed data will be available as, for instance, disaggregated updated ISTAT data or the AeDes data (Agibilità e Danno in Emergenza Sismica—"Post-earthquake damage and safety assessment and short-term countermeasures") collected, buildings by buildings, in areas struck by strong earthquakes in Italy.

The common used damage estimation methods are calibrated for tectonic earthquakes and validated with data of strong events often presenting seismic sequences with cumulative damage (see the glaring example of the 2016–2017 Central Italy earthquakes in Graziani et al., 2019). In the present work we prove that it is possible to generate reliable damage scenarios in volcanic-tectonic regions, despite some different characteristics as the small-moderate magnitude, the shallow depth, the high values of peak ground motion parameters and their fast attenuation, and the low frequency content in the near field.

The necessary conditions are that the analysis has to be carried out on a detailed scale (census sections level) and the actual characteristics of the residential buildings have to be accounted for. At the present stage of our investigations, the M_3 method (Di Pasquale et al., 2005) provides a damage scenario better reproducing the effects of the 2018 Etna earthquake.

This application may also contributes to plan measures of intervention for the improvement of the building vulnerability in a densely populated areas such as the Etna volcano particularly exposed to seismic risk.

DATA AVAILABILITY STATEMENT

The raw data supporting the conclusions of this article will be made available by the authors, without undue reservation.

AUTHOR CONTRIBUTIONS

VP and FM assessed damage scenarios and compared the results with the collected data. RA and SD'A produced intensity shaking scenario, collected, and analyzed macroseismic survey data. All authors contributed to the article and approved the submitted version.

ACKNOWLEDGMENTS

We thank the reviewers for their suggestions that improved the paper.

REFERENCES

Alparone, S., Barberi, G., Giampiccolo, E., Maiolino, V., Mostaccio, A., Musumeci, C., et al. (2020). Seismological constraints on the 2018 Mt. Etna (Italy) flank eruption and implications for the flank dynamics of the volcano. *Terranova* 32, 334–344. doi: 10.1111/ter.12463

Azzaro, R., Barbano, M. S., D'Amico, S., and Tuvè, T. (2006). The attenuation of seismic intensity on the Etna region and comparison with other Italian volcanic districts. *Ann. Geophys.* 49, 1003–1020. doi: 10.4401/ag-3113

Azzaro, R., Barberi, G., D'Amico, S., Pace, B., Peruzza, L., and Tuvè, T. (2017). When probabilistic seismic hazard climbs volcanoes: the Mt. Etna case, Italy – Part 1: model components for sources parameterization. *Nat. Hazards Earth Syst. Sci.* 17, 1981–1998. doi: 10.5194/nhess-17-1981-2017

Azzaro, R., D'Amico, S., Rotondi, R., Tuvè, T., and Zonno, G. (2013). Forecasting seismic scenarios on Etna volcano (Italy) through probabilistic intensity attenuation models: a Bayesian approach. *J. Volcanol. Geotherm. Res* 251, 149–157. doi: 10.1016/j.jvolgeores.2012.07.011

Azzaro, R., D'Amico, S., and Tuvè, T. (2016). Seismic hazard assessment in the volcanic region of Mt. Etna (Italy): a probabilistic approach based on macroseismic data applied to volcano-tectonic seismicity. *Bull. Earthq. Eng.* 14, 1813–1825. doi: 10.1007/s10518-015-9806-2

Azzaro, R., D'Amico, S., Tuvè, T., Mostaccio, A., and Scarfì, L. (2020). Terremoti con effetti macrosismici in Sicilia nel periodo gennaio 2014—Dicembre 2018. *Quad. Geofis.* 160, 1–62. doi: 10.13127/qdg/160

Bernardini, A., Giovinazzi, S., Lagomarsino, S., and Parodi, S. (2007). "The vulnerability assessment of current buildings by a macroseismic approach derived from the EMS-98 scale," in *Proceedings of 3rd Congreso National de Ingeniería Sismíca*, (Girona: Asociación Espańola de Ingeniería Sismíca), 704–718.

Bernardini, A., Salmaso, L., and Solari, A. (2008). Statistical evaluation of vulnerability and expected seismic damage of residential buildings in the Veneto-Friuli area (NE Italy). *Boll. Geofis. Teor. Appl.* 49, 427–446.

Braga, F., Dolce, M., and Liberatore, D. (1982). "A statistical study on damage buildings and an ensuing review of the M.S.K.—76 scale," in *Proceedings of 7th European conference on Earthquake Engineering*, (Athens).

Civico, R., Pucci, S., Nappi, R., Azzaro, R., Villani, F., Pantosti, D., et al. (2019). Surface ruptures following the 26 December 2018, Mw 4.9, Mt. Etna earthquake, Sicily (Italy): EMERGEO Working Group (Etna 2018). *J. Maps* 15, 831–837. doi: 10.1080/17445647.2019.1683476

Crowley, H., Colombi, M., Borzi, B., Faravelli, M., Onida, M., Lopez, M., et al. (2009). A comparison of seismic risk maps for Italy. *Bull. Earthq. Eng.* 7, 149–180. doi: 10.1007/s10518-008-9100-7

Cucci, L., D'Amico, S., De Martini, P. M., Nave, R., Pizzimenti, L., Azzaro, R., et al. (2019). *Photographic Collection of the Coseismic Geological Effects Originated by the 26th December Etna (Sicily) Earthquake. Miscellanea*, Vol. 48. Rome: INGV, 1–76.

D'Amico, S., Meroni, F., Sousa, M. L., and Zonno, G. (2016). Building vulnerability and seismic risk analysis in the urban area of Mt. Etna volcano (Italy). *Bull. Earthq. Eng.* 14, 1797–1811. doi: 10.1007/s10518-015-9804-4

De Natale, G., Petrazzuoli, S., Romanelli, F., Troise, C., Vaccari, F., Somma, R., et al. (2019). Seismic risk mitigation at Ischia island (Naples, Southern Italy): an innovative approach to mitigate catastrophic scenarios. *Eng. Geol.* 261:105285. doi: 10.1016/j.enggeo.2019.105285

Di Pasquale, G., and Orsini, G. (1997). "Proposta per la valutazione di scenari di danno conseguenti ad un evento sismico a partire dai dati ISTAT," in *Proceedings of 8th National Conference on Earthquake Engineering in Italy*, Vol. 1, Taormina, 477–486.

Di Pasquale, G. and Orsini, G. (1998). "A probabilistic model for the assessment of the earthquake economic losses in Italy," in *Proceedings of the International Conference 'Risk Analysis 98'*, Valencia, Spain, 275–284.

Di Pasquale, G., Orsini, G., and Romeo, R. W. (2005). New development in seismic risk assessment in Italy. *Bull. Earthq. Eng.* 3, 101–128. doi: 10.1007/s10518-005-0202-1

Dolce, M., Prota, A., Borzi, B., da Porto, F., Lagomarsino, S., Magenes, G., et al. (2020). Seismic risk assessment of residential buildings in Italy. *Bull. Earthq. Eng.* doi: 10.1007/s10518-020-01009-5 [Epub ahead of print],

Giovinazzi, S., and Lagomarsino, S. (2001). "Una metodologia per l'analisi di vulnerabilità sismica del costruito," in *Proceedings of the X Congresso Nazionale "L'ingegneria Sismica in Italia"*, Potenza-Matera.

Giovinazzi, S., and Lagomarsino, S. (2004). "Esposizione e vulnerabilità del costruito in provincia di Imperia," in *Italian meeting "Rischio sismico, territorio e centri storici". Sanremo (IM), 2–3 July 2004*, eds S. Lagomarsino and P. Ugolini (Milan: FrancoAngeli), 321–332.

Graziani, L., del Mese, S., Tertulliani, A., Arcoraci, L., Maramai, A., and Rossi, A. (2019). Investigation on damage progression during the 2016–2017 seismic sequence in Central Italy using the European Macroseismic Scale (EMS-98). *Bull. Earthq. Eng.* 17, 5535–5558. doi: 10.1007/s10518-019-00645-w

Grünthal, G. (1998). "European macroseismic scale 1998 (EMS-98)," in *Cahiers du Centre Européen de Géodynamique et de Séismologie*, Vol. 15, (Luxembourg: Conseil de l'Europe).

Iervolino, I. (2018). Editoriale. Il moto al suolo nel terremoto di Viagrande (CT). *Progettazione Sismica* 3, 5–8. doi: 10.1007/bf02906453

ISTAT (1991). *13° Censimento Generale Della Popolazione — Dati sulle Caratteristiche Strutturale Della Popolazione, Delle Abitazioni e Variabili Economiche*. Available online at: http://www.istat.it/it/archivio/104317 (accessed Febrary, 2021)

ISTAT (2011). *15° Censimento Generale Della Popolazione e Abitazioni*. Available online at: http://dati-censimentopopolazione.istat.it/Index.aspx?lang=it (accessed February 2021)

Kassaras, I., Kazantzidou-Firtinidou, D., Ganas, A., Kapetanidis, V., Tsimi, C., Valkaniotis, S., et al. (2018). Seismic risk and loss assessment in Kalamata (SW Peloponnese, Greece) from neighbouring shallow sources. *Boll. Geof. Teor. Appl.* 59, 1–26. doi: 10.4430/bgta0222

Kassem, M. M., Mohamed Nazri, F., and Noroozinejad Farsangi, E. (2020). The seismic vulnerability assessment methodologies: a state-ofthe-art review. *Ain Shams Eng. J.* 11, 849–864. doi: 10.1016/j.asej.2020.04.001

Lagomarsino, S., and Giovinazzi, S. (2006). Macroseismic and mechanical models for the vulnerability and damage assessment of current buildings. *Bull. Earthq. Eng.* 4, 415–443. doi: 10.1007/s10518-006-9024-z

Lagomarsino, S., Ottonelli, D., and Cattari, S. (2019). "Calibration of the macroseismic vulnerability model and derivation of the fragility curves for URM buildings," in *Proceedings of 38th National conference GNGTS*, (Rome), 418–420.

Langer, H., Tusa, G., Scarfì, L., and Azzaro, R. (2016). Ground-motion scenarios on Mt. Etna inferred from empirical relations and synthetic simulations. *Bull. Earthq. Eng.* 14, 1917–1943. doi: 10.1007/s10518-015-9823-1

Lantada, N., Irizarry, J., Barbat, A. H., Goula, X., Roca, A., Susagna, T., et al. (2010). Seismic hazard and risk scenarios for Barcelona, Spain, using the Risk-UE vulnerability index method. *Bull. Earthq. Eng.* 8, 201–229. doi: 10.1007/s10518-009-9148-z

Locati, M., Camassi, R., Rovida, A., Ercolani, E., Bernardini, F., Castelli, V., et al. (2019). *Database Macrosismico Italiano (DBMI15), versione 3.0*. Rome: Istituto Nazionale di Geofisica e Vulcanologia.

Lucantoni, A., Bosi, V., Bramerini, F., De Marco, R., Lo Presti, T., Naso, G., et al. (2001). Il rischio sismico in Italia. *Ing. Sismica* 18, 5–36.

Meroni, F., Petrini, V., and Zonno, G. (2000). "Distribuzione nazionale della vulnerabilità media comunale," in *La Vulnerabilità Degli Edifici: Valutazione a Scala Nazionale Della Vulnerabilità Sismica Degli Edifici Ordinari*, ed. A. Bernardini (Roma: GNDT-CNR), 105–131.

Meroni, F., Squarcina, T., Pessina, V., Locati, M., Modica, M., and Zoboli, R. (2017). A damage scenario for the 2012 Northern Italy earthquake and its economic losses assessment. *Int. J. Disaster Risk Sci.* 8, 326–341. doi: 10.1007/s13753-017-0142-9

Meroni, F., Zonno, G., Azzaro, R., D'Amico, S., Tuvè, T., Oliveira, C. S., et al. (2016). The role of the urban system dysfunction in the assessment of seismic risk in the Mt. Etna area (Italy). *Bull. Earthq. Eng.* 14, 1979–2008. doi: 10.1007/s10518-015-9780-8

Mosoarca, M., Onescu, I., Onescu, E., Azap, B., Chieffo, N., and Szitar-Sirbu, M. (2019). Seismic vulnerability assessment for the historical areas of the Timisoara city, Romania. *Eng. Fail. Anal.* 101, 86–112. doi: 10.1016/j.engfailanal.2019.03.013

Mota de Sá, F., Ferreira, M. A., and Oliveira, C. S. (2016). QuakeIST§earthquake scenario simulator using interdependencies. *Bull Earthq. Eng.* 14, 2047–2067. doi: 10.1007/s10518-016-9884-9

QUEST Working Group (2019). *Il Terremoto Etneo del 26 Dicembre 2018, MW4.9: Rilievo Degli Effetti Macrosismici. Rapporto INGV n. 1 del 06/02/2019*. Rome: INGV, 9. doi: 10.5281/zenodo.2558168

Riedel, I., Guéguen, P., Dalla Mura, M., Pathier, E., Leduc, T., and Chanussot, J. (2015). Seismic vulnerability assessment of urban environments in moderate-to-low seismic hazard regions using association rule learning and support vector machine methods. *Nat. Hazards* 76, 1111–1141. doi: 10.1007/s11069-014-1538-0

Rotondi, R., and Zonno, G. (2004). Bayesian analysis of a probability distribution for local intensity attenuation. *Ann. Geophys.* 47, 1521–1540. doi: 10.4401/ag-3356

Selva, J., Acocella, V., Bisson, M., Caliro, S., Costa, A., Della Seta, M., et al. (2019). Multiple natural hazards at volcanic islands:a review for the Ischia volcano (Italy). *J. Appl. Volcanol.* 8:5.

Sigbjörnsson, R., Zonno, G., and Oliveira, C. S. (2016). The European project UPStrat-MAFA: Urban disaster prevention strategies using MAcroseismic Fields and FAult Sources. *Bull. Earthq. Eng.* 14:357.

Sousa, M. L., and Campos Costa, A. (2016). Evolution of earthquake losses in Portuguese residential building stock. *Bull. Earthq. Eng.* 14, 2009–2029. doi: 10.1007/s10518-015-9809-z

Spence, R., and Le Brun, B. (2006). Special issue: earthquake scenarios for European cities – the RISK-UE project. *Bull. Earthq. Eng.* 4, 323–339. doi: 10.1007/s10518-006-9020-3

Tusa, G., Langer, H., and Azzaro, R. (2020). Localizing Ground-Motion Models in volcanic terranes: shallow events at Mt. Etna, Italy, revisited. *Bull. Seism. Soc. Am.* 110, 2843–2861. doi: 10.1785/0120190325

Working Group (2013). Gruppo di Lavoro Incaricato Della Definizione Dello Scenario di Riferimento per il Piano di Emergenza dei Campi Flegrei per il Rischio Vulcanico. Rapporto Finale. Available online at: http://www.lavoripubblici.regione.campania.it/joomla/jdownloads/Campi%20Flegrei/rapporto_gdl_campiflegrei_31gen2013.pdf (accessed February, 2021).

Zonno, G., Oliveira, C. S., Ferreira, M. A., Musacchio, G., Meroni, F., Mota-de-Sa, F., et al. (2010). Assessing seismic damage through stochastic simulation of ground shaking: the case of the 1998 Faial earthquake (Azores Islands). *Surv. Geophys.* 31, 361–381. doi: 10.1007/s10712-009-9091-1

Zonno, G., Rotondi, R., and Brambilla, C. (2009). Mining macroseismic fields to estimate the probability distribution of the intensity at site. *Bull. Seism. Soc. Am.* 99, 2876–2892. doi: 10.1785/0120090042

Zuccaro, G., and De Gregorio, D. (2019). Impact assessments in volcanic areas – the Vesuvius and Campi Flegrei cases studies. *Ann. Geophys.* 62:VO02. doi: 10.4401/ag-7827

Zuccaro, G., Perelli, F. L., De Gregorio, D., and Cacace, F. (2020). Empirical vulnerability curves for Italian masonry buildings: evolution of vulnerability model from the DPM to curves as a function of acceleration. *Bull. Earthq. Eng.* doi: 10.1007/s10518-020-00954-5 [Epub ahead of print],

Conflict of Interest: The authors declare that the research was conducted in the absence of any commercial or financial relationships that could be construed as a potential conflict of interest.

frontiers in Earth Science

ORIGINAL RESEARCH
published: 25 May 2021
doi: 10.3389/feart.2021.630116

First-Motion Focal Mechanism Solutions for 2015–2019 $M \geq 4.0$ Italian Earthquakes

Maria G. Ciaccio, Raffaele Di Stefano, Luigi Improta, Maria T. Mariucci and BSI Working Group*

Istituto Nazionale di Geofisica e Vulcanologia, Rome, Italy

A list of 100 focal mechanism solutions that occurred in Italy between 2015 and 2019 has been compiled for earthquakes with magnitude $M \geq 4.0$. We define earthquake parameters for additional 22 seismic events with $3.0 \leq M < 4.0$ for two specific key zones: Muccia, at the northern termination of the Amatrice–Visso–Norcia 2016–2018 central Italy seismic sequence, and Montecilfone (southern Italy) struck in 2018 by a deep, strike-slip Mw 5.1 earthquake apparently anomalous for the southern Apennines extensional belt. First-motion focal mechanism solutions are a good proxy for the initial rupture and they provide important additional information on the source mechanism. The catalog compiled in the present paper provides earthquake parameters for individual events of interest to contribute, as a valuable source of information, for further studies as seismotectonic investigations and stress distribution maps. We calculated the focal mechanisms using as a reference the phase pickings reported in the Italian Seismic Bulletin (BSI). We visually checked the reference picks to accurately revise manual first-motion polarities, or include new onsets when they are not present in the BSI dataset, for the selected earthquakes within the whole Italian region, with a separate focus on the Amatrice–Visso–Norcia seismic sequence area from August 24, 2016 to August 24, 2018. For the Montecilfone area, we combined the information on the geometry and kinematics of the source of the 2018 Mw 5.1 event obtained in this study with available subsurface and structural data on the Outer Apulia Carbonate Platform to improve understanding of this intriguing strike-slip sequence. Our analysis suggests that the Montecilfone earthquake ruptured a W–E trending strike-slip dextral fault. This structure is confined within the Apulia crystalline crust and it might represent the western prolongation of the Mattinata Fault–Apricena Fault active and seismogenic structures. The calculated focal mechanisms of the entire catalog are of good quality complementing important details on source mechanics from moment tensors and confirming the relevance of systematically including manually revised and more accurate polarity data within the BSI database.

Keywords: first motion solutions, focal mechanisms, seismicity, Italian region, Amatrice-Visso-Norcia seismic sequence, Montecilfone sequence, Muccia area

OPEN ACCESS

Edited by:
Nicola Alessandro Pino, National Institute of Geophysics and Volcanology (INGV), Italy

Reviewed by:
José A. Álvarez-Gómez, Complutense University of Madrid, Spain
Kostas Lentas, National Observatory of Athens, Greece

****Correspondence:***
Maria G. Ciaccio
mariagrazia.ciaccio@ingv.it

Specialty section:
This article was submitted to Solid Earth Geophysics, a section of the journal Frontiers in Earth Science

Received: *16 November 2020*
Accepted: *26 February 2021*
Published: *25 May 2021*

Citation:
Ciaccio MG, Di Stefano R, Improta L, Mariucci MT and BSI Working Group (2021) First-Motion Focal Mechanism Solutions for 2015–2019 M ≥ 4.0 Italian Earthquakes. Front. Earth Sci. 9:630116. doi: 10.3389/feart.2021.630116

INTRODUCTION

The Italian region is characterized by a high rate of tectonic origin seismicity mainly distributed along the Alpine and Apennines mountain belts, and the Calabrian Subduction zone. Relevant and long-lasting seismic sequences with mainshocks $Mw \geq 5.0$ struck the region giving important insights in the active deformation regime and therefore information for seismic risk reduction.

The BSI (Italian Seismological Bulletin[1]) analyst seismologists of INGV off-line revise both hypocenter locations and local magnitudes of earthquakes that are detected by the automatic acquisition system and then are quickly real-time analyzed by the monitoring room of INGV for civil protection duties. Revised P- and S-quality weighted onsets, hypocenter locations, amplitudes, and local magnitudes are then periodically released in the BSI publication and through the INGV FDSN web services generally for $M_L \geq 1.5$ events (INGV Seismological and Data Centre, 2006; ISIDe Working Group, 2007). Nevertheless, manually revised first-motion polarities are not yet systematically revised in the BSI dataset for further focal mechanism studies.

First-motion focal mechanism solutions are anyway an important approach, also in addition to the moment tensor estimation when available, being a good indicator of the initial rupture stages of faulting especially in very complex ruptures as seismic faults are not always planar. The first-motion data describe in fact the early part of the source which may or may not be representative of the whole source process for an earthquake; in contrast, the moment tensor solution might represent an average source process (Anderson, 1988) depending on the frequency content, the used signal length, and the applied filtering. Moreover, although for moderate to large events ($M > 4.5$) the inversion of broadband seismic waveforms well describes earthquake source properties of the main faulting process, this method might produce less stable/more noisy solutions when applied to $M < 3.5$: AUTO-TDMT procedure (automatic seismic time-domain moment tensor) implemented at INGV is triggered by local and regional events with magnitude $M_L \geq 3.5$ detected and located by the INGV monitoring center (Scognamiglio et al., 2009). Indeed, the moment tensor solution provides a good indication of the general style of deformation occurring in an area, but careful consideration of the first-motion solution is very useful for a detailed study of source mechanics, also taking advantage of the information from lower magnitudes.

We relocated all the selected earthquakes by using a multi-parameter procedure and we calculated focal mechanisms of 100 earthquakes with $M \geq 4.0$ occurred in the Italian region during the period 2015–2019[2] by using the FPFIT code (Reasenberg and Oppenheimer, 1985). Among them, 51 seismic events occurred inside the region interested by the Amatrice–Visso–Norcia (AVN) sequence, 4 in the Montecilfone area, and 2 in the Muccia area. The AVN in this paper has a time span ranging from August 2016 to August 2018 to better define the evolution of the important seismic sequence including the strongest earthquake occurred since 1980 in Italy. No earthquakes with $M \geq 4.0$ were detected in the selected period in the Alpine mountain belt or the Po Plain (**Figure 1**).

[1]http://iside.rm.ingv.it/help#BSI

[2]http://terremoti.ingv.it/

THE MULTI-PARAMETER LOCATION

The BSI locations are obtained from a simple velocity model composed of two layers on a half-space (Battelli et al., 2013); for this reason, we relocated all the selected earthquakes by using a multi-parameter procedure. To locate seismic events, we choose the linearized approach by Lahr, 1999 (the Hypoellipse code) using a best 1D velocity model for the area (**Figure 2**, modified from Chiarabba et al., 2005b), but exploring the hypocenter solutions space by changing three key *a priori* conditions that typically strongly influence the solution convergence in the linearized approach: the starting trial depth, the weight function of arrival times with distance, and the travel time residual cut.

The distance weighting function gives full weight (multiplying the assigned weight by 1) to arrival times for stations with distance less than d1 and zero weight (multiplying by 0) to arrival times for stations at epicentral distance higher than d2. Setting A1 (see **Table 1**) cuts out stations farer than 75 km giving full weight to stations closer than 25 km; settings A2 and A3 progressively extend the full weight distance and the exclusion distance including contribution of progressively farer stations that might be determinant for larger events or in case of no or few close stations.

The trial depth in the linearized problem might equally be a solution or a trap guiding the hypocenter to the absolute or a local minimum for the more unstable of the hypocenter coordinates: the focal depth. For this reason, we introduced three different trial depths at upper crustal (B1, 5 km), lower crustal (B2, 25 km), and upper mantle (B3, 75 km) depth allowing the procedure to eventually get out of local minimums and/or being trapped by 1D model velocity jumps.

Finally, the large residuals cut can have a big influence on the final location erasing the contribution of worse fitted arrival times. Bad fitting arrival times is not necessarily a symptom of large error in pickings and can be conversely related to the neglected effect of 3D heterogeneities on the travel-time computation approximations in the velocity model. For this reason, the choice of cutting them out might be correct or not and the amount of residual considered unacceptable is also a key point. A too small threshold value, especially in absence of proper stations corrections might bring to overfitting the 1D velocity model at the cost of getting complaisant but wrong locations. Moreover, an important role in the quality of the final location is played by the iteration starting from which the cut is applied. We here set a large threshold to avoid linking too much the location to the 1D model approximation and applied the cut from the 1st iteration (C1), from the 5th (C2) or never (C3).

The combination of these three different settings for each of the three sensible parameters, A, B, and C, produces 27 different configurations exploring in a discrete empirical way the hypocenter solutions space and producing 27 eventually different locations.

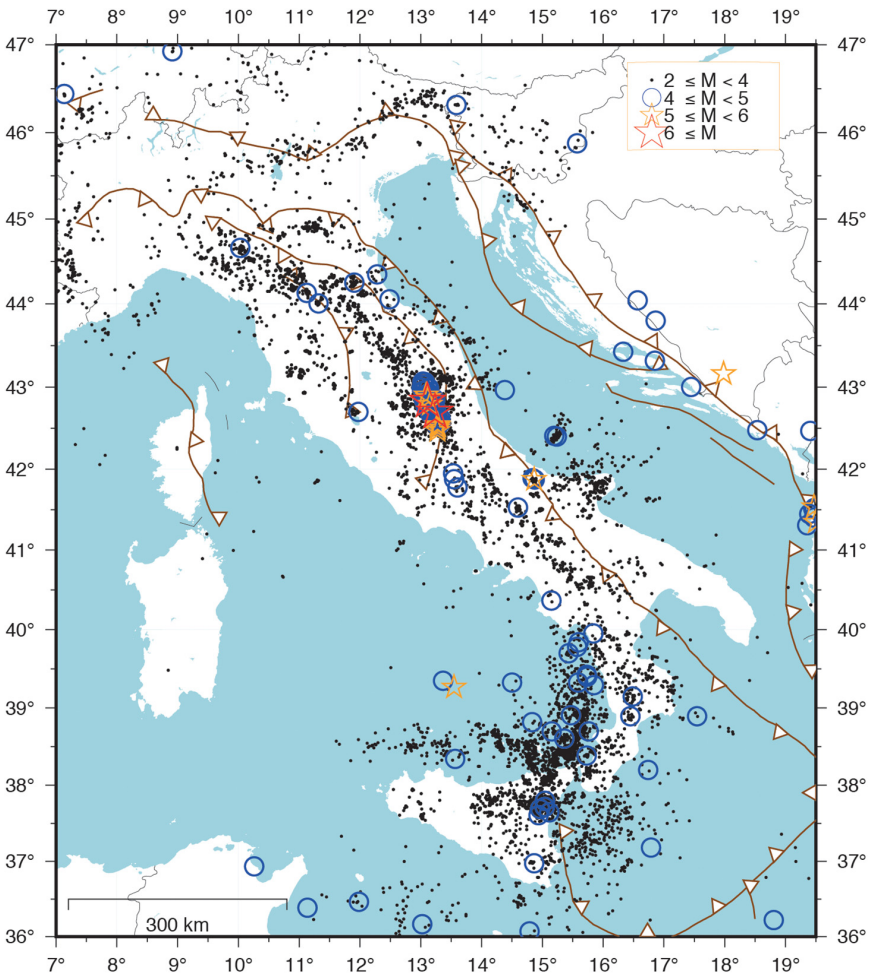

FIGURE 1 | Earthquakes, $M \geq 4.0$ (blue circles), $M \geq 5.0$ (orange stars), and $M \geq 6.0$ (red stars), that occurred in the Italian region in the period 2015–2019. Small black dots are $M \geq 2.0$ earthquakes. The main tectonic fronts of the region are reported in brown lines.

Differently from the probabilistic approach, we remain in the linearized domain and use the formal error estimation and the final rms of the array of the focal solutions to select the best location for each earthquake.

The procedure first orders the location vector by growing RMS, selecting the best 13 (half out of the total 27), then these are ordered by growing vertical error and the best 7 are selected and ordered in turn by growing horizontal error and the best 4 are taken out of which the 2 ones with lower azimuthal gaps are taken. Finally, the one with lower RMS out of these two is considered the highest quality location.

The 1D velocity model in **Figure 2** is also used to calculate the take-off angle for focal solution determination.

THE CATALOG OF FIRST-MOTION FOCAL MECHANISMS

The FPFIT code (Reasenberg and Oppenheimer, 1985) reads in the Hypoellipse output and computes double-couple fault plane solutions from *P*-wave first motion data using a grid search method. Errors in first-motion observations may occur because of station polarity reversal or incorrect direct P-arrival picks due to low signal-to-noise ratio. For these reasons, to constrain our focal solutions by reducing the number of discrepancies, we proof-checked the dataset for possible reversal polarities and we filtered the polarities based on the weight assigned to the *P*-onset by the BSI analysts (discrete classed from 0, best, to 3, worse) keeping only polarities for picks with weights 0 and 1 and rejecting those with weight 2 and 3 that can be present in the BSI dataset due to the automatic procedure applied in the monitoring seismic room of the INGV. Furthermore, since the first polarities are not routinely entered for all waveforms by the BSI analysts, we have added, where present, additional good quality polarities. We also required a minimum number of 10 *P*-polarities per event.

It may occur that, depending on the distribution and quality of first-motion data, more than one focal mechanism solution may fit equally well the impulsive polarities having as a consequence identical values of relative minima in misfit, the indication of inconsistent polarities. The variability in fault parameters

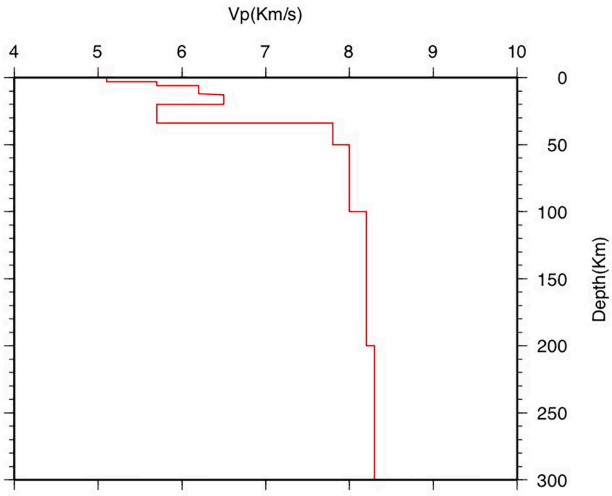

FIGURE 2 | The 1D P-wave velocity model used in the routine location of earthquakes.

TABLE 1 | Settings used in the multi-parameter procedure.

	Distance cut window		Trial depth		Large residual cut
A1	25–75	B1	5	C1	1
A2	50–150	B2	25	C2	5
A3	100–300	B3	75	C2	Never

observed among the preferred mechanisms could originate from velocity model uncertainties: in fact, the gradient of the velocity structure controls the variations of the take-off angles of the seismic rays, resulting in multiple focal mechanism solutions.

In our analysis, we only include focal mechanisms with unique solutions (**Supplementary Table 1**). Focal mechanisms with multiple solutions are anyway released in **Supplementary Table 2**. The final focal mechanism catalog contains 100 quality selected fault plane solutions for earthquakes with magnitude $M \geq 4.0$, and additional 22 solutions for seismic events with $3.0 \leq M < 4.0$ for two specific key zones: the Muccia region, at the northern termination of the Amatrice–Visso–Norcia 2016–2018 central Italy seismic sequence, and the Montecilfone (southern Italy) area struck in 2018 by deep, strike-slip Mw > 5.1 earthquakes apparently anomalous for the southern Apennines extensional belt.

Our criteria for selecting earthquakes for the analysis are principally based on the reported magnitude M which we set to $M \geq 4.0$. However, we also choose to analyze earthquakes of particular interest or seismotectonic significance with $M < 4.0$ in case of clear P-wave arrival times and polarities and favorable stations distribution. This analysis shows the importance of lowering the threshold of magnitude to get a better picture of the seismic deformation and give information about the state of stress around a fault in an area, even when earthquakes of high magnitude are absent.

For the 100 obtained fault plane solutions, we list the reference INGV event ID, Date, Magnitude (**Supplementary Table 1**), the hypocenter calculated with the multiparameter location approach, the estimated fault parameters, and their overall quality in terms of uncertainties on strike, dip, and rake and station distribution ratio (STDR). The latter quantity ranges from 0.0 to 1.0 and it is sensitive to the distribution of the data on the focal sphere, relative to the radiation pattern. Values of STDR lower than 0.5 indicate a less robust solution. In **Figure 3**, we show some statistics about the distribution of these parameters and the quality of the mechanisms obtained. The STDR is higher than 0.5, ranging from 0.5 to 0.9. For most of the focal solutions, the range in the uncertainty of each parameter (strike, dip, rake) is mostly within 20°.

Finally, we produce a classification ternary diagram plotting the plunge of the intermediate (B), tension (T), and pression axes (P) of focal mechanisms to illustrate the faulting style of the seismotectonic regimes. The diagram uses the Kaverina et al. (1996) projection technique, used also by Kagan (2005), calculated with FMC script (Álvarez-Gómez, 2019).

Due to the large density of data in the small region of the AVN seismic sequence, we decided to discuss them in a separate section. We will therefore first describe the solutions of the focal mechanisms that occurred in Italy in the 2015–2019 period and then the solutions of the AVN seismic sequence. In both areas, we also focus on sub-areas where $3.0 \leq M < 4.0$ earthquakes are analyzed.

Earthquakes $M \geq 4.0$ Occurred in Italy During 2015–2019

In Italy, during the selected 5 years, 51 earthquakes with M $\geq$ 4.0 occurred. We obtained a robust result for 49 earthquakes (**Supplementary Table 1**), 2 seismic events have multiple solutions (**Supplementary Table 2**). In **Figure 4**, we show a regional map with our new FPFIT solutions while in **Figures 5A–C**, we show the same solutions in depth along traces P1, P2, and P3.

In **Figure 6**, we show the histogram of the calculated rakes. We observe a spatial variability of the observed style of faulting reflecting the complex active tectonics of the Italian region. Statistical analysis of the kinematics of the nodal planes shows a prevalence of normal solutions with oblique/normal, left or right lateral components, while reverse and oblique/reverse mechanisms are rare.

This variability is also shown in **Figures 7**, **8**. **Figure 7** reports the azimuth of T-axes of the 49 solutions: thick lines represent the direction of T-axes with the white circle at the center of epicentral location of the respective event on the map; the length of the lines is proportional to the plunge. To classify focal mechanisms, we used the FMC program (Álvarez-Gómez, 2019) which produces the type classification (Kaverina et al., 1996) in **Figure 8**. This approximation began with the use of Frolich Apperson classification (1992) and improved later on after Kagan's work (2005).

The M $>$ 4.0 earthquakes that occurred in the northern Apennines during 2015–2019 show the extension–compression pair at the transition between the active extension zone of the Apenninic chain, oriented approximately perpendicular to the

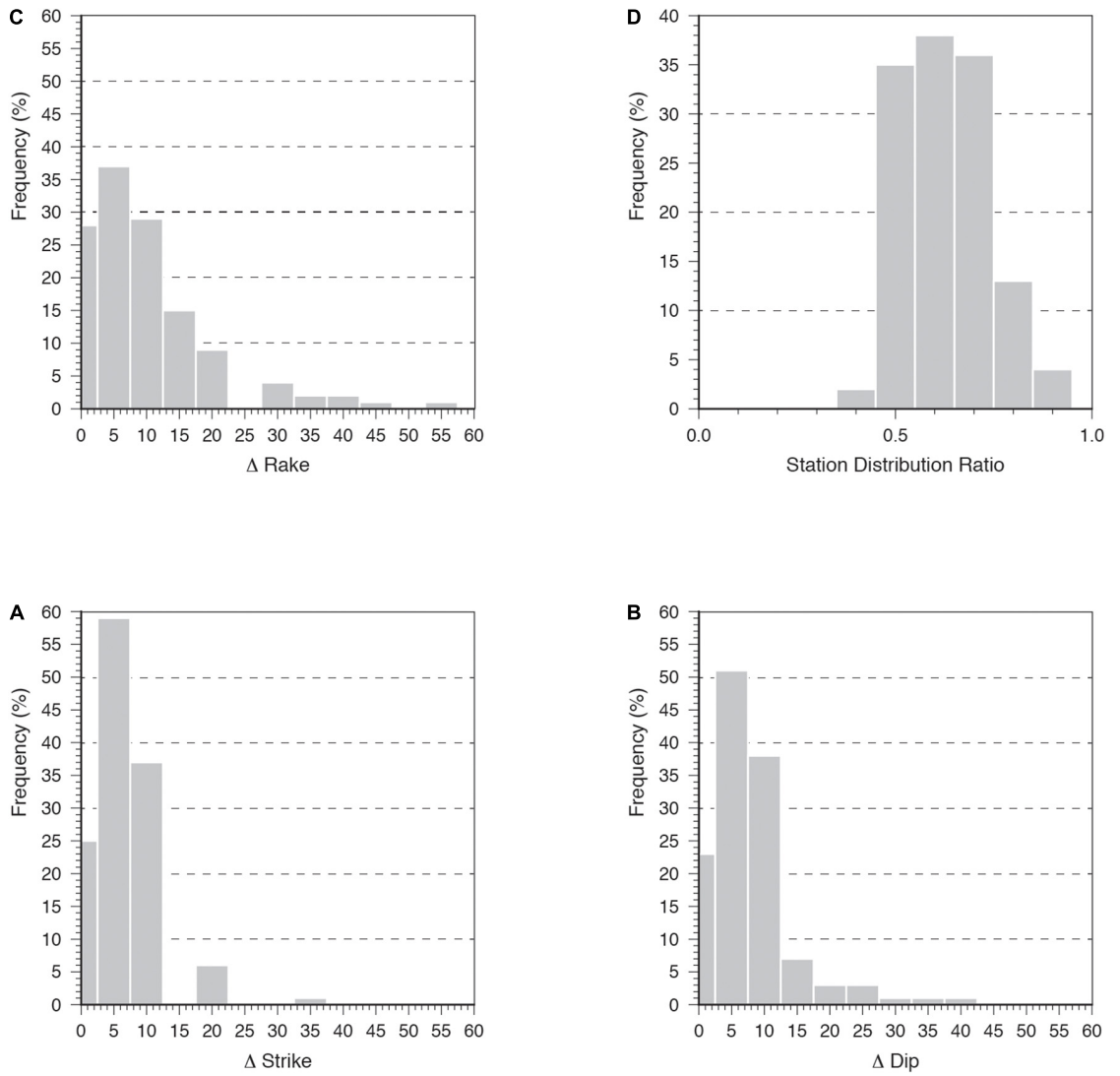

FIGURE 3 | Histograms of the uncertainties distributions of strike **(A)**, dip **(B)**, and rake **(C)** of the presented focal solutions with STDR (stations distribution ratio) **(D)**.

chain axes, and the buried compressive structures of the Po Plain (**Figure 5A**).

Strike-slip faulting are present in the region between the Apenninic axial zone and the Apulia-Gargano foreland (see the Montecilfone focus, next paragraph); the Calabrian arc and the Tyrrhenian Calabrian offshore are dominated, both at shallow and at higher depths, by active extensional deformation, while the south-eastern part of Sicily is dominated by strike-slip tectonic regime.

In particular, in the Tyrrhenian Sea, in the depth interval (0–250 km, **Figure 5B**), we find focal solutions with prevalent strike-slip solution (first 30 km) and prevalent normal component (deeper than 30 km): deeper earthquakes follow the Benioff plane dipping, at these depths, to about 70° (Selvaggi and Chiarabba, 1995). One seismic event shows a reverse solution: this earthquake is located very near to the coast (7 km from Tropea, Vibo Valentia).

In the Calabrian peninsula, two relatively shallow hypocenters (depth $<$ 50 km) have a prevalent normal component while the seismic events in the Hyblean forland, Sicily Channel, and Ionian Sea show strike-slip solutions with normal components in agreement with previous studies (Presti et al., 2013; **Figure 5C**).

Focus on 2018 Montecilfone Earthquakes

On April 25, 2018, a seismic event with *M*w 4.3 occurred in the Montecilfone area, located to the west of the Gargano Promontory (**Figure 8**), followed by a small cluster of about 10 events with $M_L < 3.0$. After less than 4 months, on August 14, a *M*w 4.6 earthquake hit the same area. The sequence culminated on August 16 with a Mw 5.1 occurred at 21 km depth and about 3 km to the south of the April 25th event. This strongest event was followed 2 h after by a Mw 4.4 event and by numerous moderate–small aftershocks. About 600 earthquakes have been recorded by the RSN with $M_L \leq 3.5$ and hypocentral depth between

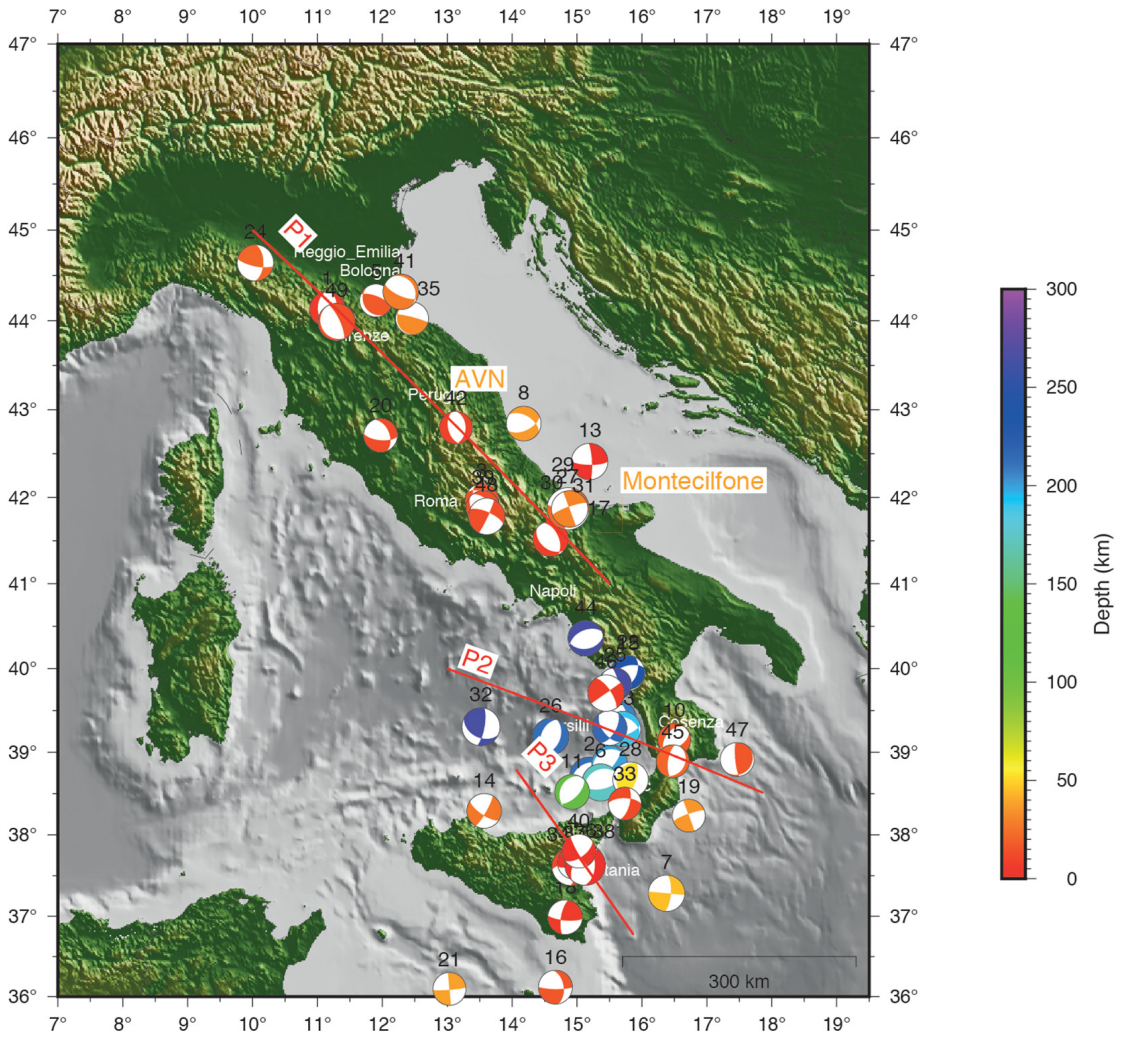

FIGURE 4 | FPFIT focal solutions for the analyzed earthquakes $M \geq 4.0$ reported in **Supplementary Table 1**, in the "Italy," "muccia," and "montecilfone" areas. AVN-Box is the area of the Amatrice–Visso–Norcia seismic sequence; P1: trace of the vertical cross section in **Figure 5A**; P2: trace of the vertical cross section in **Figure 5B**; P3: trace of the vertical cross-section in **Figure 5C**. Color scale is related to hypocenter depth.

10 and 25 km. Among them, we could determine high-quality focal mechanisms for height earthquakes having magnitude $3.0 < M_L < 4.0$ (**Figure 9**). All the solutions indicate an almost pure strike-slip, right-lateral mechanism, with subvertical focal planes mainly oriented about NS and EW.

In **Figure 9**, we show the focal mechanisms calculated in this work with first polarities compared with the available TDMT and RCMT solutions. We observe a very good agreement of the first motion and the moment tensor solution. Moreover, our first-motion polarities' focal mechanisms for $M < 4.0$ earthquakes testify that the strike-slip dextral faulting observed for the moderate events is also present at small scale suggesting almost regular fault plane geometries. By combining the hypocenter distribution and focal mechanism of all events here analyzed, we conclude that the 2018 events relate to an unknown, strike-slip structure, trending about EW and characterized by a right-lateral kinematic.

In agreement, the average focal mechanism in the Montecilfone area points out a strike-slip regime with a sub-vertical σ2 and horizontal σ1 and σ3, NW–SE and NE–SW oriented, respectively (see inset in **Figure 9**). This trend perfectly fits with the contemporary stress state in the external area of the southern Apennines (Mariucci and Montone, 2020a,b), where the minimum horizontal stress is NE–SW oriented, coherent with the extension in the inner belt, but related to a strike-slip tectonic regime as evidenced also by a few instrumental events (Potenza 1990 and Molise 2002 sequences; Di Luccio et al., 2005a,b) and main seismogenic sources (DISS Working Group, 2018).

Remarkably, such a structure broke the mid-lower crust (10–25 km depth), differently from the seismicity of the southern Apennines belt that is confined in the uppermost 15 km of the crust, and its strike appears transverse to the NW–SE direction of the large active normal faults dissecting the Apennine range westwards.

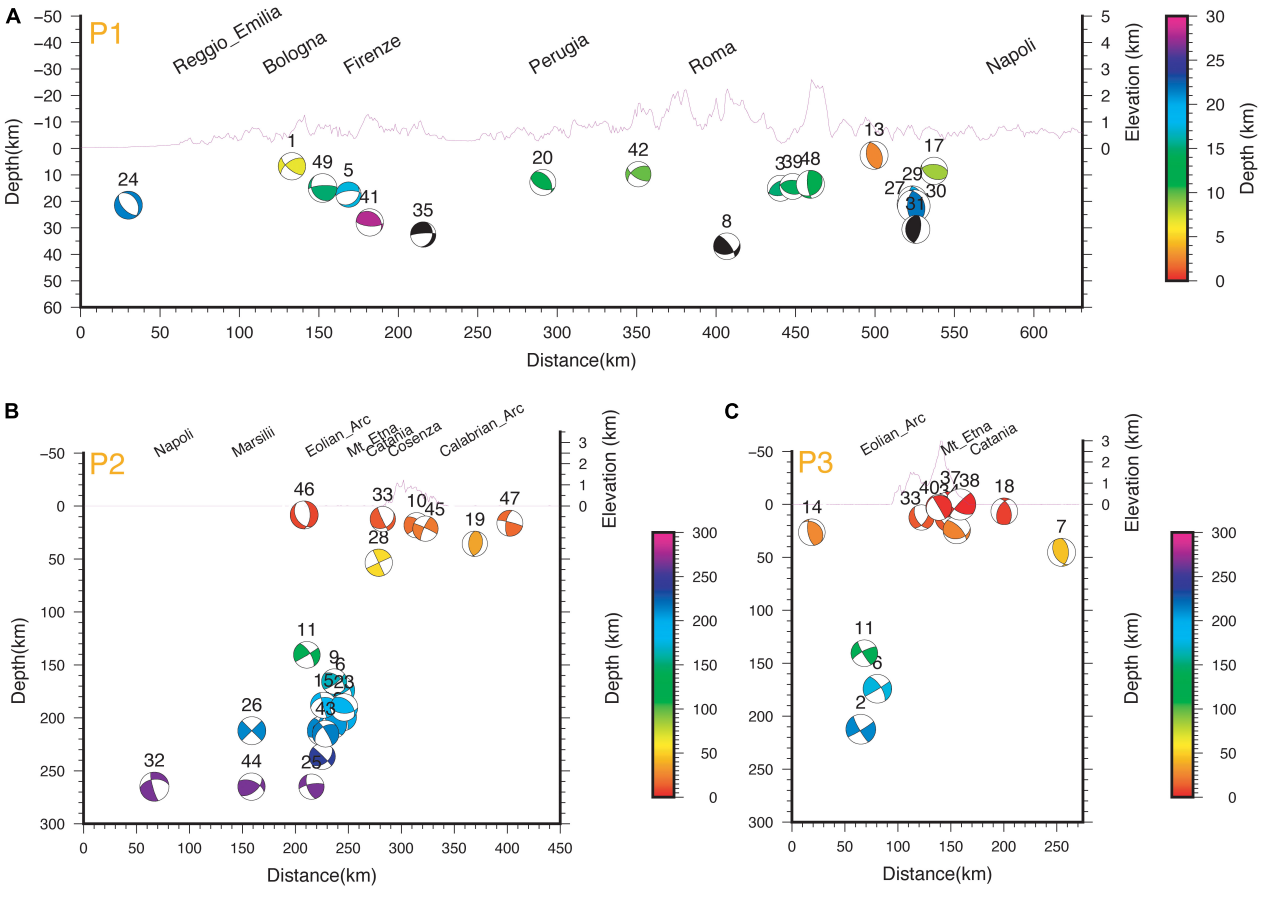

FIGURE 5 | (A–C) Seismic cross-sections along P1, P2, and P3 profile shown in **Figure 4**.

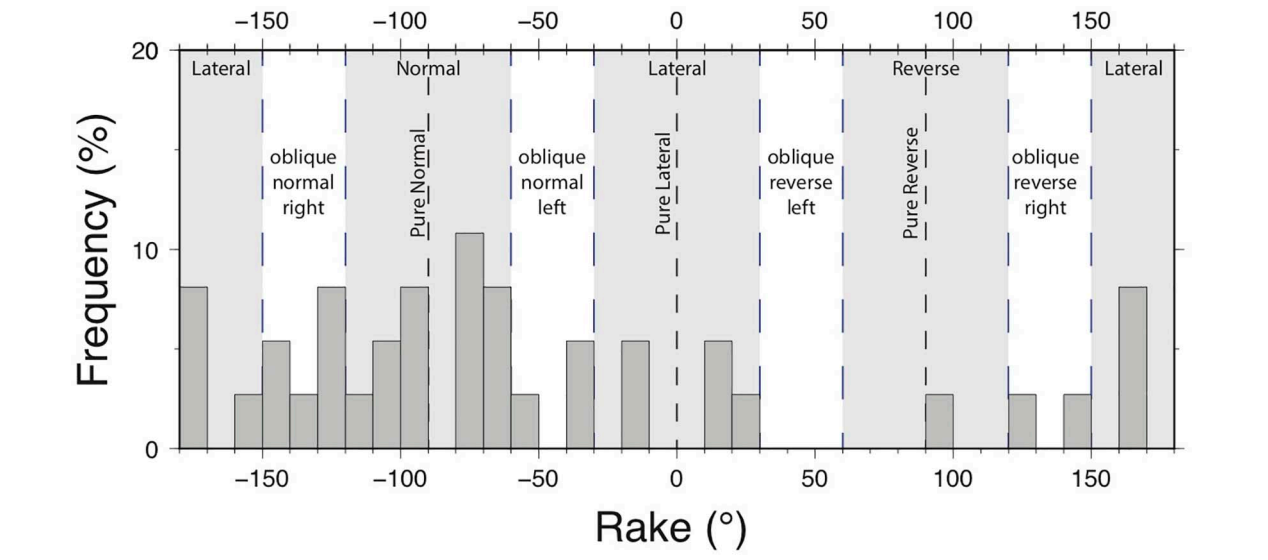

FIGURE 6 | Histogram of the rake of the calculated focal mechanisms for "Italy" area.

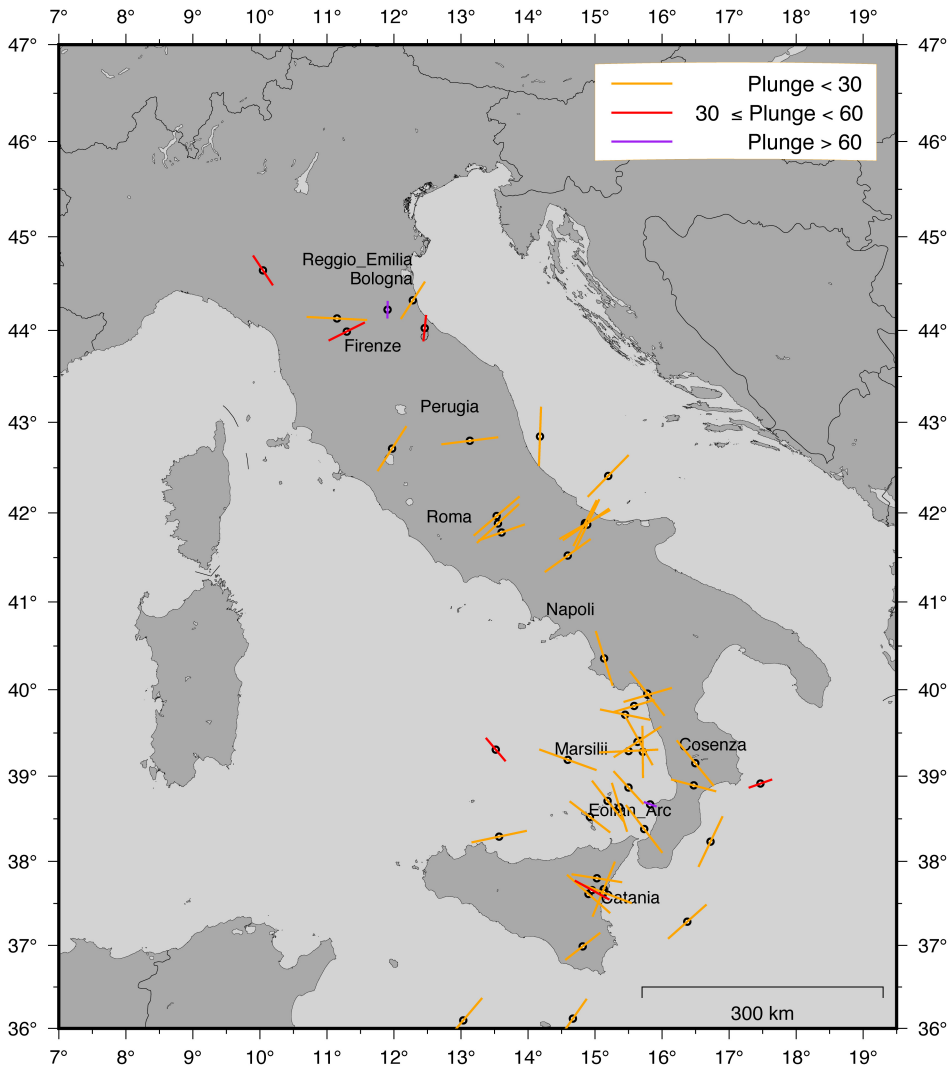

FIGURE 7 | *T*-axes of focal mechanism solutions determined in the present study for "Italy" area. The length of each bar is inverse proportional to the plunge of the axis; colors are related to the 3 groups of plunges reported in the inset.

To better understand the seismotectonic framework of the 2018 Montecilfone seismicity, we analyzed subsurface structural information available in literature. The 2018 sequence occurred in the easternmost sector of the southern Apennines thrust-and-fold belt, where the more external nappes overthrust Late Pliocene–Early Pleistocene foredeep deposits that in turn stratigraphically cover the Outer Apulian Carbonate Platform (OAP) (Menardi Noguera and Rea, 2000; Butler et al., 2004; Patacca and Scandone, 2004). The structural map of **Figure 9** shows the morphology of the top of the buried OAP, together with the main faults that displace the Apulian carbonates, from the external zone of the Apennines belt to the Apulian foreland (i.e., the western Gargano Promontory). This structural map, based on a wealth of seismic commercial profiles and well data interpreted by Nicolai and Gambini (2007), outlines two main structural trends: the regional-scale SW deepening of the OAP and local-scale structures represented by E–W to WNW–ESE oriented highs and lows. The SW deepening of the OAP from 1 km to more than 5 km depth represents the response of the Apulian carbonates to the flexure-hinge retreat of the Apulia plate margin. It is associated with NW–SE normal faults active during Late Pliocene–Early Pleistocene times that are evident in the southern part of the map. Three main deviations from the regional trend characterize the central and northwestern sectors of the survey area (**Figure 9**). High-angle transpressive faults delimit the E–W trending Chieuti High, a push-up structure active during Lower Pleistocene (Patacca and Scandone, 2004). About 5 km to the west, a WNW–ESE trending structural high aligned with the Chieuti structure has plausibly the same nature. Indeed, this structure cannot be related to the compressive structures deforming the Inner Apulia Platform thrust–fold belt being its frontal ramp located more than 30 km further west (Nicolai and Gambini, 2007). A structural low oriented E–W is bounded to the north by the Apricena fault (**Figure 9**). According to

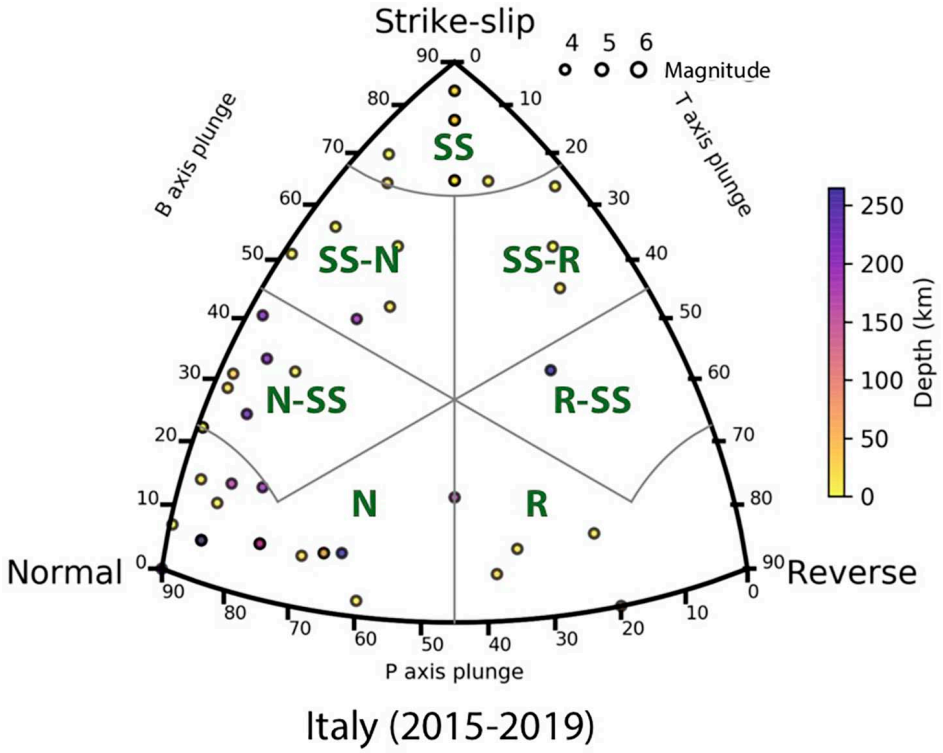

FIGURE 8 | FMC diagram for the classification of focal mechanisms in Italy area. N, normal; N-SS, normal–strike-slip; SS-N, strike-slip–normal; SS, strike-slip; SS-R, strike-slip–reverse; R-SS, reverse–strike-slip; R, reverse. The points are scaled by magnitude and colored by different depths.

Patacca and Scandone (2004), the WNW–ESE Apricena fault is a major high-angle structure that dips SSW with significant dip-slip displacement; it shows evidence of recent activity and can be identified as the source of the 1627, M6.7 Capitanata earthquake, the strongest historical event that struck the region (see the macroseismic epicenter reported in **Figure 9**). The activity of the Apricena Fault up to late Pleistocene at least is confirmed by recent high-resolution seismic reflection surveys that also seem to indicate a significant strike slip component of motion (Varriale, 2011).

Both the Chieuti and Apricena structures join the transcurrent Mattinata Fault System in the western Gargano Promontory. This is a lithospheric-scale active and seismogenic structure characterized by a complex polyphase evolution. Likely of Mesozoic origin, it was reactivated as a sinistral strike slip system from Miocene to early Pliocene and then it has slipped with dextral kinematics since late Pliocene (Di Bucci et al., 2010; and references therein).

East–west oriented structures that clearly deviate from the regional trend are also present just in the epicentral area of the 2018 Montecilfone sequence (**Figure 9**). Here, the structural map reports three parallel S-dipping high-angle faults, with the main one that measures 12 km long strike. Fault kinematics is unknown, but a dip-slip component may be hypothesized based on the southward deepening of the Apulian carbonate top. Remarkably, the epicenters of all largest earthquakes ($M > 3$) with reliable focal solutions fall in the hanging wall of the main E–W fault, near the fault trace, consistently with the southward dip of nearly vertical E–W nodal planes (**Figure 9**). Further north, WNW–ESE trending faults delimit a complex zone, where wide depressions of the OAP are bounded by E–W trending narrow ridges. We outline that the three E–W faults are located along the western prolongation of the Apricena active fault.

The OAP forms a 6–7 km thick Meso-Cenozoic carbonate multilayer overlying Permo-Triassic clastics that in turn covers a Paleozoic crystalline basement likely composed of Variscan metamorphic rocks (Mazzoli et al., 2013). Consequently, the bottom of the Apulian carbonates in the epicentral area can be set to 9–10 km depth. Considering the 10–25 km depth range of the Montecilfone seismicity, we conclude that the 2018 sequence activated the mid-lower crustal section of an E–W trending shear zone with dextral strike-slip kinematics without rupturing its upper part that presumably extends upwards up to the OAP top, as inferred by the structural map in **Figure 9**.

Prior to the 2018 seismic sequence, the Montecilfone area did not experience significant historical and instrumental seismicity. The closest activity is represented by the 2002 Molise seismic sequence, located 20 km S of Montecilfone, and characterized by two *M*w 5.8 mainshocks nucleated at 21–22 km depth on October 31 and November 1 (**Figure 9**). Both mainshocks, as well as large $M > 4$ aftershocks, are characterized by pure right-lateral strike-slip mechanisms and together with aftershock distribution unraveled the rupture of an 8–25 km deep section

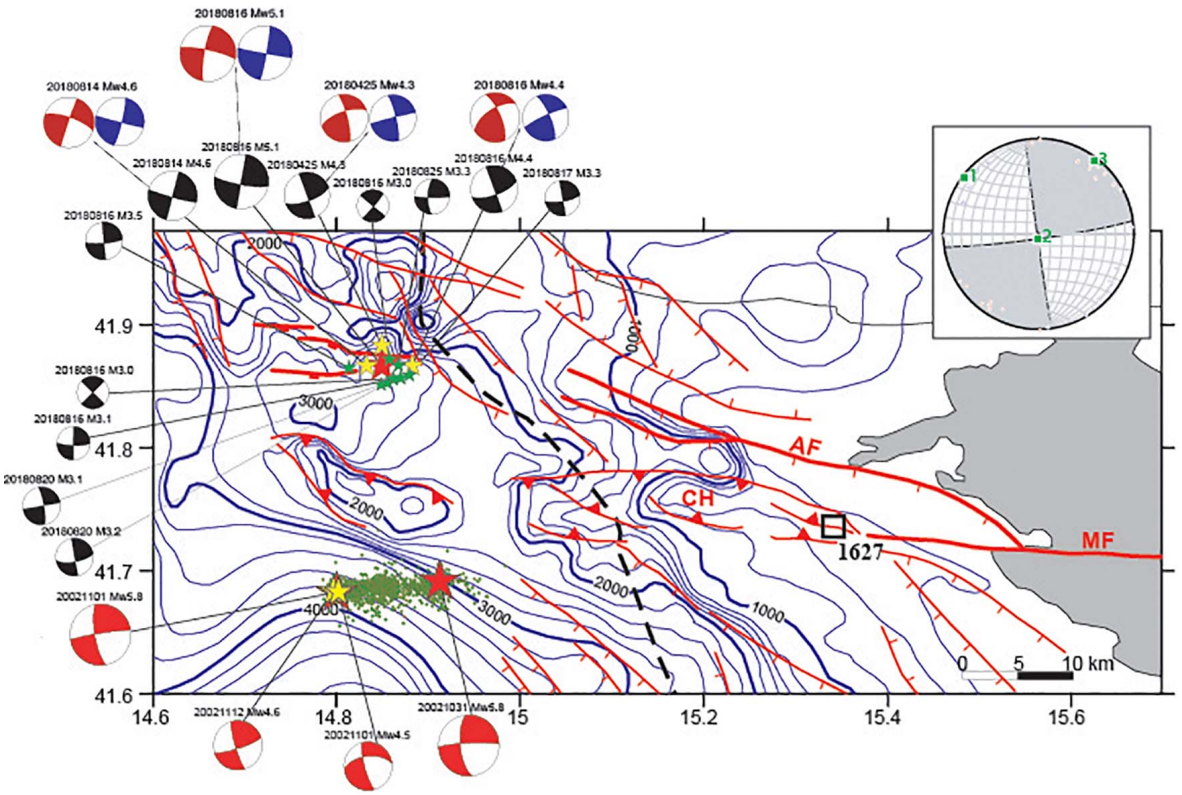

FIGURE 9 | Structural map of the Apulia Carbonate Platform in the sector between the outer Apennine belt and the western Gargano region with focal mechanisms of the mainshocks and stronger aftershocks of the 2018 Montecilfone and 2002 Molise sequences. The blue lines are isobaths (in meters) of the top of the Mesozoic–Tertiary Apulian carbonates; red lines are normal faults (or faults with prevailing dip-slip displacement) and reverse faults (modified from Nicolai and Gambini, 2007). The dashed, thick black line is the buried front of the Apennine thrust sheets. The gray area corresponds to the Mesozoic–Tertiary Apulian carbonates exposed in the Gargano region. The Mattinata Fault (MF), Apricena Fault (AF, after Patacca and Scandone, 2004), and the W–E trending faults associated with the Montecilfone sequence are outlined with thick red lines. The black square is the macroseismic epicenter of the 1627, Me6.7, Capitanata earthquake. Black beach balls of the Montecilfone events are from this study; hypocenter locations of the Molise 2002 events are from Chiarabba et al. (2005a). Red stars, *M*w > 5.0 earthquake; yellow stars, *M*w ≥ 4.0 earthquakes; green stars, *M*w ≥ 3.0 earthquakes. The box of the Montecilfone area in the Italian region is reported in **Figure 3**. The average focal mechanism attitude (unweighted moment tensor analysis; Kassaras and Kapetanidis, 2018) has been calculated considering *M* ≥ 3.0 events. Red focal mechanisms are from RCMT (rcmt2.bo.ingv.it/); blue focal mechanisms are from TDMT (cnt.rm.ingv.it/tdmt).

of the Apulian crust due to the re-activation of several pre-existing near-vertical faults striking W–E (Chiarabba et al., 2005a; Di Luccio et al., 2005a). Due to the low density and quality of hydrocarbon exploration data in the Molise 2002 source region, the structural map of the OAP has a very smooth shape and does not show deviation from the SW-dipping regional trend (**Figure 9**). Unlike, a wide depression of the Apulian carbonates bounded by a system of W–E and NE–SW faults was unraveled by Latorre et al. (2010) by migrating S-P converted phases from the OAP top recognized on most aftershock recordings. Such a structural low was interpreted as a pull-apart basin associated with a releasing bend of a W–E trending strike-slip structure activated during the 2002 sequence and representing the western prolongation, underneath the Apennines nappes of the Mattinata Fault–Chieuti High shear zone. In particular, Latorre et al. (2010) hypothesized the presence of a negative flower structure to reconcile the faults identified at the top of the OAP with the deeper E–W trending strike-slip causative faults of the two mainshocks. In such a scenario, a deep strike-slip fault system reactivates upwards secondary faults that bound the pull-apart basin dissecting with a significant dip-slip displacement the Apulian carbonates.

Here, we hypothesize a similar model for the Montecilfone sequence. In this case, the E–W trending deep strike-slip fault system activated by the 2018 sequence that also dissects the OAP top may represent the western prolongation of the Mattinata Fault–Apricena Fault active structures.

Sharing the hypocenter depths, source mechanisms, fault orientations, and structural features, the Montecilfone 2018 and Molise 2002 sequences can be considered both expressions of a distinct seismotectonic setting characterizing that wide region of southern Italy extending between the Apennine external zone and the Apulian foreland. Our finding, together with minor deep swarms with dominant strike-slip focal solutions that occurred in recent years (Trionfera et al., 2020), reinforce indeed previous seismotectonic models that emphasize the role of pre-existing W–E trending lithospheric shear zones in accommodating the Adria intraplate deformation in response

to Africa–Eurasia plate convergence (Di Bucci et al., 2010) and in producing moderate to strong deep earthquakes in the Adriatic side of the southern Apennines (Fracassi et al., 2004; Valensise et al., 2004).

Earthquakes M ≥ 4.0 Occurred During the AVN Seismic Sequence (August 24, 2016–August 24, 2018)

The AVN seismic sequence occurred throughout central Italy with an epicentral distribution geometrically coherent with the extensional system of active faults, longitudinally dissecting the Apennine chain. This sequence, started on August 24, 2016, includes the Mw 6.5 Norcia event that is the strongest earthquake that occurred over the last 30 years in Italy. The BSI group dedicated a particular analysis strategy for these earthquakes (Marchetti et al., 2016) analyzing manually over 100,000 seismic events located in an area extending for about 60 km from the Muccia village to the north, to the Montereale village to the south, where it overlaps the northernmost part of the 2009 L'Aquila seismic sequence. This careful reprocessing allowed the collection of the high-quality catalog of the 2016 central Italy AVN normal faulting sequence (Improta et al., 2019; Margheriti et al., 2019).

During this seismic sequence, 9 earthquakes had magnitudes $M \geq 5.0$ and 65 earthquakes $4.0 \leq M < 5.0$. The strongest among them were the Mw 6.0 Amatrice earthquake on August 24, the Mw 5.9 Visso earthquake on 26 October, and the Mw 6.5 Norcia earthquake on October 30. The Amatrice earthquake was not preceded by foreshocks. Their RCMT and TDMT are dominated by normal faulting, NNW–SSE striking, focal planes, consistent with the local tectonic environment. Nevertheless, the distribution of aftershock hypocenters reveals the activation of a complex faults system (Michele et al., 2016, 2020; Chiaraluce et al., 2017; Improta et al., 2019; Margheriti et al., 2019).

We here present the focal mechanism solutions for 51 earthquakes (**Supplementary Table 1**) with $M \geq 4.0$ that occurred inside the region interested by the AVN sequence; 5 earthquakes have multiple solutions.

The distribution and characteristics of the solutions are shown in **Figure 10** in map, **Figure 11** (cross-section NW–SE), and **Figure 12** (the azimuth of T-axes of the solutions). The $M > 4.0$ seismicity, aligned along more than 50 km in an average N160° direction, deepens from the north to the south, between 3 and 13 km of depth, associated mainly with normal faulting mechanisms with oblique components, striking northwest–southeast, consistent with a tensional axes oriented from SW–NE to WSW–ENE. The histogram of the rakes (**Figure 13**) presents prevalence of normal solutions with oblique/normal, left or right lateral components, while reverse and oblique/reverse mechanisms are absent; this is observed also in **Figure 14**. Among extensional seismic events with a strong transcurrent component, we note three events (September 3, 2016 10:18; July 22, 2017 02:13; and December 3, 2017 23:34) which occurred, however, in a late phase of the seismic sequence. The fault system shows dip ranging from 35 to 90°, and 2 seismic events have a dip of 15°; they are located at 5.18 km depth, with epicenter near Visso, and at 10.19 km depth, with epicenter 2 km south to Amatrice.

The mean fault plane solution for AVN is a perfect normal faulting mechanism with horizontal NW–SE oriented σ2, vertical σ1 and horizontal NE–SW oriented σ3 (see inset in **Figure 10**). The latter confirms the extension trend in the central Apennines as shown by present-day stress indicators, not only focal mechanisms but also active fault and borehole breakout data (Mariucci and Montone, 2020a,b). Therefore, this tectonic regime seems to not change with depth: from surface (fault data), to intermediate depth (well data), to seismogenic depth.

The earthquake that started the sequence deserves particular attention: in fact, it is worth noting that the Mw 6.0 Amatrice first-motion focal solution has a strike different by 30° and 21° in the anticlockwise direction with respect to the TDMT and RCMT solutions, respectively, and a significant strike-slip component possibly suggesting that the rupture started as transtensive and then evolved in pure normal faulting. This result is in agreement with the modeling of the rupture process that reported on a bilateral rupture, justifying the observed directivity (Tinti et al., 2016), and a small left-lateral strike slip component (Cirella et al., 2018) for this event. In **Figure 10**, we show the good fit of P-wave first onset polarities with the focal mechanism resulting from the inversion. We read 177 polarity observations, and between them we found 2 discrepancies for 2 stations at 60 km and 126 km distances from the epicenter: dense coverage of the focal sphere and correct picked polarities yield the robust focal mechanism computation with an azimuthal gap = 71° and the STDR = 0.71. The largest aftershock that occurred 1 h later, Mw 5.4, shows analog features: a strike direction rotated 20° and 22° in the anticlockwise direction with respect to the TDMT and RCMT solutions, respectively, and a significant strike-slip component. Discrepancies between the centroid-moment tensor and first-motion solutions require detailed investigations prompting complicated multiple rupture (Anderson, 1988).

Regarding the Mw 5.4 and Mw 5.9 Visso earthquakes, and the Mw 6.5 Norcia earthquake, they are non-present in our catalog. The Mw 5.9 Visso earthquake and its strong foreshock, Mw 5.4, are double earthquakes, both preceded by M4.5 events at 4.0 and 1.5 km distance, respectively (Improta et al., 2019). This hinders the picking of first-motion P-wave polarities and, consequently, the determination of reliable focal solutions for both Visso earthquakes. Unlike the Visso earthquakes, focal solution of the Mw 6.5 Norcia earthquake has a large number of discrepancies and highly variable parameters: the fault-plane solution shows a normal fault but its orientation is poorly constrained (particularly the strike is not very well constrained ranging from 65 to 110°).

As potential sources of these discrepancies, both model uncertainties and possible faulting complexity could be considered. The good network geometry of the Italian National Seismic Network (Rete Sismica Nazionale, RSN), implemented by additional 24 stations that were temporarily deployed (Moretti and Sismiko Team, 2016), makes us hypothesize that the uncertainty in location is unlikely to be large enough to explain the full discrepancies, even if we cannot definitively exclude the possibility. Alternatively, it is possible that the velocity model cannot describe velocity heterogeneity coming possibly

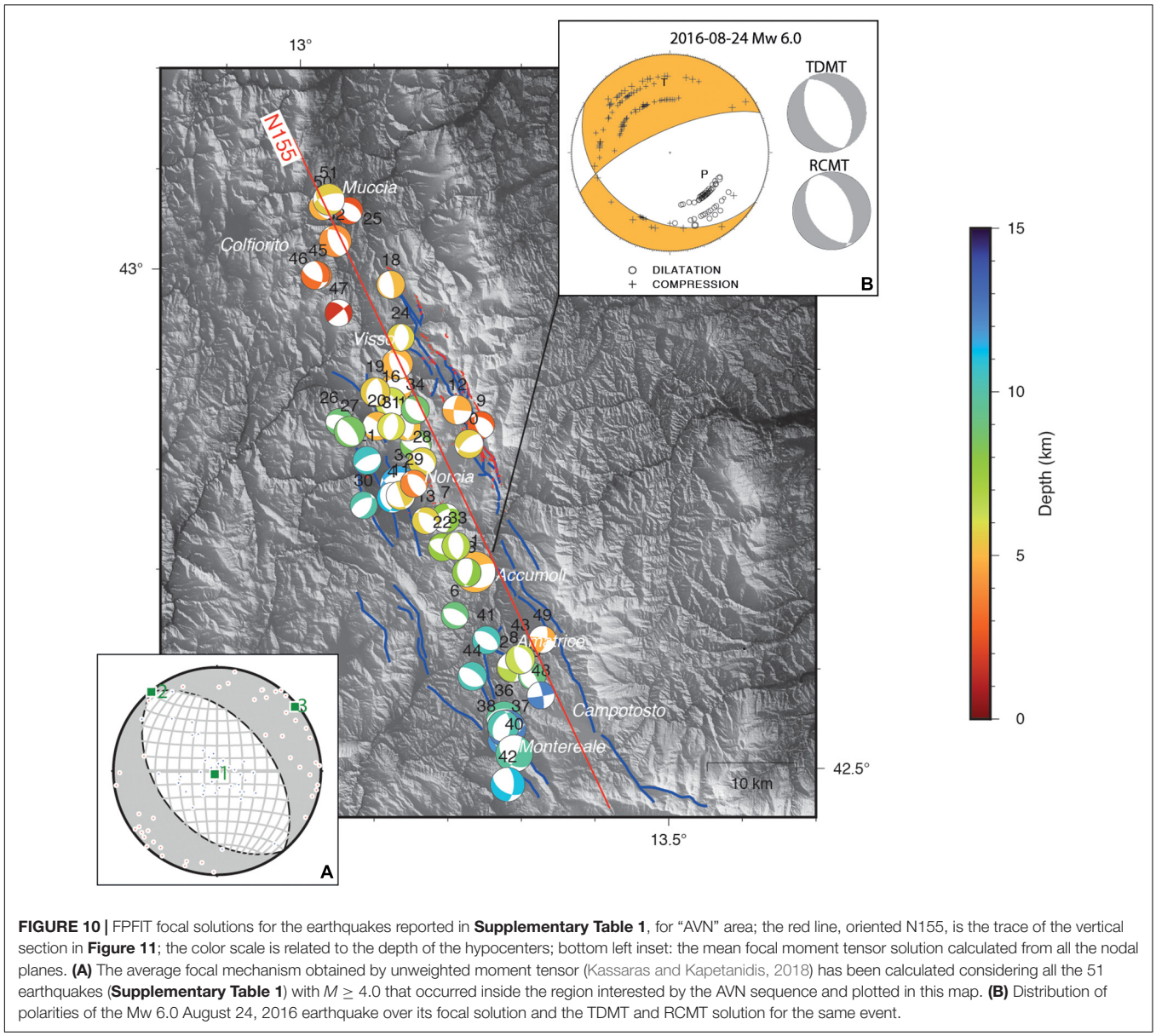

FIGURE 10 | FPFIT focal solutions for the earthquakes reported in **Supplementary Table 1**, for "AVN" area; the red line, oriented N155, is the trace of the vertical section in **Figure 11**; the color scale is related to the depth of the hypocenters; bottom left inset: the mean focal moment tensor solution calculated from all the nodal planes. **(A)** The average focal mechanism obtained by unweighted moment tensor (Kassaras and Kapetanidis, 2018) has been calculated considering all the 51 earthquakes (**Supplementary Table 1**) with $M \geq 4.0$ that occurred inside the region interested by the AVN sequence and plotted in this map. **(B)** Distribution of polarities of the Mw 6.0 August 24, 2016 earthquake over its focal solution and the TDMT and RCMT solution for the same event.

from physical explanations. Focal mechanisms in this study are constrained to double-couple sources and they cannot resolve any non–double-couple component. The strong complexity of this earthquake has been highlighted by several studies in the literature (Cheloni et al., 2017; Scognamiglio et al., 2018; Walters et al., 2018). To explain geodetic, seismological, and surface observations, many different rupture scenarios have been proposed and finite-fault inversions of the Norcia earthquake published so far rely on multi-segment rupture mechanisms. In Scognamiglio et al. (2018), the unusual non–double-couple component (compensated linear vector dipole) observed for the TDMT solution of the October 30 main shock[3] is interpreted as an evidence for a non-planar fault geometry and complex slip behavior. This is in agreement with the multi-segment rupture model obtained by the finite-fault joint inversion of strong motion and geodetic data that are characterized by the cascade activation of NNW–SSE normal faults and of a NE–SW trending oblique fault. In this contest, the first polarities can be affected by this complex rupture process resulting in FPFIT, in this case, not a suitable method for calculating the focal mechanism.

Focus on 2018 Muccia Earthquakes

During the AVN seismic sequence, in March and April 2018, two earthquakes with $M \geq 4.0$ (Mw 4.0 occurred on April 4 and Mw 4.6 on April 10), 15 seismic events with $3.0 \leq M < 4.0$ and more than 3,000 small-magnitude earthquakes occurred very close to Muccia village, in the northern area of the seismic sequence.

In **Figure 15**, we show the focal mechanisms calculated in this work with first polarities compared with the available TDMT and

[3]http://cnt.rm.ingv.it/tdmt

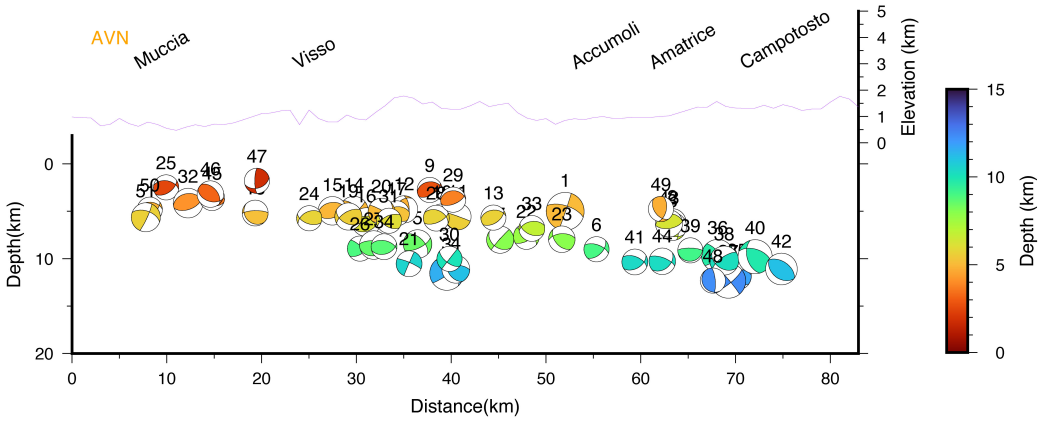

FIGURE 11 | Seismic cross-section along the trace reported in **Figure 10**.

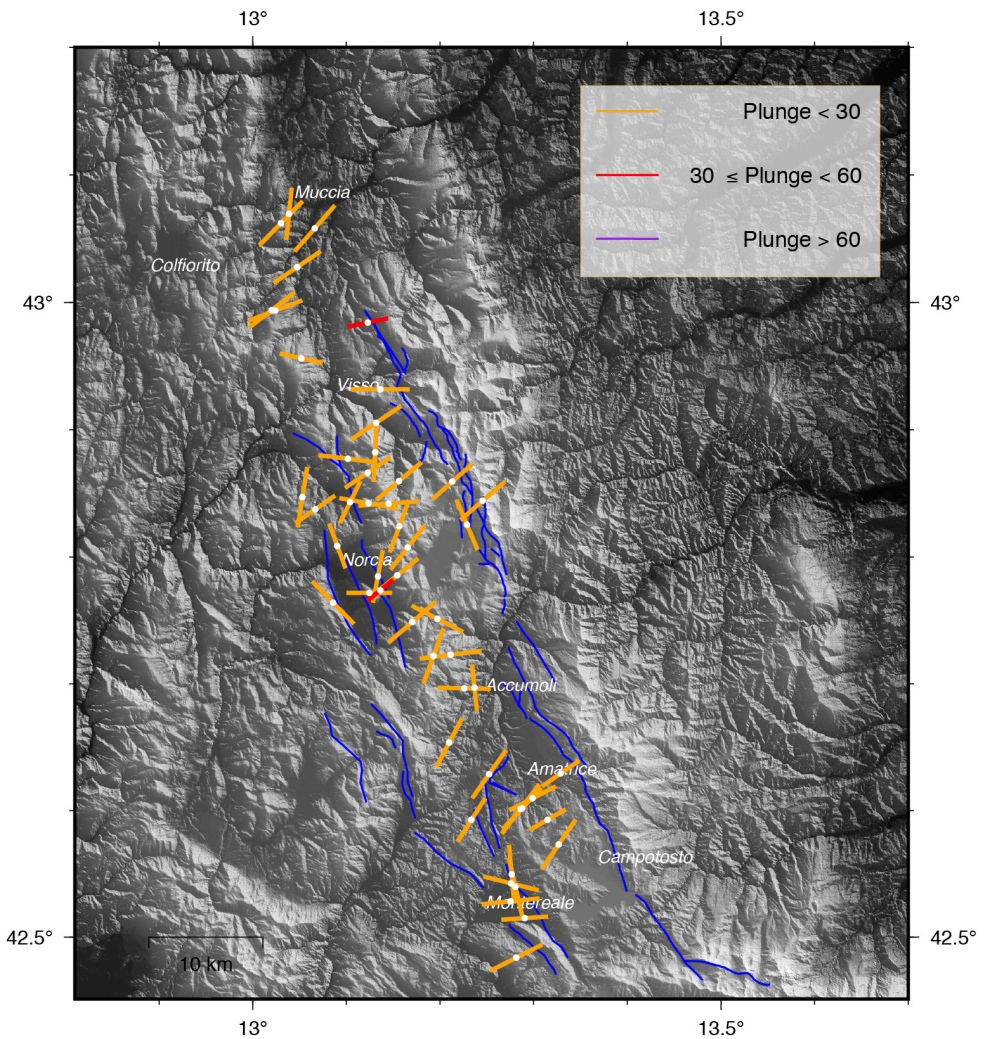

FIGURE 12 | *T*-axes of focal mechanism solutions determined in the present study for the AVN area. The length of each bar is inversely proportional to the plunge of the axis; colors are related to the 3 groups of plunges reported in the inset; blue lines are the normal faults mapped in this area while red lines are surface ruptures of the AVN seismic sequence (Pucci et al., 2017; Civico et al., 2018; Villani et al., 2018).

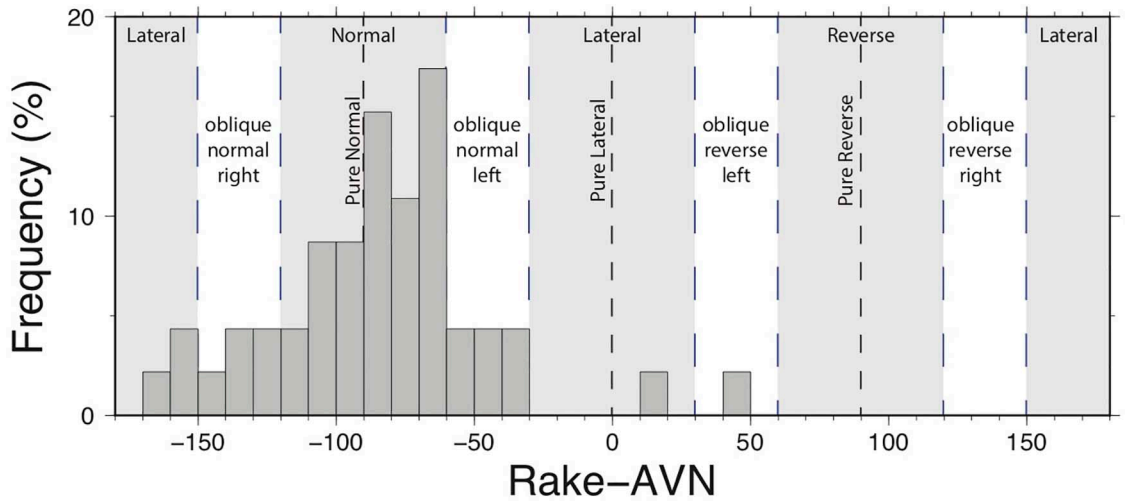

FIGURE 13 | Histogram of the rake distribution of the calculated focal mechanisms for the AVN area.

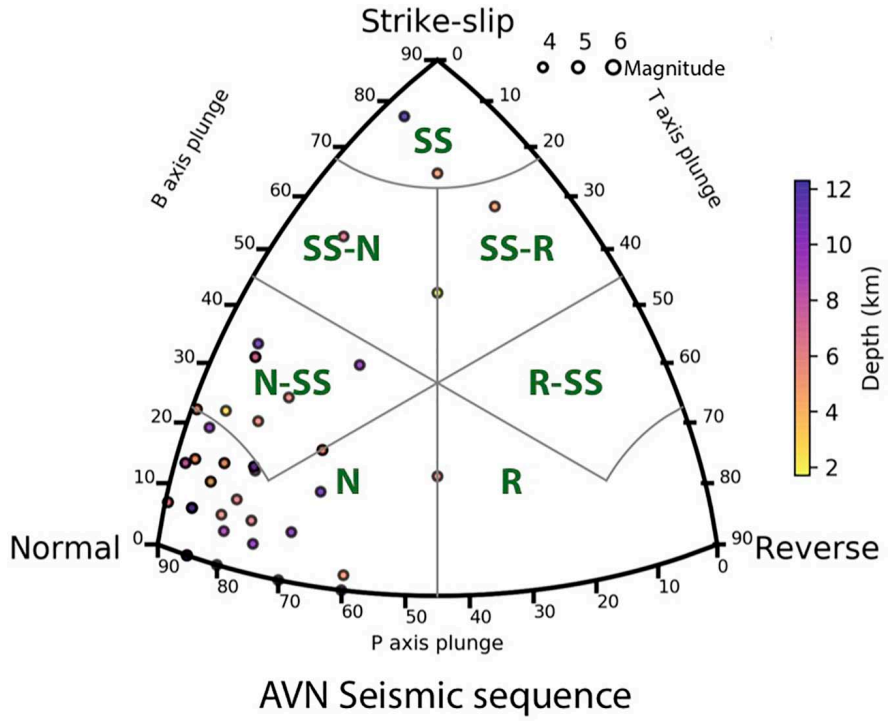

FIGURE 14 | FMC diagram for the classification of focal mechanisms AVN area. N, normal; N-SS, normal–strike-slip; SS-N, strike-slip–normal; SS, strike-slip; SS-R, strike-slip–reverse; R-SS, reverse–strike-slip; R, reverse. The points are scaled by magnitude and colored by different depths.

RCMT solutions. Also in this area we find a good agreement between the first motion and the moment tensor solutions, while focal mechanisms of minor seismicity ($M < 4.0$) calculated with FPFIT confirm the tectonic style.

The focal mechanisms are dominated by normal faulting (NW–SE nodal plane, strike near 150° for the two strongest events) often with a strike-slip component. An example of a strong strike-slip component is the April 10 M_L 3.5.

Concerning the Muccia area, the mean focal mechanism shows a normal faulting regime with a strike-slip component (**Figure 15**): although σ3 is almost horizontal and about NE–SW oriented, σ2 (NW–SE oriented) and σ1 are slightly dipping from the horizontal and vertical, respectively. The conjugate fault planes are SW and N dipping. The solution is in agreement with the main stress trend in the area and the strike component could be due to movements on minor

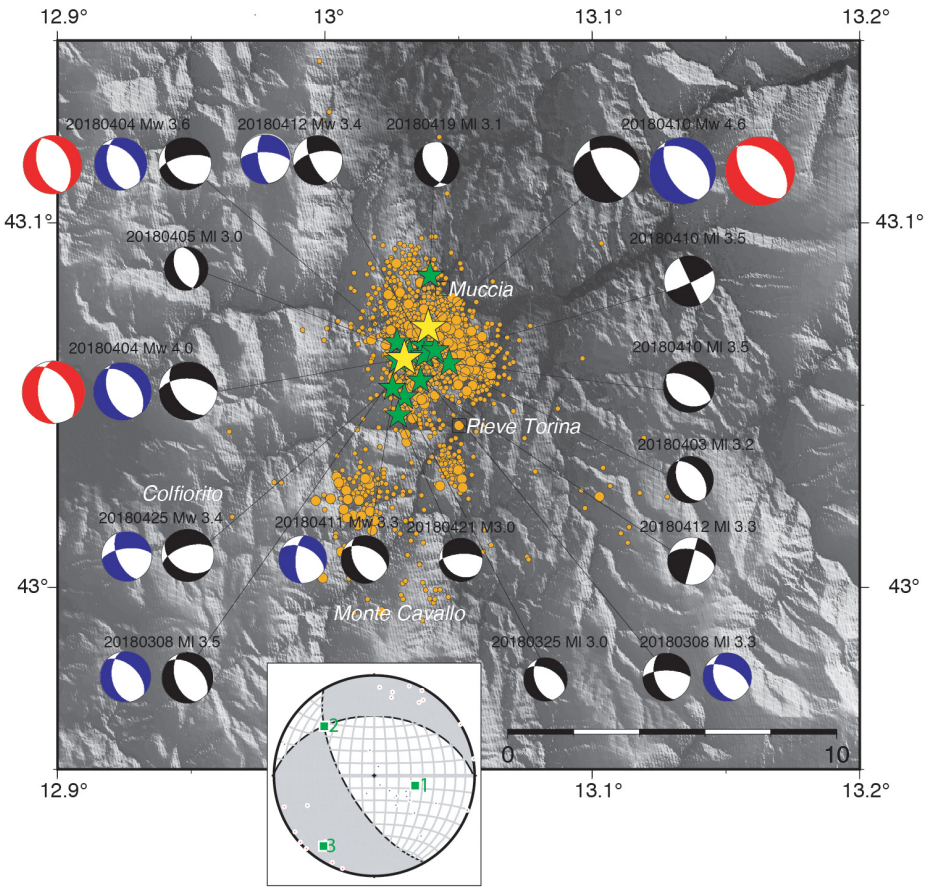

FIGURE 15 | Muccia area. Yellow stars are the *M*w ≥ 4.0 earthquakes, green stars the *M*w ≥ 3.0 earthquakes. Small orange dots are *M* ≥ 1.0; medium orange dots are *M* ≥ 2.0 earthquakes. The average focal mechanism obtained by unweighted moment tensor (Kassaras and Kapetanidis, 2018) has been calculated considering M ≥ 3.0 events. Red focal mechanisms are from RCMT (rcmt2.bo.ingv.it/); blue focal mechanisms are from TDMT (cnt.rm.ingv.it/tdmt).

faults as the earthquakes with magnitude < 4 are included in the computation.

The events analyzed are shallow, almost all having hypocenters in the first 5 km, with the exception of the normal strike-slip event, located beyond 10 km depth; variation in focal parameters and hypocentral depth may indicate the activation of secondary fault segments with respect to extensional structures on which the majority of events in the area took place. To validate this hypothesis, both the comparison with the hypocentral localizations and, above all, the calculation of the focal mechanisms of lower magnitude events will be necessary. In Michele et al. (2020), seismic sections crossing the tip of the AVN seismic sequence, where the fault's system reaches the southern termination of the 1997 Colfiorito system (Chiaraluce et al., 2003), indicate a small, shallow (above 5 km depth) synthetic/antithetic fault system.

DISCUSSION AND CONCLUSION

In this work, we present a catalog of overall 122 focal mechanism solutions that occurred in Italy between 2015 and 2019, 100 earthquakes with magnitude $M \geq 4.0$ and additional 22 seismic events with $3.0 \leq M < 4.0$.

Since January 2015, BSI analysts quickly elaborated events with $M \geq 3.5$, in the days immediately following their occurrence, and particular attention was paid to the analysis of the earthquakes with magnitude $M \geq 4.0$.

Focal mechanisms reported and discussed in this study are determined from *P*-wave first motion polarities read on the waveforms recorded by the national permanent seismological network of INGV, Rete Sismica Nazionale (RSN). The network density and its nationwide distribution allowed us to achieve a good coverage and sampling of the entire focal sphere in almost all the analyzed areas.

Starting from the picking of the BSI's analysts, we relocated the selected earthquakes by using a multi-parameter procedure (see Section "The Multi-parameter Location") based on the Hypoellipse code.

During our research, we obtained several multiple solutions when multiple mechanisms fit the impulsive polarities equally well. Because the distribution of the polarities is strongly controlled by the theoretical take-off angle, it is possible that multiple solutions are due to the vertical error coming from the

1D Earth model and the subsequent calculated take-off angle. Here, we do not consider the multiple solutions but they will be the subject of further studies that will consider vertical/lateral heterogeneities using local velocity model to calculate again the focal solutions to eventually assign a quality factor or to discard definitively.

Even if our dataset, limited to 5 years and to earthquakes with $M > 4.0$, does not permit to detect more than the gross features of the regional stress of Italian area, it is possible to observe some important features.

The strike-slip regime, east-west faulting, which occurred in southern Italy, is well clear in the focus on the Montecilfone area, at the margin between the Apenninic thrust belt to the west, and the Adriatic plate to the east where strike-slip solutions are found. Strike-slip faulting also characterizes the Ionian Sea and Sicily channel.

In the western offshore of Calabria region, we find earthquakes with prevalent normal faulting solutions and prevalent depths ranging between 100 and 215 km. For the earthquakes analyzed in this study, the P-axes mostly plunge toward the NW (**Figure 7**), coinciding with the dip direction of the Tyrrhenian slab, a consistent direction of down-dip compression in agreement with previous studies (Isacks and Molnar, 1971; Anderson and Jackson, 1987; Frepoli et al., 1996).

In the AVN seismic sequence, TDMT and RCMT present dominant normal faulting solutions along NNW–SSE trending faults, with tension axes oriented roughly perpendicular to the strike of the Apennines. The focal mechanisms here show more heterogeneous solutions with normal faults, oblique slip faults and strike-slip faults, and 80% of tension axes oriented in the range 40–70°. This variability agrees with results of previous studies dealing with relocations of high-quality aftershock catalogs (Improta et al., 2019; Michele et al., 2020) that provide evidence of activation of an extremely complex fault system; this complex system could also include inherited Pliocene reverse faults oblique to the NW–SE trending extensional structures even if, in literature, the role of these pre-existing faults is debated. Particularly interesting is the focal mechanism calculated for the Mw 6.0 Amatrice earthquake: it shows a normal solution with a significant strike-slip component possibly suggesting that the rupture started as transtensive and then evolved in pure normal faulting as highlighted from the TDMT and RCMT extensional solutions. This result agrees with the modeling of the complex rupture process that reported on a bilateral rupture and a small left-lateral strike-slip component (Tinti et al., 2016; Cirella et al., 2018).

It is worth noting that when comparing high-quality solutions obtained with first-motion polarity techniques or from waveform inversion, the differences observed between the two focal mechanisms represent real differences in the source process. Future comparison studies with RCMT and TDMT will help us to understand how much and where they are similar and how much and where they are not and verify, in the latter case, if the non–double-couple component, a measure of the deviation of a moment tensor from a double-couple mechanism, is important in the calculation.

Methods based on waveform inversion (from high-quality data) provide a stable and reliable focal mechanism: in addition, the speed and efficiency of these automated methods is clear with respect to the extremely time-consuming approach of determining the mechanism by manual attributing polarities of first motions. However, these two different methods provide different, somehow complementary, information: indication of the general style of deformation occurring in an area as for the moment tensors, and detailed study of source mechanics as for the first-motion focal mechanisms, the latter also taking advantage of the information from lower magnitudes. This is a particularly important feature due to the large number of small-magnitude earthquakes compared with high-magnitude earthquakes. On average, $2 < M < 3$ and smaller earthquakes occur several hundred times a day worldwide while very few $M \geq 5.0$ earthquakes do occur per year: during 2019, no $M \geq 9$ occurred; 1 $M = 8$ seismic event was recorded in Peru and 9 $M \geq 7.0$ (data from U.S. Geological Survey earthquake.usgs.gov). In Italy, in the same year, the RSN recorded more than 180 $M \geq 3.0$ earthquakes, 11 seismic events with $M \geq 4$ and no $M \geq 5$.

Our two focuses, Muccia and Montecilfone area, demonstrate how the analysis of focal mechanisms with the first polarities, even for earthquakes with a $M < 4.0$, provides further knowledge of the tectonic regime of the areas of interest. For the Montecilfone zone, our focal solutions for $M < 4.0$ aftershocks testify that the strike-slip dextral faulting observed for the moderate-large events is also present at small scale suggesting almost regular fault plane geometries. By combining the hypocenter distribution focal mechanisms of all events, and the structural map of the Apulia Platform here analyzed, we conclude that the 2018 events activated the mid-lower crustal section of an unknown, strike-slip structure, trending E–W and characterized by right-lateral kinematic. This structure may represent the westernmost prolongation of a complex shear zone of the Apulia Plate that includes onshore the Apricena Fault and the Mattinata Fault system both active and sources of M6 + historical earthquakes (Patacca and Scandone, 2004; Di Bucci et al., 2010). In this view, the Montecilfone seismicity and causative fault bears a remarkable resemblance to the Molise 2002 sequence that was related to an E–W trending, dextral strike-slip system representing the western prolongation of the Mattinata Fault–Chieuti High shear zone (Latorre et al., 2010). Our interpretation reinforces previous seismotectonic models that emphasize the seismogenic potential and the role of Mesozoic–Tertiary W–E trending lithospheric shear zones dissecting the flexed Apulia plate underneath the Apennines thrust belt in accommodating intraplate deformation in response to Africa–Eurasia plate convergence (Fracassi et al., 2004; Di Luccio et al., 2005b; Di Bucci et al., 2010).

The choice to deepen the study of earthquakes with small-to-medium magnitude fits well with the rising interest in recent years of the earthquake engineering community in this topic also due to the presence of upper-crustal events, in the range Mw 4.0–5.5, that occur sufficiently close to inhabited areas worldwide that actually cause damage and/or casualties (Nievas et al., 2020).

With this work, we want to underline the importance, for both the seismotectonic characterization of a wide area and

a greater comprehension of the faulting mechanism during a complex seismic sequence, of assigning polarity to the *P*-phase onsets to routinely estimate the focal mechanisms in addition to the hypocentral parameters and to the moment tensor solution estimation for a wide range of magnitudes from $M \geq 4.0$ to $M \leq 3.0$.

Our next steps are to extend the dataset in time before 2015. Moreover, we believe that it would be of great importance producing an unprecedented dataset of first-motion polarities' focal mechanisms by developing an on purpose automatic procedure of analysis taking advantage of such a large dataset of accurate manually revised polarities to educate the polarity detection algorithm.

CONSORTIUM BOLLETTINO SISMICO ITALIANO WORKING GROUP

Barbara Castello barbara.castello@ingv.it; Diana Latorre diana.latorre@ingv.it; Lucia Margheriti lucia.margheriti@ingv.it; Paola Baccheschi paola.baccheschi@ingv.it; Arianna Lisi arianna.lisi@ingv.it; Alessandro Marchetti alessandro.marchetti@ingv.it; Anna Nardi anna.nardi@ingv.it; Anna Maria Lombardi annamaria.lombardi@ingv.it; Milena Moretti milena.moretti@ingv.it; Cinzia Melorio cinzia.melorio@ingv.it; Corrado Castellano corrado.castellano@ingv.it; Patrizia Battelli patrizia.battelli@ingv.it; Alberto Frepoli alberto.frepoli@ingv.it; Alessandra Sciarra alessandra.sciarra@ingv.it; Alessandra Smedile alessandra.smedile@ingv.it; Alexia Battelli alexia.battelli@ingv.it; Antonio Rossi antonio.rossi@ingv.it; Barbara Cantucci barbara.cantucci@ingv.it; Caterina Montuori caterina.montuori@ingv.it; Corrado Thermes corrado.thermes@ingv.it; Daniele Cheloni daniele.cheloni@ingv.it; Francesco Mariano Mele franco.mele@ingv.it; Giorgio Modica giorgio.modica@ingv.it; Laura Colini laura.colini@ingv.it; Laura Scognamiglio laura.scognamiglio@ingv.it; Luca Arcoraci luca.arcoraci@ingv.it; Luca Miconi luca.miconi@ingv.it; Luca Pizzino luca.pizzino@ingv.it; Marina Pastori marina.pastori@ingv.it; Michele Berardi michele.berardi@ingv.it; Nicola Mauro Pagliuca nicola.pagliuca@ingv.it; Roberta Tozzi roberta.tozzi@ingv.it; Roberto Tardini roberto.tardini@ingv.it; Rosalba Di Maro rosalba.dimaro@ingv.it; Sabina Spadoni sabina.spadoni@ingv.it; Stefania Pinzi stefania.pinzi@ingv.it; Stefano Pintore stefano.pintore@ingv.it; Stephen Monna stephen.monna@ingv.it; Tiziana Sgroi tiziana.sgroi@ingv.it.

DATA AVAILABILITY STATEMENT

The original contributions presented in the study are included in the article/**Supplementary Material**, further inquiries can be directed to the corresponding author/s.

AUTHOR CONTRIBUTIONS

MC conceived the manuscript, computed the multi-parametric locations, produced, and analyzed the focal mechanisms. RD designed and setup the multi-parametric location method and analyzed the focal mechanisms. LI provided the geological interpretation and wrote the section dealing with the Montecilfone earthquakes. MM contributed to analyze the results and revised the manuscript. BSI Working Group revised earthquakes detected by the automatic acquisition system. All authors contributed to the article and approved the submitted version.

ACKNOWLEDGMENTS

We would like to thank JÁ-G and KL, for the very helpful comments and suggestions which have greatly improved the manuscript. We also appreciate discussions with Umberto Fracassi and Carlo Alberto Brunori. Figures are generated with The Generic Mapping Tools, Wessel and Smith (1991).

SUPPLEMENTARY MATERIAL

The Supplementary Material for this article can be found online at: https://www.frontiersin.org/articles/10.3389/feart.2021.630116/full#supplementary-material

REFERENCES

Álvarez-Gómez, J. A. (2019). FMC—Earthquake focal mechanisms data management, cluster and classification. *SoftwareX* 9, 299–307. doi: 10.1016/j.softx.2019.03.008

Anderson, H. (1988). Comparison of centroid-moment tensor and first motion solutions for western Mediterranean earthquakes. *Phys. Earth Planet. Inter.* 52, 1–7. doi: 10.1016/0031-9201(88)90052-0

Anderson, H., and Jackson, J. (1987). The deep seismicity of the Tyrrhenian Sea. *Geophys. J. R. astr. Soc.* 91, 613–637. doi: 10.1111/j.1365-246x.1987.tb01661.x

Battelli, P., Arcoraci, L., Berardi, M., Castellano, C., Marchetti, A., Mele, F., et al. (2013). Bollettino sismico italiano 2010. *Quaderni di Geofisica* 115, 1–52.

Butler, R. W. H., Mazzoli, S., Corrado, S., De Donatis, M., Di Bucci, D., Gambini, R., et al. (2004). "Applying thick-skinned tectonic models to the Apennine thrust belt of Italy — Limitations and implications," in *Thrust Tectonics and Hydrocarbon Systems*, Vol. 82, ed. K. R. McClay (Tulsa, OK: AAPG), 647–667. doi: 10.1306/m82813c34

Cheloni, D., De Novellis, V., Albano, M., Antonioli, A., Anzidei, M., Atzori, S., et al. (2017). Geodetic model of the 2016 Central Italy earthquake sequence inferred from InSAR and GPS data. *Geophys. Res. Lett.* 44, 6778–6787. doi: 10.1002/2017GL073580

Chiarabba, C., De Gori, P., Chiaraluce, L., Bordoni, P., Cattaneo, M., De Martin, M., et al. (2005a). Main shocks and aftershocks of the 2002 Molise seismic sequence, southern Italy. *J. Seismol.* 9, 487–494. doi: 10.1007/s10950-005-0633-9

Chiarabba, C., Jovane, L., and Di Stefano, R. (2005b). A new view of Italian seismicity using 20 years of instrumental recordings. *Tectonophysics* 395, 251–268. doi: 10.1016/j.tecto.2004.09.013

Chiaraluce, L., Di Stefano, R., Tinti, E., Scognamiglio, L., Michele, M., Casarotti, E., et al. (2017). The 2016 central Italy seismic sequence: a first look at the

mainshocks, aftershocks, and source models. *Seismol. Res. Lett.* 88, 757–771. doi: 10.1785/0220160221

Chiaraluce, L., Ellsworth, W. L., Chiarabba, C., and Cocco, M. (2003). Imaging the complexity of an active normal fault system: the 1997 Colfiorito (central Italy) case study. *J. Geophys. Res.* 108:2294. doi: 10.1029/2002JB002166

Cirella, A., Pezzo, G., and Piatanesi, A. (2018). Rupture kinematics and structural-rheological control of the 2016 Mw6.1 Amatrice (central Italy) earthquake from joint inversion of seismic and geodetic data. *Geophys. Res. Lett.* 45, 302–312. doi: 10.1029/2018GL080894

Civico, R., Pucci, S., Villani, F., Pizzimenti, L., De Martini, P. M., Nappi, R., et al. (2018). Surface ruptures following the 30 October 2016 Mw 6.5 Norcia earthquake, central Italy. *J. Maps* 14, 151–160. doi: 10.1080/17445647.2018.1441756

Di Bucci, D., Burrato, P., Vannoli, P., and Valensise, G. (2010). Tectonic evidence for the ongoing Africa-Eurasia convergence in central Mediterranean foreland areas: a journey among long-lived shear zones, large earthquakes, and elusive fault motions. *J. Geophys. Res.* 115:B12404. doi: 10.1029/2009JB006480

Di Luccio, F., Fukuyama, E., and Pino, N. A. (2005a). The 2002 Molise earthquake sequence: what can we learn about the tectonics of southern Italy? *Tectonophysics* 405, 141–154. doi: 10.1016/j.tecto.2005.05.024

Di Luccio, F., Piscini, A., Pino, N. A., and Ventura, G. (2005b). Reactivation of deep faults beneath southern Apennines: evidence from the 1990–1991 Potenza seismic sequences. *Terra Nova* 17, 586–590. doi: 10.1111/j.1365-3121.2005.00653.x

DISS Working Group (2018). *Database of Individual Seismogenic Sources (DISS), Version 3.2.1: A Compilation of Potential Sources for Earthquakes Larger than M 5.5 in Italy and Surrounding Areas*. Italy: Istituto Nazionale di Geofisica e Vulcanologia.

Fracassi, U., Burrato, P., Basili, R., Bencini, R., Di Bucci, D., and Valensise, G. (2004). "Shallow NE-SW extension and deep E-W right-lateral slip: coexisting seismogenic mechanisms as an expression of southern Italy geodynamics," in *Proceedings of the Gruppo Nazionale Geofisica Terra Solida Symposium, 23rd, Rome, December 2004* (Rome: Consiglio Nazionale delle Ricerche), 200–202.

Frepoli, A., Selvaggi, G., Chiarabba, C., and Amato, A. (1996). State of stress in the Southern Tyrrhenian subduction zone from fault-plane solutions. *Geophys. J. Int.* 125, 879–891. doi: 10.1111/j.1365-246x.1996.tb06031.x

Improta, L., Latorre, D., Margheriti, L., Nardi, A., Marchetti, A., Lombardi, A. M., et al. (2019). Multi-segment rupture of the 2016 Amatrice-Visso-Norcia seismic sequence (central Italy) constrained by the first high-quality catalog of early Aftershocks. *Sci. Rep.* 9:6921. doi: 10.1038/s41598-019-43393-2

INGV Seismological and Data Centre (2006). *Rete Sismica Nazionale (RSN)*. Italy: Istituto Nazionale di Geofisica e Vulcanologia (INGV).

Isacks, B., and Molnar, P. (1971). Distribution of stresses in the descending lithosphere from a global survey of focal mechanism solutions of mantle earthquakes. *Rev. Geo. Space Phys.* 9, 103–174. doi: 10.1029/rg009i001p00103

ISIDe Working Group (2007). *Italian Seismological Instrumental and Parametric Database (ISIDe)*. Italy: Istituto Nazionale di Geofisica e Vulcanologia (INGV).

Kagan, Y. Y. (2005). Double-couple earthquake focal mechanism: random rotation and display. *Geophys. J. Int.* 163, 1065–1072. doi: 10.1111/j.1365-246x.2005.02781.x

Kassaras, I. G., and Kapetanidis, V. (2018). "Resolving the tectonic stress by the inversion of earthquake focal mechanisms. application in the region of greece. a tutorial," in *Moment Tensor Solutions*, ed. S. D'Amico (Cham: Springer).

Kaverina, A. N., Lander, A. V., and Prozorov, A. G. (1996). Global creepex distribution and its relation to earthquake-source geometry and tectonic origin. *Geophys. J. Int.* 125, 249–265. doi: 10.1111/j.1365-246x.1996.tb06549.x

Lahr, J. C. (1999). *HYPOELLIPSE: A Computer Program for Determining Local Earthquake Hypocentral Parameters, Magnitude, and first-Motion Pattern*. U.S. Geological Survey Open-File Report 99–23, version 1.1. Reston, VA: USGS, 119.

Latorre, D., Amato, A., and Chiarabba, C. (2010). High-resolution seismic imaging of the Mw5.7, 2002 Molise, southern Italy, earthquake area: evidence of deep fault reactivation. *Tectonics* 29:TC4014. doi: 10.1029/2009TC002595

Marchetti, A., Ciaccio, M. G., Nardi, A., Bono, A., Mele, F. M., Margheriti, L., et al. (2016). The Italian Seismic Bulletin: strategies, revised pickings and locations of the central Italy seismic sequence. *Ann. Geophysics* 59, 1–7.

Margheriti, L., Latorre, D., Baccheschi, P., Castello, B., Lisi, A., Nardi, A., et al. (2019). *High Quality Comprehensive Earthquake Catalog of the Amatrice-Visso-Norcia Seismic Sequence (Central Italy, Italian Seismic Bulletin 2016-2018)*. San Francisco, CA: AGU Fall Meeting.

Mariucci, M. T., and Montone, P. (2020a). Database of Italian present-day stress indicators, IPSI 1.4. *Sci. Data* 7:298. doi: 10.1038/s41597-020-00640-w

Mariucci, M. T., and Montone, P. (2020b). *IPSI 1.4, Database of Italian Present-day Stress Indicators, Istituto Nazionale di Geofisica e Vulcanologia (INGV)*. Italy: INGV.

Mazzoli, S., Ascione, A., Candela, S., Iannace, A., Megna, A., Santini, S., et al. (2013). Subduction and continental collision events in the southern Apennines: constraints from two crustal cross-sections. *Rend. Online Soc. Geol. Ital.* 25, 78–84. doi: 10.3301/ROL.2013.07

Menardi Noguera, A., and Rea, G. (2000). Deep structure of the Campania-Lucanian arc (southern Apennine, Italy). *Tectonophysics* 324, 239–265. doi: 10.1016/s0040-1951(00)00137-2

Michele, M., Chiaraluce, L., Di Stefano, R., and Waldhauser, F. (2020). Fine-scale structure of the 2016–2017 Central Italy seismic sequence from data recorded at the Italian National Network. *J. Geophys. Res. Solid Earth* 125:e2019JB018440. doi: 10.1029/2019JB018440

Michele, M., Di Stefano, R., Chiaraluce, L., Cattaneo, M., De Gori, P., Monachesi, G., et al. (2016). The Amatrice 2016 seismic sequence: a preliminary look at the mainshock and aftershocks distribution. *Ann. Geophys.* 59, 1–8.

Moretti, M., and Sismiko Team (2016). Sismiko: emergency network deployment and data sharing for the 2016 Amatrice seismic sequence. *Ann. Geophys.* 59:5. doi: 10.4401/ag-7212

Nicolai, C., and Gambini, R. (2007). "Structural architecture of the Adria platform-and-basin system," in *Results of the CROP Project, Sub-Project CROP-04 Southern Apennines (Italy)*, Vol. 7, eds A. Mazzotti, E. Patacca, and P. Scandone (Rome: Bollettino della Società Geologica Italiana), 21–37.

Nievas, C. I., Bommer, J., Crowley, H., and van Elk, J. (2020). Global occurrence and impact of small-to-medium magnitude earthquakes: a statistical analysis. *Bull. Earthquake Eng.* 18, 1–35. doi: 10.1007/s10518-019-00718-w

Patacca, E., and Scandone, P. (2004). The 1627 Gargano earthquake (southern Italy): identification and characterization of the causative fault. *J. Seismol.* 8, 259–273. doi: 10.1023/B:JOSE.0000021393.77543.1e

Presti, D., Billi, A., Orecchio, B., Totaro, C., Faccenna, C., and Neri, G. (2013). Earthquake focal mechanisms, seismogenic stress, and seismotectonics of the Calabrian Arc, Italy. *Tectonophysics* 602, 153–175. doi: 10.1016/j.tecto.2013.01.030

Pucci, S., De Martini, P. M., Civico, R., Villani, F., Nappi, R., Ricci, T., et al. (2017). Coseismic ruptures of the August 24, 2016, Mw 6.0 Amatrice earthquake (central Italy). *Geophys. Res. Lett.* 44, 2138–2147. doi: 10.1002/2016gl071859

Reasenberg, P. A., and Oppenheimer, D. (1985). *FPFIT, FPPLOT and FPPAGE: FORTRAN Computer Programs for Calculating and Displaying Earthquake Fault-Plane Solutions*. US Geological Survey Open-File Report 85-739. Italy: USGS, 109.

Scognamiglio, L., Tinti, E., Casarotti, E., Pucci, S., Villani, F., Cocco, M., et al. (2018). Complex fault geometry and rupture dynamics of the M_w 6.5, 30 October 2016, Central Italy Earthquake. *JGR* 123, 2943–2964. doi: 10.1002/2018JB015603

Scognamiglio, L., Tinti, E., and Michelini, A. (2009). Real-Time determination of seismic moment tensor for the Italian region. *Bull. Seismol. Soc. Am.* 99, 2223–2242. doi: 10.1785/0120080104

Selvaggi, G., and Chiarabba, C. (1995). Seismicity and P-wave velocity image of the southern Tyrrhenian subduction zone. *Geophys. J. Int.* 121, 818–826. doi: 10.1111/j.1365-246x.1995.tb06441.x

Tinti, E., Scognamiglio, L., Michelini, A., and Cocco, M. (2016). Slip heterogeneity and directivity of the ML 6.0, 2016, amatrice earth- quake estimated with rapid finite-fault inversion. *Geophys. Res. Lett.* 43, 745–710. doi: 10.1002/2016GL071263

Trionfera, B., Frepoli, A., De Luca, G., De Gori, P., and Doglioni, C. (2020). The 2013–2018 matese and beneventano seismic sequences (Central–Southern Apennines): new constraints on the hypocentral depth determination. *Geosciences* 10:17. doi: 10.3390/geosciences10010017

Valensise, G., Pantosti, D., and Basili, R. (2004). Seismology and tectonic setting of the 2002 molise. Italy, Earthquake. *Earthquake Spectra.* 20(Suppl. 1), 23–37. doi: 10.1193/1.1756136

Varriale, F. (2011). Metodi di Imaging Sismico ad Alta Risoluzione per lo Studio di Faglie Sismogenetiche: Il Caso di Studio della Faglia di APRICENA (Puglia Settentrionale). Ph. D Thesis; Earth Sciences Department at University of Naples Federico II. Available online at: https://doi.org/10.6092/UNINA/FEDOA/8520 (accessed April 2021).

Villani, F., Pucci, S., Civico, R., De Martini, P. M., Cinti, F. R., and Pantosti, D. (2018). Surface faulting of the 30 October 2016 Mw 6.5 central Italy earthquake: detailed analysis of a complex coseismic rupture. *Tectonics* 37, 3378–3410. doi: 10.1029/2018tc005175

Walters, R. J., Gregory, L. C., Wedmore, L. N. J., Craig, T. J., McCaffrey, K., Wilkinson, M., et al. (2018). Dual control of fault intersections on stop-start rupture in the 2016 Central Italy seismic sequence. *Earth Planet. Sci. Lett.* 500, 1–14. doi: 10.1016/j.epsl.2018.07.043

Wessel, P., and Smith, W. H. F. (1991). Free software helps map and display data. *EOS Trans. AGU* 72:441. doi: 10.1029/90eo00319

Conflict of Interest: The authors declare that the research was conducted in the absence of any commercial or financial relationships that could be construed as a potential conflict of interest.

frontiers in Earth Science

ORIGINAL RESEARCH
published: 26 May 2021
doi: 10.3389/feart.2021.644142

Focal Mechanism and Seismogenic Structure of the M_S 5.1 Qingbaijiang Earthquake on February 3, 2020, Southwestern China

Min Zhao, Feng Long, Guixi Yi, MingJian Liang, Jiangtao Xie and Siwei Wang*

Sichuan Earthquake Administration, Chengdu, China

The 3 February 2020 M_S 5.1 Qingbaijiang earthquake, southwestern China, is the closest recorded $M_S \geq 5.0$ event to downtown Chengdu City to date, with an epicentral distance of only 38 km. Here we analyze seismic data from the Sichuan and Chengdu regional seismic networks, and employ a multi-stage location method to relocate the earthquakes that have occurred along the central and northern segments of the Longquanshan fault zone since 2009, including the M_S 5.1 Qingbaijiang earthquake sequence, to investigate the seismogenic structure of the region. The relocation results indicate that the seismicity along the central and northern segments of the Longquanshan fault zone has occurred mainly along the eastern branch since 2009, with the hypocentral distribution along a vertical cross-section illustrating a steep, NW-dipping parallel imbricate structure. The terminating depth of the eastern branch is about 12 km. The distribution of the M_S 5.1 Qingbaijiang earthquake sequence is along the NE–SW-striking Longquanshan fault zone. The aftershock focal depths are in the 3–6 km range, with the mainshock located at 104.475°E, 30.73°N. Its initial rupture depth of 5.2 km indicates that the earthquake occurred above the shallow decollement layer of the upper crust in this region. The hypocentral distribution along the long axis of the aftershock area highlights that this earthquake sequence occurred along a fault dipping at 56° to the NW. Our surface projection of the inferred fault plane places it near the eastern branch of the Longquanshan fault zone. We infer the M_S 5.1 mainshock to be a thrust faulting event based on the focal mechanism solution via the cut-and-paste waveform inversion method, with strike/dip/rake parameters of 22°/36°/91° and 200°/54°/89° obtained for nodal planes I and II, respectively. We identify that the seismogenic fault of the M_S 5.1 Qingbaijiang earthquake lies along the eastern branch of the Longquanshan fault zone, and nodal plane II represents the coseismic rupture plane, based on a joint analysis of the event relocation results, mainshock focal mechanism, and regional geological information. Our study provides vital information for assessing the seismic hazard of the Longquanshan fault zone near Chengdu City.

Keywords: the MS 5.1 Qingbaijiang earthquake, relocation, focal mechanism solution, seismogenic structure, the Longquanshan fault zone

OPEN ACCESS

Edited by:
Ruizhi Wen,
Institute of Engineering Mechanics, China

Reviewed by:
Jorge Jara,
École Normale Supérieure, France
Dogan Kalafat,
Boğaziçi University, Turkey

****Correspondence:***
Guixi Yi
yigx64@163.com

Specialty section:
This article was submitted to Structural Geology and Tectonics, a section of the journal Frontiers in Earth Science

Received: *20 December 2020*
Accepted: *26 April 2021*
Published: *26 May 2021*

Citation:
Zhao M, Long F, Yi G, Liang M, Xie J and Wang S (2021) Focal Mechanism and Seismogenic Structure of the M_S 5.1 Qingbaijiang Earthquake on February 3, 2020, Southwestern China. Front. Earth Sci. 9:644142. doi: 10.3389/feart.2021.644142

INTRODUCTION

The ongoing Cenozoic collision between the Indian and Eurasian plates has contributed to the uplift of the Tibetan Plateau (Molnar and Tapponnier, 1975; Houseman and England, 1986; Yin and Harrison, 2000; Tapponnier et al., 2001). However, eastward growth of the Tibetan Plateau has been impeded by the tectonically stable Yangtze Block, with the Longmenshan fold-and-thrust belt (LFTB) and the associated uplift of the Sichuan foreland basin and Longquanshan anticline forming in the eastern part of the Tibetan Plateau (Tapponnier and Molnar, 1977; Tapponnier et al., 1982; Chen et al., 1994; Burchfiel et al., 1995; Chen and Wilson, 1996; Kirby et al., 2002). The LFTB is a geologically active area of the eastern Tibetan Plateau, as indicated by the 2008 M_S 8.0 Wenchuan and 2013 M_S 7.0 Lushan earthquakes (Burchfiel et al., 2008; Hubbard and Shaw, 2009; Xu et al., 2009, 2013; Yin, 2010). Numerous studies have focused on the Longmenshan fault zone following the 2008 Wenchuan earthquake (Kirby et al., 2008; Liu-Zeng et al., 2009; Li et al., 2010; Wang et al., 2010, 2011, 2012; Zhang et al., 2010; Zhang, 2013), and also the structural characteristics and seismic hazard along the range front of the LFTB (Parsons et al., 2008; Toda et al., 2008; Hubbard and Shaw, 2009; Liu-Zeng et al., 2009; Hubbard et al., 2010). The Longquanshan fault zone, which forms the southeastern boundary of the Sichuan basin (Deng et al., 1994), has been inferred to possess a low level of seismicity that is characterized by smaller-magnitude earthquakes (Li et al., 2015; Wang and Lin, 2017); consequently, its geometric structure and seismic hazard have not been well studied. The occurrence of the 3 February 2020 M_S 5.1 Qingbaijiang earthquake therefore provides an opportunity to study the structural characteristics and potential seismic hazard of the Longquanshan fault zone, since its epicenter and associated aftershocks have been located along the central and northern segments of the fault zone.

The M_S 5.1 Qingbaijiang earthquake occurred adjacent to the highly populated and economically developed Chengdu Plain. It is the closest $M_S \geq 5.0$ event to downtown Chengdu City to date, with an epicentral distance of only 38 km. Previous studies have considered the Sichuan Basin to be a stable terrane that poses no risk of strong earthquakes (Xu et al., 2006; Hubbard et al., 2010). However, recent studies have revealed that moderate-to-strong earthquakes may also occur along the Longquanshan fault zone (Li et al., 2012, 2013; Wang and Lin, 2017). Numerous concerns regarding the future seismic hazard of the Longquanshan fault zone have been raised following this event. However, the limited data means that more studies are needed to reassess the seismic hazard in the Longquanshan area.

Constraints on seismogenic structures and their associated earthquake mechanisms are helpful for seismic risk assessments. The characteristics of various geological structures can generally be recognized by the spatial distribution of relocated earthquakes (Michael, 1988; Shearer, 1997; Presti et al., 2008; Yi et al., 2015, 2017, 2019), and the geometric and kinematic characteristics of these seismogenic structures can be inferred from their associated earthquake focal mechanisms (Zheng et al., 2009; Lv et al., 2013; Yi et al., 2015, 2017, 2019, 2020). Here we analyze seismic phase and waveform data from the Sichuan and Chengdu seismic networks, and relocate the earthquakes that have occurred along the central and northern segments of the Longquanshan fault zone since 2009, which include the M_S 5.1 Qingbaijiang earthquake sequence. We then analyze the earthquake distribution along the central and northern segments of the Longquanshan fault zone and the seismogenic structure associated with the M_S 5.1 Qingbaijiang earthquake sequence. We confirm the structure via a joint analysis of the earthquake relocation results, mainshock focal mechanism solution, and existing regional geological data, and analyze the seismogenic mechanism. Our results are a first step in better understanding the seismogenesis of the Longquanshan fault zone, and provide essential data for future studies on the formation mechanism and seismic hazard of the fault zone.

GEOLOGICAL SETTING AND HISTORICAL EARTHQUAKES

The Longquanshan fault zone forms the eastern boundary of the western Sichuan foreland basin, extending along the eastern side of the Longmenshan thrust-nappe structure and the western front of the Sichuan Basin. This 200-km-long NE–SW-trending fault zone starts in Zhongjiang County at its northern end, transects Jintang and Renshou counties, and terminates near Xinqiao Town, Leshan County, at its southern end (Li and Zeng, 1994). The Longquanshan fault zone consists of eastern and western branches that are distributed along the eastern and western limbs of the Longquanshan anticline, respectively (**Figure 1**); a conceptual model of the fault zone is shown in **Figure 2**. The western branch generally strikes NE20°–NE30°, and consists of faults that dip to the SE at 35°–70° and form an imbricate nappe structure, with these faults converging along the same main reverse fault at depth, as inferred from geological mapping (**Figure 2**; Deng et al., 1994) and seismic profiling (Wang et al., 2008; Li et al., 2013). The eastern branch is nearly parallel to the western branch, with a strike of NE10°–NE30°, and it consists of faults that dip to the NW at 28°–82° (Huang and Tang, 1995; Huang and Jiang, 2012; Li et al., 2013). The primary strata of the Longquanshan anticline are Jurassic and Cretaceous in age (Deng et al., 1994), the Longquanshan fault zone extends through these Jurassic and Cretaceous strata and terminates in the Triassic strata (Huang and Tang, 1995). The Longquanshan fault zone is divided into northern, central, and southern segments, and previous studies have generally defined the western branch as the main fault of the fault zone (**Figure 1**; Deng et al., 1994; Huang and Tang, 1995; Wang et al., 2008). The Longquanshan fault zone was originally activated during the formation of the Tibetan Plateau at the end of the Eocene (Deng et al., 1994), as inferred from seismological and geological investigations, geodetic deformation surveys (Huang and Tang, 1995; Zhang et al., 2003; Burchfiel, 2004), and focal mechanism solutions (Cheng, 1981). The secondary western Sichuan Block within the Tibetan Plateau continued to move to the SE and collided with the South China Block, resulting in the formation of small-scale folds in the interior of the Sichuan Basin (Deng et al., 1994).

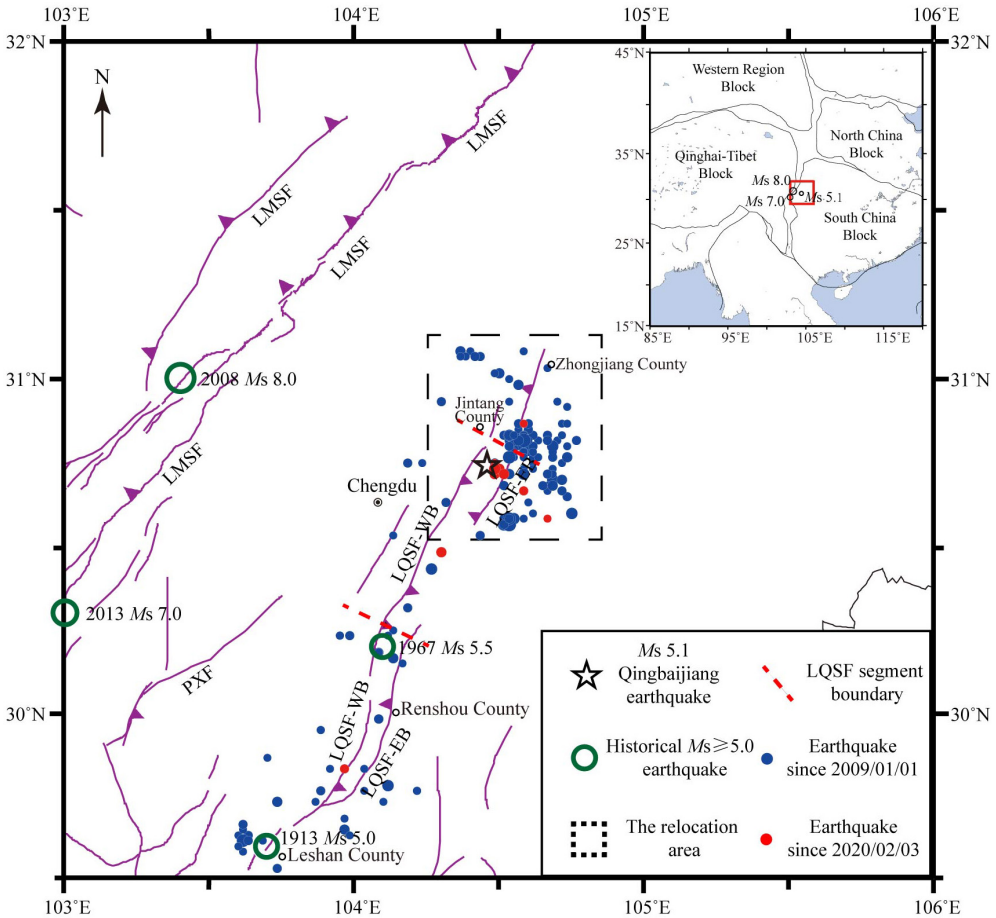

FIGURE 1 | Geological setting and epicentral map of $M_L \geq 2.0$ earthquakes since 2009 near the epicenter of the 3 February 2020 M_S 5.1 Qingbaijiang earthquake. Inset map in the upper right corner highlights the study area (red rectangle) in the main figure relative to the major crustal blocks in China. Purple lines indicate active faults: LMSF, Longmenshan fault zone; LQSF, Longquanshan fault zone; LQSF-EB, Eastern Branch of the Longquanshan fault zone; LQSF-WB, Western Branch of the Longquanshan fault zone; PXF, Pujiang-Xinjin fault.

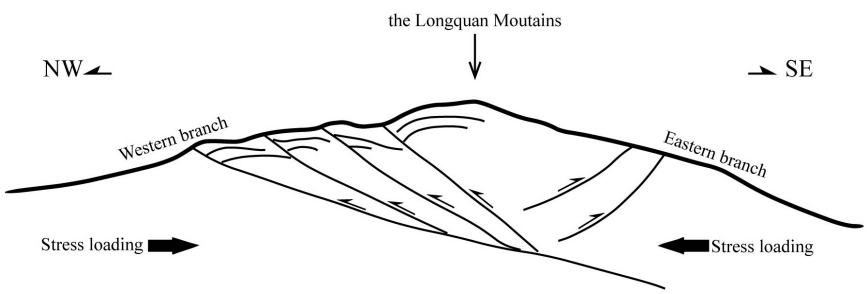

FIGURE 2 | Conceptual structural model of the Longquanshan fault zone (revised from Deng et al., 1994). The western branch consists of SE-dipping faults that form an imbricate nappe structure, with these faults converging along the same main reverse fault at depth. The eastern branch consists of NW-dipping faults with a nearly parallel arrangement.

The Longquanshan fault zone is a seismic zone that has generally hosted moderate-to-weak earthquakes, with segmented seismicity across the fault zone. Only two recorded $M_S \geq 5.0$ earthquakes have occurred along the southern segment of the fault zone (**Figure 1**), including the destructive 24 January 1967 M_S 5.5 Renshou earthquake, which is the largest event along the fault zone to date; this event had a 4 km focal depth and epicenter located on the southeastern side of the western branch (Cheng, 1981; Xu et al., 2006). Fault gouge dating has revealed that the Longquanshan fault zone was active

during the early to late Pleistocene, with the mid-Pleistocene being the most active period (Huang and Tang, 1995). Late Pleistocene activity was limited to the southern and central segments of the western branch, which might explain why moderate earthquakes have frequently occurred along these segments (Huang and Tang, 1995).

RELOCATION OF THE M_S 5.1 QINGBAIJIANG EARTHQUAKE SEQUENCE

Seismic Data and Relocation Method

The seismic phase data used for the earthquake relocation are from the Sichuan (black triangles in **Figure 3**) and Chengdu (green triangles in **Figure 3**) regional seismic networks. The M_S 5.1 Qingbaijiang earthquake sequence occurred in an area with dense, distributed seismic station coverage, thereby providing reliable data for our study. There were 55 broadband seismic stations within a 300 km epicentral distance of the mainshock, with an additional two portable short-period (SP) seismometers deployed near the epicenter immediately after the mainshock (red triangles in **Figure 3**). The minimum magnitude of completeness for the M_S 5.1 earthquake sequence was estimated to be 1.4 by the goodness-of-fit test (Wiemer and Wyss, 2000).

The events in the study area since the M_S 5.1 mainshock have been highly concentrated near the mainshock. We selected the events with epicentral distances within 15 km of the mainshock as aftershocks. The aftershocks of the M_S 5.1 event were sparse, with a scattered distribution of only 75 $M_L \geq 0.1$ aftershocks recorded by the end of October 2020 (**Figure 4**). The magnitude–time (M–t) plot (**Figure 4A**) shows that the aftershocks of the M_S 5.1 event occurred mainly during the first 2 months, whereas the aftershocks after 1 April 2020 were scattered. The frequency–time (N–t) plot (**Figure 4B**) shows that the monthly aftershock frequency of the sequence has been very low since April 2020, which indicates a rapid decay in the aftershock frequency.

We collected the phase data for 281 earthquakes since 2009 along the central and northern segments of the Longquanshan fault zone to obtain the necessary number of earthquakes for relative locations, and analyzed both the temporal and spatial characteristics of the seismicity along these segments. We relocated these earthquakes using the multi-stage method developed by Long et al. (2015). The details of our procedure are as follows.

We first located the initial earthquake locations using HYPOINVERSE2000 (Klein, 1989) based on the eastern Sichuan velocity model (Zhao and Zhang, 1987). We then selected the events that were recorded at six or more seismic stations and possessed a station distribution with a maximum azimuth gap of less than 180°. The lower limit number of observed stations in our study region was set to six, based on a series of test results, whereby the location accuracy was heavily reduced for fewer stations and the amount of relocated events decreased significantly with higher station limits, both of which inhibited the ability to accurately determine the geometry of the seismogenic fault. We calculated a new local one-dimensional (1-D) velocity model (**Table 1**) and station corrections via the VELEST program (Kissling et al., 1994, 1995) prior to the event relocations. We then employed hypoDD (Waldhauser and Ellsworth, 2000) to relocate the events using this new velocity model and applying the station corrections. We set a 3 km search radius to identify any earthquake clusters, since there were no tight earthquake distributions in the study area.

We relocated 199 earthquakes, including 60 events that were associated with the M_S 5.1 Qingbaijiang earthquake sequence. The average errors in the horizontal and vertical directions were 0.6 and 0.8 km, respectively, and the travel time residual was 0.2 s. The mainshock was located at 104.475°E, 30.731°N, with a focal depth of 5.2 km.

Analysis of the Relocation Results

The dashed rectangle in **Figure 5A** indicates the relocated epicentral distribution in the study area. The relocated earthquakes since 2009 are mainly distributed along the eastern branch of the Longquanshan fault zone and its eastern side, with most centered beneath Xinglong Town in Jintang County and Hongyuan Town in Jianyang County. The Hongyuan Town events occurred mainly in 2010. Seismicity in the Xinglong–Sanhe–Shisun area occurred mainly in 2009 and 2010, as well as after the 2013 Lushan earthquake. The influence of the 2008 M_S 8.0 Wenchuan and 2013 M_S 7.0 Lushan earthquakes on the seismicity of the Longquanshan fault zone is reflected in these observations. The aftershocks of the M_S 5.1 Qingbaijiang earthquake were ∼10 km southwest of the Xinglong earthquake cluster, and the epicenter of the M_S 5.1 mainshock was located between the eastern and western branches of the Longquanshan fault zone, ∼5 and 6 km from the eastern and western branches, respectively. The aftershock distribution strikes NE–SW, parallel to the Longquanshan fault zone, and is ∼6.0 km long and ∼2.5 km wide. The M_S 5.1 mainshock was located just north of the central part of the aftershock area (**Figure 5B**). Here we define 1 March 2020 as the boundary between the earlier and later aftershocks of the M_S 5.1 mainshock. The early aftershocks in February were generally smaller-magnitude events that were distributed to the southwest of the M_S 5.1 mainshock (red circles in **Figure 5B**), whereas the later aftershocks were relatively larger-magnitude events that were distributed to the east of the mainshock and included all of the relocated $M_L \geq 2.0$ earthquakes (green circles in **Figure 5B**).

We provide three depth profiles (A–A', B–B', and C–C' in **Figure 5A**) to further understand the seismogenic structure associated with the 2020 Qingbaijiang earthquake. These profiles focus on the M_S 5.1 Qingbaijiang earthquake sequence (B–B' and C–C' in **Figure 6**) and the earthquake clusters in the Xinglong–Sanhe–Shisun area (A–A' in **Figure 5C**).

Profile A–A' is perpendicular to the strike of the Longquanshan fault zone and intersects the main earthquake cluster in the Xinglong–Sanhe–Shisun area (**Figure 5A**). All of the relocated events within 5 km of the profile are plotted to discern the spatial distribution of the earthquake clusters. Three clusters are identified, which appear to form a parallel imbricate feature consisting of three steep NW-dipping faults

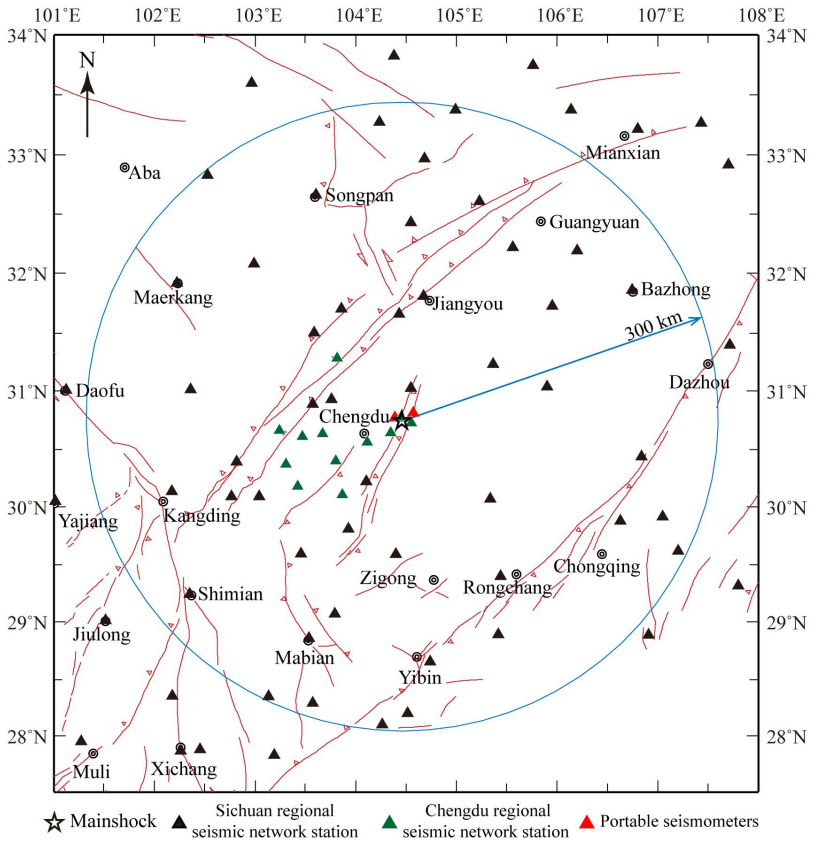

FIGURE 3 | Distribution of seismic stations (triangles) and known faults (red lines) around the epicenter of the M_S 5.1 Qingbaijiang earthquake (star). There were 55 broadband seismic stations (black and green triangles) and two portable SP seismometers (red triangles) within a 300 km epicentral distance of the mainshock.

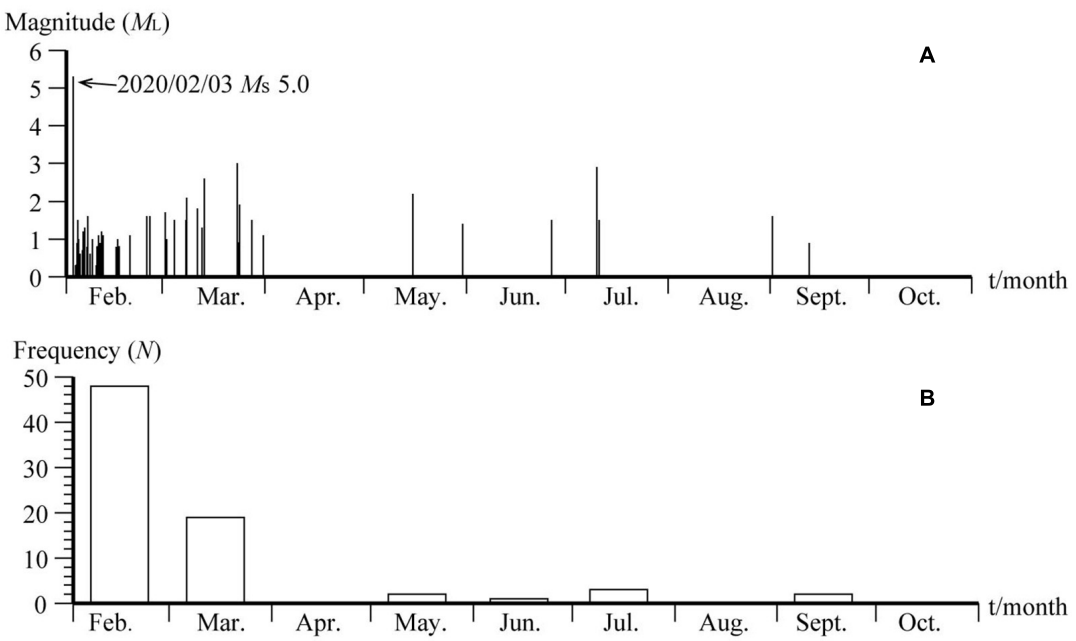

FIGURE 4 | *M–t* **(A)** and *N–t* **(B)** plots of the $M_L \geq 0.1$ events in the M_S 5.1 Qingbaijiang earthquake sequence during the 3 February–31 October 2020 period.

TABLE 1 | One-dimensional velocity model in the Longquanshan area.

Layer number	1	2	3	4	5	6	7	8	9	10	11	12
Top depth	0.0	6.0	8.0	10.0	16.0	18.0	20.0	25.0	28.0	34.0	43.0	61.0
Vp (km/s)	5.15	5.64	5.72	5.96	6.13	6.22	6.44	6.59	6.71	6.75	7.62	7.79

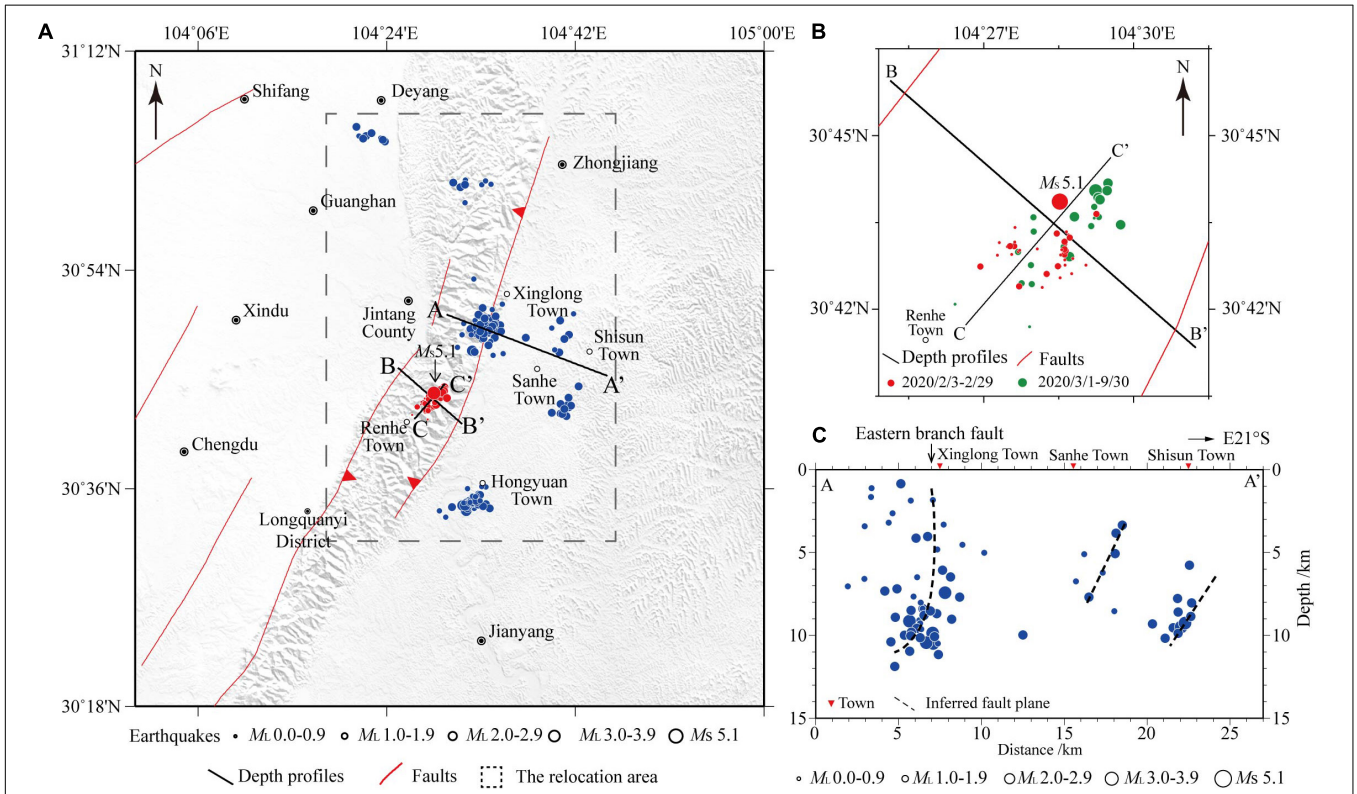

FIGURE 5 | Distribution of relocated epicenters. **(A)** Map of the relocated epicentral distribution across the central and northern segments of the Longquanshan fault zone since 2009; blue circles indicate the earthquakes since 2009, and red circles indicate the events in the 2020 M_S 5.1 Qingbaijiang earthquake sequence. **(B)** Map of the relocated epicentral distribution of the M_S 5.1 Qingbaijiang earthquake sequence. The aftershock distribution strikes NE–SW, with the M_S 5.1 mainshock located in the northern part of the aftershock area. **(C)** Depth distribution of relocated events along the A–A' profile. The three clusters appear to form a parallel imbricate feature consisting of three steep NW-dipping faults.

with focal depths concentrated in the upper 12 km of the crust. The two earthquake clusters along the eastern part of the profile are relatively small, distributed below Sanhe Town and Shisun Town, respectively, and not associated with surface ruptures. These two clusters occurred along planes dipping at ∼60° to the NW. The largest earthquake cluster near Xinglong Town has a "shovel-shaped" distribution that is nearly vertical in the uppermost crust and NW-dipping below 8 km depth. We suggest that the distribution of these earthquake clusters, which are located just below the surface expression of the eastern branch, reflects the geometry of this branch, which is consistent with regional geological and geophysical survey results (Huang and Tang, 1995).

Profiles B–B' and C–C' capture the short- and long-axis distributions of the M_S 5.1 Qingbaijiang earthquake aftershock area, respectively, showing all of the aftershocks that fall within 5 km of the profiles (**Figure 6**). The B–B' profile (**Figure 6A**) highlights a NW-dipping feature, with the aftershock distribution spanning depths of 3–6 km and the mainshock and most of the aftershocks being located above 5 km depth. The larger aftershocks ($M_L \geq 2.0$) were deeper than the smaller aftershocks. Beneath the Longquanshan anticline there is a decollement layer in the upper crust at 6–9 km depth (Hubbard et al., 2010; Jia et al., 2010; Li et al., 2015). It can therefore be inferred that the M_S 5.1 Qingbaijiang earthquake and its aftershocks occurred above this shallow detachment surface in the upper crust. The lack of aftershocks near the surface may indicate that the rupture did not extend to the surface. The distribution of the entire sequence in this section indicates that the M_S 5.1 Qingbaijiang earthquake occurred along a seismogenic fault plane dipping 56° to the NW, which is consistent with the dip direction of the eastern branch. If we extend this fault plane to the surface, it appears to meet the eastern branch fault. Therefore, we can infer that the M_S 5.1 Qingbaijiang earthquake ruptured the eastern branch of the Longquanshan fault zone at 3–6 km depth. The C–C' profile (**Figure 6B**) shows a northward deepening

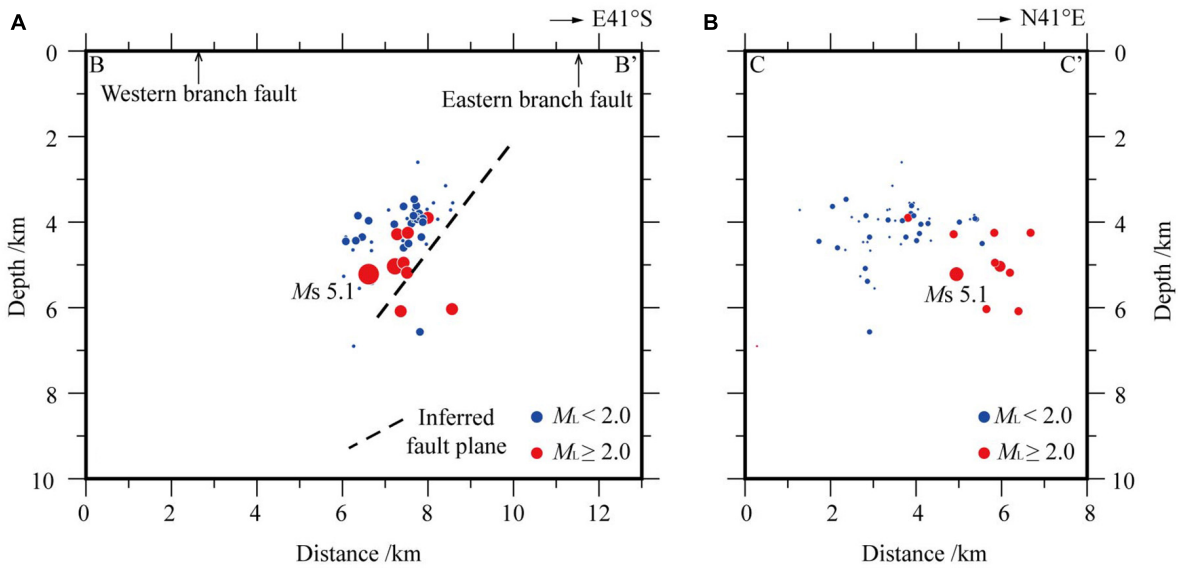

FIGURE 6 | Vertical cross-sections of the M_S 5.1 Qingbaijiang earthquake sequence. **(A)** Cross-section B–B', along the short axis of the M_S 5.1 sequence. This profile highlights a NW-dipping feature that appears to meet the eastern branch fault if it is extended to the surface. **(B)** Cross-section C–C', along the long axis of the M_S 5.1 sequence. This profile shows a northward deepening of the earthquake sequence, with smaller aftershocks in the southern part and larger aftershocks in the northern part.

of the earthquake sequence, with smaller aftershocks in the southern section that are concentrated at ∼4 km depth and larger aftershocks in the northern section that are all below 4 km depth, indicating segmentation along the eastern branch of the Longquanshan fault zone.

FOCAL MECHANISM INVERSION

Seismic Data and Focal Mechanism Solution Method

The focal mechanism solution, centroid depth, and moment magnitude of the M_S 5.1 Qingbaijiang earthquake were determined via the cut-and-paste (CAP) waveform inversion method (Zhao and Helmberger, 1994; Zhu and Helmberger, 1996). We chose the CAP method over other inversion methods since it needs fewer stations, and the inversion results are insensitive to lateral variations in the crust and less dependent on the velocity model (Tan et al., 2006; Zheng et al., 2009; Long et al., 2010; Yi et al., 2012; Luo et al., 2015). The CAP method can also constrain the focal depth using the surface wave amplitudes in the waveforms, thereby yielding a reliable focal centroid depth (Luo et al., 2015).

To calculate the focal mechanism of the mainshock, we analyzed the waveform records of permanent broadband seismic stations of the Sichuan Regional Seismological Network within a 50–300 km epicentral distance of the mainshock. We employed the frequency–wavenumber method (Zhu and Helmberger, 1996) to calculate Green's function using both a local 1-D velocity model (**Table 1**) and the model of Yi et al. (2020). We set a 2 s duration for the source time, 30 and 60 s waveform window lengths, and 0.05–0.20 Hz and 0.05–0.10 Hz band pass filters for the body waves and surface waves, respectively, in the CAP inversion. The inversion was conducted in 5° and 1 km increments to constrain the fault plane parameters and depth of the earthquake, respectively.

The obtained focal mechanism solution, centroid depth, and moment magnitude for the M_S 5.1 Qingbaijiang earthquake are shown in **Table 2**. The results for the two different velocity models are similar (**Table 2**); we selected the result based on the velocity model in **Table 1** as the focal mechanism solution for the event. The best fit to the waveforms was obtained at a 4 km centroid depth (**Figure 7**), with > 70% of the waveform components yielding correlation coefficients of > 93% (**Figure 8**).

The 4 km centroid depth of the M_S 5.1 mainshock is close to the relocated 5.2 km initial rupture depth, both of which indicate that the M_S 5.1 event occurred above the shallow detachment layer in the upper crust. The parameters of the focal mechanism solution (strike/dip/rake) are 22°/36°/91° for nodal plane I and 200°/54°/89° for nodal plane II, which indicate a thrust earthquake with a NE–SW rupture direction.

ANALYSIS OF THE SEISMOGENIC FAULT OF THE M_S 5.1 QINGBAIJIANG EARTHQUAKE AND IMPLICATIONS FOR SEISMIC HAZARD

Our preliminary analysis indicates that the seismogenic fault of the M_S 5.1 Qingbaijiang earthquake is along the eastern branch of the Longquanshan fault zone, with the coseismic rupture plane dipping 56° to the NW (nodal plane II). The initial rupture

TABLE 2 | Focal mechanism solutions for the M_S 5.1 Qingbaijiang earthquake from different velocity models.

Depth/km	Nodal plane I			Nodal plane II			*P* Axis		*T* Axis		*B* Axis		Magnitude		Velocity model
	strike/°	dip/°	rake/°	strike/°	dip/°	rake/°	azimuth/°	plunge/°	azimuth/°	plunge/°	azimuth/°	plunge/°	M_S	M_w	
4	22	36	91	200	54	89	291	9	105	81	201	1	5.1	4.61	**Table 1**
4	25	35	95	199	55	87	291	10	95	80	201	3		4.64	Yi et al. (2020)

depth obtained from the relocation analysis and the centroid depth obtained from waveform inversion suggest that this M_S 5.1 event was a moderate earthquake that occurred above the shallower detachment layer beneath the Longquanshan anticline. The sub-horizontal *P*-axis (azimuth of 291°) indicates that the tectonic stress field in the focal region is characterized by an subhorizontal principal compressive stress that trends WNW, which is consistent with the regional tectonic stress field in the South China Block (Heidbach et al., 2018; Wang and Shen, 2020). The earthquake depth, which is consistent with that of the destructive 1967 M_S 5.5 Renshou earthquake, may indicate that $M_S \geq 5.0$ destructive earthquakes along the Longquanshan fault zone have mainly occurred in the shallow part of the upper crust.

Since the 2008 Wenchuan earthquake, many studies have examined the seismic hazard of the Longquanshan fault zone. For example, Zhang et al. (2008) reported a ∼0.1 bar increase in the Coulomb stress of the Longquanshan fault zone after the Wenchuan earthquake. Qian and Han (2011) reported a 0.4–0.6 bar increase in stress along the northern segment of the Longquanshan fault zone after the Wenchuan earthquake, with this stress increase gradually decreasing from north to south along the fault zone, which is consistent with the observation that the seismicity along the fault zone was mainly clustered along the northern segment after the Wenchuan earthquake. Parsons et al. (2008) calculated the Coulomb stress change after the Wenchuan earthquake and suggested that the event increased both the stress state in the Sichuan Basin and the risk of earthquake occurrence. A comparative analysis of the seismicity before and after the 2008 Wenchuan earthquake found a significant increase in both the earthquake frequency and intensity in the Sichuan Basin (Yi et al., 2019). Moderate earthquakes occurred successively in the low-seismicity area of the Sichuan Basin, such as the 19 February 2013 M_S 4.7 Santai-Yanting earthquake, and the 29 July 2014 M_S 4.9 Zitong and M_S 4.6 Santai earthquakes, which could be related to stress loading in the Sichuan Basin due to the 2008 Wenchuan earthquake (Yi et al., 2019). However, Parsons et al. (2008) showed that the central and northern segments of the Longquanshan fault zone were in a negative zone of coseismic Coulomb stress disturbance due to the Wenchuan earthquake. Toda et al. (2008) reported a 0.1–0.3 bar stress reduction on a thrust fault to the south of Chengdu after the Wenchuan earthquake. Therefore, the influence of the 2008 Wenchuan earthquake on the seismicity and seismic hazard of the Longquanshan fault zone needs to be further investigated.

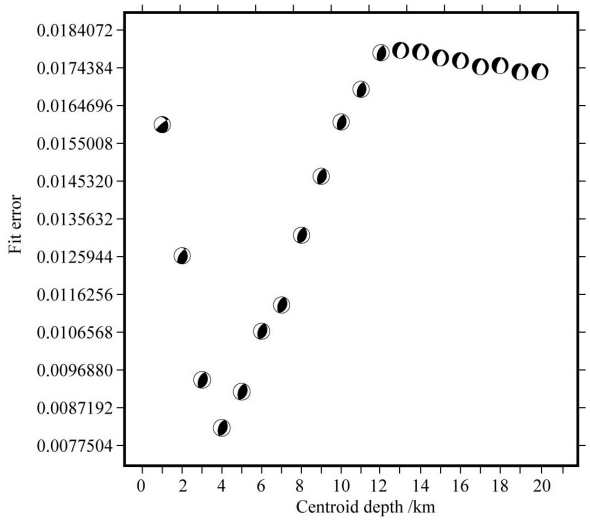

FIGURE 7 | Centroid depth variation in the residual error of the focal mechanism solution for the M_S 5.1 Qingbaijiang earthquake.

Previous studies have considered the western branch of the Longquanshan fault zone to be the main fault of the entire anticline (Deng et al., 1994; Huang and Tang, 1995; Tang et al., 1996; Wang et al., 2008; Wang and Lin, 2017), leading to the conclusion that the western branch represents a greater seismic hazard (Huang and Tang, 1995; Zhang et al., 2020). Luo et al. (2008) believe that the Longquanshan anticline formed under E–W compression related to collision between the Qinghai-Tibet Plateau and South China Block, which formed an anti-thrust pattern along the front of the Longmenshan thrust belt. The Longquanshan anticline is a shallow structure that has formed via multi-stage subduction and subsequent emplacement of deep material from the South China Block to the deeper sections of the LFTB and the West Sichuan Plateau. The eastern branch is a back-fault associated with the entire fold system, similar to the back-fault on the main fault plane of the 2013 M_S 7.0 Lushan earthquake (Long et al., 2015). However, another possibility is that the Longquanshan fault zone and LFTB are components of the same structural system, such that the Longquanshan fault zone forms the southeastern boundary of the LFTB nappe foreland basin in western Sichuan (Chen et al., 1994; Zhang et al., 2003; Liu, 2007). The eastern branch of the Longquanshan fault zone would be considered the main fault in this combined structural system, whereas the western branch would be a back-fault associated with the entire fold system. Most earthquakes, including the M_S 5.1 Qingbaijiang earthquake sequence, have occurred along the eastern branch since 2009, supporting this latter structural model. Further investigations of the dynamic

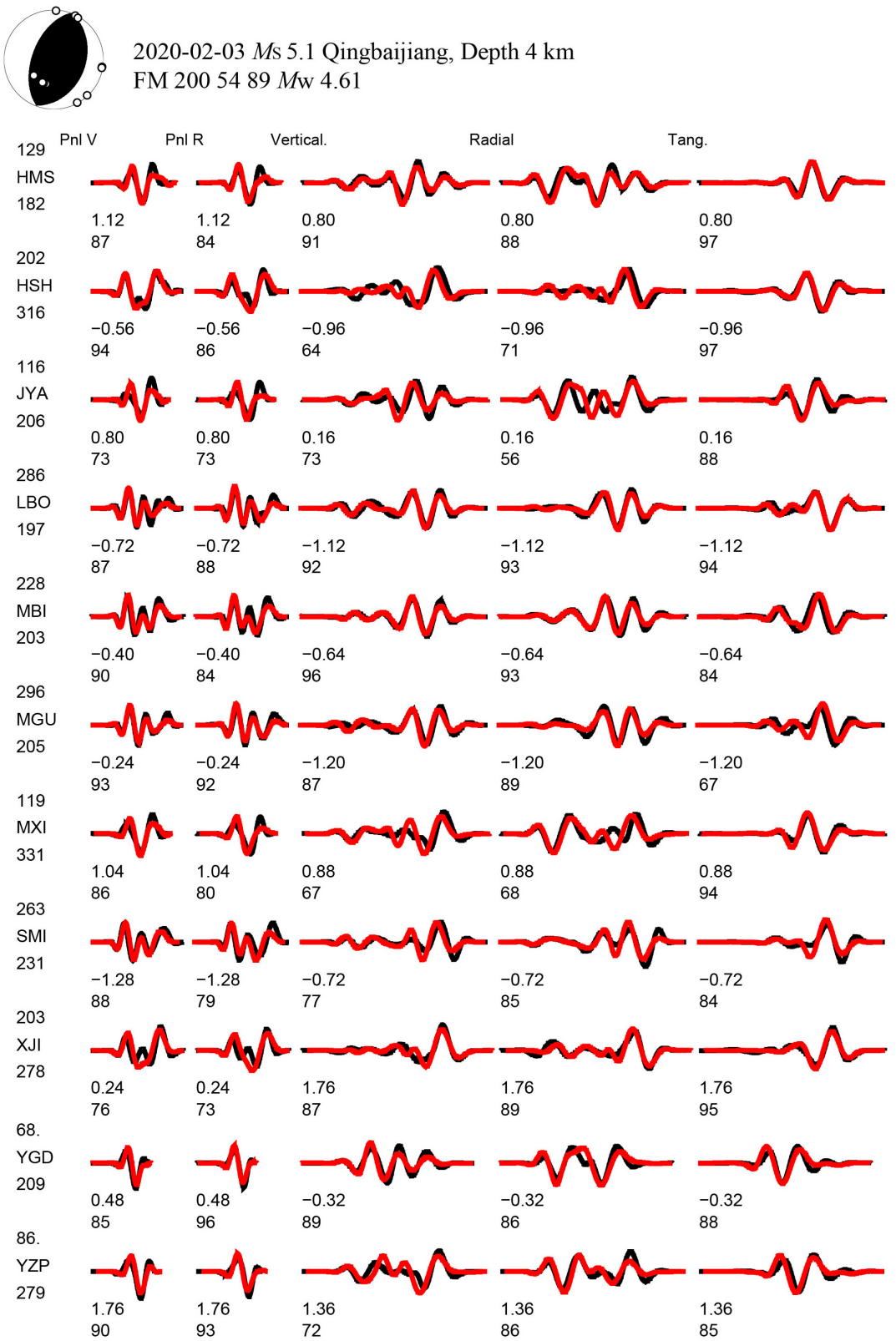

FIGURE 8 | Comparison of synthetic (red) and observed (black) waveforms at the best fitting depth for the M_S 5.1 Qingbaijiang earthquake. The relative time shift (in s; upper) and correlation coefficient (in%; lower) are provided below each trace. The station names are given to the left, with the epicentral distance (in km; upper) and azimuth (in degree; lower) provided.

origin, tectonic setting, and seismic hazard of the Longquanshan fault zone need to be undertaken to resolve these discrepancies.

CONCLUSION

We analyzed seismic phase and waveform data recorded by the Sichuan and Chengdu regional seismic networks to relocate the earthquakes that have occurred along the central and northern segments of the Longquanshan fault zone since 2009, including the M_S 5.1 Qingbaijiang earthquake sequence, using the multi-stage method. We also calculated the focal mechanism of the M_S 5.1 mainshock using the CAP waveform inversion method.

The M_S 5.1 Qingbaijiang earthquake occurred along a NE–SW-striking fault, consistent with the trend of the Longquanshan fault zone, at an initial rupture depth of 5.2 km. The earthquake clusters that have occurred along the Longquanshan fault zone since 2009, including the M_S 5.1 Qingbaijiang earthquake sequence, were located along NW-dipping features that formed a parallel imbricate pattern, which is identical to the fault geometry along the eastern branch of the Longquanshan fault zone. The mainshock had a centroid depth of 4 km and a thrust-type focal mechanism along a NW-dipping fault plane, similar to the structure of the eastern branch. Therefore, the M_S 5.1 Qingbaijiang earthquake was a pure thrusting event along the eastern branch of the Longquanshan fault zone, and nodal plane II of the focal mechanism solution represents the coseismic rupture plane. We conclude that the M_S 5.1 Qingbaijiang earthquake was a moderate earthquake above the shallow detachment layer beneath the Longquanshan Anticline and was controlled by the regional tectonic stress field, as inferred from regional geological constraints.

The focal depth of the M_S 5.1 Qingbaijiang earthquake, which is consistent with that of the 1967 M_S 5.5 Renshou earthquake, may indicate that the destructive $M_S \geq 5.0$ earthquakes along the Longquanshan fault zone occur primarily in the shallow part of the upper crust. Our study provides valuable data for future studies on the seismogenesis and seismic hazard of the Longquanshan fault zone.

AUTHOR'S NOTE

MZ, Master, engineer, mainly engaged in seismic activity research.

DATA AVAILABILITY STATEMENT

The original contributions presented in the study are included in the article, further inquiries can be directed to the corresponding author.

AUTHOR CONTRIBUTIONS

MZ mainly completed the writing of the manuscript. FL mainly completed the data processing and supported the completion of the manuscript. GY mainly formed the idea of the manuscript and supported the completion of the manuscript. ML, JX, and SW participated worked for the manuscript. All authors contributed to the article and approved the submitted version.

FUNDING

The research was supported by the National Science Foundation of China (41574047) and the National Key R&D Program of China (2018YFC150330501 and 2020YFA0710603-01).

ACKNOWLEDGMENTS

We are grateful to Prof. Zhu Lupei of San Luis University of the United States for providing the CAP program, and to the reviewers for valuable suggestions. GMT software was used to plot a part of the figures. We are very grateful to the editors and reviewers for their constructive comments and thoughtful suggestions.

REFERENCES

Burchfiel, B. C. (2004). New technology, new geological challenges. *GSA Today* 14, 4–10. doi: 10.1130/1052-51732004014<4:panngc<2.0.co;2

Burchfiel, B. C., Chen, Z. L., Liu Yupinc, L., and Royden. (1995). Tectonics of the Longmen Shan and Adjacent Regions, Central China. *Int. Geol. Rev.* 37, 661–735. doi: 10.1080/00206819509465424

Burchfiel, B. C., Royden, L. H., vander Hilst, R. D., Hager, B. H., Chen, Z., King, R. W., et al. (2008). A geological and geophysical context for the Wenchuan earthquake of 12 May 2008, Sichuan, People's Republic of China. *GSA Today* 18, 4–11. doi: 10.1130/gsatg18a.1

Chen, S. F., and Wilson, C. J. L. (1996). Emplacement of the Longmen Shan Thrust-Nappe Belt along the eastern margin of the Tibetan Plateau. *J. Struct. Geol.* 18, 413–430. doi: 10.1016/0191-8141(95)00096-V

Chen, S. F., Wilson, C., Deng, Q. D., Zhao, X. L., and Zhi, L. L. (1994). Active faulting and block movement associated with large earthquakes in the Min Shan and Longmen Mountains,northeastern Tibetan plateau. *J. Geophys. Res.* 99, 20–25. doi: 10.1029/94JB02132

Cheng, E. L. (1981). Recent tectonic stress field and tectonic movement of the Sichuan Province and its vicinity. *Acta Seismol. Sin.* 3, 231–241.

Deng, Q. D., Chen, S. F., and Zhao, X. L. (1994). Tectonics, scismisity and dynamics of Longmenshan mountains and its adjacent regions. *Seismol. Geol.* 16, 389–403.

Heidbach, O., Rajabi, M., Cui, X., Fuchs, K., Müller, B., Reinecker, J., et al. (2018). The World Stress Map database release 2016: Crustal stress pattern across scales. *Tectonophysics* 744, 484–498. doi: 10.1016/j.tecto.2018.07.007

Houseman, G., and England, P. (1986). Finite strain calculations of continental deformation: 1. Method and general results for convergent zones. *J. Geophys. Res. Solid Earth* 91, 3651–3663. doi: 10.1029/JB091iB03p03651

Huang, W., and Jiang, W. L. (2012). Discussion on the late quaternary activity and earthquake risk potential of Longquanshan Fault in Sichuan. *Northwestern Seismol. J.* 34, 50–56. doi: 10.3969/j.issn.1000-0844.2012.01.010

Huang, Z. Z., and Tang, R. C. (1995). The Longquanshan fault zone and exploration of potential earthquake ability. *Earthquake Res. Sichuan* 1, 18–23.

Hubbard, J., and Shaw, J. H. (2009). Uplift of the Longmen Shan and Tibetan plateau, and the 2008 Wenchuan (M=7.9) earthquake. *Nature* 458, 194–197. doi: 10.1038/nature07837

Hubbard, J., Shaw, J. H., and Klinger, Y. (2010). Structural Setting of the 2008 Mw 7.9 Wenchuan. China, Earthquake. *Bull. Seismol. Soc. Am.* 100, 2713–2735. doi: 10.1785/0120090341

Jia, D., Li, Y., Lin, A., Wang, M., Chen, W., Wu, X., et al. (2010). Structural model of 2008 Mw 7.9 Wenchuan earthquakes in the rejuvenated Longmen Shan thrust belt China. *Tectonophysics* 491, 174–184. doi: 10.1016/j.tecto.2009.08.040

Kirby, E., Reiners, P. W., Krol, M. A., Whipple, K. X., Hodges, K. V., Farley, K. A., et al. (2002). Late Cenozoic evolution of the eastern margin of the Tibetan Plateau: Inferences from 40Ar/39Ar and (U-Th)/He thermochronolgy. *Tectonics* 21:1001. doi: 10.1029/2000TC001246

Kirby, E., Whipple, K., and Harkins, N. (2008). Topography reveals seismic hazard. *Nat. Geosci.* 1, 485–487. doi: 10.1038/ngeo265

Kissling, E., Ellsworth, W., Eberhart-Phillips, D., and Kradolfer, U. (1994). Initial reference models in local earthquake tomography. *J. Geophys. Res. Solid Earth* 99, 19635–19646. doi: 10.1029/93JB03138

Kissling, E., Kradolfer, U., and Maurer, H. (1995). *VELEST user ES guide short introduction*. Zürich: ETH Zuerich.

Klein, F. W. (1989). HYPOINVERSE, a program for VAX computers to solve for earthquake locations and magnitudes. *U S. Geol. Survey Open File Rep.* 59, 89–314.

Li, K., Xu, X. W., and Tang, X. B. (2013). Using deformation terraces to confine the shortening and uplift of the Longquan anticline. *Seismol. Geol.* 35, 22–36. doi: 10.3969/j.issn.0253-4967.2013.01.002

Li, K., Xu, X. W., Tan, X. B., Chen, G. H., Xu, C., and Kang, W. J. (2015). Late Quaternary deformation of the Longquan anticline in the Longmenshan thrust belt, eastern Tibet, and its tectonic implication. *J. Asian Earth Sci.* 112, 1–10. doi: 10.1016/j.jseaes.2015.08.022

Li, Y. Q., Jia, D., Shaw, J. H., Hubbard, J., Lin, A. M., Wang, M. M., et al. (2010). Structural interpretation of the coseismic faults of the Wenchuan earthquake: three-dimensional modeling of the Longmen Shan fold-and-thrust belt. *J. Geophys. Res.* 115, 1–26. doi: 10.1029/2009JB006824

Li, Y., and Zeng, Y. F. (1994). On the sedimentary response to thrusting of Longmenshan trust belt in Chengdu Basin. *J. Mineral Petrol.* 14, 58–66.

Li, Z. G., Jia, D., and Chen, W. (2012). Structural geometry and deformation mechanism of the Longquan anticline in the Longmen Shan fold-and-thrust belt, eastern Tibet. *J. Asian Earth Sci.* 64, 223–234. doi: 10.1016/j.jseaes.2012.12.022

Liu, S. (2007). *Structural characteristics of the thrust fold of foreland – a case study of thrust fold at Micang and Longmen Mountains*. Ph.D. thesis. Beijing: Institute of Geology China Earthquake Administration.

Liu-Zeng, J., Zhang, Z., Wen, L., Tapponnier, P., Sun, J., Xing, X., et al. (2009). Co-seismic ruptures of the 12 May 2008, Ms 8.0 Wenchuan earthquake, Sichuan: East–west crustal shortening on oblique, parallel thrusts along the eastern edge of Tibet. *Earth Planetary Sci. Lett.* 286, 355–370. doi: 10.1016/j.epsl.2009.07.017

Long, F., Wen, X. Z., Ruan, X., Zhao, M., and Yi, G. X. (2015). A more accurate relocation of the 2013Ms7.0 Lushan, Sichuan, China, earthquake sequence, and the seismogenic structure analysis. *J. Seismol.* 19, 653–665. doi: 10.1007/s10950-015-9485-0

Long, F., Zhang, Y. J., Wen, X. Z., and Ni, S. D. (2010). Focal mechanism solution of $M_L \geq 4.0$ events in the MS6.1 Panzhihua-Huili earthquake sequence of Aug 30, 2008. *Chin. J. Geophys.* 53, 2852–2860.

Luo, Y., Zhao, L., Zeng, X. F., and Gao, Y. (2015). Focal mechanisms of the Lushan earthquake sequence and spatial variation of the stress field. *Sci. China Earth Sci.* 58, 1148–1158. doi: 10.1007/s11430-014-5017-y

Luo, Z. L., Yong, Z. Q., Liu, S. G., Sun, W., Deng, B., Yang, R. J., et al. (2008). Relationship between C-subduction and the Wenchuan earthquake and suggestions on preventing earthquakes and mitigationg disaters. *J. Chengdu Univers. Technol.* 35, 337–347. doi: 10.3969/j.issn.1671-9727.2008.04.001

Lv, J., Wang, X. S., Su, J. R., Pan, L. S., Li, Z., Yin, L. W., et al. (2013). Hypocentral location and source mechanism of the MS7.0 Lushan earthquake sequence. *Chin. J. Geophys.* 56, 1753–1763. doi: 10.6038/cjg20130533

Michael, A. J. (1988). Effects of three-dimensional velocity structure on the seismicity of the 1984 Morgan Hill, California, aftershock sequence. *Bull. Seismol. Soc. Am.* 78, 1199–1221.

Molnar, P. H., and Tapponnier, P. (1975). Cenozoic tectonics of Asia: Effects of a continental collision. *Science* 189, 419–426. doi: 10.1126/science.189.4201.419

Parsons, T., Ji, C., and Kirby, E. (2008). Stress changes from the 2008 Wenchuan earthquake and increased hazard in the Sichuan Basin. *Nature* 454, 509–510. doi: 10.1038/nature07177

Presti, D., Orecchio, B., Falcone, G., and Neri, G. (2008). Linear versus nonlinear earthquake location and seismogenic fault detection in the southern Tyrrhenian Sea. Italy. *Geophys. J. Int.* 172, 607–618. doi: 10.1111/j.1365-246x.2007.03642.x

Qian, Q., and Han, Z. J. (2011). The research in the change of the earthquake occurrence probability in Longquan Shan fault after the Wenchuan earthquake. *Prog. Geophys.* 26, 489–497. doi: 10.3969/j.issn.1004-2903.2011.02.013

Shearer, P. (1997). Improving local earthquake locations using the L1 norm and waveform cross correlation: application to the Whittier Narrows, California, aftershock sequence. *J. Geophys. Res. Solid Earth* 102, 8269–8283. doi: 10.1029/96JB03228

Tan, Y., Zhu, L. P., Helmberger, D. V., and Saikia, C. K. (2006). Locating and modeling regional earthquakes with two stations. *J. Geophys. Res.* 111:B11. doi: 10.1029/2005JB003775

Tang, R. C., Huang, Z. Z., Qian, H., Gong, Y., Wen, D. H., Ma, S. H., et al. (1996). Main features and potential seismic capability of active fault belts in Chengdu Depression. *Earthquake Res. China* 3, 285–293.

Tapponnier, P., and Molnar, P. (1977). Active faulting and tectonics in China. *J. Geophys. Res.* 82, 2905–2930. doi: 10.1029/JB082i020p02905

Tapponnier, P., Peltzer, G., Le Dain, A. Y., Armijo, R., and Cobbold, P. (1982). Propagating extrusion tectonics in Asia: new insights from simple experiments with plasticine. *Geology* 10, 611–616.

Tapponnier, P., Xu, Z., Roger, F., Meyer, B., Arnaud, N., Wittlinger, G., et al. (2001). Oblique stepwise rise and growth of the Tibet Plateau. *Science* 294, 1671–1677. doi: 10.1126/science.105978

Toda, S., Lin, J., Meghraoui, M., and Stein, R. S. (2008). 12 May 2008 M = 7.9 Wenchuan, China, earthquake calculated to increase failure stress and seismicity rate on three major fault systems. *Geophys. Res. Lett.* 35, L17305–L17301. doi: 10.1029/2008GL034903

Waldhauser, F., and Ellsworth, W. L. (2000). A double-difference earthquake location algorithm: method and application to the northern Hayward fault, California. *Bull. Seismol. Soc. Am.* 90, 1353–1368.

Wang, E., Kirby, E., Furlong, K. P., van Soest, M., Xu, G., Shi, X., et al. (2012). Two-phase growth of high topography in eastern Tibet during the Cenozoic. *Nat. Geosci.* 5:640. doi: 10.1038/ngeo1538

Wang, H., Ran, Y., Chen, L., Shi, X., Liu, R., and Gomez, F. (2010). Determination of horizontal shortening and amount of reverse-faulting from trenching across the surface rupture of the 2008 M W 7.9 Wenchuan earthquake, China. *Tectonophysics* 491, 10–20. doi: 10.1016/j.tecto.2010.03.019

Wang, M., and Lin, A. (2017). Active thrusting of the Longquan Fault in the central Sichuan basin, China, and the seismotectonic behavior in the Longmen Shan fold-and-thrust belt. *J. Geophys. Res. Solid Earth* 122, 5639–5662. doi: 10.1002/2016JB013391

Wang, M., and Shen, Z. (2020). Present-Day Crustal Deformation of Continental China Derived From GPS and Its Tectonic Implications. *J. Geophys. Res. Solid Earth* 125:2019JB018774. doi: 10.1029/2019JB018774

Wang, Q., Qiao, X., Lan, Q., Freymueller, J., Yang, S., Xu, C., et al. (2011). Rupture of deep faults in the 2008 Wenchuan earthquake and uplift of the Longmen Shan. *Nat. Geosci.* 4, 634–640. doi: 10.1038/ngeo1210

Wang, W. T., Jia, D., Li, C. Y., Zheng, W. J., and Wei, Z. Y. (2008). Preliminary investigation on deformation characteristics and activity of Longquanshan fault belt in Sichuan. *Seismol. Geol.* 30, 968–979.

Wiemer, S., and Wyss, M. (2000). Minimum magnitude of completeness in earthquake catalogs: examples from Alaska, the Western United States, and Japan. *Bull. Seismol. Soc. Am.* 90, 859–869. doi: 10.1785/0119990114

Xu, S. S., Ren, H., and Song, J. (2006). Primary study on the seismicity along the faults of Longquanshan. *Earthquake Res. Sichuan* 2, 21–27. doi: 10.3969/j.issn.1001-8115.2006.02.005

Xu, X. W., Wen, X. Z., Chen, G. H., Li, C. Y., Zheng, W. J., Zhnag, S. M., et al. (2013). Lushan M S 7.0 earthquake: A blind reserve-fault event. *Chin. Sci. Bull.* 58, 3437–3443. doi: 10.1007/s11434-013-5999-4

Xu, X. W., Wen, X. Z., Guihua, Y., Chen, G., Klinger, Y., Hubbard, J., et al. (2009). Coseismic reverse- and oblique-slip surface faulting generated by the 2008 Mw 7.9 Wenchuan earthquake, China. *Geology* 37, 515–518. doi: 10.1130/G25462A.1

Yi, G. X., Long, F., and Zhang, Z. W. (2012). Spatial and temporal variation of focal mechanisms for aftershocks of the 2008 MS8.0 Wenchuan earthquake. *Chin. J. Geophys.* 55, 1213–1227. doi: 10.6038/j.issn.0001-5733.2012.04.017

Yi, G. X., Long, F., Liang, M. J., Zhang, H. P., Zhao, M., Ye, Y. Q., et al. (2017). Focal mechanism solutions and seismogenic structure of the 8 August 2018 M7.0 Jiuzhaigou earthquake and its aftershocks, northern Sichuan. *Chin. J. Geophys.* 60, 4083–4097. doi: 10.6038/cjg20171033

Yi, G. X., Long, F., Liang, M. J., Zhao, M., and Wang, S. W. (2020). Geometry and tectonic deformation of seismogenic structures in the Rongxian-Weiyuan-Zizhong region, Sichuan Basin: insights from mechanism solutions. *Chin. J. Geophys.* 63, 3275–3291.

Yi, G. X., Long, F., Liang, M. J., Zhao, M., Wang, S. W., Gong, Y., et al. (2019). Focal mechanism solutions and seismogenic structure of the 17 June 2019 MS6.0 Sichuan Changning earthquake sequence. *Chin. J. Geophys.* 62, 3432–3447. doi: 10.6038/cjg2019N0297

Yi, G. X., Long, F., Wen, X. Z., Liang, M. J., and Wang, S. W. (2015). Seismogenic structure of the M6.3 Kangding earthquake sequence on 22 Nov. Southwestern China. *Chin. J. Geophys.* 58, 1205–1219. doi: 10.6038/cjg20150410

Yin, A. (2010). A special issue on the great 12 May 2008 Wenchuan earthquake (*M*w 7.9): Observations and unanswered questions. *Tectonophysics* 491, 1–9. doi: 10.1016/j.tecto.2010.05.019

Yin, A., and Harrison, T. M. (2000). Geologic Evolution of the Himalayan-Tibetan Orogen. *Annu. Rev. Earth Planetary Sci.* 28, 211–280. doi: 10.1146/annurev.earth.28.1.211

Zhang, G. H., Shan, X. J., and Li, W. D. (2008). The coulomb failure stress change associated with th MS8.0 Wenchuan earthquake and the risk prediction of its surrounding faults. *Seismol. Geol.* 30, 935–944. doi: 10.3969/j.issn.0253-4967.2008.04.010

Zhang, P. Z. (2013). A review on active tectonics and deep crustal processes of the Western Sichuan region, eastern margin of the Tibetan Plateau. *Tectonophysics* 584, 7–22. doi: 10.1016/j.tecto.2012.02.021

Zhang, P. Z., Wen, X. Z., Shen, Z. K., and Chen, J. H. (2010). Oblique, High-Angle, Listric-Reverse Faulting and Associated Development of Strain: TheWenchuan Earthquake of May 12, 2008, Sichuan, China. *Annu. Rev. Earth Planet. Sci.* 38, 353–382. doi: 10.1146/annurev-earth-040809-152602

Zhang, W., Zhou, R., He, Y., Liu, S., Ma, and Chao. (2020). Characteristic of Shallow Structure and Fault Activity in Western Piedmont to Longquanshan. *J. Geodesy Geodynam.* 40, 942–946. doi: 10.14075/j.jgg.2020.09.013

Zhang, Y. Q., Yang, N., Chen, W., Ma, Y. S., and Meng, H. (2003). Late Cenozoic tectonic deformation history of the east-west geomorphological boundary zone of china and uplift process of the eastern margin of the Tibetan Plateau. *Earth Sci. Front.* 10, 599–612. doi: 10.3321/j.issn:1005-2321.2003.04.026

Zhao, L. S., and Helmberger, D. V. (1994). Source estimation from broadband regional seismograms. *Bull. Seismol. Soc. Am.* 84, 91–104. doi: 10.1029/93JB02965

Zhao, Z., and Zhang, R. S. (1987). Primary study of crustal and upper mantle velocity structure of Sichuan Province. *Acta Seismol. Sin.* 1987, 44–56.

Zheng, Y., Ma, H. S., Lv, J., Ni, S. D., Li, Y. C., and Wei, S. J. (2009). The focal mechanism solution of Wenchuan Earthquake strong aftershock (MS=5.6) and its relationship with seismogenic structure. *Sci. China* 39, 413–426. doi: 10.1360/zd2009-39-4-413

Zhu, L. P., and Helmberger, D. V. (1996). Advancement in source estimation techniques using broadband regional seismograms. *Bull. Seismol. Soc. Am.* 86, 1634–1641. doi: 10.1029/96JB02296

Conflict of Interest: The authors declare that the research was conducted in the absence of any commercial or financial relationships that could be construed as a potential conflict of interest.

frontiers in Earth Science

ORIGINAL RESEARCH
published: 23 November 2021
doi: 10.3389/feart.2021.599535

Stochastic Simulation of Strong Ground Motions From Two M > 5 Uttarakhand Earthquakes

Nitin Sharma, D. Srinagesh, G. Suresh and D. Srinivas*

National Geophysical Research Institute (CSIR), Hyderabad, India

Many studies based on the geodetic data and statistical analysis of seismicity have pointed out that sufficient amount of stress accumulated in the Himalayan plate boundary may host a big earthquake. Consequently, high seismic activities and infrastructural developments in the major cities around Himalayan regions are always of major concern. The ground motion parameter estimation plays a vital role in the near real time evaluation of potentially damaged areas and helps in mitigating the seismic hazard. Therefore, keeping in mind the importance of estimation of ground motion parameters, we targeted two moderate-size earthquakes that occurred recently within a gap of 10 months in Uttarakhand region with M > 5.0 on 06/02/2017 and 06/12/2017. The ground motions are simulated by adopting a stochastic modeling technique. The source is assumed as ω^{-2}, a circular point source (Brune's model). The average value of reported anelastic attenuation from various studies, the quality factor, $Q_s = 130.4^{*}(f^{0.996})$, and stress drop values obtained through iterative procedure are considered for simulations. The stochastic spectra are generated between 0.1 and 10 Hz of frequency range. The site effect is also estimated by using the H/V method in the same frequency range. The synthetic spectra are compared with the observed Fourier amplitude spectra obtained from the recorded waveform data and converted back to the time histories. The stochastic time histories are compared with the observed waveforms and discussed in terms of amplitude (PGA). The simulated and observed response spectra at different structural periods are also discussed. The mismatch between the observed and simulated PGA values along with the GMPE existing for shallow crustal earthquakes is also discussed in the present work.

Keywords: stochastic, strong ground motion, earthquake, site effect, simulation

OPEN ACCESS

Edited by:
Jorge Miguel Gaspar-Escribano, Polytechnic University of Madrid, Spain

Reviewed by:
Vladimir Sokolov, Saudi Geological Survey, Saudi Arabia
Dinesh Kumar, Kurukshetra University, India
Danilo Galluzzo, Istituto Nazionale di Geofisica e Vulcanologia (INGV), Italy

****Correspondence:***
Nitin Sharma
withnitin@gmail.com

Specialty section:
This article was submitted to Solid Earth Geophysics, a section of the journal Frontiers in Earth Science

Received: *27 August 2020*
Accepted: *22 October 2021*
Published: *23 November 2021*

Citation:
Sharma N, Srinagesh D, Suresh G and Srinivas D (2021) Stochastic Simulation of Strong Ground Motions From Two M > 5 Uttarakhand Earthquakes. Front. Earth Sci. 9:599535. doi: 10.3389/feart.2021.599535

INTRODUCTION

The much evident Himalayan seismicity is attributed to the collision between the Indian and Eurasian plate. The Himalayan arc extends up to 2,500 km from the Indus River Valley in the west to the Brahmaputra river in the east and holds high seismic risk to the population residing in India and surrounding regions. The Western Himalayas including the states of Jammu and Kashmir, Himachal Pradesh, and Uttarakhand experience moderate to large magnitude earthquakes regularly.

The historical studies show that the Himalayas have witnessed one of the largest magnitude earthquakes among continental–continental collision boundaries. The 1897 Assam (M = 8.0), 1950 Assam–Tibet (M = 8.6), 1934 Bihar–Nepal (M = 8.0), 1999 Chamoli (M = 6.8), 2005 Kashmir (M =

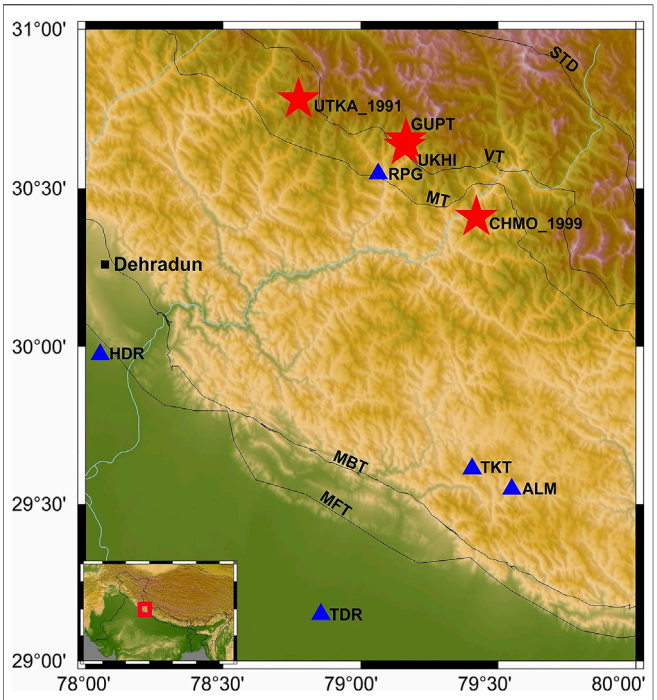

FIGURE 1 | Map showing location of earthquakes (red asterisk) and distribution of recording stations (Green triangles).

7.6), and 1991 Uttarkashi (M = 6.8) are a few earthquakes to mention which has affected around more than a million people in terms of deaths, injuries, and other damages combined.

The recent Nepal earthquake M_w = 7.8 that occurred on 25 April 2015 affected four neighboring countries. It is reported by many agencies like the Center for Disaster Management and Risk Reduction Technology (CEDIM) (2015), that the total economic loss is in the order of 10 billion U.S. dollars, which is about a half of Nepal's gross domestic product. The 2015 earthquakes will have grave long-term socioeconomic impact on people and communities in Nepal [United Nations Office for the Coordination of Humanitarian Affairs (UN-OCHA) (2015)] (Goda et al., 2015). The hazard and the consequent risk related to earthquakes will continue to rise in the Himalayan region with an increase in population and related infrastructure. Thus, it is an obligation to find and keep the scientific knowledge updated in order to better understand the ground excitations triggered by the earthquakes and the related response of the structures during the ground vibrations.

In order to understand and contribute to the seismic hazard studies in the Himalayan region, we analyzed and simulated two moderate-size earthquakes that occurred in Guptakashi (mb = 5.6) and Ukhimath (mb5.1) regions of Uttarakhand state on 06/02/2017 and 06/12/2017, respectively (NEIC and USGS). We choose these earthquakes because they occurred at the same location within a gap of 10 months and share the same epicentral zone of 1991 M_w = 6.8 Uttarakhand earthquake and 1999 M_w = 6.5 Chamoli earthquake. Moreover, the location of these earthquakes falls very near to the seismic gap capable of yielding catastrophic earthquakes in future (see **Figure 1**). Though no great earthquake has occurred in the Garhwal–Kumaun region in recent history, this section of the Himalayas between the ruptured zones of Kangra (1905) and Bihar–Nepal (1934) earthquakes has been recognized as the seismic gap, and it has been interpreted to have accumulated strain to generate huge earthquakes in the future (Khattri and Tyagi, 1983; Yeats and Thakur, 1998; Bilham, 2001; Kumar and Sharma, 2019).

Therefore, we propose to simulate the ground motions from these two earthquakes by adopting a well-known stochastic point source modeling technique. The technique assumes the spectral amplitude of the ground motion with the engineering notion that high-frequency motions are basically random vibrations (Hanks, 1979; Mc Guire and Hanks, 1980; Hanks and Mc Guire, 1981; Boore, 2003). The source of these random vibrations (earthquake) is assumed as a circular point source (Brune's model) and the amplitude spectra follows ω^{-2} fall with frequency. It is a simple technique that has been as successful as more sophisticated methods in predicting ground motion amplitudes over a broad range of magnitudes and distances. In spite of its popularity, this technique has certain limitations which cannot be neglected, especially when the distance between the source to site does not offer the agreement for point source assumption, that is, if source dimension <= epicenter distance. The technique does not consider the rupture geometry and directivity effects which cannot be ignored in case of large-magnitude earthquakes. Therefore, the finite fault approach is a preferable tool, especially for near-field simulations that can account for both fault and the directivity effects (Beresnev and Atkinson, 1997). Nevertheless, stochastic modeling has considerable advantage for being simple. The technique requires little or no information on the slip distribution on fault. Therefore, it becomes a good modeling tool for past earthquakes as well as for future events with unknown slip distributions.

Thus, our study expresses that the simple assumption of ω^{-2} circular point source (Brune's model) is good enough to synthesize seismograms from moderate-size earthquakes. In this article, we have made an attempt to reproduce the time histories by using the already-reported parameters required for simulation such as medium properties in terms of quality factor published in various literature works. An average value of the attenuation property of the medium, that is, quality factor (Q_s = $130.4*(f^{0.998})$) (Knopoff, 1964) reported by many studies (see Gupta and Kumar, 2002; Parvez et al., 2003, Joshi, 2006a; 2006b; Chopra et al., 2012; Sharma et al., 2014; Harinarayan and Kumar, 2018) for Western Himalayas is used and found reliable to reproduce the strong ground motion (herein after SGM) in good agreement with the observed data. We emphasize that averaging the parameter values from many studies that focused on the same region will reduce the associated error of the parameters and deliver the optimum values useful for the modeling. We estimated the suitable stress drop values for both the earthquakes by generating a number of time histories and comparing the RMS error for each value of stress drop between the observed and predicted PGA values. The stress drop

estimated for Guptakashi (mb = 5.6) and Ukhimath (mb5.1) are 73 and 105 bars, respectively. The values are very well in comparison with the values obtained by Joshi, 2006a, 2006b; Chopra et al., 2012; Sharma et al., 2014.

This study also emphasizes the contribution from the local site effect. The local site effect is proposed to obtain empirically which generally shows very large variations as compared to the source and medium properties. Therefore, in this study, the modeled acceleration spectra is structured by using source and medium information at first, and then it is corrected by the local site effects beneath each recording station, which is estimated empirically using the H/V method (Nakamura, 1989; 2008).

The site-corrected spectra (herein after synthetic acceleration spectra) are then compared with the Fourier amplitude spectra (herein after FAS) of the observed accelerograms obtained from the recorded waveform data. The comparison is done for frequency ranges between 0.1 and 10 Hz.

The synthetic acceleration spectra are then inverted to obtain the stochastic time series (synthetic accelerograms) and compared with observed accelerograms for amplitude (peak ground accelerations, PGA). There is a good agreement between the observed and predicted peak ground accelerations. This indicates that the considered parameters such as stress drop and attenuation properties are appropriate for strong ground motion modeling in this region.

The response spectra with 5% damping at different structural periods is also obtained from the synthetic and recorded accelerograms. The modeled pseudo spectral accelerations (PSA), velocity (PSV), and displacement (PSD) obtained are compared with the observed ones for both the earthquakes at each station.

The observed and estimated PGA values are also compared with existing GMPEs for shallow crustal seismicity (see results and discussion section). The above mentioned work on the simulation of strong ground motions is encouraging and can be adopted to predict the ground motion parameters like PGA at different distances for a hypothesized moderate to large magnitude earthquake for example, say M = 7.0 or more. However, it is emphasized that the site effect must be obtained empirically so that the observed acceleration spectra are inclusive of the local site effect. The details of data processing, methodology, and results are discussed in the following sections.

The confidence level and mismatch between the simulations and recorded data is expressed by associating the predictions with standard deviations, which are calculated from distribution of residuals ($\log_{10}Y^{obs}$—$\log_{10}Y^{pred}$), that is, common log difference between the observed and simulated data.

It is highlighted that this study is carried out to propose the idea to experiment with the existing parameters obtained from the larger dataset and check the reproducibility of ground motions and the reliability of model parameters even for small datasets. The estimated results obtained by the proposed approach assure the purposefulness of quick estimation of PGA values and preserve the reliability of ground motion parameters.

Data Processing

Two earthquakes of magnitude mb = 5.6 and mb = 5.1 occurred in the Uttarakhand region on 06/02/2017 and 06/12/2017 (Guptakashi and Ukhimath earthquakes, respectively). These earthquakes were well recorded at five stations, namely, Almorah (ALM), Haridwar (HDR), Rudraprayag (RPG), Thakurdwar (TDR), and Tarikhet (TKT) which are equipped with strong-motion broadband velocity seismographs (for details, refer Chadha et al., 2016). The recorded waveforms are converted into accelerations after applying instrument correction. The mean and the trend were also removed. Then, a zero-phase shift, Butterworth filter in the frequency band between 0.1 and 10 Hz is applied. The station location along with the epicenters is shown in **Figure 1**. The hypocenter parameters of the earthquakes are mentioned in **Table 1**.

Theory and Methodology

The stochastic method adopted in this article is construed from Boore, 2003; 2009. The basis of this technique can be cited through the works of Hanks, 1979; Mc Guire and Hanks, 1980; Hanks and Mc Guire, 1981. The technique assumes that the seismic signal recorded from the far field can be considered as band-limited, finite-duration, white Gaussian noise, and that the source spectra are described by a single corner frequency model whose corner frequency is proportional to the earthquake size. According to Brune (1970, 1971), the source scaling is expressed as $f_c \sim \omega^{-2}$.

The three main elements which constitute the seismic waveform are source (earthquake), path (the medium through which the seismic waves propagate), and the site at which the receivers are deployed and the waveform gets recorded.

These ground motions recorded by the seismograph (ground accelerations) can be expressed as a convolution of the above mentioned source, path, and site effects, which is mathematically represented by the following functional form (**Eq. 1**) (Boore and Atkinson, 1987):

$$A(f) = C \cdot M_o \cdot S(f) \cdot D(f) \cdot SE(f), \tag{1}$$

where *A(f)* is the *acceleration spectra*, *C* is a *constant*, M_o is the *seismic moment*, *SE(f)* is the *site effect*, *S(f)* represents the *source function*, and *D(f)* represents the frequency dependent attenuation function, that is, *medium effect*.

The source function in the frequency domain is represented in **Eq. 2**:

$$S(f) = \frac{(2 \cdot \mathrm{pi} \cdot f)^2}{1 + (f/f_c)^2}, \tag{2}$$

where f_c is the corner frequency which is expressed as $f_c = 2.34\beta/2\pi r_o$, β is the shear wave velocity in the crust (here it is 3.5 km/s), and r_0 is the source radius which is obtained through the stress drop and seismic moment as mentioned in **Eq. 3**:

$$\Delta\sigma = 0.4397 \cdot M_0/r_0^3, \tag{3}$$

$$C = \frac{R_{\theta\phi} \cdot \mathrm{FS} \cdot \mathrm{PR}}{4\pi\rho\beta^3}. \tag{4}$$

The constant *C* represented in **Eq. 4** is considered as the important factor for any site for a given earthquake. It is preferred for a double couple model embedded in an elastic

TABLE 1 | Description of the source and medium parameters used for simulation.

	Magnitude (mb) (USGS)	Depth (km)	Seismic moment (dyne-cm)	Corner frequency (f_c)	Source radius (r_0) km	Stress drop (bars)	Quality factor (Q_s)
Guptakashi 06/02/2017	5.6	16.1	3.12×10^{24}	0.56	2.01	73	$130.4*(f^{0.998})$
Ukhimath 06/12/2017	5.1	10.0	5.5×10^{23}	1.02	1.10	100	$130.4*(f^{0.998})$

medium, while considering only the S waves (Boore, 1983). It accounts for the combined effects of the radiation pattern ($R_{\theta\Phi}$ =*0.55*), free surface effect *FS* (here it is 2), partition of energy into two horizontal components *PR* (here it is $1/\sqrt{2}$), and density ρ (here 2.67 g/cm^3) and the shear wave velocity β (here 3.5 km/s), for the upper crust, respectively.

The decay of acceleration spectra due to elastic and anelastic attenuation (geometric and scattering effects) is represented by the **Eq. 5**:

$$D(f) = \frac{e^{(-\pi f R)/(Q\beta)}}{R} \cdot P(f, f_{max}), \quad (5)$$

where R is the hypocentral distance and $P(f_{min}, f_{max})$ represents the high-cut filter which can be interpreted as attenuation near the recording site (Hanks, 1982), with f_{max} = 10 Hz is used here (Joshi, 2006a; 2006b, V. Sri Ram et al., 2005).

The quality factor Q_s (Knopoff, 1964) in exponential term accounts for the anelastic attenuation and scattering nature of the medium.

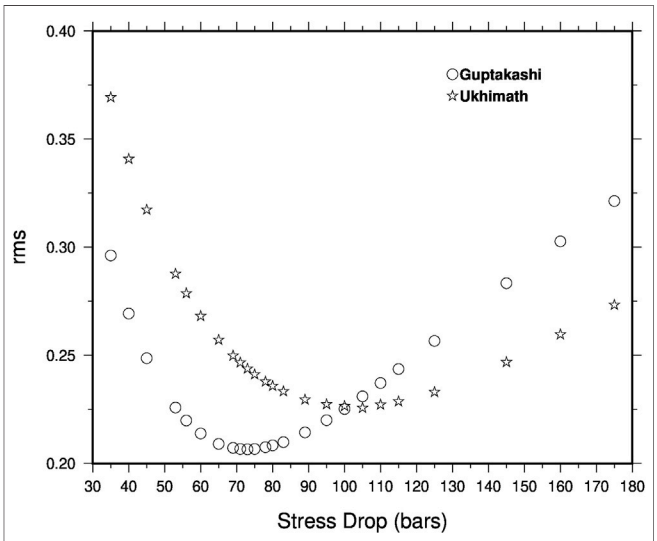

FIGURE 2 | RMS errors with respect to the stress drop values used for simulations of time histories for both Guptakashi and Ukhimath earthquakes.

Selection of Parameters

Source Parameters

The source parameters like seismic moment and stress drop of the Guptakashi and Ukhimath earthquakes are mentioned in **Table 1**. The parameter like seismic moment is obtained by using the definition proposed by Johnston (Johnston., 1996), expressed in **Eq. 6**. The seismic moment obtained is as follows:

$$\log_{10} M_o = 18.75 + 0.496mb + 0.0946mb^2. \quad (6)$$

This relation is also used to obtain the moment magnitude M_w by using the definition proposed by Hanks and Kanamori 1979, as expressed in **Eq. 7**.

$$M_w = \frac{2}{3}\log_{10} M_o - 10.7. \quad (7)$$

It appears that M_w for both Guptakashi and Ukhimath earthquakes are equal to *mb;* thus, we decided to retain the magnitude scale in *mb* for the sake of clarity.

The source parameter in the term stress drop value is estimated via the number of iterations. The values are assumed to be normally distributed ranging between 35 and 200 bars. Then the stress drop values are randomly extracted from the distribution. The time series is generated for each value to stress drop, along with all other path and site effect parameters (see sections below) and compared with the observed PGA values. The stress drop with the minimum RMS error is chosen and considered for the final simulation and modeling of the response spectra (**Figure 2**). The stress drop values obtained are 73 and 105 bars for Guptakashi (mb = 5.6) and Ukhimath (mb5.1) earthquakes, respectively.

Moreover, the work of Joshi, 2006a, 2006b; Chopra et al., 2012; Sharma et al., 2014; Kumar et al., 2014 suggest the similar values for the stress drop for the western Himalayan region.

These values are further used to calculate the corner frequency *fc* and the source radius r_0 of both the Guptakashi and Ukhimath earthquakes for the analysis (please refer to **Table 1** for the values). It should be noted that the estimation of stress drop is very critical and depends upon earthquake to earthquake. These values should be estimated for each source to minimize the random effects on the uncertainties associated with the source.

Path Effect Q and R

The decay of seismic waves with distance is classified by geometrical spreading and the aneslastic effect of the medium. Therefore, we consider the anelastic effect of the medium as an average value of the quality factor $Q_s = 130.4*(f^{0.998})$ obtained from different studies [see Parvez et al., 2003 ($Q = 127f^{0.96}$), Joshi, 2006a ($Q = 112f^{0.97}$), Sharma et al., 2014 ($Q = 159f^{1.16}$), Harinarayan and Kumar, 2018 ($Q = 105f^{0.94}$), and Gupta and Kumar, 2002 ($149f^{0.95}$)] to account for the attenuation effect due

to the medium. The decay associated with geometrical spreading is accounted as the inverse of distance (1/R). The hypocentral distance R is derived from the depth and epicentral distance information from the catalog available at USGS (https://earthquake.usgs.gov).

It is to emphasize here that we prefer the average values because the averaging not only reduces the overall errors associated with the considered parameters but also furnish the combined contributions from the individual studies done to estimate the source and the medium property of the studied region.

Time Duration and Envelop

The choice of length of the envelop and the criteria for time duration of the vibration is based on the suggestions made by Boore, 2003; Saragoni and Hart (1974). The following equations are used to shape the envelop (see **Eqs. 8–11**) and to determine the time duration of a synthetic seismogram (see **Eqs. 12**, **13**):

$$\mathrm{wt} = \mathrm{a}\left(t/t_{\eta}\right)^{b} \cdot \exp\left(-c \cdot \left(t/t_{\eta}\right)\right), \tag{8}$$

where a, b, and c values are determined such that the function *wt* should have a peak amplitude of unity. The equations for a, b, and c are as follows:

$$b = -\left(\epsilon \cdot \ln\left(\eta\right)\right)/\left(1 + \epsilon \cdot \ln\left(\epsilon\right) - 1\right), \tag{9}$$

$$c = b/\epsilon, \tag{10}$$

$$a = \left(\exp\left(1\right)/\epsilon\right)^{b}. \tag{11}$$

The values used to designed the window are $\eta = 0.05$ and $\epsilon = 0.2$ (see Saragoni and Hart, 1974; Boore, 2003).

The duration of the window is defined by the equations below:

$$t_{\eta} = \mathrm{f}\mathrm{T}_{\mathrm{gm}} \cdot T_{\mathrm{gm}}, \tag{12}$$

$$T_{\mathrm{gm}} = 1/f_{c} + 0.5 \cdot R, \tag{13}$$

where R is the hypocentral distance and $fT_{\mathrm{gm}} = 2.0$.

Local Site Effect

The local site effect varies from site to site, and these variations are large as compared to the source and medium properties. Thus, we prefer to obtain the site factor empirically by adopting the method popularly known as the H/V ratio method (see Nakamura, 1989; 2008). The technique was further extended by Lermo and Garcia (Lermo and Chávez-García, 1993). This is based on the shear wave spectral ratio of the horizontal components to the vertical component. This method nullifies the effect from the source and propagating medium, therefore endorsing the effect of local geological site conditions at a shallow level.

Many studies like those by Oubaiche et al., 2016, Nakamura (1989, 2000, 2009), Konno and Ohmachi (1998), and Bonnefoy–Claudet et al. (2008) have found a strong correlation between H/V and SH transfer function. The H/V ratio is used as a transfer function which provides the level of site amplification, but in a broader manner. Therefore, an average value within the frequency range from 0.1 to 10 Hz is used as a site amplification factor (Field and Jacob, 1993) (see **Figure 3**). Nevertheless, it should be kept in mind that this does not provide the quantitative estimation of site amplification but it gives the comprehensive idea of the site effect when compared with Vs30 values. In this case, site amplification is considered as a random variable and obtained empirically. It is to be noted that the scarce dataset and for the sake of simplicity, we considered it as a consolidated factor of site amplification and multiplied as a scalar value with the modeled acceleration spectra to get the site-corrected spectra (synthetic acceleration spectra) at each station.

The synthetic acceleration spectra are converted to acceleration time histories through the inverse Fourier transform. It is a very crucial step where the number of Fourier points should be kept beyond the time domain signal length. This is achieved by padding zero to get the nearest value in terms of power of 2.

Hence, the synthetic accelerations time histories are compared with the observed time series in terms of PGA. The details are discussed in the next section.

RESULTS AND DISCUSSION

The stochastic simulation of two earthquakes, Guptakashi and Ukhimath with magnitudes mb = 5.6 and mb = 5.1, which occurred at shallow depths of 16.1 and 10 km, respectively, has been attempted. These events are located between the epicenters of 1991 Uttarkashi (M_w 6.8) and 1999 Chamoli (M_w 6.5) earthquakes. This zone is capable of yielding a large magnitude earthquake in near future (Khattri and Tyagi, 1983; Yeats and Thakur, 1998). All the information (location, magnitude, etc.) of the earthquakes used for simulation purposes is obtained from public domain agencies [United States Geological Survey (NEIC and USGS)]. Both earthquakes are recorded at five stations [Almorah (ALM), Haridwar (HDR), Rudraprayag (RPG), Thakurdwar (TDR), and Tarikhet (TKT)] located within the hypocentral range from 14 to 170 km (**Figure 1**). The maximum PGA observed at the nearest station RPG is 165.52 and 167.255 cm/s^2 station for Guptakashi and Ukhimath earthquakes, respectively. This brings Rudrapyag district (RPG) under moderate to severe intensity zone category.

The S waves from the horizontal components are considered for the analysis. The modeled spectra are obtained by using the source and medium information as discussed in the methodology section above.

The synthetic acceleration spectra are then obtained by correcting the modeled spectra by the site amplification factor obtained after H/V ratio (Nakamura, 2008). The H/V ratio is obtained between 0.1 and 10 Hz (see **Figures 3A,B**) at each station and for both the earthquakes separately (see **Table 1**, **2**). The mean site amplification factor ranges between 1.2–1.8. This might be due to the fact that most of the sites are either rock sites or hard soil, which is not causing very high amplifications (Anbazhagan et al., 2019). The mean value of H/V ratio is calculated for this frequency range and multiplied with the modeled spectra to obtain the final corrected modeled spectra, that is, synthetic acceleration spectra. It is worth to mention here that through this practice, the station effects considered here are

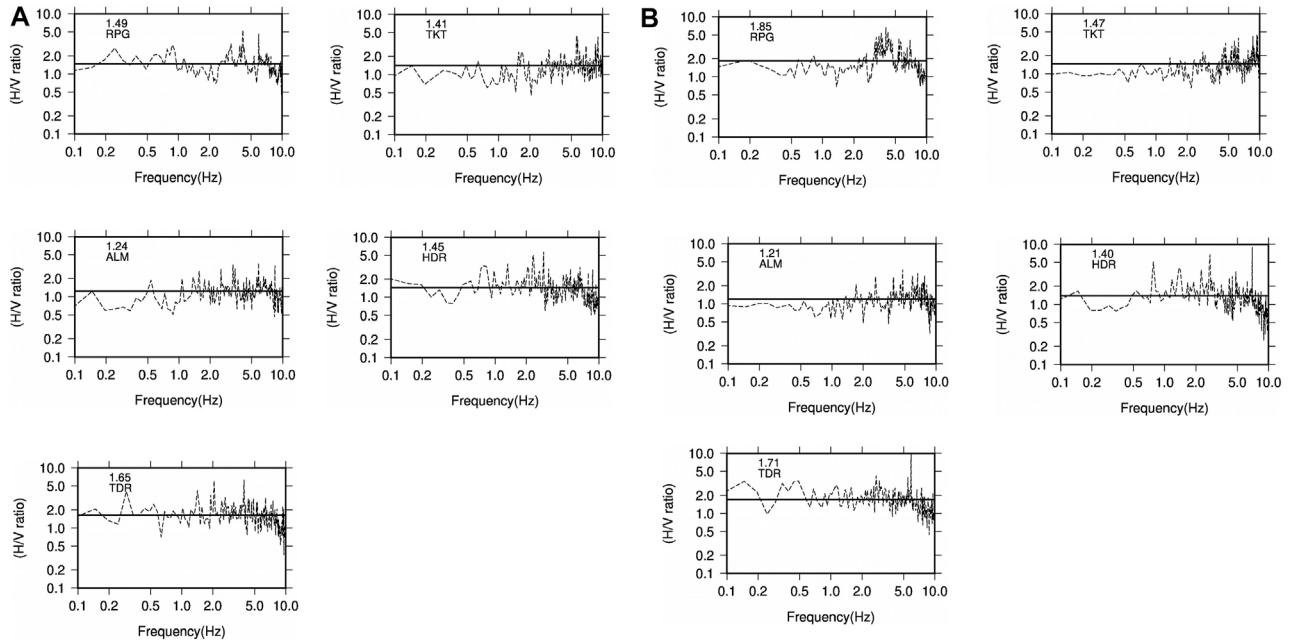

FIGURE 3 | Plots of H/V ratio at each station for Guptakashi earthquake **(3a)** and Ukhimath earthquake **(3b)**. The solid line represents the mean value of H/V ratio for all the considered frequency ranges (0.1–10 Hz). The mean values used as the site amplification factor are also mentioned in the plots.

TABLE 2 | Table showing station codes, site amplification factor, observed and predicted PGA values, and standard errors among FAS for Guptakashi earthquake, M_b = 5.6, 06/02/2017.

S.No.	Station code	Epicentral distance (km)	Site amplification factor	Observed PGA values E-W (cm/s^2)	Observed PGA values N-S (cm/s^2)	Predicted PGA values (cm/s^2)
1	RPG	15.5	1.49	73.24	165.52	153.19
2	TKT	117.7	1.41	3.87	4.76	7.94
3	ALM	128.2	1.24	9.16	7.96	5.90
4	HDR	130.9	1.45	8.02	5.96	6.65
5	TDR	169.6	1.65	6.25	9.02	4.49

not based on the average V_S30 values but include in a more general way to consider the site effects concurring to a systematic site amplification or attenuation. It is mentioned in the section above that with the constrained dataset, we considered the transfer function as a scaling factor to correct the modeled acceleration spectra for site effects. The FAS of recorded S waves (NS and EW) are then compared with the synthetic acceleration spectra (see **Figures 4A,B**).

It is interesting to note that even though with the general values of source and medium properties, the synthetic acceleration spectra provide reasonable estimates of the general shape and amplitudes of the spectra for most of the stations. The mismatch is observed at lower frequencies specially for the nearest stations like RPG, TKT, and ALM, but with an increase in the distance, the modeled and observed spectra match well even at low frequencies (HDR and TDR). It can be due to the adoption of the fixed rupture velocity used for the simulation of strong ground motions. In fact, the point source approximation is not always realized at all the epicentral distances.

Nevertheless, the synthetic accelerograms obtained by the inverse of FAS (see the methodology section) shows good agreement with the observed accelerograms, specifically in term of amplitudes. The recorded and simulated seismograms for both Guptakashi and Ukhimath earthquakes at each station are illustrated in **Figures 5A,B**. The predicted and observed PGA values for both Guptakashi and Ukhimath earthquakes can be seen **Tables 2**, **3**. The predicted values agree with the NS components because they are aligned with the radial component.

We believe that the ground motion estimation should also serve the purpose of civil engineers, as they are more interested in spectral accelerations at different structural periods. Therefore, keeping it in mind, we also calculated the pseudo spectral accelerations (PSA), velocity (PSV), and displacement (PSD) with standard 5% damping factors at different structural periods ranging between 0.1 and 10 s. The spectral ordinates are calculated at each station and for both the earthquakes (**Figures 6A,B**). These spectral acceleration, velocities, and

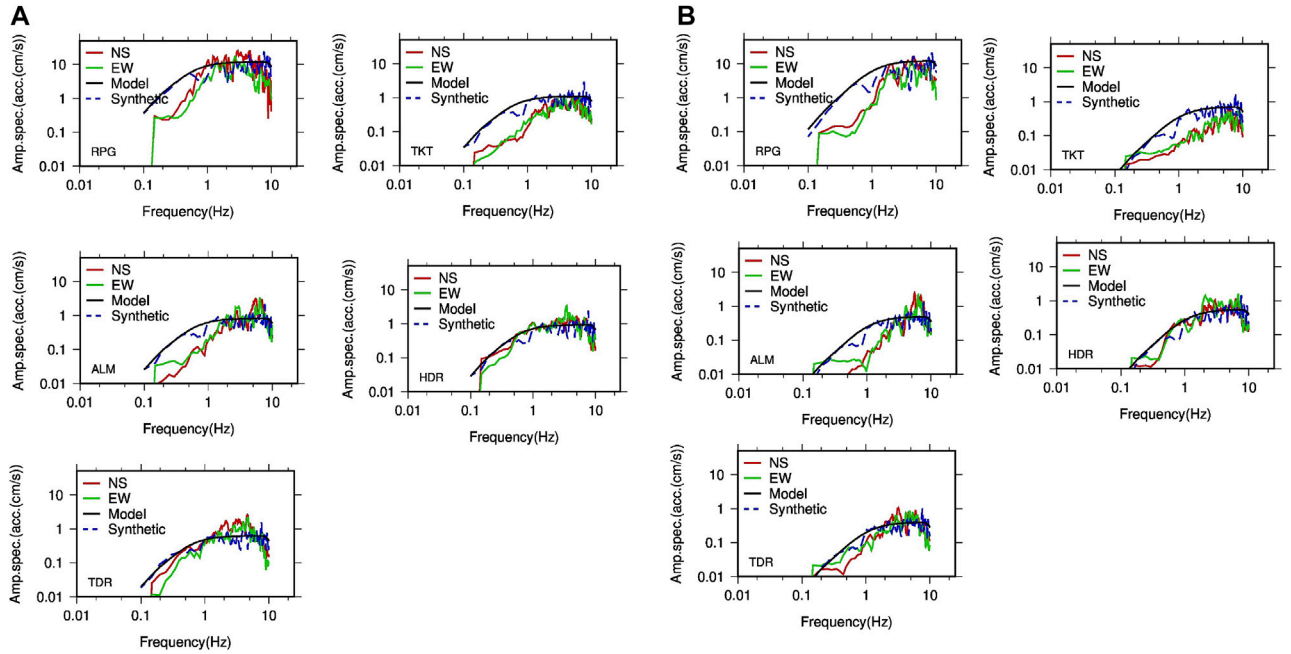

FIGURE 4 | Comparison of the observed and synthetic Fourier amplitude spectra (FAS) for Guptakashi earthquake **(4A)** and Ukhimath earthquake **(5B)**. The comparison shows good match between modeled and observed ones..

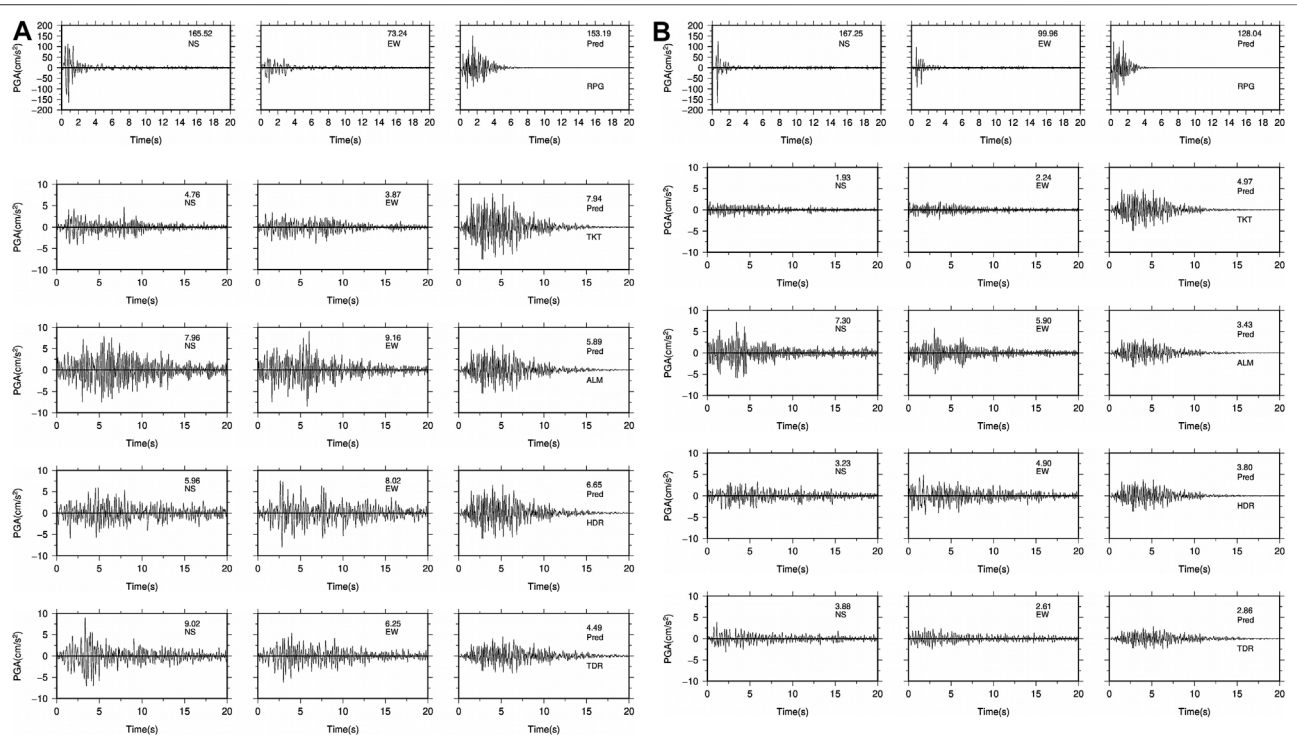

FIGURE 5 | Comparison of recorded horizontal (NS and EW) components of accelerograms and the synthetic accelerograms for both Guptakashi **(5A)** and Ukhimath earthquakes **(5B)**. The PGA values are mentioned along with the horizontal component and station codes.

TABLE 3 | Table showing station codes, site amplification factor, observed and predicted PGA values, and standard errors among FAS for Ukhimath Earthquake, M_b = 5.1, 06/12/2017.

S.No.	Station code	Epicentral distance (km)	Site amplification factor	Observed PGA values E-W (cm/s^2)	Observed PGA values N-S (cm/s^2)	Predicted PGA values (cm/s^2)
1	RPG	13.5	1.85	99.96	167.25	128.04
2	TKT	115.6	1.47	2.24	1.93	4.97
3	ALM	126.2	1.21	5.90	7.30	3.43
4	HDR	129.2	1.40	4.90	3.23	3.80
5	TDR	167.3	1.71	2.61	3.88	2.86

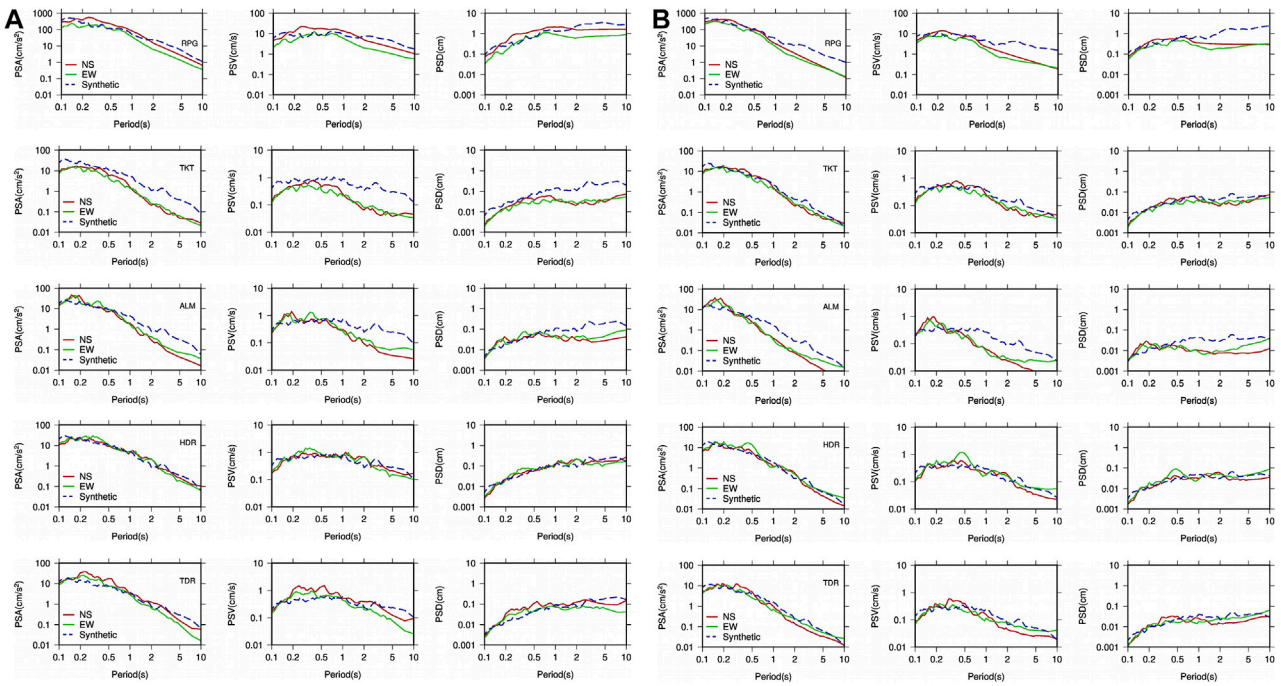

FIGURE 6 | Pseudo spectral accelerations, velocities, and displacements estimated from the observed data and its comparison with the synthetic one.

displacement obtained from the observed data are compared with the synthetic ones.

There are deviations observed specially at lower frequencies, which result in under- and over-prediction of the observed response spectra. Even though the general shape of the response spectra is maintained for synthetic data, these deviations are predominant before 0.5 s, especially at RPG, TKT, and ALM stations. The predictions at lower period are overestimated. The distant stations HDR and TDR have an overall good match. This mismatch reminds the fact that there are some random factors which might not be fully captured during the evaluation of source (e.g., stress drop), medium (Q_s, quality factor), and site properties. The synthetic models do have some limitations in defining the complex source, medium, and site properties perfectly. Moreover, the point source approximations cannot be achieved at all the source to receiver distances.

Further, we have used the mean values which vary from region to region, especially the Q_s value, which also varies with epicentral distances, but we have considered the common and averaged attenuation value for all the stations. The epistemic uncertainties associated with model parameters specifically with the Qs and site effect will definitely affect the results. We tried to encounter random effects associated with earthquake uncertainties. We estimated stress drop values for the individual earthquakes by iteratively generating a number of time histories using different values of stress drop. The values which provide minimum RMS errors are considered for simulations (see **Figure 2**). Overall, we found good agreement between observed and predicted data in terms of both amplitudes and the response spectra.

Residual Analysis

We estimated the residuals which is common logarithmic ($\log_{10}$) difference between the observed (NS and EW components) and the predicted PGA values for both the earthquakes at each station (see **Figure 7**). It is observed that the total scattering of residuals lies between +0.33 and −0.41 and total standard deviation estimated is 0.22. The computed

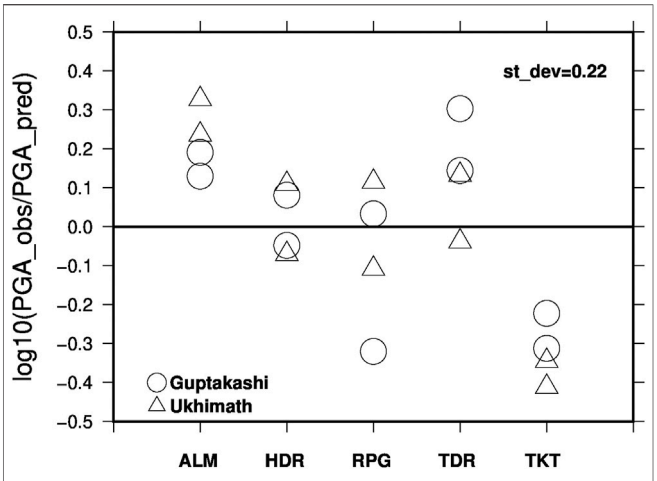

FIGURE 7 | Comparison of the observed and predicted PGA values with GMPEs are shown here. The solid line indicates the mean values and +/− 1sigma is represented by the dashed lines. Asterisks represent the predicted values and the observed PGA values are represented by circles.

residuals for each station demonstrates how well the simulations replicate the real data. The work by Bommer et al., 2004 and Strasser et al., 2008 with 40 years of data also summaries the values of standard deviations which tend to lie between 0.15 and 0.35 in $\log_{10}$ units for most of the ground motion prediction models. This further clarifies that our proposed idea is very well justified.

Comparison With Existing GMPEs

The results motivated us to compare our predicted and observed PGA values with some of the popular GMPEs developed for Western Himalayas and similar shallow crustal seismic environment. It is very interesting to note that our predicted and observed values are very well explained by some of the robust GMPEs, while some of the equations under/over predict our PGA values either at small distances or at large distances. The GMPEs, for example, developed by Emolo et al., 2015 for the south Korean Peninsula, and the GMPEs developed by Bommer et al., 2003 for European scenarios appeared to explain the observed and predicted PGA values within +/−1 sigma at small distances as compared to large distances (see **Figure 8**). While the GMPEs developed by Iyenger and Gupta, 2004; Joshi et al., 2012 could not explain the data very well at small distances, they over predicted the PGA values for Guptakashi earthquake. This must be due to the regional dependencies which must be taken into account while developing or selecting the GMPEs to perform seismic hazards. Overall, the GMPES could not convincingly explain the observed values for small to large distance ranges even though the magnitude is kept same. Therefore, it is to emphasize the fact that there is always a need to update the ground motion prediction models with the addition of more data in terms of broad magnitude and distance ranges.

The present study emphasizes the prospects to reproduce the results for different earthquakes by using the model parameters, which are already obtained by other studies through inversion of large datasets in the same region. Moreover, this work also proposed the idea to experiment with the parameters obtained from the largest dataset and check the reproducibility of ground motions with these parameters even for small datasets.

This idea will not only help in gaining clarity over existing studies but also help in identifying the uncaptured properties of the source, medium, and site to minimize the associated errors by refining the model parameters. For example, the aleatory and epistemic uncertainties associated with model parameters should always be considered while modeling the ground motion, especially when there is a larger dataset.

CONCLUSION

1) The stochastic modeling technique is adopted to simulate strong ground motions. The simulation is done for two earthquakes that occurred in Uttarkashi with magnitude M > 5 on 06/02/2017 and 06/12/2017 [Guptakashi (mb = 5.6) and Ukhimath (mb = 5.1), respectively].

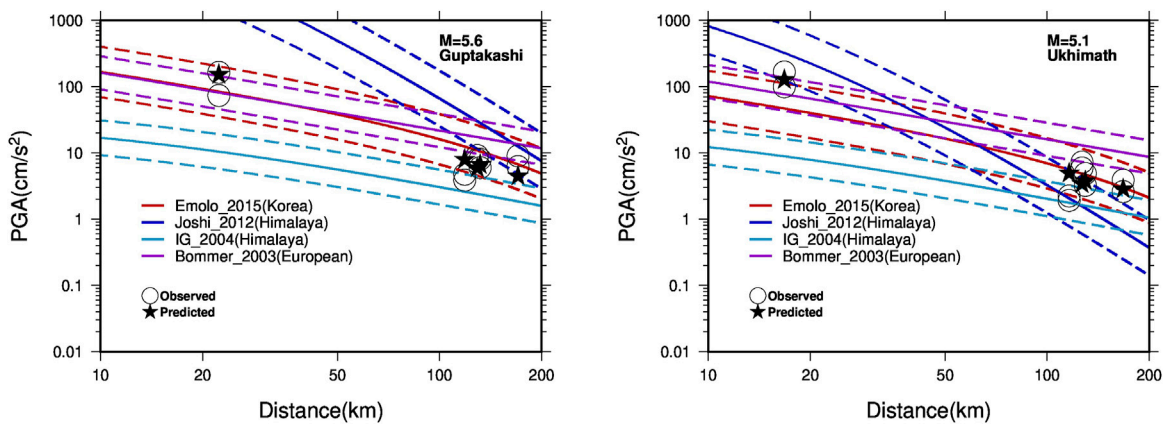

FIGURE 8 | Distribution of residuals for the PGA values at each station for both Guptakashi and Ukhimath earthquakes.

2) The synthetic spectra shows good agreement with the observed Fourier amplitude spectra (FAS) obtained from the recorded waveform data. The stochastic time series is also compared with the observed waveforms in terms of amplitude (PGA). The response spectra obtained from the simulated waveform and from the observed ones were found to be a good match, when compared.
3) The overall good match between the observed and predicted ground motion parameters prove that the simple assumption of circular crack model (ω^{-2}, point source) and parameters derived from public agencies are sufficient enough for the model, and the ground motions are generated from earthquakes.
    1) The mismatch observed at lower frequencies, especially at near field stations, can be due to the adoption of fixed rupture velocity used for the simulation of strong ground motions. Moreover, the simple/point source model does have some limitation in defining the complex source, medium, and site properties perfectly.
    2) The random or between-event uncertainties should be considered while modeling the ground motion, when associated with the different sources even in the same region. The epstemic uncertainties associated with the medium might decrease with the addition of information unlike aleatory uncertainties.
    3) These preliminary results obtained not only validate the technique but are also encouraging to extend the technique further and to simulate strong ground motions for a hypothetical large magnitude earthquake for M = 7.0 and above in the Himalayan region.
    4) Such techniques are very useful in anticipating the potentially damaged zone for the future earthquake, and hence mitigating the seismic hazard.
    5) The comparison of our predictions and observed PGA data with existing GMPEs shows that our predictions are very well explained by many robust GMPEs developed for similar shallow crustal seismic environment in Asia and Europe. Moreover, it is also observed that there are certain discrepancies in the predicted PGA values and can be ascribed to the fact that the ground motion parameters are region specific; hence, prediction models are needed to be developed and updated with time. Therefore, in a nutshell, it can be concluded that the proposed work and results obtained in this study are very optimistic and contribute toward the understanding of strong ground motions in the Himalayan region.

DATA AND RESOURCES

The seismograms used in this study were recorded by stations from the Indo-Gangetic Plains network (CIGN), maintained by the Council of Scientific and Industrial Research-National Geophysical Research Institute (NGRI). The earthquake information used for simulation purpose is obtained from the catalog available at the United States Geological Survey (NEIC and USGS), https://earthquake.usgs.gov/.

DATA AVAILABILITY STATEMENT

The raw data supporting the conclusions of this article will be made available by the authors, without undue reservation.

AUTHOR CONTRIBUTIONS

NS designed the problem, carried out the analysis, and drafted the manuscript. DS suggested necessary modifications in the manuscript. GS and DS retrieved the data from the stations and provided instrument information.

ACKNOWLEDGMENTS

The authors acknowledge the support and grant received from the projects MLP—6401-28 (DSN) of National Geophysical Research Institute funded by Council of Scientific and Industrial Research, Government of India. The authors are also thankful to the Director, CSIR—NGRI, Hyderabad, for his kind support and permission to publish the research work. All the figures are prepared using the Generic Mapping tool (Wessel and Smith, 1991). The simulation is done using MATLAB Software. The authors are extremely thankful to the editor and the reviewers for their constructive comments which have definitely improve the study and the manuscript.

REFERENCES

Anbazhagan, P., Srilakshmi, K. N., Bajaj, K., Moustafa, S. S. R., and Al-Arifi, N. S. N. (2019). Determination of Seismic Site Classification of Seismic Recording Stations in the Himalayan Region Using HVSR Method. *Soil Dyn. Earthquake Eng.* 116, 304–316. doi:10.1016/j.soildyn.2018.10.023

Beresnev, I. A., and Atldnson, G. M. (1997). Modeling Finite-Fault Radiation from the 09 N Spectrum. *Bull. Seism. Soc. Am.* 87, 67–84.

Bilham, R., Gaur, V. K., and Molnar, P. (2001). Himalayan Seismic Hazard. *Science* 293 (5534), 1442–1444. doi:10.1126/science.1062584

Bommer, J. J., Abrahamson, N. A., Strasser, F. O., Pecker, A., Bard, P.-Y., Bungum, H., et al. (2004). The challenge of Defining Upper Bounds on Earthquake Ground Motions. *Seismological Res. Lett.* 75 (1), 82–95. doi:10.1785/gssrl.75.1.82

Bommer, J. J., Douglas, J., and Strasser, F. O. (2003). Style-of-Faulting in Ground-Motion Prediction Equations. *Bull. Earthquake Eng.* 1, 171–203. doi:10.1023/A:1026323123154

Bonnefoy-Claudet, S., Köhler, A., Cornou, C., Wathelet, M., and Bard, P.-Y. (2008). Effects of Love Waves on Microtremor H/V Ratio. *Bull. Seismological Soc. America* 98 (1), 288–300. doi:10.1785/0120070063

Boore, D. M., and Atkinson, G. M. (1987). Stochastic Prediction of Ground Motion and Spectral Response Parameters at Hard-Rock Sites in Eastern North America. *Bull. Seismological Soc. America* 77 (2), 440–467.

Boore, D. M. (2009). Comparing Stochastic point-source and Finite-Source Ground-Motion Simulations: SMSIM and EXSIM. *Bull. Seismological Soc. America* 99 (6), 3202–3216. doi:10.1785/0120090056

Boore, D. M. (2003). Simulation of Ground Motion Using the Stochastic Method. *Pure Appl. Geophys.* 160, 635–676. doi:10.1007/PL00012553

Boore, D. M. (1983). Stochastic Simulation of High-Frequency Ground Motions Based on Seismological Models of the Radiated Spectra. *Bull. Seismol. Soc. Am.* 73, 1865–1894.

Chadha, R. K., Srinagesh, D., Srinivas, D., Suresh, G., Sateesh, A., Singh, S. K., et al. (2016). CIGN, A Strong-Motion Seismic Network in Central Indo-Gangetic Plains, Foothills of Himalayas: First Results. *Seismological Res. Lett.* 87 (1), 37–46. doi:10.1785/0220150106

Chopra, S., Kumar, V., Suthar, A., and Kumar, P. (2012). Modeling of strong Ground Motions for 1991 Uttarkashi, 1999 Chamoli Earthquakes, and a Hypothetical Great Earthquake in Garhwal-Kumaun Himalaya. *Nat. Hazards* 64, 1141–1159. doi:10.1007/s11069-012-0289-z

Emolo, A., Sharma, N., Festa, G., Zollo, A., Convertito, V., Park, J. H., et al. (2015). Ground-Motion Prediction Equations for South Korea Peninsula. *Bull. Seismological Soc. America* 105 (5), 2625–2640. doi:10.1785/0120140296

Field, E., and Jacob, K. (1993). The Theoretical Response of Sedimentary Layers to Ambient Seismic Noise. *Geophys. Res. Lett.* 20, 2925–2928. doi:10.1029/93gl03054

Goda, K., Kiyota, T., Pokhrel, R. M., Chiaro, G., Katagiri, T., Sharma, K., et al. (2015). The 2015 Gorkha Nepal Earthquake: Insights from Earthquake Damage Survey. *Front. Built Environ.* 1, 8. doi:10.3389/fbuil.2015.00008

Gupta, S. C., and Kumar, A. (2002). Seismic Wave Attenuation Characteristics of Three Indian Regions: A Comparative Study. *Curr. Sci.* 82, 407–413.

H, H., and Kumar, A. (2018). Estimation of Source and Site Characteristics in the North-West Himalaya and its Adjoining Area Using Generalized Inversion Method. *Ann. Geophys.* 62 (5), SE559. doi:10.4401/ag-7922

Hanks, T. C. (1979). Bvalues and ω−γseismic Source Models: Implications for Tectonic Stress Variations along Active Crustal Fault Zones and the Estimation of High-Frequency strong Ground Motion. *J. Geophys. Res.* 84, 2235–2242. doi:10.1029/jb084ib05p02235

Hanks, T. C. (1982). f max. *Bull. Seismological Soc. America* 72, 1867–1879. doi:10.1785/bssa07206a1867

Hanks, T. C., and McGuire, R. K. (1981). The Character of High-Frequency Strong Ground Motion. *Bull. Seismol. Soc. Am.* 71, 2071–2095. doi:10.1785/bssa0710062071

Iyenger, R. N., and Ghosh, S. (2004). Microzonation of Earthquake hazard in Greater Delhi Area. *Curr. Sci.* 87, 1193–1202.

Johnston, A. C. (1996). Seismic Moment Assessment of Earthquakes in Stable continental Regions—I. Instrumental Seismicity. *Geophys. J. Int.* 124 (Issue 2), 381–414. doi:10.1111/j.1365-246x.1996.tb07028.x

Joshi, A. (2006a). Analysis of strong Motion Data of the Uttarkashi Earthquake of 20th October 1991 and the Chamoli Earthquake of 28th March 1999 for Determining the Mid Crustal Q Value and Source Parameters. *J. Earth Tech.* 43, 11–29.

Joshi, A. (2006b). Use of Acceleration Spectra for Determining the Frequency-dependent Attenuation Coefficient and Source Parameters. *Bull. Seismological Soc. America* 96, 2165–2180. doi:10.1785/0120050095

Joshi, A., Kumar, A., Lomnitz, C., Castaños, H., and Akhtar, S. (2012). Applicability of Attenuation Relations for Regional Studies. *Geofísica internacional* 51 (4), 349–363. doi:10.22201/igeof.00167169p.2012.51.4.1231

Khattri, K. M., and Tyagi, A. K. (1983). Seismicity Patterns in the Himalayan Plate Boundary and Identification of the Areas of High Seismic Potential. *Tectonophysics* 96, 281–297. doi:10.1016/0040-1951(83)90222-6

Knopoff, L. (1964). Q. *Rev. Geophys.* 2 (4), 625–660. doi:10.1029/rg002i004p00625

Konno, K., and Ohmachi, T. (1998). Ground-Motion Characteristics Estimated from Spectral Ratio between Horizontal and Vertical Components of Microtremor. *Bull. Seismol. Soc. Am.* 88, 228–241. doi:10.1785/bssa0880010228

Kumar, S., and Sharma, N. (2019). The Seismicity of Central and North-East Himalayan Region. *Contrib. Geophys. Geodesy* 49 (3), 265–281. doi:10.2478/congeo-2019-0014

Lermo, J., and Chávez-García, F. J. (1993). Site Effect Evaluation Using Spectral Ratios with Only One Station. *Bull. Seismol. Soc. Am.* 83 (5), 1574–1594. doi:10.1785/bssa0830051574

McGuire, R. K., and Hanks, T. C. (1980). RMS Accelerations and Spectral Amplitudes of strong Ground Motion during the San Fernando, California Earthquake. *Bull. Seismol. Soc. Am.* 70, 1907–1919. doi:10.1785/bssa0700051907

Nakamura, Y., (2008). "On H/V Spectrum," in The 14th World Conference on Earthquake Engineering, Beijing, China, October 12-17, 2008.

Nakamura, Y. (1989). A Method for Dynamic Characteristics Estimation of Subsurface Using Microtremor on the Ground Surface. *Q. Rep. Railway Tech. Res. Inst.* 30 (1), 25–30.

Nakamura, Y. (2009). "Basic Structure of QTS (HVSR) and Examples of Applications," in *Increasing Seismic Safety by Combining Engineering Technologies and Seismological Data.NATO Science for Peace and Security, Series C: Environmental*. Editors M. Mucciarelli, M. Herak, and J. Cassidy(Springer: Dordrecht).

Nakamura, Y. (2000). "Clear Identification of Fundamental Idea of Nakamura's Technique and its Applications," in Proc. of the 12th World Conference on Earthquake Engineering, Auckland, New Zealand, 30 January 30–February 4, 2000.

Oubaiche, E. H., Chatelain, J. L., Hellel, M., Wathelet, M., Machane, D., Bensalem, R., et al. (2016). The Relationship between Ambient Vibration H/V and SH Transfer Function: Some Experimental Results. *Seismological Res. Lett.* 87 (5), 1112–1119. doi:10.1785/0220160113

Parvez, I. A., Vaccari, F., and Panza, G. F. (2003). A Deterministic Seismic hazard Map of India and Adjacent Areas. *Geophys. J. Int.* 155, 489–508. doi:10.1046/j.1365-246X.2003.02052.x

Saragoni, G. R., and Hart, G. C. (1974). Simulation of Artificial Earthquakes. *Earthq. Eng. Struct. Dyn.* 2, 249–267.

Sharma, J., Chopra, S., and Roy, K. S. (2014). Estimation of Source Parameters, Quality Factor (QS), and Site Characteristics Using Accelerograms: Uttarakhand Himalaya RegionQS), and Site Characteristics Using Accelerograms: Uttarakhand Himalaya Region. *Bull. Seismological Soc. Americaulletin Seismological Soc. America* 104 (1), 360–380. doi:10.1785/0120120304

Strasser, F. O., Bommer, J. J., and Abrahamson, N. A. (2008). Truncation of the Distribution of Ground-Motion Residuals. *J. Seismol* 12 (1), 79–105. doi:10.1007/s10950-007-9073-z

Yeats, R. S., and Thakur, V. C. (1998). Reassessment of Earthquake hazard Based on a Fault-bend Fold Model of the Himalayan Plate-Boundary Fault. *Curr. Sci.* 74, 230–233.

Conflict of Interest: The authors declare that the research was conducted in the absence of any commercial or financial relationships that could be construed as a potential conflict of interest.

Publisher's Note: All claims expressed in this article are solely those of the authors and do not necessarily represent those of their affiliated organizations, or those of the publisher, the editors, and the reviewers. Any product that may be evaluated in this article, or claim that may be made by its manufacturer, is not guaranteed or endorsed by the publisher.

Advantages of publishing in Frontiers

OPEN ACCESS
Articles are free to read for greatest visibility and readership

FAST PUBLICATION
Around 90 days from submission to decision

HIGH QUALITY PEER-REVIEW
Rigorous, collaborative, and constructive peer-review

TRANSPARENT PEER-REVIEW
Editors and reviewers acknowledged by name on published articles

Frontiers
Avenue du Tribunal-Fédéral 34
1005 Lausanne | Switzerland

Visit us: www.frontiersin.org
Contact us: frontiersin.org/about/contact

REPRODUCIBILITY OF RESEARCH
Support open data and methods to enhance research reproducibility

DIGITAL PUBLISHING
Articles designed for optimal readership across devices

FOLLOW US
@frontiersin

IMPACT METRICS
Advanced article metrics track visibility across digital media

EXTENSIVE PROMOTION
Marketing and promotion of impactful research

LOOP RESEARCH NETWORK
Our network increases your article's readership